Measurement of Polarization Observables in the Reaction $\gamma p \to p\pi^0\pi^0$ with the CBELSA/TAPS Experiment

Dissertation
zur
Erlangung des Doktorgrades (Dr. rer. nat.)
der
Mathematisch-Naturwissenschaftlichen Fakultät
der
Rheinischen Friedrich-Wilhelms-Universität Bonn

vorgelegt von
Nils Stausberg
aus
Dachau

Bonn, 2025

Angefertigt mit Genehmigung der Mathematisch-Naturwissenschaftlichen Fakultät der Rheinischen Friedrich-Wilhelms-Universität Bonn

Gutachterin/Betreuerin:	Prof. Dr. Ulrike Thoma
Gutachter:	Prof. Dr. Reinhard Beck
Tag der Promotion:	10.12.2025
Erscheinungsjahr:	2026

Abstract

Quantum Chromodynamics (QCD), the theory of the strong interaction, presents significant challenges as perturbation theory cannot be applied in the energy region where hadrons form. A promising approach to probe QCD in this region is the study of the excitation spectrum of baryons. However, classical (unpolarized) cross section measurements alone are insufficient to isolate the contributions of individual excited states. To disentangle overlapping resonance contributions, measurements of polarized cross sections are performed, which further constrain the spin degrees of freedom. Extracted polarization observables are then used in partial wave analysis to gain insight into resonance parameters and their properties. The CBELSA/TAPS experiment at the ELSA accelerator facility in Bonn makes an important contribution to the field of baryon spectroscopy by studying meson photoproduction off protons or neutrons.

In this work, the reaction $\gamma p \to p\pi^0\pi^0$ has been analyzed using a linearly polarized photon beam and a transversely polarized target. The cross section for these multi-meson final states remains large at energies where many predicted resonances remain unobserved. They are sensitive to higher-mass resonances with significant branching ratios to other excited states. Despite these advantages, the existing database for multi-meson photoproduction still leaves room for improvement.

Four different periods of data taking were analyzed. In total, 8.17×10^5 events on quasi-free protons with a $p\pi^0\pi^0$ final state were selected in a beam photon energy range of $650-3\,100\,\mathrm{MeV}$ and an average reconstruction efficiency of $22\,\%$. At the same time, the average background was reduced to $< 2\,\%$. Events on bound protons were successfully subtracted using reference measurements with carbon foam as a target material. Using an event-based likelihood fit, polarization observables were extracted for different combinations of five kinematic variables. The single polarization observables P_x and P_y were extracted in a beam photon energy range of $650 - 3\,100\,\mathrm{MeV}$ with high statistics. The double polarization observables P_x^s, P_y^s, P_x^c, and P_y^c were extracted in a beam photon range of $850 - 1\,700\,\mathrm{MeV}$. This is the first measurement of these double polarization observables at such high energies.

In addition, a recent upgrade of the CBELSA/TAPS experiment has improved both the readout electronics and the trigger system. Therefore, this work also includes an investigation of the newly available time information for the Crystal Barrel detector and its incorporation into the reconstruction process of particles. The time information was further used to validate the pile-up detection and correction of the newly installed sampling-analog-to-digital converters (SADCs), revealing significant shortcomings. These shortcomings were subsequently resolved in a separate work.

Contents

CHAPTER 1

Introduction

The Standard Model of particle physics [1–4] provides a comprehensive framework for understanding the fundamental constituents of matter and their interactions. In the Standard Model, elementary particles are divided into two categories: leptons and quarks (cf. Table 1.1). Both leptons and quarks are classified as fermions due to their half-integer spin and are organized in three generations, ordered by increasing mass. Each particle carries specific charges that determine the nature of its interactions: the electric charge is responsible for electromagnetic interaction, the color charge for the strong interaction, and the weak charge for the weak interaction. While all particles carry weak charge, electric and color charge are not universal. For instance, electrons (e^-), muons (μ^-), and tau (τ^-) each have -1 units of electric charge. Quarks carry either $-1/3$ (d, s, b) or $+2/3$ (u, c, t) units of electric charge and also carry color charge. Neutrinos (ν_e, ν_μ, ν_τ), in contrast, carry only weak charge. Each particle has a corresponding antiparticle characterized by opposite charges.

The interactions between the elementary particles are mediated by gauge bosons, which are particles with integer spin. Photons (γ) mediate the electromagnetic force, gluons (g) mediate the strong force, while $W^\pm$ and Z^0 bosons mediate the weak force. These interactions are mathematically described by quantum electrodynamics (QED) for electromagnetic processes, quantum chromodynamics (QCD) for strong processes and the Glashow-Weinberg-Salam theory for electroweak processes.[1] The last fundamental force in nature, gravity, is not described by the Standard Model. It is too weak to play a significant role in elementary particle physics.

The fundamental forces differ significantly in their strength and range. The strong force is the strongest, but operates only at short distances, on the scale of atomic nuclei (femtometers). The electromagnetic force, although weaker than the strong force, has an infinite range and dominates our everyday lives. The weak force operates at even shorter distances than the strong force and is weak due to the large masses of its mediators.

The historic success of the Standard Model lies in its ability to explain the discovery of many new particles in the 1960s. A quark model introduced by Gell-Mann and Zweig classified these particles into symmetry groups (multiplets) based on properties such as their charge and strangeness [5, 6]. The new particles could then be explained by a small number of elementary particles, called quarks. Quarks manifest themselves as color-neutral bound systems called hadrons. In the basic form of the quark model, there are two types of hadrons: mesons, which describe bound states of a quark and an antiquark ($q\bar{q}$), and baryons, which describe bound states of three quarks (qqq). However, there are also other exotic hadrons that go beyond this simple classification scheme such as tetraquarks, pentaquarks or glueballs

[1] The Glashow-Weinberg-Salam theory of electroweak processes describes the unification of the electromagnetic and weak interactions.

(cf. Quark Model in [7]). Although they are part of ongoing research, they are not discussed in this work.

A more recent success in experimental particle physics was the discovery of the Higgs boson, a scalar particle (spin 0), which is predicted by the Standard Model [8]. The Higgs boson arises as a consequence of the electroweak symmetry breaking via the Higgs mechanism. This symmetry breaking is responsible for giving mass to all elementary fermions as well as the weak gauge bosons. Despite the success, significant challenges remain in the Standard Model, such as in fully understanding the strong interaction via QCD.

Table 1.1: The Standard Model of particle physics. For each particle there is an antiparticle with opposite charge, except for the gauge bosons γ and Z^0. The Higgs boson is not listed but completes the model. The strength is given without a unit and can only be used for a qualitative comparison. The tables are adapted from [4, 9]. The weak charge is not explicitly indicated.

	Generations			Electric charge [e]	Color
	1	2	3		
Leptons	e^-	μ^-	τ^-	-1	–
	ν_e	ν_μ	ν_τ	0	–
Quarks	u	c	t	$+2/3$	r,g,b
	d	s	b	$-1/3$	r,g,b

Interaction	Couples to	Gauge bosons	Mass [GeV]	Strength
Strong	Color charge	8 gluons (g)	0	10
Electromagnetic	Elect. charge	Photon (γ)	0	10^{-2}
Weak	Weak charge	W and Z bosons ($W^\pm$, Z^0)	$\approx 10^2$	10^{-13}

1.1 QCD in Comparison to QED

Quantum electrodynamics (QED) was historically the first successful quantum field theory developed to describe the electromagnetic interactions between electrically charged particles [10]. The force in QED is mediated by the exchange of neutral photons (γ) and is characterized by the electromagnetic coupling constant α_{QED}. The coupling constant has a small dependence on the momentum transfer Q ($Q \propto 1/r$; $r \equiv$ distance) due to screening effects caused by vacuum polarization[2] (cf. Fig. 1.1 (left)). As a consequence, the coupling

[2] Vacuum polarization refers to the creation of $e^\pm$ pairs during the exchange of a virtual photon, resulting in a dielectric behavior of the vacuum [4].

constant increases at high Q, since less of the bare charge is shielded at smaller distances. However, the overall small value of the coupling constant allows perturbation theory to be used effectively in QED.

In contrast to QED, a solution to quantum chromodynamics (QCD) poses significant challenges. In QCD, the strong coupling constant α_{QCD} behaves in the opposite way to the electromagnetic coupling constant (cf. Fig. 1.1 (right)). This is because gluons carry color charge and couple to themselves. The self-coupling of the gluons dominates the screening effects and leads to an opposite behavior. At high momentum transfers Q the strong coupling constant decreases, a phenomenon known as asymptotic freedom [11, 12]. In this regime, perturbation theory can be applied. At small momentum transfers, however, α_{QCD} increases, leading to the confinement of quarks and the formation of hadrons [13]. Here $\alpha_{\mathrm{QCD}} \approx 1$ and perturbation theory with α_{QCD} as expansion parameter is not applicable. Theoretical methods alternative to conventional perturbation theory, iterated with detailed experimental studies, must be used to gain an understanding of the internal structures and dynamics of systems bound by the strong force. A promising approach to understanding the strong force in the large α_{QCD} regime is the study of the excitation spectrum of baryons.

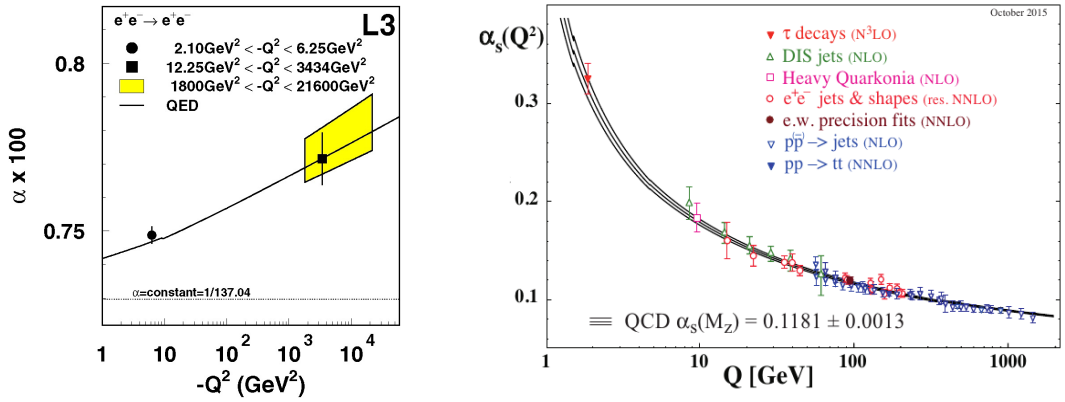

EM coupling constant α_{QED} [14]

Strong coupling constant α_{QCD} [7]

Figure 1.1: The electromagnetic (EM) coupling constant α_{QED} and the strong coupling constant α_{QCD} as a function of the momentum transfer Q ($Q \propto 1/r$; $r \equiv$ Distance).

1.2 Baryon Spectroscopy

Baryon spectroscopy provides a theoretical and experimental approach to probing the non-perturbative regime of the strong interaction. One of the main goals of baryon spectroscopy is to achieve a comprehensive understanding of the excited states of baryons. The excited states correspond to different energy levels higher than the ground state and reflect different excitation patterns. Theoretical models are used to predict the excitation spectrum and provide valuable insights. However, theoretical predictions alone are not sufficient without experimental confirmation. Therefore, an experimental measurement of the baryon excitation spectrum is also important.

1.2.1 Models and Calculations

Two types of theoretical methods are described below: Constituent quark models [15] and lattice QCD [13]. Constituent quark models provide an intuitive, effective description of the baryon structure, while lattice QCD provides a first-principles calculation based on the QCD Lagrangian. Several other methods relevant to baryon spectroscopy are listed at the end.

1.2.1.1 Constituent Quark Models

Constituent quark models describe baryons as bound states of three constituent quarks. The constituent quarks can be thought of as effective degrees of freedom that capture the collective behavior of virtual quark-antiquark pairs and gluons surrounding the bare quarks. This model provides a simple and intuitive approach to baryon spectroscopy. One of the first calculations was made by Isgur and Karl [15].[3]

In the quark model, the effective inter-quark potential is often described as a linearly rising potential with some short-range residual interaction. The linear rise accounts for the confinement of the quarks within the baryon. An example of such a model is the Bonn model, which includes a linearly rising potential along with instanton-induced two- and three-body residual interactions [16, 17]. The Bethe-Salpeter equation is solved to obtain the wave functions and their energy levels. An extension of the Bonn model introduces additional flavor-dependent interactions with the aim of providing a better description of the experimental data [18].

A comparison of nucleon resonances calculated in the Bonn model with experimental data is shown in Fig. 1.2. A good agreement is found for resonance masses below $\sim 1\,800\,\mathrm{MeV}$. However, even here not all the mass positions are fully understood. A prominent example is the $N(1440)\frac{1}{2}^+$. It is the first radial excitation of the proton and has a lower mass than expected when compared to the first orbital (angular) excitation $N(1535)\frac{1}{2}^-$. Only by introducing the additional flavor-dependent interaction can this mass ordering be described.[4] The situation becomes more complex at higher masses, where many predicted resonances have not yet been confirmed by the data. This raises the question of the correct degrees of freedom within the quark model, which is responsible for the richness of the spectrum. As a result, alternatives such as quark-diquark configurations have been investigated. However, recent work favors the idea of a three-body rather than a quark-diquark description to explain systematic effects in the branching ratios at higher masses [19–21]. It should be emphasized that quark models are mostly phenomenological, relying on effective descriptions of the strong interaction. The parameters and potentials used in these models are not derived from first principles of QCD. A more fundamental approach based directly on QCD leads us to the numerical approach of lattice QCD.

[3] A non-relativistic constituent quark model that includes a one-gluon exchange mechanism to describe residual interactions.

[4] The additional interaction was introduced purely phenomenologically [18].

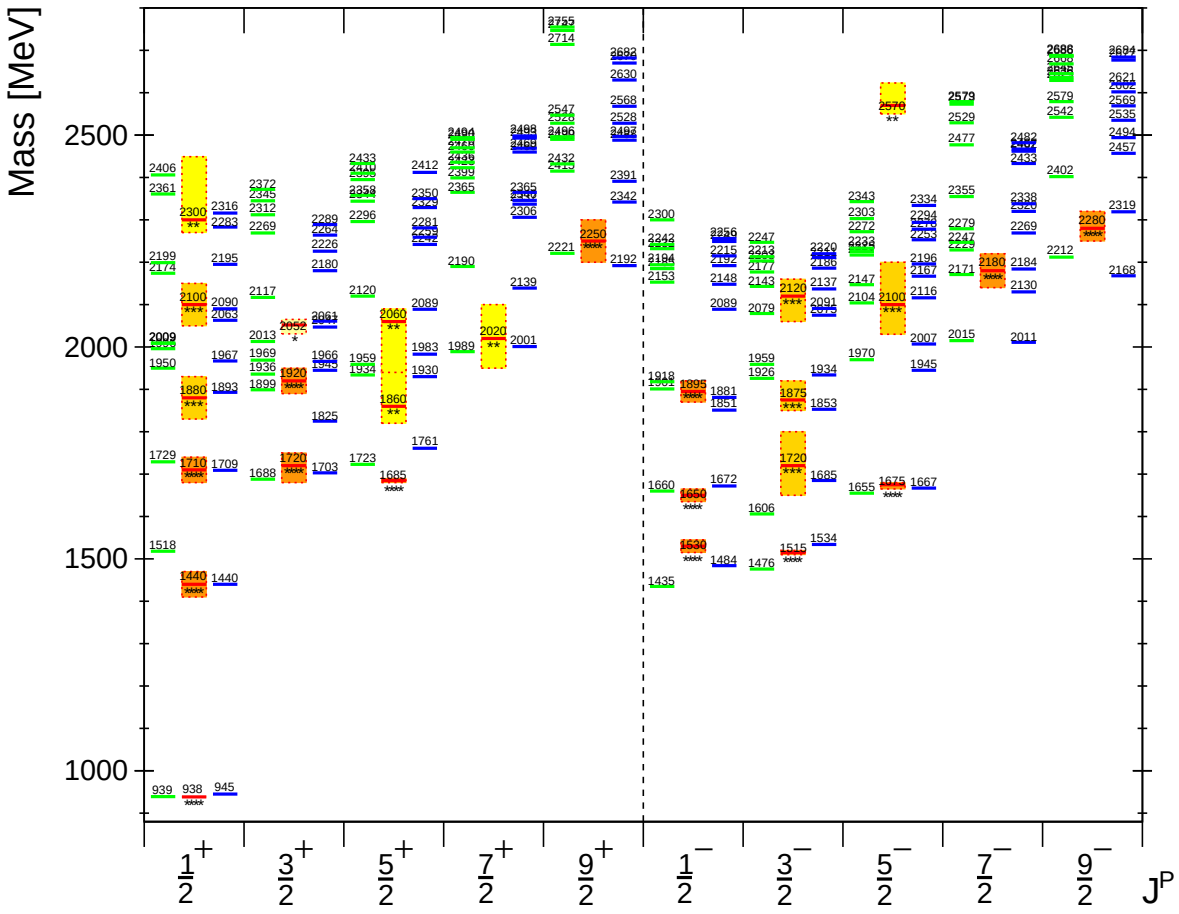

Figure 1.2: The spectrum of nucleon resonances up to $J^P = \frac{9}{2}^{\pm}$. The Bonn model is shown as green lines [17], while the extension with flavor-dependent interactions is shown as blue lines [18]. Experimental data from the PDG (2023) are shown as colored boxes [7]. The uncertainty of the experimental data is given by the height of the boxes and its establishment by the number of stars.

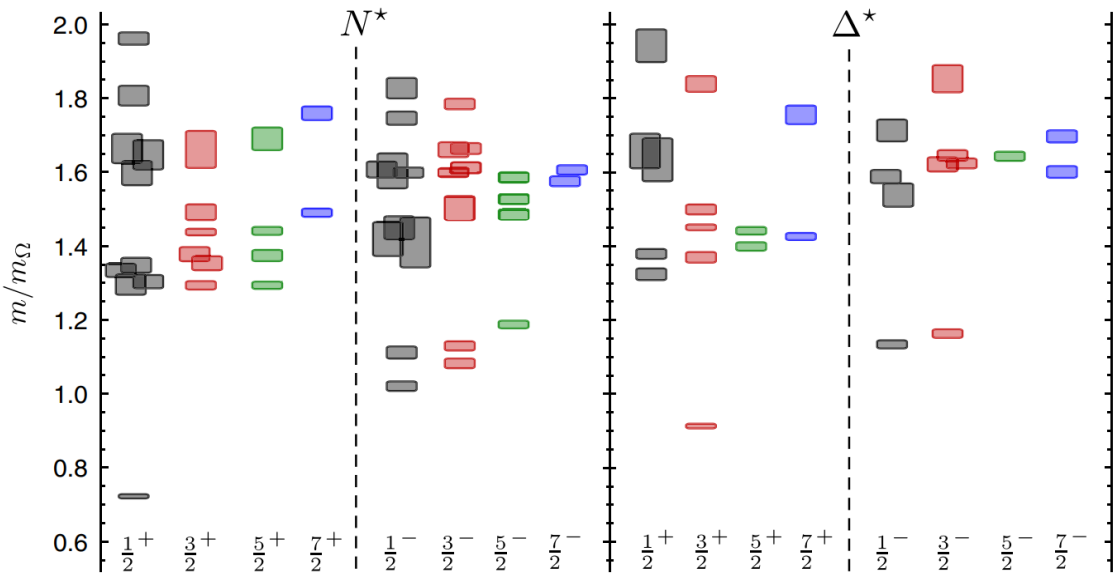

Figure 1.3: The spectrum of nucleon N and Δ resonances up to $J^P = \frac{7}{2}^\pm$ from a lattice with $m_\pi = 396\,\text{MeV}$. The masses are in units of the calculated Ω mass [24].

1.2.1.2 Lattice QCD

Lattice QCD is a numerical approach to solving QCD on a discretized space-time lattice [13]. In lattice QCD, calculations are performed by evaluating full path integrals[5] numerically to describe the behavior of quarks and gluons. To avoid finite size effects, a sufficiently large and fine lattice is required. While some calculations have been performed at or close to the continuum limit, many lattice QCD calculations are still carried out at finite lattice spacings due to computational limitations. A careful choice of lattice size and spacing is required, and extrapolation techniques are used to obtain physical predictions [23]. These constraints often lead to unphysical quark masses that are larger in lattice QCD. This effect is quantified by the pion mass m_π. Lattice QCD provides a non-perturbative framework for studying the baryon spectrum and has successfully reproduced a wide range of low-lying baryon states. However, similar to the constituent quark models, there are still missing states that have yet to be discovered in experimental data or understood within this framework. A lattice QCD spectrum of the nucleon N and Δ resonances is shown in Fig. 1.3.

1.2.1.3 Other Methods

In addition to constituent quark models and lattice QCD, several other methods are used to understand the baryon spectrum. Effective field theory (EFT) provides a systematic framework for describing the low-energy interactions of hadrons [25, 26]. The Dyson-Schwinger and Bethe-Salpeter equations provide non-perturbative techniques to study the

[5] A path integral is a mathematical formulation in quantum mechanics that computes the probability amplitude by summing over all paths between initial and final states. For non-relativistic quantum mechanics cf. [22].

quark-gluon dynamics within baryons [27–29]. Holographic QCD, inspired by the AdS/CFT correspondence[6], provides another approach to understanding the strong interactions [30, 31]. While the focus of this chapter has been on constituent quark models and lattice QCD, it is important to acknowledge the existence of the alternative methods and their contributions to the field of baryon spectroscopy. By combining insights from different theoretical approaches and comparing them with experimental data, it is possible to deepen the understanding of the excitation spectra of baryons and the underlying dynamics of the quark interactions. In this context, photoproduction experiments play a central role by providing direct experimental access to baryon resonances.

1.2.2 Photoproduction as an Experimental Tool

Photoproduction experiments provide a tool for studying the excitation spectrum of baryons, with the goal of identifying as many excited states as possible. While early studies relied on pion-nucleon scattering [32, 33], recent advances have made extensive use of photoproduction data [20, 34, 35]. However, classical (unpolarized) cross section measurements alone do not provide sufficient information to disentangle the contributions of the different excited states (resonances) from the data. They overlap strongly in energy due to their short lifetimes τ and large widths ($\Gamma \sim 1/\tau$). Additionally, only their squared amplitudes contribute to the total cross section, and thus small contributions may remain unobserved (cf. Fig. 1.4). To disentangle overlapping resonance contributions, polarization observables are used. They provide essential information about the spin amplitudes, including interference terms. By performing a partial wave decomposition, the amplitudes can be expressed in terms of contributions with well-defined total angular momentum and parity quantum numbers J^P. This decomposition allows the isolation of individual resonance contributions.

Experiments that have contributed greatly to baryon spectroscopy using photoproduction are CBELSA/TAPS at ELSA e.g. [20, 37–39], A2 at MAMI e.g. [40–43] and CLAS at JLab e.g. [44–47]. In the following, special emphasize is given to the case of two-pseudoscalar meson photoproduction.[7]

1.2.2.1 Polarization Observables

Polarization observables are defined as asymmetries of the differential cross section for certain polarization configurations, normalized to the unpolarized cross section [48]

$$\mathcal{O} = \frac{1}{\left(\frac{\mathrm{d}\sigma}{\mathrm{d}\Omega}\right)_0} \cdot \left[\left(\frac{\mathrm{d}\sigma}{\mathrm{d}\Omega}\right)^a - \left(\frac{\mathrm{d}\sigma}{\mathrm{d}\Omega}\right)^b\right]. \tag{1.1}$$

Here, a and b correspond to different polarization configurations of the initial state particles (beam or target) and the final state particles (recoil). While the unpolarized cross section relates only to the sum of the squared spin amplitudes, the polarization observables are also sensitive to interference terms. This allows for the extraction of more detailed information about these amplitudes.

[6] **A**nti-**d**e **S**itter/**c**onformal **f**ield **t**heory correspondence
[7] The relevant reaction in this work is $\gamma p \to p\pi^0\pi^0$.

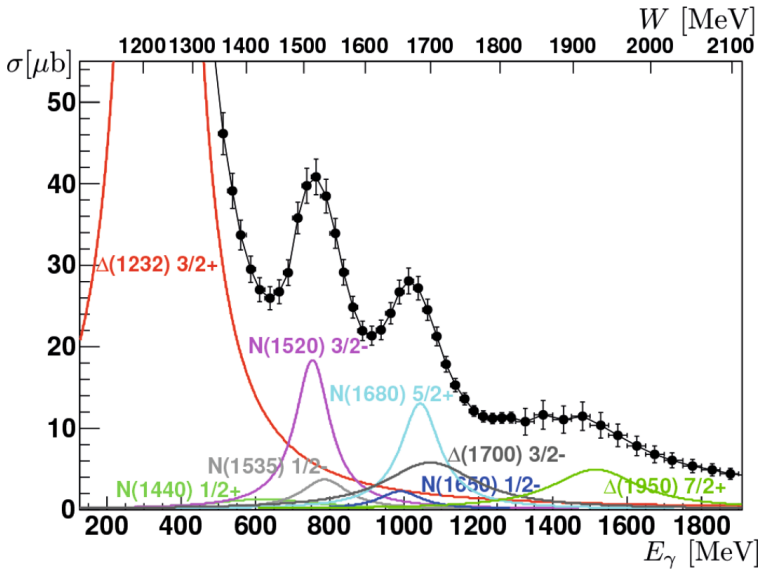

Figure 1.4: The total cross section for the reaction $\gamma p \to p\pi^0$ [36]. Contributing resonances are shown in different colors. In all cases a Breit-Wigner parametrization is used for illustrative purposes.

For two-pseudoscalar meson photoproduction, $N_A = 8$ different spin amplitudes fully describe the process [49]. Theoretically, $N_A^2 = 64$ polarization observables are measurable. They are listed in Table 1.2. In addition to the unpolarized cross section I_0, there are single polarization observables with respect to the beam polarization $\mathcal{B}$, target polarization $\mathcal{T}$ or recoil polarization $\mathcal{R}$. Furthermore, double polarization ($\mathcal{BT}$, $\mathcal{BR}$, $\mathcal{TR}$) and triple polarization ($\mathcal{BTR}$) observables can be defined. In general, by using certain subsets (combinations) of only a few polarization observables one can disentangle all the different contributions and obtain valuable information about the underlying amplitudes in so-called complete experiments. In [50] a graph-based method is used which, in the case of two-pseudoscalar meson photoproduction, allows to select a minimal set of 16 observables.[8] The obtained sets are completely free of ambiguities. However, each set still includes the measurement of one triple polarization observable ($\mathcal{BTR}$) which increases the experimental complexity.

The cross section can be expressed in terms of the polarization observables. For two-pseudoscalar meson photoproduction, the cross section has the form [49]

$$\begin{aligned}\frac{\mathrm{d}\sigma}{\mathrm{d}\Omega} = \left(\frac{\mathrm{d}\sigma}{\mathrm{d}\Omega}\right)_0 \cdot \Big(1 &+ \vec{\Lambda}\cdot\vec{P} + \vec{\sigma}\cdot\vec{P}' + \Lambda^\alpha \sigma^{\beta'} \mathcal{O}_{\alpha\beta'} \\ &+ \delta_\odot \left[I^\odot + \vec{\Lambda}\cdot\vec{P}^\odot + \vec{\sigma}\cdot\vec{P}^{\odot\prime} + \Lambda^\alpha \sigma^{\beta'} \mathcal{O}^\odot_{\alpha\beta'}\right] \\ &+ \delta_l \sin(2\phi) \left[I^s + \vec{\Lambda}\cdot\vec{P}^s + \vec{\sigma}\cdot\vec{P}^{s\prime} + \Lambda^\alpha \sigma^{\beta'} \mathcal{O}^s_{\alpha\beta'}\right] \\ &+ \delta_l \cos(2\phi) \left[I^c + \vec{\Lambda}\cdot\vec{P}^c + \vec{\sigma}\cdot\vec{P}^{c\prime} + \Lambda^\alpha \sigma^{\beta'} \mathcal{O}^c_{\alpha\beta'}\right]\Big).\end{aligned} \tag{1.2}$$

[8] Under the assumption of data with infinite experimental precision.

Table 1.2: Polarization observables for two-pseudoscalar meson photoproduction assuming a polarized beam $\mathcal{B}$, a polarized target $\mathcal{T}$ and a measurement of the recoil polarization $\mathcal{R}$. The table is adapted from [48]. For an explanation of the notation, see [49]. The I_0 corresponds to the unpolarized cross section. Due to their length, the expressions of the observables in terms of spin amplitudes are not given.

Type	Observables $\mathcal{O}$
	I_0
$\mathcal{B}$	I^s, I^c $I^\odot$
$\mathcal{T}$	P_x, P_y, P_z
$\mathcal{R}$	$P_{x'}$, $P_{y'}$, $P_{z'}$
$\mathcal{BT}$	P_x^s, P_y^s, P_z^s, P_x^c, P_y^c, P_z^c $P_x^\odot$, $P_y^\odot$, $P_z^\odot$
$\mathcal{BR}$	$P_{x'}^s$, $P_{y'}^s$, $P_{z'}^s$, $P_{x'}^c$, $P_{y'}^c$, $P_{z'}^c$ $P_{x'}^\odot$, $P_{y'}^\odot$, $P_{z'}^\odot$
$\mathcal{TR}$	$\mathcal{O}_{xx'}$, $\mathcal{O}_{xy'}$, $\mathcal{O}_{xz'}$, $\mathcal{O}_{yx'}$, $\mathcal{O}_{yy'}$, $\mathcal{O}_{yz'}$, $\mathcal{O}_{zx'}$, $\mathcal{O}_{zy'}$, $\mathcal{O}_{zz'}$
$\mathcal{BTR}$	$\mathcal{O}^s_{xx'}$, $\mathcal{O}^s_{xy'}$, $\mathcal{O}^s_{xz'}$, $\mathcal{O}^s_{yx'}$, $\mathcal{O}^s_{yy'}$, $\mathcal{O}^s_{yz'}$, $\mathcal{O}^s_{zx'}$, $\mathcal{O}^s_{zy'}$, $\mathcal{O}^s_{zz'}$, $\mathcal{O}^c_{xx'}$, $\mathcal{O}^c_{xy'}$, $\mathcal{O}^c_{xz'}$, $\mathcal{O}^c_{yx'}$, $\mathcal{O}^c_{yy'}$, $\mathcal{O}^c_{yz'}$, $\mathcal{O}^c_{zx'}$, $\mathcal{O}^c_{zy'}$, $\mathcal{O}^c_{zz'}$ $\mathcal{O}^\odot_{xx'}$, $\mathcal{O}^\odot_{xy'}$, $\mathcal{O}^\odot_{xz'}$, $\mathcal{O}^\odot_{yx'}$, $\mathcal{O}^\odot_{yy'}$, $\mathcal{O}^\odot_{yz'}$, $\mathcal{O}^\odot_{zx'}$, $\mathcal{O}^\odot_{zy'}$, $\mathcal{O}^\odot_{zz'}$

The choice of coordinates and the kinematic dependencies are discussed in detail in Chapter 8.

Although polarization observables provide crucial sensitivity to interference effects and spin amplitudes, the data alone do not directly yield resonance parameters such as mass, width, or branching ratios. To extract these parameters, the measured observables must be analyzed within a theoretical framework capable of decomposing the complex amplitude structure into contributions with defined quantum numbers. This analysis is known as partial wave analysis (PWA).

1.2.2.2 Partial Wave Analysis

Partial wave analysis (PWA) extracts detailed information about the resonance properties from the measured polarization observables. Therefore, the amplitudes are expanded into partial waves corresponding to specific orbital angular momentum states. In a simplified case of spinless particles in a $2 \to 2$ scattering process (used here for illustration), the scattering amplitude A is expanded as

$$A(s, \theta) \propto \sum_{l=0}^{\infty} (2l + 1) A_l(s) P_l(\cos\theta), \tag{1.3}$$

with the Mandelstam variable s, the scattering angle θ and the Legendre polynomials $P_l(\cos\theta)$. The partial wave amplitudes $A_l(s)$ carry the energy dependence and contain the information about the process dynamics. By parametrizing both resonant and non-resonant contributions within these partial waves and fitting the polarization observables, the contribution of different partial waves to the scattering process can be isolated. This method allows the extraction of resonance properties such as mass, width, and branching ratios, even in the presence of multiple overlapping resonances.

When parametrizing resonances, it is important to consider that the scattering S-matrix, which defines the scattering amplitudes A via its matrix elements, is an analytic function in the complex s-plane. Singularities in the S-matrix arise from branch points (associated with the opening of new channels) and poles (corresponding to resonances if they lie on the unphysical Riemann sheet). The pole position in the complex plane determines the resonance parameters: the real part corresponds to the mass, while the imaginary part is half of the total width (cf. Resonances in [7]). In cases where a resonance is narrow and isolated, a common parametrization is the constant-width Breit-Wigner form [7]

$$A_a(s) = \frac{N_a(s)}{M_{\mathrm{BW}}^2 - s - iM_{\mathrm{BW}}\Gamma_{\mathrm{BW}}}, \tag{1.4}$$

where M_{BW} and Γ_{BW} are the Breit-Wigner mass and Breit-Wigner width, respectively. $N_a(s)$ includes kinematic factors and couplings related to the specific process. It should be noted, however, that the Breit-Wigner parameters do not have a strict physical meaning. The Breit-Wigner mass and width approximate the physical resonance parameters only in the limit of a narrow and isolated resonance. Also, the parameters are typically reaction dependent. Instead, a more sophisticated approach such as the K-matrix formalism must be used to parameterize resonances and account for the complex dynamics of coupled channel scattering as well as unitarity constraints [51, 52]. With the K-matrix, the scattering amplitude can be expressed as

$$A(s) = \mathbf{K}\left(\mathbf{I} - i\boldsymbol{\rho}\mathbf{K}\right)^{-1}, \tag{1.5}$$

where $\mathbf{K}$ is the so-called K-matrix and ρ is the phase space. A choice of the K-matrix is

$$K_{ab}(s) = \sum_R \frac{g_a^R g_b^R}{M_R^2 - s} + f_{ab}(s), \tag{1.6}$$

where g_a^R and g_b^R are the coupling constants of the resonance R to the initial and final states of the process $a \to b$. The non-resonant transition is described by $f_{ab}(s)$. M_R is the bare mass of the resonance. The physical mass and width of the resonance ($M_{\mathrm{pole}} - i\frac{1}{2}\Gamma_{\mathrm{pole}}$) can be obtained by scanning the complex s-plane for poles or by calculating the zeros of the denominator of the parameterized amplitude [53]

$$\det\left(\mathbf{I} - i\boldsymbol{\rho}\mathbf{K}\right)\prod_R \left(M_R^2 - s\right) = 0. \tag{1.7}$$

A fully model-independent partial wave decomposition is challenging, particularly for reactions involving more than two final-state particles. Consequently, partial wave analysis is

typically performed within model-dependent frameworks. Prominent examples include the Bonn-Gatchina model [53–55], MAID [56–58], SAID [59–61], and the Jülich-Bonn [62–64] model. These models differ in their methodology, such as dispersion relations, channels considered, and databases used. The impact of including recent polarization data on pion photoproduction in the different partial wave analysis models is described in [65].

Regardless of the theoretical framework, the reliability of the extracted resonance parameters depends on the quality and completeness of the experimental data. Accurate and extensive polarization observables are essential inputs to constrain models and reduce ambiguities. Therefore, an overview of the current experimental database for two-neutral pion photoproduction, the reaction relevant to this work, is given below.

1.2.2.3 Database for $\gamma p \to p\pi^0\pi^0$

Multi-meson photoproduction is becoming increasingly important in baryon spectroscopy. At higher energies, where many predicted resonances remain unobserved, the cross section for multi-meson photoproduction is still large. In addition, multi-meson final states are sensitive to resonances with higher masses and significant branching ratios to other excited states [19–21]. For example, in the first step of this sequential decay, i.e. in the decay to the intermediate excited state, the first meson is emitted. When the intermediate excited state decays back to the ground state, the second meson is emitted. These high-lying resonances may remain unobserved in single-meson photoproduction. Among the final states of two-pion photoproduction, the $\pi^0\pi^0$ final state is particularly interesting because the number of born terms and t-channel processes are strongly reduced. For example, there is no diffractive ρ production, since the decay of the ρ into $\pi^0\pi^0$ is forbidden. There is also no contribution from the Delta-Kroll-Rudermann term, which describes the direct dissociation of the proton into $\Delta^{++}\pi^-$.

Despite the advantages, the existing database for two-neutral pion photoproduction still leaves room for improvement. A summary of already published polarization observables for two-neutral pion photoproduction with their corresponding beam photon energy ranges is given in Table 1.3. The most extensively measured observable is the unpolarized cross section I_0, which has been studied early on and over a wide energy range. Other measurements have focused on using a polarized beam to extract single polarization observables, such as $I^\odot$, I^s and I^c. Only a limited number of measurements are available for double polarization observables. For example, measurements with a longitudinally polarized target and a circularly polarized beam were performed by Ahrens et al. in 2005 [66] and Dieterle et al. in 2020 [67]. These experiments focused on the extraction of the helicity dependent cross sections $\sigma_{1/2}$ and $\sigma_{3/2}$. Measurements with a transversely polarized target and a linearly polarized beam have so far only been performed by Seifen et al. in 2020 [20]. In this case, the extraction of double polarization observables was limited to an energy range of $650 - 950\,\mathrm{MeV}$. In summary, the two-neutral pion photoproduction database would greatly benefit from more extensive measurements of double polarization observables, such as P_x^s, P_y^s, P_x^c and P_y^c. These additional measurements would enhance the capabilities of the partial wave analysis and improve the precision of resonance parameters.

Table 1.3: Summary of published observables in two-neutral pion photoproduction. The table is adapted from [48] and is extended. I_0 corresponds to the unpolarized cross section. For the other polarization observables, the notation defined in [49] is used whenever possible. The threshold for two-neutral pion photoproduction is at $\sim 309\,\mathrm{MeV}$.

Observables	Energy range E_γ	Facility	Reference	Year
P_x, P_y P_x^s, P_y^s, P_x^c, P_y^c	$650 - 2\,600\,\mathrm{MeV}$ $650 - 950\,\mathrm{MeV}$	CBELSA/TAPS	Seifen et al. [20]	2020
$P_z^\odot$, $\sigma_{1/2}$, $\sigma_{3/2}$	$431 - 1\,455\,\mathrm{MeV}$	Crystal Ball/TAPS	Dieterle et al. [67]	2020
I_0	$432 - 1\,374\,\mathrm{MeV}$	Crystal Ball/TAPS	Dieterle et al. [68]	2015
I_0 I^s, I^c	$600 - 2\,500\,\mathrm{MeV}$ $970 - 1\,650\,\mathrm{MeV}$	CBELSA/TAPS	Sokhoyan et al. [21]	2015
$I^\odot$	$600 - 1\,400\,\mathrm{MeV}$	Crystal Ball/TAPS	Oberle et al. [69]	2013
I_0	$309 - 1\,400\,\mathrm{MeV}$	Crystal Ball/TAPS	Kashevarov et al. [70]	2012
I_0 $I^\odot$	$309 - 800\,\mathrm{MeV}$ $550 - 820\,\mathrm{MeV}$	Crystal Ball/TAPS	Zehr et al. [71]	2012
$I^\odot$	$560 - 810\,\mathrm{MeV}$	Crystal Ball/TAPS	Krambrich et al. [72]	2009
I_0	$400 - 1\,300\,\mathrm{MeV}$	CB-ELSA	Thoma et al. [73]	2008
I_0, $\sigma_{1/2}$, $\sigma_{3/2}$	$400 - 800\,\mathrm{MeV}$	DAPHNE	Ahrens et al. [66]	2005
I_0	$309 - 425\,\mathrm{MeV}$	TAPS	Kotulla et al. [74]	2004
I_0, I^s, I^c	$650 - 1\,450\,\mathrm{MeV}$	GRAAL	Assafiri et al. [75]	2003
I_0	$309 - 820\,\mathrm{MeV}$	TAPS	Wolf et al. [76]	2000
I_0	$309 - 792\,\mathrm{MeV}$	TAPS	Härter et al. [77]	1997
I_0	$464 - 779\,\mathrm{MeV}$	DAPHNE	Braghieri et al. [78]	1995

1.3 Aim of This Work

Considerable progress has been made in recent years with the collection of extensive data on single-meson photoproduction. However, the study of multi-meson final states is becoming increasingly important as described above. This work aims to contribute to the database available for partial wave analysis in two-neutral pion photoproduction $\gamma p \to p\pi^0\pi^0$. Previous studies have determined single (P_x, P_y) and double polarization observables (P_x^s, P_y^s, P_x^c, P_y^c) in the energy ranges of $650 - 2\,600\,\text{MeV}$ and $650 - 950\,\text{MeV}$, respectively [20] (cf. Table 1.3). This work extends the analysis to the energy ranges of $650 - 3\,100\,\text{MeV}$ and $850 - 1\,700\,\text{MeV}$. A multidimensional analysis of the polarization observables is performed to capture all relevant kinematic dependencies. By including this additional data, ambiguities in the partial wave analysis solutions can be reduced and the accuracy of the extracted resonance parameters such as masses, widths and branching ratios can be improved.

In addition, a thorough understanding of the detector system is crucial for accurate extraction of polarization observables. A recent upgrade of the CBELSA/TAPS experiment improved the readout electronics and the trigger system [79–82]. During the upgrade, the readout of time information in the Crystal Barrel detector was improved. Therefore, this work also includes a detailed investigation of the time information and its incorporation into the reconstruction process of particles. Furthermore, the time information in the Crystal Barrel detector is used to validate the performance of the pile-up detection and pile-up correction of the newly installed sampling-analog-to-digital converters (SADCs).

The thesis is structured into three parts. Part I focuses on explaining the CBELSA/TAPS experiment, the data readout for the Crystal Barrel detector and calibrations for the Crystal Barrel detector (cf. Chapter 2-4). Part II examines the time information in the Crystal Barrel detector, to improve the internal reconstruction process and to validate specific features of the newly used SADCs (cf. Chapter 5). Part III explains the analysis and extraction of polarization observables (cf. Chapter 6-9).

CHAPTER 2

CBELSA/TAPS Experiment

The CBELSA/TAPS experiment is a fixed target experiment[1] at the Elektronen-Stretcher-Anlage ELSA of the University of Bonn. It focuses on the study of photoproduced reactions on nucleons and the extraction of polarization observables to gain a good understanding of the spectrum and the properties of baryon resonances. For this purpose, nucleon excitations are studied in reactions such as

$$\gamma + N \to R \to N + X. \tag{2.1}$$

R indicates a resonance that could be produced in the photoproduction off the nucleon N and X any number of decay products. The initial state photons γ are produced in the process of bremsstrahlung of electrons which are extracted from the ELSA accelerator. While in this work the excitation of protons p is studied, the excitation of neutrons n is also possible. For each case, a suitable target material is available. Furthermore, it is possible to polarize the target in transverse or longitudinal direction. In combination with linearly or circularly polarized photons, not only single but also double polarization observables can be extracted. Examples of common reactions studied with the CBELSA/TAPS experiment include

$$\gamma + p \to p + \pi^0 \tag{2.2a}$$
$$\gamma + p \to p + \eta \tag{2.2b}$$
$$\gamma + p \to p + \pi^0\pi^0, \tag{2.2c}$$

where the mesons decay almost instantaneously and with high probability to photons.[2]

To detect the final decay products, several detectors are positioned around the target. The most important are the two calorimeters with good energy resolution for photons: the Crystal Barrel detector and the MiniTAPS detector. They are complemented by charge-sensitive detectors to detect the proton. With these detectors, the CBELSA/TAPS experiment is particularly well suited for the study of photoproduced reactions. An overview of the experiment is shown in Fig. 2.1. The ELSA accelerator and the individual detector components of the CBELSA/TAPS experiment are described in the following.

[1] The target nucleon is at rest.

[2] The π^0 meson decays with a probability of 98.82 % to 2γ while the η decays with 39.36 % to 2γ and with 32.57 % to $3\pi^0$ [7].

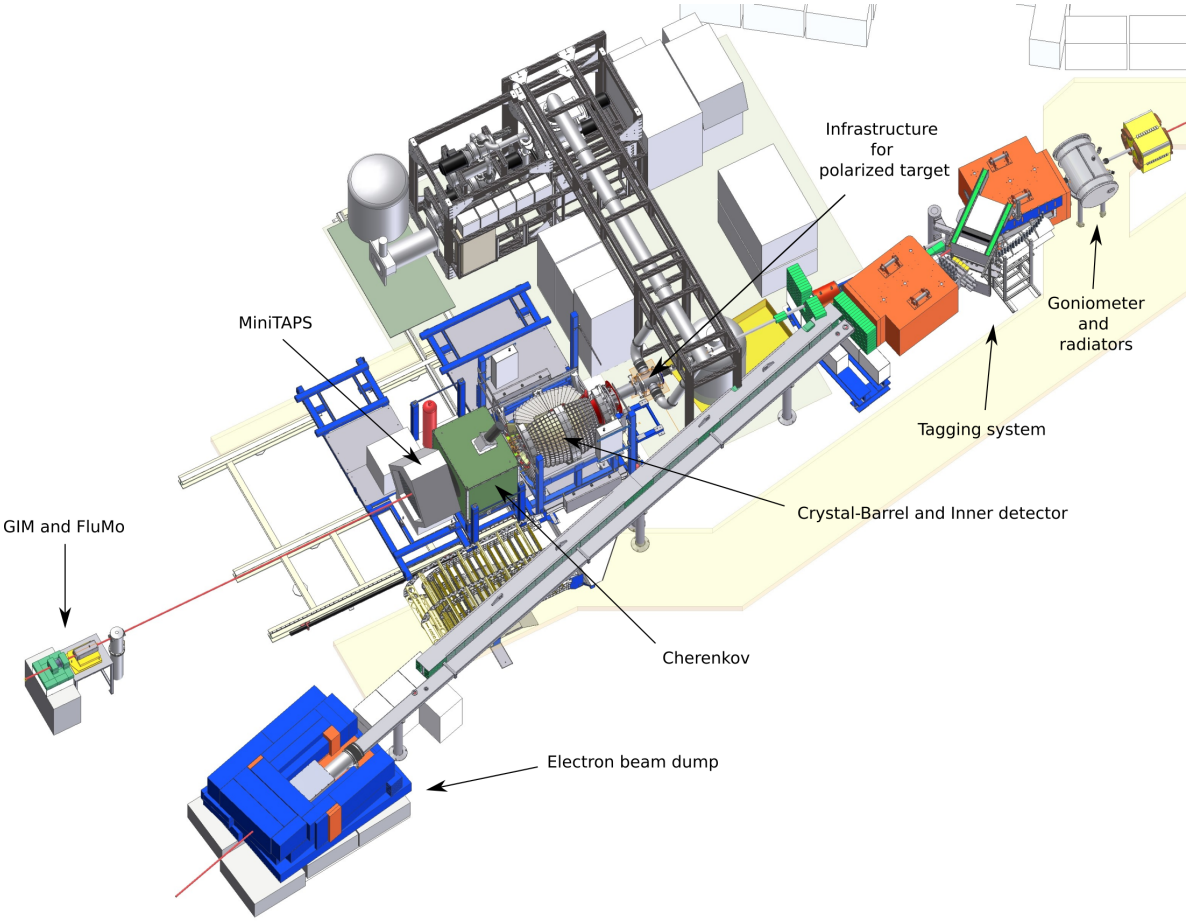

Figure 2.1: Overview of the CBELSA/TAPS experiment at ELSA in Bonn [83]. The extracted electron beam provided by ELSA enters the experimental area in the upper right corner.

2.1 ELSA

The accelerator at ELSA provides an electron beam of variable energy up to 3.5 GeV.[3] It consists of three stages: a linear accelerator, a booster synchrotron, and a stretcher ring [84].

The linear accelerator (LINAC 2) is used for the initial acceleration of electrons emitted from an electron source. Its frequency of 50 Hz is tuned to the booster synchrotron, where electrons are injected at an energy of 26 MeV. The booster synchrotron is capable of further accelerating electrons up to 1.6 GeV. In the current setup, however, only acceleration up to 1.2 GeV is required. The combination of linear accelerator and booster synchrotron is used as an injector for the final stretcher ring, where electrons can be further accelerated to a maximum energy of 3.5 GeV. The stretcher ring, with a circumference of 164 m, is the largest stage of the accelerator. It supplies the experiments with electrons of adjustable energy and current. The main mode of operation is post-acceleration. A typical post-acceleration cycle

[3] However, a stable beam with sufficient beam current and long extraction times can only be provided up to 3.2 GeV.

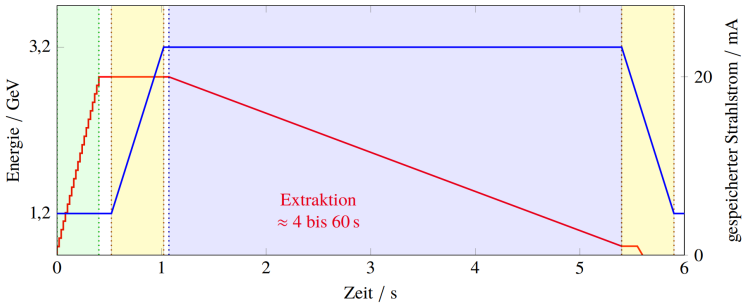

Figure 2.2: Energy and beam current during a cycle in post-acceleration mode [86]. The colored areas correspond to different phases within the cycle: injection, acceleration (ramping), extraction.

is shown in Fig. 2.2. At the beginning of the cycle, electrons are injected from the booster synchrotron at 1.2 GeV. Several injections are needed to completely fill the stretcher ring and to achieve the desired current. Shortly after, the electrons are accelerated to a target energy of 3.2 GeV with a maximum rate of 7 GeV s^{-1}. Then the extraction for the experiment starts, providing a continuous electron beam for several seconds. At the end, the energy is returned to 1.2 GeV, which again corresponds to the booster synchrotron to start the next cycle.

In the context of this work, the post-acceleration mode with a target energy of 3.2 GeV and an extraction time of 4 s was used for data taking. This resulted in a beam intensity at the experiment of ~ 1 nA. The typical ratio of the time electrons can be supplied to the experiment to the full cycle length is about 80 % [85].[4]

2.2 Photon Beam

For photoproduction experiments, the electrons extracted from ELSA must be converted into photons. This is achieved via the process of bremsstrahlung in radiator material which is mounted on a goniometer. Depending on the type of radiator, different characteristics of the photon beam can be obtained (cf. Section 2.2.1). A tagging system is then used to provide energy and time information of the photons (cf. Section 2.2.2).

2.2.1 Goniometer and Radiators

The Goniometer holds multiple radiators of different types (cf. Fig. 2.4 (left)). An electrical control system precisely adjusts the position of the individual radiators and centers them in the electron beam. In a radiator, electrons are deflected and generate bremsstrahlung. The electrons slow down in the presence of nuclei by radiating energy in the form of a photon [87]. To prevent the e^- from scattering more than once, the radiators are built very thin. This allows to characterize the energy of the photon by

$$E_\gamma = E_e^{\text{in}} - E_e^{\text{out}} \tag{2.3}$$

where E_e^{in} is the energy of the electron before and E_e^{out} after the radiator.

[4] This number is also known as the duty factor.

Unpolarized Photons For unpolarized photons, a foil made of amorphous copper is used as a radiator. Inside the amorphous copper, the scattering partners are isotropically distributed. The energy distribution of the unpolarized photons is then described by the Bethe-Heitler cross section [88]

$$\sigma_{\mathrm{B.H}} = Z^2 \alpha r_0^2 \frac{\mathrm{d}k}{k} \frac{4}{E_0^2} \left[E_0^2 + E^2 - \frac{2}{3} E_0 E \right] \left[\log\left(\frac{2E_0 E}{k} \right) - \frac{1}{2} \right]. \tag{2.4}$$

Here, α is the electromagnetic coupling constant, r_0 the Bohr-radius, E_0 and E the energy of the electron before (E_e^{in}) and after (E_e^{out}) the creation of the photon and k the energy of the photon (E_γ). The energy distribution for unpolarized photons is proportional to $1/k$.

Linear Polarized Photons For linearly polarized photons, a diamond crystal is used as a radiator. Unlike amorphous copper, the diamond crystal consists of a cubic distribution of scattering partners. The lattice can only absorb the recoil momentum, if it is a multiple n of a reciprocal lattice vector (Laue condition). This leads to coherent bremsstrahlung, where the plane of the electric field vectors is well defined. As a result, the photons are linearly polarized [89]. The cross section is defined as the superposition of the incoherent cross section according to Eqn. 2.4 and the coherent cross section

$$\sigma = \sigma_{\mathrm{incoherent}} + \sigma_{\mathrm{coherent}}. \tag{2.5}$$

The incoherent part accounts for inhomogeneities in the lattice structure due to thermal motion.

In Fig. 2.3 a comparison between the intensity distribution for an amorphous radiator and a diamond is shown. Enhancements due to coherent bremsstrahlung occur at certain energies related to reciprocal lattice vectors in the diamond.[5] As the photon energy increases, reciprocal lattice vectors move out of the allowed kinematic region for the recoil momentum, resulting in a decrease in intensity. Instead, others enter the region and begin to contribute. For each data taking, the position of the coherent edge is accurately set by aligning the diamond crystal with the incident electron beam.[6] To determine the degree of linear polarization δ_l, an intensity spectrum is recorded with both the amorphous copper as radiator and the diamond crystal. The ratio of the spectra is called the enhancement spectrum and can be compared with analytical expectations based on ANB[7] calculations [93].

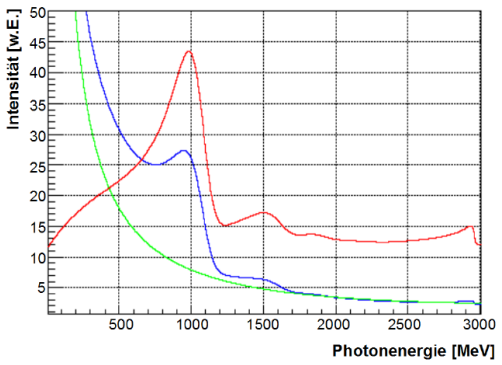

Figure 2.3: Intensity distribution of an amorphous radiator and a diamond. A relative comparison is also shown [90].

[5] Any reciprocal lattice vector within the allowed kinematic range for the recoil momentum contributes.
[6] The Stonehenge technique is used for precise alignment [91, 92].
[7] **AN**alytical **B**remsstrahlung

Circular Polarized Photons For circular polarized photons an amorphous radiator and longitudinal polarized electrons are used. The longitudinal polarized electrons lead to a well defined helicity transfer from the electrons to the bremsstrahlung photons. The resulting degree of circular polarization $\delta_\gamma^\odot$ depends only on the degree of polarization of the electrons δ_e and the transferred energy $x = E_\gamma/E_e$. Quantum electrodynamic calculations yield [94]

$$\delta_\gamma^\odot = \frac{1 + \frac{1}{3}(1-x)}{1 + (1-x)^2 - \frac{2}{3}(1-x)} x \cdot \delta_e. \tag{2.6}$$

To determine $\delta_\gamma^\odot$, the energy transfer and the polarization of the incoming electrons must be measured. While the energy transfer is measured with the Tagging system, the polarization degree of the electrons is determined with a Møller radiator [95] (cf. Fig. 2.4 (left)). A foil with electrons of known polarization is used as a scattering partner for the incoming electrons. Since the $e^- e^-$-scattering cross section depends on the spin orientations,[8] the degree of polarization can be determined from the asymmetries of the event yields.

2.2.2 Tagging System

The analysis of photoproduced reactions requires a precise measurement of the incoming photon energy E_γ. The photons are produced by bremsstrahlung of an electron in the radiator and carry the energy

$$E_\gamma = E_e^{\text{in}} - E_e^{\text{out}}. \tag{2.7}$$

While the energy of the electrons supplied by ELSA E_e^{in} is known, the energy of the electrons after the bremsstrahlung E_e^{out} must be measured. To measure the outgoing electrons, a tagging system is placed shortly after the Goniometer (cf. Fig. 2.4 (right)). In a constant magnetic field generated by a dipole magnet, the electrons are deflected according to their energy. Depending on the magnetic field and the strength of the deflection, the energy of the outgoing electrons and thus of the photons can be determined.[9] The Tagging system consists of a hodoscope that can be divided into Tagger bars and Tagger fibers. Tagger bars are 96 bars of organic scintillators. An overlap between the bars allows the requirement of coincident hits, reducing the influence of background. The Tagger bars are complemented by 480 Tagger fibers for better segmentation in the range of high energy electrons with small deflection. This increases the resolution for low energy photons. The Tagging system can cover a photon energy range between 11.9 % and 97.9 % of the incoming electron energy E_e^{in} [96].

2.3 Detectors

Different detector components are used to measure the final state products. For an overview see Fig. 2.5. The energy and angular information of the photons are measured by two calorimeters: the Crystal Barrel detector positioned around the target and the MiniTAPS

[8] A parallel electron spin configuration leads to a smaller scattering rate than an antiparallel spin configuration.
[9] For high energy transfers to the photon, a large deflection is expected. For small energy transfers a small deflection is expected.

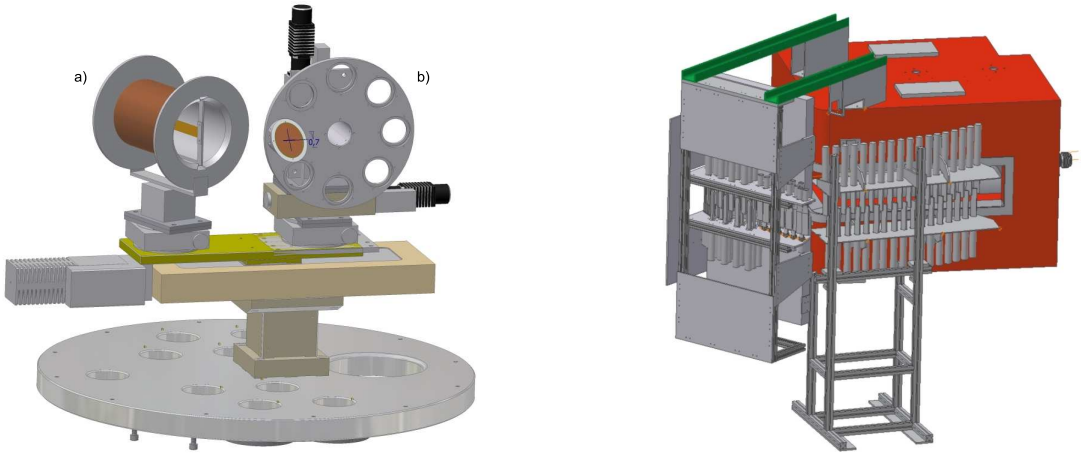

Goniometer with Møeller coil (a) and radiator mount with diamond crystal (b)

Tagging system

Figure 2.4: Layout of the Goniometer and the Tagging system [83].

detector, which is positioned further forward. The so-called Inner detector is used to identify charged particles. Further, charge-sensitive plastic scintillators are positioned in front of the MiniTAPS detector and in the forward direction of the Crystal Barrel detector. Electromagnetic background is suppressed using a Cherenkov detector as a veto signal for the trigger mechanism.[10] At the end of the beam line, detector components are installed to measure the photon flux.

A unified coordinate system is used to describe all detector components. θ defines the polar angle relative to the beam line starting at 0° in the forward direction and ending at 180° in the backward direction. ϕ defines the azimuthal angle around the beam line starting at 0° and ending at 360°. In this chapter a general description of each detector component is given. In Chapter 3, the readout of the Crystal Barrel detector, the main calorimeter of the experiment, is explained in more detail. Also, more specific information on the event reconstruction from these detectors and the energy and angular resolutions achieved in the experiment is given in Chapter 6.

2.3.1 Crystal Barrel Detector

The Crystal Barrel detector is the main calorimeter of the experiment [98]. It covers the entire ϕ-range and most of the θ-range from 11.2° to 156°. The calorimeter consists of 1320 CsI(Tl)[11] crystals, which in most cases[12] point head-on toward the center. Each crystal covers a region of $6^\circ \times 6^\circ$ ($\theta \times \phi$) except for the first three rings in the forward direction where each crystal covers $6^\circ \times 12^\circ$ instead. This region is also known as the Forward detector and ranges from 11.2° to 27.5° in θ. Similarly, for the last ring, the crystal size is $6^\circ \times 12^\circ$.

[10] A trigger system starts the readout only when certain conditions are met. A veto signal is part of the conditions and can prevent the readout from starting.

[11] **T**hallium doped **C**esium **I**odide

[12] An exception are the first three rings in the forward direction.

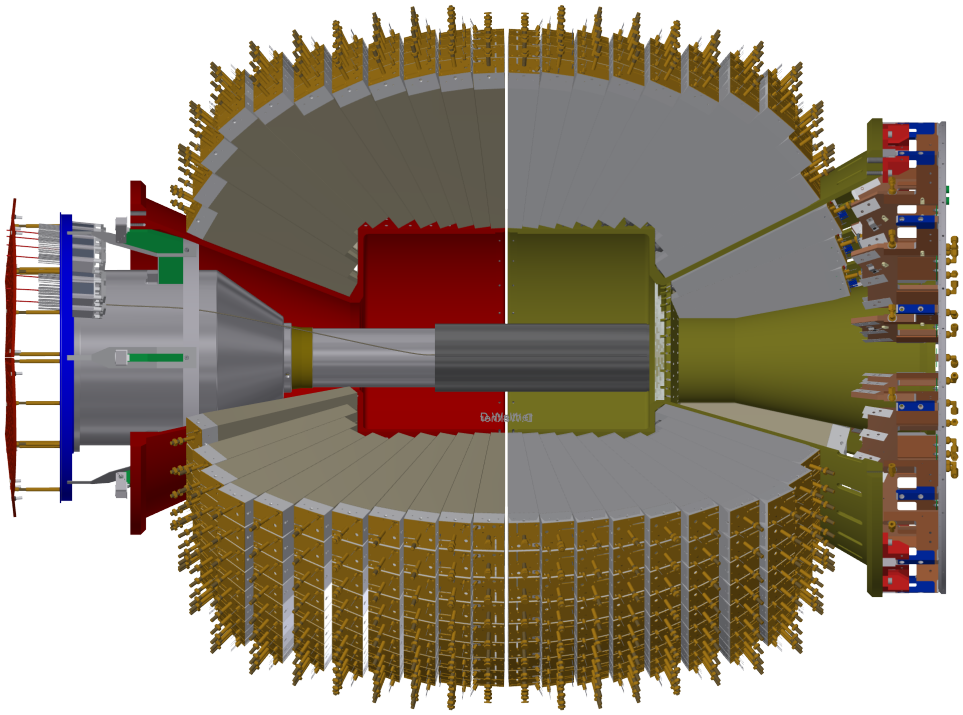

Figure 2.5: Cut through the Crystal Barrel detector [97]. The incoming beam (left to right) impinges on the target enclosed by the Inner detector (black). The MiniTAPS detector is positioned further along the beam line and is not shown in the image.

There are 24 rings in total, each holding 60 crystals, except for the first three and the last ring, which hold 30 crystals each. Each crystal has a length of 30 cm. This corresponds to a total of 16 radiation lengths[13], with a radiation length of $X_0 = 1.86\,\text{cm}$ for CsI(Tl) [7]. This ensures almost complete energy deposition even for high energy photons.

For the Forward detector, charge-sensitive plastic scintillators are placed in front of the crystals, allowing the detection of charged particles [99]. There are 60 plates per ring, arranged in two layers, each covering $6^\circ \times 12^\circ$. This allows for the requirement of coincident hits which reduces the influence of background. Each plate is 3 mm thin.

In addition to energy, the Crystal Barrel detector also provides time and directional information. Directional information is reconstructed based on the segmentation of the calorimeter. The readout of this information is explained in detail in Chapter 3.

[13] Longitudinal expansion after which the energy of an electron is reduced by bremsstrahlung to $1/e$ of the initial energy.

2.3.2 MiniTAPS

The MiniTAPS detector consists of 216 hexagonal BaF_2[14] crystals [100] (cf. Fig. 2.6 (left)). It is positioned 2.1 m further in the forward direction along the beam line and covers a θ-range from 1° to 12° complementing the Crystal Barrel detector. Each crystal has a length of 25 cm, which with a radiation length of $X_0 = 2.03\,\text{cm}$ for BaF_2 corresponds to 12 radiation lengths in total [7]. Again, charge-sensitive plastic scintillators plates are placed in front of each crystal to detect charged particles. Each plate is 5 mm thin. Similar to the Crystal Barrel detector, the MiniTAPS detector provides energy, time, and direction information.

2.3.3 CO_2 Cherenkov Detector

Electromagnetic reactions must be suppressed due to their high cross section. Since they are dominant in the very forward direction at small angles, a CO_2 Cherenkov detector is installed between the Crystal Barrel detector and MiniTAPS [101]. The Cerenkov detector has a size of $1\,\text{m} \times 1.2\,\text{m} \times 1.2\,\text{m}$ in length, width, and height. With a refraction index of $n = 1.00043$ electrons and positrons produce Cherenkov light above 17.4 MeV. For comparison, other particles such as charged pions or muons produce Cherenkov light only at much higher values of 4.7 GeV and 3.6 GeV. The Cherenkov light is focused by a mirror and detected by a photomultiplier. The photomultiplier then acts as a veto signal for the trigger (cf. Section 2.5).

2.3.4 Photonflux- and Gamma Intensity Monitor

For an analysis such as the determination of cross sections, the photon flux must be known precisely. Therefore, a combination of a Photonflux- (FluMo) and a Gamma Intensity Monitor (GIM) is installed at the end of the beam line [102] (cf. Fig. 2.6 (right)). The GIM consists of a 4×4 matrix of PbF_2[15] crystals, in which photons are detected by using the Cherenkov light of charged particles in electromagnetic showers. This works reliably up to a certain rate. Above that, saturation effects occur due to the limited double pulse resolution of the readout [103]. To overcome this, the FluMo is used. The FluMo is placed in front of the GIM. It detects e^-e^+-pairs of photons converted on a lead foil. Since only a fraction of the photons are converted, the detector must be calibrated with the GIM at low rates. After calibration, the FluMo works reliably at rates where the GIM saturates. A charge-sensitive scintillator is placed at the front, which acts as a veto for charged particles coming with the photon beam. A photon camera is also installed to monitor the position of the beam during data taking.

2.3.5 Inner Detector

The Inner detector is of cylindrical shape and surrounds the target (cf. Fig. 2.7 (left)). It is used to detect charged particles and to identify their intersection point with the detector [104–106]. The detector covers a θ-range from 13° to 156° and the full ϕ-range. It consists of 513 organic scintillating fibers with a diameter of 2 mm and a length of 400 mm. The forward end of the fibers is reflective, while the backward end is connected to light guides

[14] **Ba**rium **F**luoride
[15] Lead Fluoride

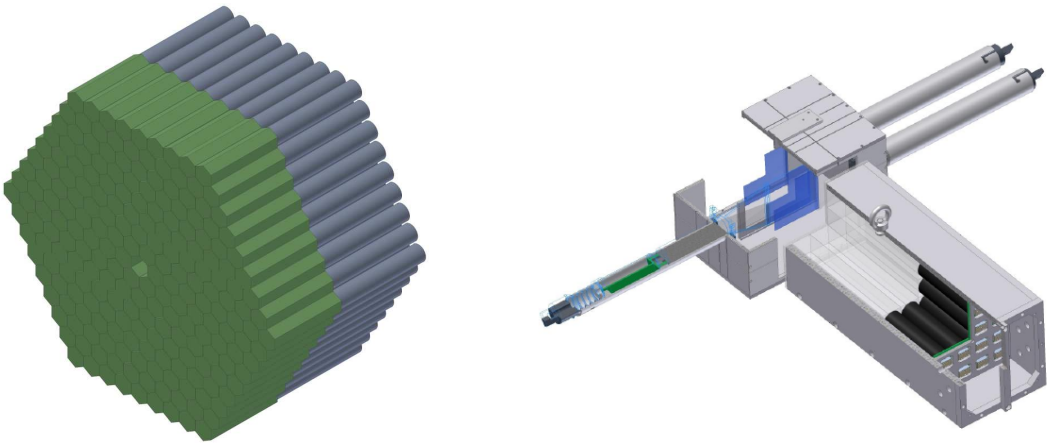

MiniTAPS FluMo and GIM

Figure 2.6: Layout of the MiniTAPS detector and the setup of the Photonflux- (FluMo) and Gamma intensity monitor (GIM) [83].

and photomultipliers. The fibers are arranged in three layers. The outer layer is aligned parallel to the beam axis, while the middle and inner layers are tilted by $+25.7°$ and $-24.5°$ respectively. This allows the reconstruction of a unique crossing point with a signal in only two fibers in different layers.

2.4 Target

Several targets are available, each with its own application. For cross section measurements or for beam polarization experiments with protons as interaction partners, a Liquid Hydrogen target (LH_2) is used.[16] It provides a large number of free protons as interaction partners and good statistics. In the case of double polarization experiments, the target must be polarizable. For this case there is a Frozen Spin target using butanol (C_4H_9OH) as the target material.[17] For reference measurements, a third type of target exists that uses carbon foam. Each target type is described in more detail below.

Liquid Hydrogen Target In cases where the target does not need to be polarized, liquid hydrogen (LH_2) is used as the target material. It consists of a high concentration of free protons as interaction points. The protons in liquid hydrogen can be treated as free particles due to their low binding energy. This makes the target ideal for measuring cross sections or for single polarization experiments, where only the photon beam is polarized. The Liquid Hydrogen target consists of a cooling circuit, a cold head, and a heat exchanger. The target cell has a length of 5.26 cm and a diameter of 3 cm. The cell operates at a temperature of 20 K [107].

[16] Liquid deuterium (LD_2) is used to study reactions with neutrons as interaction partners.
[17] Deuterated butanol is used to study reactions with neutrons as interaction partners.

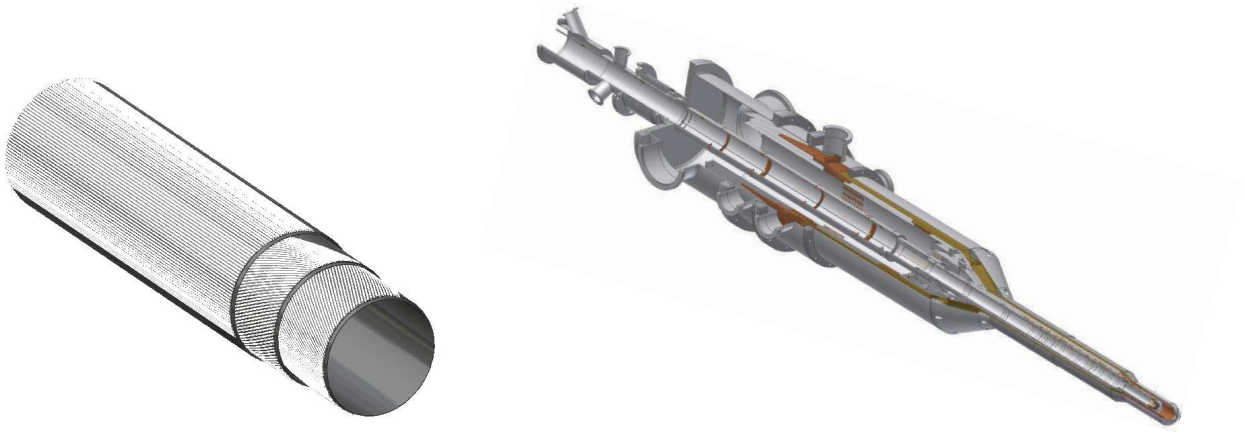

Inner detector

Frozen Spin target with cryostat

Figure 2.7: Layout of the Inner detector and the Frozen Spin target with cryostat. The target is placed at the tip of the cryostat [83].

Frozen Spin Target For double polarization experiments the Mainz-Dubna Frozen Spin target with butanol (C_4H_9OH) is used [108] (cf. Fig. 2.7 (right)). Frozen butanol pallets are placed in the target cell. A cryostat cools the temperature to about 250 mK. At this temperature, a superconducting solenoid magnet with a field strength of 2.5 T achieves almost complete polarization of the electrons. Dynamic nucleon polarization (DNP) is then used to transfer the polarization to the nucleons via microwave radiation. The polarization can be chosen to be parallel or antiparallel to the magnetic field. The magnet is removed before the measurement begins to make room for the detector components. To extend the relaxation time[18] the target is cooled to its operating temperature of about < 30 mK. Furthermore, a holding coil is placed inside the cryostat with a magnetic field strength of 0.5 T [109]. This ensures reliable polarization with relaxation times of several hundred hours. After that, the data taking has to be stopped and the target has to be repolarized. The degree of polarization is determined by nuclear magnetic resonance measurement (NMR) [110].

By using butanol as the target material, only part of the nucleons can be polarized. Nucleons bound in carbon and oxygen within butanol cannot be polarized and must be explicitly considered in the analysis of the data. Therefore, a reference measurement with carbon foam as target material is necessary.

Carbon Foam Carbon foam is used as a reference target material to account for the fraction of non-polarizable nucleons bound in carbon and oxygen within the Frozen Spin target. For optimal comparison, the entire detector setup must remain the same between the butanol and the reference measurements. The carbon foam is filled into a cylinder and placed in the exact same cryostat with the same coolant that is used for the Frozen Spin target. The data taken with the carbon foam can then be subtracted from the data taken with butanol to remove the influence of the unpolarized nucleons.

[18] To *freeze* the aligned spins, hence the name Frozen Spin target.

2.5 Trigger System

Reactions that are of no interest but have a high cross section must be suppressed during data taking. A readout of these events would lead to unnecessary dead time in the experiment. Therefore, a trigger system is implemented. Only when at least one of a number of predefined conditions is met will the readout start. The current conditions in the experiment require at least two hits in the calorimeters. If MiniTAPS is involved and at most one hit is detected in the Crystal Barrel detector, an additional check is performed for the Cherenkov veto signal. The veto is not checked if two hits or more are detected in the Crystal Barrel detector. The conditions are listed in Table 2.1.

Table 2.1: Set of trigger conditions. As soon as one condition is met, the readout will start. `taps1` and `taps2` refer to at least one or at least two hits in MiniTAPS. `cb1` and `cb2` refer to at least one or at least two hits in the Crystal Barrel detector. `cherenkov` refers to the veto signal of the Cherenkov detector.

Condition
`taps1` $\wedge$ `cb1` $\wedge$ `NOT cherenkov`
`taps2` $\wedge$ `NOT cherenkov`
`cb2`

The information about the number of hits in the calorimeters must be provided within $300-500\,\mathrm{ns}$. For the Crystal Barrel detector this fast behavior is achieved by a combination of a cluster finder and a cluster adder [81]. For each crystal, it is checked whether the neighbors match a certain hit pattern. The hit pattern is chosen so that it is valid for only one crystal in a continuous cluster of energy depositions (cluster finder). This provides information about the number of clusters or equivalent hits. This process is performed in parallel. In a second step, the number of clusters is added and sent to the trigger (cluster adder). In the case of MiniTAPS, a similar algorithm is proposed in [111]. However, a simpler method is currently used. The MiniTAPS detector is divided into four sectors of 54 crystals each. Any number of energy depositions within a sector are counted as a single cluster.

2.6 Software

In addition to a sophisticated detector setup, appropriate software is needed to record, process, and analyze the data. The detector setup needs to be monitored and calibration managed on a large scale. Furthermore, simulations of the detector response are required to validate the data. A variety of software tools are used for these purposes.

2.6.1 ExPlORA

The data recorded during the experiment must be reconstructed and analyzed in an efficient way. Therefore, a framework called ExPlORA[19] is used [112]. ExPlORA was designed

[19] **Ex**tendable **Pl**ugable **O**bjectoriented **R**ootified **A**nalysis

specifically for the CBELSA/TAPS experiment and is under continuous development. It is written in C++ and operated by XML files. It can be easily extended with plugins, allowing a modular use of different functionalities. ExPlORA is built on top of ROOT, an object-oriented data analysis framework developed at CERN [113]. ROOT provides functionality for statistical analysis, visualization, and data management.

During the analysis, it is also necessary to simulate particles within the existing detector setup. For this purpose, **V**irtual**M**onte**C**arlo (VMC) is used [114]. VMC is embedded in ExPlORA and allows detailed investigation of expected detector responses. It relies on Geant[20] [115, 116] to track particles and to simulate their interaction with material. From there, VMC calculates the detector response using Monte Carlo methods[21] and produces output as it would occur in reality. It is critical that the simulation be as close to reality as possible. This requires accurate knowledge of the detector geometry and detector response.

2.6.2 Data Acquisition System

During the measurement, a **D**ata **A**cquisiton **S**ystem (DAQ) is responsible for receiving, processing, and storing the data [117]. While the system is written in C++, the components communicate via TCP/IP protocol[22]. During data taking, multiple processes run in parallel on different computers. For each detector component, a local event builder reads the data, processes it, and passes it to the network. The local event builder consists of separate threads connected by ring buffers: the readout thread, the process thread, and the data thread. This way, the different steps are decoupled from each other and the readout thread can be ready for a new event while the other threads are still busy. Each local event builder passes the data to the network, where it is sent to the global event builder. The global event builder collects the data and checks it for completeness. If successful, the data is passed via a buffer to a thread that is responsible for compressing and storing the data. It is saved in data structures provided by the ROOT framework. The global event builder then passes the data to a thread responsible for the online monitor, which displays the recorded data in near real time [118].

The DAQ is controlled by a central service (demon). The demon is responsible for monitoring the status of the DAQ components as well as allowing adjustments such as starting and stopping runs and configuring the detectors. A graphical user interface DAQt is implemented, which is directly connected to the DAQ demon.[23] Additionally, the DAQt writes all meta information of the recorded data to a database. This information can be easily accessed and viewed via a web interface implemented in PHP [119].

2.6.3 Slowcontrol

The Slowcontrol corresponds to a network of sensors and controllable devices which are installed for various detector systems [120, 121]. The Slowcontrol is responsible for monitoring, analyzing, and storing sensor data in a database. It can also be used to configure certain

[20] **GE**ometry **AN**d **T**racking
[21] Numerical method for generating significant distributions by a large number of repetitions.
[22] **T**ransmission **C**ontrol **P**rotocol/**I**nternet **P**rotocol
[23] The DAQt is implemented using the Qt software, which is a solution for creating graphical user interfaces.

parts of the experiment. Examples of measured data include temperature, voltage supplies, fan trays, position of the goniometer, thresholds of discriminator modules and more. The Slowcontrol can be accessed via a web interface implemented in PHP [122]. A Grafana[24] dashboard is also available for visualizations and alerts.

2.6.4 Analyse Database

Most detector components require some form of calibration. While some of the calibrations are performed once for each period of data taking, others are performed multiple times to account for variations. In addition to calibrations, more general information such as the measured polarization has to be stored. All this information must be made available during analysis. Therefore, the Analyse Database exists [123], which is read when ExPlORA is started. The database is based on Postgres and the corresponding web interface is developed in AppFuse, an open source Java (EE) framework.

While the web interface allows you to upload and interact with the database, the process can be error prone. The range of data for which the information is valid must be carefully selected. To complicate matters, there may be multiple versions of the same information, each with its own priority.[25] While this is technically necessary, it is important to ensure that it is maintained correctly. The web interface of the Analyse Database does not provide a good overview for this. Therefore, in addition to the original web interface, a complementary interface has been developed in this work to provide an overview of the various information in the Analyse Database and to document their status and performance (cf. Fig. 2.8) [124]. It is divided into two components. The first component visualizes the status of each calibration by frequently querying the Analyse Database. Data recorded by the experiment with missing or outdated calibration is highlighted. The second component allows the documentation of the performance of each calibration by text or by uploading PDF or ROOT files. The interface is written in Python using Django as the web framework.

[24] Grafana is an open source solution for interactive visualizations in a web application by connecting to a data source such as a Postgres database.

[25] The version with the highest priority is used by ExPlORA.

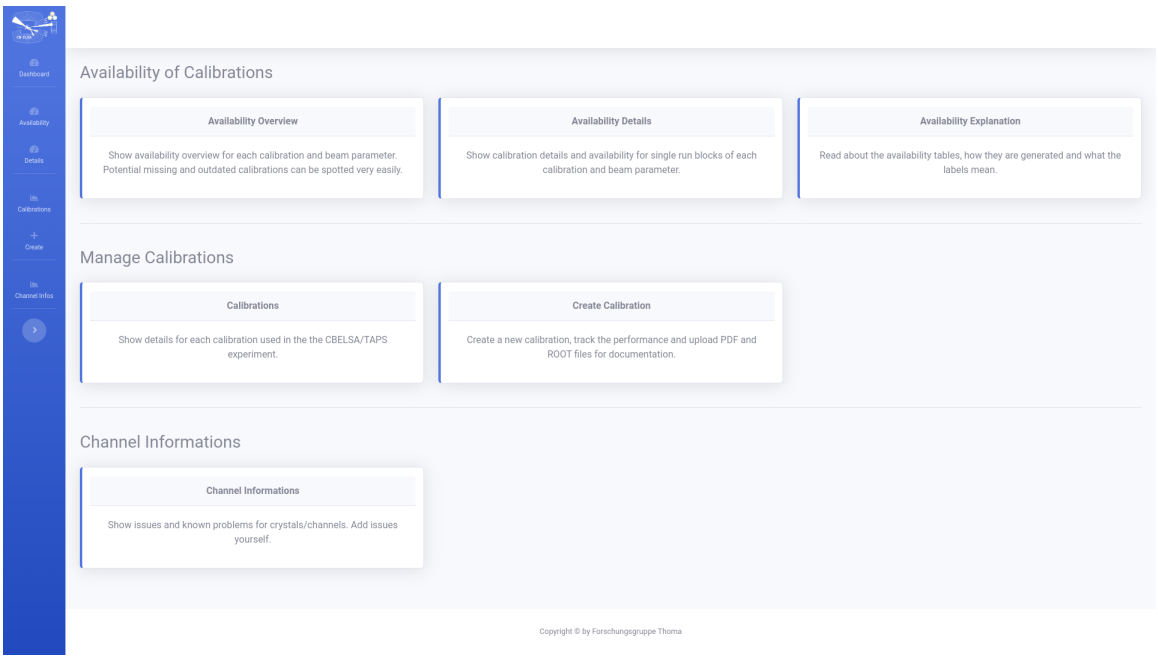

Overview

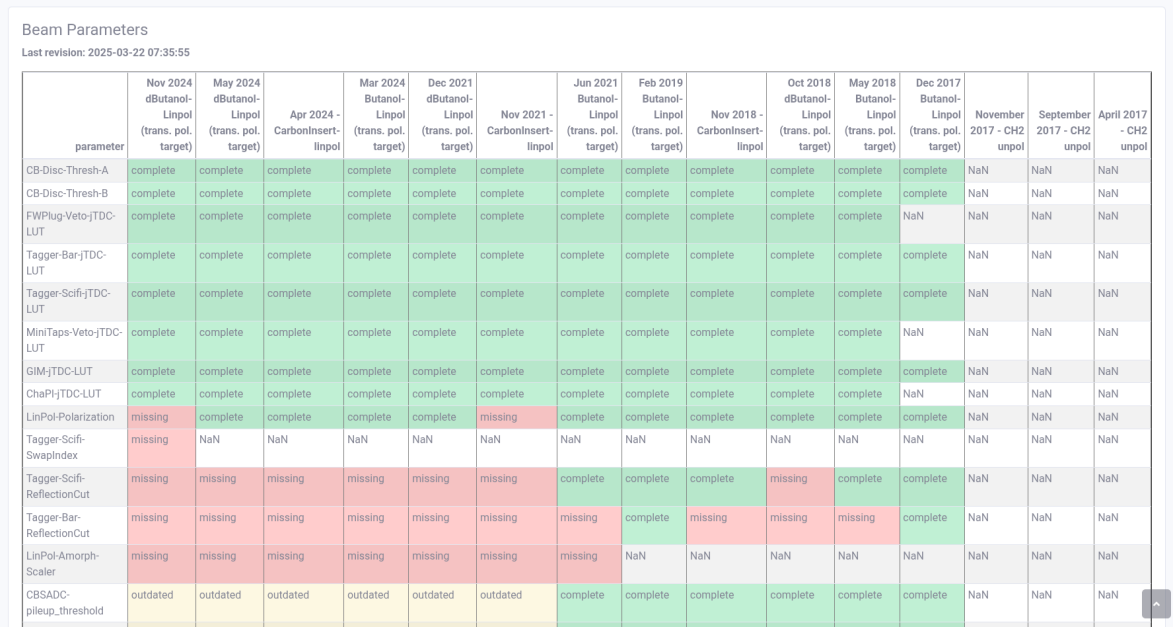

Beam Parameters

Last revision: 2025-03-22 07:35:55

parameter	Nov 2024 dButanol-Linpol (trans. pol. target)	May 2024 dButanol-Linpol (trans. pol. target)	Apr 2024 - CarbonInsert-linpol	Mar 2024 Butanol-Linpol (trans. pol. target)	Dec 2021 dButanol-Linpol (trans. pol. target)	Nov 2021 - CarbonInsert-linpol	Jun 2021 Butanol-Linpol (trans. pol. target)	Feb 2019 Butanol-Linpol (trans. pol. target)	Nov 2018 - CarbonInsert-linpol	Oct 2018 dButanol-Linpol (trans. pol. target)	May 2018 Butanol-Linpol (trans. pol. target)	Dec 2017 Butanol-Linpol (trans. pol. target)	November 2017 - CH2 unpol	September 2017 - CH2 unpol	April 2017 - CH2 unpol
CB-Disc-Thresh-A	complete	complete	complete	complete	complete	complete	complete	complete	complete	complete	complete	complete	NaN	NaN	NaN
CB-Disc-Thresh-B	complete	complete	complete	complete	complete	complete	complete	complete	complete	complete	complete	complete	NaN	NaN	NaN
FWPlug-Veto-jTDC-LUT	complete	complete	complete	complete	complete	complete	complete	complete	complete	complete	complete	NaN	NaN	NaN	NaN
Tagger-Bar-jTDC-LUT	complete	complete	complete	complete	complete	complete	complete	complete	complete	complete	complete	complete	NaN	NaN	NaN
Tagger-Scifi-jTDC-LUT	complete	complete	complete	complete	complete	complete	complete	complete	complete	complete	complete	complete	NaN	NaN	NaN
MiniTaps-Veto-jTDC-LUT	complete	complete	complete	complete	complete	complete	complete	complete	complete	complete	complete	NaN	NaN	NaN	NaN
GIM-jTDC-LUT	complete	complete	complete	complete	complete	complete	complete	complete	complete	complete	complete	complete	NaN	NaN	NaN
ChaPl-jTDC-LUT	complete	complete	complete	complete	complete	complete	complete	complete	complete	complete	complete	NaN	NaN	NaN	NaN
LinPol-Polarization	missing	complete	complete	complete	complete	missing	complete	complete	complete	complete	complete	complete	NaN	NaN	NaN
Tagger-Scifi-SwapIndex	missing	NaN	NaN	NaN	NaN	NaN	NaN	NaN	NaN	NaN	NaN	NaN	NaN	NaN	NaN
Tagger-Scifi-ReflectionCut	missing	missing	missing	missing	missing	missing	complete	complete	complete	missing	complete	complete	NaN	NaN	NaN
Tagger-Bar-ReflectionCut	missing	missing	missing	missing	missing	missing	missing	complete	missing	missing	missing	complete	NaN	NaN	NaN
LinPol-Amorph-Scaler	missing	missing	missing	missing	missing	missing	missing	NaN	NaN	NaN	NaN	NaN	NaN	NaN	NaN
CBSADC-pileup_threshold	outdated	outdated	outdated	outdated	outdated	outdated	complete	complete	complete	complete	complete	complete	NaN	NaN	NaN

Availability of beam parameters

Figure 2.8: Overview page and availability of beam parameters (as one example) of the new web interface that complements the Analyse Database web interface [124]. It provides an overview of the various information in the Analyse Database and can be used to document the status and performance of calibrations.

CHAPTER 3

Readout of the Crystal Barrel Detector

There are two types of information that specify the signals detected in the calorimeter. The first one is energy information, which correlates with the scale of a signal. It is particularly important for later determination of particle properties, such as their four-momentum[1] (cf. Chapter 6). The second type of information is time, which indicates when a signal occurs. Time information allows multiple detector signals to be correlated and provides information for trigger decisions. The information from the calorimeter is extracted during a process called *readout*. There are several requirements for the readout electronics. Energy information must be extracted over a wide dynamic range[2] with a low signal-to-noise ratio (SNR).[3] This requires a processing that allows for as much accumulated signal as possible. In contrast, time information must be provided with low latency but high resolution.[4] To include the Crystal Barrel detector as a first-level trigger, a logical signal must be generated within the first $\sim 300 - 500\,\mathrm{ns}$ [80, 125]. This fast behavior is achieved by using relatively short time characteristics, thus using only a small part of the signal. The conflicting requirements for extracting energy and time information lead to the need for carefully selected electronics. A schematic drawing of the current readout for the Crystal Barrel detector is shown in Fig. 3.1. The readout can be divided into two parts: The front-end refers to components placed directly behind each crystal. The back-end refers to components placed further away from the detector.

A recent modification of the experiment improved the readout electronics and the trigger system [79–82], allowing not only for higher data quality and improved rate capability but also for increased trigger efficiency. After modification, the trigger efficiency for neutral final state was significantly increased up to 90 % over a wide angular range [126]. Some of these modifications and their motivation are discussed below.

3.1 Front-End Electronics

The front-end is responsible for the primary detection of a signal in inorganic scintillators and for the amplification of small electrical signals arising from avalanche photodiodes (APDs). The placement of these components directly behind the crystal is necessary to minimize noise. After amplification, the influence of noise sources is reduced during transmission via connecting cables.

[1] Together with the directional information provided by the segmentation of the calorimeter.
[2] Range of detectable energy information.
[3] Using the QDC and SADC (energy) branch in Fig. 3.1.
[4] Using the TDC (timing) branch in Fig. 3.1.

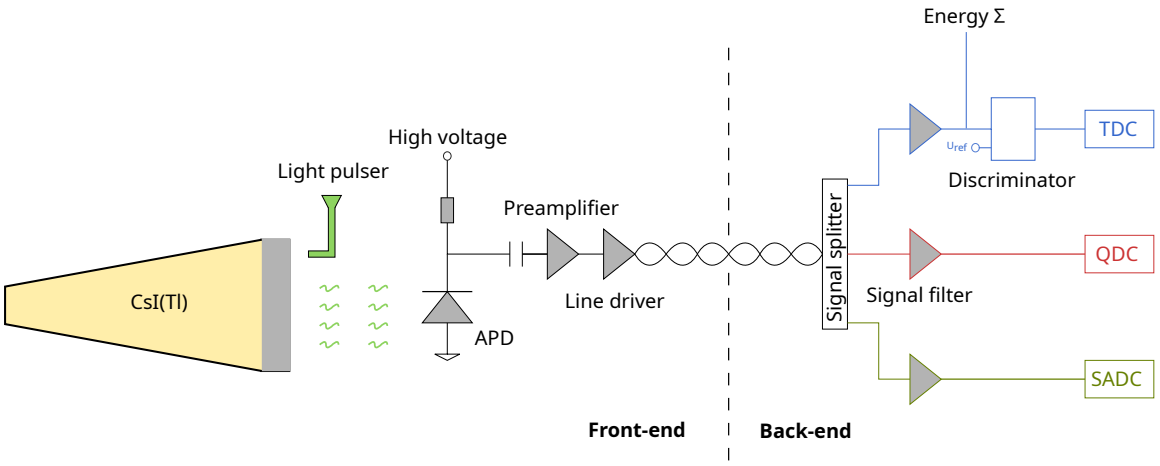

Figure 3.1: Schematic overview of the readout electronics in the Crystal Barrel detector. Components that appear to be separated may be on the same physical board.

3.1.1 CsI(Tl) as an Inorganic Scintillator

An inorganic scintillator consisting of CsI(Tl)[5] is installed just before the front-end electronics. In the case of energy deposition, e^-/h-pairs are created in the conduction and valence band of the crystal. When the pairs recombine via luminescence centers, visible light is emitted for which the crystal is transparent. The intensity of the light is proportional to the energy deposited [128]. In general, a scintillator can be characterized by its light yield and its decay time. While CsI(Tl) has a high light yield of 54 photons per keV, its natural time characteristics are rather slow [129]. Other advantages include low cost and resistance to thermal and mechanical shock. The emission spectrum has a maximum at about 550 nm [7]. Each crystal has a length of 30 cm, allowing almost complete energy deposition even for high energy photons.[6] The shape of the emitted light pulse is determined by the characteristics of different processes: the formation of e^-/h-pairs, the thermalization time, the transition to luminescence centers and the final decay of these centers. This non-trivial behavior is often parametrized by a sum of exponential functions with different decay times [87]. In [129] different components of the decay times are mentioned for CsI(Tl) ranging between $\tau = 0.6 - 3.5\,\mu s$. In [127] even higher decay times up to 17.7 µs

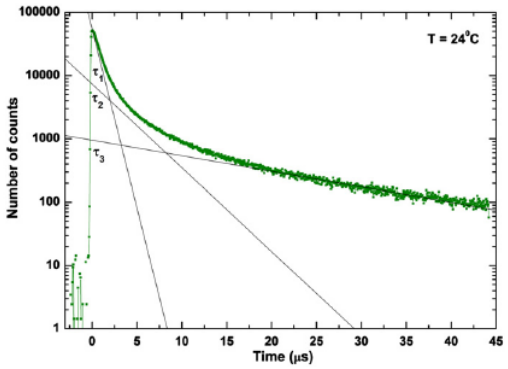

Figure 3.2: The decay time of a CsI(Tl) light pulse and its components, measured at room temperature (24 °C) [127].

[5] **T**hallium activated **C**esium **I**odide

[6] With a radiation length of $X_0 = 1.86\,cm$ for CsI(Tl), this corresponds to a total of 16 radiation lengths [7].

are given (cf. Fig. 3.2). The primary (average) decay time for photons is about 1 µs [129].

3.1.2 Avalanche photodiodes

Prior to the modification of the readout, the scintillation light was processed by PIN photodiodes[7] and by photomultipliers. Due to the high latency associated with the PIN photodiode readout, the Crystal Barrel detector could not meet the timing requirements for the integration into the first-level trigger. To resolve this issue and provide sufficiently fast timing information, an appropriate signal filter was introduced (cf. Section 3.2.1). At the same time, improving the signal-to-noise ratio (SNR) was essential to enable lower trigger thresholds, which required intrinsic gain in the processing of the scintillation light. Replacing the PIN photodiodes with two avalanche photodiodes (APDs) per crystal[8] successfully addressed these requirements [80]. At the same time, the photomultipliers were also changed to APDs. It was then discussed to use the Crystal Barrel detector within a magnetic field, which would not have been possible with photomultipliers. This allows for the future integration of a time projection chamber inside the Crystal Barrel detector.

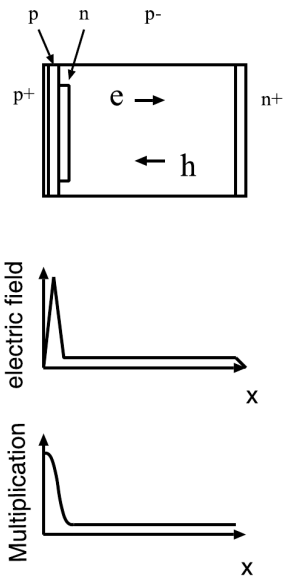

Figure 3.3: *Reverse-type* APD. The area of intrinsic multiplication is located just below the surface [130].

Avalanche photodiodes consist of a positively and negatively doped layer. A special doping profile in combination with a high reverse bias voltage leads to an intrinsic gain [87]. As a result, APDs offer a better SNR than previously used PIN photodiodes. Of the various types available, *reverse-type* APDs are used. Here, the area of intrinsic multiplication is located just below the surface (cf. Fig. 3.3). This prevents the amplification of dark current from electrons.[9] In addition, an intrinsic gain of about 50 is set as the best compromise between sufficient SNR for energy and time information and a good temperature stabilization[10] [80]. A high voltage (HV) supply is used to provide the necessary reverse bias voltage. The HV is set individually for each APD and corrects for any temperature dependence around the target operating temperature of 27.5 °C. The target temperature is achieved by stabilizing the temperature of all the crystals using an oil circuit. Monitoring of the intrinsic gain is possible with the light pulser system (cf. Section 3.3). This ensures a constant gain during measurement [79, 131].

[7] Layers in a PIN photodiode are a **p**-type semiconductor layer, an undoped **i**ntrinsic semiconductor layer and a **n**-type semiconductor layer.

[8] Using two APDs per crystal improves the signal-to-noise ratio by a factor of $\sqrt{2}$ (assuming uncorrelated noise). It also provides a fallback, in case one of the APDs fails.

[9] The dark current from holes (h) is still amplified.

[10] The temperature dependence increases at higher gains, making stabilization more difficult.

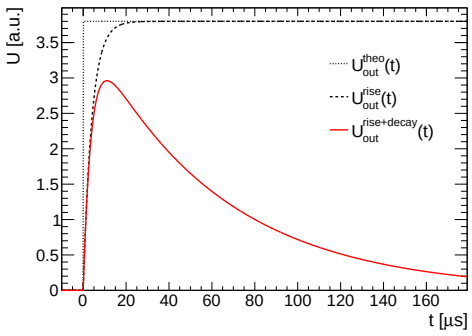

Time characteristics

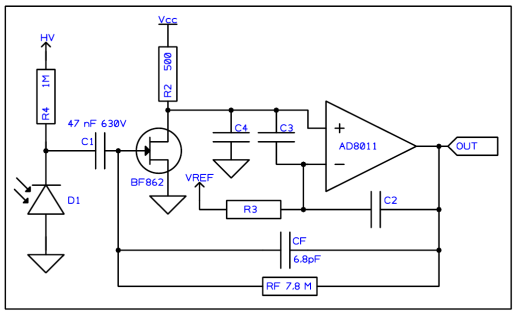

Preamplifier circuit

Figure 3.4: Left: Theoretical time characteristics of the preamplifier output with a rise time of 10 µs and a decay time constant of $\tau_{\text{decay}} = 54\,\mu\text{s}$, simulating the situation in the experiment. Right: Simplified representation of the existing charge sensitive preamplifier consisting of an inverting operational amplifier with capacitive feedback [80]. Besides the feedback capacitor, additional capacitors are used for loop stabilization and decoupling of the APD signal from high bias voltage.

3.1.3 Charge Sensitive Preamplifier

A charge sensitive preamplifier is used to integrate and amplify the signals arising from the avalanche photodiode. The output of the preamplifier is a voltage proportional to the integrated incoming charge. Integration and amplification are performed by an inverting operational amplifier with capacitive feedback. The incoming charge is integrated by means of the feedback capacitor C_f, whose resulting charge Q_f is equal to the signal charge Q_s. For pointlike input signals and an ideal preamplifier, a voltage level of $U_{\text{out}}^{\text{theo}}(t) = U_0 = Q_s/C_f$ is instantaneously reached at the output. However, the slow time characteristics of the CsI(Tl) crystals are far off from pointlike signals, resulting in a rise time behavior of the preamplifier described by [128]

$$U_{\text{out}}^{\text{rise}}(t) = U_0 \cdot \left(1 - e^{-\frac{t}{\tau_{\text{rise}}}}\right) \tag{3.1}$$

where τ_{rise} is the rise time constant. In the case of multiple input signals, the output voltage will be continuously integrated, resulting in a step-like accumulation (pile-up). To prevent saturation, the feedback capacitor is discharged via a resistor R_f. As a result, the output voltage decays exponentially with

$$U_{\text{out}}^{\text{decay}}(t) = U_0 \cdot e^{-\frac{t}{\tau_{\text{decay}}}} \qquad \text{with} \qquad \tau_{\text{decay}} = C_f \cdot R_f. \tag{3.2}$$

As a result, the output voltage U_0 is not fully reached, reducing the expected amplification. This is called the ballistic deficit. The size of the ballistic deficit depends on the selected time constants. With the current settings, the ballistic deficit is about $0.7 \cdot U_0$ [80]. The behavior of the preamplifier is shown in Fig. 3.4 (left).

The behavior of the charge sensitive preamplifier is highly dependent on the selected feedback capacitance and resistance. They determine the amplification, and thus the SNR, as

well as the decay time. During the recent modification of the experiment, a new dual-channel preamplifier[11] was installed per crystal (cf. Fig. 3.4 (right)). A study of optimal values was performed, which resulted in $C_f = 6.8\,\text{pF}$ and $\tau_{\text{decay}} = 54\,\mu\text{s}$ [80, 132]. Due to the slow time characteristics of the scintillating light the output signal reaches its maximum after 10 µs.

3.1.4 Line Driver

After amplification, the signal is transmitted to the back-end electronics via connecting cables. A line driver is used to improve the quality of the transmission. The signal is transmitted using differential signaling, which sends both the original signal and its inverted version. This cancels out external noise, as this affects both signals in the same way, leaving the difference between them untouched. As a first step in the back-end, the differential signal is converted back to a single-ended signal for further processing. The line driver also allows for small gain adjustments to correct for differences in the light yield of the crystals. As part of the recent modification, the line driver was also renewed to allow for a wider frequency range during transmission [80].

3.2 Back-End Electronics

In the back-end, energy information must be extracted over a wide dynamic range with a high signal-to-noise ratio. In contrast, time information must be provided with low latency for trigger decisions. To meet both requirements, a multi-backend logic was introduced as part of the readout modification. The signal is therefore split into three parts. Each part is processed by a dedicated branch optimized for its use case. The first branch uses time-to-digital converters (TDCs) to digitize the time information. The second branch uses charge-to-digital converters (QDCs) to digitize energy information. The third branch uses sampling-analog-to-digital converters (SADCs) as a more advanced way to digitize both the energy and time information. Starting with data taking in June 2021, the SADC branch is used as a replacement of the previous energy readout that relied on QDCs. During the modification of the readout, data were taken with the following configurations: only using the QDC branch;[12] using the QDC and SADC branch in parallel;[13] using the SADC branch only.[14] The TDC branch was used in all cases. Each branch has its own signal filter optimized for its requirements.

3.2.1 Signal Filter

Signals coming from the charge sensitive preamplifier have a long decay time of $\tau_{\text{decay}} = 54\,\mu\text{s}$. This will lead to pile-up of the subsequent signals. To separate these pulses, a high-pass filter (CR) is applied that only responds to the rising edge of the preceding signal.[15] In

[11] One channel for each of the two APDs per crystal.
[12] Data taking in December 2017, May 2018, October 2018, November 2018, and February 2019.
[13] Part of data taking in June 2021 and November 2021.
[14] Since data taking in June 2021, except for periods when QDCs were used in parallel.
[15] Not all pile-up events can be separated with equal precision. Pile-up events that are close enough will still lead to pile-up in the output of the signal filter.

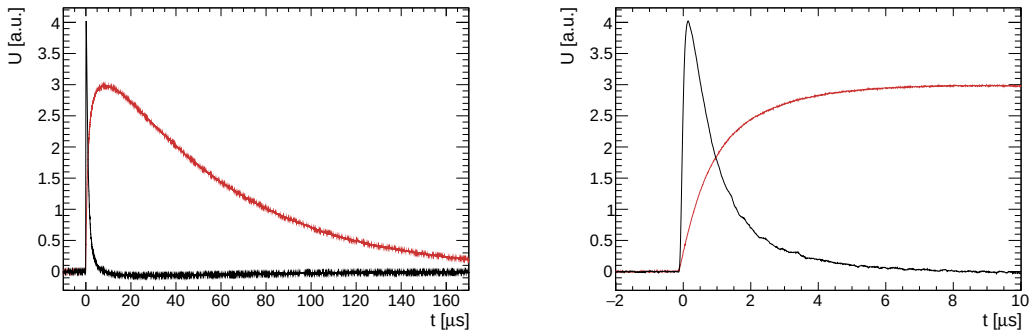

Complete signal

Rising edge of the signal

Figure 3.5: Comparison of the output signal of the charge sensitive preamplifier with the output of the **signal filter** in the TDC branch. The signal generated by the preamplifier reaches its maximum after 10 µs. Its decay time is about $\tau = 54\,\mu s$. In contrast, the shaped signal reaches its maximum after about 300 ns and has a decay time of the order of 1 µs. All signals were recorded on an oscilloscope in a laboratory where an equivalent readout was constructed for a single crystal as it is used in the experiment.

addition, the output of the preamplifier exhibits frequency-dependent $1/f$-noise (APD shot noise) and frequency-independent white noise (thermal noise). The noise is suppressed by using a low-pass filter (RC) after the high-pass filter [128]. The combination of high-pass and low-pass filters $(CR)^N$-$(RC)^M$ is called a signal filter, or equivalently a shaper. N and M are the number of high-pass and low-pass filters, respectively. The effect of the signal filter in the TDC branch is shown in Fig. 3.5. In some cases, the output signal shows an undershoot. This is due to the slow discharge behavior of the feedback capacitor in the preamplifier. The CR high-pass filter reacts to the decay of the incoming signal, resulting in a drop below the baseline. To correct this, pole-zero cancellation is used, which is the compensation of the undershoot by a resistor in parallel with the capacitor of the first high-pass filter.

3.2.2 The TDC Branch (Time)

To obtain a logical signal that meets the requirements for trigger decisions, the signal is shaped with a $(CR)^1 - (RC)^2$ signal filter [80]. The signal filter is designed to output signals that reach their maximum within the first 300 ns and that have a decay time of about $\tau_{\text{decay}} = 1\,\mu s$ (cf. Fig. 3.5). This allows time information to be extracted within the trigger requirements using leading edge discriminators.

3.2.2.1 Discriminators

Discriminators are used to digitize time information from an analog signal. There are two types of discriminators. The first is a leading edge discriminator, which outputs a logic pulse when the incoming signal reaches a certain threshold. The second type is a constant fraction discriminator. Here, a logic pulse is output when the incoming signal reaches a certain fraction of its peak value.

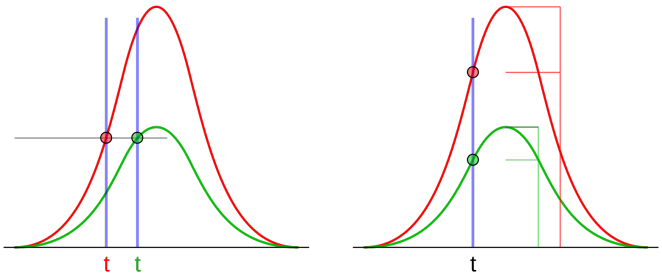

Figure 3.6: Comparison of a leading edge discriminator (left) and a constant fraction discriminator (right) [135].

Leading Edge Discriminators By comparing the incoming signal to a reference voltage, the discriminator effectively sets a threshold. When the voltage of the signal exceeds the reference voltage, a logic pulse is generated. A major drawback of the leading edge discriminator is the dependence of the logic pulse and timing information on the signal shape. Signals with higher energy have a steeper leading edge than signals with lower energy at the same threshold. At this threshold, the first signal would be assigned an earlier timestamp than the second signal, even if both signals originated at the same time (cf. Fig. 3.6 (left)). The dependence of time on the energy of the signal is called time walk.

Constant Fraction Discriminators In the case of constant fraction discriminators, the threshold is fixed at a certain fraction of the peak value of the signal. This is done by delaying and subtracting the signal, resulting in a zero crossing that is independent of the signal scale (cf. Fig. 3.6 (right)). As a result, the time information is free of time walk. The main drawback of the constant fraction discriminator is a certain delay because the whole signal must be considered and not only its leading edge.

While the MiniTAPS detector uses constant fraction discriminators, for the Crystal Barrel detector the resulting delay would prevent its use as a fist-level trigger [133]. Instead, leading edge discriminators are used, requiring a correction of the time walk behavior (cf. Section 4.1.4). A dual comparator[16] allows the extraction of two times at different thresholds for each signal [134]. A full discriminator module can support up to 92 crystals, each with such a dual-threshold setting.

3.2.2.2 Time-to-Digital Converter

The final time information is extracted by connecting the discriminators to time-to digital converters (TDCs). A TDC determines the time difference between a signal and a reference signal. In the case of the CBELSA/TAPS experiment, the reference time corresponds to

[16] A comparator is a key component of a leading edge discriminator, comparing the input signal with the reference voltage.

the time of the trigger, while the signal corresponds to a specific detector. A more detailed explanation of the functionality of TDCs in general and their use in the CBELSA/TAPS experiment is given in [81, 103].

During the recent modification, the previously used CATCH[17] multihit TDCs [136] were replaced by jTDCs [137, 138]. The main reason for this change was the high rate and buffering capability of jTDCs. Detectors using jTDCs are the bars, and fibers in the Tagger, the Forward Veto, MiniTAPS Veto, Inner and Cherenkov detector and the Gamma Intensity Monitor. While jTDCs are used in most detector components they are not practical for the larger Crystal Barrel detector because they only support 99 channels each, resulting in high resource consumption. Instead, another type of time-to-digital converter (pTDC) has been developed in [81]. For completeness, both the pTDC and the jTDC are described below, although the jTDC is not used in the Crystal Barrel detector. However, the jTDC will be relevant for the calibrations discussed in Chapter 4.

jTDC A jTDC is a time-to-digital converter implemented on an FPGA. With the Xilinx Spartan 6, 99 input channels are supported [138]. High rate compatibility is achieved by using a BRAM-recorder.[18] On each clock cycle, the address is incremented, allowing the input information (hit or not hit) to be stored without buffering. The BRAM is clocked at 200 MHz, resulting in a double pulse resolution of 5 ns. Furthermore, a double-page memory[19] ensures continuous data taking even during readout. To improve time resolution, a tapped-delay-line method is used, sampled at 400 MHz.[20] In the tapped-delay-line method, a chain (carry chain) of flip-flops delays and tracks the propagation of the signal within a sampling interval. At the beginning of a new interval, the position of the signal within the carry chain provides additional fine resolution. The coarse resolution is provided by the clock itself. In order to use the fine time resolution a calibration must be performed (cf. Section 4.1.2) to account for an individual propagation time for each carry chain element. After calibration, the theoretical time resolution of a jTDC is of the order of 30 ps RMS [138].

pTDC The pTDC uses an integrated deserializer component instead of a tapped-delay-line [81]. The time resolution of this approach is lower compared to a jTDC due to the lack of the fine time resolution, but so is the resource consumption. It allows for more than 185 input channels on a single pTDC module. Each deserializer is a chain of flip-flops operating at an effective frequency of 800 MHz to sample the signal. This results in a bin width of 1.25 ns, which meets all the requirements of the Crystal Barrel detector.

Similar to the jTDC, the pTDC uses a ring buffer[21] equipped with BRAM elements. The buffer allows for a trigger window (gate) of about $\pm 10\,\mu s$ around the trigger time of the experiment in which the pTDC is sensitive to input data. In comparison, the gate of the QDC, which is used to measure energy information, has a much shorter length of 6 µs starting at the trigger time of the experiment. The same is true for the integrating window of the

[17] **C**OMPASS **A**ccumulate, **T**ransfer and **C**ontrol **H**ardware

[18] BRAM refers to on-chip memory.

[19] Page refers to a different address block in the memory that is addressed by flipping a bit.

[20] The sampling rate of the clock at 200 MHz is doubled by double data rate (DDR), where the rising and falling edges of the clock signal are used for sampling.

[21] In a full ring the newest entry replaces the last.

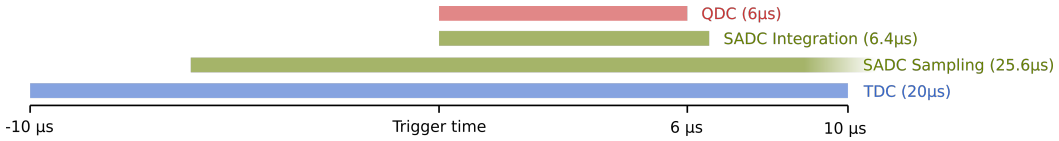

Figure 3.7: Comparison of the trigger window (gate) of the pTDC with the gate of the QDC and with the integration and sampling gate of the SADC. The times are given relative to the experiment trigger.

SADC. As a result, the time information of pTDCs can be used to investigate coincident time background and pile-up detection (cf. Fig. 3.7; cf. Chapter 5). In contrast to the jTDC, no further calibration is required since the deserializer components use a fixed effective frequency.

3.2.3 The QDC Branch (Energy)

While the signal filter in the TDC branch produces signals as short as possible, the signal filter in the QDC branch is optimized for more accumulated signal to improve the SNR for energy measurement. Therefore, a $(CR)^3$-$(RC)^3$ signal filter is used [139]. To extract energy information, the signal filter is connected to a charge-to-digital converter.

3.2.3.1 Charge-to-Digital Converter

A charge-to-digital converter (QDC) integrates and digitizes the charge information of an input signal using a 96-channel 12-bit Fastbus ADC [140]. A capacitor is used for the integration. The integration window (gate) is set to start at trigger time and to end after 6 µs to allow a good amount of accumulated signal and a high SNR (cf. Fig. 3.7). To increase the dynamic range of the detectable energy information while maintaining good energy resolution for low energy signals, a dual-range logic is used. The incoming signal is divided into three parts in an 8:1:1 ratio. While the first two parts of the signal each charge a capacitor, the last part is used for test purpose only. A comparator is used to decide which voltage to digitize. Low energy signals are digitized with their full integral, giving good energy resolution. High energy signals are digitized in their downscaled form, resulting in a wide dynamic range. The first mode is called low-range and the second one is called high-range. A high-range flag is set to distinguish between the two cases. Since the ratio between the low- and high-range can vary, a calibration must be performed to determine the exact factor for each channel (cf. Section 4.2.2). The dead time of the QDC limits the readout rate to a maximum of 2 kHz. This is one of the reasons why SADCs were integrated as an alternative readout.

3.2.4 The SADC Branch (Energy & Time)

Extracting energy information using QDCs has several drawbacks. The dead time of the QDCs is the limiting factor for the readout rate. In addition, the signal is integrated regardless of the shape of the pulse, which can lead to pile-up errors. The TDCs used to extract time information also have limitations. Threshold discriminators can only generate time information for signals above a certain height. As a result, low energy signals below the

threshold have no time assigned. New sampling techniques and processing on FPGAs solve these problems. This allows for a higher rate and improved data quality through pile-up detection, event-based pedestal subtraction and time information even for low-energy signals. Such an FPGA-based sampling ADC has been designed and included in the experiment in [82, 141]. A $(CR)^1$-$(RC)^2$ signal filter is used which is complemented by a $(RC)^1$ component on the SADC itself. Thus, an effective $(CR)^1$-$(RC)^3$ behavior is achieved. The first data taking with full SADC readout took place in June 2021 partly in parallel with the QDC readout. Later measurement periods use only SADCs to benefit from increased data readout rates.[22]

3.2.4.1 Sampling-Analog-to-Digital Converter

The sampling-analog-to-digital converter (SADC) is implemented on an FPGA and digitizes voltage waveforms with a fixed sampling rate [82, 141]. While the sampling runs at 80 MHz, the post-processing on the FPGA reduces the rate to 20 MHz by adding four samples at a time. A so-called feature extraction allows the extraction of certain information from the waveform already on the FPGA. Common features are the integral, the maximum and the time of the waveform. It is then possible to pass on only these features for storage instead of the full waveform.

In addition to the higher readout rate of the SADC, the sampling technique combined with the feature extraction leads to several advantages of the SADC compared to the readout within the QDC and TDC branches. For example, event-based pedestal subtraction can be performed during data taking by using sampled information between signals. For QDCs, a special clock-triggered measurement must be performed before each run.[23] Here, a potential drift in the measurement during a run cannot be corrected. Furthermore, as the SADC can also analyze the pulse shape of the signal, pile-up detection is possible. During later analysis, pulses flagged as pile-up can be recovered using the waveforms stored on disk [141]. To minimize disk space, waveforms are saved only in the case of a detected pile-up and optionally for some additional randomly selected events for further analysis. Another advantage is the lack of discriminator thresholds. While TDCs can extract time information only above a certain discriminator threshold, SADCs have no such limitation. Here, time information can be extracted down to 1 MeV[24] [142]. The constant fraction functionality also eliminates the need for time walk correction. Nevertheless, the time resolution provided by the TDCs is better over a wide energy range (cf. Section 5.1). During the first periods of data taking, the SADCs lacked multihit functionality. It was implemented for data taking after June 2021 [142].

3.3 The Light Pulser System

The light pulser system allows the simulation of energy deposition in the scintillating material of each crystal by using a signal of a well-defined height with high frequency [79]. When

[22] An exception is data taking in November 2021, where data were also partially recorded with QDCs.

[23] A period of data taking is divided into several runs, each run corresponding to approximately 30 min of data taking.

[24] This does not mean that time information is always available at such low energies. In some cases, the integral is > 1 MeV, but no peak (and no time) can be determined.

the readout was modified, the light pulser system was also renewed. Most notable is the change from gas discharge lamps to LEDs. This results in a higher flash rate, higher intensity, and finer adjustability of the simulated signals. Without the APD bias voltage applied, an average energy equivalent of 300 MeV can be achieved at maximum light intensity. With the bias voltage applied, the full energy range of the readout can be covered. In [79] a flash rate of 1.4kHz is mentioned.

The light pulser system is divided into six different sectors, each of which can have different settings. Each sector corresponds to a collection of crystals in the Crystal Barrel detector. The first three sectors cover the entire upstream part of the detector, while the other three sectors cover the downstream part of the detector. The light pulser system serves two main purposes: to calibrate the dual-range logic of the QDCs (cf. Section 4.2.2) and to monitor the stability of the APD gain.

3.4 The Energy Sum (∑)

During data taking, as many useful events as possible should be recorded. The dead time of recording uninteresting events must therefore be minimized. For this reason, an energy sum is currently being developed which further increase the selectivity of the Trigger system. The energy sum corresponds to modules that sum up all the analog signals in the Crystal Barrel detector. Since the information must be available at trigger time, signals from the TDC branch are used. When calibrated, the output is proportional to the total energy deposited in the detector [143, 144]. This can now be used to exclude uninteresting events. An example of such events are events with low-energy beam photons, where the high-energy electron could not have been detected by the tagging system.[25] By setting an appropriate threshold for the energy sum, these events can be filtered out already during data taking. The threshold has to be determined carefully in simulations.

[25] The Tagging system can cover a photon energy range between 11.9 % and 97.9 % of the incoming electron energy E_e^{in} [96].

CHAPTER 4

Calibrations for the Crystal Barrel Detector

For accurate energy and time information, the detector output must be calibrated. While Section 4.1 explains the calibration methods for the time readout, Section 4.2 explains the calibrations related to the energy readout.

4.1 Calibration of the Time Readout

Raw values from TDCs are converted to time in a process known as time calibration (cf. Section 4.1.1). Time calibration is performed not only for the Crystal Barrel detector, but for all detectors using TDCs. In the case of jTDCs, an additional calibration of the carry chains is required. It is also explained here for completeness, although jTDCs are not explicitly used in the Crystal Barrel detector (cf. Section 4.1.2). In addition, the recent modification of the readout has resulted in the need for additional calibration methods. The use of leading edge discriminators in the Crystal Barrel detector requires a correction of the time walk behavior (cf. Section 4.1.4). This in turn requires the exact determination of the threshold heights, which are set within the discriminator modules (cf. Section 4.1.3).

4.1.1 Time Calibration

TDCs digitize relative time differences in units of their channel width. The conversion of the raw TDC values T to a meaningful time t is given by

$$t = g \cdot T + a. \tag{4.1}$$

The calibration factor g is used to convert raw TDC values to time. The offset a compensates for different transmission times due to cable lengths and electronic behavior. The calibration factor g can be calculated if the frequency of the sampling clock and thus the bin width of the TDC channels is known. Only for the MiniTAPS detector a more complex determination of g is needed [103]. Also, for the fine time resolution of jTDCs, an additional calibration is required to obtain the effective bin width. The offset a must be determined on a per-channel basis for each beam time. Therefore, the times of the photons from each detector are first compared to the trigger time. Any systematic deviation is due to differences in the time-of-flight behavior of the photons and non-zero transmission times, and can be used as a first coarse calibration a_{coarse}. After the coarse calibration, the time of each TDC channel relative to the trigger signal is distributed around 0 ns.[1]

[1] It is not exactly at 0 ns due to the finite resolution of the detectors.

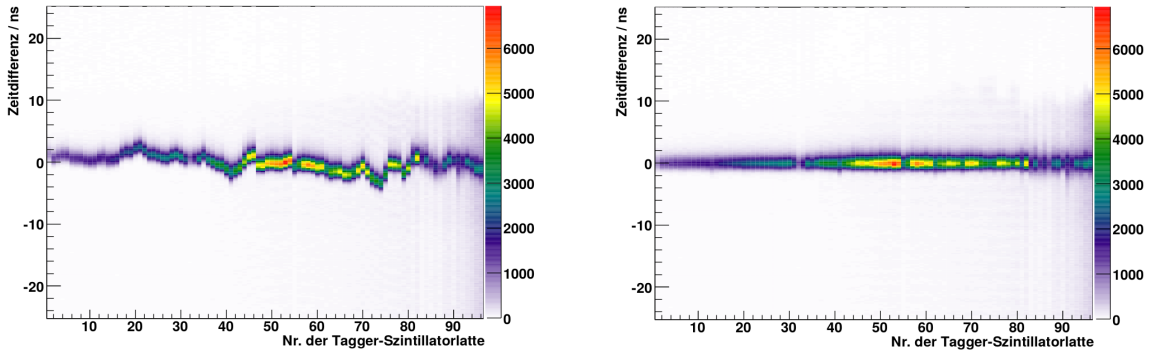

After coarse and before fine calibration

After coarse and after fine calibration

Figure 4.1: Time difference between the Tagger bars and the Cherenkov detector before and after fine time calibration [103].

The coarse calibration is limited by the time resolution of the trigger signal. For higher accuracy, the time differences of each detector to a reference detector with good time resolution are examined in a second step. In this way, the influence of the trigger signal disappears as

$$\Delta t = (t_{\text{det}} - t_{\text{trig}}) - (t_{\text{ref. det}} - t_{\text{trig}}) = t_{\text{det}} - t_{\text{ref. det}}. \tag{4.2}$$

The position of the prompt peak[2] Δt_{prompt} can then be used for a more precise calibration offset

$$a_{\text{fine}} = a_{\text{coarse}} + \Delta t_{\text{prompt}}. \tag{4.3}$$

The Tagger bars are used as a reference detector because of their good time resolution. For fine calibration of the Tagger bars, the Cherenkov detector is used, which also has a good time resolution. In Fig. 4.1 the time difference of Tagger bars to the Cherenkov detector is shown before and after fine time calibration. In this way, the resulting accuracy of the calibration is limited by the time resolution of the Cherenkov detector. Further improvement is possible by iteratively calibrating the Tagger bars with the MiniTAPS detector as reference and vice versa. Both detectors are expected to provide better time resolution than the Cherenkov detector. The final calibration values for all detectors can then be determined by using the Tagger bars as reference again, but now with optimized resolution.

4.1.2 Calibration of jTDCs

Time information from jTDCs consists of two components: the coarse time resolution of the clock and the fine time resolution given by the position of the leading edge within the carry chain. With proper calibration of the carry chain, it is possible to combine both parts. The coarse time resolution is defined by the effective sampling frequency of 400 MHz (2.5 ns) which corresponds to half a clock cycle of a 200 MHz clock with dual data rate[3] (DRR). Based on the position of the leading edge within the carry chain, each sampling interval

[2] Distribution of the different Δt.

[3] Sampling is performed on the rising and the falling edge of the clock signal.

can be divided into N_{max} further intervals. N_{max} corresponds to the maximum number of carry chain elements on the FPGA through which the signal can propagate in a full sampling interval. Thus, the information of a jTDC can be converted to time as

$$\begin{aligned} t &= t_{\text{coarse}} + t_{\text{fine}} \\ &= \frac{1}{400\,\text{MHz}} \left(N_{\text{sampling}} + C\left(\text{TDC}_{\text{channel}}, N_{\text{carry chain}}\right)\right) \end{aligned} \tag{4.4}$$

where $N_{\text{carry chain}}$ is the final position of the signal within the chain. The calibration coefficient $C\left(\text{TDC}_{\text{channel}}, N_{\text{carry chain}}\right)$ takes into account the different propagation time of each carry chain element. It corresponds to the fraction of a sampling interval that has to be added. For each detector using jTDCs,[4] the calibration coefficient must be determined for all carry chain elements over all TDC channels.

A suitable method for calibration has been proposed in [138] and implemented for the CBELSA/TAPS experiment in [145]. By examining the frequency distribution of carry chain elements, information about relative differences in propagation times can be obtained. Because the input signals at the jTDC are not correlated with the sampling clock, carry chain elements with shorter propagation times will have fewer entries than carry chain elements with longer propagation times. An example of such a frequency distribution and the resulting calibration values can be seen in Fig. 4.3. In [145] the dependence of the calibration on temperature and rate was investigated. While a dependence on temperature is clearly observed, the resulting uncertainty is significantly lower than the best time resolution achieved in the experiment. Furthermore, the calibration values do not show a significant dependence on the rates observed in the experiment. The only significant discrepancies occur at times when the FPGA firmware is changed, resulting in discrete jumps in some calibration values.[5] Therefore, a separate calibration must be performed for each time interval with constant firmware.

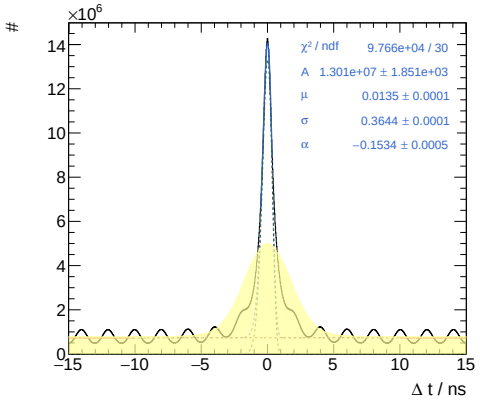

Figure 4.2: Time distribution of Tagger bars relative to themselves **with** and without carry chain calibration of jTDCs [145].

The time difference of coincident hits in the Tagger bars with and without jTDC carry chain calibration is shown in Fig. 4.2. Without calibration (yellow area) the time resolution

[4] Detectors using jTDCs are the bars and fibers in the Tagging system, the Forward Veto, the MiniTAPS Veto, the Inner and Cherenkov detector, and the Gamma Intensity Monitor. An exception is the December 2017 data, where only the bars and fibers in the Tagging system and the Gamma Intensity Monitor were equipped with jTDCs.

[5] Firmware updates can change the internal routing of signals within the FPGA, which can have a significant impact on the timing characteristics.

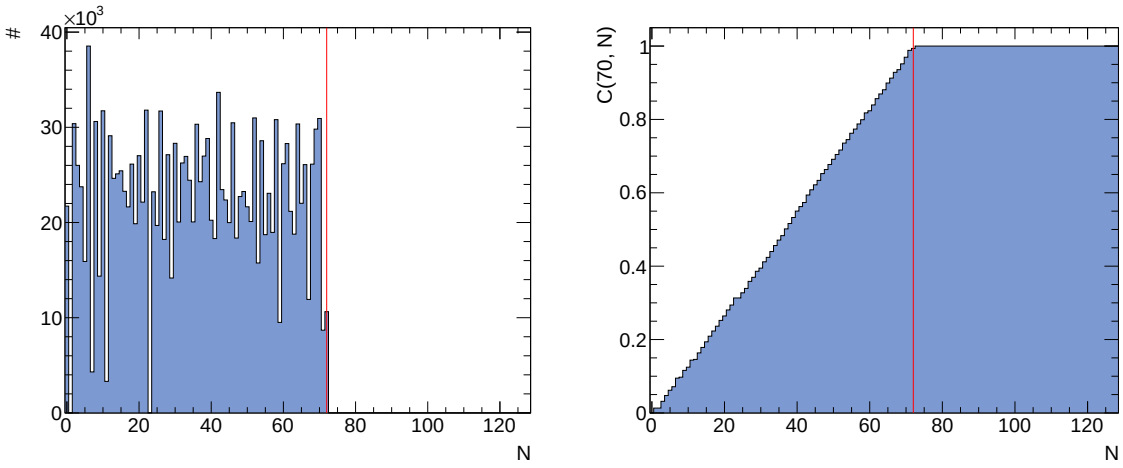

Frequency distribution of the carry chain

Calibration values

Figure 4.3: Frequency distribution of the carry chain for Tagger bar 70 and the corresponding calibration values. The maximum carry chain index $N_{\max}$ that can be reached in one full sampling interval corresponds to the red line [145].

is limited by the sampling frequency of 400 MHz. After calibration, the peak distribution is much narrower and the bunch structure of ELSA becomes visible. While in [145] the calibration of the jTDC calibration is performed for data taken in December 2017 and May 2018, in this work it is performed for later data.

4.1.3 Threshold Determination

Each TDC channel in the Crystal Barrel detector is connected to a preceding threshold discriminator. The threshold height (position) of a discriminator can be adjusted by applying a reference voltage to the comparator component. The exact height varies from crystal to crystal due to electronic tolerances, differences in the light yield of the crystals or a non-identical APD or preamplifier gain. Since the time information depends on the threshold heights, their values must be accurately determined in units of energy. In [145] a method was developed to determine the threshold heights. A ratio R between the number of hits detected above the threshold and all hits is used

$$\mathrm{R}(E) = \frac{\text{above threshold}}{\text{all}}. \tag{4.5}$$

Below the threshold the ratio is zero, above the threshold the ratio is one. Considering noise and finite energy resolution, the step-like transition at the position of the threshold is convolved with a Gaussian of width σ_{noise}. This results in an S-shaped curve given by

$$\mathrm{R}(E) = \frac{1}{2} \cdot \left(1 - \mathrm{erf}\left(\frac{\Theta - E}{\sqrt{2} \cdot \sigma_{\text{noise}}}\right)\right) \tag{4.6}$$

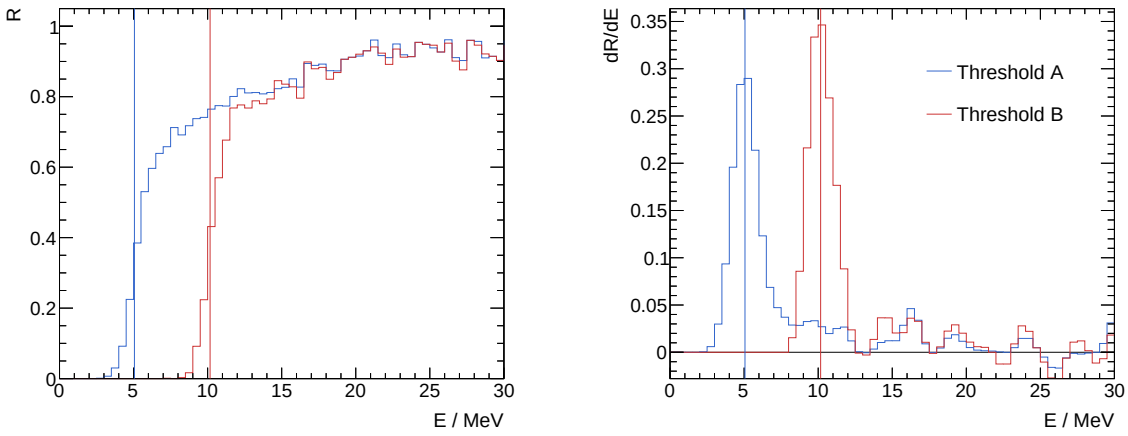

$R(E)$ Derivative of $R(E)$

Figure 4.4: Ratio R (cf. Eqn. 4.5) as well as its derivative for crystal 242 during data taking in December 2017. The vertical lines correspond to the final threshold heights obtained by fitting Gaussian functions to the peaks [145].

where Θ corresponds to the position of the threshold. To determine the position of the threshold, the derivative of the ratio $R(E)$ is calculated, resulting in a Gaussian with mean Θ and width σ_{noise}. The height of a threshold is then defined by fitting a Gaussian function to the derivative of $R(E)$. This method is robust because it is largely independent of the exact shape of the transition. An example of the ratio $R(E)$, its derivative, and the corresponding determined threshold positions are shown in Fig. 4.4. The thresholds can be characterized by their height (position) Θ and the amount of smearing σ_{noise}, which is related to noise and energy resolution.

Threshold height The dual-threshold discriminators allow two thresholds for each crystal. The lower threshold is called A and the upper threshold is called B. In Fig. 4.5 (top) the determined threshold heights are shown for the June 2021 data. In order to suppress low energy electromagnetic background events, the threshold height is increased step by step in the forward direction. The last ring in the Crystal Barrel detector also has increased thresholds to deal with an increasing rate of low energy events.[6] In Table 4.1, average threshold heights for the different crystal regions are listed. In [145] the thresholds were determined for data taken in December 2017 and May 2018, whereas in this work this calibration is performed for later data.

Threshold smearing The positions of the thresholds are smeared due to noise and finite energy resolution. The amount of smearing is given by as σ_{noise} and is shown in Fig. 4.5 (bottom) σ_{noise}. Excluding the most forward crystals the smearing is well below 1 MeV.

[6] A possible source of these low energy events in the last ring is the cryostat of the Mainz-Dubna Frozen Spin target. The increasing rate of low energy events was detected only after the switch to this target. However, it is not clear why this is the case. Another possibility is scattering effects of the beam at the collimator.

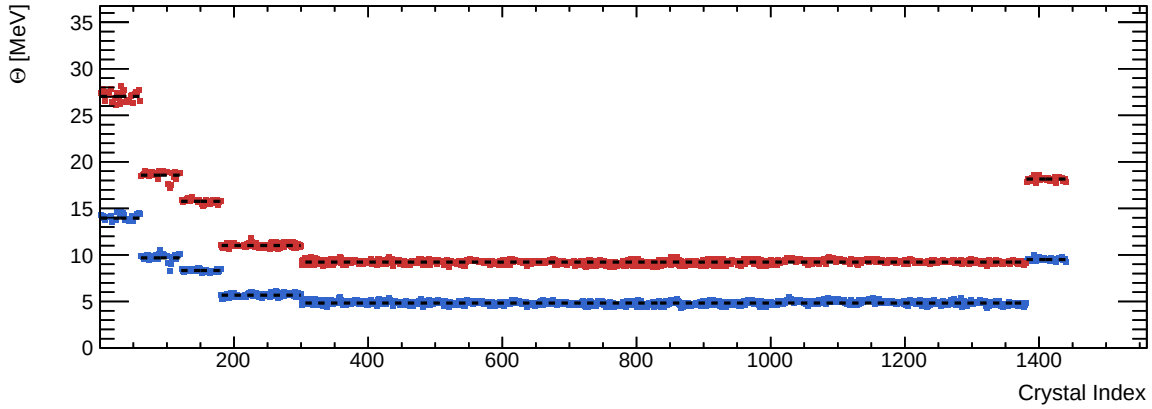

Position of the thresholds

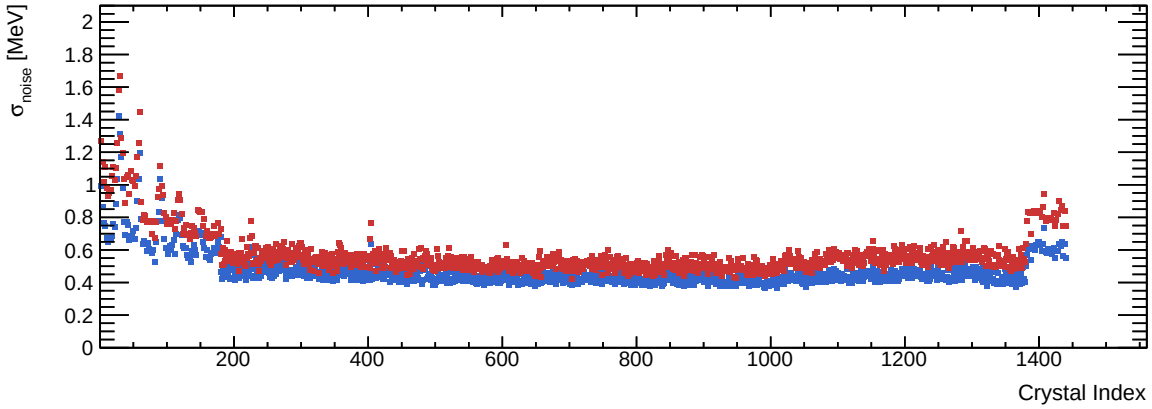

Smearing of the thresholds

Figure 4.5: Threshold A and threshold B for each crystal for the June 2021 data.

Table 4.1: Average threshold heights of crystals with similar threshold configuration (cf. Fig. 4.5 (top)) for the June 2021 data. Thresholds for other periods of data taking may be different.

Crystal index	Ring	Θ [MeV]	
		A	B
1 – 60	1	14.0	27.0
61 – 120	2	9.7	18.6
121 – 180	3	8.3	15.8
181 – 300	4 – 5	5.7	11.0
301 – 1 380	6 – 23	4.8	9.2
1 381 – 1 440	24	9.5	18.2

4.1.4 Time Walk Correction

The use of leading edge discriminators introduces the need for time walk correction. Time walk describes the dependence of the time information on the energy of the signal as well as on the threshold height. The time walk behavior can be seen particularly well in the time difference between the Tagging system and the crystals as a function of energy

$$\Delta t(E) = t_{\text{Tagger}} - t_{\text{Crystal}}(E). \tag{4.7}$$

By using the time difference, the poor resolution of the trigger time is removed. Due to time walk, a strong energy dependence of $\Delta t(E)$ is expected. This is clearly the case for the Crystal Barrel detector where time walk occurs up to 300 ns (cf. Fig. 4.6 (top)).

In [145] a time walk correction function has been developed that is valid for all threshold configurations. During the reconstruction process the correction is applied to all given times. Depending on the energy and threshold of the crystal, a time offset is applied to compensate for the walk.[7] As shown in Fig. 4.6 (middle) & (bottom), the correction improves the time walk by two orders of magnitude. Small deviations in the low energy range are negligible when compared to the time resolution in the same range.

4.2 Calibration of the Energy Readout

The output of QDCs or SADCs is converted to energy information in a process known as energy calibration (cf. Section 4.2.1). For QDCs, an additional high-range calibration is required to determine the exact ratio between the low- and high-range (cf. Section 4.2.2).

4.2.1 Energy Calibration

The raw values of the QDCs or SADCs are linearly dependent on the energy. The gain g must be determined for each ADC, i.e. for each crystal in the Crystal Barrel detector. After calibration, the energy can be calculated as

$$E = \left(\text{ADC}^{\text{low}} - \text{ADC}^{\text{low}}_{\text{pedestal}}\right) \cdot g. \tag{4.8}$$

ADC^{low} corresponds to the output of the ADC in low-range.[8] $\text{ADC}^{\text{low}}_{\text{pedestal}}$ corresponds to the baseline measured at zero intensity and must be subtracted. The gain is determined by comparing the reconstructed π^0 invariant mass with the literature value. The choice of the π^0 invariant mass for the comparison has several advantages. Besides the high probability of producing the π^0, the π^0 also decays into two photons with a high probability of 98.82 % [7]. The invariant mass of the π^0 is then reconstructed using

$$M^{\text{rec}}_{\pi^0} = E_{\gamma_1} E_{\gamma_2} \left(1 - \cos(\alpha_{\gamma_1\gamma_2})\right), \tag{4.9}$$

[7] The correction is only valid for times related to the measured energy information i.e., times around the trigger.

[8] The distinction between low- and high-range is only relevant for QDCs and is explained in more detail in Section 4.2.2.

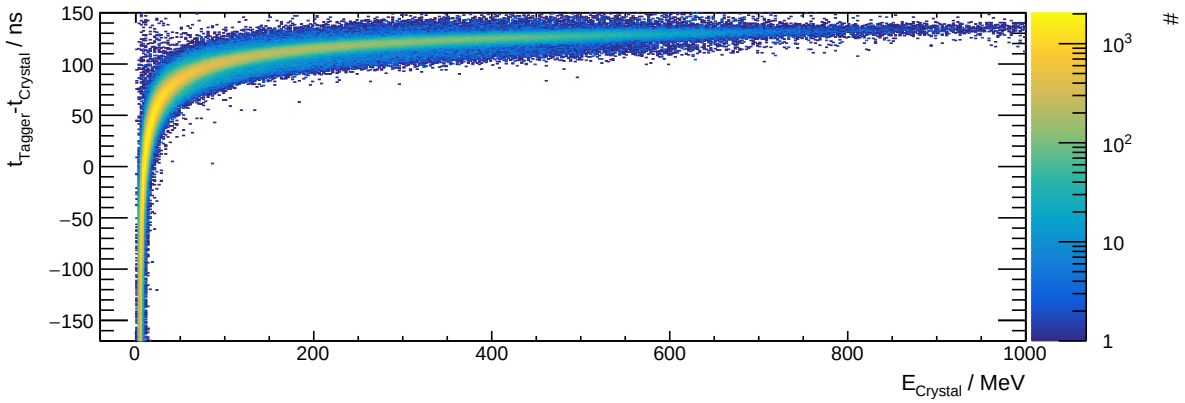

Uncorrected time walk of threshold A for crystals with index 181 to 300

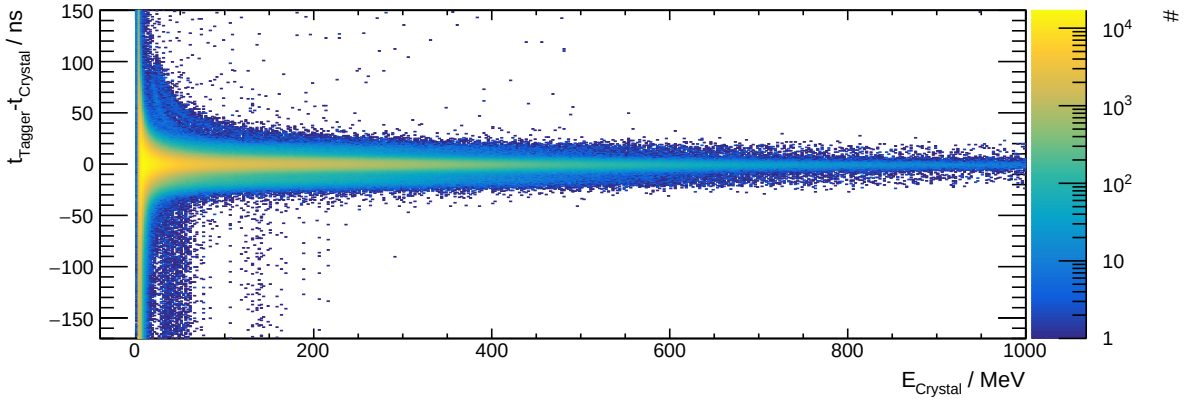

Corrected time walk of threshold A

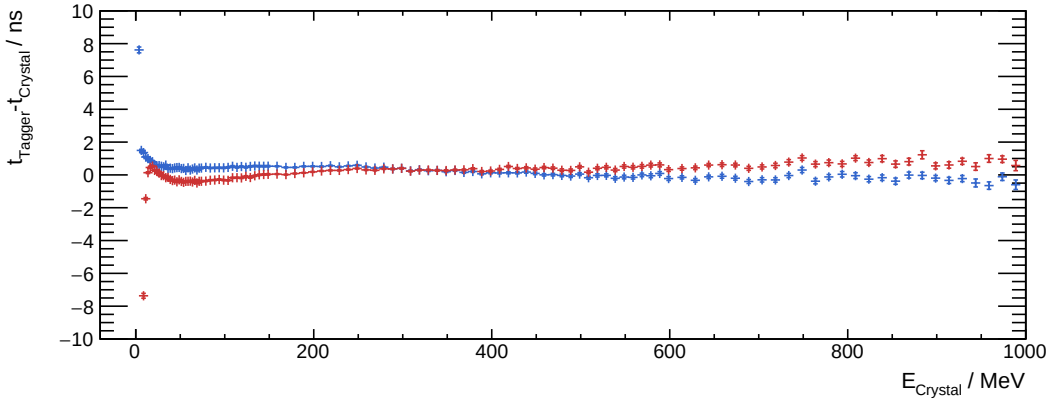

Mean of corrected time walk of threshold A and threshold B

Figure 4.6: Comparison of the time walk behavior of the Crystal Barrel detector before and after the correction [145]. Only crystals with energy deposition by photons from a π^0 decay for the December 2017 data are shown.

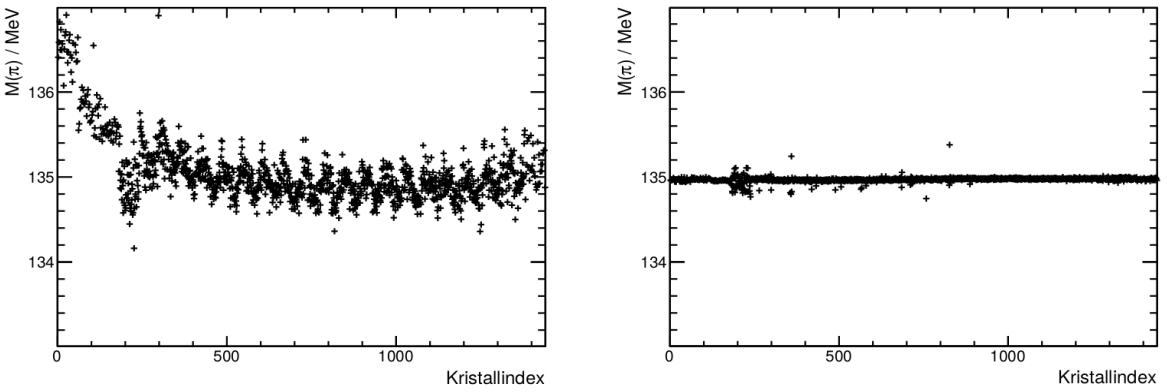

Before calibration After calibration

Figure 4.7: Reconstructed π^0 mass for each crystal inside the Crystal Barrel detector before and after energy calibration [146]. The deviations in the crystal indices around 180 are due to the transition between the main and the forward part of the Crystal Barrel detector.

with the photon energies $E_{\gamma_{1/2}}$ and the opening angle $\alpha_{\gamma_1\gamma_2}$. Photons entering the material deposit their energy in multiple crystals via electromagnetic showers. As a result, the photon energies depend on all the gains for those crystals. Also, the opening angle is indirectly affected by an energy-weighted reconstruction of the direction (cf. Section 6.1.3). To calibrate the gain factor for a single crystal, only events where that crystal has the highest energy are selected. In this way, the gain factor of that crystal has the greatest influence on the photon energy and the reconstructed invariant mass. By comparing the reconstructed mass with its literature value, the gain of this crystal can be adjusted with [146]

$$g_{\text{after}} = \left(\frac{M_{\pi^0}^{\text{lit}}}{M_{\pi^0}^{\text{rec}}} \cdot (1-d) + d \right) \cdot g_{\text{before}}. \tag{4.10}$$

Since the new gain depends on the gain of the other crystals, this process must be repeated in several iterations. In each iteration, the gain of each crystal is adjusted once. A damping factor d is introduced to account for systematic effects that could lead to overcorrection and lack of convergence even after several iterations. The process is stopped when the reconstructed mass is at the literature value. The effect of the energy calibration is shown in Fig. 4.7. For the very first calibration, carefully selected values were determined in [147] and used as a starting point. Afterwards, the most recent gains are used as a starting point to perform a calibration on new data.

4.2.2 High-Range Calibration

For QDCs, an additional high-range calibration is required to determine the exact range factor r between the low- and high-range for each ADC. After calibration, high-range values

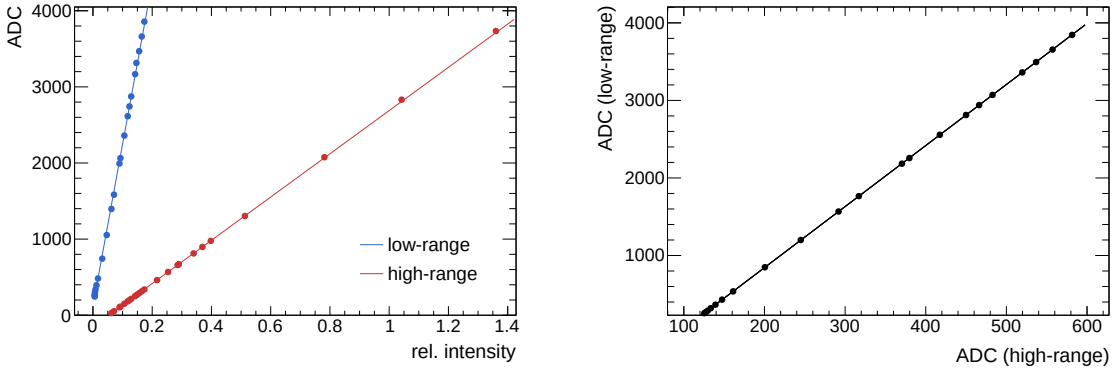

ADC vs. Intensity ADC vs. ADC

Figure 4.8: Left: ADC values in low- and high-range as a function of normalized intensity. The ratio of the slopes corresponds to the calibration factor r. Right: The ADC values in the low-range as a function of the ADC values in the high-range. The slope is directly related to the calibration factor. Data are shown for crystals 1354 (left) and 1264 (right) during data taking in June 2021.

can be converted to low-range values using

$$\begin{aligned} \mathrm{ADC}^{\mathrm{low}} &= \mathrm{ADC}^{\mathrm{high}} \cdot r + \left(\mathrm{ADC}^{\mathrm{low}}_{\mathrm{pedestal}} - r \cdot \mathrm{ADC}^{\mathrm{high}}_{\mathrm{pedestal}}\right) \\ &= \mathrm{ADC}^{\mathrm{high}} \cdot r + r^{\mathrm{offset}}. \end{aligned} \tag{4.11}$$

While $\mathrm{ADC}^{\mathrm{low}}_{\mathrm{pedestal}}$ can be measured at zero intensity, this is not the case for $\mathrm{ADC}^{\mathrm{high}}_{\mathrm{pedestal}}$. Therefore, an explicit determination of the range offset r^{offset} is used instead. After converting the high-range values to low-range value, the energy calibration can be used to obtain final energy information.

There are two methods for determining the range factor and offset [79]. Both methods use the light pulser system to simulate energy deposition in scintillating material with signals of well-defined intensity and high rate. The intensity can be adjusted by using a 12bit digital-to-analog converter (DAC). In both methods discussed below, data is recorded from each crystal for a given set of intensities using the low-range of the ADC as well as a forced readout of the high-range.[9] These light pulser runs are referred to as low-range runs and high-range runs, respectively.

ADC vs. Intensity The relationship between DAC values and the emitted intensity of the light pulser was investigated in [79]. This relationship can be used to determine the linear dependence of low- and high-range ADC values on the intensity (cf. Fig. 4.8 (left)). The ratio of the slopes then corresponds to the calibration factor r. The offset r^{offset} is determined using the measured low-range pedestal (at zero intensity) and the y-axis intercept for the high-range dependence as the high-range pedestal (cf. Eqn. 4.11). The *ADC vs. Intensity* method has the disadvantage of a non-linear relationship between the DAC values and the

[9] Forced readout refers to a readout of the high-range even in cases where the signal is below the threshold for downscaling.

emitted intensity, which must be carefully determined. The preferred calibration method is therefore the one described next.

ADC vs. ADC To avoid converting the DAC settings to intensities, the ADC values for low- and high-range can be compared directly. The only requirement is that the selected DAC values must occur simultaneously in low- and high-range. However, DAC values in the low-range will, by design, only populate small values in the high-range. Complicating matters further, the high-range pedestal can vary greatly from crystal to crystal. The required overlap area between low- and high-range may be only a few percent of the total available range. This results in the need for highly optimized DAC settings that apply to all crystals. In [148] the DAC settings have been optimized to allow as much data as possible while still being evenly distributed. In cases where the overlap area is insufficient, the *ADC vs. Intensity* method can be used as an alternative. Fig. 4.8 (right) shows the relationship between low- and high-range values for the optimized DAC settings. The slope is directly related to the calibration factor R and the y-axis intercept to the offset r^{offset}.

CHAPTER 5

Time Information in the Crystal Barrel Detector

Time information is extracted as part of the readout process (cf. Chapter 3), allowing for the correlation of signals from multiple detectors. This correlation helps to eliminate random coincidences during event reconstruction and selection. For the widely used multihit TDCs, two different scenarios can occur. In the first scenario, a single signal within a crystal generates only one timestamp.[1] This timestamp uniquely represents the time of the signal and can be easily used for further analysis. However, as a second scenario, situations may arise where a single signal produces multiple timestamps, often caused by noise fluctuations on top of the signal or by multiple signals occurring within the same TDC window (gate). In such cases, the most meaningful timestamp must be selected for accurate analysis

This chapter investigates the time resolution achieved in the experiment and introduces a new method for selecting meaningful timestamps. Some of the results obtained in this chapter are already visualized in Fig. 5.1. Only with time information it is now possible to gain a detailed understanding of the processes that take place inside the crystals. This detailed understanding has also led to additional applications. Specifically, the findings have allowed the validation of the pile-up detection and correction capabilities of the SADCs, revealing significant shortcomings in the pile-up detection, which were later resolved in [141]. Furthermore, the integration of timing information into the existing clustering method used for particle reconstruction in the Crystal Barrel detector is presented.

5.1 Time Resolution

The time resolution achieved in the experiment varies for the different detector components and their readout electronics. In [145] a detailed investigation of the time resolution for all detectors was performed, using the Tagger bars or MiniTAPS as reference.[2] This removes the influence of the trigger signal as

$$\Delta t = (t_{\text{det}} - t_{\text{trig}}) - (t_{\text{ref. det}} - t_{\text{trig}}) = t_{\text{det}} - t_{\text{ref. det}}. \tag{5.1}$$

All time resolutions are listed in Table 5.1.

The time resolution depends strongly on the energy of the incoming signals. Therefore, Table 5.1 lists not only the average time resolution $\overline{\text{FWHM}}$[3], but also the best (peak) time

[1] Due to the use of dual-threshold discriminators, each threshold generates one timestamp.
[2] Tagger bars and the MiniTAPS detector are known for their good time resolution.
[3] **F**ull **W**idth at **H**alf **M**aximum

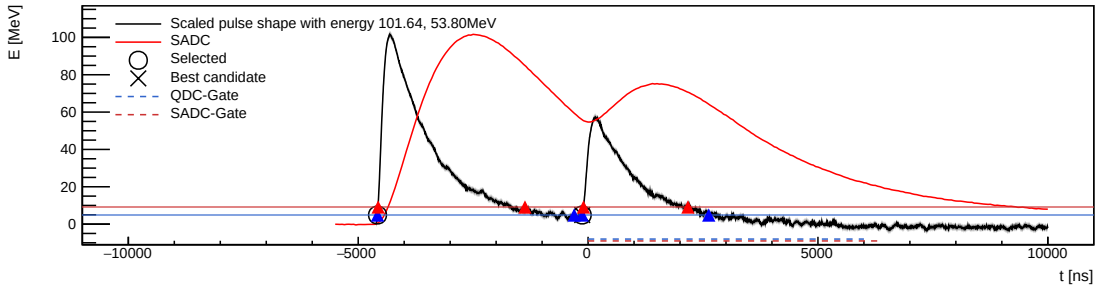

Figure 5.1: Example of an event inside a crystal with timestamps and pulses displayed. The discriminator thresholds threshold A and threshold B are shown as horizontal lines. Using an oscilloscope, **pre-recorded sample pulses in the TDC branch** are used to better visualize the dynamics inside the crystals. The pre-recorded samples are scaled and shifted using only time information, showing two signals with an energy of 101.64 MeV and 53.80 MeV (calculated only via time). The waveform recorded in the SADC branch is also shown for comparison. This event is a pile-up event which affects energy information, as explained in more detail in Section 5.3.2.

resolution $\mathrm{FWHM}_{\mathrm{peak}}$. The peak time resolution corresponds to the best time resolution which is obtained by considering only high energy photons. Finally, a comparison with the values determined in [103] is given, which show the time resolution before the modification of the experiment readout. An overview of the fits which were performed to extract the time resolution can be found in [145].

The detectors with the best time resolution are the Tagger bar and the MiniTAPS detector. This is consistent within the results from [103]. However, a notable difference is observed for the Forward detector, where the time resolution has decreased compared to the previous measurement. This can be explained by the change from photomultiplier to avalanche photodiodes during the modification of the readout.[4] In addition, the time resolution depends strongly on the energy of the photons as shown by the differences between $\overline{\mathrm{FWHM}}$ and $\mathrm{FWHM}_{\mathrm{peak}}$. Therefore, a different selection of photon energies may dilute the direct comparability of these results with the values reported in [103]. Finally, the time resolution of the Crystal Barrel calorimeter was determined for the first time, giving an average FWHM of 7.6 ns.

5.1.1 Time Resolution of the Crystal Barrel Detector

In the following, the time resolution of the Crystal Barrel detector is examined in more detail and compared with the time resolution of the SADC branch. This time resolution will be used as a key component for time clustering within the Crystal Barrel detector as described in Section 5.4.

5.1.1.1 TDC Branch

For a more detailed study, a series of time distributions of the Crystal Barrel detector using the Tagger bars as a reference detector (cf. Eqn. 5.1) are fitted using the Novosibirsk

[4] For further details, see Section 3.1.2.

Table 5.1: Average and peak time resolution ($\overline{\text{FWHM}}$ and $\text{FWHM}_{\text{peak}}$) of different detector- and reference detector pairs [145]. $\text{FWHM}_{\text{peak}}$ corresponds to the best (peak) time resolution obtained by considering only high energy photons. Due to low statistics, it was not possible to determine $\text{FWHM}_{\text{peak}}$ for Tagger fibers (in coincidence with the MiniTAPS detector). Only signals from photons originating from a π^0 decay during data taking in May 2018 are considered. The values are also compared with values determined in [103] before the readout was modified.

Detector	Ref. detector	$\overline{\text{FWHM}}$ [ns]	$\text{FWHM}_{\text{peak}}$ [ns]	$\overline{\text{FWHM}}_{[103]}$ [ns]
Tagger bars	Tagger bars	(0.8592 ± 0.0002)	(0.525 ± 0.005)	(0.635 ± 0.003)
Tagger fibers	Tagger bars	(1.4384 ± 0.0004)	(1.05 ± 0.02)	(1.694 ± 0.006)
Inner detector	Tagger bars	(2.188 ± 0.001)	(1.82 ± 0.01)	(2.093 ± 0.013)
CB detector	Tagger bars	(7.591 ± 0.008)	(2.53 ± 0.31)	–
Forward detector	Tagger bars	(4.70 ± 0.01)	(2.69 ± 0.10)	(1.861 ± 0.016)
Forward-Vetos	Tagger bars	(4.93 ± 0.01)	(4.06 ± 0.09)	(4.434 ± 0.013)
Cherenkov detector	Tagger bars	(1.231 ± 0.002)	(1.228 ± 0.002)	(1.194 ± 0.014)
GIM	Tagger bars	(3.0775 ± 0.0006)	(2.222 ± 0.005)	(3.1 ± 0.3)
MiniTAPS	Tagger bars	(0.85 ± 0.01)	(0.654 ± 0.005)	(0.872 ± 0.006)
MiniTAPS-Vetos	Tagger bars	(3.34 ± 0.02)	(2.25 ± 0.19)	(3.06 ± 0.05)
Tagger bars	MiniTAPS	(0.87 ± 0.02)	(0.66 ± 0.03)	(0.830 ± 0.006)
Tagger fibers	MiniTAPS	(1.28 ± 0.03)	–	(1.45 ± 0.03)

function [149]

$$N(x;\alpha,\mu,\sigma,A) = A \cdot \exp\left(-\frac{1}{2q^2}\ln^2\left(1-\alpha\cdot\frac{x-\mu}{\sigma}\right)-\frac{q^2}{2}\right), \quad \text{with} \quad q = \frac{2}{2\sqrt{\ln(4)}}\cdot\sinh\left(\alpha\cdot\frac{2\sqrt{\ln(4)}}{2}\right)^{-1}. \tag{5.2}$$

The Novosibirsk function represents an asymmetric Gaussian-like peak, where α is a measure of the asymmetry.[5] In the case of $\alpha \to 0$, the asymmetrical shape disappears and the Novosibirsk function converges to a Gaussian. Equivalent to a Gaussian, the FWHM is given as [151]

$$\text{FWHM} \approx 2.35 \cdot \sigma. \tag{5.3}$$

By using Tagger bars as a reference, both the Crystal Barrel detector and the Tagger bars contribute to the measured resolution

$$\text{FWHM}^2 = \text{FWHM}^2_{\text{Crystal Barrel}} + \text{FWHM}^2_{\text{Tagger bars}}. \tag{5.4}$$

However, since the time resolution of the Tagger bars is much better (cf. Table 5.1), their influence is negligible. Example fits are shown in Fig. 5.2 and in Section A.2 in the Appendix.

[5] The functional form is taken from [149] and differs from the usual choice defined in [150]. It has the advantage of a low correlation between the parameter α and the amplitude A of the function.

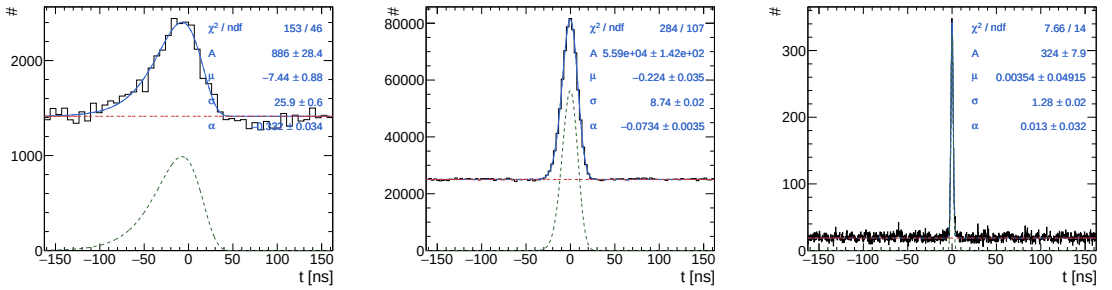

Θ_A, $1-60$, $12-14\,\mathrm{MeV}$ Θ_B, $301-1\,380$, $16-18\,\mathrm{MeV}$ Θ_B, $121-180$, $358-378\,\mathrm{MeV}$

Figure 5.2: Example fits of a Novosibirsk function (cf. Eqn. 5.2) to time distributions of the Crystal Barrel detector using Tagger bars as reference detector (TDC branch). Only signals from photons originating from a π^0 decay during data taking in May 2018 are considered. The resulting time resolution is shown in Fig. 5.3. Further fits are shown in Section A.2 in the Appendix.

In [87] the time resolution of an analog signal is defined as

$$\sigma_t = \frac{\sigma_{\mathrm{noise}}}{\left|\frac{\mathrm{d}U}{\mathrm{d}t}\right|} \tag{5.5}$$

where $\frac{\mathrm{d}U}{\mathrm{d}t}$ is the slope of the signal at the discriminator threshold. The time resolution of the Crystal Barrel detector therefore depends not only on the energy but also on the threshold settings. This can be seen very well in Fig. 5.3, where the energy dependent time resolution is shown for different crystal ranges and threshold configurations. Crystals with lower thresholds have better time resolution at low energies compared to those with higher thresholds, while at high energies this relationship is reversed. This behavior occurs because, at low energies, lower thresholds sample a steeper part of the leading edge, whereas at high energies, higher thresholds are positioned on a steeper region. While the time resolution reaches values around 1 ns at high energies, it decreases rapidly at energies close to the threshold.

To parameterize the dependence on energy and threshold, a function of the form

$$\sigma_t^{\mathrm{TDC}}(E,\Theta) = [0]\,(\Theta) + \frac{[1]\,(\Theta)}{(E-[2](\Theta))^{0.75}} \tag{5.6}$$

is fitted to the data. The function is purely phenomenological, the only requirement being that it is valid for all threshold and energy configurations of the experiment. Each parameter $[i](\Theta)$ is a function of the threshold. A two-dimensional fit yields the parameters

$$\begin{aligned}
[0](\Theta) &= \mathrm{p0}/\Theta + \mathrm{p1} = (3.57 \pm 0.02)/\Theta + (0.706 \pm 0.003) \\
[1](\Theta) &= \mathrm{p0}/\Theta + \mathrm{p1} = (51.2 \pm 0.3)/\Theta + (35.06 \pm 0.06) \\
[2](\Theta) &= \Theta + \mathrm{p0} = \Theta + (-0.163 \pm 0.003).
\end{aligned} \tag{5.7}$$

The fit is shown as solid lines in Fig. 5.3 which fits the data well. Eqn. 5.6 now allows a simple calculation of the time resolution of the TDC branch in the Crystal Barrel detector. The

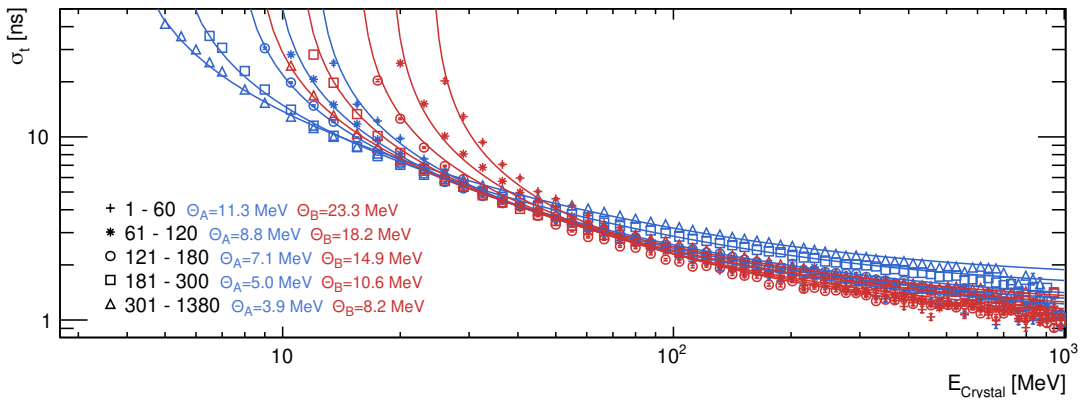

Figure 5.3: Time resolution of the TDC branch of the Crystal Barrel detector as function of energy. To resolve the dependence on the discriminator threshold, the time resolution is shown for each crystal section with different threshold configurations for threshold A and threshold B. Only signals from photons originating from a π^0 decay during data taking in May 2018 are considered. Example fits are shown in Fig. 5.2 and in Section A.2 in the Appendix.

parametrization of the threshold height ensures valid values even for arbitrary configurations in the experiment.

5.1.1.2 SADC Branch

The SADC branch does not rely on the same signal filter as the TDC branch, but uses a different architecture optimized for its own application. This already changes the signal shapes significantly. In addition, the sampling of the SADC allows time information to be determined with methods of a constant fraction discriminator. This not only eliminates the need for time walk correction but also allows time information to be obtained from signals with energies as low as 1 MeV[6] [142]. There is also no dependence on different threshold heights used for triggering. Until the November 2021 data taking, the time resolution of the SADC is limited by its sampling interval.[7] For later data, linear interpolation between samples is possible for improved time resolution [142]. In Fig. 5.4 the time resolution with and without interpolation is shown as a function of energy. It is also compared with the time resolution in the TDC branch at the highest and lowest threshold heights set in the experiment. It can clearly be seen that the time resolution provided by the TDC branch is more accurate over a wide energy range. Only at low energies is the situation opposite. Here, the TDCs only provide time information down to the thresholds set in the experiment. The

[6] This does not mean that time information is always available at such low energies. In some cases, the integral is > 1 MeV, but no peak (and no time) could be determined.

[7] The signal is sampled with a sampling interval of 50 ns. The trigger signal is sampled at a higher rate with a sampling interval of 12.5 ns.

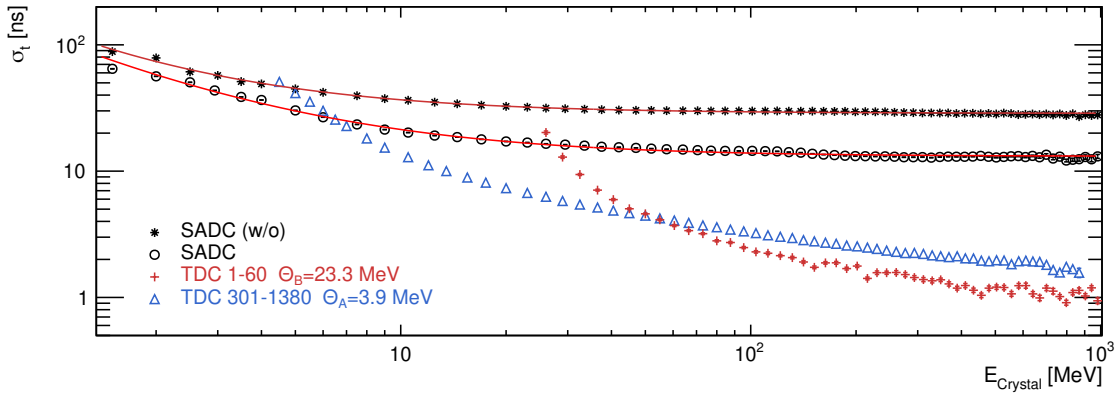

Figure 5.4: Time resolution of the **SADCs** branch of the Crystal Barrel detector with and without (w/o) interpolation as function of energy. It is further compared with the time resolution in the TDC branch at the highest and lowest threshold heights set in the experiment. The dependencies are fitted using Eqn. 5.8. Only signals from photons originating from a π^0 decay during data taking in June 2021 for SADC (w/o) and December 2021 for SADC are considered.

dependencies of the SADC are fitted, resulting in the following parametrization

$$\sigma_t^{\text{SADC (w/o)}}(E) = \frac{(85.90 \pm 0.07)}{E - (0.172 \pm 0.001)} + (26.93 \pm 0.07)$$
$$\sigma_t^{\text{SADC}}(E) = \frac{(74.3 \pm 0.2)}{E - (0.213 \pm 0.007)} + (13.24 \pm 0.01). \tag{5.8}$$

5.2 Method for Selecting TDC Times

Up to and including the December 2021 data, the discriminators have been set to trigger only on the leading edge, i.e. only on positive crossings (from below the threshold). Still, situations may arise where one signal generates multiple timestamps. This can be due to noise on top of the signals causing multiple positive threshold crossings. This is particularly pronounced for the trailing edge where the signal decays more slowly. The internal hysteresis mechanism of the discriminators[8] [134] is not able to remove all this noise. In addition, random coincidences can also lead to multiple timestamps in a crystal. For data taken after December 2021, the discriminators also trigger on the trailing edge, i.e. for negative crossings (from above the threshold). In this case, by definition, multiple timestamps are available for each signal. As this work is based on data prior to December 2021, it is important to note that only positive crossings need to be considered in the following. A recorded example of multiple timestamps is shown in Fig. 5.5. In such a case, one time out of all the available timestamps must be selected. A simple and robust method is to select the timestamp closest to the experiment trigger at 0 ns. While this is indeed implemented as the default method

[8] Hysteresis defines how far below/above the threshold the signal must move to trigger a change of state. This prevents the influence of oscillatory behavior around the threshold.

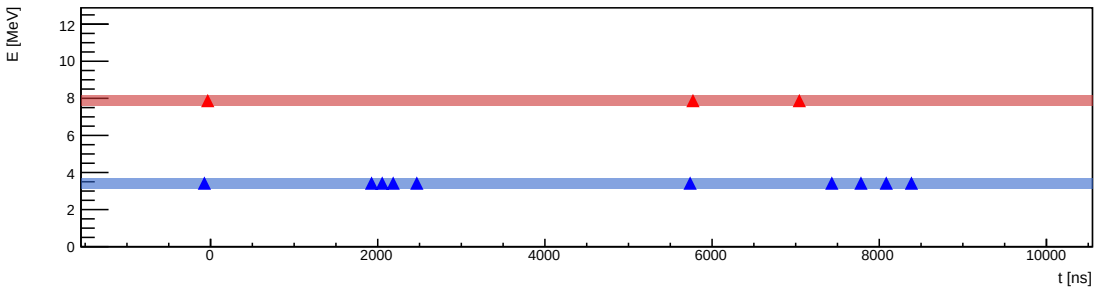

Figure 5.5: Timestamps recorded for the crystal with index 261 and an energy of 163 MeV during data taking in May 2018. The discriminator thresholds threshold A and threshold B are shown as horizontal lines. Times are given relative to the experiment trigger at 0 ns.

for the event reconstruction in ExPlORA, it throws away a lot of information about the processes within the crystals. Therefore, a more advanced method is presented that also allows the investigation of pile-up events and random coincidences within the Crystal Barrel detector. This will be used for later validation of the pile-up detection and correction features of the SADC.

In the following, the lower threshold is referred to as threshold A while the upper threshold is referred to as threshold B. A particular combination of detected timestamps at threshold A and threshold B is referred to as a pattern.[9]

5.2.1 Signal Shape in the TDC Branch

In case of multiple timestamps per signal, their placement is related to the shape of the signal. The shape of the signal in turn depends on the readout, as described in Chapter 3. Most prominent is the influence of the signal filter, which shapes the output of the preamplifier to short time constants. Due to the linear behavior of the preamplifier and the signal filter, the shape of the output signal is independent of the size of the input (the energy). A change of the size of the input will only result in a scaling of the output. In theory, therefore, a parametrization of the signal shape from first-principles will allow us to relate the timestamps to the individual signals by comparing their positions with the parametrization. While this would be feasible for the direct output of the signal filter, it is hardly possible for the input signals at the discriminator module. Despite the linearity of the preamplifier and the signal filter an energy-dependent shape appears.[10] This can be seen very clearly in Fig. 5.6, where the direct output of the signal filter is compared with the input signal at the discriminator. This is due to the transformer at the beginning of the discriminator circuit, which is used to convert the differential signal into a single-ended signal. The transformer exhibits core saturation effects, resulting in a non-linear dependence on the internal magnetic flux and in distorted signal shapes. Besides distorted signal shapes, undershoots occur with an amplitude of $4 - 8\,\%$ of the signal voltage, lasting up to $80 - 100\,\mu s$ (cf. Fig. A.1 in the Appendix).

[9] In Fig. 5.5 a *ABAAAAABBAAAA* pattern is shown.

[10] This does not affect the signals used for the energy sum which is tapped after the signal filter and before the discriminator module.

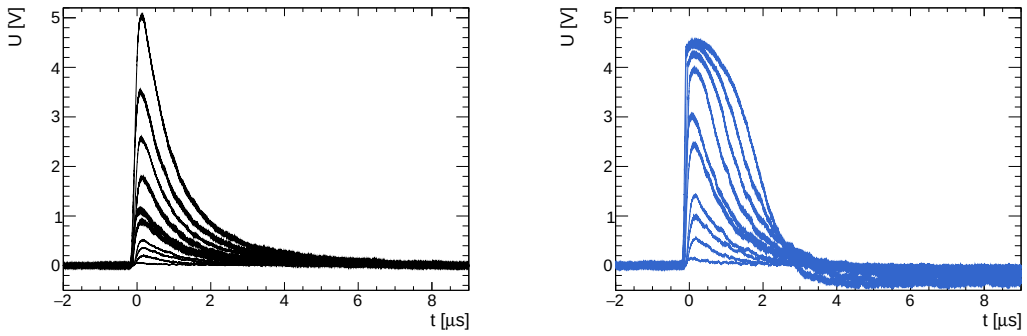

Output of the signal filter

Input signal at the discriminator

Figure 5.6: Comparison of output signals at the **signal filter** to input signals at the discriminator module. For the input signals at the discriminator module an energy dependent shape can be seen. All signals were recorded on an oscilloscope in a laboratory where an equivalent readout was constructed for a single crystal as it is used in the experiment.

Both the energy-dependent signal shape and the undershoot do not affect the quality of time information during event reconstruction or selection. The time range of the undershoot is not yet long enough to affect subsequent events. Also, the final time information is extracted at the leading edge, where the distortion of the signal is not yet present. However, the distortion prevents a parametrization of the signal shape from first-principles to provide a good selection mechanism for timestamps inside crystals. Instead, the required information must be extracted from the recorded data, taking into account all the distortion.

5.2.2 Grouping of Timestamps to Signals

In order to select the most suitable time for a crystal, the timestamps must be grouped to the signals from which they originate. For each signal, the timestamps at the leading edge must be separated from the timestamps at the trailing edge. The latter ones are discarded as noise, generated by random threshold crossings of the slowly decaying signal.[11] The timestamps at the leading edge can be used to assign a well-defined time to each signal. The time of the signal closest to the trigger is then assigned to the crystal for further reconstruction processes. In the following, this time will be referred to as the default time. The next section will explain this process in more detail.

5.2.2.1 Energy

Artificial dead time is used to group the timestamps and to discard the ones at the trailing edge. It refers to the time range after a leading edge of a signal in which all other timestamps are ignored. They are considered as noise on the trailing edge as the discriminators only trigger on positive crossings (from below the threshold). The artificial dead time must be long enough to include all the noise generated by the signal. This length is primarily determined

[11] For the data considered in this work, the discriminators are configured to trigger only on positive crossings (from below the threshold).

by the scale, i.e. the energy of the signal. However, the energy information provided by QDCs or SADCs cannot be used due to the different gate lengths compared to the TDCs. Using the energy information would limit the selection mechanism to signals prominently within the QDC or SADC gate, neglecting information from a much wider TDC gate (cf. Fig. 3.7). Furthermore, energy information from QDCs could be distorted by pile-up. Therefore, in order to apply artificial dead time, the energy information has to be determined directly from time. The time difference at the leading edge Δt_{AB} or the time-over-threshold Δt_{TOT} can be used for this.

Time difference Δt_{AB} The time difference at the leading edge Δt_{AB} can be used as an alternative to measured energy information. It is defined as

$$\Delta t_{AB} = t_B - t_A, \tag{5.9}$$

where t_A is the timestamp generated by the leading edge at threshold A and t_B the timestamp generated by the same leading edge at threshold B. This time difference is related to energy, as high energy signals result in fast crossings of the thresholds while low energy signals result in slow crossings. The same effect is already used for a first time walk correction within the trigger logic of the experiment [81].

In Fig. 5.7 (left) the relation between Δt_{AB} and energy (QDC) is shown for crystals exhibiting a pure AB pattern around trigger time.[12] Each point corresponds to the most probable value of its underlying energy distribution determined by a fit using a Novosibirsk function. To account for the dependence on the threshold height, the energy is normalized by the threshold difference $\Delta\Theta = \Theta_B - \Theta_A$ (cf. Fig. 5.7 (right)). The normalization takes advantage of the approximate linearity of the leading edge around the threshold. Examples of the underlying distributions and fits are shown in Section A.3 in the Appendix. To parameterize the overall relation, a function of the following form is fitted to the combined normalized data

$$\frac{E}{\Theta_B - \Theta_A}\Big(\Delta t_{AB}\Big) = [0] \cdot \exp\Big[[1] \cdot \log\Big(\Delta t_{AB} - [2]\Big)\Big] + [3]. \tag{5.10}$$

The fit gives the parameters

$$\begin{aligned}
[0] &= (1\,480 \pm 1)\\
[1] &= (-1.7741 \pm 0.0001)\\
[2] &= (2.484 \pm 0.001)\\
[3] &= (1.82422 \pm 0.00005).
\end{aligned}$$

The parametrization is of phenomenological nature and is only intended to reproduce the dependence and allow for extrapolation.

[12] For simple AB patterns, more complex behavior is suppressed. As the pattern (signal) is required to be around the trigger time ($-200 - 200\,\mathrm{ns}$), a good correlation with the measured energy of the crystal is ensured.

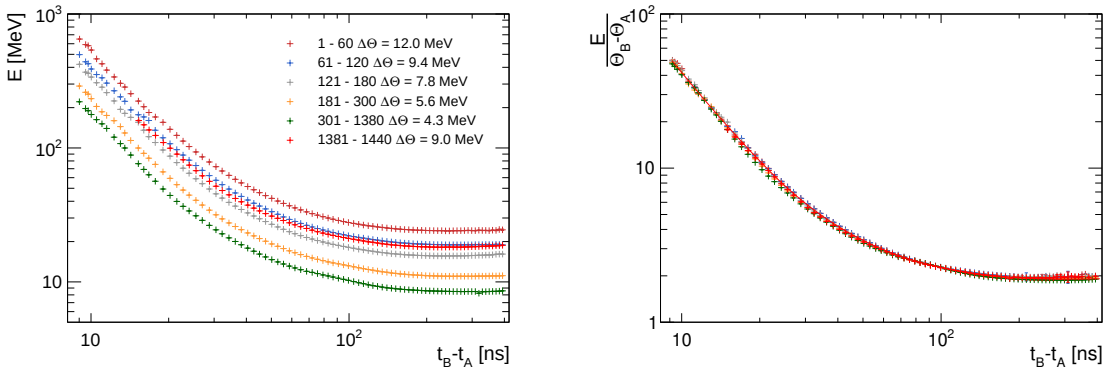

Without normalization Normalized by $\Delta\Theta$

Figure 5.7: Energy (QDC) as function of the time difference $\Delta t_{AB} = t_B - t_A$ for crystals showing a pure AB pattern around the trigger time ($-200 - 200$ ns) for May 2018 data (left). Normalization by the threshold difference $\Delta\Theta = \Theta_B - \Theta_A$ removes the dependence on the threshold height (right). A fit to the combined normalized data is shown in red and results in Eqn. 5.10.

Time-over-threshold Δt_{TOT} Time-over-threshold information can also be used as an alternative to measured energy information. Time-over-threshold is defined as the time difference between two timestamps at threshold A or B, one at the leading edge (1) and one at the trailing edge (2)

$$\Delta t_{\mathrm{TOT}} = t_{A_2/B_2} - t_{A_1/B_1}. \tag{5.11}$$

Δt_{TOT} is only available in case of timestamps at the trailing edge. Up to and including the December 2021 data taking the discriminators were set to trigger only on positive crossings. In this case, timestamps on the trailing edge are only available when noise leads to positive crossings. For later data, the discriminators also trigger on negative crossings. In this case, time-over-threshold is always available when a threshold is crossed.[13] In this work, only the timestamps of positive crossings are available.

In Fig. 5.8 (left) the relation between Δt_{TOT} and energy (QDC) is shown for crystals exhibiting a pure AA or ABB pattern around the trigger time.[14] Again, each point corresponds to the most probable value of its underlying energy distribution as determined by a fit using a Novosibirsk function. While at low energies Δt_{TOT} increases with energy as expected, at high energies it starts to decrease again. The reason for this is the distorted signal shape at the input of the discriminator (cf. Fig. 5.6). As a result, Δt_{TOT} is no longer unique at high energies. To remove the influence on the threshold height, the energy is normalized by Θ as the signals scale linearly with the input (cf. Fig. 5.7 (right)). This works well for low Δt_{TOT} where the distortions are not yet visible. Examples of the underlying distributions are shown

[13] In addition, different types of timestamps are generated for positive (from below) and negative (from above) threshold crossings, so that the two situations can be distinguished.

[14] For these patterns, more complex behavior is suppressed. ABA patterns can also be used for time-over-threshold information at threshold A. However, they do not provide much new information. As the pattern (signal) is required to be around the trigger time ($-200 - 200$ ns), a good correlation with the measured energy of the crystal is ensured.

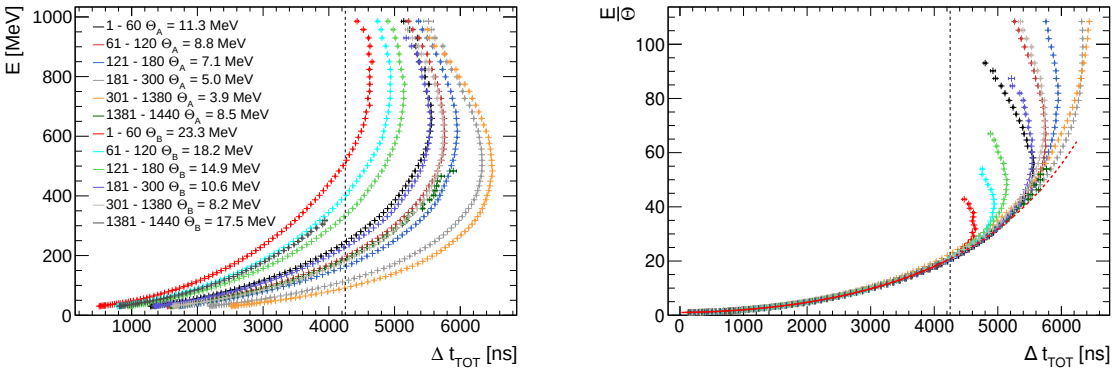

Without normalization

Normalized by Θ

Figure 5.8: Energy (QDC) as a function of time-over-threshold $\Delta t_{\mathrm{TOT}} = t_{A_2/B_2} - t_{A_1/B_1}$ for crystals exhibiting a pure AA or ABB pattern around the trigger time ($-200 - 200$ ns) during data taking in May 2018 (left). Normalization by Θ removes the dependence on the threshold height for low values (right). At high values, a dependence on the threshold still exists due to energy-dependent signal shapes at the input of the discriminator. A fit to the combined normalized data for $\Delta t_{\mathrm{TOT}} \leq 4\,250$ ns (vertical black line) is shown in red and results in Eqn. 5.12.

in Section A.3 in the Appendix. A fit to the combined normalized data yields

$$\frac{E}{\Theta}\left(\Delta t_{\mathrm{TOT}}\right) = [0] \cdot \exp\Big[[1] \cdot (\Delta t_{\mathrm{TOT}} - [2])\Big] + [3] \cdot \left(\Delta t_{\mathrm{TOT}}\right)^{[4]} + [5] \tag{5.12}$$

with parameters

$$\begin{aligned}
[0] &= (5.181 \pm 0.001) \times 10^{-4} \\
[1] &= (7.6526 \pm 0.0008) \times 10^{-4} \\
[2] &= (-8\,373 \pm 1) \\
[3] &= (5.579 \pm 0.001) \times 10^{-7} \\
[4] &= (2.02093 \pm 0.00003) \\
[5] &= (0.6879 \pm 0.0001).
\end{aligned}$$

After $\Delta t_{\mathrm{TOT}} \sim 4\,250$ ns there are deviations between the fit and the data. Furthermore, as already pointed out, for a given Δt_{TOT}, the energy information starts to be not unique anymore. Depending on the threshold height, signals with energy above ~ 475 MeV for $\Theta = 3.9$ MeV or above ~ 775 MeV for $\Theta = 23.3$ MeV are affected. As a result, high energy signals will be assigned too low energies when calculated via time-over-threshold.

Comparison For validation, the energy determined using time information is compared to the energy information measured by QDCs. In Fig. 5.9, the correlation for energy based

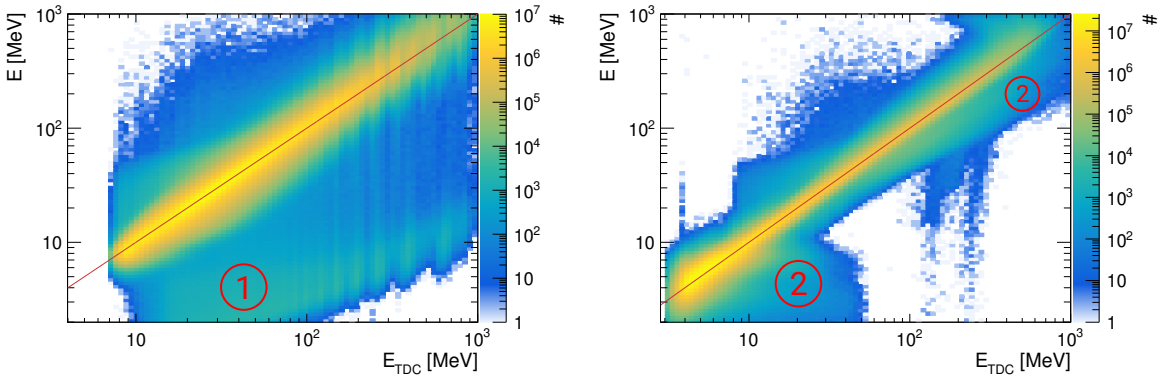

E_{TDC} via Δt_{AB} for AB pattern

E_{TDC} via Δt_{TOT} for AA and ABB pattern

Figure 5.9: Comparison of the energy information E_{TDC} determined only by time with the energy information E provided by the QDCs during data taking in May2018. To ensure a valid comparison, only signals at trigger time $(-200 - 200\,\mathrm{ns})$ within the QDC gate are selected.

on Δt_{AB} and Δt_{TOT} is shown for signals around the trigger time.[15] While there is a clear correlation, there are also some deviations. The energy determination using Δt_{AB} shows an enhancement at low E (marked as 1). This enhancement is caused by signals that have a time stamp at threshold B due to the influence of noise, although their energy is too low. As a result, the time difference Δt_{AB} is too small, causing E_{TDC} to be too high. The energy determination using Δt_{TOT} also shows deviations at low E (marked as 2). There is a similar deviation at higher E. Both deviations are due to pile-up events which prolong the time-over-threshold information. At low E the time-over-threshold at threshold A is used, whereas at high E threshold B is used.

When comparing the two alternatives, energy determination using time-over-threshold information gives a better correlation and is more favorable. Therefore, if time-over-threshold information is available, it will be preferred in the following. If no two timestamps are available at a given threshold, the time difference at the leading edge Δt_{AB} is used instead.

5.2.2.2 Artificial Dead Time

Artificial dead time is used to group the timestamps and at the same time to discard trailing edge timestamps. The required length of the artificial dead time is defined by the time difference between the timestamp at threshold A at the leading edge (A_1) and potential A timestamps related to the same signal but created by noise at the trailing edge (A_2)

$$\tau_{\mathrm{dead}} = t_{A_2} - t_{A_1}. \tag{5.13}$$

The energy information from Δt_{TOT} or Δt_{AB} is used to determine its length. In this way, artificial dead time can also be applied to signals that are not prominently within the gate for energy measurement. In Fig. 5.10 (left) the relation between energy (TDC) and τ_{dead}

[15] Signals around trigger time $(-200 - 200\,\mathrm{ns})$ lay prominently within the gate used for energy measurement. This allows a comparison with energy information measured by QDCs.

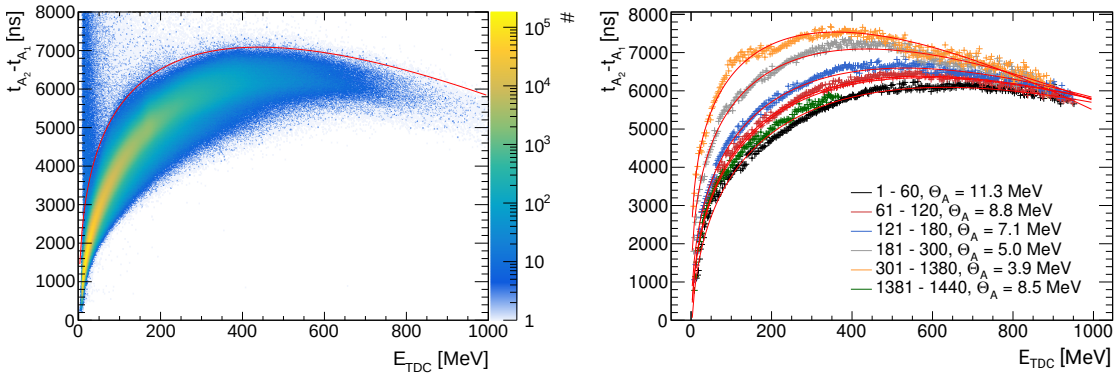

Figure 5.10: Artificial dead time $\tau_{\text{dead}} = t_{A_2} - t_{A_1}$ as function of energy (TDC) for crystal indices $181 - 300$ with pure ABA pattern around the trigger time ($-200 - 200$ ns) during data taking in May 2018 (left). The transition points between noise at the trailing edge and random coincidences are determined for each region with constant threshold (right). The dependence on energy and threshold is fitted using Eqn. 5.14.

is shown for crystal indices $181 - 300$ with pure ABA (A_1BA_2) pattern around the trigger time ($-200 - 200$ ns). Selecting only ABA patterns increases the probability that only one signal is present. In this case the last A timestamp is related to noise on the trailing edge.[16] It can be seen that low energy signals stay only briefly above the threshold. Thus, only short artificial dead times are needed. In comparison, high energy signals require long artificial dead times up to 7 000 ns. The decreasing behavior for high energies is again related to the distorted signal shapes (cf. Fig. 5.6). For each energy, the distribution of the artificial dead time is mostly broad as the position of the noise at the trailing edge can vary. In addition, random coincidences where the last A timestamp is not related to noise but to a new signal, result in a flat background at low energies. To obtain an appropriate dead time that takes into account all the noise associated with a signal, but not the timestamps of a new signal, the transition point between noise and random coincidences must be determined for each energy. The transition point is defined as the point where the slope of a linear function fitted to the surrounding points starts to show a flat behavior. Some example distributions are shown in Fig. A.10 in the Appendix. Fig. 5.10 (right) shows the transition points for each region with different threshold configuration. The artificial dead time as a function of energy and threshold is fitted and marked as a red line. The fit gives

$$\tau_{\text{dead}}(E, \Theta_A) = [0](\Theta_A) \cdot E^{[1](\Theta_A)} + [2](\Theta_A) \cdot E + [3](\Theta_A) \tag{5.14}$$

[16] It is assumed, that the set of all ABA patterns is sufficient to reflect the behavior of other patterns with more noise, such as $ABAAA$.

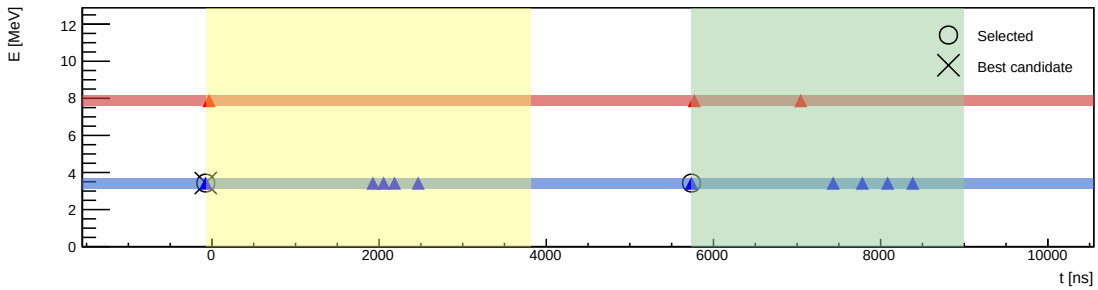

Figure 5.11: Timestamps recorded for the crystal with index 261 and energy 163 MeV during data taking in May 2018. The discriminator thresholds threshold A and threshold B are shown as horizontal lines. Timestamps that fall within the areas of artificial dead time determined with energy information from the time difference of an AB pattern (Δt_{AB}) or using time-over-threshold information (Δt_{TOT}) are discarded. The selected timestamp closest to the trigger is used as the best candidate for the crystal.

with parameters

$$
\begin{aligned}
[0](\Theta_A) &= \mathrm{p0}/\Theta_A + \mathrm{p1} = (2\,173 \pm 32)/\Theta_A + (715 \pm 20) \\
[1](\Theta_A) &= \mathrm{p0}/\Theta_A + \mathrm{p1} = (-0.26 \pm 0.01)/\Theta_A + (0.430 \pm 0.005) \\
[2](\Theta_A) &= \mathrm{p0}/\Theta_A + \mathrm{p1} = (-16 \pm 1)/\Theta_A + (-6.6 \pm 0.2) \\
[3](\Theta_A) &= \mathrm{p0}/\Theta_A + \mathrm{p1} = (12\,153 \pm 259)/\Theta_A + (-2\,420 \pm 63).
\end{aligned}
$$

All three parametrization, Δt_{AB} to energy, Δt_{TOT} to energy and energy to artificial dead time τ_{dead} can be combined to group timestamps to signals and to discard timestamps corresponding to noise. Therefore, the full length of the artificial dead time is applied after each leading edge of a signal (defined by an AB pattern). If another AB pattern occurs within the artificial dead time, clearly defining the beginning of a new signal, the artificial dead time is stopped early. The use of artificial dead time is shown in Fig. 5.11. Each selected timestamp defines the time of a single signal. Of these timestamps, the one closest to the trigger is set as the default time of the corresponding crystal.

5.2.2.3 Clustering of A Timestamps

In the case that a signal exceeds threshold B, the associated AB pattern clearly defines its leading edge. In such a situation, the energy can be calculated and artificial dead time can be applied. For low energy signals this is not the case, as only timestamps at threshold A are generated. In this case, it is not yet clear which timestamps belong to the same signal (cf. Fig. 5.12). To account for these low-energy signals the timestamps at threshold A are grouped into signals using a single-linkage principle. First, each timestamp at threshold A is considered to be a group in itself. In a bottom-up fashion, groups that are closer than a predefined time difference are aggregated. This process is repeated until no further aggregation is possible. Each remaining group is considered to have originated from a signal

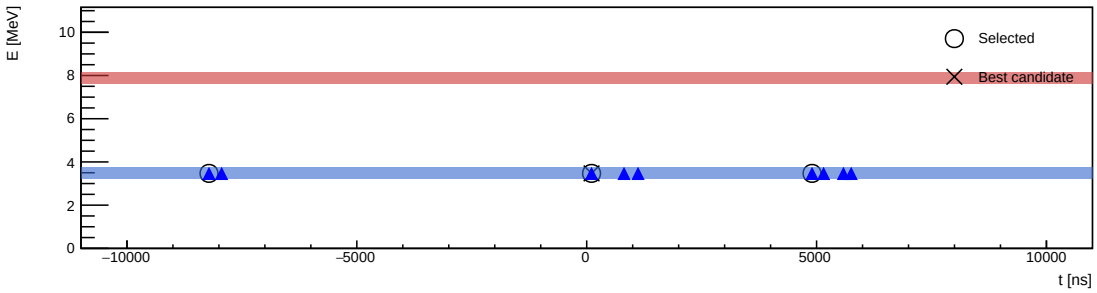

Figure 5.12: Timestamps recorded for crystal with index 833 and energy 5.5 MeV during data taking in May 2018. The discriminator thresholds threshold A and threshold B are shown as horizontal lines. Timestamps at threshold A are grouped using a single-linkage principle with a maximal allowed time difference given by Eqn. A.1. The selected timestamp closest to trigger is used as the best candidate for the crystal.

with a time given by the timestamp at the leading edge.[17] The maximum time difference allowed within a group is determined by examining subsequent time differences in crystals containing only timestamps at the threshold A. For more information on the clustering of A timestamps, see Section A.4 in the Appendix.

5.2.3 Limitations

The method presented above allows us to gain insights into different phenomena within the crystals by using the full multihit functionality of the TDCs. However, there are certain limitations:

1. Signals with an energy below the threshold $E < \Theta_A$ do not have a time assigned. Depending on the position of the crystals these are signals with an energy below $4.8 - 14\,\text{MeV}$.[18] This is the case for $\sim 66\,\%$ of all crystals with an energy deposition above 1 MeV.

2. For data up to and including December 2021, signals with low energy $\Theta_A < E < \Theta_B$ may have only one timestamp assigned. As a result, no time-based energy can be calculated because neither Δt_{AB} nor Δt_{TOT} information is available. Depending on the threshold positions of the crystals, this can happen for signals with an energy below $9.2 - 27\,\text{MeV}$.[18] This is the case for $\sim 9\,\%$ of all crystals with an energy deposition above 1 MeV. For later data, time-over-threshold information is available for all signals as soon as threshold A is crossed.

3. A second signal that occurs on the trailing edge of a preceding signal before threshold A is reached cannot be detected. Such a pile-up may look like a normal signal in terms of the generated timestamps. This could also be the case if the preceding signal reaches Θ_A, but the energy of the second signal does not allow for a timestamp at threshold B.

[17] The timestamp at the leading edge is defined as the first timestamp within a group.
[18] The values are valid for June 2021 data (cf. Table 4.1).

While the first limitation effects also further reconstruction processes like time clustering (cf. Section 5.4) the other limitations only influence the investigation of selected TDC times presented in Section 5.3. The following work will refer to elements in this list if their effect is significant.

5.3 Investigation of Selected TDC Times

It is now possible to take full advantage of the multihit functionality of TDCs in the Crystal Barrel detector. Each signal occurring within the TDC gate is assigned both time and energy information, even if the signal is not in the QDC or SADC gate. This allows to study the behavior of pile-up in more detail. The results will also be used later to validate the pile-up detection and pile-up correction of SADCs.

5.3.1 Coincident Time Background

Without time information only an energy deposition is measured. In the case of QDCs, it is not known with certainty that this energy deposition results from only one signal.[19] It is not known, how often random coincidences occur in and around the gate for energy measurement. By using the time information from the TDCs, this is no longer the case. The probability of random coincidences within the TDC gate can be investigated.[20]

Table 5.2 gives the probability that a crystal with energy deposition has not only one but several signals (with time information) within the TDC gate of ~ -10 to 10 µs

$$R(N) = \frac{\text{Energy depositions with N signals with time}}{\text{All energy depositions}}. \tag{5.15}$$

Only energy depositions above 1 MeV are considered. It is important to note that the first limitation presented in Section 5.2.3 strongly influences the numbers. Signals with an energy below the threshold $E < \Theta_A$ are not assigned a time. About 34 % of the crystals with energy depositions contain a single signal with time, while only 0.3 % contain two signals with time. Three signals with time are even less likely to happen with only 0.002 %. The numbers are valid for the May 2018 data. They may vary for other measurement periods due to different threshold configurations. From the numbers it can be seen that already one random coincidence (with time) within the large TDC gate is unlikely. Figure 5.13 shows the position of the coincident events in the Crystal Barrel detector. For crystals with no time, the distribution reflects the setting of threshold A. As expected, at low thresholds (θ-index $6-23$) there are fewer events without time than in regions with high thresholds. In the case that one signal with time is detected, the effect is opposite. For crystals with two or three detected signals with time the distribution is mostly flat. Only in the forward direction there is an increment of coincident signals, located at two positions in ϕ. This plane corresponds to the plane of the electromagnetic background ($e^{+/-}$) which is enhanced in the Crystal Barrel detector by the transverse magnetic field used for target polarization.

[19] The readout using SADCs is capable of detecting pile-up, i.e. events with more than two signals.

[20] A random coincidence detected within the TDC gate does not necessarily lead to pile-up. Pile-ups are discussed in detail in the next section.

Table 5.2: Probability that a crystal with energy deposition will have a given number of signals with time information within the TDC gate of ~ -10 to 10 µs during data taking in May 2018.

Number of pulses with time	0	1	2	3
Probability $R(N) \cdot 100\,\%$	65.7 %	34 %	0.3 %	0.002 %

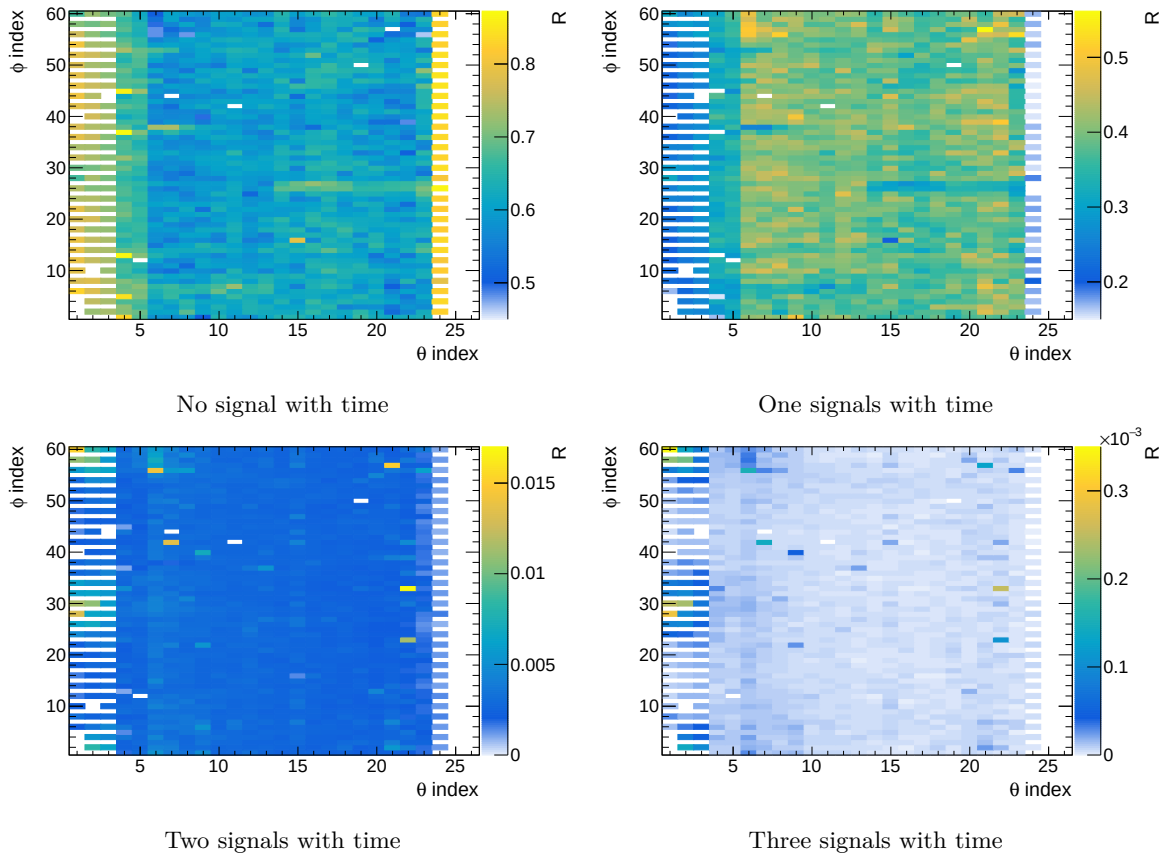

Figure 5.13: Distribution of random coincidences inside the Crystal Barrel detector during data taking in May 2018. The proportion R (cf. Eqn. 5.15) is shown for crystals with no, one, two and three signals with time in the TDC gate of ~ -10 to 10 µs. Outliers with high R are due to deviations in their threshold heights. If the deviations are too large, the crystals appear as white spots in the image.

5.3.2 Pile-up

In the case of multiple signals within a crystal (the terms signal and pulse are used interchangeably in the following), a distortion of the measured energy information cannot be excluded. Coincident pulses occurring before or after the prompt pulse (the primary pulse around the trigger time) can lead to a false increase in energy. While it is not possible to detect pile-up with the QDC readout, a recent modification of the experiment has led to the integration of SADCs. They are used as a new readout for energy and as an alternative readout for time information. Among other benefits, SADCs provide functionality to flag crystals that exhibit pile-up behavior and to correct their energy information.

The proposed method for TDC times also allows for the detection and correction of pile-ups. Therefore, the TDCs can be used as an independent source to validate the SADCs. While the SADCs detect pile-up within the SADC branch, the method using TDCs detects pile-up within the TDC branch. Here, the signal filter shapes the pulses to shorter time constants. This has several advantages. The short shaping time in the TDC branch results in a high double pulse resolution. Furthermore, due to the large gate length of ~ -10 to $10\,\mu s$, coincident pulses can already be detected before the gate for the energy measurement starts.

5.3.2.1 Pile-up Detection

Pile-up is defined as the superposition of two or more signals. When a superposition occurs entirely within the gate for energy measurement, the measured energy is equal to the sum of the energy of each signal. More generally, pile-up in the Crystal Barrel detector can be defined as situations where at least two signals are fully or partially within the gate for energy measurement. The following events would be classified as pile-up, assuming a prompt signal around the trigger:

1. The trailing edge of a preceding pulse reaches the start of the gate for energy measurement.

2. A second pulse superimposes the prompt pulse.

3. A second pulse comes after the prompt pulse but is still partially within the gate for energy measurement.

Fig. 5.14 shows one example of each of these cases in real data. Pre-recorded sample pulses are used to give a better visualization on the pulse shapes[21]. The pre-recorded samples are scaled and shifted using only the time information from TDCs. It is important to note that the pulses in the TDC branch are not comparable to the pulses in the QDC or SADC (energy) branch. They are shaped differently (cf. Fig. 5.16). As a result, pulses which are separated in the TDC branch can very well lead to a pile-up in the energy branch.

In the case of pile-up, the measured energy is distorted and shifted to higher values. The resulting error is strongly coupled to the energy of the prompt pulse and the pile-up pulse as

[21] The sample pulses were recorded on an oscilloscope in the laboratory using the same readout electronics and configuration as in the experiment.

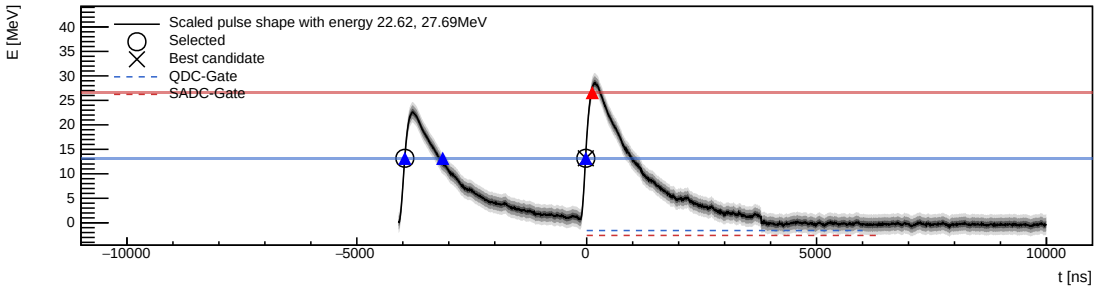

Preceding pile-up

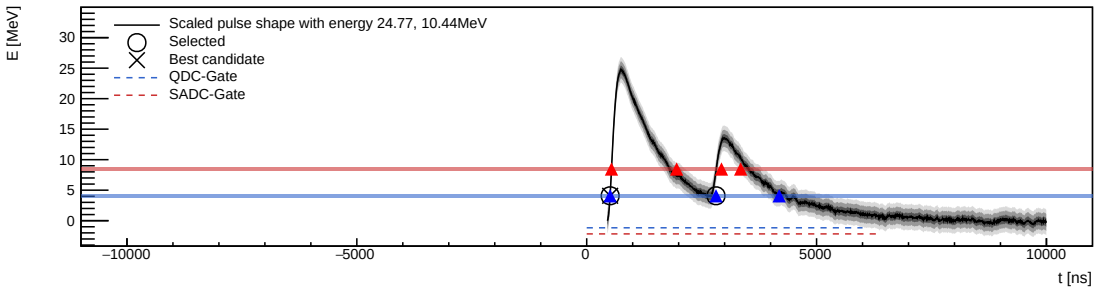

Superimposed Pile-up

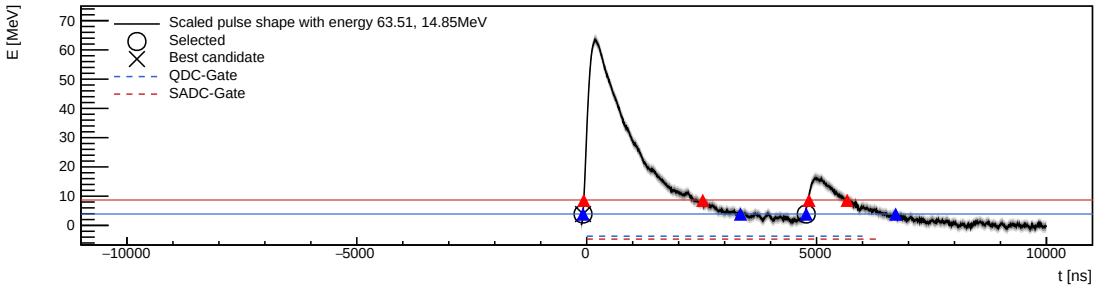

Trailing pile-up

Figure 5.14: Events which are classified as pile-up. The discriminator thresholds threshold A and threshold B are shown as horizontal lines. As before, artificial dead time is used to discard timestamps associated with noise on top of the leading edge, but this time it is not drawn explicitly. Instead, with an oscilloscope pre-recorded sample pulses are used to give a better visualization of the signal shapes. The pre-recorded samples are scaled and shifted using only the time information from the TDCs. The position and length of the QDC and SADC window (gate) are also marked. It is important to note that pile-up is defined within the energy branch, where pulses have longer time constants due to the different shaping characteristics. Therefore, pulses that are separated in the TDC branch can actually lead to pile-up in the energy branch.

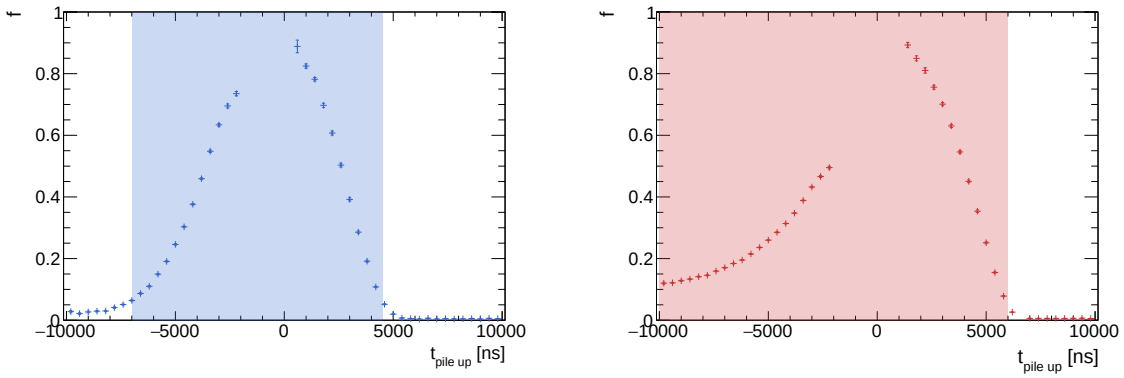

QDC SADC

Figure 5.15: Dependence of the influence of pile-up f (cf. Eqn. 5.16) on the position of pile-up relative to the trigger $t_{\text{pile-up}}$ for QDC readout (May 2018 data) or SADC readout (June 2021 data). Events with two pulses and a prompt pulse around trigger are selected. Pulses which fall inside $-7\,000$ to $4\,750$ ns for QDCs and $-10\,000$ to $6\,000$ ns for SADCs are treated as pile-ups with significant influence.

well as to the position (time) of the pile-up pulse. The influence of pile-up can be characterized by

$$f\left(t_{\text{pile-up}}\right) = \frac{E_{\text{crystal}} - E_{\text{prompt}}}{E_{\text{pile-up}}}, \tag{5.16}$$

where E_{prompt} is the energy of the prompt pulse only (determined by TDC times) and $E_{\text{pile-up}}$ is the energy of the pile-up pulse only (determined by TDC times). E_{crystal} is the energy measured by the QDC or SADC. The influence f corresponds to the fraction of the pile-up energy that is deposited in the gate used for energy measurement. If a pile-up has no effect (i.e. completely outside of the energy measurement gate), the measured energy E_{crystal} and the energy of the prompt pulse E_{prompt} are equal and $f = 0$. When a pile-up has full effect (i.e. fully within the energy measurement gate), the energy measurement includes both the prompt pulse and the pile-up pulse $E_{\text{crystal}} = E_{\text{prompt}} + E_{\text{pile-up}}$, resulting in $f = 1$. It is important to note that the influence f does not directly relate to the error of the energy measurement, for which the energies involved must also be taken into account.

In Fig. 5.15 (left) f is shown as a function of the time of the pile-up relative to the trigger for energy measurements using QDCs. About $7\,000$ ns before the trigger, on average about 5 % of the energy of the pile-up is added to the measurement. The influence increases as the pile-up gets closer to the trigger. Just before the trigger, the pile-up pulse prevents the prompt pulse from being detected, resulting in a gap in the data points of f. The same is true just after the trigger, where the prompt pulse prevents the detection of the pile-up pulse. It is important to note that despite the inability to determine f in this area, pile-up still occurs. At trigger, the pile-up pulse is completely within the gate for energy measurement and f is at its maximum. At later times, the influence decreases again as more of the pile-up pulse runs out of the gate. f falls below 5 % at about $4\,750$ ns after trigger.

For pile-up detection, the time range in which pile-up pulses influence the measurement

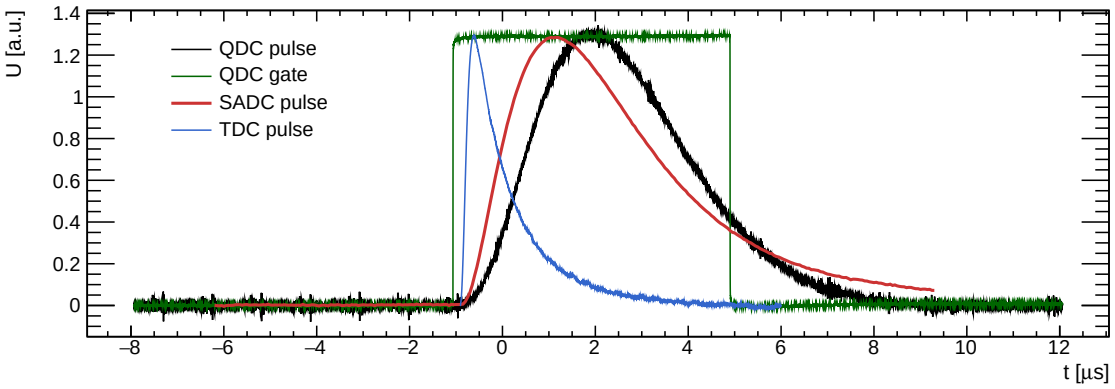

Figure 5.16: A pulse recorded with an oscilloscope in the **QDC branch** relative to the QDC gate used for energy measurement. A pulse recorded with an oscilloscope recorded in the TDC branch and the waveform in the SADC branch are added for comparison. The pulses are only for general comparison of the shape and do not provide any additional information such as position or noise. The SADC gate for the energy measurement is not explicitly drawn but has a length of 6.4 µs.

must be defined. Using $f \cdot 100\,\% = 5\,\%$ as the threshold a second pulse occurring within

$$t = -7\,000 \text{ to } 4\,750\,\text{ns} \tag{5.17}$$

is treated as pile-up for QDCs. The magnitude of the error is then defined by the energies of the pulses involved. In case of SADCs, the pulses are longer due to different shaping characteristics and the gate is slightly wider. Both yield a different characteristic of f (cf. Fig. 5.15 (right)). For SADCs, a larger time range of

$$t = -10\,000 \text{ to } 6\,000\,\text{ns}. \tag{5.18}$$

is defined for pile-up detection. Both time ranges must correlate with the pulse shapes and the length of the gates used for energy measurement. A comparison of a recorded pulse in the QDC and SADC branch is shown in Fig. 5.16. It can clearly be seen that the SADC pulse is shaped to longer times, which explains the earlier start of the pile-up detection time range. The SADC gate is also longer than the QDC gate, which explains the later end of the pile-up detection time range. The reason why the pile-up time range ends before and not at the end of the gates is due to the slow rise of the leading edge at the beginning of a pulse. This slow rise takes a while to have a significant effect on the energy measurement.

5.3.2.2 Pile-up Frequency and Error

In Section 5.3.1, the frequency of the coincident background within the TDC gate was examined. However, due to the different QDC and SADC gates, the frequency for pile-up events does not need to be comparable. Only by using Eqn. 5.17 and 5.18 the proportion of actual pile-ups within the Crystal Barrel detector can also be determined from the TDC information. Fig. 5.17 (left) shows the position of pile-up in the Crystal Barrel detector. As with the coincidences, the highest pile-up rates occur in the forward direction, at two

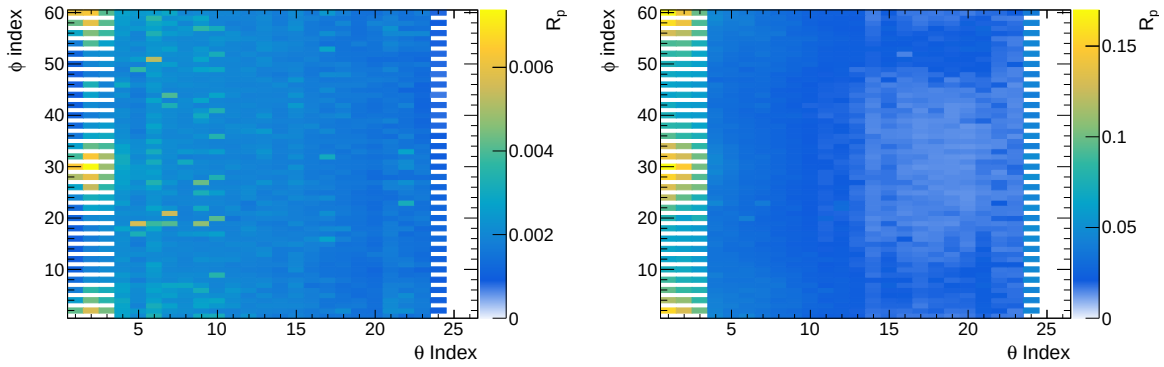

Pile-up detection with TDC

Pile-up detection with SADC

Figure 5.17: Proportion of pile-up R_p within the Crystal Barrel detector for all energy depositions above 1 MeV for the June 2021 data. In the case of TDCs (left), outliers with high R_p are due to deviating threshold heights.

positions in ϕ. Here, the electromagnetic background ($e^{+/-}$) is enhanced due to the transverse magnetic field used for target polarization. Considering all energy depositions above 1 MeV the maximum proportion of pile-up in these regions is $\sim 0.7\,\%$ for the June 2021 data. The average share of pile-up in the Crystal Barrel detector is $\sim 0.2\,\%$. It is important to note that these numbers are affected by the limitations presented in Section 5.2.3. Pulses with an energy below the threshold $E < \Theta_A$ have no time assigned and therefore cannot be detected as pile-ups. Also, certain topologies of pile-up are missing. The SADC does not suffer from the same limitation and thus detects a higher pile-up rate (cf. Fig. 5.17 (right)).

The actual error due to pile-up depends on the time of the pile-up pulse and the energies of the pulses involved. The error can be defined as

$$\begin{aligned}\delta E &= \frac{E_{\text{crystal}} - E_{\text{prompt}}}{E_{\text{prompt}}} \\ &= \frac{E_{\text{prompt}} + f\left(t_{\text{pile-up}}\right) \cdot E_{\text{pile-up}} - E_{\text{prompt}}}{E_{\text{prompt}}} \\ &= f\left(t_{\text{pile-up}}\right) \cdot \frac{E_{\text{pile-up}}}{E_{\text{prompt}}}. \end{aligned} \tag{5.19}$$

E_{crystal} is the energy measured by the QDC or SADC. E_{prompt} and $E_{\text{pile-up}}$ are the energy of the prompt pulse and the pile-up pulse, respectively, determined from the TDC information. The influence[22] of the pile-up on the energy measurement depends on the time of the pile-up relative to the trigger and is given by $f\left(t_{\text{pile-up}}\right)$. By using the information from Fig. 5.15, the error for different combinations of

$$t_{\text{pile-up}} \qquad \text{and} \qquad R = \frac{E_{\text{pile-up}}}{E_{\text{prompt}}} \tag{5.20}$$

[22] The influence f corresponds to the fraction of the pile-up energy that is deposited in the gate used for the energy measurement.

Table 5.3: Probability of the cumulative error $\delta E \cdot 100\,\%$ in case a pile-up occurs. Values for the QDC and the SADC branch are listed. As an example, the top-left cell shows that 10 % of pile-up events in the QDC branch result in an error below 1.4 %. Inversely, there is a 10 % probability that a single pile-up event will result in an error below 1.4 %. Note that these numbers do not indicate the frequency, i.e. how often pile-ups occur.

	c.d.f					
	10 %	20 %	40 %	60 %	80 %	90 %
QDC branch	$< 1.4\,\%$	$< 3\,\%$	$< 8\,\%$	$< 17.8\,\%$	$< 39.4\,\%$	$< 68.4\,\%$
SADC branch	$< 2.2\,\%$	$< 4.4\,\%$	$< 11.2\,\%$	$< 22\,\%$	$< 45.2\,\%$	$< 72\,\%$

can be calculated. In the following, such combinations will be referred to as topologies. Fig. 5.18 (left) shows the calculated error δE for different simulated topologies. Areas above which the error $\delta E \cdot 100\,\%$ exceeds 1 %, 10 %, 50 %, 100 % and 500 % are marked with red lines. As before, inside the white area around the trigger, the prompt or pile-up pulse prevents the other from being detected and there is no information for $f(t_{\text{pile-up}})$. In Fig. 5.18 (right) the density of topologies for recorded data is shown. High values of $\log_2(R)$ are less likely because the pile-up pulse is often of lower energy. While a constant behavior is observed before the trigger, the pile-up density is much higher after the trigger. Here, the slowly decaying trailing edge allows for pile-up pulses that would otherwise be too low in energy to reach the discriminator thresholds. By comparing the density of the topologies with the associated error, an estimate of the total error can be made. In most cases, the error in pile-up is less than 50 %. Comparing the readout using QDCs and SADCs, the error is slightly larger for the SADC readout. This is to be expected, as the shaping characteristics differ. The rising edge is steeper and the decay time is longer (cf. Fig. 5.16). The gate for energy measurement is also slightly larger. For a more general examination of the errors, the cumulative density function (c.d.f.)[23] of δE is calculated, integrating over any dependence on topologies (cf. Fig. 5.19). Again, a slightly larger error can be seen within the SADC readout. However, it should be noted that for the SADCs, unlike QDCs, the influence of pile-up can be corrected. Table 5.3 lists some example probabilities for cumulative errors. It is clear that the occurrence of pile-up can severely distort the energy information of a crystal. However, it is important to note that the overall frequency of pile-up in the experiment is low, so only a small proportion of events are affected. Furthermore, all the numbers are additionally affected by the limitations presented in Section 5.2.3. A large number of low energy pile-ups are not detected by the TDC due to the discriminator thresholds. Therefore, in reality, the probability of cumulative errors is overestimated to some extent. Overall, taking into account the frequency of pile-ups, the impact of pile-ups on the data quality of the experiment can be estimated to be small.

[23] The cumulative probability function specifies the probability that a variable takes a value less than or equal to the evaluation point.

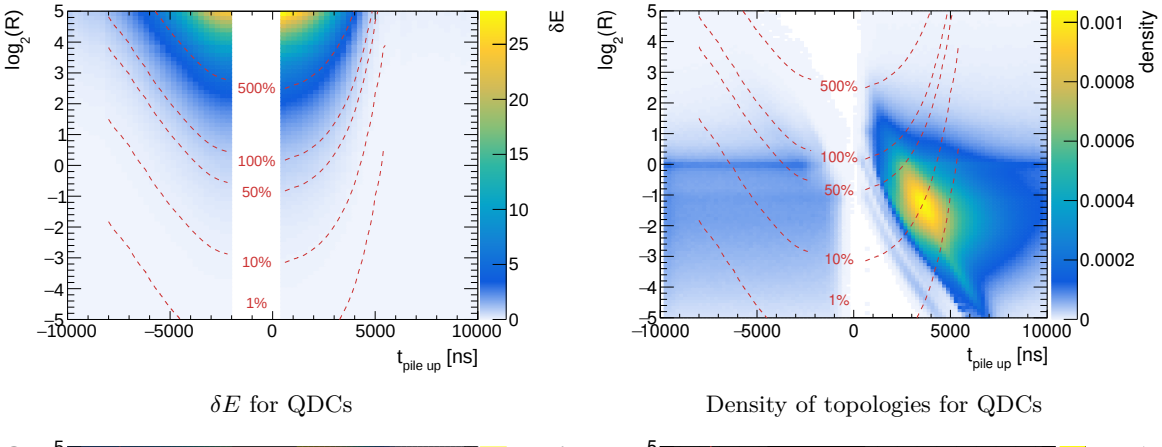

δE for QDCs

Density of topologies for QDCs

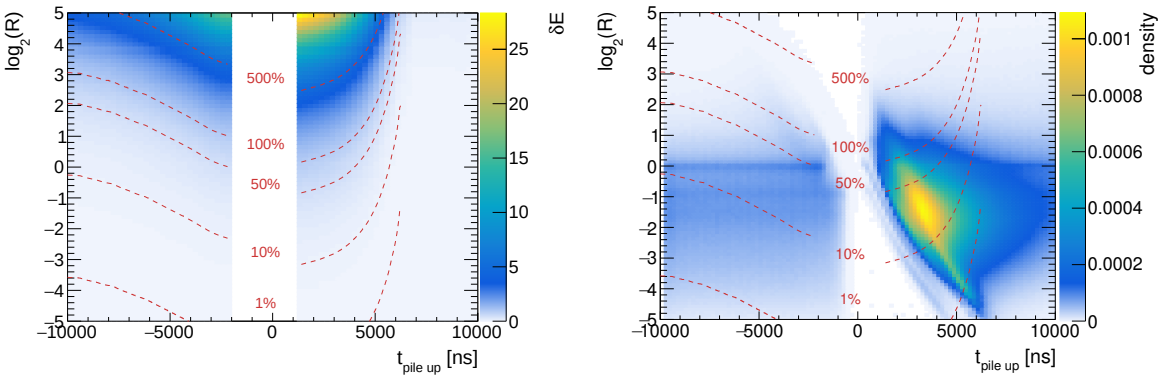

δE for SADCs

Density of topologies for SADCs

Figure 5.18: Left: The error of pile-up δE (cf. Eqn. 5.19) for simulated topologies (cf. Eqn. 5.20). Right: The density of topologies for recorded data. Areas above which the error $\delta E \cdot 100\,\%$ exceeds $1\,\%$, $10\,\%$, $50\,\%$, $100\,\%$ and $500\,\%$ are marked as red lines. White spots in the distributions refer to situations where pile-ups are not detected due to limitations of the TDCs. Data from data taking in May 2018 (QDCs) and June 2021 (SADCs) are shown.

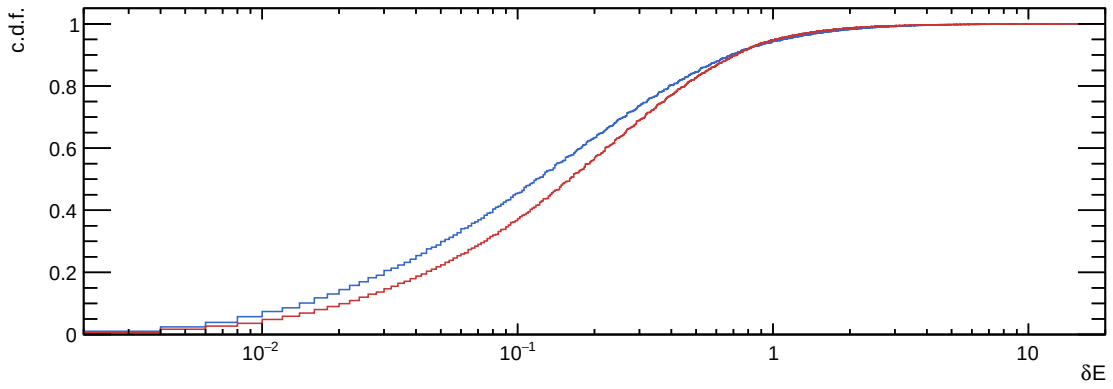

Figure 5.19: Cumulative density function (c.d.f.) of the error δE (cf. Eqn. 5.19) for the readout using QDCs during the data taking in May 2018, and for the readout using SADCs during the data taking in June 2021.

5.3.2.3 Pile-up Correction

Pile-up can be corrected by using the time difference at the leading edge Δt_{AB} or the time-over-threshold Δt_{TOT} to calculate the energy of the prompt pulse. Unlike for the measured energy, there is no influence from other pulses. Nevertheless, the energy information determined by time is not as precise (cf. Section 5.2.2.1). Furthermore, for data after (and including) June 2021, SADCs are available that are ideally suited to the task of pile-up detection and correction. Therefore, the ability to detect and correct pile-ups using TDC information is only used to provide insight and an independent cross-check of the performance of the SADCs.

5.3.3 Comparison to SADC

During the data taking in June 2021, the SADCs were used for the first time for the entire Crystal Barrel detector. In order to cross-check their performance in terms of pile-up detection, the TDCs can be used, which provide a completely independent way of determining such information.

5.3.3.1 Comparison of Pile-up Detection

In Fig. 5.17 the proportion of pile-ups within the Crystal Barrel detector detected by TDCs or SADCs is shown for the June 2021 data. A more detailed comparison is given in Table 5.4.

Table 5.4: Comparison of the proportion of pile-up events detected by SADC or TDC for all energy depositions above 1 MeV during the data taking in June 2021. The proportions are specified for the SADC and TDC independently as well as for the case where only the SADC or only the TDC detects pile-up.

SADC	TDC	SADC and not TDC	TDC and not SADC
4.92 %	0.24 %	4.80 %	0.12 %

The first thing to note is that SADCs detect significantly more pile-ups than TDCs. The reason for this is the limitation of the TDCs to detect only pulses with at least the energy of threshold A. Due to the high frequency of low-energy pulses, a large number of low-energy pile-ups remain unseen. In addition, certain pile-up topologies are difficult to detect (cf. Section 5.2.3). Examples of events where the SADC but not the TDC detects pile-up are shown in Fig. 5.20. In all cases the timestamps generated by the TDC indicate a single prompt pulse. Only the sampled waveform in the SADC branch indicates a distortion of the signal (top, middle). In some cases, the SADC even flags an event as a pile-up without showing any obvious visual distortion of the sampled pulse (bottom).

Of particular interest are those cases where the TDC, despite its limitations, detects pile-up but the SADC does not. Representative examples are shown in Fig. 5.21. In some cases, the double pulse resolution of the SADC branch is not good enough to discriminate pile-up which is close to the prompt pulse (top). This is not a problem in the TDC branch as the shaping is designed for shorter time constants. In the other cases, the clear pile-up behavior

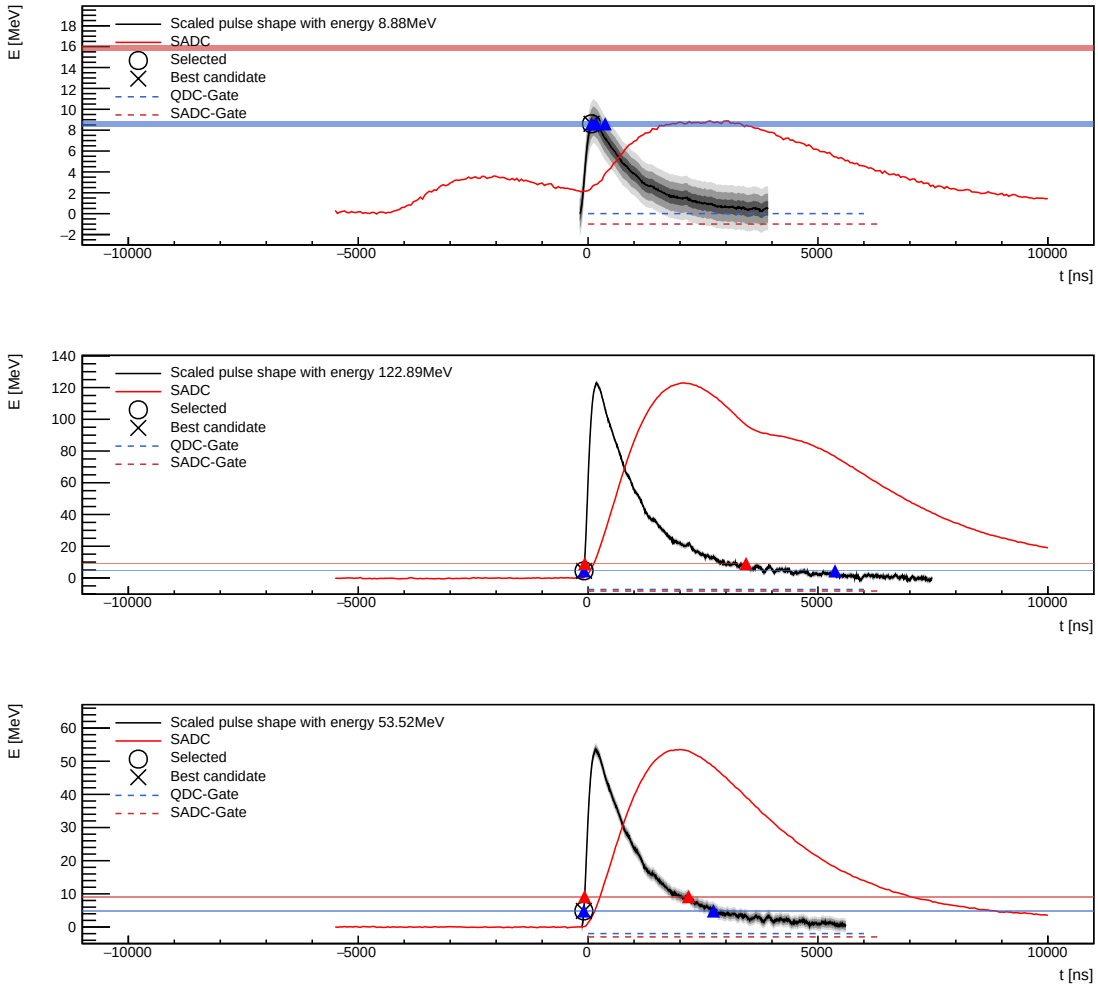

Figure 5.20: Events detected as pile-up by SADC but not by TDC. The discriminator thresholds threshold A and threshold B are shown as horizontal lines. As before, artificial dead time is applied but this time it is not drawn explicitly. Instead, with an oscilloscope **pre-recorded sample pulses** are used to give a better visualization on the dynamics inside the crystals. The pre-recorded samples are scaled and shifted only using time information. The waveform recorded in the SADC branch is also displayed.

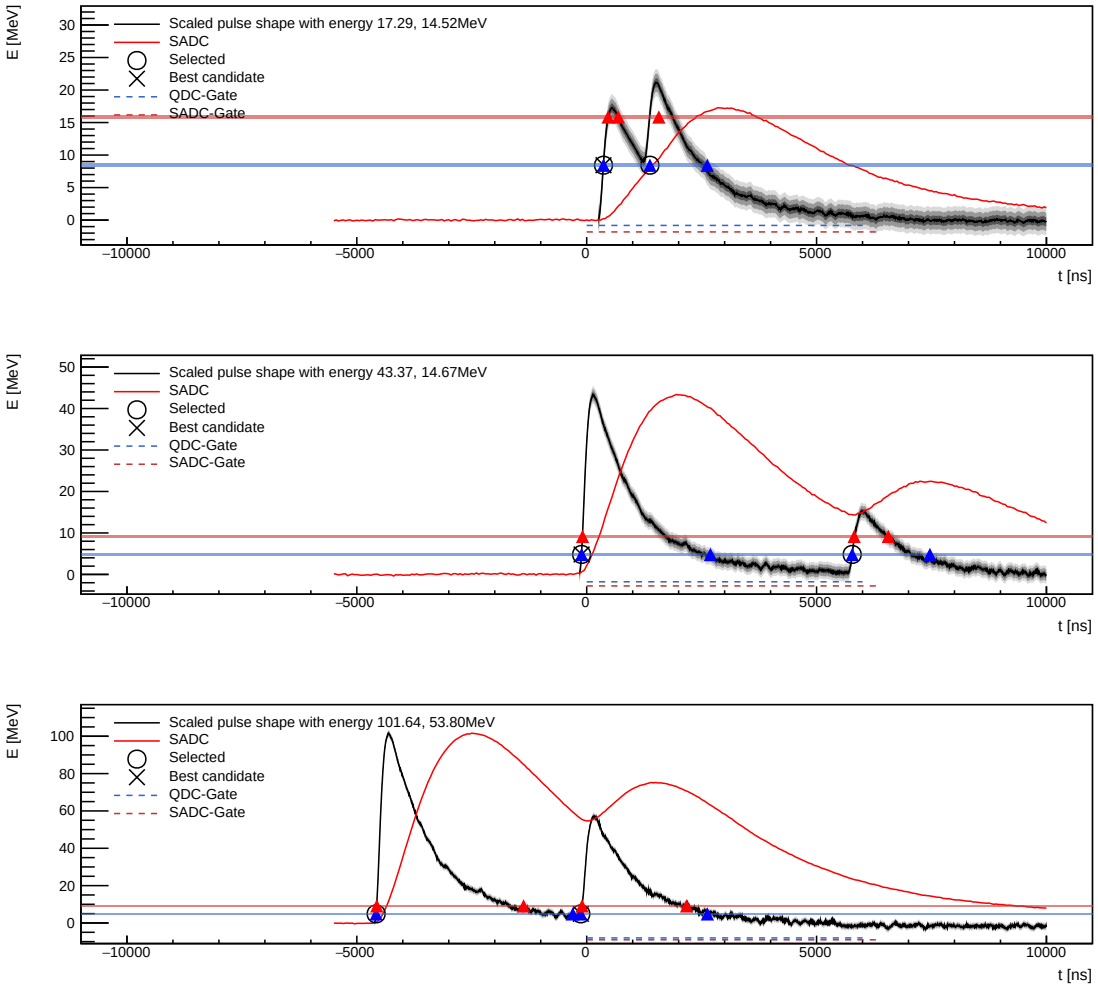

Figure 5.21: Events detected as pile-up by TDC but not by SADC. The discriminator thresholds threshold A and threshold B are shown as horizontal lines. As before, artificial dead time is applied, but this time it is not drawn explicitly. Instead, with an oscilloscope **pre-recorded sample pulses** are used to give a better visualization on the dynamics inside the crystals. The pre-recorded samples are scaled and shifted only using time information. The waveform recorded in the SADC branch is also displayed.

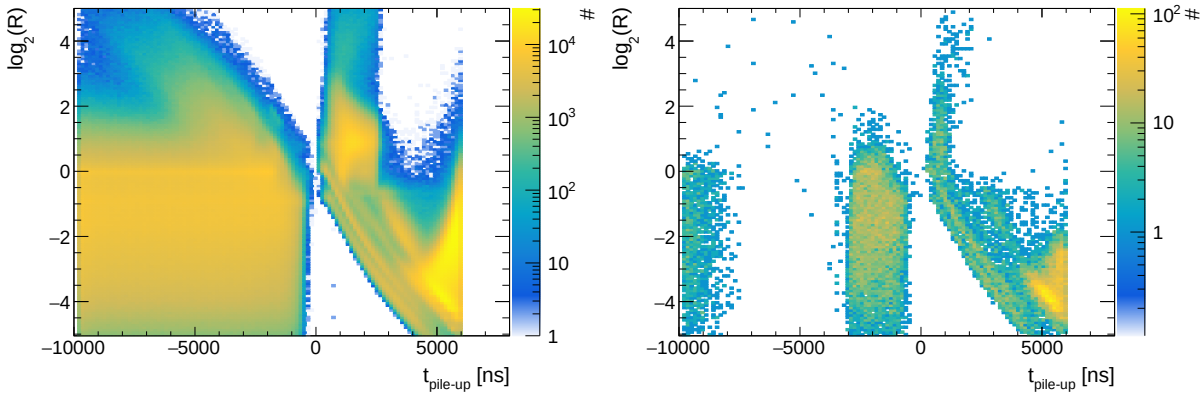

Figure 5.22: Topology of pile-ups detected by TDC but missed by SADC for June 2021 (left) and May 2022 (right) data. Only events with two pulses and one prompt pulse around the trigger ($-200-200$ ns) are selected. The cut at $t_{\text{pile-up}} = 6\,000$ ns results from the TDC definition of pile-up (cf. Eqn. 5.18).

of leading or trailing pulses should have been recognized by the SADC (middle, bottom). In Fig. 5.22 (left) the topology of pile-up detected by the TDC but missed by SADC is shown. As before, the topology is defined as the dependence on the intensity of pile-up and prompt pulse determined from the TDC information and the time of the pile-up:

$$t_{\text{pile-up}} \qquad \text{and} \qquad R = \frac{E_{\text{pile-up}}}{E_{\text{prompt}}}. \tag{5.21}$$

The missed pile-up pulses before the trigger show a mostly flat behavior. At early times and at low ratios (low pile-up energy compared to the prompt energy), these may be negligible events that do not significantly distort the energy measurement. However, at higher ratios and closer to the trigger, the impact that should be detected by the SADC is greater. The fact that the SADC is not able to detect these cases indicates that the SADC has significant shortcomings in the pile-up detection. The diagonal bands after trigger result from the different thresholds in the experiment.[24]

The results of this work led to a more detailed investigation of the pile-up detection of the SADC. In the initial approach, the pile-up detection of the SADC was based on the ratio of the integral to the height of the pulse (pile-up ratio[25]). A pile-up has been detected as soon as

$$\left|\frac{\text{integral}}{\text{peak height}} - 0.64\right| > 3\,\% + \frac{0.25\,\text{MeV}}{\text{peak height}} \tag{5.22}$$
$$\Leftrightarrow \qquad |\text{integral} - 0.64 \cdot \text{peak height}| > 3\,\% \cdot \text{peak height} + 0.25\,\text{MeV},$$

[24] The white area just before the trigger for high ratios and just after the trigger for low ratios are related to topologies where the TDC is unable to detect pile-up because the prompt pulse prevents the detection of the pile-up pulse and vice versa.

[25] Not to be confused with $R = E_{\text{pile-up}}/E_{\text{prompt}}$ which is used in this work together with $t_{\text{pile-up}}$ to define the topology of the pile-up (cf. Eqn. 5.21).

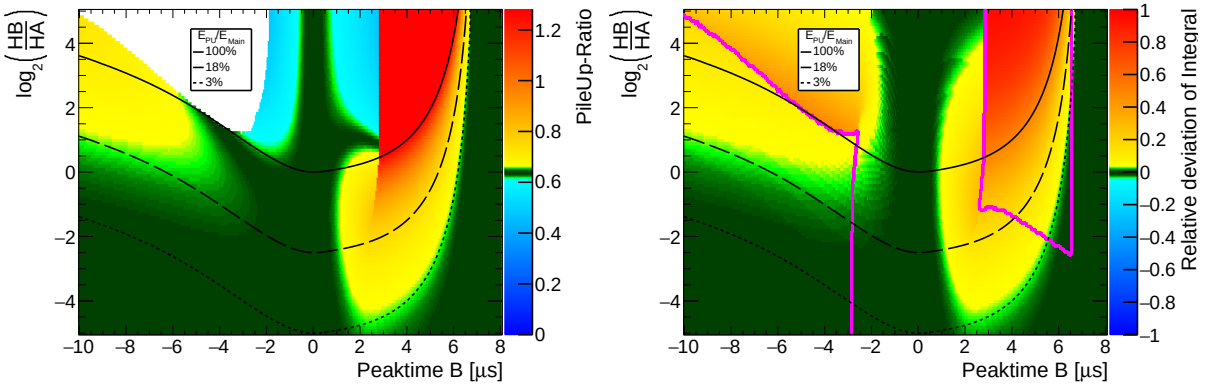

Former pile-up detection LUT-based pile-up detection

Figure 5.23: Simulation of the sensitivity of the pile-up detection of SADCs with the former pile-up detection using the pile-up ratio (left) and the new LUT-based pile-up detection using integral deviation (right) [141]. While peak time A (not explicitly marked in the figures) refers to the prompt pulse (at 0 ns) peak time B refers to the pile-up. H_B and H_A are their simulated intensities. The pile-up ratio (z-axis on the left) is defined as the ratio between the integral and the height of the resulting pulse within the gate used for energy measurement (cf. Eqn. 5.22). The relative deviation of the integral (z-axis on the right) is defined between the measured integral and the expected value (cf. Eqn. 5.23 to 5.24). The pink lines correspond to the area where two peaks can be separated. In this area, instead of using the relative deviation of the integral, pile-up is detected by two or more peaks with influence on the gate for energy measurement.

where $0.64 \cdot$ peak height is an expected integral for a valid (non-pile-up) pulse. The TDC analysis in this of this work shows, that this pile-up ratio is not able to discriminate pile-up in every situation. As a result, the pile-up ratio was examined in more detail in [141]. Fig. 5.23 (left) shows a simulation of the sensitivity of pile-up detection in the SADCs using the pile-up ratio. The topologies highlighted in green are not marked as pile-up because their pile-up ratio looks as if it would stem from a valid pulse. A comparison of the topology of missed pile-ups in Fig. 5.22 with the green areas in the simulation in Fig. 5.23 finds a good agreement. A change in the SADC pile-up detection algorithm has significantly improved the situation for later and future data [141]. Instead of using the pile-up ratio, the improved algorithm distinguishes between two situations. If two or more peaks are detected by the SADC their influence on the gate for energy measurement is checked using a predictive integral[26] in the form of a look-up-table (LUT). A peak is defined as relevant if the following condition is met

$$\text{peak height} \cdot \text{LUT}\,(\text{peak time}) > 0.5\,\text{MeV} + 1\,\% \cdot \text{integral}, \tag{5.23}$$

where peak height $\cdot$ LUT (peak time) is the predictive integral as function of the peak time. If two or more peaks are relevant, pile-up is detected. If only one peak is detected, the relative deviation of the measured integral from the predictive integral is used:

$$\text{integral} - \text{peak height} \cdot \text{LUT}\,(\text{peak time}) > 0.5\,\text{MeV} + 1\,\% \cdot \text{integral}. \tag{5.24}$$

[26] The integral is an energy equivalent.

Fig. 5.22 (top right) shows the TDC topology of pile-ups missed by SADC after the improvements for cosmic data recorded in May 2022. Some areas can be identified that still have missed pile-ups:

1. At the very beginning of the TDC gate (~ -10 to $-8\,\mu s$). These are pile-up events detected by the TDC that have a small influence on the energy measurement. They are primarily located at low ratios and only deposit a negligible proportion of their energy in the gate for energy measurement.

2. Just before the trigger (~ -3 to $0\,\mu s$). In these cases, the double pulse resolution of the SADC is unable to resolve two separate peaks. Therefore, the relative deviation of the integral is used for separation. Here, as in the case of the pile-up ratio, certain topologies cannot be resolved.

3. After trigger (~ 0 to $4\,\mu s$) the double pulse resolution again does not allow the separation of two peaks. Furthermore, small pile-up at the top of the trailing edge lead to band-like structures.[27] The latter type of pile-ups has a negligible influence on the energy measurement.

4. At the very end (~ 4 to $6\,\mu s$). Here, too, pile-up may be negligible, since the gate for the energy measurement stops shortly after, resulting in little energy being deposited by the pile-up.

The areas also agree well with another simulation of the sensitivity of pile-up detection using the new LUT-based approach (cf. Fig. 5.23 (right)). For topologies within the area marked by pink lines, separation of peaks is possible. In this case, pile-ups are detected by two or more peaks affecting the gate for energy measurement. Only close to the trigger is the double pulse resolution not good enough and the relative deviation of the integral must be used. Here, as already with the pile-up ratio, there are ambiguities that can lead to pile-ups being missed.

5.3.3.2 Comparison of Pile-up Correction

SADCs are able to correct measured energy information for the potential influence of pile-up. To ensure a valid correction, the pile-up correction of the TDCs can be used as a cross-check. Therefore, the correlation between the corrected energies of SADC and TDC is examined. In Fig. 5.24 (top left) the correlation between the uncorrected and the corrected energy using SADCs is shown. As expected, the pile-up correction leads to a reduction in energy. The same behavior can be seen in (top right) where TDC information is used for the correction. Existing deviations are related to the deviations in energy determination as discussed in Section 5.2.2.1. If the SADC and TDC pile-up corrections are comparable, their corrected energy information should be well correlated with each other. This is indeed the case (bottom left).

[27] In some cases, fluctuations at the top of the signal could also be interpreted as pile-up.

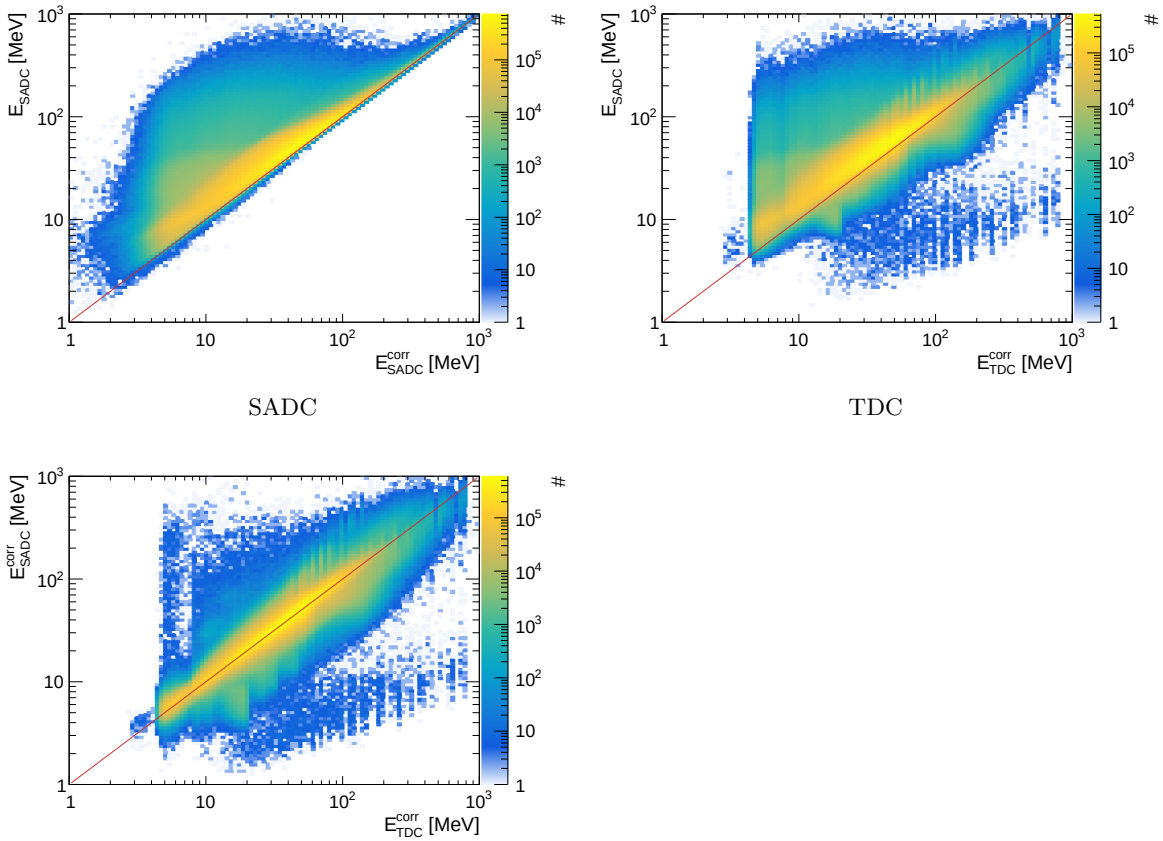

Figure 5.24: Top: Correlation between the uncorrected and corrected energy for pile-up events using the SADC or the TDC for June 2021 data. Bottom: Correlation between the energy corrected by the SADC and the energy corrected by the TDC.

5.4 Time Clustering

When photons interact with the material of scintillating crystals, electromagnetic showers are produced. As a result, one photon leads to several crystals with energy and time information. During event reconstruction, neighboring crystals with energy information are clustered. Each group is then assigned a reconstructed particle. For more information on the reconstruction process, refer to Chapter 6.

While the previous clustering algorithm for the Crystal Barrel detector only considers spatial relations between neighboring crystals, the new modification of the experiment allows for the additional use of time information. An improvement of the clustering process will lead to better energy and angular information of reconstructed photons. In Fig. 5.25 the position of the crystals inside the Crystal Barrel detector is shown after spatial clustering. For event 1 (left) the spatial clustering successfully separates 3 clusters. They all occur in a consistent time of $\Delta t = 50\,\text{ns}$. While event 2 (right) also separates 3 clusters, the time information

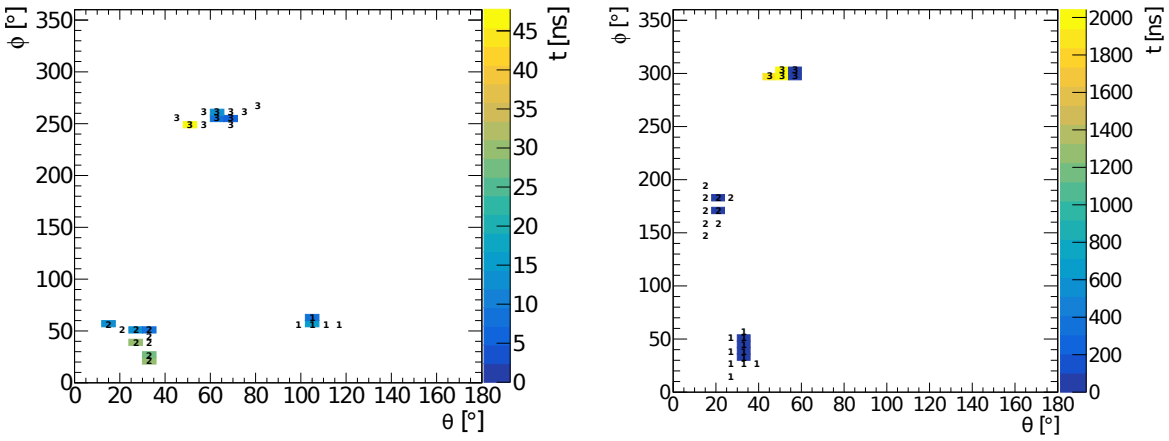

Figure 5.25: Position of crystals within the Crystal Barrel detector after spatial clustering. Clusters are labeled with numbers. While crystals with time information are colored according to the color axis, crystals without time remain white. Below $\theta \approx 30^\circ$ the Forward detector starts, leading to an increased spacing between the bins due to larger crystal sizes. Both events were recorded during May 2018 with time information from the TDCs.

is much more diverse. Within cluster 3 hits occur $\sim 2\,000$ ns after other neighboring hits. These hits are random coincidences, which lay close in space, but which occur later in time. They therefore distort the energy and angular information. Time clustering is the effort to remove such random coincidences. Therefore, time clustering is applied as a subsequent step to spatial clustering. During time clustering, a cut on time differences within a spatial cluster is applied. If a time difference exceeds a predefined cut-off value the cluster is divided into smaller ones. Spatial clustering is then applied again to search for new neighboring relations. The steps of the combined clustering process are as follows:

1. Performing spatial clustering on all crystals with energy deposition.

2. Performing time clustering for each spatial cluster.

3. Performing spatial clustering again to consider potential changes in neighboring relations.

5.4.1 Energy and Threshold Dependent Cut-Off Value

The cut-off value for time clustering is dictated by the time resolution of the crystals. It must account for all times that can be explained by the time resolution, but it should be small enough to remove everything else. The dependence of time resolution on energy and threshold is carefully determined in Section 5.1 and will be used in the following.

The allowed time difference between two crystals within a spatial cluster is primarily

determined by their combined time resolutions. It is given by[28]

$$\Delta t_{\text{cut}} = c\,(E_1, E_2) \cdot n \cdot \sqrt{\sigma_t(E_1, \Theta_1)^2 + \sigma_t(E_2, \Theta_2)^2}, \tag{5.25}$$

where n is some factor that increases the σ interval to account for all correct events. A conservative value of $n = 5$ is used. $c\,(E_1, E_2)$ is a correction factor to account for asymmetric time distributions at low energies near the threshold. The correction factor is defined as

$$c\,(E_1, E_2) = \frac{1}{0.05 \cdot \min(E_1, E_2)} + 1, \tag{5.26}$$

where $\min(E_1, E_2)$ is the lower energy of the two crystals involved.[29] To apply the cut-off value Δt_{cut}, the time differences of all crystals within a spatial cluster are calculated with respect to the crystal with highest energy.[30] Crystals with a time difference within the cut-off value are treated as one valid cluster. The process is then repeated for the remaining crystals. The time cluster closest to the trigger is then saved for further reconstruction. In the case of time information from TDCs, low energy hits below the threshold do not have a time assigned. They must be considered as potentially belonging to any neighboring cluster. This is less frequent the case for SADCs, which can provide time information down to $< 1\,\text{MeV}$. In Figure 5.26 and 5.27 the time differences of crystals within a spatial cluster is shown for times from TDCs and SADCs. Only clusters related to photons from a π^0-decay recorded in May 2018 (TDC) and June 2021 (SADC) are used. Due to the dependence on threshold and energy, only a few representative parameter constellations are shown. The cut-off value is indicated as a red line. It is easy to see that the cut-off value still accounts for all correct photon clusters.

5.4.2 Performance

Time clustering leads to more precise energy and angular information, thereby reducing the influence of random coincidences on the particle reconstruction process. The effect of time clustering is shown in Figure 5.28, where the $\gamma\gamma$-invariant mass distribution is compared between simple spatial clustering and time clustering. Time clustering is performed once using time information from TDCs and once using time information from SADCs. In both cases, only a small improvement can be seen, suggesting that the current rate of random coincidences does not yet significantly affect the reconstruction process. However, time clustering using SADCs shows more noticeable improvement. This is because the SADCs provide time information for lower energies, while the TDCs are limited by the discriminator thresholds. In addition to more reconstructed events, a slight shift of the invariant mass to lower energies is observed. The reason for this is that time clustering always removes energy but never adds energy to spatial clusters. The shift of the π^0-invariant mass away from the literature value can be explained by the now obsolete energy calibration. After recalibration with time clustering, the position is again in agreement with the literature value. Due to

[28] When SADC times are used for time clustering, the dependence on the threshold Θ vanishes.
[29] Examples of correction factors are $c(10\,\text{MeV}) = 3$, $c(25\,\text{MeV}) = 1.8$, $c(40\,\text{MeV}) = 1.5$, $c(100\,\text{MeV}) = 1.2$.
[30] The crystal with the highest energy is used as the reference, as it has best time resolution.

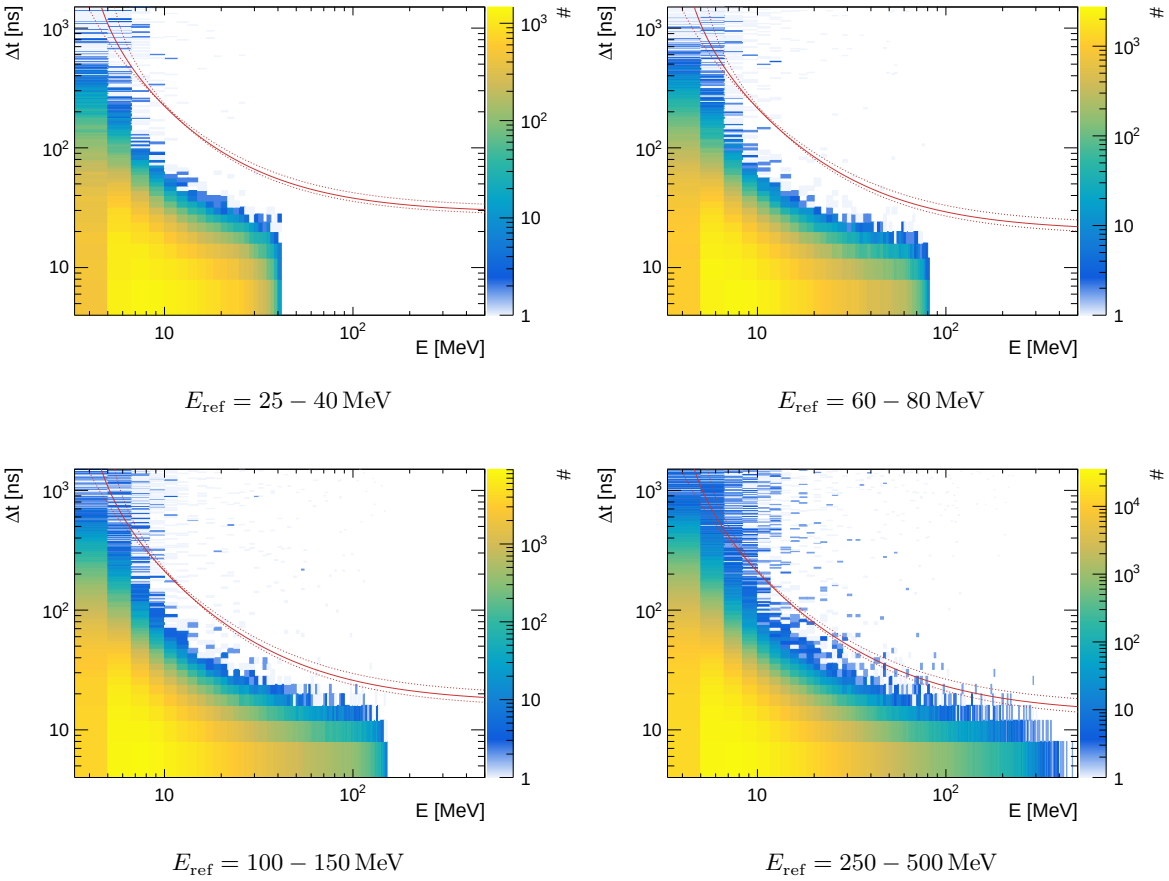

Figure 5.26: TDC time differences of crystals within each spatial cluster to the crystal with the highest energy E_{ref}. Only crystals within the index range $301 - 1\,380$ ($\Theta = 3.94\,\mathrm{MeV}$) are shown. The energy and threshold dependent cut-off value Δt_{cut} (cf. Eqn. 5.25) is indicated as a red line. The dashed lines represent the cut-off value for the Θ-threshold heights $\pm 1\,\mathrm{MeV}$. Only clusters related to photons from a π^0-decay recorded during May 2018 are used.

the later installation of SADCs, time clustering is performed using TDC information for data from December 2017 to June 2021. In June 2021 and for later data, SADCs are fully available and time clustering will be performed using SADC time information.

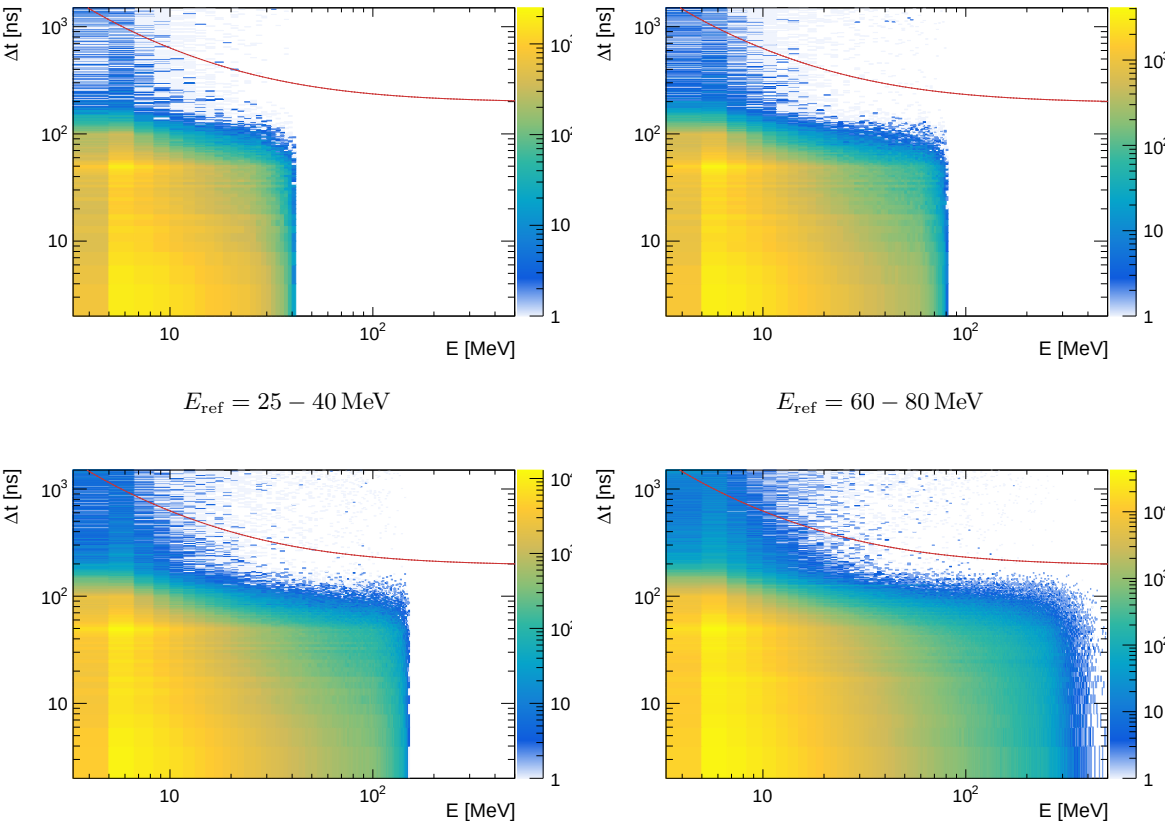

$E_{\mathrm{ref}} = 25 - 40\,\mathrm{MeV}$ $E_{\mathrm{ref}} = 60 - 80\,\mathrm{MeV}$

$E_{\mathrm{ref}} = 100 - 150\,\mathrm{MeV}$ $E_{\mathrm{ref}} = 250 - 500\,\mathrm{MeV}$

Figure 5.27: SADC time differences of crystals within each spatial cluster to the crystal with the highest energy E_{ref}. Only crystals within the index range $301 - 1\,380$ are shown. The energy dependent cut-off value Δt_{cut} (cf. Eqn. 5.25) is indicated as a red line. Only clusters related to photons from a π^0-decay recorded during June 2021 are used.

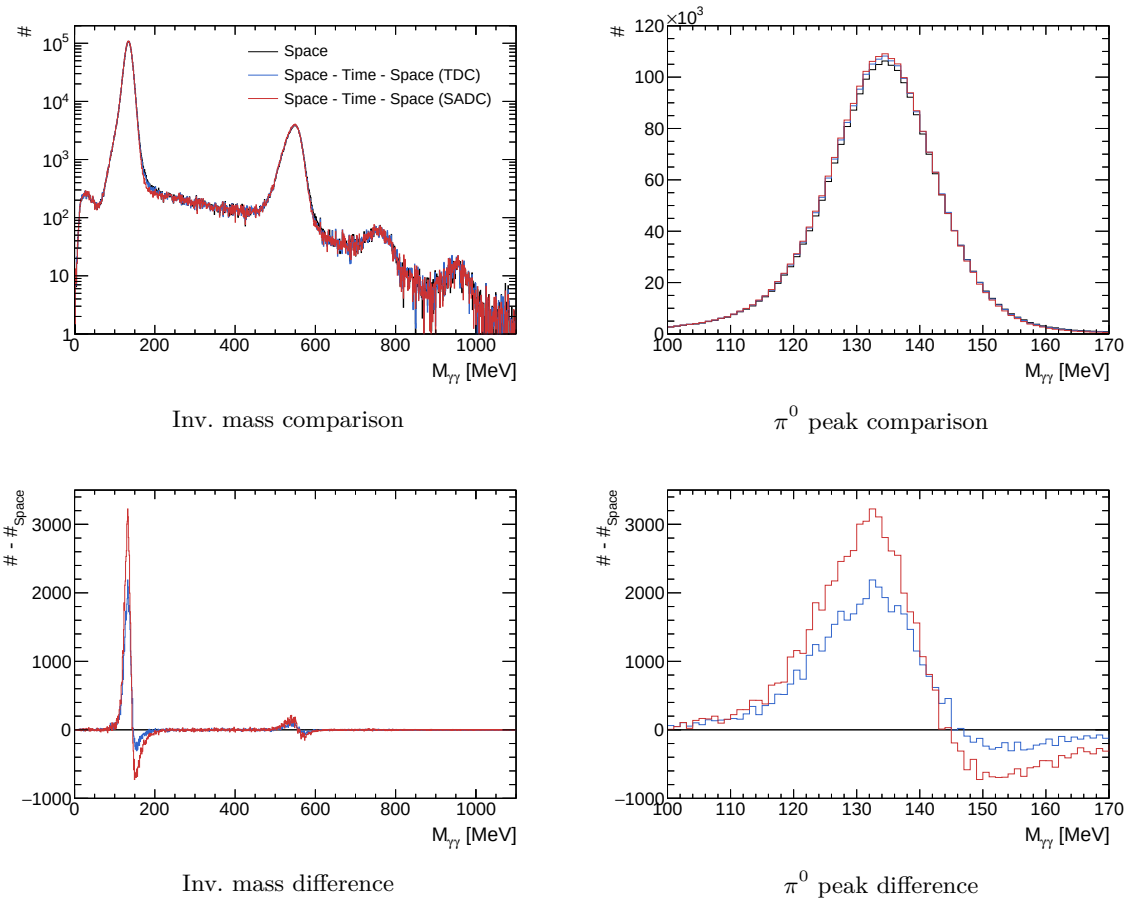

Inv. mass comparison

π^0 peak comparison

Inv. mass difference

π^0 peak difference

Figure 5.28: Comparison of the $\gamma\gamma$ invariant mass distribution between **plain spatial clustering** and time clustering with TDC time information or SADC time information. Top: A direct comparison is shown. Bottom: The difference between time clustering to simple spatial clustering is shown. In both cases, the June 2021 data is used.

CHAPTER 6

Event Reconstruction

After the readout and the calibration of the raw data, energy and time information is provided on a per-hit basis.[1] For an analysis of the data, a reconstruction of the properties of detected particles is required. Important properties are the four-momenta (four-vector), time and charge information. If the type of particle is known, it is sufficient to measure energy and directional information instead of the full four-vector. The event reconstruction process involves the determination of these properties of each final state particle as well as of the beam photon. For the beam photon, only the energy measurement is required, as its direction is defined by the experimental setup.

6.1 Photon Reconstruction

The calorimeters of the CBELSA/TAPS experiment are particularly well suited to detect photons. Thus, in the following only photons are considered as final state particles. While other particles such as the proton can also be detected they may not be fully stopped in the calorimeters and their energy cannot be reliably measured.

6.1.1 Shower Formation

In general, photons can interact with material through various processes, including the photoelectric effect, Compton effect, and pair production (cf. Passage of Particles Through Matter in [7]). By these interactions, photons deposit their energy in the detector material. The probability of interaction depends on the material and energy of the photons. In the energy range relevant for the experiment, pair production becomes the dominant effect (cf. Fig. 6.1). Pair production involves a photon converting into an e^-e^+-pair. The electron can then emit another photon through bremsstrahlung, leading to the creation of another e^-e^+-pair. This cascading effect, known as a shower, results in energy deposition within a certain volume of material. Essential characteristics of showers in material are the critical energy E_c and the radiation length X_0. The critical energy describes the point at which the energy loss of an electron due to bremsstrahlung is equal to the energy loss due to ionization.[2] The radiation length describes the mean distance over which an electron looses all but $1/e$ of its energy by bremsstrahlung [7]. The transverse distribution of a shower can be described by the Molière radius, defined as $R_M = X_0 \frac{21\,\mathrm{MeV}}{E_c}$. About 90 % of the shower energy is deposited within a cylinder of radius R_M while about 99 % is deposited within $3.5 \cdot R_M$ [7]. During

[1] Here, a hit refers to a signal from a detector element such as a crystal in the Crystal Barrel detector.
[2] Alternative definitions exist, e.g. in [152].

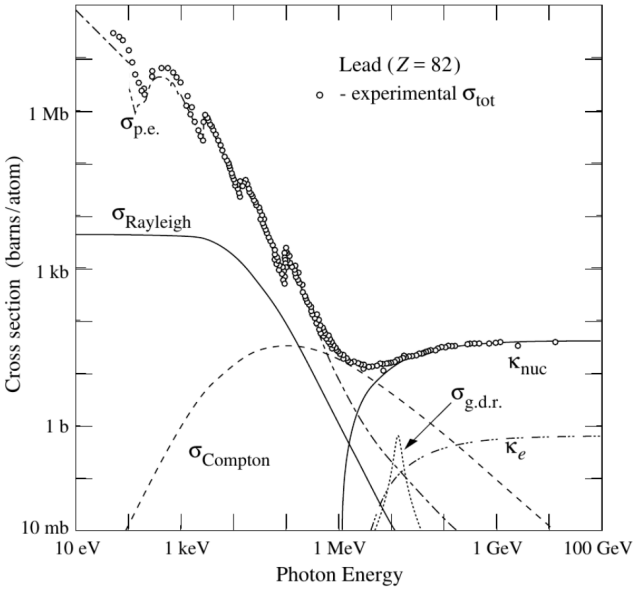

Figure 6.1: Cross sections of photons as a function of energy in lead [7]. Important contributions are the photoelectric effect $\sigma_{\text{p.e.}}$, Compton scattering σ_{Compton} and pair production at the nucleus κ_{nuc}. Other contributions are Rayleigh scattering σ_{Rayleigh}, pair production at the shell electrons κ_e and the photoelectric effect at the nucleus $\sigma_{\text{g.d.r.}}$. In the energy range relevant for the experiment, pair production becomes the dominant effect.

energy deposition, the scintillation process generates low-energy photons whose number is proportional to the energy deposited. The readout is then responsible for processing and digitizing this information. For more information on the readout, see Chapter 3.

6.1.2 Energy Reconstruction

The process of energy reconstruction is largely identical for the Crystal Barrel detector and MiniTAPS. Therefore, it is explained in detail for the Crystal Barrel detector and only the differences are described for MiniTAPS.

6.1.2.1 Crystal Barrel Detector

For each event, a set of crystals with energy deposition is recorded. To suppress noise, only energy depositions in crystals with $E > 1\,\text{MeV}$ are considered for reconstruction. These energy depositions are then grouped into clusters associated with incident particles. The clustering process consists of the following steps:

1. Grouping neighboring crystals with energy deposition.

2. Performing time clustering on each spatial cluster to separate signals that occur close in space but at different times. This is done by applying an energy-dependent time cut, as described in detail in Section 5.4. For each spatial cluster, only the time cluster closest to the trigger is kept.

3. Performing spatial clustering again to account for possible changes in neighborhood relations after time clustering.

After clustering, a central crystal[3] with energy $E_{\text{central}} > 20\,\text{MeV}$ and a total cluster energy $E_{\text{cluster}} > 20\,\text{MeV}$ is required to further suppress the background.[4] Clusters can be classified as either single-particle clusters (1-PED[5]) or multi-particle clusters (e.g. 2-PED) (cf. Fig. 6.2). A 1-PED cluster is formed by a single incident particle and the particle energy is equal to the sum of all the individual energy depositions within the cluster. Multi-particle clusters are formed by overlapping showers of multiple incoming particles. In this case, the cluster must be split into these multiple incident particles. Therefore, local maxima within the cluster are identified, each corresponding to the central crystals of an incident particle. Again, the requirement is an energy $E_{\text{central}} > 20\,\text{MeV}$ for each local maximum. The energy depositions are then distributed to the incident particles using their theoretically expected energy as weight [153]. For a crystal i, the expected energy is calculated using an exponential description of the transverse distribution of a shower

$$E_i^{\text{theo}} = E_{\text{central}} \cdot \exp\left(-\frac{d_i}{R_M}\right). \tag{6.1}$$

Here, R_M is the Molière-radius[6] and d_i the distance of the i-th crystal to the central crystal. Finally, the energy of a crystal i associated with a particle pk is given by

$$E_i^{pk} = E_i \cdot \frac{E_i^{\text{theo},pk}}{\sum_j E_i^{\text{theo},pj}}. \tag{6.2}$$

The energies of the central crystals are corrected once to remove the contributions from neighboring PEDs before they are being used in Eqn. 6.1 to calculate the expected energy of the other crystals. Also, an energy-dependent penetration depth is explicitly considered in the calculation of the distances d_i. For more information see [153].

An energy correction function (ECF) is applied to the reconstructed energies to account for energy deposition in non-sensitive materials such as the support structures or the titanium covers of the crystals, as well as for energy loss in the boundary regions of the detector [146]. The ECF depends on the energy and the polar angle θ of the reconstructed particles and was developed based on Monte Carlo simulations of the detector. In a first step, the ECF ensures that the most probable values[7] of photon energy distributions match the expected values. However, during the development of the ECF, it was found that despite this correction, the reconstructed invariant masses of the mesons are shifted to lower values. This is a result of product distributions which are constructed from on the asymmetric energy distributions in

[3] The crystal with the highest energy in the cluster.

[4] In this particular case, the total cluster energy is already ensured by requiring a central crystal with $E_{\text{central}} > 20\,\text{MeV}$.

[5] **P**article-**E**nergy-**D**eposit

[6] The Molière radius is an exponential description of the transverse distribution of a shower. The radius is defined as $R_M = X_0 \frac{21\,\text{MeV}}{E_c}$ [7].

[7] The maxima of the distributions. In the case of asymmetric distributions, this is not equal to the expectation value.

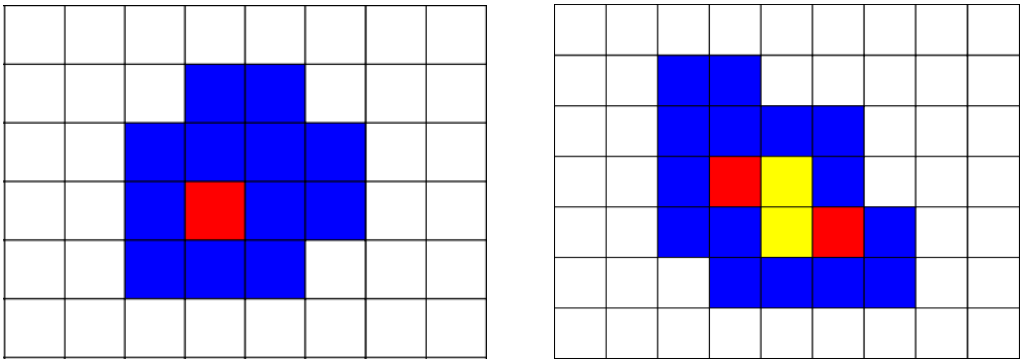

1-PED 2-PED

Figure 6.2: Difference between 1-PED and 2-PED cluster events [153]. For the 2-PED event, two separate maxima are shown in red. Crystals bordering both maxima are marked in yellow.

the invariant mass calculation [154]. While this shift in the invariant mass can be compensated in the data by energy calibration (cf. Section 4.2), it is difficult to do so for the Monte Carlo simulations, where no energy calibration is applied. Instead, the ECF is modified as it is applied to both data and Monte Carlo events. After modification, the ECF ensures that the reconstructed π^0 invariant mass is on average equal to the literature value [146]. This version of the ECF is known as *sigma85* and is used by default for reconstruction in the Crystal Barrel detector. The energy resolution for the Crystal Barrel detector is [125]

$$\left(\frac{\sigma_E}{E}\right)^2 = \left(\frac{(2.39 \pm 0.05)\,\%}{\sqrt[4]{E/\mathrm{GeV}}}\right)^2 + \left(\frac{(0.46 \pm 0.08)\,\%}{\sqrt{E/\mathrm{GeV}}}\right)^2 + \left(\frac{(0.048 \pm 0.007)\,\%}{E/\mathrm{GeV}}\right)^2. \tag{6.3}$$

6.1.2.2 MiniTAPS Detector

Energy reconstruction in the MiniTAPS detector is similar to energy reconstruction in the Crystal Barrel detector. However, there are a few differences. One such difference is in the energy thresholds. Only energy depositions with $E > 17\,\mathrm{MeV}$ for the inner two rings and $E > 13\,\mathrm{MeV}$ for the rest are considered in MiniTAPS. The higher value for the inner rings accounts for the higher rate close to the beam.[8] After clustering, a central crystal with an energy above 20 MeV and a total cluster energy above 25 MeV is required. Furthermore, instead of using an energy dependent time cut to remove random coincidences within a cluster, a constant maximum time difference of 5 ns is used. Similar to the Crystal Barrel detector, an energy correction function (ECF) is applied for energy reconstruction in MiniTAPS [155]. The ECF depends on the energy and the point of impact of the photon. The energy resolution for MiniTAPS is [156]

$$\frac{\sigma_E}{E} = 1.91\,\% + \frac{0.59\,\%}{\sqrt{E/\mathrm{GeV}}}. \tag{6.4}$$

[8] The constant fraction discriminator thresholds are also set to higher values compared to the outer rings.

6.1.3 Directional Reconstruction

The reconstruction of the direction is also very similar for the Crystal Barrel detector and MiniTAPS. Therefore, the process for the Crystal Barrel detector will be explained again first and only the differences for MiniTAPS will be described.

6.1.3.1 Crystal Barrel Detector

The direction with respect to the center of the target is reconstructed from the position of the crystals within a PED cluster. For higher resolution, the center of the shower is determined by calculating a weighted average in polar (θ) and azimuthal (ϕ) directions [147]

$$\theta_{\mathrm{PED}} = \sum_i w_i \theta_i \qquad \phi_{\mathrm{PED}} = \sum_i w_i \phi_i. \tag{6.5}$$

For single-particle cluster, the weight for each crystal i is given by

$$w_i = \frac{\tilde{w}_i}{\sum_i \tilde{w}_i}, \quad \text{with} \quad \tilde{w}_i = \max\left\{0; 4.25 + \ln\left(\frac{E_i}{E_{\mathrm{cluster}}}\right)\right\}. \tag{6.6}$$

The logarithmic weighting accounts for the expected exponential decrease of energy in the transverse direction of the shower. The value of 4.25 leads to a cut-off at $1.4\,\% \cdot E_{\mathrm{cluster}}$ in energy, below which crystals are not considered for directional reconstruction. For multi-particle clusters, first the energy correction is applied as already described for the energy reconstruction. This time, however, only the crystals directly neighboring the central crystal of each PED are taken into account. By using the weighted determination of the direction, angular resolutions of about $1.4 - 2.2^\circ$ for photons with $E = 100\,\mathrm{MeV}$ and $0.7 - 1.2^\circ$ for photons with $E = 1\,000\,\mathrm{MeV}$ are achieved which is significantly better than the granularity of the crystals alone [146]. For other types of particles such as protons or charged pions, which may deposit their energy in a single crystal, the angular resolution is still dominated by the granularity of the crystals.

6.1.3.2 MiniTAPS Detector

In the case of the MiniTAPS detector, the crystals do not point head-on towards the vertex, resulting in asymmetric shower distributions with respect to the entry point of the incident particle. As a consequence, the directions determined from the crystal positions have to be corrected depending on the penetration depth of the showers [155] (cf. Fig. 6.3). Uncorrected angles would otherwise be overestimated. Angular resolution in the order of $0.2 - 0.8^\circ$ is achieved for MiniTAPS [155].

6.2 Time

Time information for particles is available from both calorimeters and charge-sensitive detectors. For the MiniTAPS detector, a time resolution of FWHM = 0.85 ns is achieved with respect to Tagger bars. For the Crystal Barrel detector, the time resolution is strongly dependent on the energy and the discriminator thresholds set in the experiment, varying

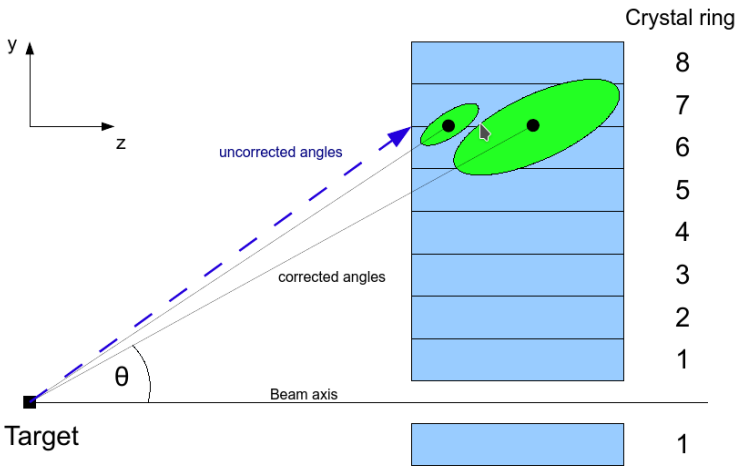

Figure 6.3: Illustration of the angle correction in MiniTAPS depending on the penetration depth of the showers [155].

from 1 ns for high energies to 20 ns for low energies (cf. Fig. 5.3). Time resolutions for other detector components are listed in Table 5.1.

Time information from TDCs is available as soon as the energy deposition in a crystal exceeds the predefined thresholds set in the discriminator modules. The central crystal always meets this criterion because its energy must be above 20 MeV, exceeding the highest discriminator thresholds.[9] When multiple crystals have time information, the central crystal is used to define the time of the incident particle. This takes advantage of the better time resolution at higher energies. In scenarios where energy information is only available from charge-sensitive detectors but not from the calorimeters, the time information from the charge-sensitive detectors is used as an alternative source. This ensures that time information is always available for the analysis.

6.3 Identification of Charged Particles

In addition to the energy and time information from the calorimeters, other detector components are dedicated to the identification of charged particles. These detectors are also capable of providing time and directional information, allowing charge identification to be matched with the reconstructed clusters in the calorimeters. Charge information is provided by three detector systems: the Inner detector, scintillating plates in the forward direction of the Crystal Barrel detector (Forward Veto detector) and scintillating plates in front of MiniTAPS (MiniTAPS Veto detector).

6.3.1 Inner Detector

The Inner detector consists of 513 scintillating fibers which are arranged in three layers. The first step of reconstruction is to cluster the activated fibers within each layer. The clustering

[9] Referring to threshold A, i.e. the lower threshold.

process requires a maximum time difference of 14 ns for fibers within a cluster. Based on the clusters, crossing points of two layers can be determined. Again, a maximum time difference of 14 ns is applied. Due to the geometry of the Inner detector, hits in two fibers in two different layers already define a unique crossing point in the Inner detector. A crossing point through three layers corresponds to three of these two-crossing points. Thus, if possible, three reconstructed two-crossing points are combined into a single three-crossing point. During this process, a distance cut is applied to remove coincident background that does not actually correspond to part of a three-crossing point. More information about this distance cut can be found in [157]. Fibers that are part of a three-crossing point are then removed and not used for further isolated two-crossing points. This reduces the amount of ghost hits due to ambiguities in case of multiple hits in the Inner detector [158].

6.3.2 Forward Veto Detector

There are 180 scintillating plates positioned in front of the first three rings of the Crystal Barrel detector. With a separation of $6^\circ \times 12^\circ$ in θ and ϕ, they overlap in azimuthal direction. This allows to require coincident hits of two plates with a maximum time difference of 20 ns. While the polar resolution is given by the size of the plates, the azimuthal resolution is improved to 6° by the overlap.

6.3.3 MiniTAPS Veto Detector

A scintillating plate is placed in front of each crystal in MiniTAPS. Unlike the Forward Veto detector, there is no overlap between the plates and a single hit is sufficient to identify charge. In this case, the center of the plate is used as incident point. The resolution is determined by the size of the plates which have a front face diameter of 5.9 cm.

6.3.4 Linking to Clusters

Charge information and reconstructed clusters in the calorimeters may belong to the very same particle. To match the charge information with the clusters, their individually reconstructed directions and time information are compared.

For the Inner detector and the Crystal Barrel detector, charge information is matched with calorimeter hits if the following conditions are met

$$|\Delta t| = 50\,\text{ns} \qquad |\Delta\phi| < 12^\circ \qquad |\Delta\theta| < 12^\circ,$$

where Δt is the maximum time difference and $\Delta\phi$, $\Delta\theta$ are the azimuthal and polar angle differences, respectively. An exception is the Liquid Hydrogen target (LH_2), where $\Delta\theta$ is increased to 50°.[10] For the Forward Veto detector and the Crystal Barrel detector the matching conditions are

$$|\Delta t| = 50\,\text{ns} \qquad |\Delta\phi| < 14^\circ \qquad |\Delta\theta| < 10^\circ.$$

[10] The LH_2 target is significantly longer than the Frozen Spin target, which degrades the polar resolution. The effect is most pronounced for the Inner detector, which is close to the target.

In the case of the MiniTAPS Veto detector and the MiniTAPS calorimeter, the distance on the surface of the detector is used for comparison, instead of angular differences. The conditions for matching charge information and clusters are

$$|\Delta t| = 15\,\text{ns} \qquad |\Delta d| < 6.51\,\text{cm}.$$

A motivation of these conditions is given in [159] and, with small variations, in [158]. In this work, only the allowed time differences Δt for the Inner- and Crystal Barrel detector as well as the Forward Veto- and Crystal Barrel detector are chosen differently. A higher value of $|\Delta t| = 50\,\text{ns}$ is used to account for the time resolution within the new detector setup (cf. Table 5.1).

6.4 The Beam Photon

Up to this point, only the properties of the final state particles have been discussed. For a complete description of the reaction, the energy and time of the incoming photon must also be determined.[11] To obtain the energy and time information of the beam photon, the Tagging system is used that measures the deflection of the outgoing electrons.

6.4.1 Tagging System

The Tagging system consists of two components: the Tagger bars and the Tagger fibers. Overlapping bars allow the requirement of coincident hits from two bars. Neighboring hits are then clustered, with a maximum time difference of 4 ns. Similarly, neighboring hits in fibers are clustered, but with a slightly larger maximum time difference of 7 ns due to the lower time resolution. Also, due to partial lack of fiber overlap, hits in only one fiber are also considered. In regions where bars and fibers overlap, their clusters are matched for optimal reconstruction [103, 160]. Again, a maximum time difference of 4 ns is required for a match. In regions where only bars exist, only their information is used. To reconstruct the energy information, the positions of the hits in the Tagger bars and fibers are related to the energy using a polynomial dependence. This dependence is carefully determined based on a beam calibration and the magnetic field set in the tagger. The average of all energies within the cluster is then calculated. If energy information is available from fibers, these are used solely because of their better spatial and improved energy resolution. For time information, the times of bars and fibers are also averaged. However, time information from bars is weighted twice as much as that from fibers because bars have better time resolution.

[11] The direction of the beam photon is defined by the experimental setup (along the z-axis).

CHAPTER 7

Event Selection for the $p\pi^0\pi^0$ Final State

During data taking, a wide range of information on various types of events is recorded. For a reliable analysis of the $p\pi^0\pi^0$ final state, a precise event selection is essential. Therefore, a procedure has been developed that maximizes the available statistics while keeping the background contamination to a minimum.

For a fixed target experiment, the process of $\pi^0\pi^0$ photoproduction off the proton can be expressed in terms of four-momenta as

$$\begin{aligned}\begin{pmatrix} E_\gamma \\ \vec{p}_\gamma \end{pmatrix} + \begin{pmatrix} m_p \\ \vec{0} \end{pmatrix} &= \begin{pmatrix} E_{p'} \\ \vec{p}_{p'} \end{pmatrix} + \begin{pmatrix} E_{\pi_1^0} \\ \vec{p}_{\pi_1^0} \end{pmatrix} + \begin{pmatrix} E_{\pi_2^0} \\ \vec{p}_{\pi_2^0} \end{pmatrix} \\ &= \begin{pmatrix} E_{p'} \\ \vec{p}_{p'} \end{pmatrix} + \begin{pmatrix} E_{\gamma_1} \\ \vec{p}_{\gamma_1} \end{pmatrix} + \begin{pmatrix} E_{\gamma_2} \\ \vec{p}_{\gamma_2} \end{pmatrix} + \begin{pmatrix} E_{\gamma_3} \\ \vec{p}_{\gamma_3} \end{pmatrix} + \begin{pmatrix} E_{\gamma_4} \\ \vec{p}_{\gamma_4} \end{pmatrix}, \end{aligned} \tag{7.1}$$

assuming a decay of each π^0 into two γ.[1] E_γ and $\vec{p}_\gamma$ is the energy and momentum of the incoming photon and m_p the mass of the target proton at rest. $E_{p'}$ and $\vec{p}_{p'}$ is the energy and momentum of the outgoing proton in the final state. $E_{\gamma_{1-4}}$ and $\vec{p}_{\gamma_{1-4}}$ are the energies and momenta of the photons resulting from the decay of the two π^0. During event selection, charge information is used to identify the outgoing proton and to ensure that the photons are uncharged.[2] Time information is used to ensure a correlation of all interacting particles. In addition, conservation of energy and momentum is used to verify that a reaction is indeed described by Eqn. 7.1.

The event selection is performed for the following periods of data taking: December 2017, May 2018, February 2019, and June 2021. They represent the butanol data available after modification of the experiment up to the time of writing. The data were taken with a transversely polarized target and a linearly polarized beam. A detailed explanation of each data taking period can be found in Chapter 9. In the following, some figures are presented only for the May 2018 data, as an example. However, in case of statistical limitations, all data periods are combined. A good agreement between the different periods is ensured beforehand. Furthermore, beam flux normalization is applied as it is explained in detail in Section 8.3.1.

[1] A π^0 decays into two γ with a probability of 98.82 % [7].
[2] Later, the requirement of uncharged γ is relaxed a bit, as described in Section 7.3.

7.1 Combinatorics

After the event reconstruction described in Chapter 6, a set of four-momenta candidates is available for each event.[3] From Eqn. 7.1, a final state consisting of five particles is expected: one proton and two photon pairs resulting from the decay of the two π^0.

The assignment of the four-momenta candidates to the different particle types is not unique. Without any assumptions all combinations must be considered. Assuming that there is no prior information about the charge, each of the particles must be tentatively treated as the proton once. From the other four particles the two π^0 can be constructed in three different ways. This leads to a total of 15 combinations just considering the final state. In addition, due to the high rate of the beam, multiple beam photons are tagged per event (cf. Fig. 7.1). As before, each beam photon must be considered once. The incorrect combinations are assumed to be eliminated later on in the event selection process. Incorrect combinations remaining after event selection contribute to the final background contamination. To reduce the number of combinations, charge information that defines the proton will be used in the following. For a more detailed discussion of the use of charge information, see Section 7.3.

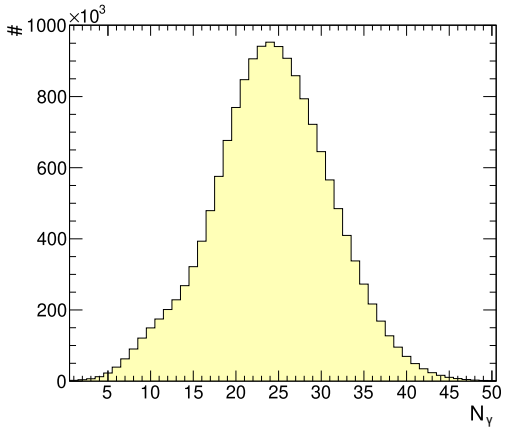

Figure 7.1: Multiplicity of beam photons N_γ during data taking in May 2018 without any additional cuts for 5-PED events.

7.2 Event Classes

There are three classes of events that can be distinguished depending on the detection of the outgoing proton: 5-PED, 4.5-PED and 4-PED, where PED refers to a reconstructed final state particle. The event classes are particularly well separated within the kinematic region spanned by the kinetic energy $E_{p'}^{\text{kin}}$ and the polar angle $\theta_{p'}$ of the outgoing (missing[4]) proton (cf. Fig. 7.2). The event classes extracted from the data are compared with a Monte Carlo phase space simulation[5] that assumes a photon flux following the Bethe-Heitler cross section (c.f. Eqn. 2.4). The Monte Carlo simulation is used to verify that the event classes are correctly reconstructed. In all cases, event selection is applied (cf. Section 7.4). For the experimental data, carbon subtraction (cf. Section 8.3) and flux normalization (cf. Section 8.3.1.) are also performed. To allow for a direct comparison of structural features

[3] Only for the photon, the real four-momenta can be measured. The proton cannot be fully reconstructed. Only its direction but not its energy is available.

[4] As the outgoing proton can not be fully reconstructed, the missing proton is used instead. The missing proton is recalculated using the initial state information and the four-momenta of the four γ. For the calculation of the missing proton refer to Eqn. 7.6.

[5] For the simulation, the position of the Inner detector was updated to match the current setup (valid for all data taking periods in this work). This also applies to the aluminum tube, which is still in place [161].

between data and Monte Carlo, all distributions are normalized to a total integral of one. The event classes are explained in more detail below.

5-PED In 5-PED events, all final state particles are reconstructed. The photons as well as the proton are detected in the calorimeters. This is the case for most of the kinematic regions, as can be seen in Fig. 7.2 (top).

4.5-PED In 4.5-PED events, the proton is only detected in charge-sensitive detectors but not in a calorimeter. This can happen for two reasons: an angular range is only covered by a charge-sensitive detector but not by the sensitive material of a calorimeter, or the kinetic energy of the proton is too low to leave a signal in the calorimeter. Both can be seen in Fig. 7.2 (middle). The enhancement at low kinetic energies corresponds to protons that, after leaving a signal in a charge-sensitive detector, do not have enough energy to leave another signal in the calorimeter. The horizontal line just below $\theta_{p'_m} \approx 30^\circ$ up to high kinetic energies corresponds to insensitive material in the calorimeter at the transition to the Forward detector. while the Inner detector still covers this region. For the selection of 4.5-PED events, the signals from charge-sensitive detectors must occur within $-100\,\text{ns} \leq t \leq 85\,\text{ns}$ around the trigger. This is the same time range as specified in the general selection procedure described in Section 7.4. If multiple signals from charge-sensitive detectors are available, the signal which is closest (based on the opening angle) to the missing proton p'_m is used. The other signals are discarded.

4-PED In 4-PED events, the proton is not detected at all. Nevertheless, there is enough information available to recalculate the missing proton p'_m from the other measured quantities (cf. Fig. 7.2 (bottom)). 4-PED events occur at even lower kinetic energies than 4.5-PED events. Here, the protons do not even leave a signal in the charge-sensitive detectors. A horizontal line appears at about $\theta_{p'_m} \approx 12^\circ$ up to high kinetic energies. This line corresponds to the transition to the MiniTAPS detector, where only insensitive material exists and no charge-sensitive detector.

The comparison with the Monte Carlo for 4-PED events is complicated by low statistics and carbon subtraction.[6] Both lead to fluctuations at higher kinetic energies. Still, for all event classes, a good agreement between data and Monte Carlo can be observed. This confirms that the event classes are selected according to expectations when analyzing the data. The proportion of each PED class is given in Table 7.1. Despite the dominant contribution of 5-PED events, it is important to note that for a complete analysis, all event classes must be included. This is the only way to cover the whole kinematic region.

7.3 Charge Information

Charge information can be used to identify the outgoing proton. This reduces the number of combinations that need to be considered for each event (cf. Section 7.1). If one charged

[6] A detailed explanation of carbon subtraction is given in Section 8.3.

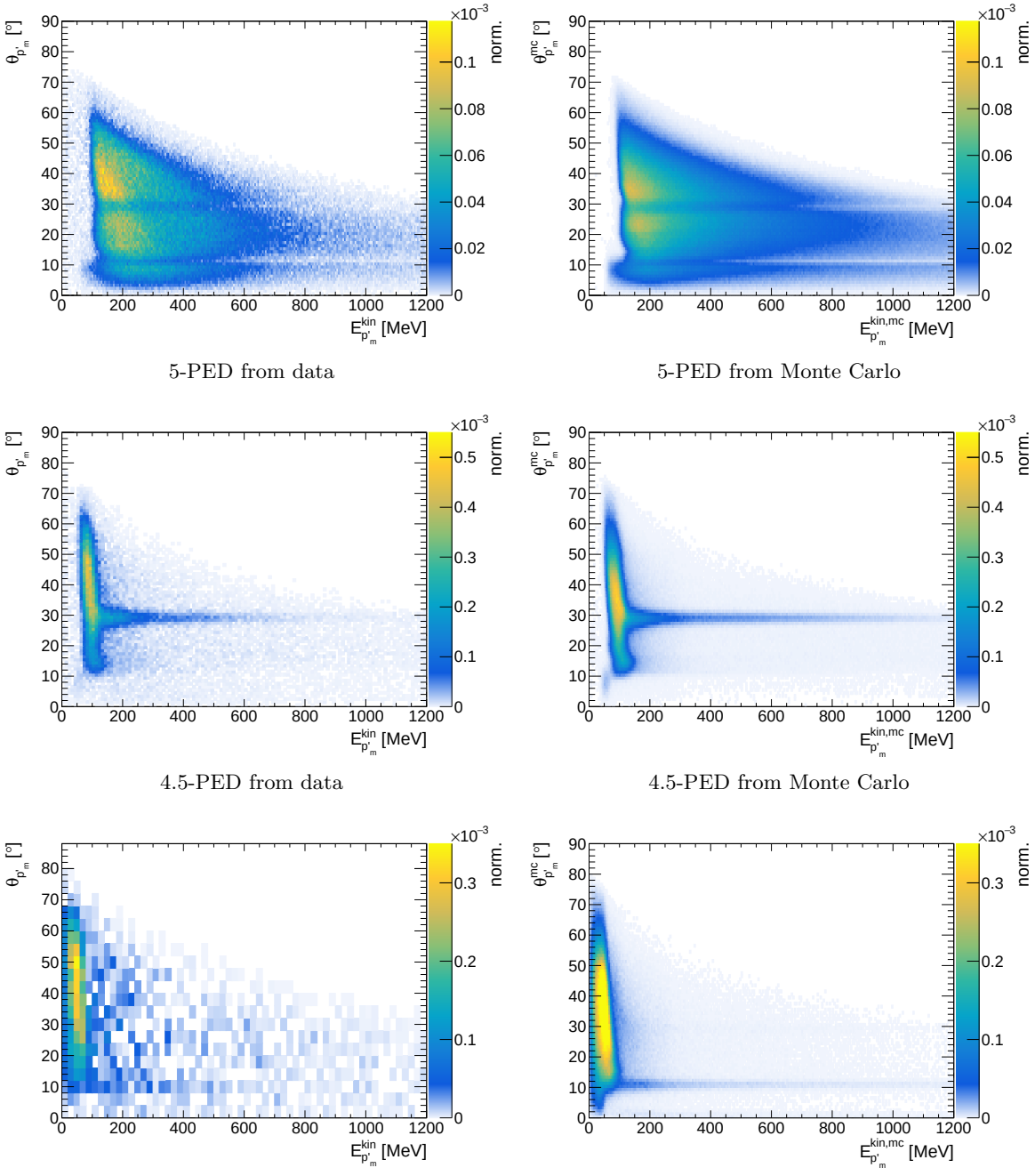

5-PED from data

5-PED from Monte Carlo

4.5-PED from data

4.5-PED from Monte Carlo

4-PED from data

4-PED from Monte Carlo

Figure 7.2: Distribution of the event classes 5-PED, 4.5-PED and 4-PED as a function of the kinetic energy $E_{p'_m}$ and the polar angle $\theta_{p'_m}$ of the missing proton. Left: Data from December 2017, May 2018, February 2019 and June 2021 are shown. In addition to event selection (cf. Section 7.4), carbon subtraction (cf. Section 8.3) and flux normalization (cf. Section 8.3.1) are performed. Right: Event classes from a Monte Carlo phase space simulation (only structural differences can be checked).

Table 7.1: Proportion of each event class after event selection during data taking in December 2017, May 2018, February 2019 and June 2021. For June 2021 no 4-PED events are used (cf. Section 8.3.2.3). Event selection (cf. Section 7.4), carbon subtraction (cf. Section 8.3) and flux normalization (cf. Section 8.3.1.) are applied.

5-PED	4.5-PED	4-PED
83 %	13 %	4 %

particle and four uncharged particles are required, the proton can be uniquely identified. This reduces the number of combinations by a factor of five. In the experiment, however, it may happen that photons convert into e^-e^+-pairs within the material between the interaction point and the detector. This is particularly important to consider for the Frozen Spin target due to the additional material of the cryostat. Here, the conversion probability of a photon is estimated to be in the region of 10 %. Given four photons in the final state, the probability for conversion of k photons is described by the binomial distribution

$$P(k) = \binom{4}{k} 0.1^k (1-0.1)^{4-k} \quad \text{with} \quad \binom{n}{k} = \frac{4!}{k!(4-k)!}. \tag{7.2}$$

This gives an estimated probability of conversion of 29 % for one photon, and 5 %, 0.3 %, and 0.01 % for the conversion of 2, 3, or all 4 photons within a single event, respectively. In case of conversion, the opening angle of the electron-positron pair is small enough so that all the energy is deposited in a single cluster. Requiring uncharged photons would rule out these events. On the other hand, considering charged photons increases the combinatorial complexity. It is therefore not clear from the beginning how to use the charge information best. Three different approaches are therefore compared.

`charged` In a `charged` analysis, the proton is required to be the only charged particle. The photons must be uncharged. This reduces the number of combinations by a factor of five down to three combinations, which minimizes the background contribution. However, it is not possible to account for the conversion of photons.

`semicharged` In a `semicharged` analysis, the proton is still required to be charged. But at the same time up to one charged photon is allowed. This allows for a potential conversion of one of the photons. If a charged photon is present, the number of combinations increases by a factor of two to six combinations compared to the `charged` analysis. A conversion of more than one photon is not taken into account, as the probability of more photons being converted is greatly reduced.

`dontcarecharged` Within a `dontcarecharged` analysis no charge information is used at all. All 15 possible combinations must be considered.

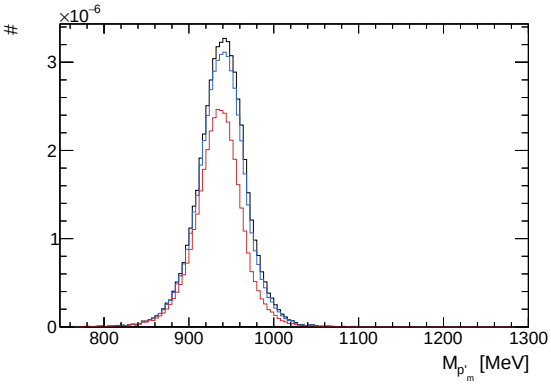

5-PED, full kinematic fit

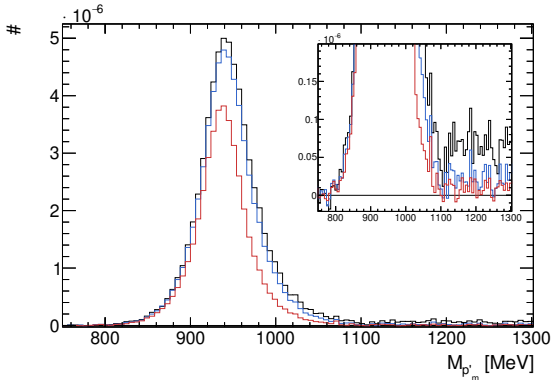

5-PED, $\pi^0\pi^0$ fit

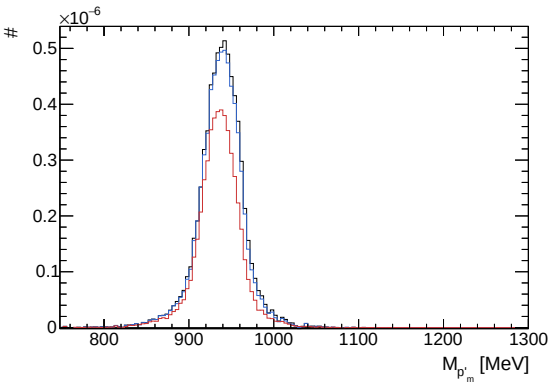

4.5-PED, full kinematic fit

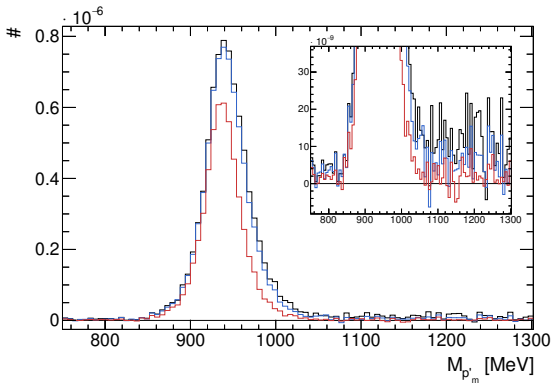

4.5-PED, $\pi^0\pi^0$ fit

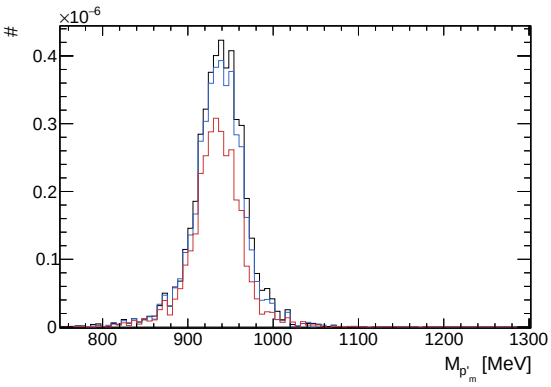

4-PED, full kinematic fit

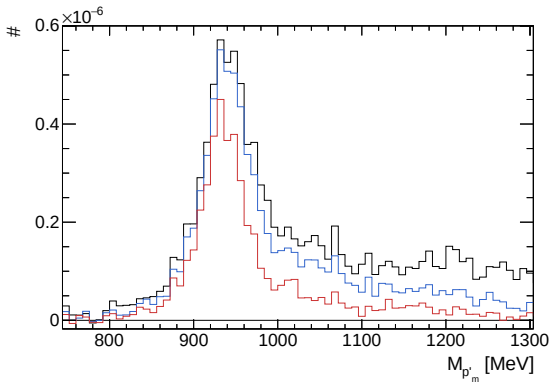

4-PED, $\pi^0\pi^0$ fit

Figure 7.3: Comparison of the missing mass for a `charged`, `semicharged` and **`dontcarecharged`** analysis. Left: Missing mass distribution after the full kinematic fit (cf. Section 7.4.3). In this case, the background is no longer visible due to the fulfilled kinematic requirements. The amount of statistics can be estimated from the integral. Right: Missing mass distribution after the $\pi^0\pi^0$ fit (cf. Section 7.7.1). The background corresponds to the right-hand increment. In each case, the combined data of December 2017, May 2018, February 2019, and June 2021 are used. In addition to event selection (cf. Section 7.4), carbon subtraction (cf. Section 8.3) and flux normalization (cf. Section 8.3.1) are performed. Note that the binning differs between the images for better visualization. An overlay is used when the peak is dominant.

Fig. 7.3 shows a comparison of the different approaches. For each case, the invariant mass distribution of the missing proton (missing mass) at the end of the event selection is shown. The amount of statistics in the final event sample can be estimated from the integral of the distributions on the left. The amount of background corresponds to the right-hand increment in the distributions on the right. More details on the background estimation are given in Section 7.7.

The comparison shows that the `semicharged` analysis has the best signal-to-noise ratio for 5-PED and 4.5-PED events. Compared to the `semicharged` analysis, the `dontcarecharged` analysis does not significantly improve the statistics further but instead shows a slight increase in the background contribution. For 4-PED events, the background increases significantly when the charge requirement is relaxed. This is due to the limited number of constraints on event selection for this particular event class. As a result of the comparison, a `semicharged` analysis is performed for 5-PED and 4.5-PED events, while a `charged` analysis is used for 4-PED events. This improves the statistics for 5-PED and 4.5-PED by 33 % compared to a standard `charged` analysis.

7.4 Selection

In order to select only $p\pi^0\pi^0$ events for analysis, certain constraints are applied. In the following, the constraints resulting from time information and kinematics are presented.

7.4.1 Time Cuts

Time information can be used to ensure correlation between all the interacting particles. Non-correlated particles result from random coincidences. Two criteria are used to remove the random coincidences: the time of each individual particle in the final state (particle time) and the time difference between the initial and the final state of a reaction (reaction time).

Particle Time Particles that truly participated in the reaction are detected around the trigger time $t = 0\,\text{ns}$. Therefore, only final state particles with a time within $-100\,\text{ns} \leq t \leq 85\,\text{ns}$ are considered. In this way, particles that are not part of the reaction are excluded. The time range is carefully selected using the time distribution of all final state particles as shown in Fig. 7.4 (left). The flat background corresponds to random coincidences. The cut on individual particle times is performed before the event classes (PEDs) are constructed, as the number of particles can change.

Reaction Time Due to the limited time resolution of the trigger, the individual particle times cannot be used to ensure correlation between the initial and the final state of a reaction. Instead, the reaction time is used, which is defined as the time difference between the beam photon and the average time of the mesons in the final state

$$t_{\text{reaction}} = t_{\text{beam}} - \bar{t}_{\text{mesons}}. \tag{7.3}$$

This removes the effect of the trigger. The time of the mesons $\bar{t}_{\text{mesons}}$ is determined by averaging all the photon times associated with the mesons. The time of the proton, which

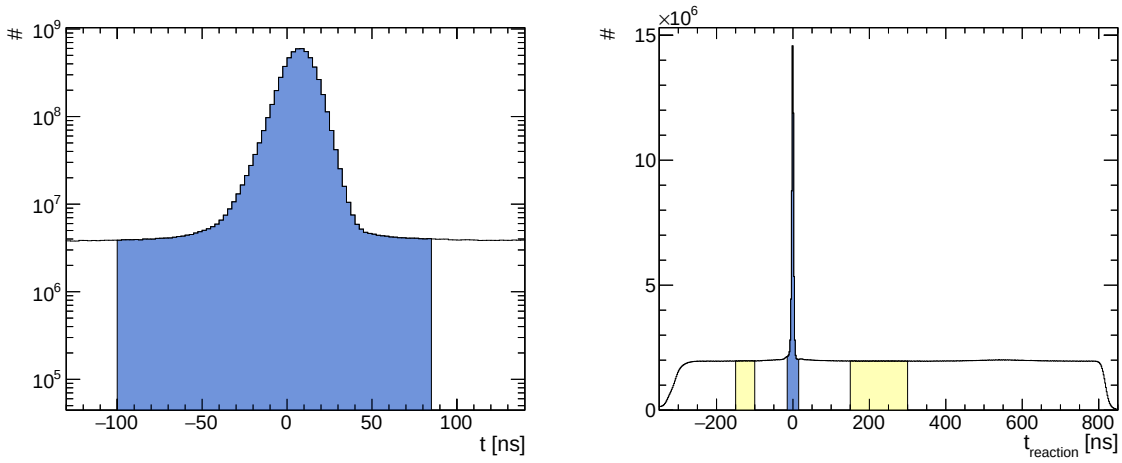

Time relative to trigger

Reaction time

Figure 7.4: Left: Time of all reconstructed final state particles relative to trigger. The cut is displayed in blue. Right: Reaction time from Eqn. 7.3. The cut on the prompt peak is displayed in blue while the selected sideband is shown in yellow. The data is based on May 2018 as an example.

may travel slower, is excluded. The reaction time is shown in Fig. 7.4 (right). The prompt peak around 0 ns results from correct combinations between the initial beam photon and the final state. Wrong combinations are flatly distributed. A cut at the prompt peak $-15\,\text{ns} \leq t_{\text{reaction}} \leq 15\,\text{ns}$ removes most of the incorrect combinations. However, some background remains below the prompt peak. This part is removed by sideband subtraction.

Sideband Subtraction The background below the peak is removed by sideband subtraction. Therefore, a part of the flat background (sideband) is retained in the region $-150\,\text{ns} \leq t_{\text{reaction}} \leq -100\,\text{ns}$ and $150\,\text{ns} \leq t_{\text{reaction}} \leq 300\,\text{ns}$ (cf. Fig. 7.4 (right)). Events from the sideband behave exactly like events below the peak. Thus, the sideband events can be subtracted from the prompt events using the ratio of the widths of the different bands as the weight

$$\omega = \frac{\Delta t_{\text{prompt}}}{\Delta t_{\text{sideband}}} = \frac{30\,\text{ns}}{50\,\text{ns} + 150\,\text{ns}} = 0.15. \tag{7.4}$$

In this work, sideband subtraction is performed on all the data to eliminate any influence of false beam photons.

7.4.2 Kinematic Cuts

The conservation of energy and momentum in Eqn. 7.1 defines the behavior of the final state. Measured energy and angle information can therefore be used to discard events that behave differently. The criteria used are explained below. The missing mass and invariant mass criteria are only mentioned for completeness. In the final selection of the events, a kinematic fit is applied instead, which replaces both (cf. Section 7.4.3).

Coplanarity The beam photon travels along the z-axis while the target proton is at rest. There is no transverse momentum in the initial state. The same must be true for the total transverse momentum in the final state. Thus, the outgoing proton p' and the system of the two mesons $\pi^0\pi^0$ must be coplanar. The azimuthal angle difference is then given by

$$\Delta\phi = \left|\phi_{p'} - \phi_{\pi^0\pi^0}\right| = 180^\circ. \tag{7.5}$$

To calculate coplanarity, the proton must be measured. Therefore, coplanarity can only be used as a selection criteria for 5-PED and 4.5-PED events, but not for 4-PED events.

Missing Mass The reaction is overdetermined, which allows one particle to be treated as a missing particle. The missing particle is calculated from the other measured quantities. Due to the lack of full detection[7], the proton is conveniently treated as the missing particle p'_m. The invariant mass of the missing proton can then be compared to the expected value of 938.27 MeV [7]

$$\begin{aligned} M^2_{p'_m} = \begin{pmatrix} E_{p'_m} \\ \vec{p}_{p'_m} \end{pmatrix}^2 &= \left[\begin{pmatrix} E_\gamma \\ \vec{p}_\gamma \end{pmatrix} + \begin{pmatrix} m_p \\ \vec{0} \end{pmatrix} - \begin{pmatrix} E_{\pi^0_1} \\ \vec{p}_{\pi^0_1} \end{pmatrix} - \begin{pmatrix} E_{\pi^0_2} \\ \vec{p}_{\pi^0_2} \end{pmatrix} \right]^2 \\ &= (938.27\,\mathrm{MeV})^2 . \end{aligned} \tag{7.6}$$

Polar Angle Difference As before, the proton can be treated as missing particle p'_m. The polar angle of the missing proton can then be compared to the measured proton

$$\Delta\theta = \left|\theta_{p'} - \theta_{p'_m}\right| = 0^\circ. \tag{7.7}$$

Similar to the coplanarity the proton must be measured for the polar angle difference. Therefore, the polar angle difference can be used as a selection criteria for 5-PED and 4.5-PED but not for 4-PED events.

Invariant Mass The coplanarity, the missing mass and the polar angle difference do not depend on the type of mesons involved in the reaction. To select the target reaction, a cut on the invariant mass of both π^0 (134.98 MeV [7]) is performed

$$\begin{aligned} M^2_{\gamma\gamma} &= \begin{pmatrix} E_{\pi^0} \\ \vec{p}_{\pi^0} \end{pmatrix}^2 \\ &= (134.98\,\mathrm{MeV})^2 . \end{aligned} \tag{7.8}$$

Even for proper $\gamma p \to p\pi^0\pi^0$ events, the criteria defined above are not fulfilled exactly but each criteria is distributed around its expected values due to the finite resolution of the detectors. To ensure as much statistics as possible while keeping background contamination

[7] Only the direction can be reliably measured, not the energy.

low, ranges are defined within which events are accepted. If one criteria is not fulfilled, the reaction is discarded. The ranges correspond to 2σ of the underlying distributions, which in the case of a normal distribution corresponds to 95.45 % of the events.[8]

To complicate matters, the shapes of the distributions vary as the kinematics change. One way to describe the variations is by expressing them as functions of the beam energy E_γ and the cosine of the polar angle of the mesons $\cos(\theta_{\pi^0\pi^0})$ in the CMS of the reaction. Thus, the final cut ranges are determined as a function of these variables. In addition, the fraction of bound protons in the butanol target introduces further smearing due to Fermi motion. The non-zero momentum of these bound protons violates the fixed-target assumption, leading to broader distributions. Carbon subtraction allows to remove these variations and to extract narrower cut ranges. The procedure of carbon subtraction is explained in detail in Section 8.3. In Section B.1 in the Appendix, the extracted cut ranges are shown as a function of E_γ and $\cos(\theta_{\pi^0\pi^0})$ for each of the criteria discussed above. All periods of data taking and all PED event classes are used simultaneously for their determination.

After applying the time and kinematic cuts, the probability that reactions other than the target reaction remain is greatly reduced. The effect of the cuts is shown in Fig. 7.5 for 5-PED events. Equivalent pictures for 4.5-PED and 4-PED are shown in Section B.2 in the Appendix.

7.4.3 Kinematic Fit

The use of kinematic cuts already reduces the background significantly. However, not all background can be removed.
In Fig. 7.6 the remaining ambiguities (combinatorial background) are shown as the multiplicity of reactions per event. This multiplicity does not take into account reactions with different beam photons since these are already considered in the sideband subtraction. It can be seen that while only one reaction can be correct, there are events where multiple combinations remain.

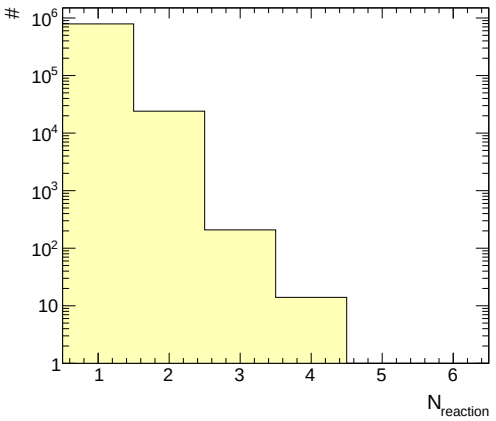

Figure 7.6: Multiplicity of 5-PED, 4.5-PED and 4-PED reactions after application of time cuts and kinematic cuts for the May 2018 data as an example. The multiplicity does not include reactions with different beam photons.

A kinematic fit can be used to assign a probability (confidence) to each reaction with respect to a particular hypothesis (a particular type of reaction). In the case of multiple candidates, the reaction with the highest confidence can then be selected, reducing the combinatorial background. In addition, the kinematic fit can be used to apply a general cut to the confidence level to further reduce the overall background. Confidence for other types of background reactions (anti-hypotheses) can also be calculated and used. In this way, competing reactions can

[8] 1σ corresponds to 68.27 %, 2σ to 95.45 % and 3σ to 99.73 % [162].

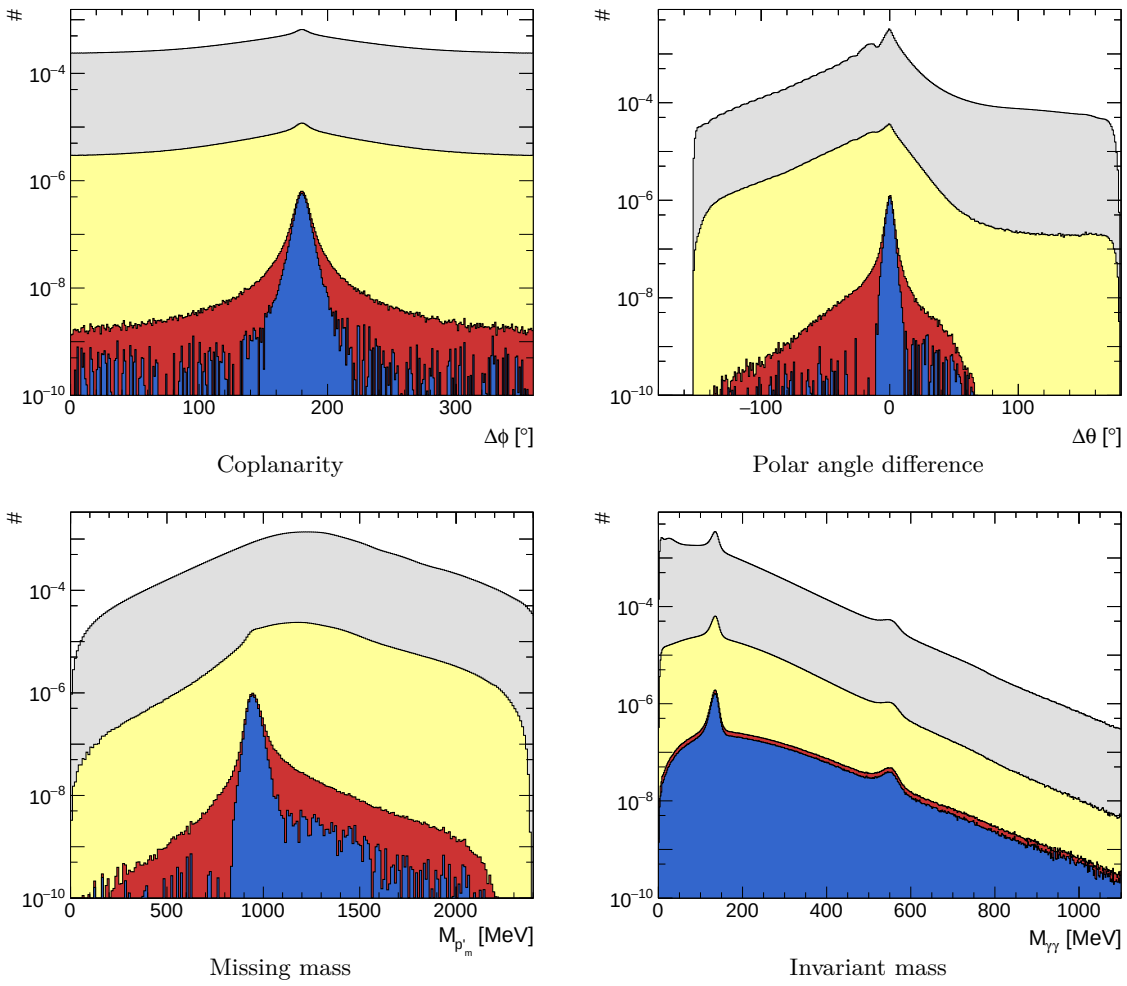

Figure 7.5: Effect of the cuts on the kinematic variables for 5-PED events. The distributions before any cuts, before kinematic cuts but with time cuts and the distributions after kinematic cuts are shown. In each case, all kinematic cuts are applied except the one shown in the picture. For completeness, the distribution after carbon subtraction is also shown. Flux normalization is applied (cf. Section 8.3.1). The combined data from December 2017, May 2018, February 2019, and June 2021 are used. Note that the y-axis is logarithmic.

be specifically suppressed.

7.4.3.1 Method

The kinematic fit minimizes the deviation of measured quantities with respect to certain constraints. During the minimization process, the measured values are varied within their estimated errors until the constraints are exactly satisfied. The constraints are given by the conservation of energy and momentum and the masses of the particles involved in the hypothesis. They can be expressed as

$$f_k(\vec{x}, \vec{\eta}) = 0 \quad k = 1, 2, \ldots, m,$$

where f_k are the m constraints, $\vec{\eta}$ are the true values and $\vec{x}$ the unknown (not measured) values that can be additionally determined by the fit. The measured values $\vec{y}$ differ from the true values by an error

$$\vec{\epsilon} = \vec{y} - \vec{\eta}.$$

The errors are assumed to be normal distributed and centered around zero. Minimization of

$$M = \vec{\epsilon}^{\mathrm{T}} C_y^{-1} \vec{\epsilon} \tag{7.9}$$

while satisfying the constraints f_k, leads to the solution for $\vec{x}$ and $\vec{\eta}$ [163]. C_y is the covariance matrix, which for uncorrelated errors corresponds to a diagonal matrix of the different uncertainties σ_i^2. For the minimization, the method of the Lagrange multiplier or the orthogonal transformation can be used [163]. In each case, as many constraints m are needed as there are unknowns r in $\vec{x}$. M follows a χ^2 distribution with $m - r$ degrees of freedom. For a given hypothesis, the P-values are uniformly distributed between 0 and 1.[9] The P-value describes the probability that an event reaches a χ^2 equal to or greater than the one calculated with the hypothesis. In other words, it describes how likely it is that an event is consistent with the hypothesis. Background that does not match the hypothesis accumulates at low P-values. In the following, the P-values are referred to as the confidence level (CL). The confidence level can be used to select only those reactions that are most likely to be the reaction of interest. Furthermore, within the kinematic fit, the fitted energy E[10] and the fitted angles θ and ϕ of the particles are optimized to minimize M and to satisfy the constraints. This results in improved values for these quantities, which can be used to improve the accuracy of the subsequent analysis.

7.4.3.2 Hypotheses

The hypothesis refers to the choice of constraints. For the event selection one hypothesis and one anti-hypothesis is used.

[9] Assuming perfectly known errors for the different values fitted.

[10] $\sqrt{E}$ is used instead of E to correct for asymmetric energy distributions. The distribution of $\sqrt{E}$ follows a more Gaussian shape, which is beneficial for the kinematic fit.

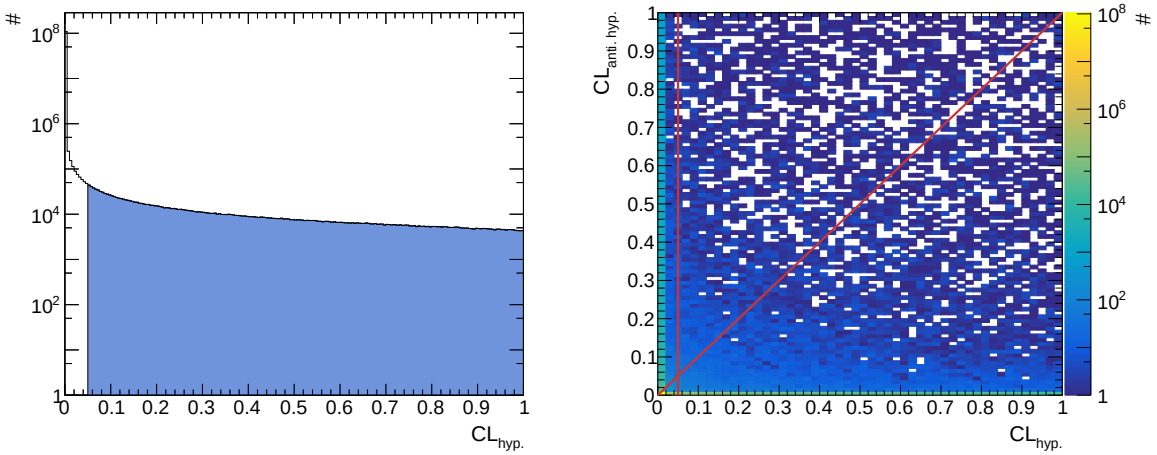

Hypothesis | Anti-Hypothesis vs. Hypothesis

Figure 7.7: Left: Confidence level for the hypothesis $CL_{hyp.}$. The events that pass the cut are shown in blue. Right: Anti-hypothesis $CL_{anti.\ hyp.}$ versus hypothesis $CL_{hyp.}$. The cut on the hypothesis is shown as a vertical line, while the requirement that $CL_{hyp.} > CL_{anti.\ hyp.}$ is shown as a diagonal line. The hypothesis is $\gamma p \to p'_m \pi^0 \pi^0$ and the anti-hypothesis is $\gamma p \to p'_m \pi^0 \eta$.

Hypothesis $\gamma p \to p'_m \pi^0 \pi^0$ The target reaction is used as a hypothesis. As before, the proton is recalculated from the conservation of energy and momentum and is treated as missing particle. In this way, only the masses of the final state particles remain as constraints. For each event, only the reaction with the highest confidence is kept, reducing the combinatorial background. Furthermore, a general cut on the confidence is applied. In Fig. 7.7 (left) the CL is shown. The signal events are expected to be uniformly distributed between 0 and 1 and the background events are expected to peak at low values. While the background events indeed peak at low values (note the logarithmic y-axis), the signal events are not uniformly distributed. This is the result of asymmetric (non-Gaussian) distributions within the experiment, which is especially the case for the energy distributions. Using $\sqrt{E}$ instead of E in the kinematic fit cannot fully compensate for this. The effect is discussed in more detail in [164]. To complicate matters, the fraction of bound protons in the butanol target has additional Fermi motion, which violates the assumption of a fixed target experiment. Deviations are therefore expected. Nevertheless, a good separation of signal and background events is possible.

A cut at $CL > 0.05$ reduces most of the background and rejects only some signal events. The cut represents a trade-off between statistics and background contamination of the final event sample.

Anti-Hypothesis $\gamma p \to p'_m \pi^0 \eta$ The $p'_m \pi^0 \eta$ final state has a high potential to be a background contribution. η decays into $\gamma\gamma$ with a probability of 39.36 % [7] ending in exactly the same detection pattern ($p\gamma\gamma\gamma\gamma$) as the hypothesis. To keep the background from the anti-hypothesis as low as possible, the confidence for both the hypothesis and for the anti-hypothesis is calculated for each reaction. If the confidence for the anti-hypothesis

is higher than the confidence for the hypothesis, the reaction is discarded. In Fig. 7.7 (right) the confidence of the hypothesis is compared to the confidence of the anti-hypothesis. In most cases, the kinematic fit assigns a high confidence to either the hypothesis or the anti-hypothesis, leading to an accumulation along the x-axis or y-axis. As a result, the cut on $\mathrm{CL}_{\mathrm{hyp.}}$ for the hypothesis already rejects most of the $p'_m\pi^0\eta$ events. Only in a few cases, mostly at lower CL, η events are removed by the additional anti-hypothesis requirement.

Besides $p'_m\pi^0\eta$, there are other types of reactions that can lead to the same detection pattern. In Table 4.1 in [159] the influence of different final states has been investigated using simulated data. Of all the states considered, $p'_m\pi^0\eta$ is the only one with a significant influence on the $p\pi^0\pi^0$ final state.

The kinematic fit is applied after the time cuts but before the kinematic cuts. After the fit, the conservation of energy and momentum is exactly satisfied, and the masses are by definition equal to their literature values. This eliminates the need to use kinematic cut ranges for the missing and invariant mass criteria.[11] Only the angle information for 5-PED and 4.5-PED events can still be used to perform further cuts. In this case, the cut ranges determined in Section 7.4.2 will be used. The effect of the kinematic fit is shown in Fig. 7.8 for 5-PED events. Equivalent pictures for 4.5-PED and 4-PED events are shown in Section B.3 in the Appendix.

7.5 Efficiency

The event selection not only removes background. Some of the signal events are also discarded to achieve the best signal-to-noise ratio. The reconstruction efficiency ϵ is a measure of how well the detector, the reconstruction and the selection process together retain signal events. It is defined as the fraction of simulated signal events that survive event selection

$$\epsilon = \frac{N_{\mathrm{rec.}}}{N_{\mathrm{sim.}}}. \tag{7.10}$$

The efficiency is determined using a set of 60×10^6 phase space simulated reactions of the type $\gamma p \to p\pi^0\pi^0$ assuming a photon flux that follows the Bethe-Heitler cross section (c.f. Eqn. 2.4). The global efficiency is found to be 22 %. However, depending on the kinematic region, more than 30 % of the events remain. In Fig. 7.9, the efficiency is plotted as a function of the beam energy E_γ and $\cos(\theta_{\pi^0\pi^0})$ for each PED class as well as for the total. As already discussed in Section 7.2, the different regions in which each PED class dominates become visible. At high $\cos(\theta_{\pi^0\pi^0})$ the proton is emitted in the backward direction with low energy, resulting in 4.5-PED and 4-PED events. The horizontal lines for 4.5-PED and 4-PED events at low $\cos(\theta_{\pi^0\pi^0})$ correspond to the transition to the Forward detector and the MiniTAPS detector, respectively.

To further reduce background contamination, in the following an efficiency cut is applied as the last step of event selection. For each PED class, a reconstruction efficiency

[11] In other words, by applying requirements at the CL level of the kinematic fit, a cut is already performed on the masses.

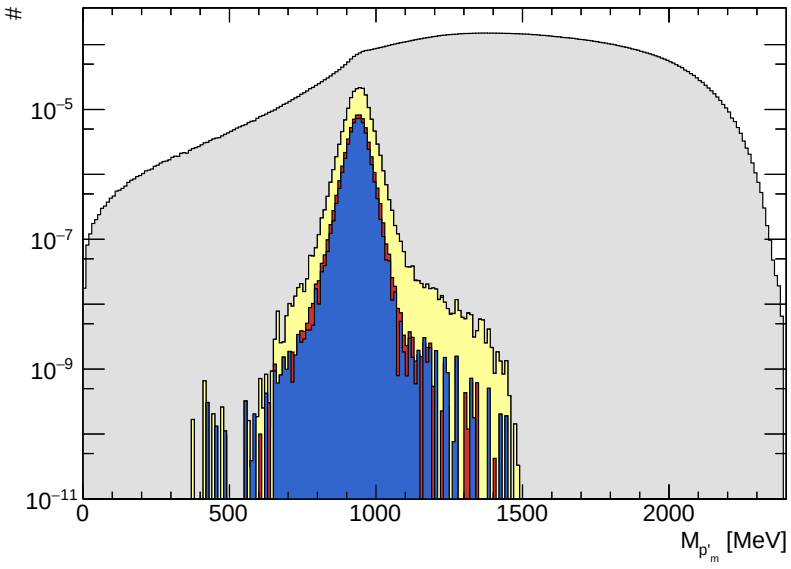

Figure 7.8: Effect of the kinematic fit on the missing mass distribution for 5-PED events. Since the missing mass after the kinematic fit is limited to the literature value, the measured values are shown instead. The distribution after time cuts but before cuts on the CL is shown as well as the distribution with cut on the hypothesis and additional cut on the anti-hypothesis. The anti-cut has only a small effect and is not visible (the yellow distribution is on top of the green distribution). The distribution after angle cuts is also shown, as is the final distribution after carbon subtraction. In each case, flux normalization is applied (cf. Section 8.3.1). Note that the y-axis is logarithmic.

$\epsilon\left(E_\gamma, \cos(\theta_{\pi^0\pi^0})\right) \geq 0.02$ (2 %) is required. This ensures that only events in kinematic regions where signal events are expected contribute to the final event sample. The effectiveness of this cut in reducing the background contribution is discussed in Section 7.7.

7.6 Distribution of Events

A three-body final state can be described by five different kinematic variables. One choice is $(E_\gamma, \cos(\theta), M, \phi^*, \theta^*)$. Here, E_γ is the photon energy of the beam. $\cos(\theta)$ is the cosine of the polar angle of the $\pi^0\pi^0$ system or the $p\pi^0$ system (quasiparticle) in the final state. M is the invariant mass of the system. ϕ^* is the angle between the reaction plane and the secondary decay plane spanned by the particles defining the quasiparticle. θ^* is the angle of one of the particles defining the quasiparticle relative to the reaction plane. A detailed description of the kinematic variables is given in Chapter 8.

The distribution of the selected events in these kinematic variables depends on several factors such as the cross section and the reconstruction efficiency. Fig. 7.10 shows the distribution of the events after event selection for the different kinematic variables as a function of the beam energy E_γ. The high statistic at low beam energies is clearly observed, reflecting the $1/E_\gamma$ dependence of the generated bremsstrahlung photons (cf. Section 2.2.1).

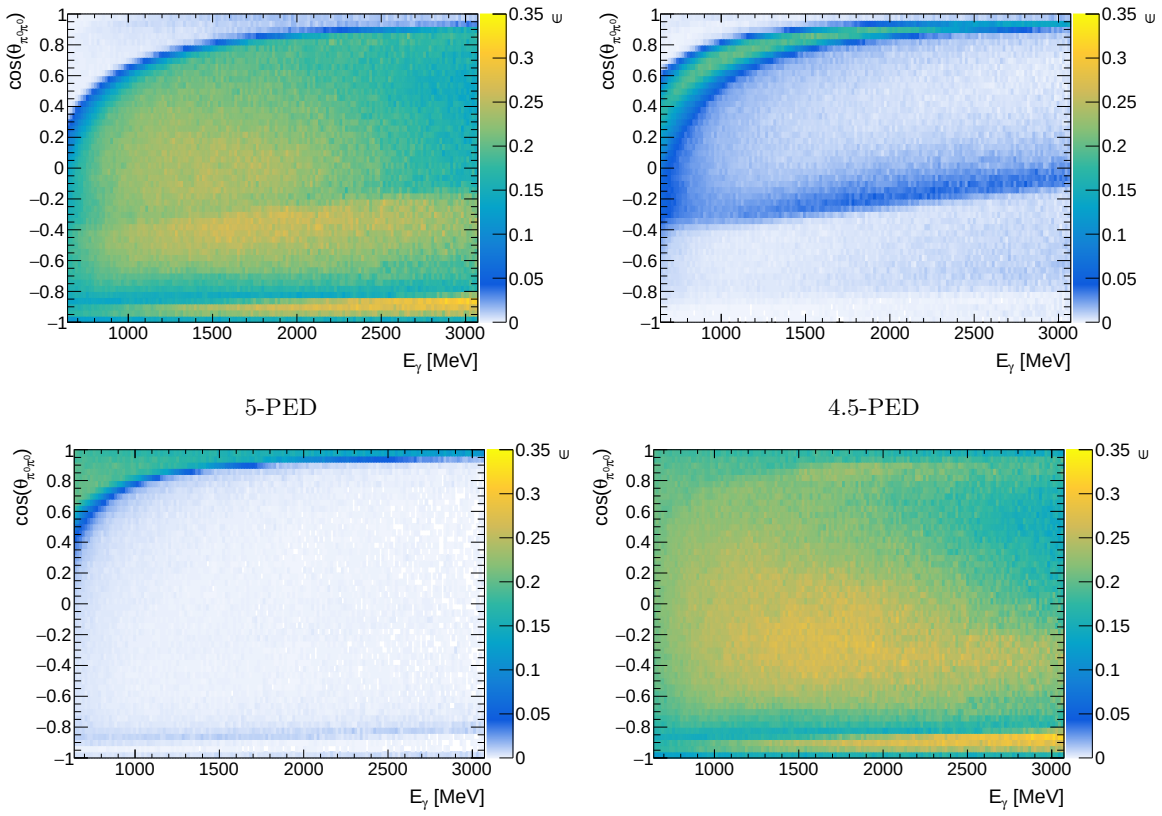

Figure 7.9: Reconstruction efficiency ϵ (cf. Eqn. 7.10) for the different PED classes after event selection with kinematic fit as a function of the beam energy E_γ and the cosine of the polar angle of the mesons in the CMS $\cos(\theta_{\pi^0\pi^0})$. For the determination of the efficiency a set of 60×10^6 phase space simulated reactions of the type $\gamma p \to p\pi^0\pi^0$ with a $1/E_\gamma$ distribution is used to simulate the photon flux.

The dependence of the cross section on E_γ is also observed as well as its angular dependence. In Section B.4 in the Appendix, the distributions are shown for other combinations of kinematic variables.

7.7 Background

The goal of the event selection is to achieve the best possible selection of the $p\pi^0\pi^0$ final state. However, even after implementing all the selection criteria described above, there will still be background. To estimate the percentage of background, the invariant mass distribution of the missing proton (missing mass) is used. The missing mass distribution is particularly sensitive to the remaining background because it includes most of the detected particles in its calculation. However, it cannot directly distinguish between the combinatorial background originating from the photons and competing final states such as $p'\pi^0\eta$. These background contributions may have a similar missing mass distribution as the signal events, making them

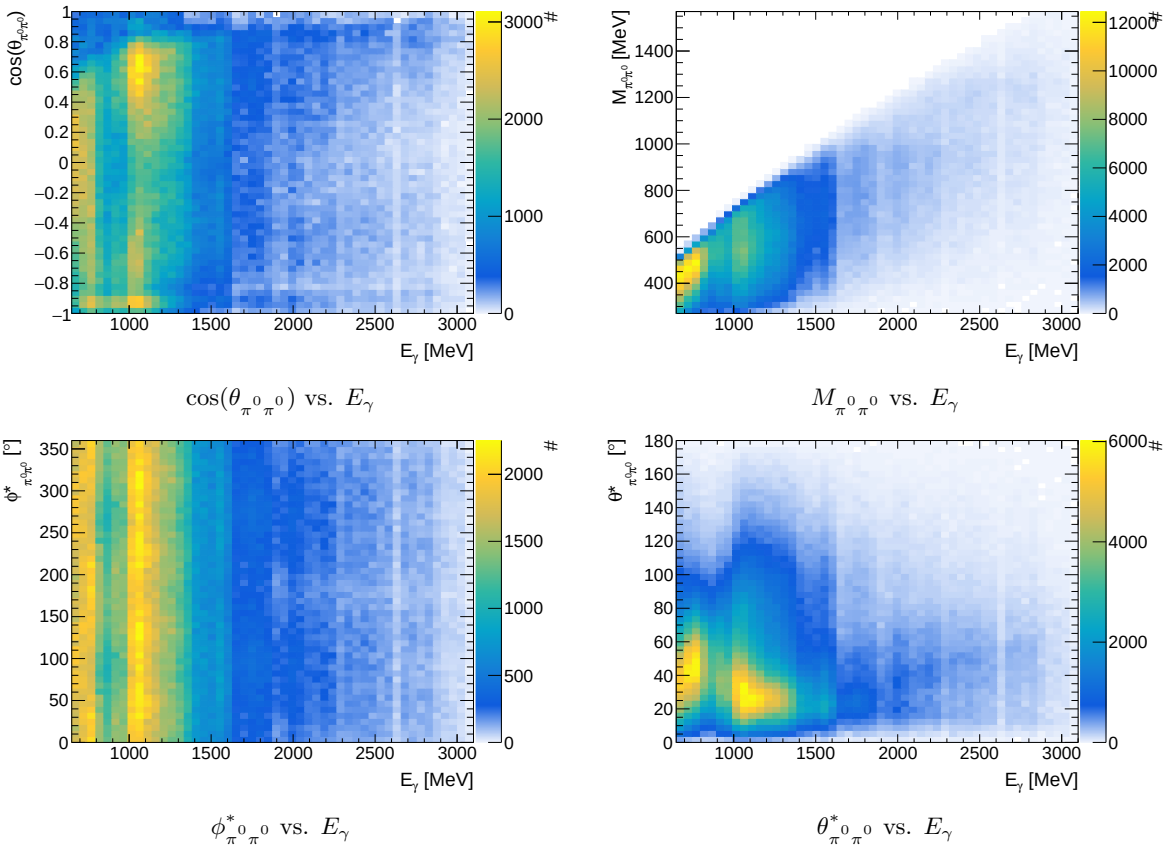

$\cos(\theta_{\pi^0\pi^0})$ vs. E_γ $M_{\pi^0\pi^0}$ vs. E_γ

$\phi^*_{\pi^0\pi^0}$ vs. E_γ $\theta^*_{\pi^0\pi^0}$ vs. E_γ

Figure 7.10: Distribution of $p\pi^0\pi^0$ events after event selection for the different kinematic variables as function of beam energy E_γ. Carbon subtraction (cf. Section 8.3) is performed. All PED classes from December 2017, May 2018, February 2019 and June 2021 are used. In Section B.4 in the Appendix, the distributions are shown for other combinations of kinematic variables.

impossible to separate. However, such contamination is avoided by applying a cut on the confidence level of the hypothesis and anti-hypothesis in the kinematic fit (cf. Section 7.4.3).

After the kinematic fit, the missing mass is constrained to its literature value and does not allow any separation of signal and background. The original measured values[12] cannot be used either as they were already part of all the selection criteria and behave as signal events by definition. Thus, a more profound method is needed for background estimation.

7.7.1 $\pi^0\pi^0$ Fit

The kinematic fit constrains all the masses of the particles in the final state. To use the missing mass for background estimation, its corresponding constraint must be removed. Therefore, instead of performing a full kinematic fit, only the $\pi^0\pi^0$ are fitted. In the fit, the photons are combined with the mesons in every possible way. A confidence is calculated for each combination. The combination with the highest confidence is then selected. As before,

[12] The measured (original) values are still available for the constrained and optimized quantities.

a cut on the CL of the hypothesis ($\pi^0\pi^0$) and the anti-hypothesis ($\pi^0\eta$) is performed using exactly the same criteria as in the case of the full kinematic fit. In this way, the $\pi^0\pi^0$ fit can be used to parameterize signal and background.

7.7.2 Binned Q-Factor Method

To separate the signal from the background, a parametrization is fitted to the missing mass distribution. The signal events are described by a variation of the Crystal Ball function as discussed in [165]

$$f_{\mathrm{s}}(x) = \begin{cases} e^{\frac{k_L^2}{2} + k_L\left(\frac{x-\mu}{\sigma}\right)} & \text{for} \quad \frac{x-\mu}{\sigma} \leq -k_L \\ e^{-\frac{1}{2}\left(\frac{x-\mu}{\sigma}\right)^2} & \text{for} \quad -k_L < \frac{x-\mu}{\sigma} \leq k_H \\ e^{\frac{k_H^2}{2} - k_H\left(\frac{x-\mu}{\sigma}\right)} & \text{for} \quad k_H < \frac{x-\mu}{\sigma}. \end{cases}$$

The function is continuously differentiable and consists of two exponential tails which are stitched to a Gaussian core. k_L and k_H describe the transition from the core to the exponential tail in units of the width σ. This function is particularly useful for modeling loss processes, as it is the case for the photon energies used in the reconstruction of invariant masses. A Chebyshev polynomial of degree 2 is used to describe background events

$$\begin{aligned} f_{\mathrm{bg}}(x) &= 1 + c_1 \cdot T_1(x) + c_2 \cdot T_2(x) \\ &= 1 + c_1 \cdot x + c_2 \cdot \left(2x^2 - 1\right). \end{aligned} \tag{7.11}$$

The degree is a compromise between description of the background and stability of the fit. Signal and background can be combined in a final fit model of the missing mass distribution

$$F(x) = I \cdot \left[\mu \cdot f_{\mathrm{s}}^{\mathrm{norm}}(x) + (1-\mu) \cdot f_{\mathrm{bg}}^{\mathrm{norm}}(x)\right]. \tag{7.12}$$

$f_{\mathrm{s}}^{\mathrm{norm}}$ and $f_{\mathrm{bg}}^{\mathrm{norm}}$ are the normalized versions of the signal and background. They are combined proportionally weighted by the fraction of signal events μ. I corresponds to the overall scale (integral) of the distribution. Fig. 7.11 shows the fits to the missing mass distributions for the different event classes. Each fit describes the data well and justifies the chosen model.

While $1-\mu$ gives a realistic background contribution after applying the $\pi^0\pi^0$ fit, it overestimates the background in the final event sample after performing the full kinematic fit. This is due to the additional constraint on the missing mass in the full kinematic fit, which further reduces the background. To account for this, a Q-factor is calculated for each missing mass x. A Q-factor refers to the probability of signal events at a given point in the distribution

$$Q(x) = \frac{\mu \cdot f_{\mathrm{s}}^{\mathrm{norm}}(x)}{\mu \cdot f_{\mathrm{s}}^{\mathrm{norm}}(x) + (1-\mu) \cdot f_{\mathrm{bg}}^{\mathrm{norm}}(x)}. \tag{7.13}$$

Assuming that the general shape of the signal and background does not change, the Q-factors can then be applied to the missing mass distribution after the full kinematic fit. For this

purpose, the measured quantities are used. They are shown in Fig. 7.11 as red distributions. The extracted background contributions are listed in Table 7.2 with and without the cut on the reconstruction efficiency $\epsilon \geq 0.02$ (cf. Section 7.5). As expected, the background is highest for 4-PED events. But here, the cut on the efficiency reduces the contribution significantly from 27.41 % down to 11.07 %.

The extracted background corresponds to a global value that integrates over all kinematic dependencies. To account for variations, the background must be determined as a function of the relevant kinematic variables. Due to statistical limitations, an event-based Q-factor method is used.

Table 7.2: Fraction of the background ξ after event selection. The values are obtained by a fit to the missing mass distributions in Fig. 7.11. Values are given for no cut on the efficiency $\epsilon \geq 0$ and with cut $\epsilon \geq 0.02$. The combined data of December 2017, May 2018, February 2019 and June 2021 are used.

	$\epsilon \geq 0$			$\epsilon \geq 0.02$		
	5-PED	4.5-PED	4-PED	5-PED	4.5-PED	4-PED
Background ξ [%]	0.69 %	2.61 %	27.41 %	0.41 %	2.39 %	11.07 %
χ^2/ndf	1.85	1.13	1.76	1.68	1.27	1.15

7.7.3 Event-Based Q-Factor Method

To determine the background as a function of all kinematic variables $(E_\gamma, \cos(\theta), M, \phi^*, \theta^*)$, an event-based Q-factor method is used instead of a binned approach [166]. This ensures sufficient statistics for reliable fits of the signal and background function to the data.

7.7.3.1 Method

At the end of the event based Q-factor method, each event in the final event sample is assigned a probability Q that it is a signal event. This probability can then be used to estimate the background contribution in the data. The event-based Q-factor method consists of three steps. All three steps are shown in Fig. 7.12 assuming two arbitrary dimensions for explanation purpose.

Step 1: Initialize In the first step (cf. Fig. 7.12 (top left)), the final event sample after the full kinematic fit is considered[13]. This is the same event sample that will be used to extract the polarization observables. The butanol events are shown schematically as black dots. For each of these events, a Q-factor (Step 2) and a P-factor (Step 3) are determined. An example event is marked with a green star.

[13] The combined data of December 2017, May 2018, February 2019 and June 2021 and all event classes 5-PED, 4.5-PED and 4-PED.

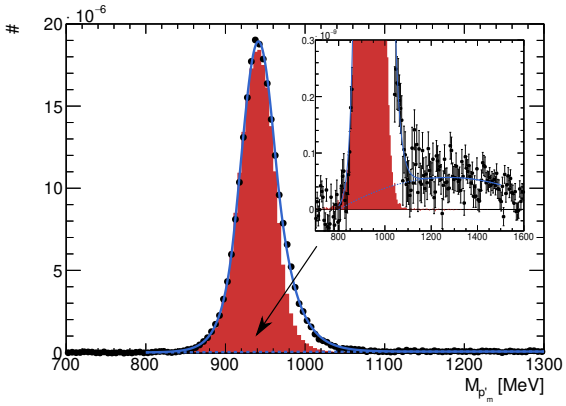

5-PED, $\chi^2/\mathrm{ndf} = 1.85$, $\xi = 0.69\,\%$

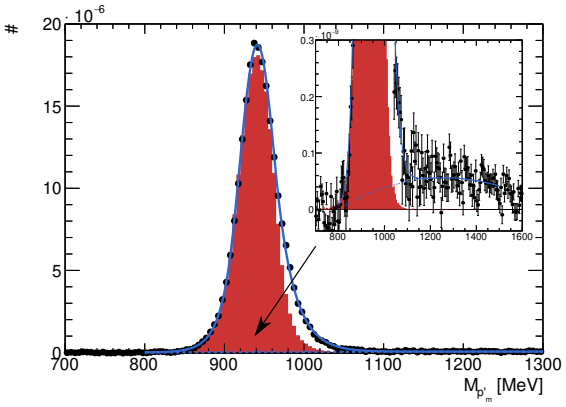

5-PED for $\epsilon > 0.02$, $\chi^2/\mathrm{ndf} = 1.68$, $\xi = 0.41\,\%$

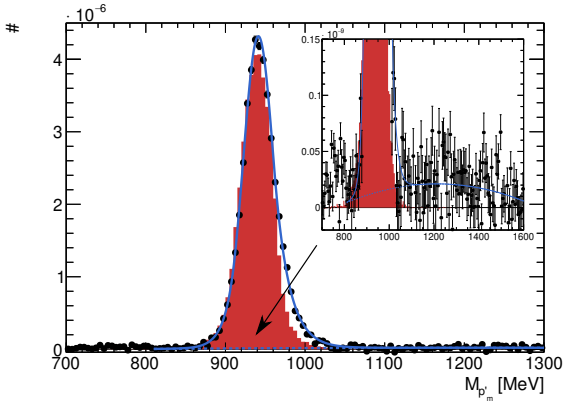

4.5-PED, $\chi^2/\mathrm{ndf} = 1.13$, $\xi = 2.61\,\%$

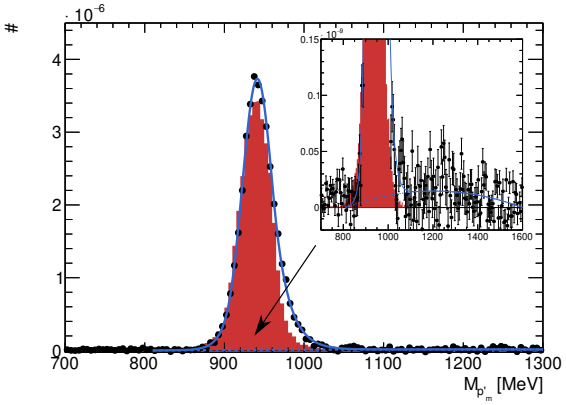

4.5-PED for $\epsilon > 0.02$, $\chi^2/\mathrm{ndf} = 1.27$, $\xi = 2.39\,\%$

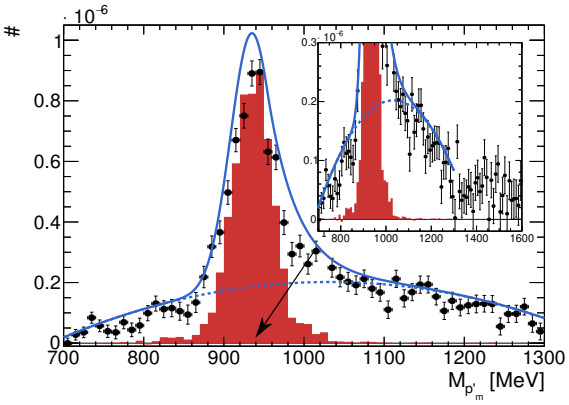

4-PED, $\chi^2/\mathrm{ndf} = 1.76$, $\xi = 27.41\,\%$

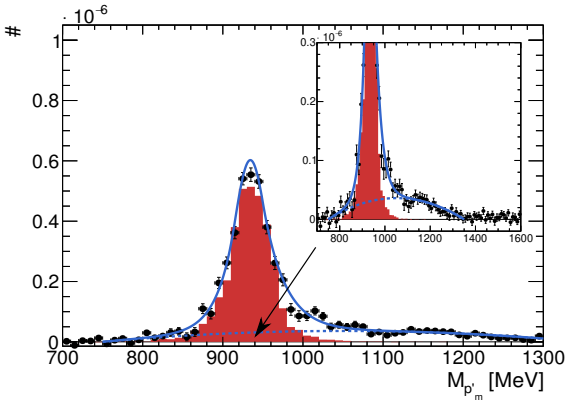

4-PED for $\epsilon > 0.02$, $\chi^2/\mathrm{ndf} = 1.15$, $\xi = 11.07\,\%$

Figure 7.11: Fit of Eqn. 7.12 to the missing mass distribution **after the $\pi^0\pi^0$ fit** for each event class. The missing mass distribution after the full kinematic fit using the measured quantities is also shown. The background ξ is calculated with the Q-factors in Eqn. 7.13. Left: No cut on the efficiency for each PED class is applied. Right: A cut on $\epsilon \geq 0.02$ is performed (cf. Section 7.5). In each case, the combined data of December 2017, May 2018, February 2019 and June 2021 are used. An overlay highlights the background fit.

Step 2: *Q*-factor In the second step (cf. Fig. 7.12 (top right)), the butanol events are shown after the $\pi^0\pi^0$ fit (black dots). In addition, events from the sideband (blue dots) and from the carbon reference measurement (red dots) are shown to illustrate the sideband and carbon subtraction (think of assigning negative weights to these points).[14] Only in this step signal and background can be parameterized, as only the $\pi^0\pi^0$ fit is applied and not the full kinematic fit. For each point from Step 1, a hypersphere is constructed that contains a certain statistical significance. Within this hypersphere, the missing mass distribution of the proton is used to parameterize the signal and background as described by Eqn. 7.12. The Q-factor is then determined by the fraction of signal at the position of the point in the missing mass distribution using Eqn. 7.13. The parametrization of the signal and background for the example event is shown in an overlay. The position of the example event is indicated as a vertical line.

Step 3: *P*-factor Step 1 includes all butanol events. Consequently, a Q-factor is also assigned to the sideband and carbon events within the butanol. The background, which is calculated from all the Q-factors, is later on used as a systematic error on the extracted polarization observables (cf. Section 8.5). For the polarization observables, however, sideband events are explicitly considered in their determination (cf. Section 8.4) and carbon events do not contribute as a source of error due to their non-polarizable nature. Thus, the inclusion of sideband and carbon events in the background estimation would lead to inaccuracies in the systematic error later on. This is especially true for 4-PED events with a high amount of carbon, which tends to be located at higher missing masses. Therefore, in addition to the Q-factor, a P-factor is also determined. It refers to the probability that the event is not a sideband or carbon event. In Step 3 (cf. Fig. 7.12 (bottom left)), the event sample is considered again after the full kinematic fit. This time, however, events from the sideband (blue dots) and from the carbon reference measurement (red dots) are also included. A hypersphere is constructed with the same size as in Step 2. Within this hypersphere, the distribution of butanol events $N_{\mathrm{B}}(x)$ is compared with the distribution after subtracting the sideband and carbon $N_{\mathrm{B}}^{\mathrm{sub}}(x)$. The probability that the example event is not a sideband or carbon event is then given by the ratio of the two distributions at the position of the example event

$$P(x) = \frac{N_{\mathrm{B}}^{\mathrm{sub}}(x)}{N_{\mathrm{B}}(x)}. \tag{7.14}$$

As before, the distributions are shown in the overlay with the example event as a vertical line.

After Step 1–3, a Q and P-factor is determined for each event in the five-dimensional space spanned by all kinematic variables. The resulting background contribution ξ can then be

[14] Sideband and carbon subtraction can only be applied when binning the data. This is not the case for Step 1, so subtraction cannot be applied there.

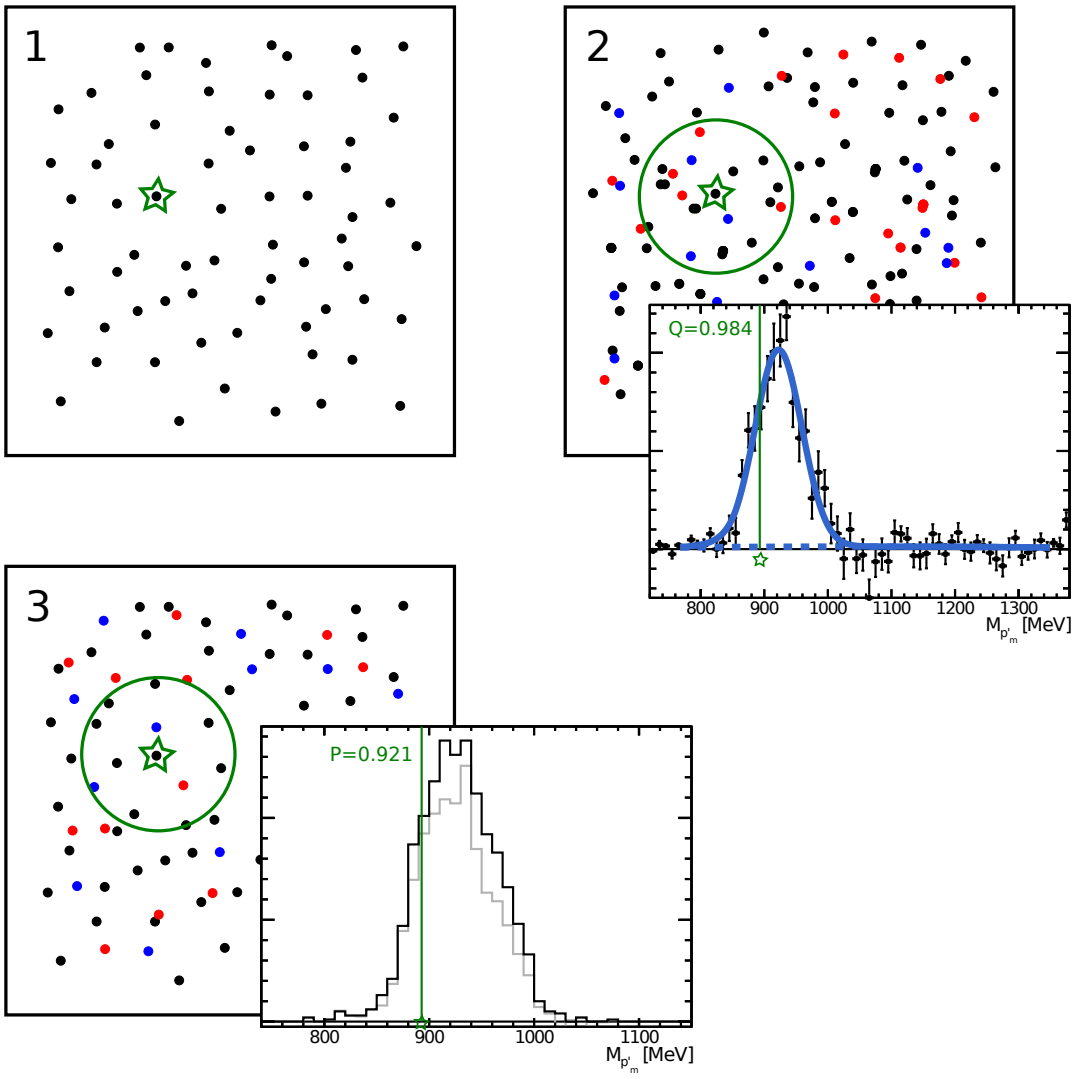

Figure 7.12: Steps for an event-based determination of the Q- and P-factor in two arbitrary dimensions. **Butanol events**, carbon events and sideband events are schematically shown as dots. In Step 1, the final butanol event sample after the full kinematic fit is shown. An example event is marked with a green star. Step 2 is then used to calculate the Q-factor. Here, the butanol event sample is shown after the $\pi^0\pi^0$ fit, along with carbon and sideband events for subtraction. Signal and background are parametrized using the missing mass in a hypersphere around the example event, which gives the Q-factor. Step 3 is used to calculate the P-factor. In this step, the final event sample after the full kinematic fit is shown again, this time also with carbon events and sideband events for subtraction. The P-factor is calculated by comparing the missing mass distribution with and without subtraction in the same hypersphere as before around the example event. The overlays show the missing mass distributions of the proton at Step 2 and 3. See the text for a more detailed explanation.

calculated via a weighted average

$$\xi = \frac{\sum_i (1 - Q_i) \cdot P_i}{\sum_i P_i}. \tag{7.15}$$

The use of the P-factor as a weight in the calculation ensures that the influence of sideband and carbon events within butanol is minimized, as they should not play a role in the systematic error on polarization observables.

7.7.3.2 Size of the Hypersphere

An important choice is the size of the hypersphere. It controls the amount of statistics available to fit the missing mass distribution but also determines the fuzziness of the calculated background contribution. To account for the different density of events, the Euclidean distance is normalized to the standard deviation σ_k along each axis. In this way, the distance d_{ij} between points p^{ij} is defined as

$$d_{ij}^2 = \sum_{k \neq r} \left(\frac{p_k^i - p_k^j}{\sigma_k} \right)^2. \tag{7.16}$$

Here, k iterates over the different axes in the coordinate space i.e. the kinematic variables $(E_\gamma, \cos(\theta), M, \phi^*, \theta^*)$. The axis r refers to the axis that contains the information of the missing mass distribution and is excluded from the metric. Using the normalized Euclidean distance, a hypersphere corresponds to an ellipse in normal Euclidean space. Within the ellipse, axes with more dense information will have a smaller radius compared to axes with less dense information. To also account for energy-dependent variations in the distribution of events, an energy-dependent standard deviation is used for normalization.[15] This is particularly important for the distribution of the invariant mass M, where the energy dependence is most pronounced. In the following, the size of the hypersphere is chosen so that the integral of the fitted missing mass distribution reaches 1500 events. This value represents a compromise between statistics for the fit and size of the sphere. In Section B.5 in the Appendix fits to the missing mass distribution of a random collection of points are shown. It can be seen that a further reduction of the number of events within a hypersphere is hardly possible, especially for the distributions with higher background contribution.

The resulting size of the hyperspheres can be characterized by the distances between all points within each hypersphere along each axis (cf. Fig. 7.13). The width σ of the distance distributions characterizes the average size of the hyperspheres containing $\sim 68.27\,\%$ of the events. Since the normalized Euclidean distance is used, the σ is approximately the same for all kinematic variables. Shifts and asymmetries in the distributions are due to the construction of hyperspheres in boundary regions due to kinematic constraints. In these regions, the events tend to lie in the direction of the kinematically allowed range. This effect is particularly pronounced for kinematic variables such as $M_{\pi^0\pi^0}$, where many events lie close to these boundaries (cf. Fig 7.10).

Another way of looking at the size of the hyperspheres is by considering the total radius

[15] The only exception is the energy itself.

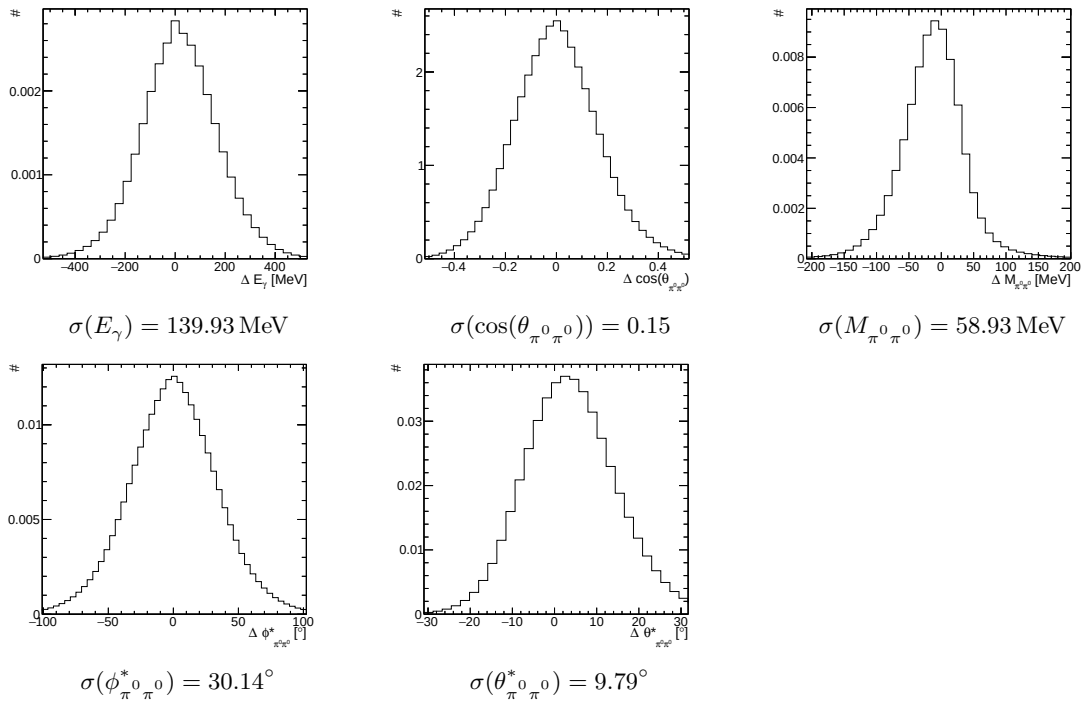

$\sigma(E_\gamma) = 139.93\,\text{MeV}$ $\sigma(\cos(\theta_{\pi^0\pi^0})) = 0.15$ $\sigma(M_{\pi^0\pi^0}) = 58.93\,\text{MeV}$

$\sigma(\phi^*_{\pi^0\pi^0}) = 30.14^\circ$ $\sigma(\theta^*_{\pi^0\pi^0}) = 9.79^\circ$

Figure 7.13: Distributions of the distances between all points within each hypersphere along each axis $(E_\gamma, \cos(\theta_{\pi^0\pi^0}), M_{\pi^0\pi^0}, \phi^*_{\pi^0\pi^0}, \theta^*_{\pi^0\pi^0})$. The width σ of the distance distributions is determined by a Gaussian fit and characterizes the average size of the hyperspheres containing $\sim 68.27\,\%$ of the events.

along each semi-axis. The total radius along a semi-axis of a given hypersphere is defined as the distance between the minimum and maximum points along that axis. The radius as a function of beam energy is shown in Section B.5 in the Appendix. It can clearly be seen that the hyperspheres become larger as the beam energy increases, due to the lower event density in this region.

7.7.3.3 Background ξ

In total, over 2×10^7 fits are performed to determine all Q-factors and P-factors. Eqn. 7.15 can then be used to calculate the background contribution in all bins.[16] In Fig. 7.14 (top left) the background ξ is shown as a function of E_γ and $\cos(\theta_{\pi^0\pi^0})$. A background well below $2\,\%$ is present over a wide kinematic range. At high energies, the background increases up to $4\,\%$. The highest background contribution of about $9\,\%$ comes from the region with high $\cos(\theta_{\pi^0\pi^0})$ values. This is also the region where 4-PED events dominate (cf. Fig. 7.9). Fig. 7.14 also shows the background for all the other kinematic variables as a function of beam energy E_γ. The high background contribution at low $M_{\pi^0\pi^0}$ with high E_γ is an artifact of the kinematic situation. Only a few statistical signal events are to be expected in this region. Consequently, the remaining events are more likely to be background. In Section B.5 in the Appendix, the

[16] Later, the polarization observables are determined for specific kinematic regions, which are called bins. For each of these bins, a background estimate is required.

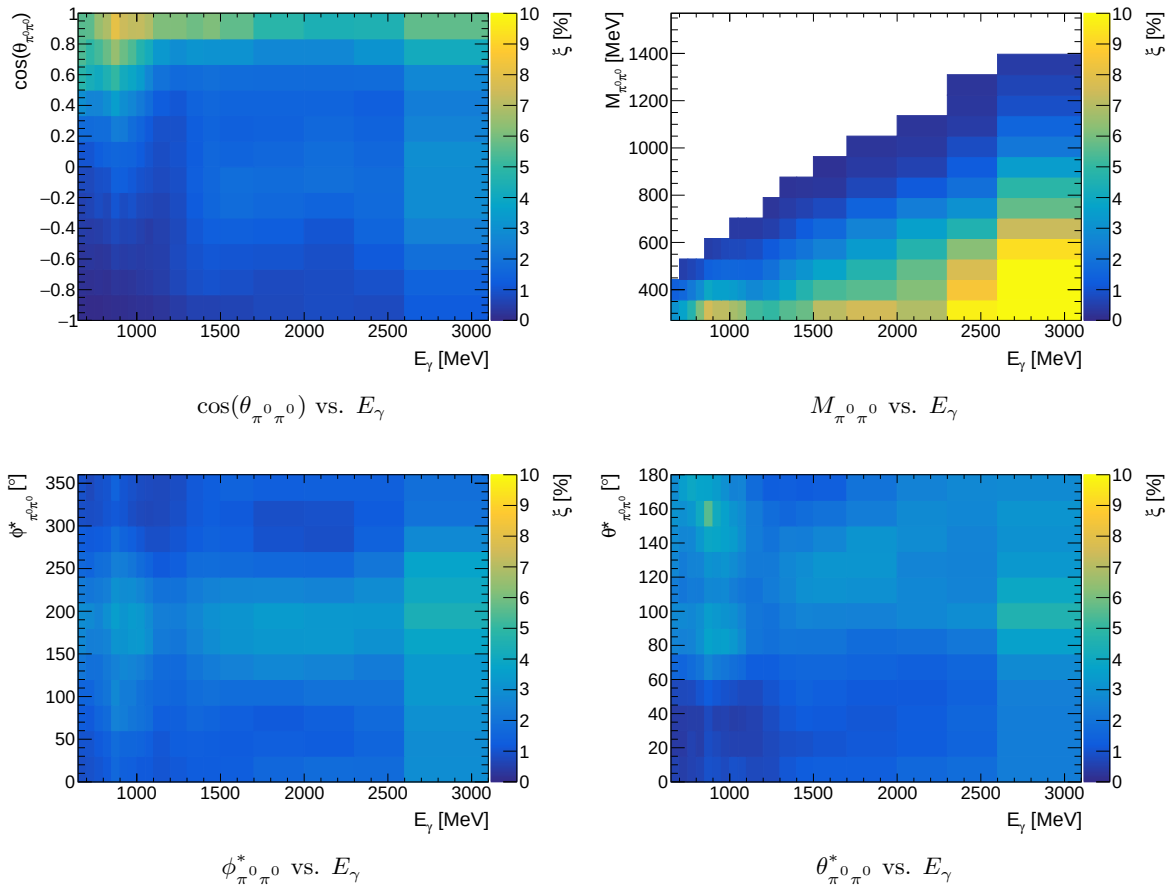

$\cos(\theta_{\pi^0\pi^0})$ vs. E_γ $M_{\pi^0\pi^0}$ vs. E_γ

$\phi^*_{\pi^0\pi^0}$ vs. E_γ $\theta^*_{\pi^0\pi^0}$ vs. E_γ

Figure 7.14: Background ξ for $(\cos(\theta_{\pi^0\pi^0}), M_{\pi^0\pi^0}, \phi^*_{\pi^0\pi^0}, \theta^*_{\pi^0\pi^0})$ as function of E_γ. In Section B.5 in the Appendix, the background is shown for several other kinematic regions.

background is shown for several other kinematic regions.

The global background contribution determined with Eqn. 7.15 for the combined data of December 2017, May 2018, February 2019 and June 2021 as well as considering all event classes 5-PED, 4.5-PED and 4-PED is 1.8 %. This is in good agreement with the binned background results in Table 7.2.

CHAPTER 8

Determination of Polarization Observables

The cross section for photoproduction off the proton depends on the spin configuration of the initial state particles (beam and target) as well as the final state particles, i.e. the proton (recoil). This can be used to disentangle the contributing amplitudes, including the resonances and their properties. For a transversely polarized target ($\Lambda_x \neq 0, \Lambda_y \neq 0, \Lambda_z = 0$) and a linearly polarized beam (δ_l), the cross section for two-pseudoscalar meson photoproduction (cf. Eqn. 1.2) is reduced to

$$\begin{aligned}\frac{\mathrm{d}\sigma}{\mathrm{d}\Omega} = \left(\frac{\mathrm{d}\sigma}{\mathrm{d}\Omega}\right)_0 \cdot \Big(1 &+ \Lambda_x \cdot P_x + \Lambda_y \cdot P_y \\ &+ \delta_l \sin(2\phi_B)\left[I^s + \Lambda_x \cdot P_x^s + \Lambda_y \cdot P_y^s\right] \\ &+ \delta_l \cos(2\phi_B)\left[I^c + \Lambda_x \cdot P_x^c + \Lambda_y \cdot P_y^c\right]\Big).\end{aligned} \tag{8.1}$$

Recoil polarization is not measured in this work and is omitted. The polarization observables are defined as follows: P_x, P_y and I^s, I^c represent single polarization observables with respect to target polarization $\mathcal{T}$ and beam polarization $\mathcal{B}$. Double polarization observables (beam and target) $\mathcal{BT}$ are denoted as P_x^s, P_y^s, P_x^c, and P_y^c. The angle ϕ_B describes the orientation of the beam polarization relative to the reaction plane. In the case of a two-body final state such as $\gamma p \to p\pi^0$, the reaction plane is spanned by the beam photon and the meson or recoil nucleon in the CMS of the reaction. In the case of a three-body final state, the beam photon and the combined momentum of two of the three final state particles define the reaction plane. Thus, for the reaction $\gamma p \to p\pi^0\pi^0$, there are two possibilities (cf. Fig. 8.1). In this work, the different possibilities are referred to with $\pi^0\pi^0$ and $p\pi^0$ as subscripts.

In the experiment, the polarization is determined in the laboratory frame. Here, the angles of the target polarization vector and the beam polarization vector are defined as β and α. However, in Eqn. 8.1, the quantities Λ_x, Λ_y and ϕ_B are given with respect to the reaction plane, which differs from the laboratory frame by a rotation around the z-axis. To express all quantities in the laboratory frame, the angle φ between the laboratory frame and the reaction plane can be calculated. With this angle Λ_x, Λ_y and ϕ_B can be expressed in the laboratory frame as

$$\begin{aligned}\Lambda_x &= \cos(\beta - \varphi) \cdot \Lambda \\ \Lambda_y &= \sin(\beta - \varphi) \cdot \Lambda \\ \phi_B &= \alpha - \varphi.\end{aligned} \tag{8.2}$$

A visualization of the target polarization and the beam polarization vector is shown in Fig. 8.2.

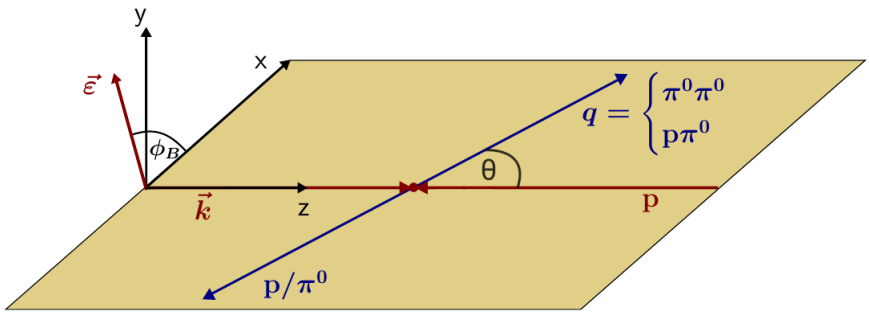

Figure 8.1: Definition of the reaction plane for $\gamma p \to p\pi^0\pi^0$. There are two different ways to define the quasiparticle q ($\pi^0\pi^0$ or $p\pi^0$). The reaction plane is then spanned by the beam photon and the quasiparticle in the CMS of the reaction. The angle ϕ_B describes the orientation of the beam polarization relative to the reaction plane. The illustration is taken from [159].

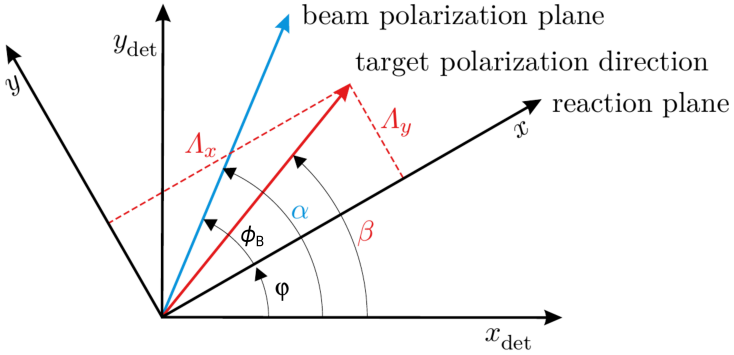

Figure 8.2: Definition of the coordinate system with the target polarization vector and the beam polarization vector. y_{det} and x_{det} refer to the laboratory frame, while y and x describe the reaction plane. The z-axis points along the axis of the beam (in the direction of the reader). The illustration is adapted from [158].

This leads to the following definition of the cross section used to extract the polarization observables

$$\begin{aligned}\frac{d\sigma}{d\Omega} = \left(\frac{d\sigma}{d\Omega}\right)_0 \cdot \Big(1 &+ \Lambda\cos(\beta-\varphi)\cdot P_x + \Lambda\sin(\beta-\varphi)\cdot P_y \\ &+ \delta_l \sin(2(\alpha-\varphi))\left[I^s + \Lambda\cos(\beta-\varphi)\cdot P_x^s + \Lambda\sin(\beta-\varphi)\cdot P_y^s\right] \\ &+ \delta_l \cos(2(\alpha-\varphi))\left[I^c + \Lambda\cos(\beta-\varphi)\cdot P_x^c + \Lambda\sin(\beta-\varphi)\cdot P_y^c\right]\Big).\end{aligned} \tag{8.3}$$

8.1 Polarization Degree

In the experiment, the target is transversely polarized and the beam is linearly polarized. In the following, details of the target and the beam polarization are discussed, which are

important for the analysis of the data.

Target polarization Λ

To maintain the desired degree of target polarization, repolarization is performed periodically every few days during data taking. The angle of the target polarization vector in the laboratory frame is $\beta = 90^\circ$. This angle is used to calculate the polarization with respect to the reaction plane (cf. Eqn. 8.2).[1] To reduce systematic effects, the polarization orientation is periodically switched by 180° during data taking. The different polarization orientations are referred to as $\Lambda_\pm$. Fig. 8.3 (left) shows the target polarization for each period of data taking used in this work. The breaks in the polarization correspond to periods of repolarization or interruptions in the measurements for various reasons. The average target polarization for each data taking is listed in Table 8.1. It is noticeable that the target polarization for December 2017 is significantly lower compared to the polarization of the other periods. A detailed examination of the extracted polarization observables shows that the polarization was measured too low. This is compensated by applying a correction factor of 1.44 to the target polarization for December 2017. A more detailed explanation of the correction is given in Section 9.1.1.

Table 8.1: Average target polarization for each data taking. For December 2017, next to the measured values also corrected values are given in parentheses.

	December 2017	May 2018	February 2019	June 2021
Λ_+	+51.6 % (+74.3 %)	+78.5 %	+77.8 %	+72.9 %
Λ_-	−49.9 % (−71.9 %)	−79.2 %	−77.6 %	−75.3 %

Beam Polarization δ_l

The beam in the experiment is linearly polarized. The degree of polarization depends on the energy of the beam photons. The angle of the beam polarization vector in the laboratory frame is $\alpha = 45^\circ$. Similar to the target polarization, the orientation of the beam polarization is periodically switched by 90° to reduce systematic effects during data taking. Fig. 8.3 (right) shows the beam polarization as a function of energy for each period of data taking. Note the two different positions of the coherent edge.[2] The position of the coherent edge is an important choice and has a strong effect on the degree of polarization. The position of the coherent edge and the maximum beam polarization achieved for each data taking are listed in Table 8.2.

[1] The value of β has been investigated in [145] and found to be consistent with the expectation.
[2] For an explanation of beam polarization and the coherent edge, cf. Section 2.2.1.

Table 8.2: Coherent edge and maximum beam polarization $\delta_l^{\max}$ for each period of data taking.

	December 2017	May 2018	February 2019	June 2021
Coherent edge	1 350 MeV	1 350 MeV	1 600 MeV	1 600 MeV
$\lvert\delta_l^{\max}\rvert$	55.3 %	55.1 %	45.9 %	44.7 %

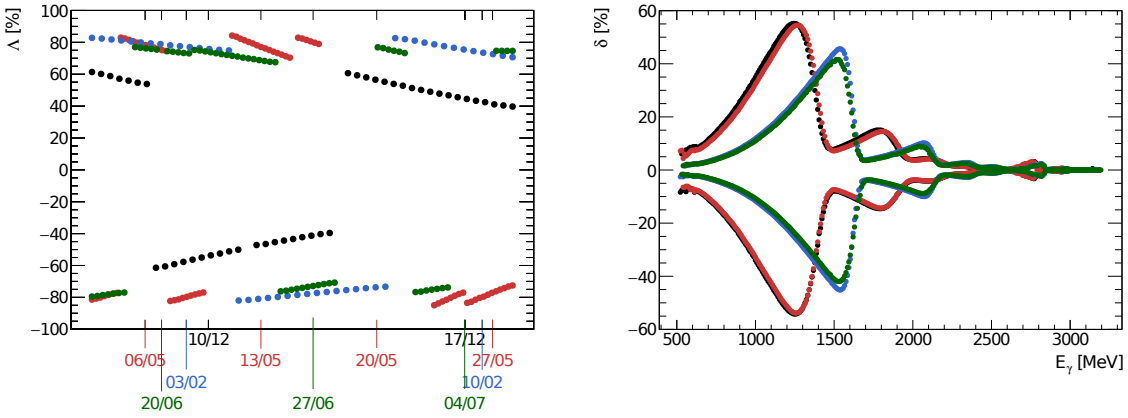

Target polarization Beam polarization

Figure 8.3: Polarization for the data taking in **December 2017** (uncorrected values), May 2018, February 2019 and June 2021. The target polarization is shown as a function of time, while the beam polarization is shown as a function of beam energy E_γ.

8.2 Kinematics

The kinematics of a reaction can be described by a set of independent variables that characterize the initial and final states of the particles involved. For a two-body final state, such as single-pseudoscalar meson photoproduction, two variables are required. Typically, the beam photon energy E_γ and the cosine of the polar angle of the meson in the CMS $\cos(\theta)$ are chosen. In the case of a three-body final state five independent variables are needed to fully describe the kinematics. In this work, the same set of variables as in [159] is used for better comparability. The kinematic variables are defined as

$$E_\gamma \quad \cos(\theta_{\pi^0\pi^0/p\pi^0}) \quad M_{\pi^0\pi^0/p\pi^0} \quad \phi^*_{\pi^0\pi^0/p\pi^0} \quad \theta^*_{\pi^0\pi^0/p\pi^0}. \tag{8.4}$$

E_γ corresponds to the beam photon energy and $\cos(\theta)$ is the cosine of the polar angle of the quasiparticle in the CMS. The quasiparticle can be defined by either the $\pi^0\pi^0$ or the $p\pi^0$ system. M is the invariant mass of the quasiparticle. ϕ^* is the angle between the reaction plane and the secondary decay plane spanned by the particles defining the quasiparticle. θ^* is the angle of one of the particles defining the quasiparticle relative to the reaction plane.[3] The two choices for the quasiparticle lead to different reaction planes and thus to different

[3] The π^0 in the case of $\pi^0\pi^0$ and the p in the case of $p\pi^0$.

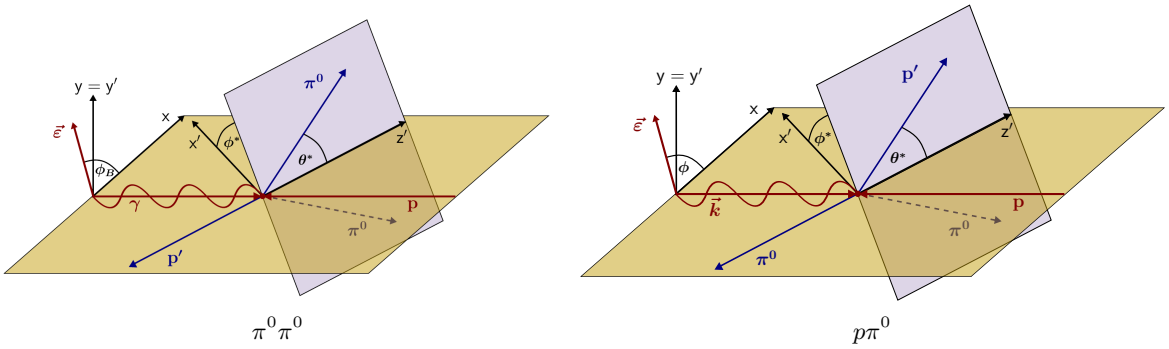

Figure 8.4: Kinematic variables describing the reaction $\gamma p \to p\pi^0\pi^0$ (cf. Eqn. 8.4). The two choices of the quasiparticle are shown: $\pi^0\pi^0$ and $p\pi^0$. The illustrations are taken from [159].

behavior of the polarization observables. In this work the choice of the quasiparticle is indicated by using $\pi^0\pi^0$ or $p\pi^0$ as subscripts for the corresponding variables. The kinematic variables and the two choices of the quasiparticle are illustrated in Fig. 8.4.

It is important to note that the indistinguishability of the two π^0 requires symmetrization. Both orderings $\pi^0_1\pi^0_2$ and $\pi^0_2\pi^0_1$ have to be considered in all calculations. As a result of this symmetrization, it follows for $\phi^*_{\pi^0\pi^0}$ and the polarization observables $\mathcal{O}$

$$\phi^*_{\pi^0_1\pi^0_2} = \phi^*_{\pi^0_2\pi^0_1} + 180^\circ \qquad \to \qquad \mathcal{O}(\phi^*) = \mathcal{O}(\phi^* + 180^\circ).$$

Examples of this symmetry are shown in Fig. 9.13 and 9.14 in Chapter 9. However, as soon as $\theta^*_{\pi^0\pi^0}$ is also considered (i.e. not integrated over), the symmetry is broken, since the symmetrization of $\left(\phi^*_{\pi^0\pi^0}, \theta^*_{\pi^0\pi^0}\right)$ has to be considered at the same time.

8.2.1 Connection to Single Pseudoscalar Meson Photoproduction

Integrating over the angles ϕ^* and θ^* simplifies the three-body dynamics to a quasi-two-body configuration (see Fig. 8.1). In this case, the kinematic variables in Eqn. 8.4 are reduced to

$$E_\gamma \quad \cos(\theta_{\pi^0\pi^0/p\pi^0}) \quad M_{\pi^0\pi^0/p\pi^0}. \tag{8.5}$$

This quasi-two-body system effectively mimics the conditions of single-pseudoscalar meson photoproduction, for which the polarized cross section is defined as [167]:

$$\begin{aligned}\frac{\mathrm{d}\sigma}{\mathrm{d}\Omega} = \left(\frac{\mathrm{d}\sigma}{\mathrm{d}\Omega}\right)_0 \cdot \Big(1 &- \delta_l \cos(2(\alpha-\varphi)) \cdot \Sigma + \Lambda \sin(\beta-\varphi) \cdot T \\ &- \delta_l \Lambda \sin(2(\alpha-\varphi)) \cos(\beta-\varphi) \cdot H \\ &- \delta_l \Lambda \cos(2(\alpha-\varphi)) \sin(\beta-\varphi) \cdot \hat{P}\Big).\end{aligned} \tag{8.6}$$

Here, T and Σ are single polarization observables with respect to target polarization $\mathcal{T}$ and beam polarization $\mathcal{B}$. H and $\hat{P}$ are double polarization observables with respect to

beam and target polarization $\mathcal{BT}$. In the case of single-pseudoscalar meson photoproduction, the double polarization observable $\hat{P}$ is equal to the recoil polarization observable P. By comparison with the polarized cross section of the three-body final state (Eqn. 8.3), the following correspondences between the observables can be identified:

$$P_x = 0,\ P_y \widehat{=} T \qquad I^s = 0,\ I^c \widehat{=} -\Sigma \qquad P_x^s \widehat{=} -H,\ P_y^s = 0 \qquad P_x^c = 0,\ P_y^c \widehat{=} -\hat{P} \tag{8.7}$$

However, in this context, $\hat{P}$ no longer corresponds to the recoil polarization observable $P_{y'}$ in two-pseudoscalar meson photoproduction. For a detailed explanation refer to Appendix D in [159]. The observables P_x and P_y for the quasi-two-body final state are shown in Fig. 9.11 and 9.12 in Chapter 9. Here, P_x is 0 as expected according to Eqn. 8.7.

Parity conservation must also be satisfied. As shown in [49], the symmetry properties of the spin amplitudes under parity transformation can be used to infer the behavior of observables under the substitution $\phi^* \leftrightarrow 2\pi - \phi^*$. Specifically, the observables exhibit the following symmetry behavior:

$$\begin{aligned} &P_x,\ I^s,\ P_y^s,\ P_x^c \text{ are odd in } \phi^*\text{: } \mathcal{O}(2\pi - \phi^*) = -\mathcal{O}(\phi^*) \\ &P_y,\ I^c,\ P_x^s,\ P_y^c \text{ are even in } \phi^*\text{: } \mathcal{O}(2\pi - \phi^*) = +\mathcal{O}(\phi^*) \end{aligned}$$

As a result, integrating over ϕ^* effectively cancels the contribution of observables that are odd in ϕ^* (cf. Eqn. 8.7). This symmetry is clearly reflected in the extracted observables: P_x, which is odd in ϕ^*, vanishes on integration, while P_y, which is even, remains non-zero. This behavior is illustrated in Fig. 9.13 and Fig. 9.14 in Chapter 9.

8.3 Carbon Subtraction

Butanol (C_4H_9OH) is used as target material. Butanol consists of polarizable quasi-free protons in hydrogen (H) and non-polarizable protons bound in carbon (C) and oxygen (O). As a result, reactions on polarized and non-polarized protons are present in the selected event sample

$$\begin{aligned} \gamma + p_{\text{free}} &\rightarrow p + \pi^0\pi^0 \\ \gamma + p_{\text{bound}} &\rightarrow p + \pi^0\pi^0. \end{aligned}$$

For the extraction of polarization observables, only reactions on polarizable quasi-free protons are of interest. Reactions on bound protons reduce the effective degree of polarization and dilute the observables. To correct the dilution, a reference measurement is performed using carbon foam as target material. The target density of the foam corresponds approximately to the density of the bound nucleons in the butanol target. To ensure that the conditions of the reference measurement are equivalent to those of the butanol measurement, the entire experimental setup is kept the same.[4] In this way, the reference measurement only needs to be scaled by a factor to subtract the effect of reactions on bound nucleons in the butanol data. The scaling factor takes into account small differences in the target densities. Different

[4] The carbon foam is filled into a cylinder and placed in the exact same cryostat with the same coolant that is used for the Frozen Spin target.

measurement times and energy dependent changes of the beam flux are corrected by flux normalization (cf. Section 8.3.1). After determining the scaling factor c, the number of reactions on quasi-free protons N_{H} in the butanol data N_{B} can be calculated as

$$N_{\mathrm{H}} = N_{\mathrm{B}} - c \cdot N_{\mathrm{C}}^{\mathrm{ref}}, \tag{8.8}$$

where $N_{\mathrm{C}}^{\mathrm{ref}}$ is the reference measurement on carbon foam.

In Table 8.3, the reference measurements for the different periods of data taking are listed. While in most cases a reference measurement with the same setting for the coherent edge exists, this is not the case for February 2019. At that time, a reference measurement was scheduled shortly afterwards, but the accelerator failed before. Maintenance work did not allow for another reference measurement until November 2021. To ensure equivalent conditions in the experimental setup, a reference measurement from November 2018 will be used instead. This measurement is closer in time but was performed at a different coherent edge.

Table 8.3: Butanol measurements and corresponding reference measurements with carbon foam as target material. Each measurement is given with the month and year of data taking as well as the setting of the coherent edge in MeV. In May 2018, measurements with butanol (B) and carbon (C) were performed in the same month. For completeness, the associated scaling factor c after flux normalization is also listed.

Butanol	Carbon foam	c
December 2017 (1 350 MeV)	May 2018 (C, 1 350 MeV)	(0.83 ± 0.02)
May 2018 (B, 1 350 MeV)	May 2018 (C, 1 350 MeV)	(0.87 ± 0.02)
February 2019 (1 600 MeV)	November 2018 (1 350 MeV)	(0.85 ± 0.03)
June 2021 (1 600 MeV)	November 2021 (1 600 MeV)	(0.83 ± 0.02)

8.3.1 Beam Flux Normalization

The scaling factor c takes into account small differences in target density between the data and reference measurements. In principle, the scaling factor can also account for different measurement times and global differences in the beam flux. Only energy dependent changes cannot be corrected.[5] In February 2019, the data measurement was performed with a different coherent edge than the reference measurement, resulting in such energy dependent changes. Therefore, a normalization of the beam flux is required. In the following, the normalization is performed for all periods of data taking.

In beam flux normalization, the event yields are normalized to the integrated number of photons hitting the target as a function of energy. The beam flux Φ_γ is calculated with

$$\Phi_\gamma = N_{\mathrm{Tagger}} \cdot P_\gamma \cdot P_\gamma^{\mathrm{corr}} \cdot f_{\mathrm{live}}, \tag{8.9}$$

[5] An energy dependent scaling factor would be needed which is harder to calculate.

where N_{Tagger} is the number of reconstructed photons within the Tagging system in a time window Δt (cf. Section 8.3.1.1). The time window is arbitrary but should be large enough to minimize statistical errors. It must also exclude the hadronic trigger to prevent any effect on the measured energy distributions of the photons. $P_\gamma \cdot P_\gamma^{\text{corr}}$ describes the probability that a photon reconstructed in the Tagging system also reaches the target (cf. Section 8.3.1.2). f_{live} corresponds to a scaling factor to scale the photon flux for the small time window Δt to the full livetime of the experiment (cf. Section 8.3.1.3). The procedure for determining the beam flux for the experimental setup before the modification of the readout[6] is described in detail in [103, 158]. Here, a similar method is proposed and applied to the new data.

8.3.1.1 N_{Tagger}

For the calculation of N_{Tagger}, reconstructed photons within the time window $\Delta t = 100-700\,\text{ns}$ are counted. To avoid the influence of a slightly changing TDC window between the data taking in December 2017 and the subsequent ones starting in May 2018, the left side of the TDC window is not used (cf. Fig. 8.5 (left)). Furthermore, the influence of the hadronic trigger is eliminated by starting at 100 ns, which is far enough away from the trigger at 0 ns. The hadronic trigger only needs to be excluded for high-rate runs (standard data runs). For low-rate runs[7], the Tagging system is used for triggering. Here, the time window is increased to $\Delta t = -20 - 700\,\text{ns}$ for more statistics.

8.3.1.2 P_γ

The number of reconstructed photons in the Tagging system is not directly equal to the number of photons hitting the target. The number of photons is reduced by the collimator behind the Tagging system. Also, additional background in the Tagging system will lead to an overestimation of the number of photons reaching the target. Therefore, the true number of photons in the target is calculated with

$$N_{\text{Target}} = N_{\text{Tagger}} \cdot P_\gamma \cdot P_\gamma^{\text{corr}}. \tag{8.10}$$

The photon definition probability P_γ describes the probability that a reconstructed photon will also reach the target and can be determined from the coincidences between hits in the Tagging system and the GIM which is positioned behind the target

$$P_\gamma = \frac{N_{\text{Tagger}\wedge\text{GIM}}}{N_{\text{Tagger}}}. \tag{8.11}$$

The coincidence between the Tagging system and the GIM is defined by events satisfying a time difference of $-8\,\text{ns} \leq t_{\text{Tagger}} - t_{\text{GIM}} \leq 15\,\text{ns}$. Random coincidences are removed by subtracting events from the sideband selected as -28 to $-19\,\text{ns}$ and 19 to 35 ns. To account for the limited double-pulse resolution of the GIM[8] the peak and sideband events

[6] For more information on the readout, see Chapter 3.

[7] Runs with lower beam current and using the Tagging system as trigger (tagger-or trigger), which are recorded from time to time. They are used in the following to correct the photon definition probability P_γ.

[8] Already a hit in one of the GIM crystals is interpreted as a photon. To avoid overcounting in cases where a photon leads to signals in multiple crystals, all hits following up to 12 ns after a first hit are removed. This

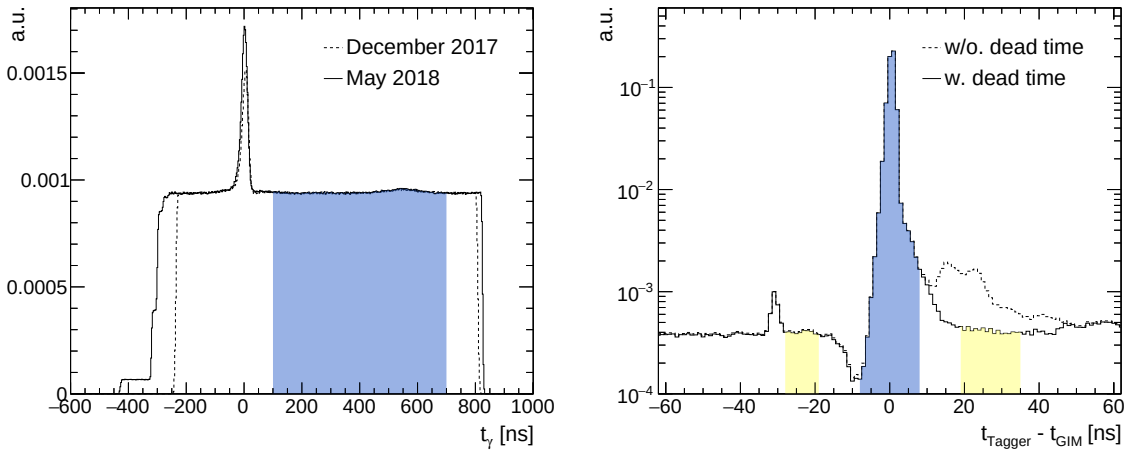

TDC window

Time difference

Figure 8.5: Left: TDC window for a high-rate run during data taking in May 2018. December 2017 is shown for comparison to illustrate the changes in the TDC window. The time window for the flux determination is shown in blue for a high-rate run ($\Delta t = 100 - 700\,\text{ns}$). Right: Time difference between the reconstructed photons in the Tagging system and the GIM with (w) and without (w/o) artificial dead time on Tagger fibers for a high-rate run in May 2018. Coincidences are time differences within the blue area (-8 to $15\,\text{ns}$). The background is subtracted using sideband events within the yellow regions (-28 to $-19\,\text{ns}$ and 19 to $35\,\text{ns}$). The small peak on the left is from afterpulses within the GIM but has no effect on the selected time ranges. The dip before the prompt peak is from the dead time of the GIM $t_{\text{dead}}^{\text{GIM}} = 12\,\text{ns}$. Note the logarithmic scale on the y-axis.

are normalized to their corresponding livetime. This is necessary because there is more dead time around the coincidence peak due to more hits in the peak interval compared to a time interval of the same size in the sideband. The live times are determined on an event-by-event basis as described in more detail in [158]. The final number of coincident hits is then given by

$$N_{\text{Tagger}\wedge\text{GIM}} = N_{\text{Tagger}\wedge\text{GIM}}^{\text{peak}} - \frac{t_{\text{live}}^{\text{peak}}}{t_{\text{live}}^{\text{sideband}}} \cdot N_{\text{Tagger}\wedge\text{GIM}}^{\text{sideband}}. \tag{8.12}$$

The distribution of the time differences between the Tagging system and the GIM is shown in Fig. 8.5 (right). In order to remove the influence of afterpulses from the Tagger fibers, an artificial dead time $t_{\text{dead}}^{\text{fibers}} = 45\,\text{ns}$ is additionally applied.[9]

For standard data runs, the high rate leads to a saturation of the GIM detector. Therefore, during the data taking, runs with lower beam current (low-rate runs) are also recorded.[10] By comparing the P_γ from such a low-rate run with an adjacent high-rate run, a correction of

results in a dead time of $t_{\text{dead}}^{\text{GIM}} = 12\,\text{ns}$.

[9] The artificial dead time affects the reconstruction in the Tagger in such a way that the afterpulses are removed without affecting the real events. The dead time is also applied for the general analysis to match the flux determination.

[10] Low-rate runs are recorded every few days.

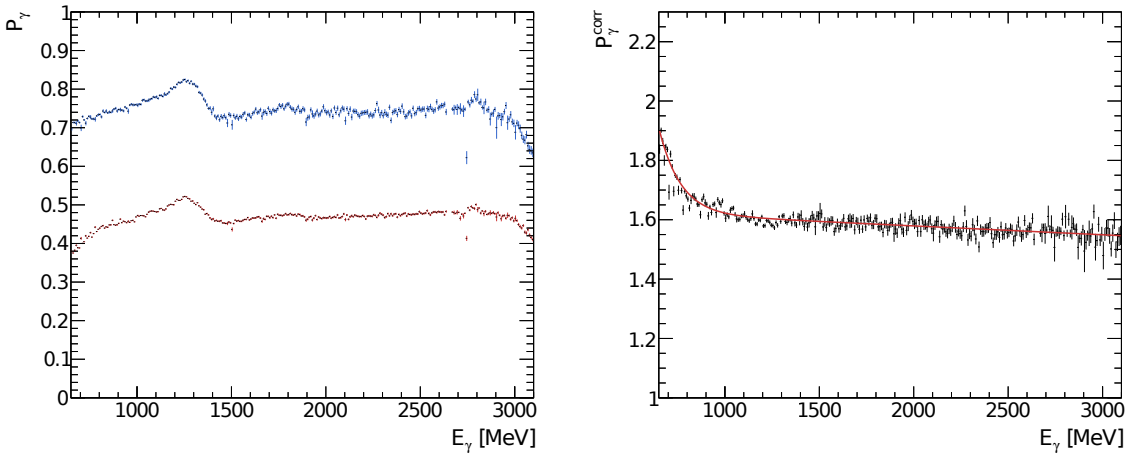

P_γ P_γ^{corr}

Figure 8.6: Left: Photon definition probability P_γ as a function of the beam photon energy E_γ for a low-rate (run number 201583) and a high-rate run (run number 201577). Right: Correction factor P_γ^{corr} (cf. Eqn. 8.13). The final correction is determined by fitting an exponential function with linear offset to the data.

the saturation can be calculated

$$P_\gamma^{\text{corr}} = \frac{P_\gamma^{\text{low-rate}}}{P_\gamma^{\text{high-rate}}}. \tag{8.13}$$

For each period of data taking, several low-rate runs are recorded so that multiple corrections are available each at different times. The correction closest in time is used to correct the P_γ of each high-rate run. An exception is when the beam current is adjusted. In this case, a correction valid for the updated beam current must be used. Furthermore, the correction is determined and applied separately for each of the polarization settings in the experiment.

In Fig. 8.6 (left), the P_γ is shown for an example pair of a low-rate run and a high-rate run for May 2018 data. The enhancement at the coherent edge at 1 350 MeV results from smaller opening angles in the case of coherent bremsstrahlung. As a result, the collimator behind the Tagging system has less effect and the number of photons reaching the target increases. In Fig. 8.6 (right), the correction P_γ^{corr} is shown. The final correction is obtained by fitting an exponential function with linear offset to the data, removing any fluctuations.

8.3.1.3 f_{live}

N_{Tagger} only corresponds to the number of tagged beam photons within the time range Δt. Livetime-gated scaler modules can be used to scale this number to the total livetime of the experiment. From and including December 2017, 96 scaler count all hits for individual bars during livetime.[11] To determine the livetime factor, the scaler values are compared to the

[11] Before that, only coincidences were counted with 95 scalers.

number of TDC hits within Δt

$$f_{\text{live}} = \frac{N_{\text{Tagger}}^{\text{live, scaler}}}{N_{\text{Tagger}}^{\Delta t,\text{TDC}}}. \tag{8.14}$$

A further complication arises from the dead time of the Cherenkov detector, which acts as a veto trigger. In the case of a veto, the livetime-gated scaler continues to count even though no more trigger signals are accepted. In these situations, the livetime calculated with Eqn. 8.14 is overestimated. In most of the data relevant to this work, the veto of the Cherenkov detector is only checked for the case where there is no hit or only one hit in the Crystal Barrel detector[12] (cf. Section 2.5). However, this is almost never the case for the $p\pi^0\pi^0$ final state because of the high probability of ≥ 2 hits in the Crystal Barrel detector. For this data, the dead time of the Cherenkov detector can therefore be neglected. Only for the first runs during data taking in December 2017, the veto of the Cherenkov detector was always checked.[13] For these runs, the livetime factor is modified by

$$f_{\text{live}} \cdot \epsilon_{\text{veto}},$$

where $\epsilon_{\text{veto}} = 0.88$ is the relative livetime of the Cherenkov detector. The value is obtained from a dedicated scaler that counts all clock cycles with an active veto of the Cherenkov detector.[14]

8.3.1.4 Φ_γ

The flux is determined for each run. The flux integrated over all runs for each period of data taking is shown in Fig. 8.7 (left). The difference in the statistics and the different positions of the coherent edge can be clearly seen. Fig. 8.7 (right) shows the flux for the four different polarization settings for May 2018 as an example. The flux for the different settings is comparable, confirming that the data were collected with roughly the same measurement time for each setting, which is one of the goals of data taking.

8.3.2 Calculation of the Scaling Factor c

The beam flux normalization already takes into account energy dependent differences in flux and different measurement times. As a result, the scaling factor only needs to account for the different target densities. It can be determined either directly from the target material densities or from data.

[12] Trigger pattern `trig42_i` and `trig42_k` (up to the point of writing).

[13] Trigger pattern `trig_42g` and `trig_42h`. Effected run numbers are 200024–200271, 200286–200316 and 200410–200412.

[14] The veto scaler is only available for data starting with run 200343 during data taking in December 2017. By this time, most runs with trigger pattern `trig_42g` and `trig_42h` have already been recorded. Therefore, ϵ_{veto} was determined using the veto scaler for later runs and applied to the runs without veto scaler. It was ensured beforehand that the beam current did not change for the affected runs.

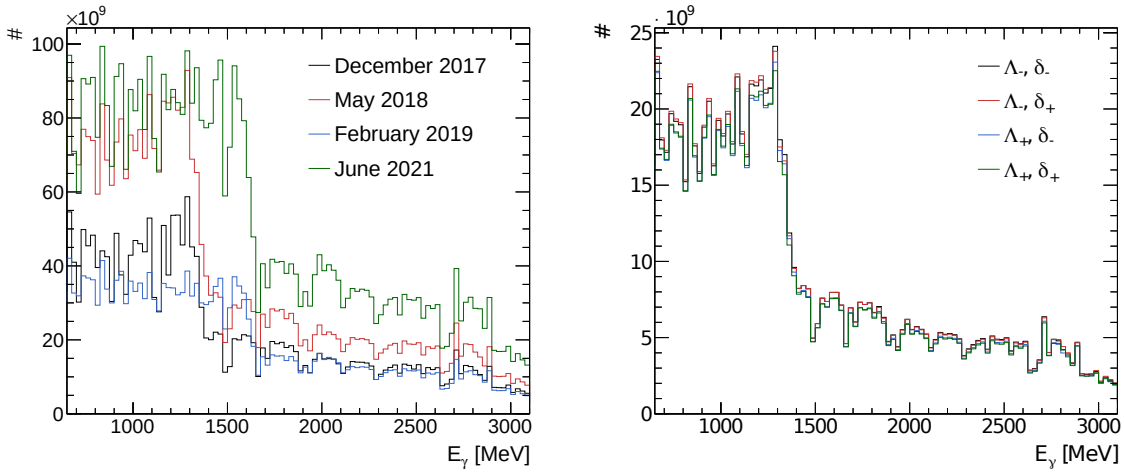

Integrated For each pol. setting

Figure 8.7: The integrated beam flux for each period of data taking (left) and the beam flux for each polarization setting $(\Lambda_\pm, \delta_\pm)$ for May 2018 as an example (right). An energy binning of 25 MeV is used for better visualization.

8.3.2.1 Calculation from Target Densities

To calculate the scaling factor c from the target materials, the target densities of bound protons

$$n_p^{\text{bound}} = \frac{\rho \cdot l_{\text{eff}} \cdot N_p^{\text{bound}} \cdot N_A}{m_{\text{mol}}} \tag{8.15}$$

must be determined for the butanol target and the carbon foam. Here, ρ is the density and m_{mol} is the molar mass of the target materials. l_{eff} describes the length of the targets. For the butanol target, the length is modified by a filling factor of (0.61 ± 0.05),[15] which accounts for the empty space between the butanol beads that are in the target cell [168]. N_p^{bound} is the number of bound protons in the material and N_A is the Avogadro constant. All values are listed in Table 8.4. In addition to the target materials, a PTFE (polytetrafluoroethylene) window used to cover the target cell must also be considered. The setup of the target cell is identical for both measurements, so the PTFE container must also be considered for the measurement with carbon foam [109]. The scaling factor is

$$c = \frac{n_{p,\text{B}}^{\text{bound}} + n_{p,\text{PTFE}}^{\text{bound}}}{n_{p,\text{C}}^{\text{bound}} + n_{p,\text{PTFE}}^{\text{bound}}} = \frac{(0.298 \pm 0.024) + 0.032}{0.307 + 0.032} = (0.97 \pm 0.07). \tag{8.16}$$

8.3.2.2 Calculation from Data

The scaling factor can also be determined directly from the data. Here, the Fermi motion of the bound protons is used. Their non-zero momentum leads to a violation of the assumption

[15] In [168], different filling factors are given for different target lengths. A factor of 0.61 is a realistic value for a target length of 2 cm [109]. However, an error of ±0.05 is assumed due to the high uncertainty of the value.

Table 8.4: Material values [7, 169] and lengths [161] for the butanol target, the carbon foam and the PTFE window. The target density of bound protons is calculated using Eqn. 8.15. The length of the butanol target is modified by the filling factor of (0.61 ± 0.05) [168]. The uncertainty in the filling factor dominates in the calculation of the target density. As a result, only butanol has errors assigned.

Target	ρ [g/cm^3]	l_{eff} [cm]	m_{mol} [g mol^{-1}]	N_p^{bound}	n_p^{bound} [b^{-1}]
Butanol (C_4H_9OH)	0.94	$2.00 \cdot (0.61 \pm 0.05)$	74.12	32	(0.298 ± 0.024)
Carbon foam (C)	0.50	2.04	12.01	6	0.307
PTFE window (C_2F_4)	2.20	0.05	100.02	48	0.032

that the target nucleon is at rest. As a result, distributions such as coplanarity are broadened. In regions of coplanarity, where quasi-free protons are negligible, the scaling factor can then be determined as follows

$$c = \frac{N_B}{N_C^{\text{ref}}}, \tag{8.17}$$

where N_B is the number of events in that region during data taking with the butanol target and N_C^{ref} the number of events in the very same region for the reference measurement with carbon foam.

The coplanarity distribution of 5-PED events is well suited to calculate the scaling factor. In the case of vanishing transverse momentum in the initial state, the coplanarity distribution is centered around 180° (cf. Section 7.4.2). In contrast, bound protons with additional initial momentum are distributed more towards the tails of the distribution. The scaling factor is first determined as a function of the width of an anti-cut on the coplanarity distribution

$$180^\circ \pm \Delta\phi_{\text{anti-cut}}. \tag{8.18}$$

If the anti-cut is too small, the quasi-free protons are not negligible and the scaling factor is too high. However, once the region where carbon dominates is reached, the scaling factor converges to a constant value. The application of the anti-cut and the effect of carbon scaling is shown in Fig. 8.8. By combining the data from December 2017, May 2018, February 2019 and June 2021, a global scaling factor of

$$c = (0.86 \pm 0.01) \tag{8.19}$$

is determined.

A comparison with the scaling factor based on the target material densities (cf. Eqn. 8.16) shows that the value obtained from the data is smaller than expected. One explanation could be the uncertainty of the filling factor, which dominates in the calculation of the target density of butanol. Because of this uncertainty, the value directly obtained from data is used in the following. The scaling factor is validated using the missing mass distribution after the $\pi^0\pi^0$ fit in Fig. 8.9. This distribution is especially sensitive to errors due to the accumulation of carbon at higher missing masses. Nevertheless, a good working carbon scaling can be

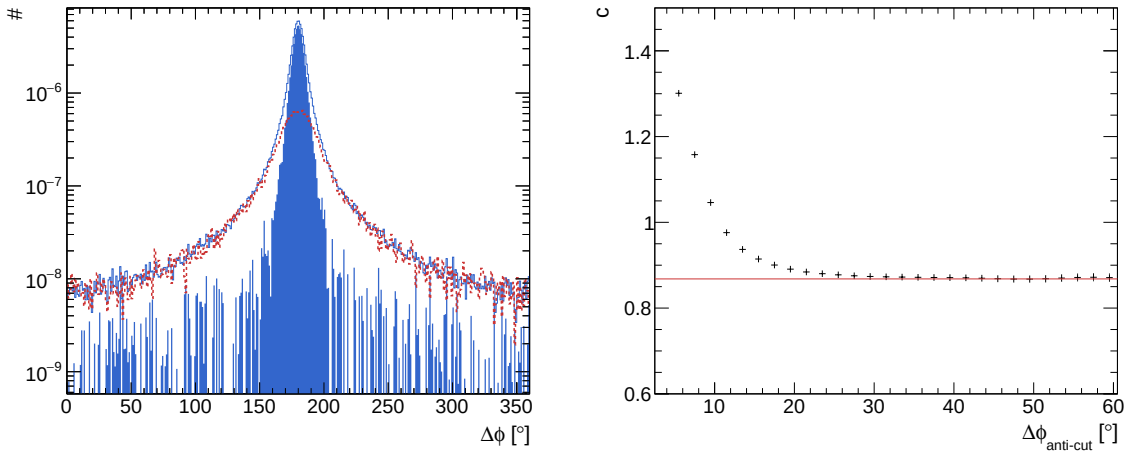

Coplanarity distribution

Scaling factor c

Figure 8.8: Coplanarity distribution for 5-PED events after the full kinematic fit (left). Carbon subtraction is demonstrated using the scaling factor $c = 0.86$. The butanol distribution before carbon subtraction and the scaled carbon distribution are shown. The butanol distribution after carbon subtraction is shown as filled area. The scaling factor is determined using an anti-cut $180^\circ \pm \Delta\phi_{\text{anti-cut}}$ on the coplanarity distribution (right). Combined data from the December 2017, May 2018, February 2019 and June 2021 data taking is shown.

seen. Leftovers on the right hand side of the distribution correspond to the background in the event sample. For more information on background refer to Section 7.7. More resulting distributions after carbon scaling can be found in Appendix B.

In Fig. 8.10, the scaling factor is shown for each period of data taking as a function of the beam energy E_γ or $\cos(\theta_{\pi^0\pi^0})$. Since the flux normalization takes into account the energy dependent differences in the flux, a constant behavior is expected. Furthermore, the scaling factor after flux normalization should be consistent between the different periods of data taking. Both are clearly the case. The remaining fluctuations are taken into account in the systematic uncertainties (cf. Section 8.5). The scaling factors for each period of data taking are listed in Table 8.3. However, for the following analysis, the scaling factor from Eqn. 8.19 is used, which is determined simultaneously on all periods of data taking in this work.

8.3.2.3 Exclusion of 4-PED Events for June 2021 Data

As noted in several places in this work, 4-PED events are excluded from the analysis for the June 2021 data.[16] The reason for this is a non-functional carbon scaling. Similar to the other periods of data taking, the scaling factor for June 2021 is determined using 5-PED events and the coplanarity distribution. The resulting scaling factor is consistent with the scaling factors for the other periods (cf. Table 8.3 or Fig. 8.10) and can be applied to 5-PED and 4.5-PED events. However, when the scaling factor is applied to 4-PED events, there are significant deviations in the butanol distribution after subtraction (cf. Fig. 8.11). Instead of removing only the influence of carbon, too much data is subtracted, resulting in negative values.

[16] Otherwise, all event classes are used for each period of data taking.

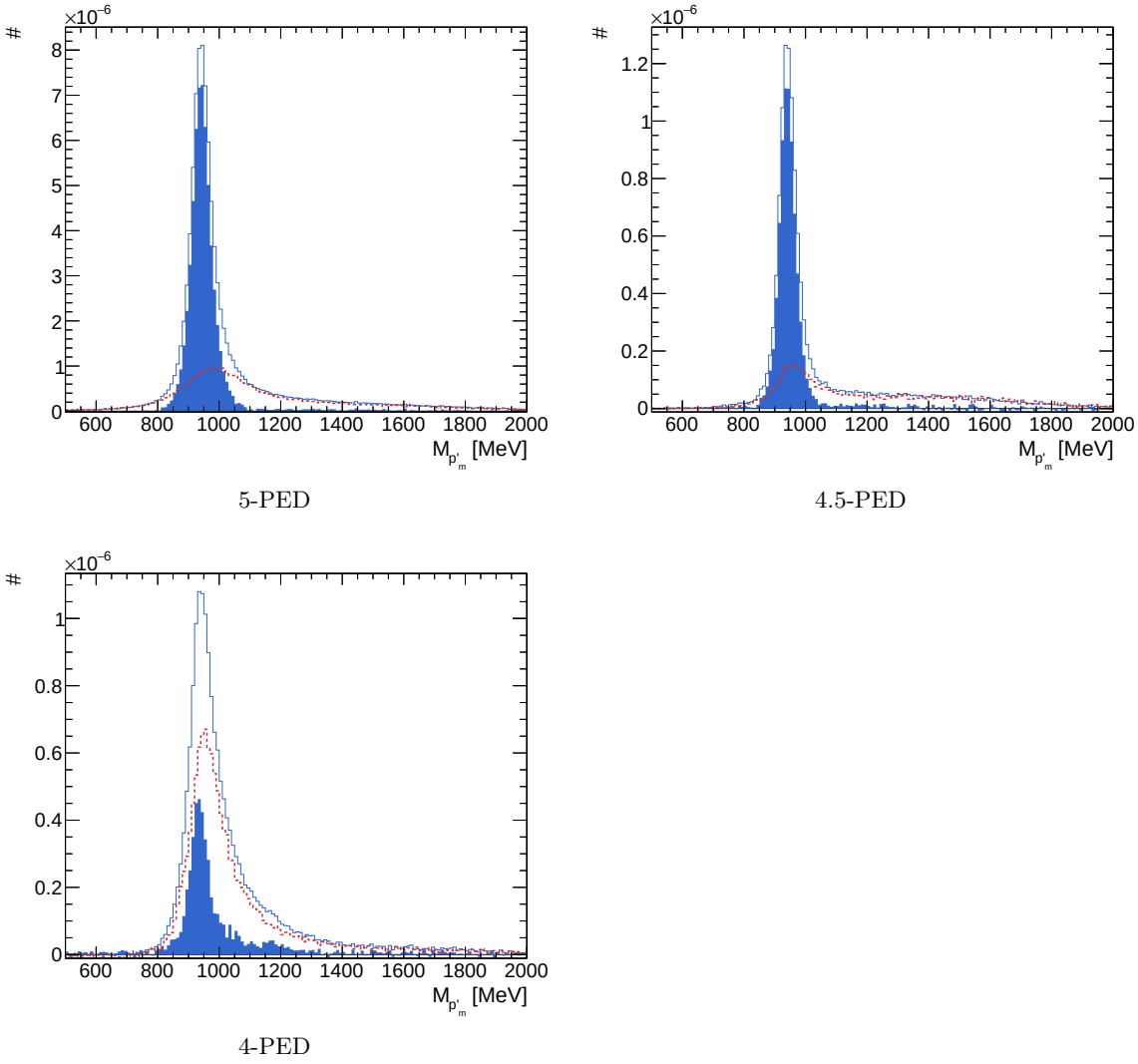

5-PED

4.5-PED

4-PED

Figure 8.9: Application of carbon scaling for 5-PED, 4.5-PED and 4-PED events using the missing mass distribution after the $\pi^0\pi^0$ fit as an example. In all cases $c = 0.86$ is used as the scaling factor. The butanol distribution before carbon subtraction and the scaled carbon distribution are shown. The butanol distribution after carbon subtraction is shown as a filled area. Combined data from December 2017, May 2018, February 2019 and June 2021 are shown.

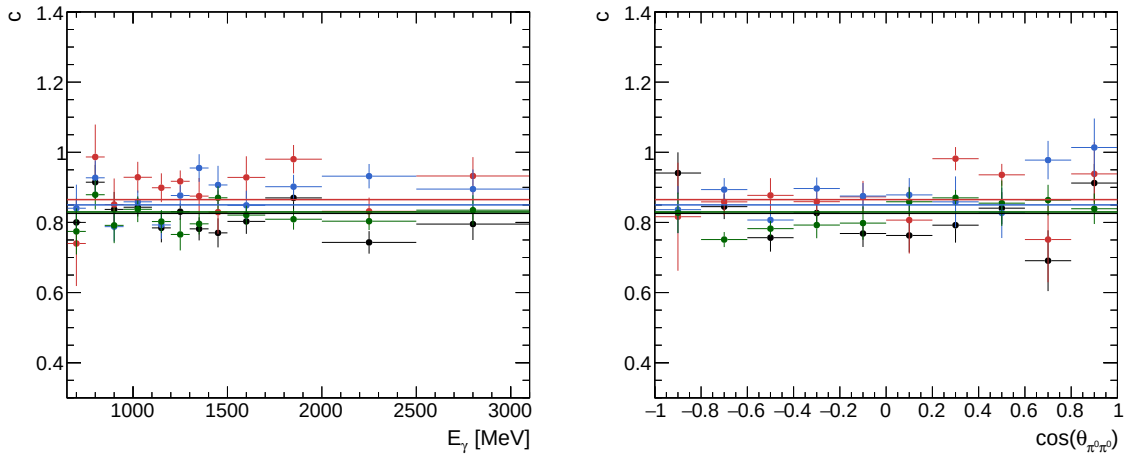

Figure 8.10: The scaling factor c as a function of the beam energy E_γ or $\cos(\theta_{\pi^0\pi^0})$. The different periods of data taking **December 2017**, May 2018, February 2019 and June 2021 are compared. The horizontal lines correspond to global scaling factors. In each case (also for the global scaling factors), 5-PED events and the coplanarity distribution are used.

The impact of excluding 4-PED events for the June 2021 data is manageable. As explained in Section 7.1, 4-PED events affect only a small kinematic range. Nevertheless, about one third of 4-PED events are lost (cf. Table 9.1). It is therefore of great interest to solve this problem in the future. The same effect is also observed in other analyses based on the same data [170]. At the moment the problem is still under investigation.

8.3.3 Dilution Factor d

The protons bound in carbon and oxygen dilute the polarization observables. Since the cross section for oxygen behaves similarly to the cross section for carbon, any difference between oxygen and carbon is neglected in the following [171]. The polarized cross section for butanol data is then given by

$$\frac{\mathrm{d}\sigma}{\mathrm{d}\Omega}^B = \frac{\mathrm{d}\sigma}{\mathrm{d}\Omega}\left(P_x, P_y, I^s, I^c, P_x^s, P_y^s, P_x^c, P_y^c\right)^H + \frac{\mathrm{d}\sigma}{\mathrm{d}\Omega}\left(I_C^s, I_C^c\right)^C .$$

All observables are included in the cross section of the hydrogen data. For carbon only the beam observables contribute due to the non-polarizable bound protons in the target.

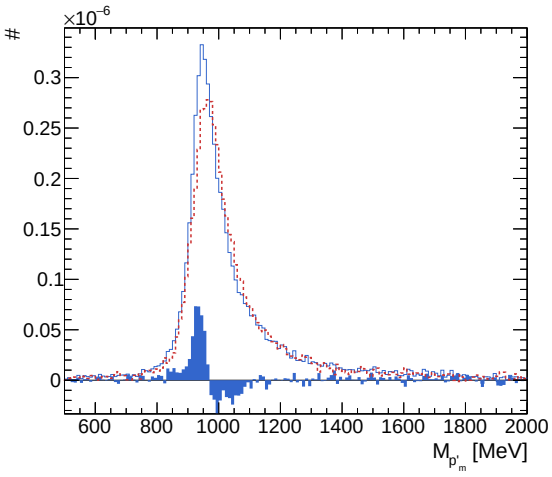

Figure 8.11: Application of carbon scaling for 4-PED events for the June 2021 data using the missing mass distribution after the $\pi^0\pi^0$ fit as an example. A scaling factor of $c = 0.83$ is used. The butanol distribution before carbon subtraction and the scaled carbon distribution are shown. The butanol distribution after carbon subtraction is shown as a filled area.

Substituting the expression for the polarized cross section (cf. Eqn. 8.1) we get

$$\begin{aligned}\frac{\mathrm{d}\sigma}{\mathrm{d}\Omega}^{B} = \left[\left(\frac{\mathrm{d}\sigma}{\mathrm{d}\Omega}\right)_0^H + \left(\frac{\mathrm{d}\sigma}{\mathrm{d}\Omega}\right)_0^C\right] \cdot \Big(1 + d\cdot\Lambda_x P_x + d\cdot\Lambda_y P_y \\ + \delta_l \sin(2\phi_B)\left[d\cdot I^s + (1-d)\cdot I_C^s + d\cdot\Lambda_x P_x^s + d\cdot\Lambda_y P_y^s\right] \\ + \delta_l \cos(2\phi_B)\left[d\cdot I^c + (1-d)\cdot I_C^c + d\cdot\Lambda_x P_x^c + d\cdot\Lambda_y P_y^c\right]\Big).\end{aligned} \tag{8.20}$$

For simplicity, the following expression has already been replaced

$$d = \frac{\left(\frac{\mathrm{d}\sigma}{\mathrm{d}\Omega}\right)_0^H}{\left(\frac{\mathrm{d}\sigma}{\mathrm{d}\Omega}\right)_0^H + \left(\frac{\mathrm{d}\sigma}{\mathrm{d}\Omega}\right)_0^C}. \tag{8.21}$$

It becomes clear that the observables $\mathcal{O}_B$ extracted from the butanol data are diluted by a factor of

$$\mathcal{O}_B = d\cdot\mathcal{O}. \tag{8.22}$$

Using the proportionality of the cross section to the event yield the dilution factor d can be expressed as

$$d = \frac{N_H}{N_H + N_C} = \frac{N_B - c\cdot N_C^{\mathrm{ref}}}{N_B}. \tag{8.23}$$

In the last step, Eqn. 8.8 is used to express the unknown event yield of hydrogen N_H using the event yield of the reference measurement with carbon foam N_C^{ref}. The event yield of the reference measurement is scaled by the carbon scaling factor c. This allows the extracted

observables to be corrected. An exception are the beam polarization observables, where the dilution depends on the observables of the carbon itself

$$I_B^{s/c} = d \cdot I^{s/c} + (1 - d) \cdot I_C^{s/c}. \tag{8.24}$$

Without knowledge of the beam polarization in carbon, the dilution of the beam polarization cannot be corrected. For this reason, the beam polarization observables are not extracted as a result of this work. They can be analyzed with higher accuracy using data measured with a liquid hydrogen target. An example of such an analysis is [164].

In Fig. 8.12, the dilution factor is shown for each period of data taking as a function of the beam energy E_γ or $\cos(\theta_{\pi^0\pi^0})$. As before with the scaling factor, the dilution factor is expected to be the same for the different data takings. This is clearly the case for 5-PED and 4.5-PED events. Only for the sum of 5-PED, 4.5-PED, and 4-PED events does the June 2021 data behave differently. This is because for June 2021 4-PED events are not included in this analysis.

A decrease of the dilution factor with increasing energies is observed. This can be explained by wider cut ranges at high energies (cf. Fig. B.1 to B.2 in the Appendix). They allow more carbon events to be reconstructed within the cut ranges, thus lowering the dilution factor. Other structures arise from the shape of the cross section or from acceptance effects. Furthermore, a decrease of the dilution factor can be seen as soon as all PED classes are used. The reason for this is that 4-PED events are particularly sensitive to carbon since no angular cuts can be applied[17] (cf. Section 7.4.2). Also, the influence of reactions on bound neutrons is present in 4-PED events, since the nucleon and its charge are not measured. In Fig. 8.13, the dilution factor for all kinematic variables is plotted as a function of beam energy E_γ. Again, a decrease is clearly visible at high values of $\cos(\theta_{\pi^0\pi^0})$, where the 4-PED events are located. In Section C.1 in the Appendix, the dilution factor for several other kinematic regions is shown. For the final results of this work, the dilution factor is determined using the same binning as the extracted polarization observables.[18]

8.4 Event Based Likelihood Fit

An event-based likelihood fit is used to extract the polarization observables [158, 172]. Therefore, the polarized cross section (cf. Eqn. 8.3) is interpreted as a probability density function $f_{\text{phys}}(\varphi)$. The likelihood $\mathcal{L}$ that a set of events is described by a particular f_{phys} is defined as the multiplication of the probabilities of the individual events

$$\begin{aligned} \mathcal{L} &= f_{\text{phys}}(\text{event } 1) \cdot f_{\text{phys}}(\text{event } 2) \cdot \ldots \cdot f_{\text{phys}}(\text{event } n) \\ &= \prod_{i=1}^{n} f_{\text{phys}}(\text{event } i). \end{aligned} \tag{8.25}$$

[17] For the calculation of coplanarity and the polar angle difference the proton must be measured, which is not the case for 4-PED events.

[18] There is no requirement on the statistics, that is, no minimum number of events required within a bin.

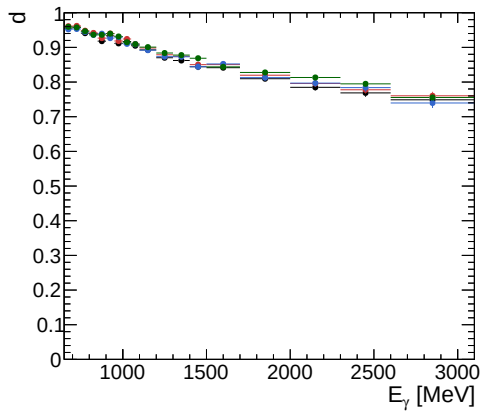

E_γ for 5-PED

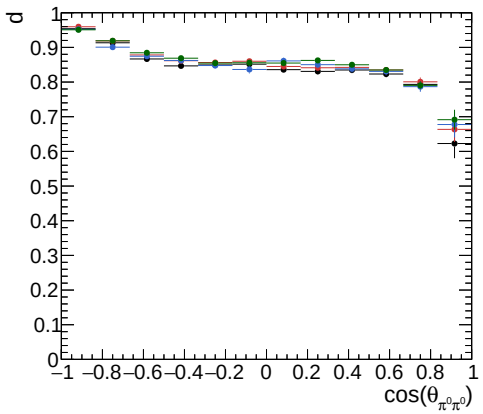

$\cos(\theta_{\pi^0\pi^0})$ for 5-PED

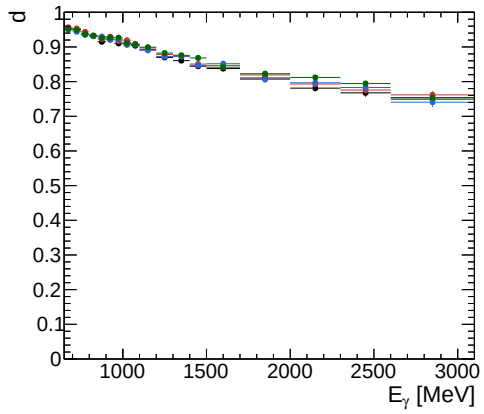

E_γ for 5-PED, 4.5-PED

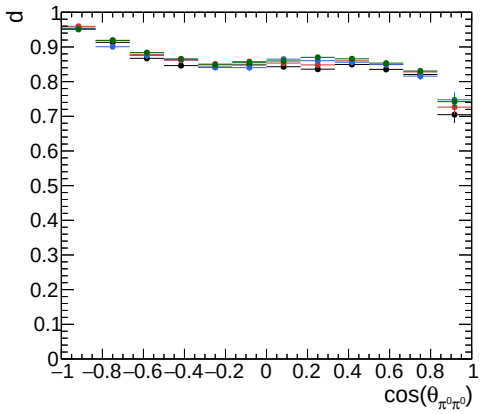

$\cos(\theta_{\pi^0\pi^0})$ for 5-PED, 4.5-PED

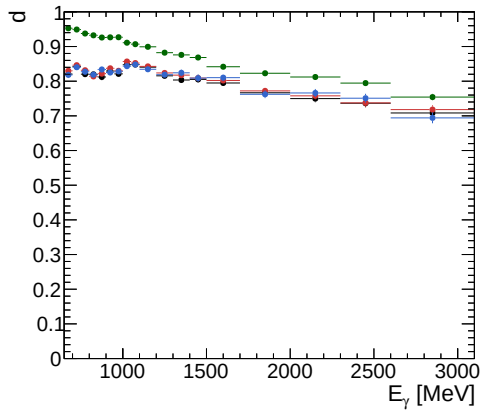

E_γ for 5-PED, 4.5-PED, 4-PED

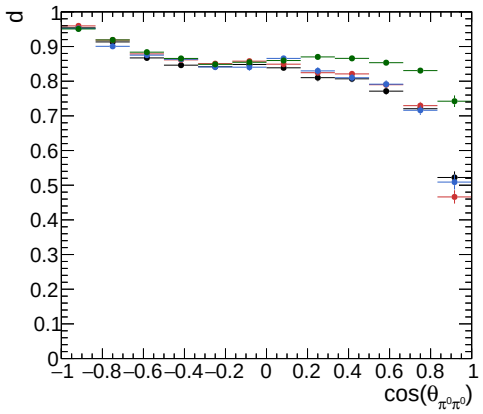

$\cos(\theta_{\pi^0\pi^0})$ for 5-PED, 4.5-PED, 4-PED

Figure 8.12: The dilution factor d as a function of the beam energy E_γ (left) or $\cos(\theta_{\pi^0\pi^0})$ (right). The different periods of data taking **December 2017**, May 2018, February 2019 and June 2021 are compared. Top: Only 5-PED events are used. Middle: Both 5-PED and 4.5-PED events are used. Bottom: 5-PED, 4.5-PED and 4-PED events are used. Here, June 2021 behaves differently, because 4-PED events are excluded (cf. Section 8.3.2.3).

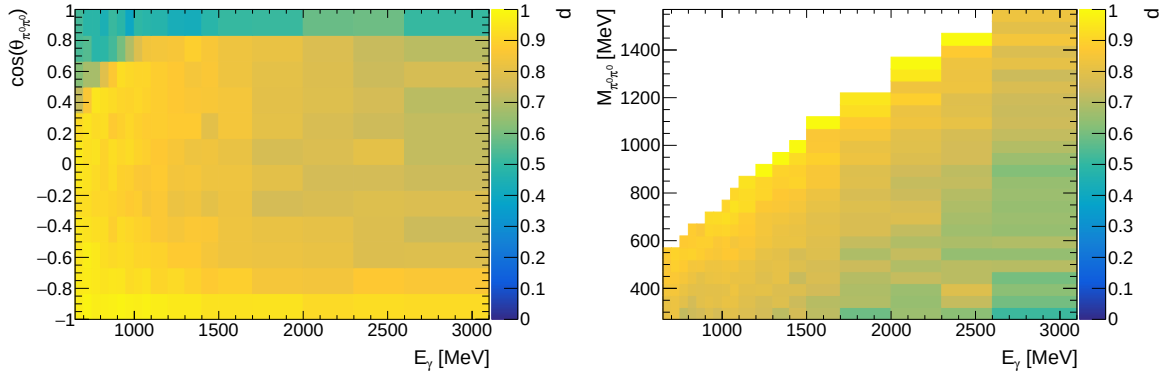

$\cos(\theta_{\pi^0\pi^0})$ vs. E_γ

$M_{\pi^0\pi^0}$ vs. E_γ

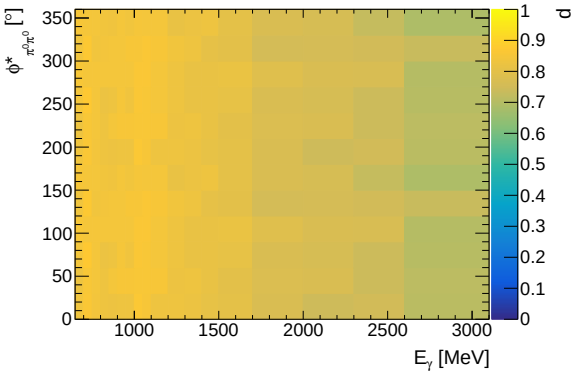

$\phi^*_{\pi^0\pi^0}$ vs. E_γ

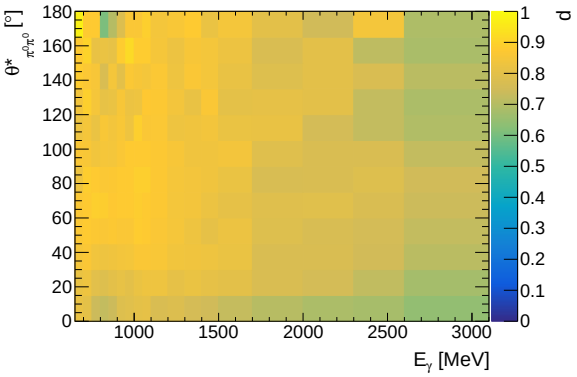

$\theta^*_{\pi^0\pi^0}$ vs. E_γ

Figure 8.13: Dilution factor d for $(\cos(\theta_{\pi^0\pi^0}), M_{\pi^0\pi^0}, \phi^*_{\pi^0\pi^0}, \theta^*_{\pi^0\pi^0})$ as function of E_γ for the combined data from December 2017, May 2018, February 2019 and June 2021. In Section C.1 in the Appendix, the dilution factor for several other kinematic regions is shown.

To find the best fitting f_{phys}, meaning to extract the polarization observables as parameters of the function, $\mathcal{L}$ must be maximized. However, for numerical reasons it is more practical to minimize the negative log-likelihood instead

$$-\log\left(\mathcal{L}\right) = -\sum_{i=1}^{n} \log\left(f_{\text{phys}}(\text{event } i)\right). \tag{8.26}$$

The probability density function of the cross section f_{phys} can be rewritten as a Fourier series [159]

$$f_{\text{phys}}(\varphi) = 1 + \sum_{k=1}^{3} a_k \sin(k\varphi) + b_k \cos(k\varphi) \tag{8.27}$$

with the coefficients

$$
\begin{aligned}
a_1 =& + d\Lambda \left[P_x \sin(\beta) - P_y \cos(\beta)\right] \\
& - \frac{1}{2} d\delta_l \Lambda \left[(P_x^s - P_y^c)\left(\sin(2\alpha)\sin(\beta) + \cos(2\alpha)\cos(\beta)\right)\right] \\
& + \frac{1}{2} d\delta_l \Lambda \left[(P_x^c + P_y^s)\left(\sin(2\alpha)\cos(\beta) - \cos(2\alpha)\sin(\beta)\right)\right] \\
b_1 =& + d\Lambda \left[P_x \cos(\beta) + P_y \sin(\beta)\right] \\
& - \frac{1}{2} d\delta_l \Lambda \left[(P_x^s - P_y^c)\left(\cos(2\alpha)\sin(\beta) - \sin(2\alpha)\cos(\beta)\right)\right] \\
& + \frac{1}{2} d\delta_l \Lambda \left[(P_x^c + P_y^s)\left(\sin(2\alpha)\sin(\beta) + \cos(2\alpha)\cos(\beta)\right)\right] \\
a_2 =& + \delta_l \left[-I^s \cos(2\alpha) + I^c \sin(2\alpha)\right] \\
b_2 =& + \delta_l \left[+I^s \sin(2\alpha) + I^c \cos(2\alpha)\right] \\
a_3 =& - \frac{1}{2} \delta_l d\Lambda \left[(P_x^s + P_y^c)\left(-\sin(2\alpha)\sin(\beta) + \cos(2\alpha)\cos(\beta)\right)\right] \\
& + \frac{1}{2} \delta_l d\Lambda \left[(P_x^c - P_y^s)\left(\sin(2\alpha)\cos(\beta) + \cos(2\alpha)\sin(\beta)\right)\right] \\
b_3 =& + \frac{1}{2} \delta_l d\Lambda \left[(P_x^s + P_y^c)\left(\cos(2\alpha)\sin(\beta) + \sin(2\alpha)\cos(\beta)\right)\right] \\
& + \frac{1}{2} \delta_l d\Lambda \left[(P_x^c - P_y^s)\left(-\sin(2\alpha)\sin(\beta) + \cos(2\alpha)\cos(\beta)\right)\right]
\end{aligned}
$$

In the case of an event-based likelihood fit, the effects of the detector acceptance along φ must be explicitly considered. This can be achieved by using a normalized Fourier series decomposition of the acceptance [158]

$$
f_{\text{det}}(\varphi) = 1 + \sum_{k=1}^{\infty} c_k \sin(k\varphi) + d_k \cos(k\varphi). \tag{8.28}
$$

It can be shown that it is sufficient to consider the coefficients c_k and d_k for $k \leq 6$ without loss of information in the polarization observables [158, 159]. Finally, by multiplying f_{phys} by f_{det} and normalizing, we obtain the total probability density function

$$
\begin{aligned}
f(\varphi) =& \frac{f_{\text{phys}}(\varphi) \cdot f_{\text{det}}(\varphi)}{\frac{1}{2\pi} \int f_{\text{phys}}(\varphi) \cdot f_{\text{det}} \, \mathrm{d}\varphi} \\
=& \frac{\left(1 + \sum_{k=1}^{3} a_k \sin(k\varphi) + b_k \cos(k\varphi)\right) \cdot \left(1 + \sum_{k=1}^{6} c_k \sin(k\varphi) + d_k \cos(k\varphi)\right)}{1 + \frac{1}{2} \sum_{k=1}^{3} a_k c_k + b_k d_k}.
\end{aligned} \tag{8.29}
$$

The last aspect to be considered are the background events bg, which arise from random coincidences of beam photons. Other remaining background in the event sample is not considered in the fit but will be taken into account later in the systematic error. To remove the influence of the random beam photons, the selected sideband events[19] are also fitted with

[19] For more information on sideband events, see Section 7.4.1.

their own probability distribution. This results in the overall likelihood function

$$\begin{aligned}\mathcal{L} = \prod_{i=1}^{n} \Big(& \tau \cdot f(\varphi_i, d^i, \delta_{l,i}, \Lambda_i, \mathcal{O}_{1-8}, c_1, \ldots, c_6, d_1, \ldots d_6) \\ & + (1-\tau) \cdot f(\varphi_i, d^i, \delta_{l,i}, \Lambda_i, \mathcal{O}^{\mathrm{bg}}_{1-8}, c_1^{\mathrm{bg}}, \ldots, c_6^{\mathrm{bg}}, d_1^{\mathrm{bg}}, \ldots d_6^{\mathrm{bg}}) \Big) \\ \cdot \prod_{j=1}^{m} & f(\varphi_j, d^j, \delta_{l,j}, \Lambda_j, \mathcal{O}^{\mathrm{bg}}_{1-8}, c_1^{\mathrm{bg}}, \ldots, c_6^{\mathrm{bg}}, d_1^{\mathrm{bg}}, \ldots d_6^{\mathrm{bg}}),\end{aligned} \tag{8.30}$$

where $f(\varphi)$ is given by Eqn. 8.29. $\mathcal{O}_{1-8}$ refers to the set of the eight observables. d is the dilution factor, Λ the target polarization and δ_l the beam polarization. τ refers to the fraction of signal events

$$\tau = \frac{n - w \cdot m}{n} \qquad \text{with} \qquad w = 0.15, \tag{8.31}$$

where n is the number of selected events, m is the number of events within the sideband, and w is the weight of sideband events calculated in Eqn. 7.4. A total of 40 parameters are determined: eight observables $I^s, I^c, P_x, P_y, P_x^s, P_x^c, P_y^s, P_y^c$, twelve detector asymmetry coefficients $c_1, \ldots, c_6, d_1, \ldots d_6$, and the same number of parameters for the background (sideband) events.

8.4.1 Toy Monte Carlo Simulation

The implemented likelihood method is validated using a Monte Carlo simulation. The data are simulated according to the polarized cross section. The input is a random constellation of polarization observables. After applying the event-based likelihood fit, the extracted observables can be compared with the observables used as input for the simulation.

For a realistic scenario, the event yields for signal events, background due to random beam photon coincidences, and sideband events are simulated using the Poisson distribution

$$\begin{aligned} N^{\mathrm{signal}} &= \mathrm{Poisson}(\tau \cdot N) \\ N^{\mathrm{bg}} &= \mathrm{Poisson}((1-\tau) \cdot N) \\ N^{\mathrm{bg}}_{\mathrm{sideband}} &= \mathrm{Poisson}(\tfrac{1-\tau}{w} \cdot N), \end{aligned} \tag{8.32}$$

where N is the event yield, τ is the fraction of signal events, and w is the weight of sideband events. For the simulation, $\tau = 0.86$ and $w = 0.15$ are assumed, which reflects the situation in real data. All the parameters used in the simulation are listed in Table 8.5. The event yield is chosen differently for the different polarization settings to model a complex case. For simplicity, the dilution factor is assumed to be 1. In addition, a blind spot in φ is simulated as a worst-case scenario for the detector inefficiency[20] (cf. Fig. 8.14 (left)). For illustration, the cross section for each polarization setting is shown in Fig. 8.14 (right).

[20] Such an inefficiency is not expected in the detector and is used only for a thorough test of the event-based likelihood fit.

Table 8.5: Parameters and event yields used as input to the polarized cross section to simulate one Monte Carlo data set. The event yields are chosen differently for different polarization settings to model a complex case. For the same reasons, the background observables are chosen with opposite signs to the signal observables. 6400 Monte Carlo data sets are simulated with these parameters to test the event-based likelihood fit.

$\beta^{\uparrow}$	$90°$	$\Lambda^{\parallel}_{\uparrow}$, $\delta^{\parallel}_{\uparrow}$	0.65, 0.75	I^s, I^c, $I^{s,\mathrm{bg}}$, $I^{c,\mathrm{bg}}$	$+0.3$, -0.5, -0.3, $+0.5$	$N^{\parallel}_{\uparrow}$	600
$\beta^{\downarrow}$	$90+180°$	$\Lambda^{\parallel}_{\downarrow}$, $\delta^{\parallel}_{\downarrow}$	0.80, 0.60	P_x, P_y, P_x^{bg}, P_y^{bg}	-0.1, $+0.4$, $+0.1$, -0.4	$N^{\parallel}_{\downarrow}$	800
$\alpha^{\parallel}$	$45°$	$\Lambda^{\perp}_{\uparrow}$, $\delta^{\perp}_{\uparrow}$	0.70, 0.55	P_x^s, P_y^s, $P_x^{s,\mathrm{bg}}$, $P_y^{s,\mathrm{bg}}$	$+0.2$, $+0.3$, -0.2, -0.3	$N^{\perp}_{\uparrow}$	450
$\alpha^{\perp}$	$45+90°$	$\Lambda^{\perp}_{\downarrow}$, $\delta^{\perp}_{\downarrow}$	0.85, 0.50	P_x^c, P_y^c, $P_x^{c,\mathrm{bg}}$, $P_y^{c,\mathrm{bg}}$	-0.8, $+0.6$, $+0.8$, -0.6	$N^{\perp}_{\downarrow}$	750

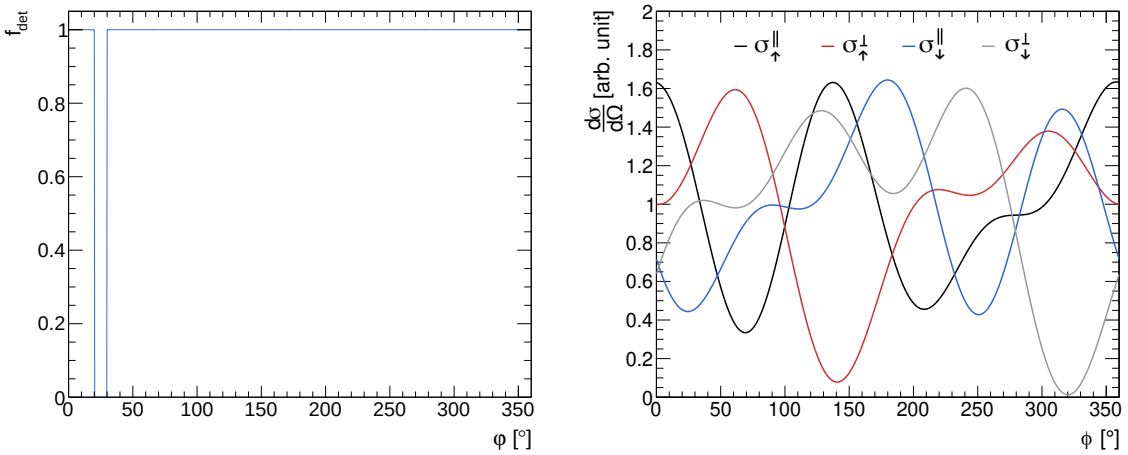

Inefficiency in φ | Cross sections for each setting

Figure 8.14: Left: Simulated inefficiency in φ which is used for an in-depth test of the event-based likelihood fit. Right: Cross sections for each polarization setting with the parameters specified in Table 8.5.

A total of 6400 Monte Carlo data sets are simulated. The resulting distributions for the extracted polarization observables are shown in Fig. 8.15. There is good agreement with the input parameters. As expected, the distributions for the single polarization observables are also narrower than those for the double polarization observables. The normalized residuals (pulls) are shown in Fig. 8.16. They are calculated as the deviations of the extracted polarization observables from the corresponding input parameters, normalized to the statistical error

$$\mathrm{pull}(n) = \frac{\mathcal{O}(n) - \mathcal{O}^{\mathrm{sim}}(n)}{\Delta\mathcal{O}(n)} \quad \text{with} \quad n = 0 \ldots 6400. \tag{8.33}$$

If the resulting distributions correspond to normal distributions with mean 0 and width 1, the extracted values are in agreement with the simulation. In each case, a normal distribution is present, so that a correct working likelihood fit can be assumed. For completeness, the distributions of the background observables and all coefficients for the inefficiency are shown in Section C.2 in the Appendix.

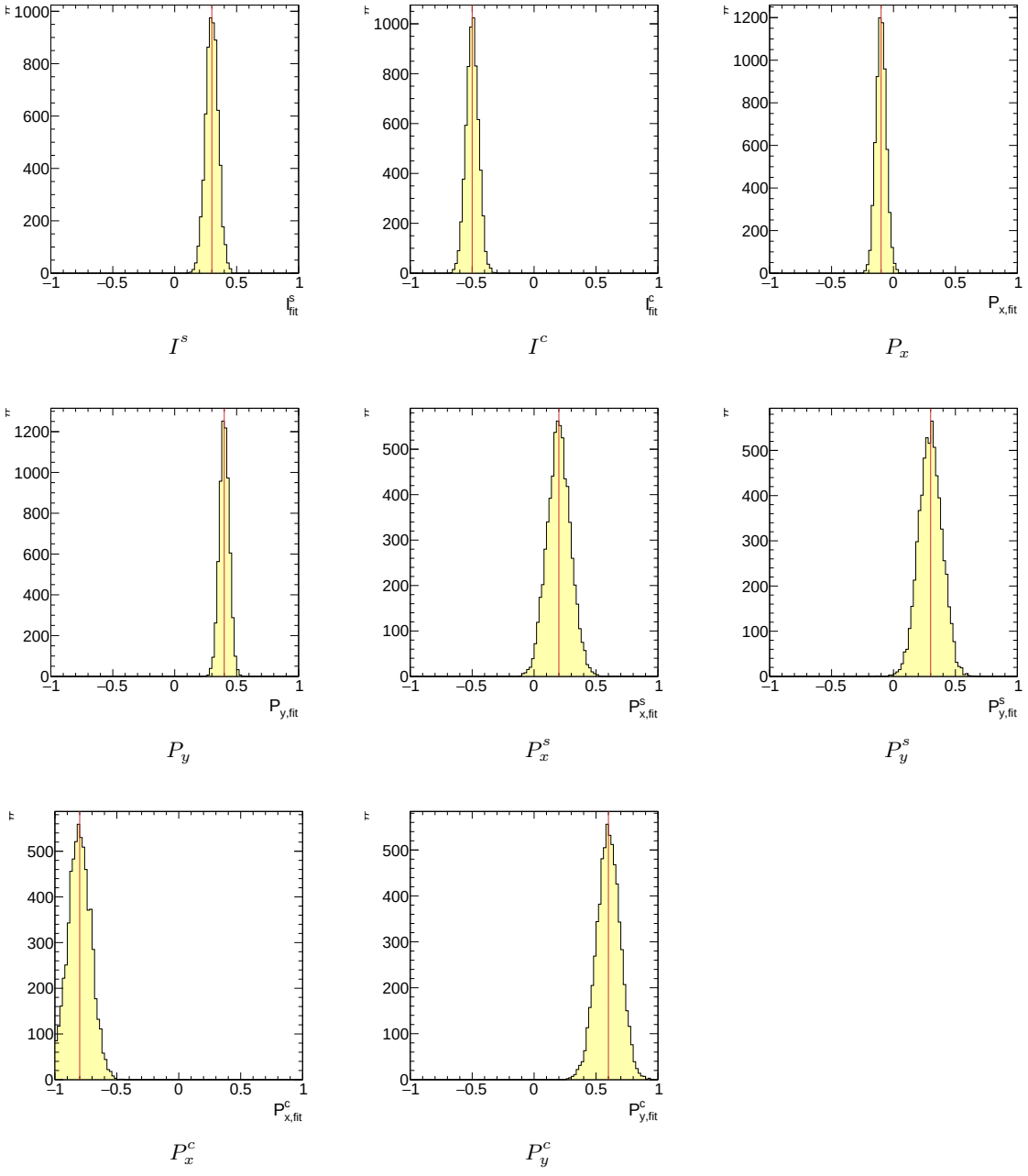

Figure 8.15: Distributions of extracted polarization observables after 6400 Monte Carlo simulations. The input parameters are listed in Table 8.5 and marked as red lines. The corresponding distributions of the normalized residuals are shown in Fig. 8.16.

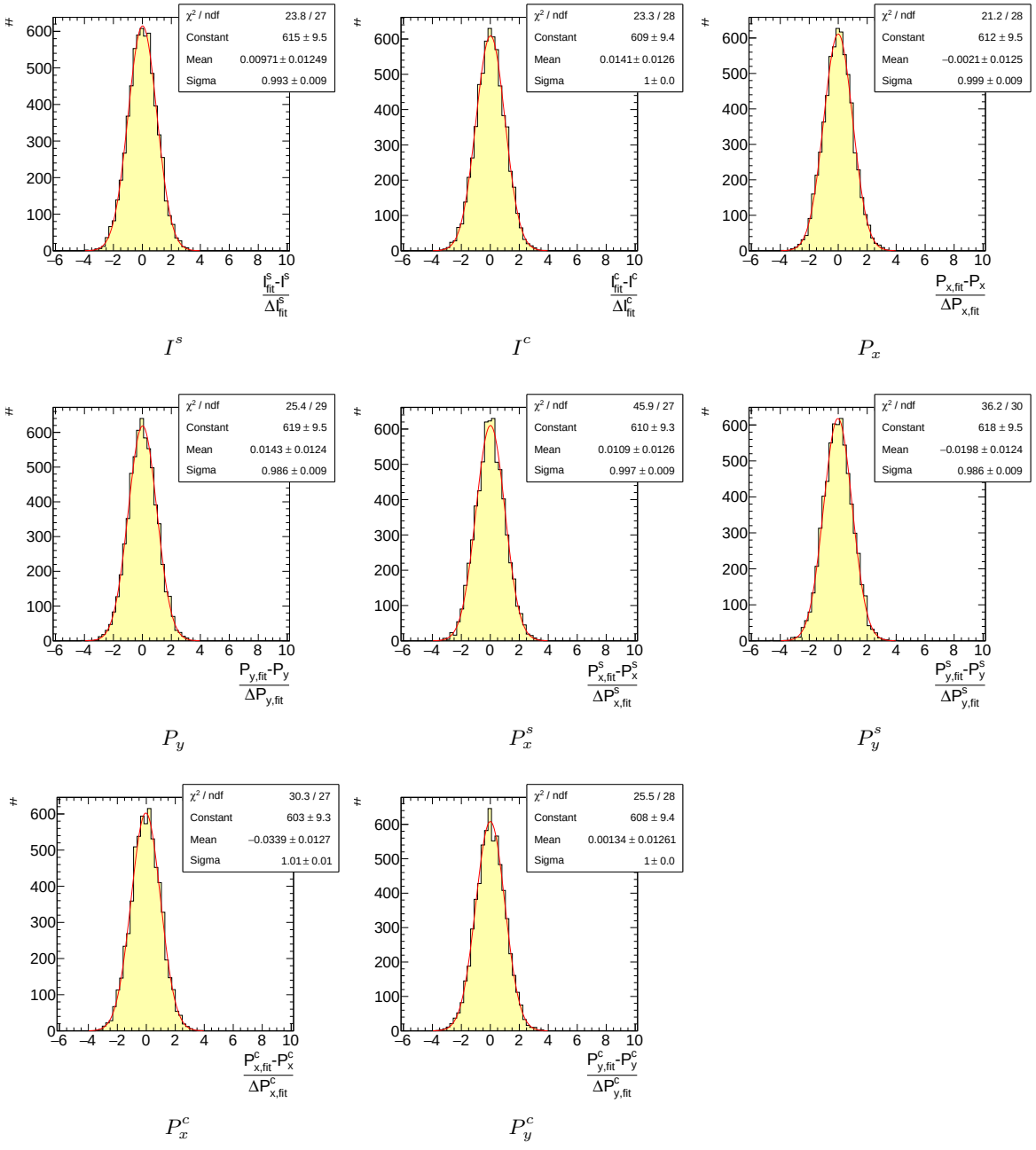

Figure 8.16: Normalized residuals of the polarization observables after 6400 Monte Carlo simulations (cf. Eqn. 8.33). If the resulting distribution corresponds to a normal distribution with mean 0 and width 1, the extracted values are in agreement with the simulation.

8.5 Systematic Uncertainties

For the final results of the polarization observables, not only the statistical error of the likelihood fit, but also the systematic uncertainties must be considered. Input parameters that have uncertainties are the target polarization Λ, the beam polarization δ_l, and the dilution factor d. In addition, the remaining background ξ in the final event sample can also bias the extracted observables. A method for quantifying the total systematic error in the final results is presented in the following. The method is based on considerations in [158].

8.5.1 Polarization Degree

One source of systematic error is the uncertainty associated with the target and beam polarization. The uncertainty of the target polarization arises primarily from the temperature measurement during calibration of the nuclear magnetic resonance (NMR) measurement. The relative systematic error in target polarization is estimated to be [109]

$$\frac{\Delta\Lambda}{\Lambda} = 2\,\%. \tag{8.34}$$

Similarly, beam polarization introduces a systematic error into the analysis. To estimate the systematic error, deviations of the calculated ANB[21] spectrum and the measured enhancement spectrum were analyzed in [173]. Based on this comparison, the relative systematic uncertainty in the beam polarization is estimated to be

$$\frac{\Delta\delta_l}{\delta_l} = 5\,\%. \tag{8.35}$$

An increase in the systematic uncertainty of the beam polarization near the position of the coherent edge was proposed in [158]. However, more recent studies find no evidence to support the need for such an adjustment [164]. Therefore, a global estimate is used in this work.

The degree of polarization enters as a multiplicative factor in the extraction of polarization observables, leading to a direct propagation of the relative systematic uncertainty to the extracted observables

$$\begin{aligned}
\frac{\Delta\mathcal{O}^{\mathcal{T}}_{\mathrm{pol}}}{\mathcal{O}^{\mathcal{T}}} &= \frac{\Delta\Lambda}{\Lambda} \\
\frac{\Delta\mathcal{O}^{\mathcal{B}}_{\mathrm{pol}}}{\mathcal{O}^{\mathcal{B}}} &= \frac{\Delta\delta_l}{\delta_l} \\
\frac{\Delta\mathcal{O}^{\mathcal{TB}}_{\mathrm{pol}}}{\mathcal{O}^{\mathcal{TB}}} &= \sqrt{\left(\frac{\Delta\Lambda}{\Lambda}\right)^2 + \left(\frac{\Delta\delta_l}{\delta_l}\right)^2}.
\end{aligned} \tag{8.36}$$

Here, $\mathcal{O}^{\mathcal{T}}$ and $\mathcal{O}^{\mathcal{B}}$ are single polarization observables with respect to the target polarization ($\mathcal{T}$) and the beam polarization ($\mathcal{B}$), respectively. Double polarization observables dependent on both target and beam polarization are denoted as $\mathcal{O}^{\mathcal{TB}}$.

[21] **AN**alytical **B**remsstrahlung

8.5.2 Dilution Factor

The systematic error of the dilution factor is derived from the systematic error of the scaling factor. A global scaling factor is used across all periods of data taking. The systematic error of the scaling factor is estimated to be $\Delta c = 10\,\%$ and accounts for the small fluctuations between the different periods (cf. Fig. 8.10). The propagation of the systematic error from the scaling factor to the dilution factor is given by

$$\Delta d = \Delta c \cdot \frac{N_C^{\mathrm{ref}}}{N_B} = \frac{\Delta c}{c} \cdot (1 - d). \tag{8.37}$$

As with the polarization degrees, the dilution factor is used as a multiplicative factor in the extraction of polarization observables, leading to a direct propagation of the relative systematic uncertainty to the extracted observables

$$\frac{\Delta \mathcal{O}_{\mathrm{d}}}{\mathcal{O}} = \frac{\Delta d}{d}. \tag{8.38}$$

8.5.3 Background

Remaining background ξ in the final event sample can bias the extracted observables, as the measured observables represent a mixture of signal and background contributions

$$\mathcal{O}_{\mathrm{meas}} = (1 - \xi)\mathcal{O} + \xi \mathcal{O}_{\mathrm{bg}}. \tag{8.39}$$

The fraction of background events ξ is carefully examined in Section 7.7. While it is, in principle, possible to correct the extracted observables for their background contributions [159], such a correction requires a precise and reliable determination of ξ. Any systematic uncertainty in the estimation of ξ would otherwise be directly reflected in the final results. Therefore, in this work, no correction is applied and $\mathcal{O}_{\mathrm{meas}} = \mathcal{O}$ is assumed. Instead, the potential influence of background is taken into account in the total systematic uncertainty.

In [158], a realistic estimate for the systematic uncertainty due to background, $\Delta \mathcal{O}_{\mathrm{bg}}$, is derived as

$$\Delta \mathcal{O}_{\mathrm{bg}} \lesssim \xi. \tag{8.40}$$

In the following, $\Delta \mathcal{O}_{\mathrm{bg}} = \xi$ is chosen as a conservative estimate.

8.5.4 Combination of Systematic Errors

To combine the different sources of systematic uncertainty, the first step is to convert the relative uncertainties $\Delta \mathcal{O}_{\mathrm{sys}}^{\mathrm{rel}}$ into absolute uncertainties $\Delta \mathcal{O}_{\mathrm{sys}}^{\mathrm{abs}}$. A straightforward approach would be to use

$$\Delta \mathcal{O}_{\mathrm{sys}}^{\mathrm{abs}} = \Delta \mathcal{O}_{\mathrm{sys}}^{\mathrm{rel}} \cdot |\mathcal{O}| \tag{8.41}$$

but this neglects the statistical uncertainty $\Delta \mathcal{O}_{\mathrm{stat}}$ associated with the measured observables. To account for the statistical error, Eqn. 8.41 is convolved with the probability distribution of the estimate for $\mathcal{O}$. This distribution is modeled as a Gaussian with mean $\mathcal{O}$ and standard

deviation $\sigma_{\mathcal{O}} = \Delta\mathcal{O}_{\text{stat}}$. The convolution integral is given by [158]

$$\begin{aligned}\Delta\mathcal{O}^{\text{abs}}_{\text{sys}} &= \int_{-\infty}^{\infty} \Delta\mathcal{O}^{\text{rel}}_{\text{sys}} \cdot |\mathcal{O} - x| \cdot \mathcal{N}(x, \sigma_{\mathcal{O}})\,\mathrm{d}x \\ &= \int_{-\infty}^{\infty} \Delta\mathcal{O}^{\text{rel}}_{\text{sys}} \cdot |\mathcal{O} - x| \cdot \frac{1}{\sqrt{2\pi\sigma^2_{\mathcal{O}}}} \exp\left(-\frac{x^2}{2\sigma^2_{\mathcal{O}}}\right)\mathrm{d}x. \end{aligned} \tag{8.42}$$

This integral is evaluated numerically over the range $[-5\sigma_{\mathcal{O}}, 5\sigma_{\mathcal{O}}]$.

The total systematic uncertainty is then obtained through Gaussian error propagation. For the different types of observables, the following expressions are used

$$\begin{aligned}\Delta\mathcal{O}^{\mathcal{T}} &= \sqrt{\left[\int_{-5\sigma_{\mathcal{T}}}^{5\sigma_{\mathcal{T}}} \sqrt{\left(\frac{\Delta\Lambda}{\Lambda}\right)^2 + \left(\frac{\Delta d}{d}\right)^2} \cdot |\mathcal{O}^{\mathcal{T}} - x| \cdot \mathcal{N}(x, \sigma_{\mathcal{T}})\,\mathrm{d}x\right]^2 + \xi^2} \\ \Delta\mathcal{O}^{\mathcal{B}} &= \sqrt{\left[\int_{-5\sigma_{\mathcal{B}}}^{5\sigma_{\mathcal{B}}} \sqrt{\left(\frac{\Delta\delta_l}{\delta_l}\right)^2} \cdot |\mathcal{O}^{\mathcal{B}} - x| \cdot \mathcal{N}(x, \sigma_{\mathcal{B}})\,\mathrm{d}x\right]^2 + \xi^2} \\ \Delta\mathcal{O}^{\mathcal{TB}} &= \sqrt{\left[\int_{-5\sigma_{\mathcal{TB}}}^{5\sigma_{\mathcal{TB}}} \sqrt{\left(\frac{\Delta\Lambda}{\Lambda}\right)^2 + \left(\frac{\Delta\delta_l}{\delta_l}\right)^2 + \left(\frac{\Delta d}{d}\right)^2} \cdot |\mathcal{O}^{\mathcal{TB}} - x| \cdot \mathcal{N}(x, \sigma_{\mathcal{TB}})\,\mathrm{d}x\right]^2 + \xi^2}. \end{aligned} \tag{8.43}$$

As before, $\mathcal{O}^{\mathcal{T}}$ and $\mathcal{O}^{\mathcal{B}}$ refer to single polarization observables associated with target polarization ($\mathcal{T}$) and beam polarization ($\mathcal{B}$), respectively. Double polarization observables dependent on both target and beam polarization are denoted as $\mathcal{O}^{\mathcal{TB}}$.

CHAPTER 9

Discussion of the Results

In this chapter, the results for the polarization observables P_x, P_y, P_x^s, P_y^s, P_x^c and P_y^c for $\gamma p \to p\pi^0\pi^0$ are presented and discussed. The results are checked for consistency between the different periods of data taking relevant to this work. Their combination is used to obtain the final results that are compared with existing data as well as with predictions from recent partial wave analyses solutions.

9.1 Different Periods of Data Taking

In this work, four periods of data taking are analyzed. They are listed in Table 9.1 together with their coherent edge and the number of extracted $p\pi^0\pi^0$ events after carbon subtraction. The different data takings were recorded over a period of four years, during which the

Table 9.1: Characteristics of the different periods of data taking used in this work. For December 2017 the first runs (200024 – 200208) are discarded as the configuration of the experiment was not yet finalized. The number of $p\pi^0\pi^0$ events is given after carbon subtraction for the sum of all PED classes. The relative proportion of each data taking is given in parentheses. In every case, the event selection presented in Chapter 7 is applied.

Data taking	Coherent edge	Run range	Total events	$p\pi^0\pi^0$
December 2017	1 350 MeV	200209 – 200941	0.86×10^9	1.44×10^5 (18 %)
May 2018	1 350 MeV	201475 – 202308	1.22×10^9	2.55×10^5 (31 %)
February 2019	1 600 MeV	205482 – 206052	0.80×10^9	1.47×10^5 (18 %)
June 2021	1 600 MeV	206832 – 207832	1.90×10^9	2.71×10^5 (33 %)

experiment was continuously improved. Most notable is the change from a QDC to a full SADC readout at the beginning of June 2021. After that pile-up correction is available and used.[1] Furthermore, for all periods of data taking time information is used for the first time as described in Chapter 5, including time clustering.

In June 2021, there were also some challenges in stabilizing the coherent edge. In addition to drifts away from the nominal position, discrete jumps occurred that shifted the coherent edge by up to 100 MeV. This led to the need for a modified treatment of the linear polarization in the analysis. For these data, the linear polarization is determined on a per-spill[2] basis

[1] The effect of the pile-up correction is described in [141].

[2] A spill refers to one extraction cycle from the accelerator and lasts about 4 seconds.

instead of for runs. This allows to take into account the volatile behavior of the coherent edge [174].

9.1.1 Correction of Target Polarization in December 2017

In [145], the $p\pi^0$ final state was analyzed for the December 2017 and May 2018 data. There, a discrepancy was found between the polarization observables extracted from the two periods. An investigation of the target asymmetry T revealed that, for the data to be consistent, the target polarization in December 2017 needs to be scaled by a factor of (1.41 ± 0.02). This discrepancy is attributed to an underestimation of the target polarization during that period. The NMR coil used to measure the target polarization was positioned outside of the target cell for December 2017, whereas in the other periods it was placed inside. The outer placement can lead to the formation of a thin ice layer on the coil, containing non-dynamically polarizable protons. This layer of ice artificially lowers the measured degree of polarization. The explanation is supported by previous measurements by the A2 collaboration at MAMI, where a direct comparison of an outer placement of the coil with an inner placement confirmed that the outer placement leads to a systematically reduced polarization [173].

In [145] the correction factor for December 2017 was determined by calculating the ratio of the target asymmetry for each data point[3]

$$\frac{P_y^{\text{Dec2017}}}{P_y^{\text{May2018}}}. \tag{9.1}$$

For verification, the factor is determined again. This time, instead of calculating the ratio, a more sophisticated method is used.

If the extracted observables for the two periods of data taking are consistent, their residuals normalized to the statistical error must follow a normal distribution with mean 0 and width 1. Thus, assuming a factor f for the December 2017 data, the quantity

$$g = \frac{P_y^{\text{May2018}} - f \cdot P_y^{\text{Dec2017}}}{\sqrt{\left(\Delta P_y^{\text{May2018}}\right)^2 + \left(f \cdot \Delta P_y^{\text{Dec2017}}\right)^2}} \tag{9.2}$$

must be normal distributed once the correct factor is found. Therefore, minimizing the negative log-likelihood

$$-\log\left(\mathcal{L}\right) = -\sum_{i=1}^{n} \log[\phi(g(\text{bin } i))]\,, \qquad \phi(g) = \frac{1}{\sqrt{2\pi}} \exp\left(-\frac{g^2}{2}\right) \tag{9.3}$$

gives the best estimate for f. For the minimization, the target asymmetry P_y in bins of E_γ and $\cos(\theta_{\pi^0\pi^0})$ is used, since it is a single polarization observable and independent of the beam polarization. The negative log-likelihood and the minimization results are shown in Fig. 9.1 (left). The minimization is performed for the $p\pi^0\pi^0$ data from this work as well as

[3] The mean of the resulting distribution was used as the correction factor.

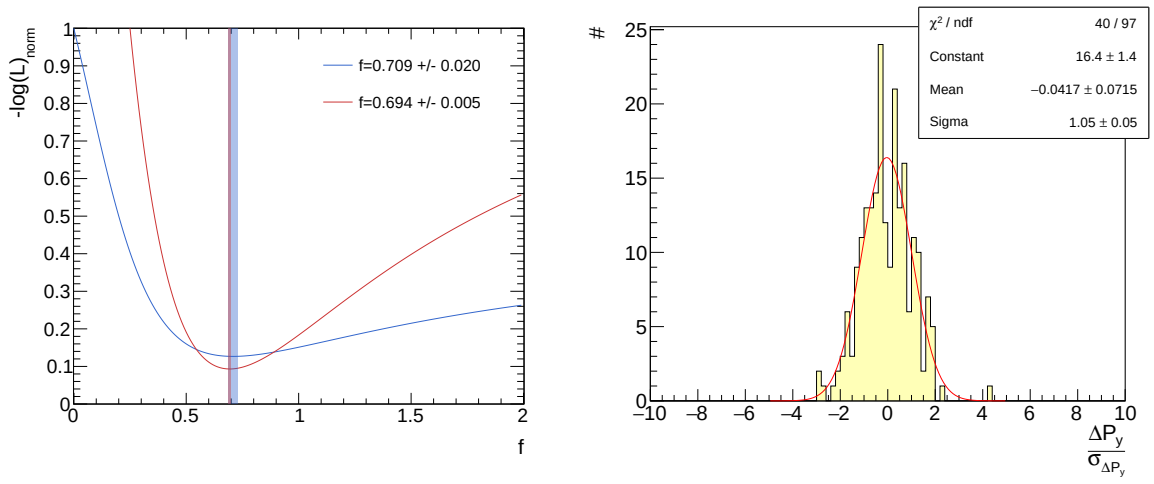

$-\log(\mathcal{L})$ Normalized residuals

Figure 9.1: Left: Minimization of $-\log(\mathcal{L})$ (cf. Eqn. 9.3). The resulting factor f is shown for $p\pi^0\pi^0$ data from this work as well as for $p\pi^0$ data from [145]. Right: Difference in the target asymmetry P_y for $p\pi^0\pi^0$ data from December 2017 (corrected) to May 2018, normalized to the statistical errors.

for the $p\pi^0$ data from [145]. The resulting factors are

$$\begin{aligned}(f)^{p\pi^0\pi^0} &= (0.709 \pm 0.020) \quad \Leftrightarrow \quad \left(\frac{1}{f}\right)^{p\pi^0\pi^0} = (1.41 \pm 0.04) \\ (f)^{p\pi^0} &= (0.694 \pm 0.005) \quad \Leftrightarrow \quad \left(\frac{1}{f}\right)^{p\pi^0} = (1.44 \pm 0.01).\end{aligned} \tag{9.4}$$

f corresponds to the factor used in Eqn. 9.3 to scale the December 2017 data, while $\frac{1}{f}$ corresponds to the correction of the target polarization. The values agree within their errors and are close to the value determined in [145]. In the following, an error-weighted average of $\overline{\frac{1}{f}} = (1.44 \pm 0.01)$ is used as the scaling factor for the target polarization. The measured degrees of polarization for December 2017 are corrected to

$$\begin{aligned}\Lambda_+^{\text{corr}} &= +51.6\,\% \cdot 1.44 = +74.3\,\% \\ \Lambda_-^{\text{corr}} &= -49.9\,\% \cdot 1.44 = -71.9\,\%.\end{aligned} \tag{9.5}$$

A comparison of the uncorrected and corrected target asymmetries for the December 2017 data is shown in Fig. 9.2. Furthermore, the distribution of the normalized residuals for the corrected data from December 2017 to May 2018 is shown in Fig. 9.1 (right). As expected, the normalized residuals are normal distributed. The correction factor is also confirmed in [144] which is an independent analysis of the same data.

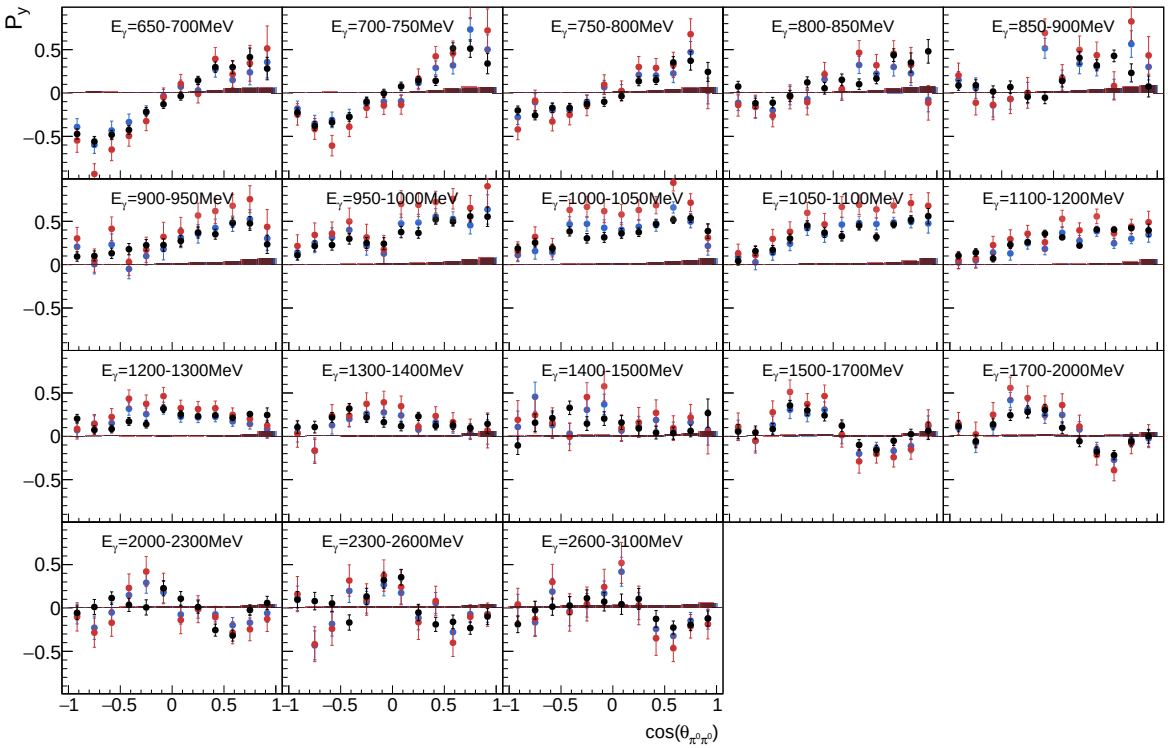

Figure 9.2: Target asymmetry P_y as a function of $\left(E_\gamma, \cos(\theta_{\pi^0\pi^0})\right)$ for data taking in **May 2018**, December 2017 (uncorrected) and December 2017 (corrected) ($\Lambda_{\text{corr}} = 1.44 \cdot \Lambda$). The systematic uncertainties are shown as bars on the x-axis.

9.1.2 Comparison of the Different Periods of Data Taking

For the final results, the different periods of data taking are combined into a single event-based likelihood fit. It is therefore necessary to ensure that the individual results are consistent within statistical uncertainties. In Fig. 9.3, the target asymmetry P_y for 5-PED and 4.5-PED events is compared for each of these periods. 4-PED events are excluded because they are not used for June 2021 (cf. Section 8.3.2.3). A comparison including the 4-PED events but without June 2021 is shown in Section D.1 in the Appendix. In all cases, the target polarization for December 2017 is corrected by a factor as described above. Already qualitatively, a good agreement can be seen.

For a more detailed comparison, the residuals normalized to the statistical error are compared for each combination of the four periods of data taking (cf. Fig. 9.4). If the values agree within their statistical uncertainties the distributions must follow a normal distribution with mean 0 and width 1, which is largely the case. Small deviations can be explained by the systematic uncertainty of the target polarization which is independent for each period of data taking. The same comparison can be made for double polarization observables. However, high statistical errors make comparison and interpretation more difficult. A comparison for the double polarization observable P_x^s is shown in Fig. 9.5 and 9.6.

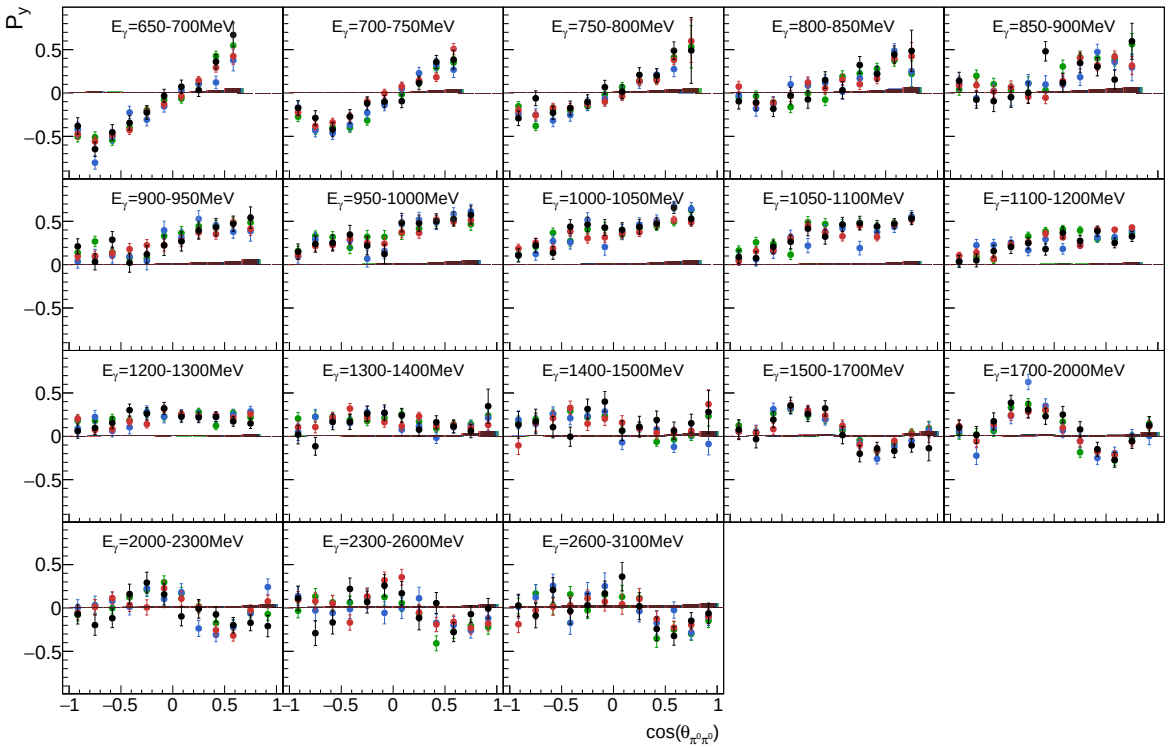

Figure 9.3: Target asymmetry P_y as a function of $\left(E_\gamma, \cos(\theta_{\pi^0\pi^0})\right)$ for 5-PED and 4.5-PED events. The different periods of data taking **December 2017**, May 2018, February 2019 and June 2021 are compared. The systematic uncertainties are shown as bars on the x-axis.

9.2 Comparison to Existing Data

So far, comparisons have been made between different periods of data taking. However, it is also important to compare the results with existing data from an independent analysis. For such a comparison, the results of Seifen et al. [20] are used. This is the only study on $p\pi^0\pi^0$ with equivalent polarization settings and with an overlap in the same kinematic region (see Table 1.3). In Seifen et al., data were also measured with a transversely polarized target and a linearly polarized beam, and the single polarization observables P_x, P_y as well as the double polarization observables P_x^s, P_y^s, P_x^c, P_y^c were extracted. Only the coherent edge of the beam polarization has been set to 950 MeV, which is significantly lower than for the data in this work (1 350 MeV and 1 600 MeV). As a result, there is no significant overlap of the extracted double polarization observables. Only for the single polarization observables, a detailed comparison can be performed. Furthermore, in Seifen et al. only 5-PED and 4.5-PED events are used. Thus, the 4-PED events in this work are also excluded in the following comparison. Moreover, to be consistent with the definitions in Seifen et al., in the case where $p\pi^0$ span the secondary decay plane, the $\cos(\theta)$ of the recoiling π^0 (definition in Seifen et al.) is used instead of the $\cos(\theta)$ of the $p\pi^0$ system (definition in this work). This redefinition is used here for comparison purpose only. Finally, the same binning of the kinematic variables is used as in Seifen et al.

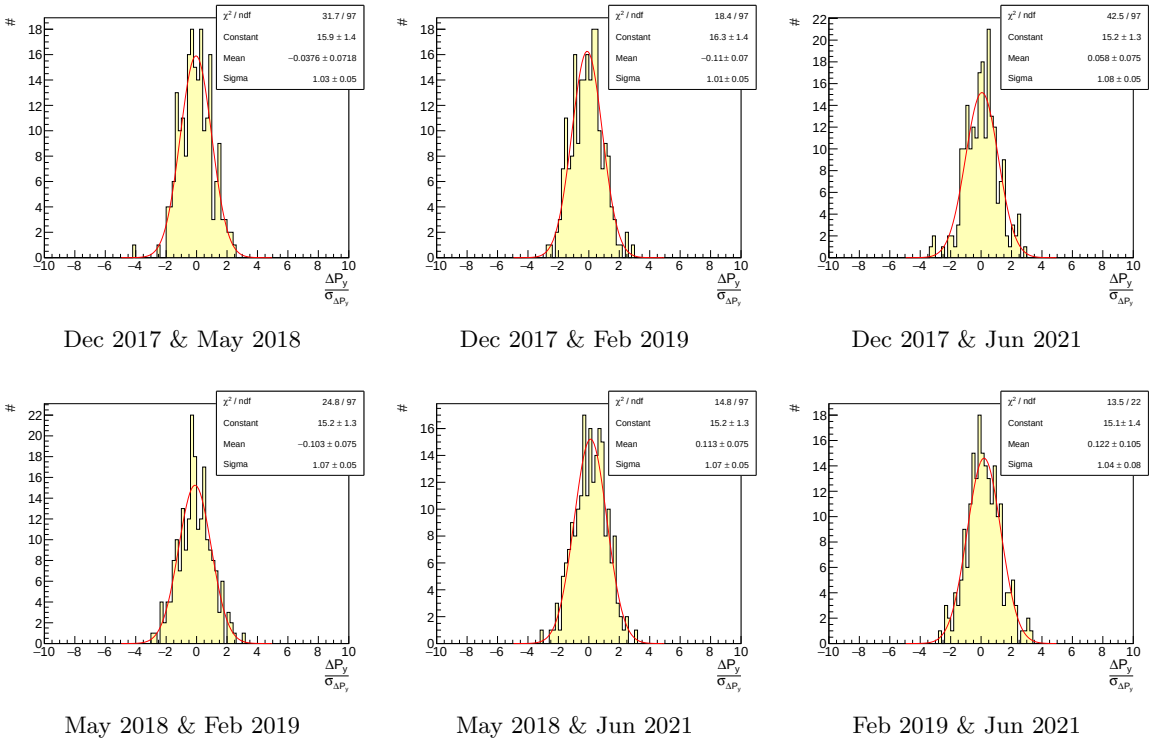

Figure 9.4: Residuals of the target asymmetry P_y for 5-PED and 4.5-PED events normalized to the statistical error for each combination of the four different periods of data taking December 2017, May 2018, February 2019 and June 2021.

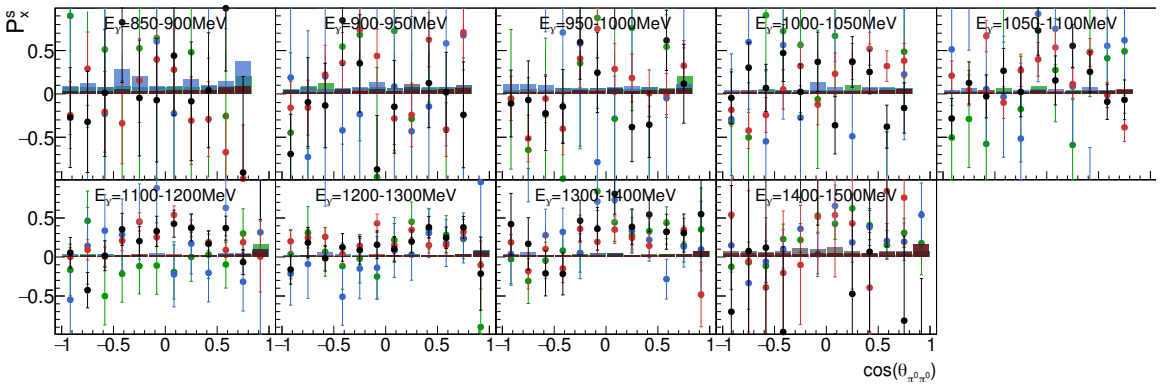

Figure 9.5: Target asymmetry P_x^s as a function of $\left(E_\gamma, \cos(\theta_{\pi^0\pi^0})\right)$ for 5-PED and 4.5-PED events. The different periods of data taking **December 2017**, May 2018, February 2019 and June 2021 are compared. The systematic uncertainties are shown as bars on the x-axis.

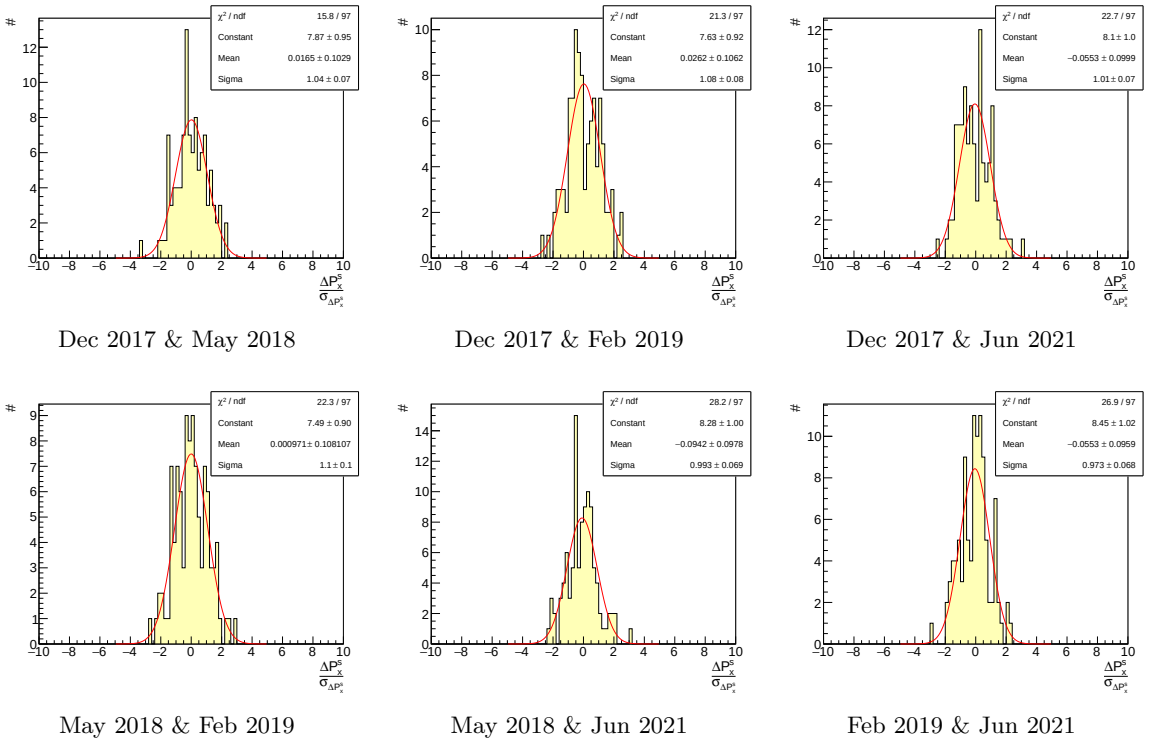

Figure 9.6: Residuals of the target asymmetry P_x^s for 5-PED and 4.5-PED events normalized to the statistical error for each combination of the four different periods of data taking December 2017, May 2018, February 2019 and June 2021.

A comparison of the target polarization P_y as function of E_γ and $\cos(\theta_{\pi^0\pi^0})$ is presented in Fig. 9.7. Their normalized residuals are shown in Fig. 9.8 well matching a normal distribution with mean 0 and width 1. For an even more thorough comparison, the target asymmetry P_x and P_y is extracted for a specific energy range E_γ and as function of three kinematic variables ($\cos(\theta_{p\pi^0})$, $M_{p\pi^0}$, $\phi^*_{p\pi^0}$). The four-dimensional comparison is shown in Fig. 9.9 for an energy range of $E_\gamma = 800 - 950\,\text{MeV}$. Other energy ranges are shown in Section D.2 in the Appendix. In all comparisons, small deviations can be explained within the systematic uncertainty of the target polarization, which is independent for the data sets. Furthermore, in Seifen et al. the polarization observables are corrected for their background influence. In this work, however, the background is included in the systematic error. Despite these differences, a good agreement can be seen for the full energy range.

For completeness, a comparison of the double polarization observables is shown in Fig. 9.10. It can be clearly seen that this work complements the existing data by extending the double polarization observables to higher energies. However, due to the lack of overlap, a systematic comparison is not possible.

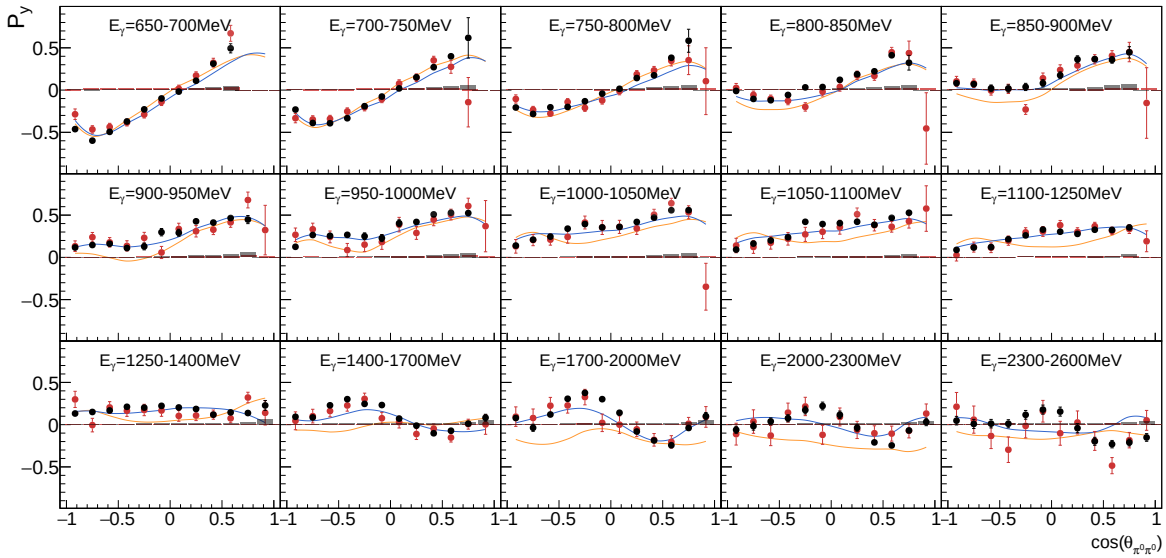

Figure 9.7: Target asymmetry P_y as function of $\left(E_\gamma, \cos(\theta_{\pi^0\pi^0})\right)$ for 5-PED and 4.5-PED events. The **combined data of this work** is shown in comparison to Seifen et al. [20]. The systematic uncertainties are shown as bars on the x-axis. For completeness, model predictions of BnGa-2022 and BnGa-2014 are already presented.

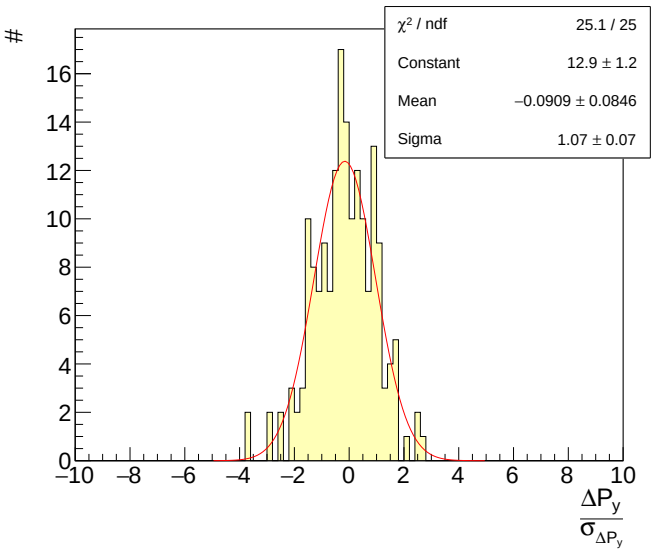

Figure 9.8: Difference in the target asymmetry P_y as a function of $\left(E_\gamma, \cos(\theta_{\pi^0\pi^0})\right)$ normalized to the statistical error for data from this work compared to data from Seifen et al. [20].

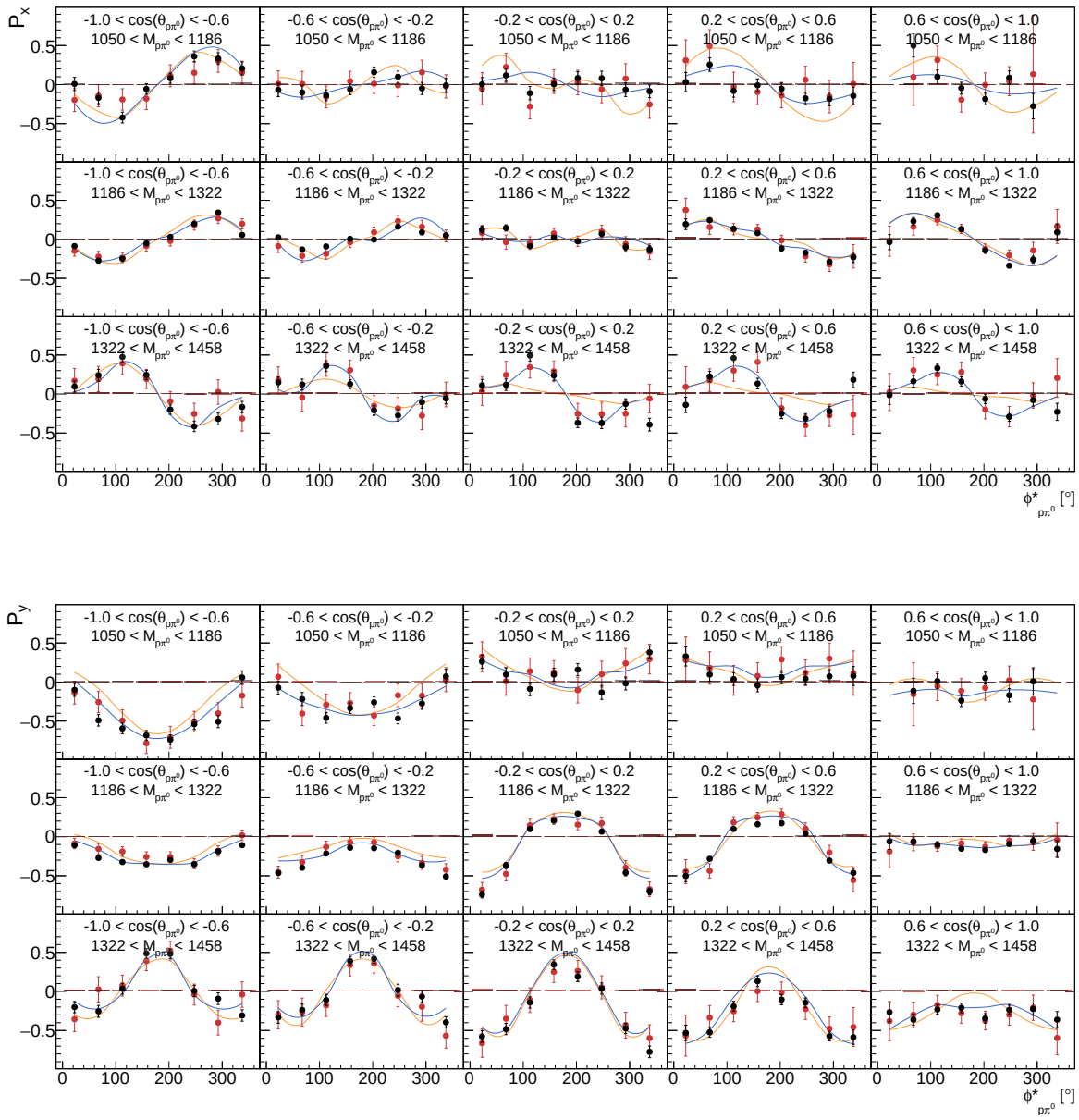

$E_\gamma = 800 - 950\,\mathrm{MeV}$

Figure 9.9: Target asymmetries P_x, P_y as function of $\left(\cos(\theta_{p\pi^0}), M_{p\pi^0}, \phi^*_{p\pi^0}\right)$ in a specific energy range $E_\gamma = 800 - 950\,\mathrm{MeV}$ for 5-PED and 4.5-PED events. The **combined data of this work** is shown in comparison to Seifen et al. [20]. The systematic uncertainties are shown as bars on the x-axis. Comparisons in other energy ranges are given in Section D.2 in the Appendix. For completeness, model predictions of BnGa-2022 and BnGa-2014 are already presented.

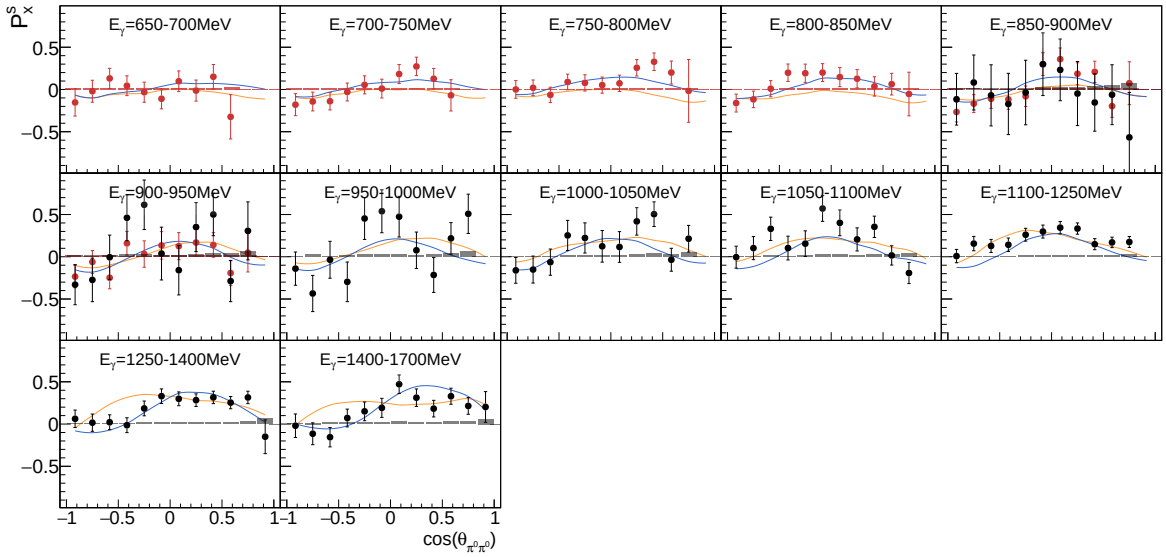

P_x^s

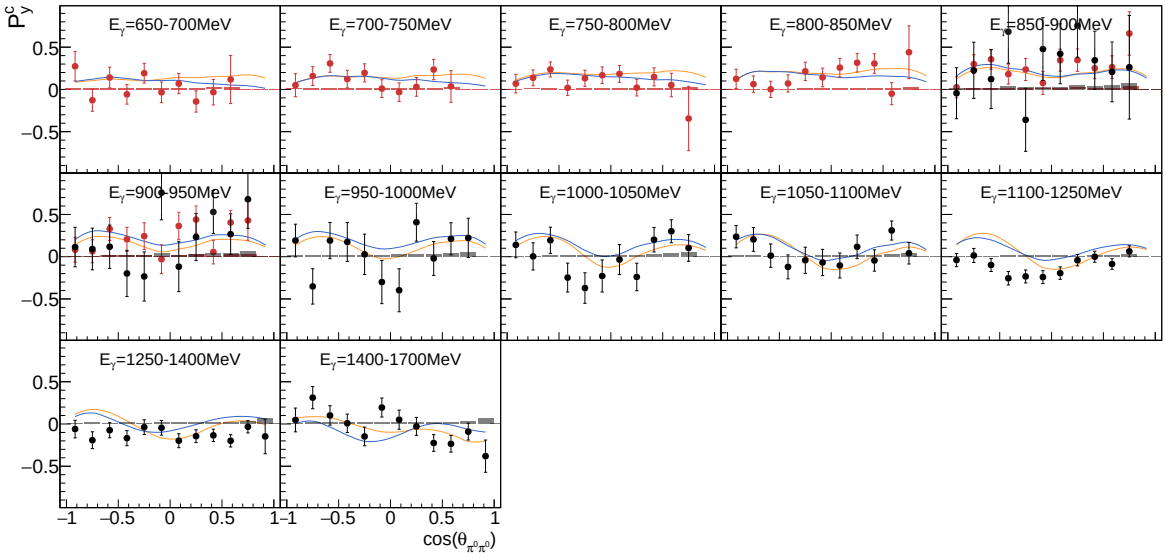

P_y^c

Figure 9.10: Double polarization observables P_x^s, P_y^c as function of $\left(E_\gamma, \cos(\theta_{\pi^0\pi^0})\right)$ for 5-PED and 4.5-PED events. The **combined data of this work** is shown in comparison to Seifen et al. [20]. The systematic uncertainties are shown as bars on the x-axis. For completeness, model predictions of BnGa-2022 and BnGa-2014 are already presented.

9.3 Comparison to Model Predictions

For the comparison with Seifen et al. only 5-PED and 4.5-PED events were used to ensure identical settings. In the following, 4-PED events are also included, representing all the available statistics in this work. The extracted observables are compared with the predictions available from several frameworks. In this work, particular emphasis is placed on the Bonn-Gatchina PWA[4] [53–55, 65]. The Bonn-Gatchina PWA provides easily accessible predictions for the $p\pi^0\pi^0$ final state. Moreover, the predictions can be used in all relevant kinematic regions. Two different solutions are used for comparison.

Bonn-Gatchina 2014 The BnGa-2014 solution is based on a pure K-matrix approach [53]. While this solution already includes data from a variety of channels and experiments, it does not yet include the data from Seifen et al. [20]. This makes this solution, along with the most recent one, interesting for comparison.

Bonn-Gatchina 2022 The BnGa-2022 solution is the latest version. Instead of a pure K-matrix formalism, the N/D technique is used. For more information on this method, see [20, 21, 65]. Also, additional data such as the results from Seifen at al. are included in this solution [20, 54].

A full five-dimensional representation of the extracted observables is not possible due to statistical limitations. Therefore, the observables are presented for different combinations of kinematic variables, while integrating over the other variables. In Section 9.3.1, the extracted observables are presented as a function of two kinematic variables. In Section 9.3.2, four-dimensional representations are presented. These two sections are used for a qualitative presentation of the results and visual comparison with the model predictions. In Section 9.3.3, a more quantitative comparison is made.

9.3.1 Polarization Observables in Two Dimensions

For the following, a binning of the observables is used which is fine tuned to the statistics in this work. A fine binning is used for single polarization observables. In contract, for double polarization observables a coarser binning is chosen to account for their larger statistical uncertainties. In addition, the energy binning for double polarization observables is tuned to the high beam polarization region.

P_x, P_y

In Fig. 9.11 and 9.12, the target polarization observables P_x and P_y are shown as a function of $(E_\gamma, \cos(\theta_{\pi^0\pi^0}))$. This choice of kinematic variables represents a quasi-two-body dynamics[5] for which the relations $P_x = 0$ and $P_y = T$ hold (cf. Eqn. 8.7). In Fig. 9.13 and 9.14, the

[4] **P**artial **W**ave **A**nalysis

[5] It is integrated over the angles between decay plane and reaction plane $(\phi^*_{\pi^0\pi^0}, \theta^*_{\pi^0\pi^0})$, which reduces the three-body dynamic to a quasi-two-body dynamics (cf. Chapter 8).

target polarization observables P_x and P_y are shown once again, but this time as a function of $(E_\gamma, \phi^*_{\pi^0\pi^0})$. Thus, the quasi-two-body dynamics is no longer valid and $P_x \neq 0$. Due to parity conservation, P_x is odd in ϕ^*, while P_y is even in ϕ^* (cf. Section 8.2.1).

In general, a good qualitative agreement with the model prediction of BnGa-2022 is present. This is also to be expected as the data from Seifen et al. already constrains the model in this kinematic region for single polarization observables. This data is not included in the BnGa-2014 solution, which shows larger deviations. Only at higher energies deviations become visible also for the BnGa-2022 solution. One example is P_y at energies around $E_\gamma = 2\,000\,\text{MeV}$. More figures on the single polarization observables in different kinematic regions, also for the $p\pi^0$ instead of the $\pi^0\pi^0$ system, are presented in Appendix E.

P_x^s, P_y^s, P_x^c, P_y^c

In Fig. 9.15 and 9.16 double polarization observables P_x^s, P_y^s, P_x^c, P_y^c are shown as a function of $(E_\gamma, \cos(\theta_{\pi^0\pi^0}))$ and $(E_\gamma, \phi^*_{\pi^0\pi^0})$. In this energy range there is no data yet included in the model predictions for these observables. However, both the BnGa-2022 and BnGa-2014 solutions can follow the data to some extent. For P_y^c there are some more significant deviations. They are expressed in terms of a χ^2/N in Section 9.3.3. As before, further figures on the double polarization observables in different kinematic regions, also for the $p\pi^0$ instead of the $\pi^0\pi^0$ system, are presented in the Appendix F.

9.3.2 Polarization Observables in Four Dimensions

A full five-dimensional representation of the polarization observables is hardly possible. Due to statistical limitations, at most a four-dimensional representation can be extracted. Such a four-dimensional representation is shown in the following for both single and double polarization observables. Each figure corresponds to a selected energy range. In each figure (energy range), the extracted observables are presented as a function of $(\cos(\theta), M, \phi^*)$.

P_x, P_y

The four-dimensional target asymmetry P_y is extracted for the energy range

$$E_\gamma = 650 - 1\,850\,\text{MeV} \qquad \text{with a binning of} \qquad \Delta E_\gamma = 150\,\text{MeV}.$$

Only the last energy bin is increased to 300 MeV for more statistics. In Fig. 9.20 to 9.23, the four-dimensional representation of P_y for the higher energy range $1\,100 - 1\,850\,\text{MeV}$ is shown. This is the first time that the observables have been extracted in four dimensions at such high energies. In the Appendix G all energy ranges for the target asymmetries P_x, P_y are shown for both the $\pi^0\pi^0$ and the $p\pi^0$ system.

P_x^s, P_y^s, P_x^c, P_y^c

The double polarization observables can only be extracted in a small energy range corresponding to the region of high beam polarization. Therefore, only two energy bins are used

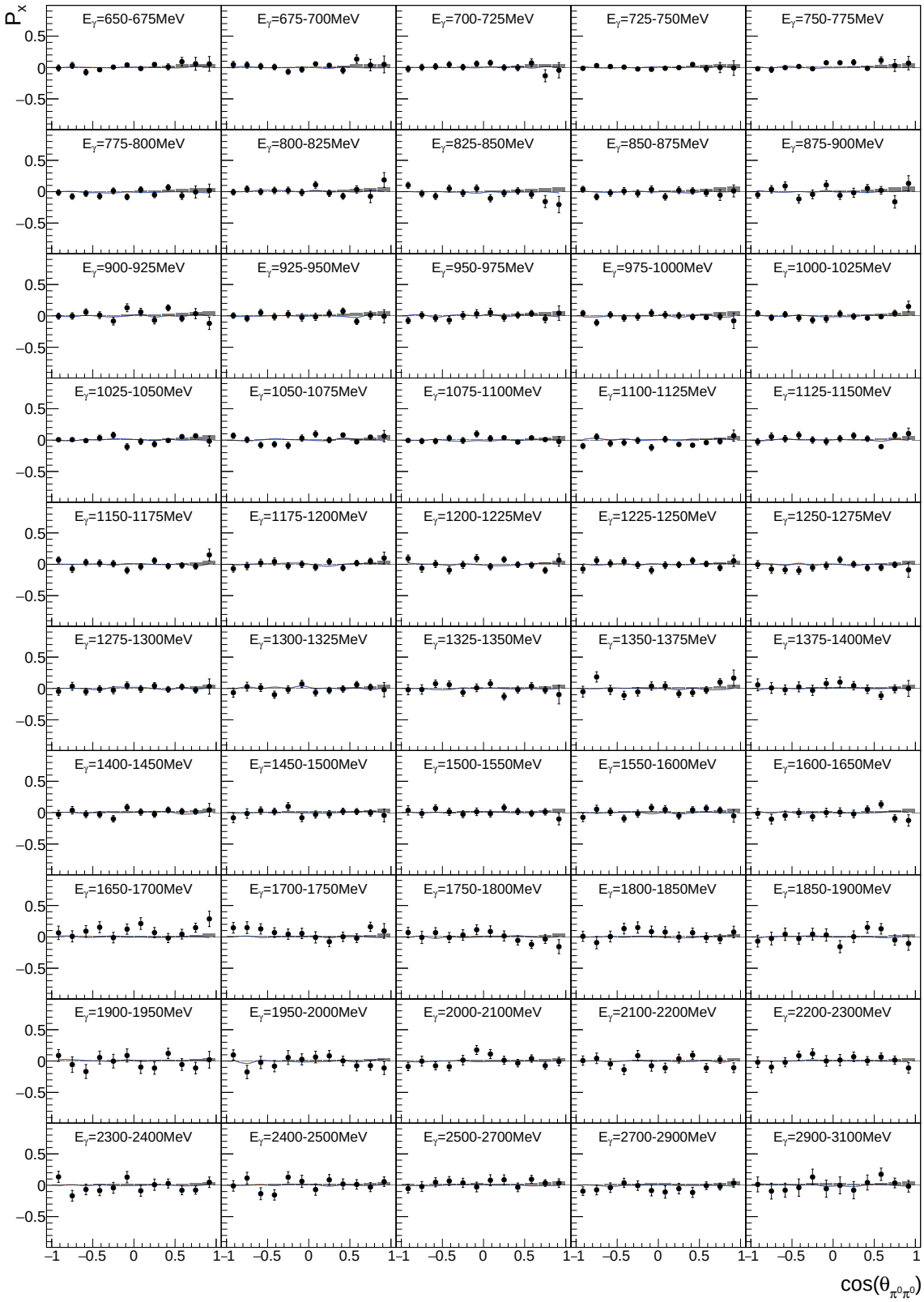

Figure 9.11: Target asymmetry P_x as function of $\left(E_\gamma, \cos(\theta_{\pi^0\pi^0})\right)$. The **combined data of this work** is shown as well as the model predictions BnGa-2022 and BnGa-2014. The systematic uncertainties are shown as bars on the x-axis.

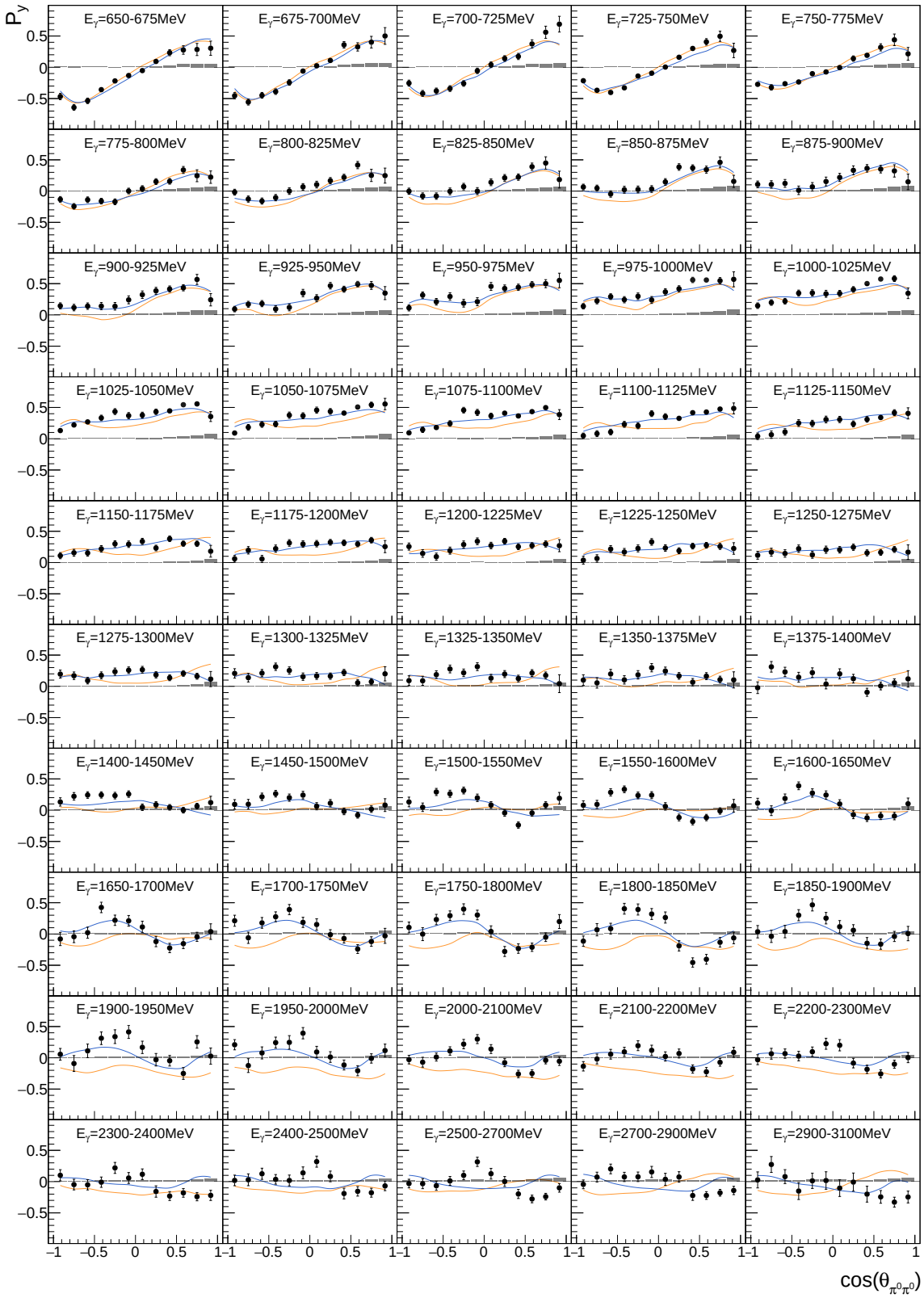

Figure 9.12: Target asymmetry P_y as function of $\left(E_\gamma, \cos(\theta_{\pi^0\pi^0})\right)$. The **combined data of this work** is shown as well as the model predictions BnGa-2022 and BnGa-2014. The systematic uncertainties are shown as bars on the x-axis.

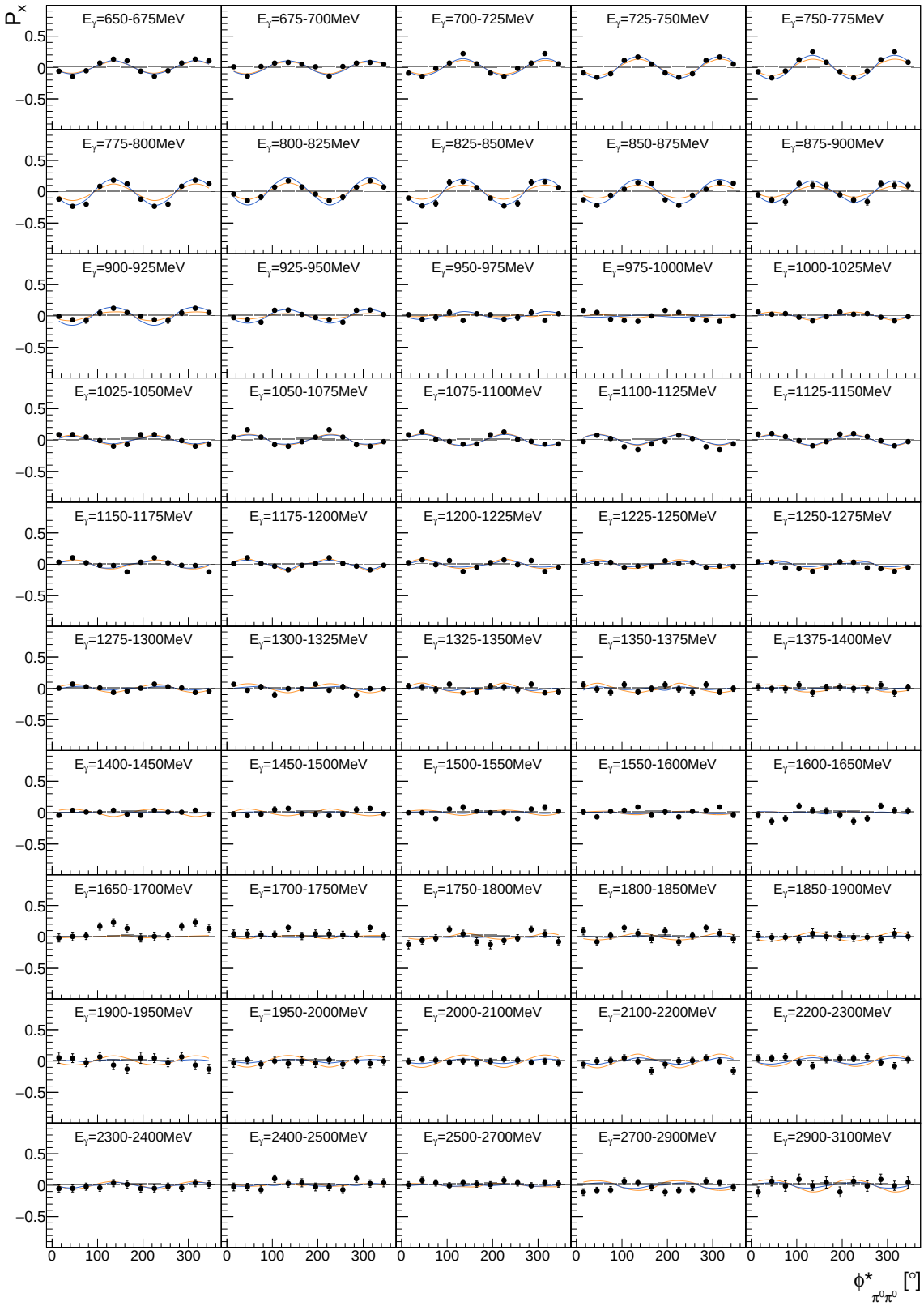

Figure 9.13: Target asymmetry P_x as function of $\left(E_\gamma, \phi^*_{\pi^0\pi^0}\right)$. The **combined data of this work** is shown as well as the model predictions BnGa-2022 and BnGa-2014. The systematic uncertainties are shown as bars on the x-axis.

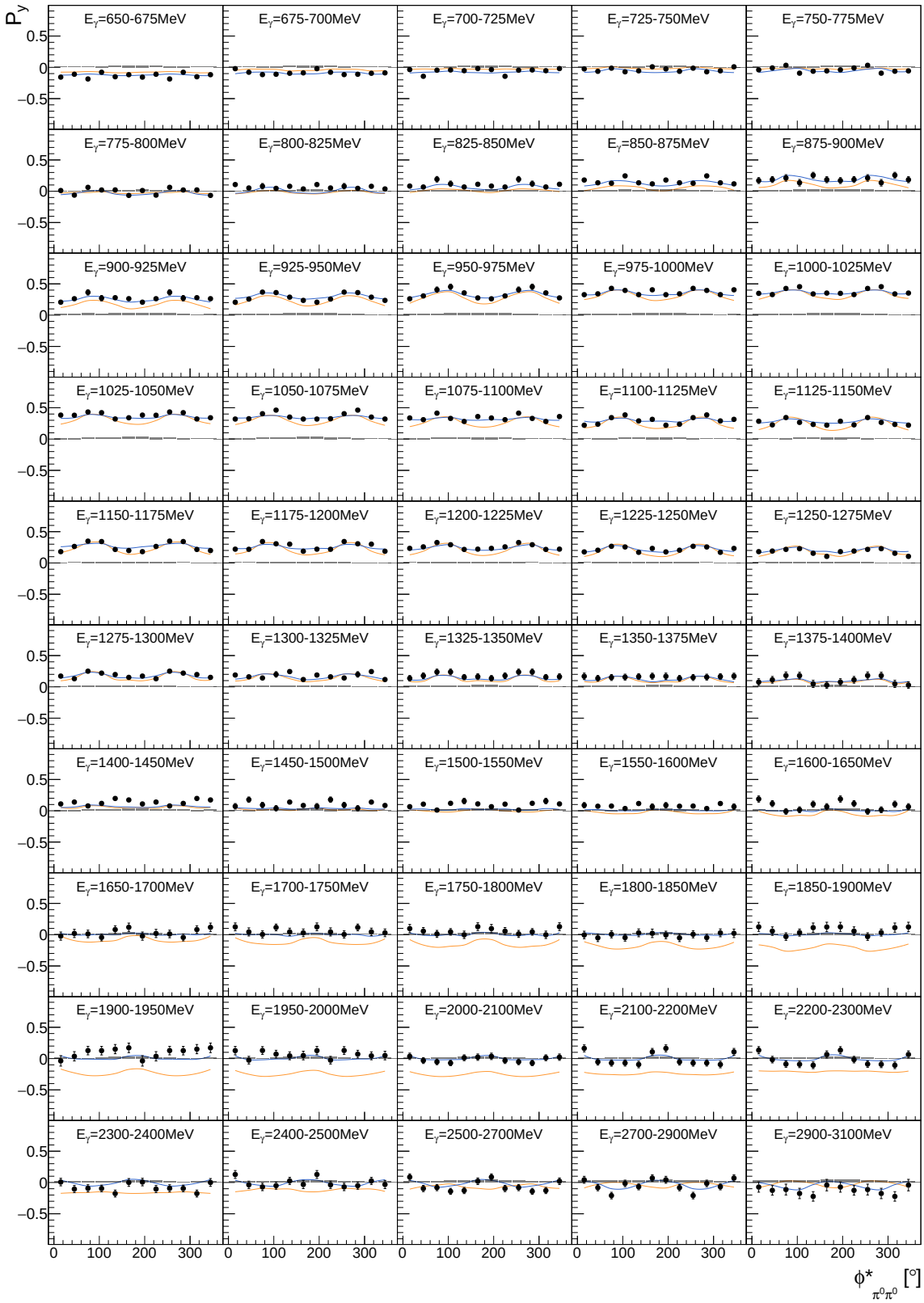

Figure 9.14: Target asymmetry P_y as function of $\left(E_\gamma, \phi^*_{\pi^0\pi^0}\right)$. The **combined data of this work** is shown as well as the model predictions BnGa-2022 and BnGa-2014. The systematic uncertainties are shown as bars on the x-axis.

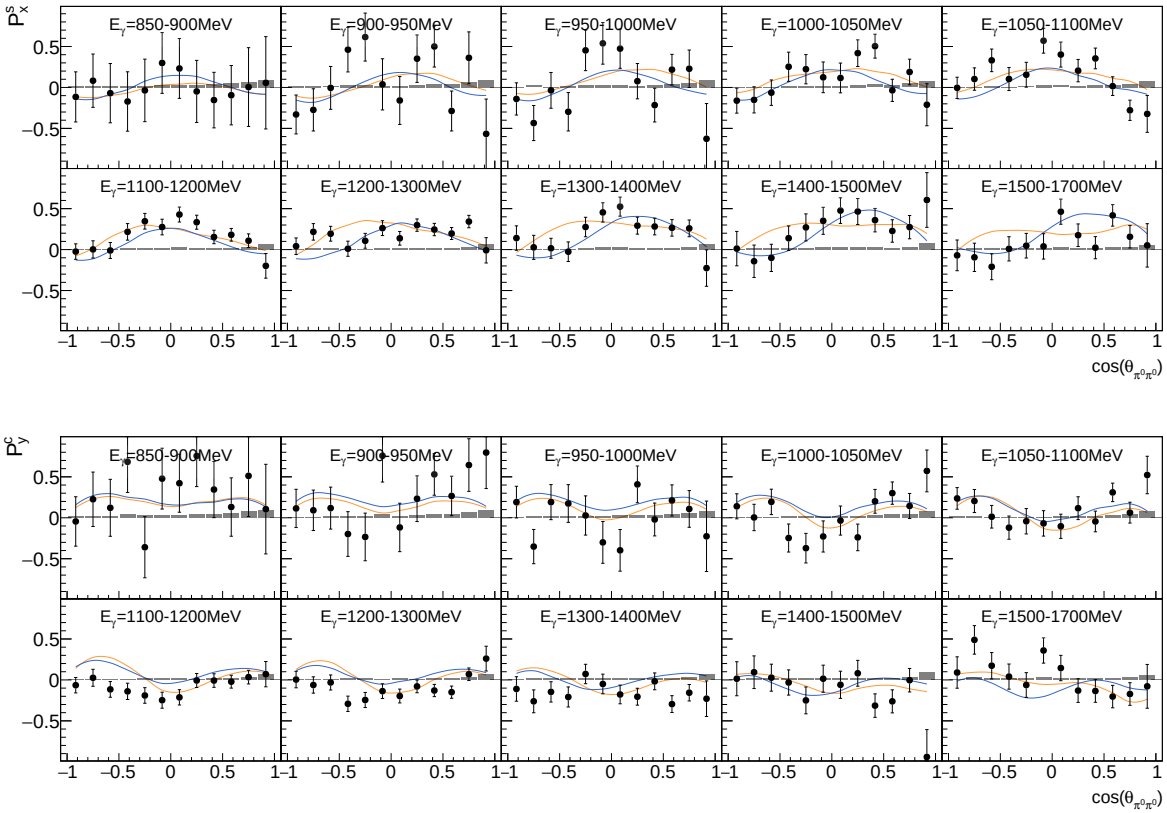

Figure 9.15: Double polarization observable P_x^s, P_y^c as function of $\left(E_\gamma, \cos(\theta_{\pi^0\pi^0})\right)$. The **combined data of this work** is shown as well as the model predictions BnGa-2022 and BnGa-2014. The systematic uncertainties are shown as bars on the x-axis.

for the four-dimensional representation of the double polarization observables

$$E_\gamma = 1\,000 - 1\,600\,\text{MeV} \qquad \text{with a binning of} \qquad \Delta E_\gamma = 300\,\text{MeV}.$$

The four-dimensional representation of the double polarization observable P_y^c is shown as an example in Fig. 9.24. This observable contained larger deviations in its two-dimensional representations. In the Appendix H all energy bins are shown for all double polarization observables P_x^s, P_y^s, P_x^c, P_y^c. The results are presented in both the $\pi^0\pi^0$ and $p\pi^0$ system.

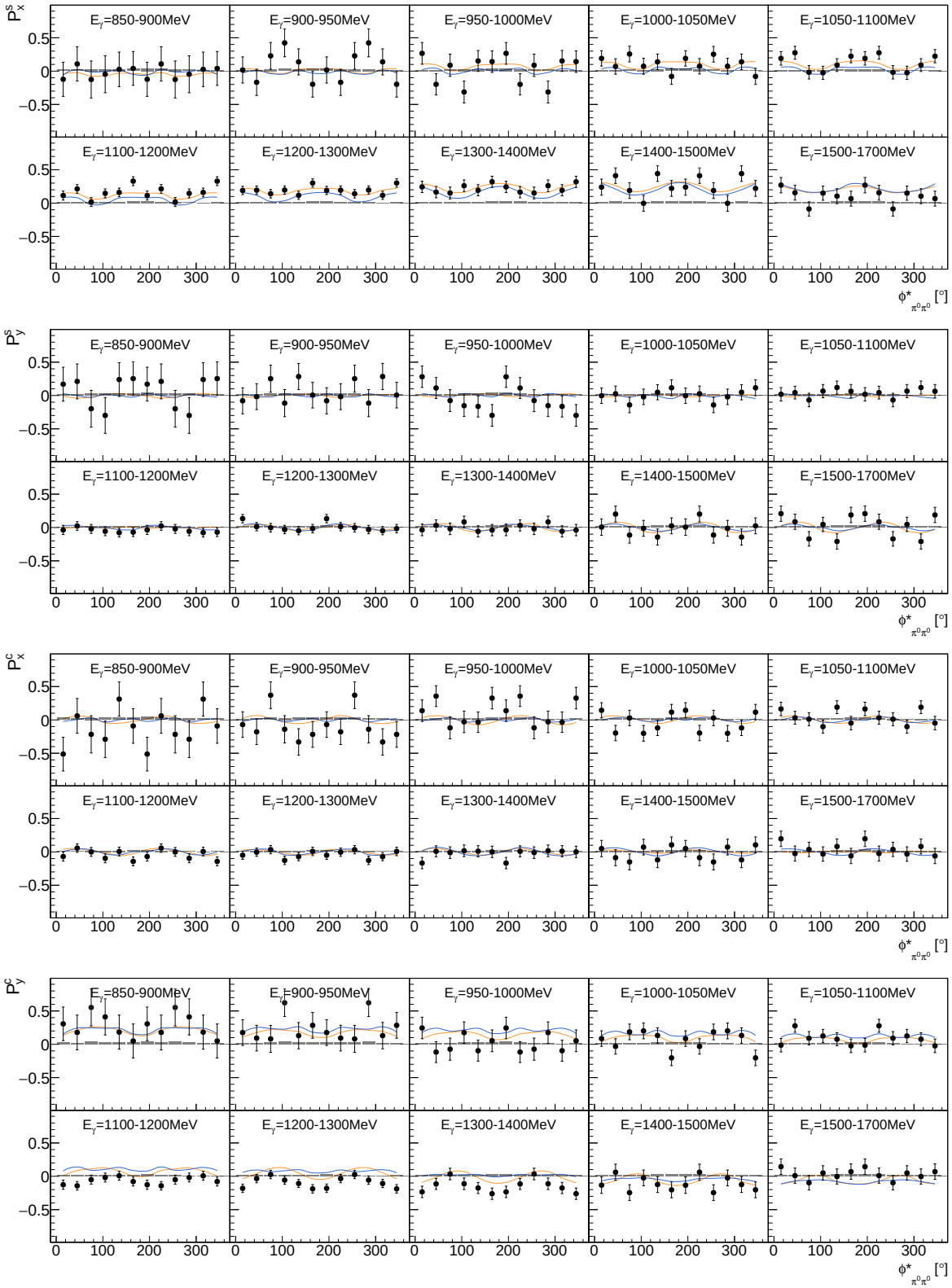

Figure 9.16: Double polarization observable P^s_x, P^s_y, P^c_x, P^c_y as function of $\left(E_\gamma, \phi^*_{\pi^0\pi^0}\right)$. The **combined data of this work** is shown as well as the model predictions BnGa-2022 and BnGa-2014. The systematic uncertainties are shown as bars on the x-axis.

9.3.3 χ^2/N of BnGa-2022 and BnGa-2014

For a quantitative study of the agreement between the extracted results and the model predictions, the χ^2/N criterion is used. It is defined as

$$\chi^2/N = \frac{1}{N}\sum_{i=1}^{N}\left(\frac{\mathcal{O}_i^{\mathrm{BnGa}} - \mathcal{O}_i^{\mathrm{data}}}{\sqrt{\left(\Delta\mathcal{O}_{\mathrm{stat},i}^{\mathrm{data}}\right)^2 + \left(\Delta\mathcal{O}_{\mathrm{sys},i}^{\mathrm{data}}\right)^2}}\right)^2 \tag{9.6}$$

where N is the number of data points.

In Fig. 9.17 (top) the calculated χ^2/N for the target polarization observable $P_y(\sqrt{s}, \cos(\theta_{\pi^0\pi^0}))$ and $P_y(\sqrt{s}, \phi^*_{\pi^0\pi^0})$ as function of $\sqrt{s}$ is shown. For the calculation of the χ^2/N the center of mass energy $\sqrt{s}$ is used instead of the beam photon energy E_γ allowing a better comparison with resonance regions. The calculated χ^2/N is in agreement with the previous visual observations. In the case of single polarization observables, there is a good agreement between the data of this work and the BnGa-2022 solution. Here the data from Seifen et al. already constrain the solution. It is only at higher energies in $(\sqrt{s}, \cos(\theta_{\pi^0\pi^0}))$ that discrepancies start to appear. On average, the comparison with BnGa-2022 a χ^2/N of 2.2 (left) and 1.3 (right) is reached. In contrast, the BnGa-2014 solution shows significantly poorer agreement, with average χ^2/N values of 6.8 (left) and 5.4 (right). This is to be expected, since in this case the data from Seifen et al. do not yet constrain the solution. It should be noted that the significance of the χ^2/N values decreases at higher energies, where increased statistical uncertainties prevent small deviations from being reliably resolved.

In Fig. 9.17 (bottom), the χ^2/N for the double polarization observable $P_y^c(\sqrt{s}, \cos(\theta_{\pi^0\pi^0}))$ and $P_y^c(\sqrt{s}, \phi^*_{\pi^0\pi^0})$ is shown, which contained larger differences from the model predictions. In the energy range shown, neither BnGa-2014 nor BnGa-2022 are constrained by measured data. Especially in the range of $\sqrt{s} = 1\,725 - 1\,875\,\mathrm{MeV}$ significant deviations can be seen. In this range the data extracted in this work will have a high impact on the next generations of BnGa solutions. For P_y^c the BnGa-2014 achieves a better average χ^2/N of 2.0 (left) and 1.9 (right) compared to the BnGa-2022 with 2.3 (left) and 2.8 (right). However, looking at the data in Fig. 9.15 (bottom), BnGa-2022 seems to represent the overall shape slightly better, although there are larger deviations in some places.

For a more detailed analysis of the impact of the data extracted in this work, a two-dimensional representation of the χ^2/N is shown in Fig. 9.18 for P_y and in Fig. 9.19 for P_y^c. As before, for P_y, the deviations from the BnGa-2022 solution, especially at center of mass energies $1\,900 - 2\,300\,\mathrm{MeV}$,[6] are much better when compared to the BnGa-2014 solution. Here the data from Seifen et al. already constrain the solution. This is not the case for the double polarization observable P_y^c, where the χ^2/N remains high. As before, especially at $\sqrt{s} = 1\,700 - 1\,850\,\mathrm{MeV}$ there are significant deviations.

In summary, the single polarization observables in the Bonn-Gatchina model BnGa-2022 are already reasonably well constrained by the data from Seifen et al. However, deviations remain, particularly at higher energies. For double polarization observables, more pronounced discrepancies are observed. It is noticeable that BnGa-2022 better describes the data in

[6] At higher energies, the resolution of the χ^2/N criteria decreases due to higher statistical uncertainties.

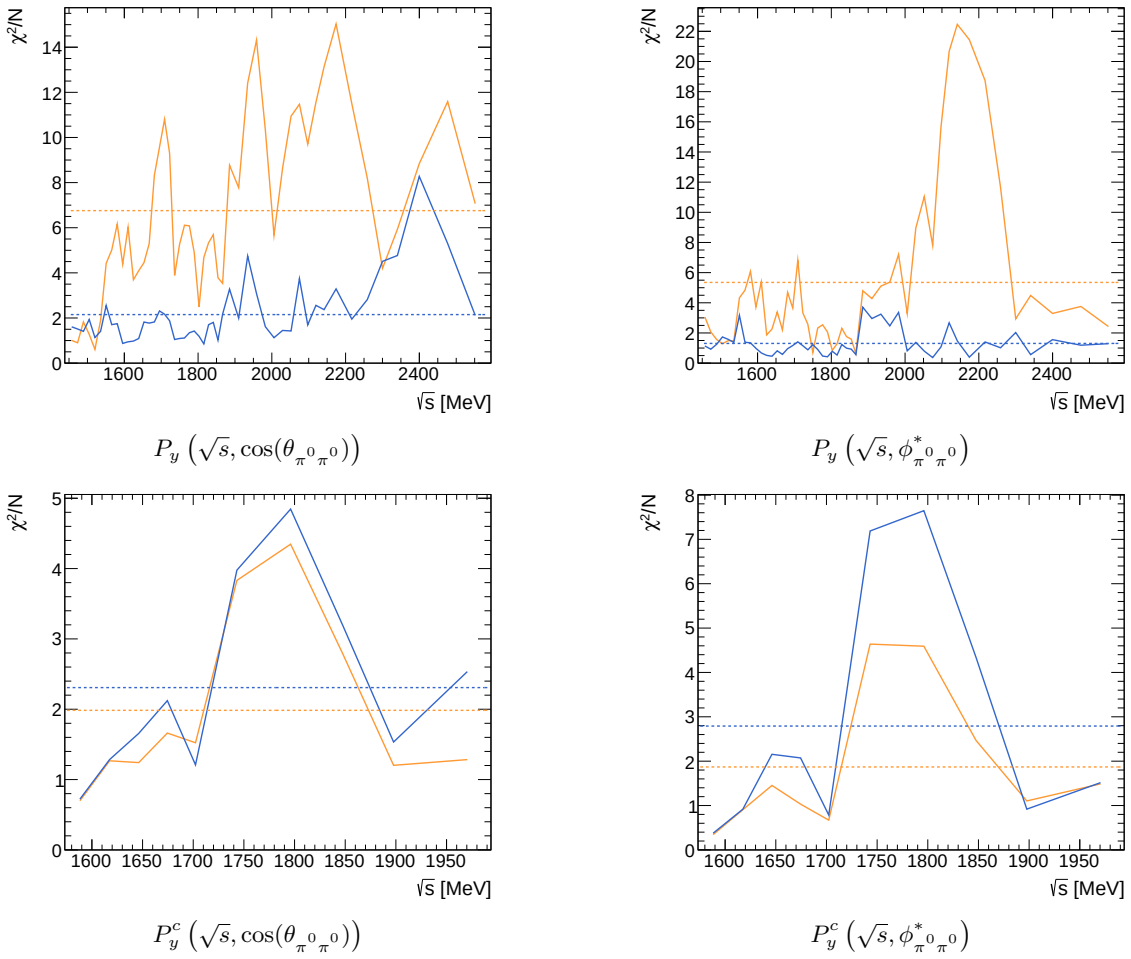

Figure 9.17: χ^2/N (cf. Eqn. 9.6) of the target asymmetry P_y (top) and the double polarization observables P^c_y (bottom) in bins of $\left(\sqrt{s}, \cos(\theta_{\pi^0\pi^0})\right)$ (left) and $\left(\sqrt{s}, \phi^*_{\pi^0\pi^0}\right)$ (right) as a function of $\sqrt{s}$ compared to BnGa-2014 and BnGa-2022.

some kinematic regions, while BnGa-2014 again better describes the data in other regions. Incorporating the data from this work into the Bonn-Gatchina model will help to contribute to further refine the predictions.

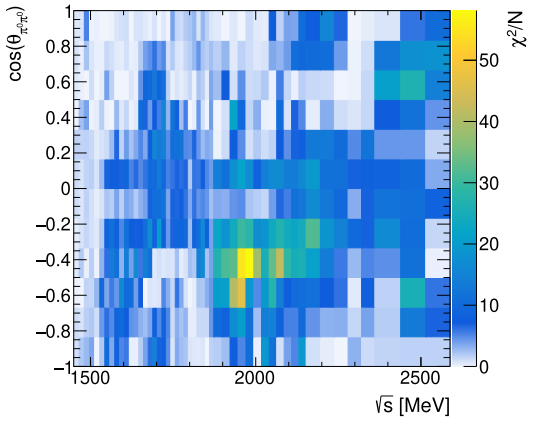

$P_y\left(\sqrt{s}, \cos(\theta_{\pi^0\pi^0})\right)$ with BnGa-2014

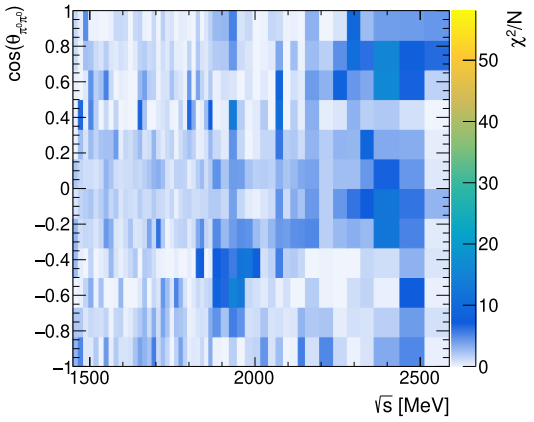

$P_y\left(\sqrt{s}, \cos(\theta_{\pi^0\pi^0})\right)$ with BnGa-2022

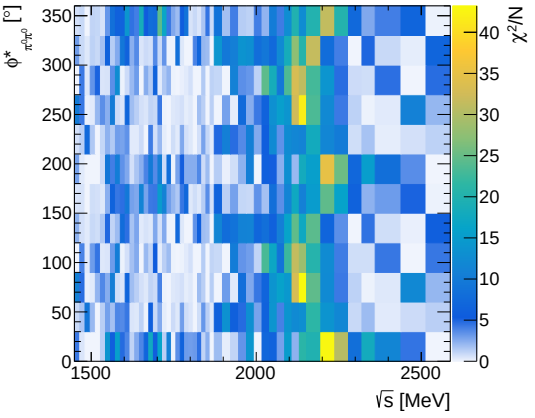

$P_y\left(\sqrt{s}, \phi^*_{\pi^0\pi^0}\right)$ with BnGa-2014

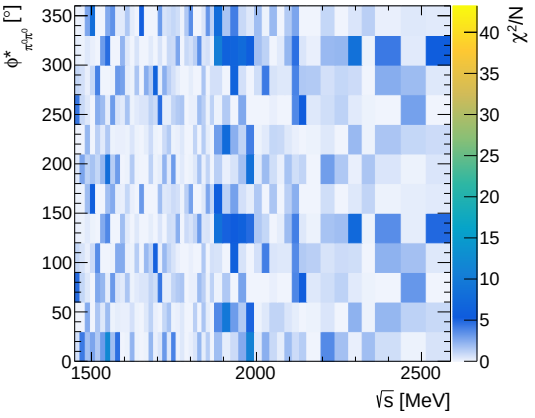

$P_y\left(\sqrt{s}, \phi^*_{\pi^0\pi^0}\right)$ with BnGa-2022

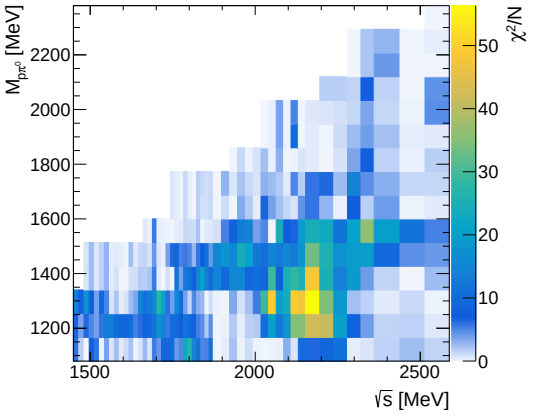

$P_y\left(\sqrt{s}, M_{p\pi^0}\right)$ with BnGa-2014

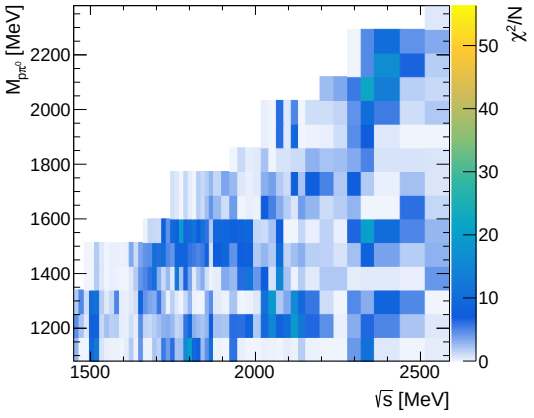

$P_y\left(\sqrt{s}, M_{p\pi^0}\right)$ with BnGa-2022

Figure 9.18: χ^2/N (cf. Eqn. 9.6) of the target asymmetry $P_y\left(\sqrt{s}, \cos(\theta_{\pi^0\pi^0})\right)$ (top), $P_y\left(\sqrt{s}, \phi^*_{\pi^0\pi^0}\right)$ (middle) and $P_y\left(\sqrt{s}, M_{p\pi^0}\right)$ (bottom) in two dimensions compared to BnGa-2014 (left) and BnGa-2022 (right).

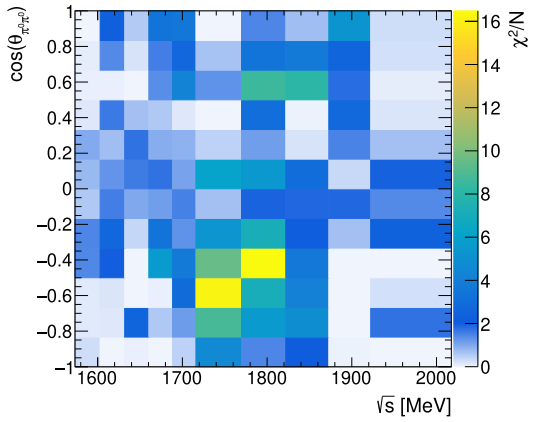

$P_y^c\left(\sqrt{s}, \cos(\theta_{\pi^0\pi^0})\right)$ with BnGa-2014

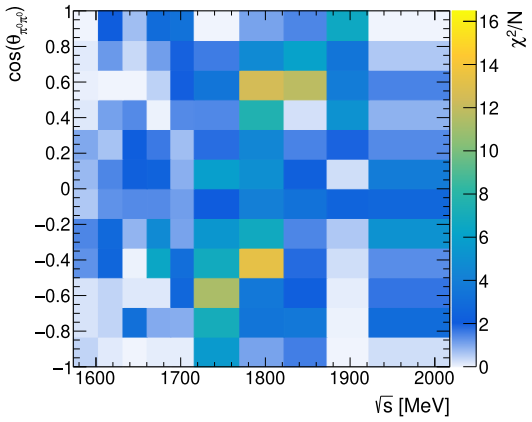

$P_y^c\left(\sqrt{s}, \cos(\theta_{\pi^0\pi^0})\right)$ with BnGa-2022

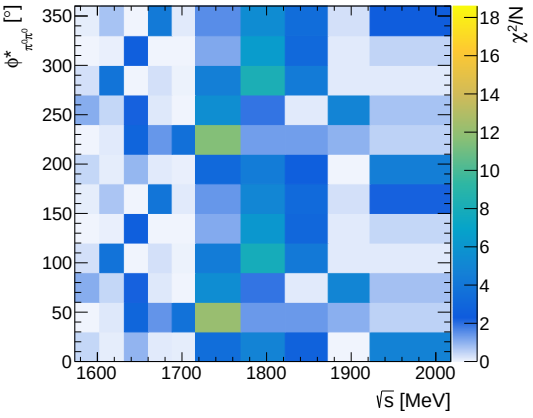

$P_y^c\left(\sqrt{s}, \phi^*_{\pi^0\pi^0}\right)$ with BnGa-2014

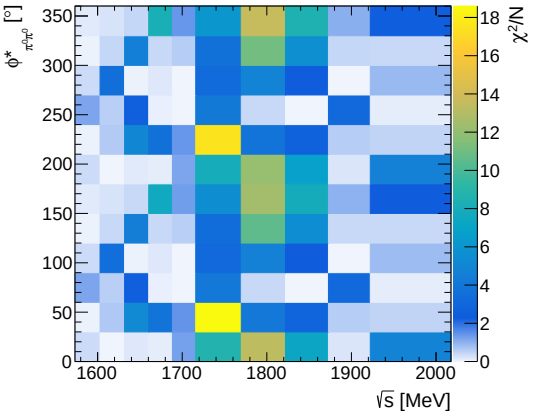

$P_y^c\left(\sqrt{s}, \phi^*_{\pi^0\pi^0}\right)$ with BnGa-2022

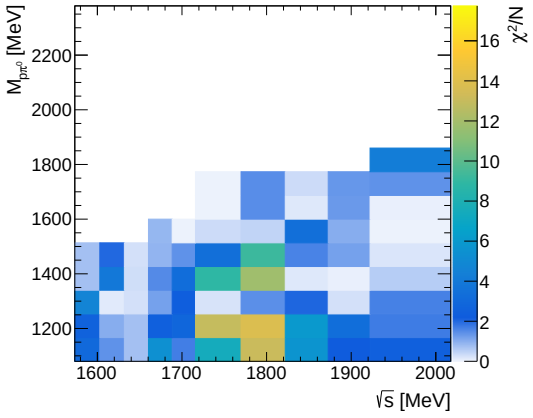

$P_y^c\left(\sqrt{s}, M_{p\pi^0}\right)$ with BnGa-2014

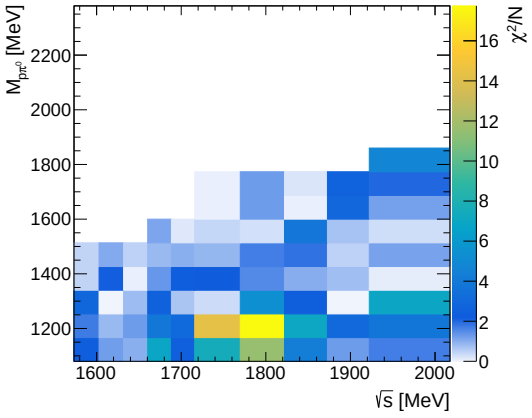

$P_y^c\left(\sqrt{s}, M_{p\pi^0}\right)$ with BnGa-2022

Figure 9.19: χ^2/N (cf. Eqn. 9.6) of the double polarization observables $P_y^c\left(\sqrt{s}, \cos(\theta_{\pi^0\pi^0})\right)$ (top), $P_y^c\left(\sqrt{s}, \phi^*_{\pi^0\pi^0}\right)$ (middle) and $P_y^c\left(\sqrt{s}, M_{p\pi^0}\right)$ (bottom) compared to BnGa-2014 (left) and BnGa-2022 (right).

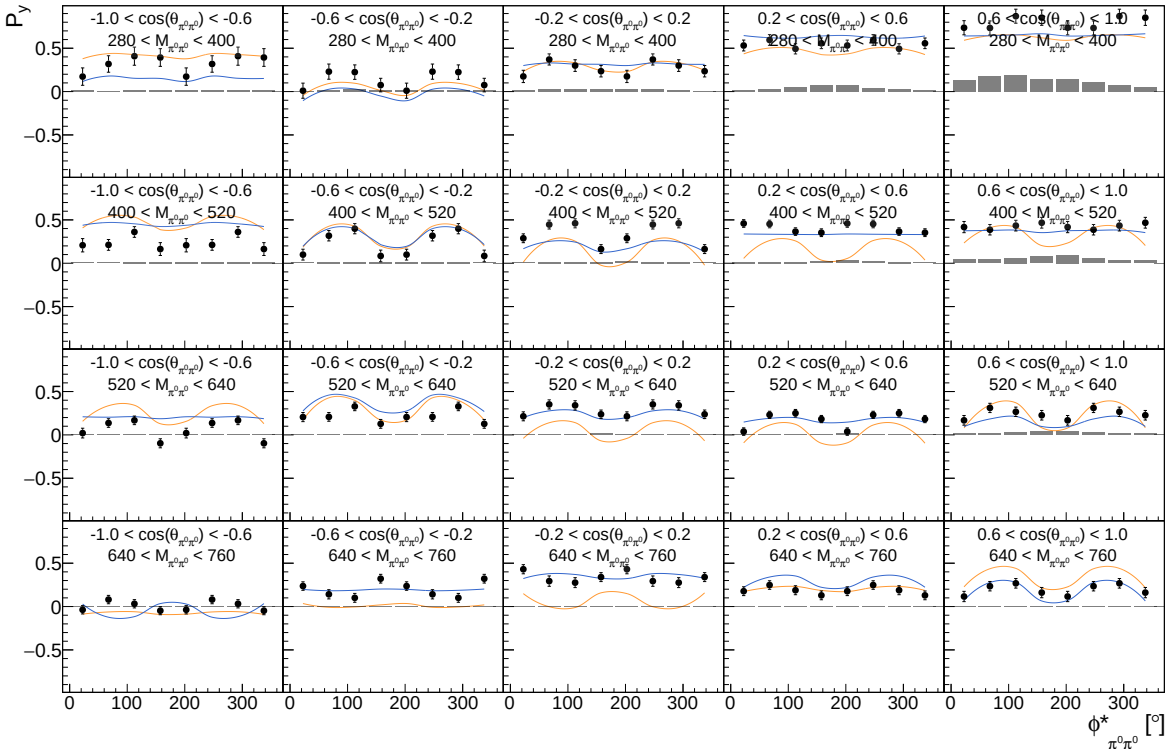

$E_\gamma = 1\,100 - 1\,250\,\text{MeV}$

Figure 9.20: Target asymmetry P_y for a specific energy range $E_\gamma = 1\,100 - 1\,250\,\text{MeV}$ as function of $\left(\cos(\theta_{\pi^0\pi^0}), M_{\pi^0\pi^0}, \phi^*_{\pi^0\pi^0}\right)$. The **combined data of this work** is shown as well as the model predictions BnGa-2022 and BnGa-2014. The systematic uncertainties are shown as bars on the x-axis.

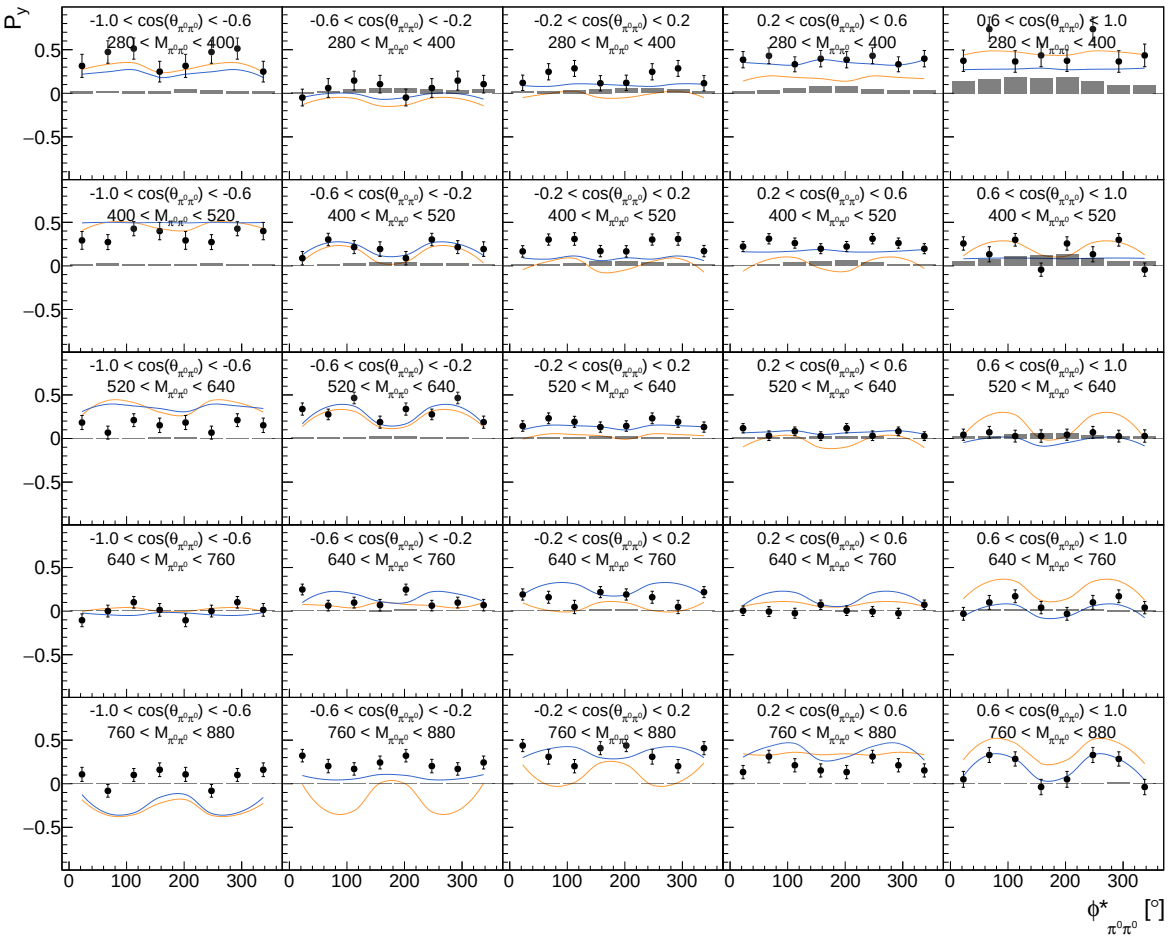

$E_\gamma = 1\,250 - 1\,400\,\text{MeV}$

Figure 9.21: Target asymmetry P_y for a specific energy range $E_\gamma = 1\,250 - 1\,400\,\text{MeV}$ as function of $\left(\cos(\theta_{\pi^0\pi^0}), M_{\pi^0\pi^0}, \phi^*_{\pi^0\pi^0}\right)$. The **combined data of this work** is shown as well as the model predictions BnGa-2022 and BnGa-2014. The systematic uncertainties are shown as bars on the x-axis.

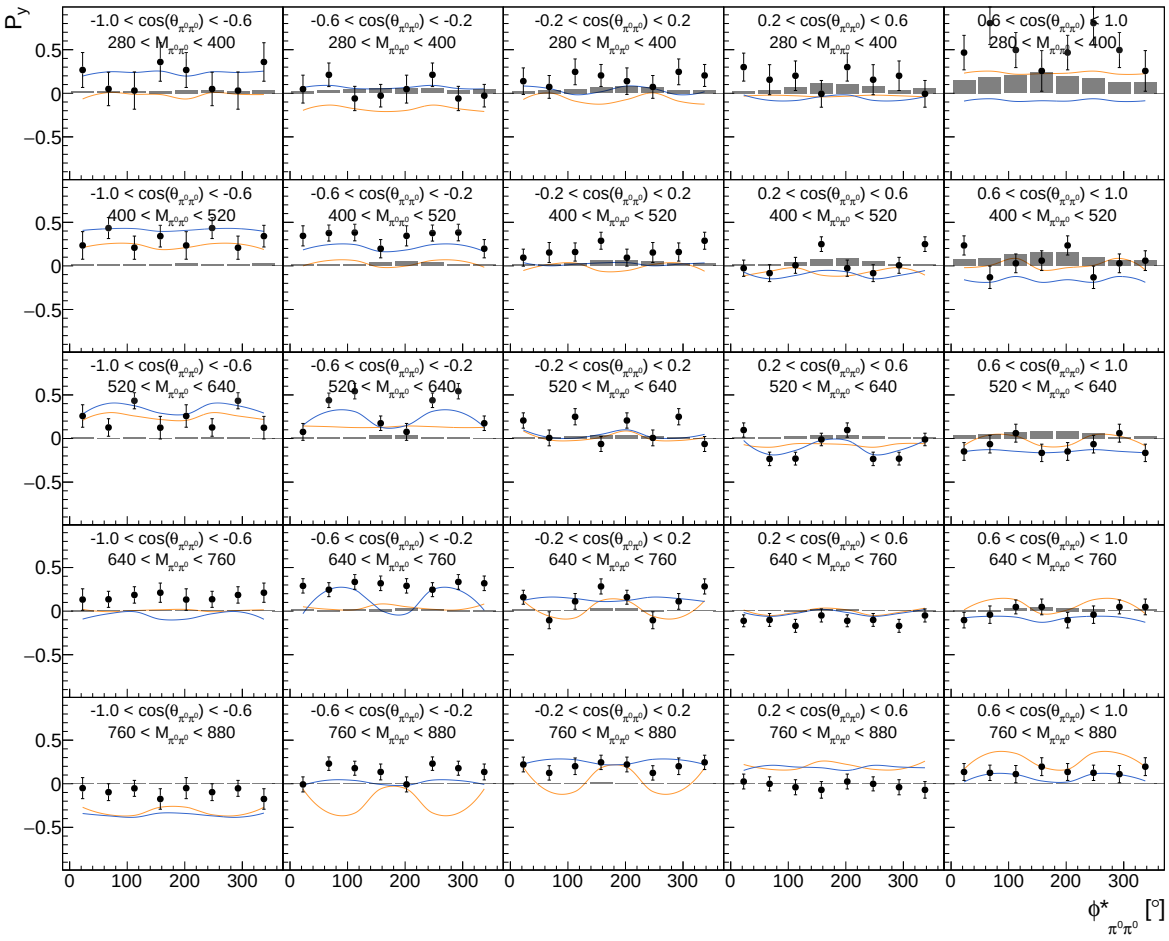

$E_\gamma = 1\,400 - 1\,550\,\text{MeV}$

Figure 9.22: Target asymmetry P_y for a specific energy range $E_\gamma = 1\,400 - 1\,550\,\text{MeV}$ as function of $\left(\cos(\theta_{\pi^0\pi^0}), M_{\pi^0\pi^0}, \phi^*_{\pi^0\pi^0}\right)$. The **combined data of this work** is shown as well as the model predictions BnGa-2022 and BnGa-2014. The systematic uncertainties are shown as bars on the x-axis.

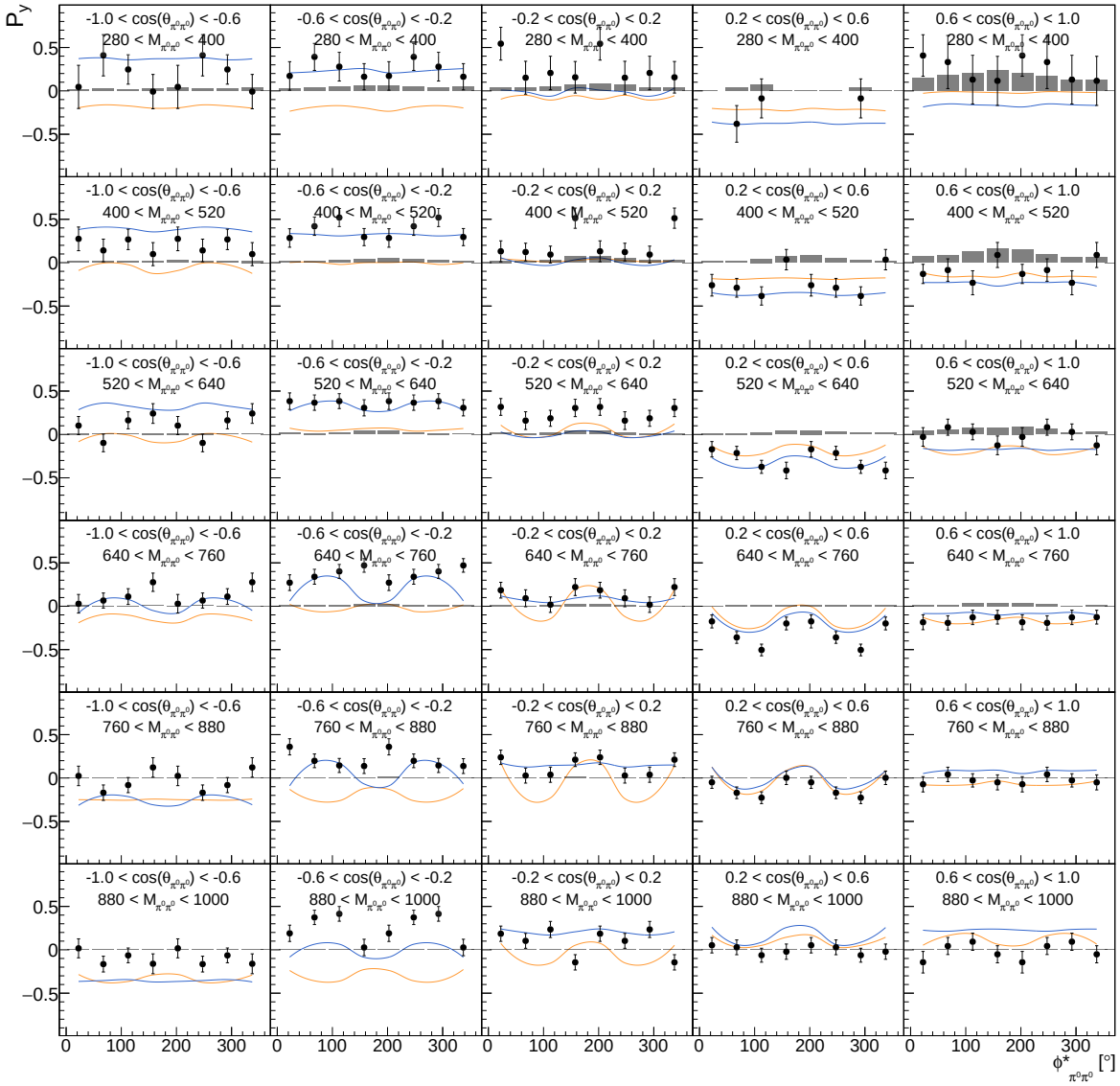

$E_\gamma = 1\,550 - 1\,850\,\mathrm{MeV}$

Figure 9.23: Target asymmetry P_y for a specific energy range $E_\gamma = 1\,550 - 1\,850\,\mathrm{MeV}$ as function of $\left(\cos(\theta_{\pi^0\pi^0}), M_{\pi^0\pi^0}, \phi^*_{\pi^0\pi^0}\right)$. The **combined data of this work** is shown as well as the model predictions BnGa-2022 and BnGa-2014. The systematic uncertainties are shown as bars on the x-axis.

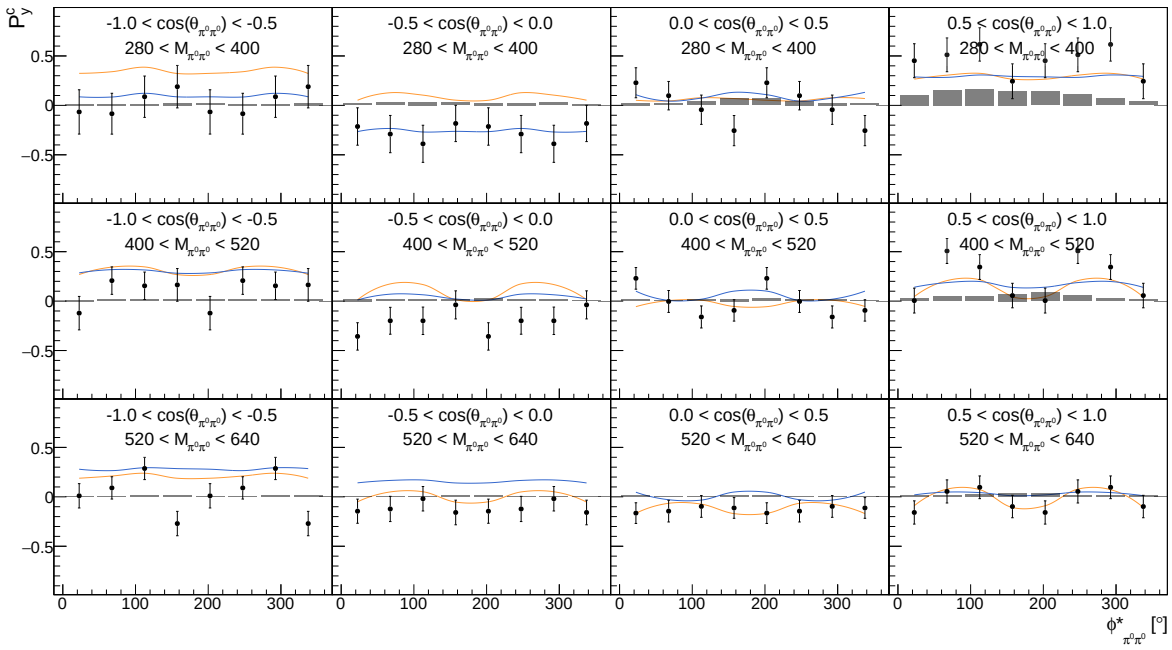

$E_\gamma = 1\,000 - 1\,300\,\text{MeV}$

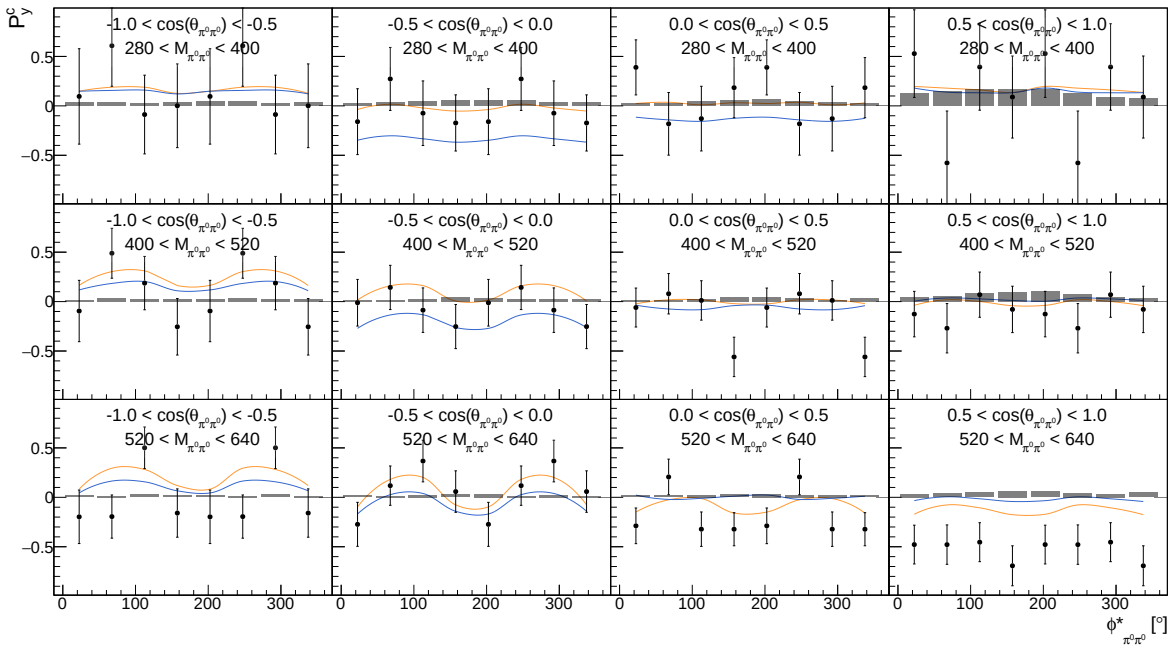

$E_\gamma = 1\,300 - 1\,600\,\text{MeV}$

Figure 9.24: Double polarization observable P_y^c for energy ranges $E_\gamma = 1\,000 - 1\,300\,\text{MeV}$ and $E_\gamma = 1\,300 - 1\,600\,\text{MeV}$ as function of $\left(\cos(\theta_{\pi^0\pi^0}), M_{\pi^0\pi^0}, \phi^*_{\pi^0\pi^0}\right)$. The **combined data of this work** is shown as well as the model predictions BnGa-2022 and BnGa-2014.

CHAPTER 10

Summary and Outlook

The theory of Quantum Chromodynamics (QCD) poses significant challenges. In the energy region where hadrons form, perturbation theory cannot be applied. A promising approach to probe QCD in this region is the study of the excitation spectrum of baryons. However, classical (unpolarized) cross section measurements alone are insufficient to isolate the contributions of individual excited states due to their large width. To disentangle overlapping resonance contributions, polarized cross sections are measured, which further constrain the spin degrees of freedom. Extracted polarization observables are then used in partial wave analysis (PWA) to gain insight into resonance parameters and their properties. The CBELSA/TAPS experiment makes an important contribution to the field of baryon spectroscopy investigating the photoproduction of mesons off the proton p or neutron n. In this work, the $\gamma p \to p\pi^0\pi^0$ reaction is analyzed.

A recent upgrade of the CBELSA/TAPS experiment improved both the readout electronics and trigger system, allowing higher data quality, improved rate capability and higher trigger efficiency. As part of the modification, time information for the full Crystal Barrel detector became available for the first time. In this work, the time information was investigated in detail. It was used to independently validate the pile-up detection and pile-up correction functionality of the newly installed sampling-analog-to-digital-converters (SADCs). Based on this work, significant shortcomings in pile-up detection were identified, which have been resolved in [141]. In addition, time information was included in the clustering of energy depositions in the Crystal Barrel detector. This ensures improved particle reconstruction not only for this work, but also for future work.

Based on the improved reconstruction process, an analysis was performed on data recorded by the CBELSA/TAPS experiment using a linearly polarized photon beam and a transversely polarized butanol target. Four different periods of data taking were combined: December 2017, May 2018, February 2019, and June 2021. To achieve an optimal coverage of all kinematic regions, in addition to 5-PED and 4.5-PED events, the more difficult-to-handle 4-PED events were also included in the analysis. In total, 8.17×10^5 events on quasi-free protons with a $p\pi^0\pi^0$ final states were selected in a beam photon energy range of $650 - 3\,100\,\mathrm{MeV}$ and an average reconstruction efficiency of $22\,\%$. At the same time, the average background was reduced to $< 2\,\%$. Events on bound protons were successfully subtracted using reference measurements with carbon foam as a target material.

Using an event-based likelihood fit, polarization observables were extracted for different combinations of the kinematic variables $(E_\gamma, \cos(\theta), M, \phi^*, \theta^*)$. The secondary decay plane was chosen as either $\pi^0\pi^0$ or $p\pi^0$. The single polarization observables P_x and P_y were extracted in a beam photon energy range of $650 - 3\,100\,\mathrm{MeV}$ with high statistics. The double polarization observables P_x^s, P_y^s, P_x^c, and P_y^c were extracted in a beam photon range of

$850 - 1\,700$. This is the first measurement of these double polarization observables at such high energies. Moreover, the inclusion of 4-PED events enabled this analysis to extract results also at the very forward angles of $\cos(\theta_{\pi^0\pi^0})$. The results were compared with existing data, where available, and with model predictions from the Bonn-Gatchina partial wave analysis.

The results of this work will help to further disentangle the ambiguities in partial wave analysis. The next step is to incorporate the results of this work (cf. Appendix E to H) into an updated solution of the Bonn-Gatchina model. This will improve the accuracy of resonance parameters and branching ratios. In this way, this work contributes to the understanding of strongly bound systems in QCD.

APPENDIX A

Time in the Crystals Barrel Detector

This appendix presents additional material to Chapter 5. In Section A.1, a close comparison of the output of the signal filter to the input of the discriminator module is shown. In Section A.2 energy dependent time distributions and example fits of a Novosibirsk function to these time distributions are presented. This results in the final time resolution of the Crystal Barrel detector which is shown in Fig. 5.3. The Section A.3 contains all the distributions and some example fits needed for developing the method for selecting TDC times in the Crystal Barrel detector. The Section A.4 contains more information about the clustering of timestamps at threshold A.

A.1 Signals in the TDC Branch

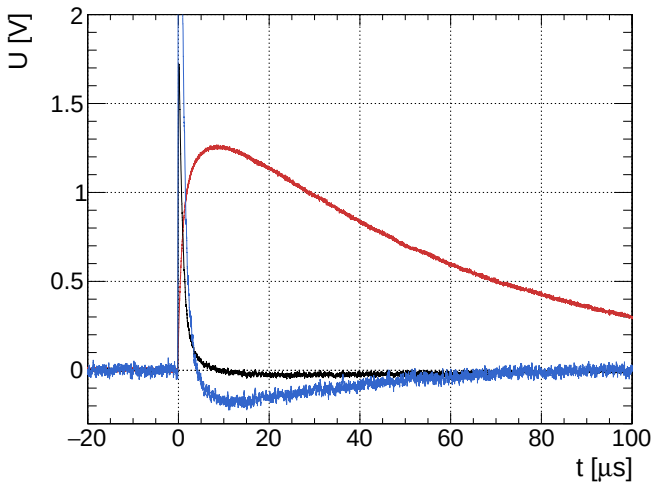

Figure A.1: Comparison of the output signal of the **signal filter** to the input signal at the discriminator module. For completeness, the output signal of the preamplifier is shown as well. The signal at the discriminator input exhibits an undershoot due to core saturation effects of the transformer. Such undershoots have an amplitude of $4 - 8\,\%$ of the signal's voltage and last up to $80 - 100\,\mu s$ depending on the size of the signal. All signals were recorded on an oscilloscope in a laboratory where an equivalent readout was constructed for a single crystal as it is used in the experiment.

A.2 Time Resolution of the Crystal Barrel Detector

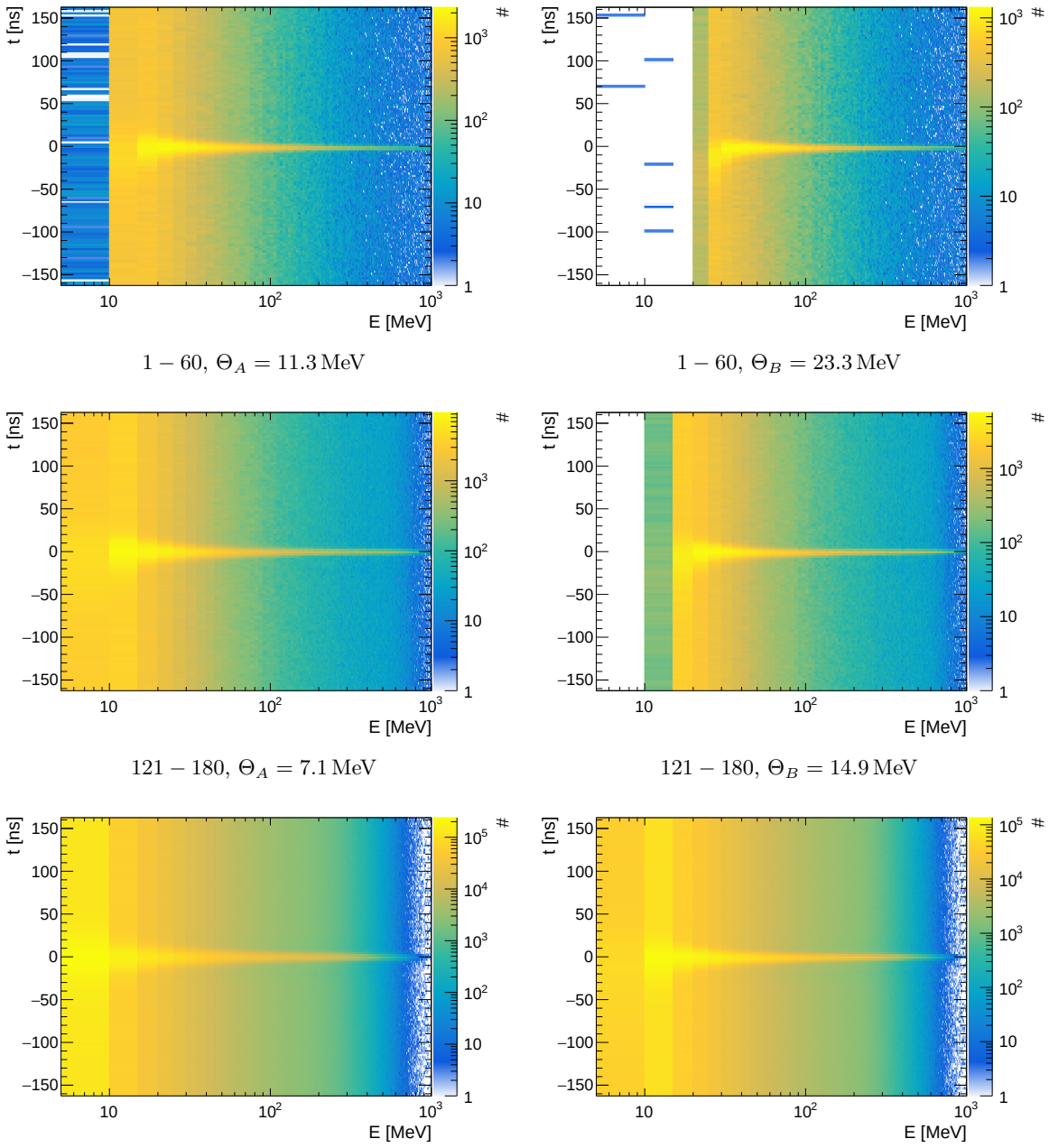

$1 - 60$, $\Theta_A = 11.3\,\mathrm{MeV}$ $1 - 60$, $\Theta_B = 23.3\,\mathrm{MeV}$

$121 - 180$, $\Theta_A = 7.1\,\mathrm{MeV}$ $121 - 180$, $\Theta_B = 14.9\,\mathrm{MeV}$

$301 - 1\,380$, $\Theta_A = 3.9\,\mathrm{MeV}$ $301 - 1\,380$, $\Theta_B = 8.2\,\mathrm{MeV}$

Figure A.2: Examples of energy dependent time distributions of coincident hits in the Crystal Barrel detector using Tagger bars as reference detector (TDC branch). Different crystal regions with different threshold configuration are shown. Only signals from photons originating from a π^0 decay during data taking in May 2018 are considered. Example fits to single distributions are shown in Fig. A.3.

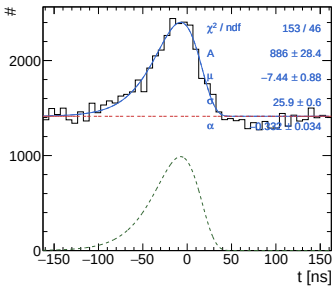

Θ_A, $1-60$, $12-14\,\mathrm{MeV}$

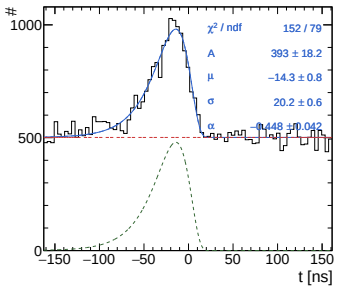

Θ_B, $1-60$, $24-27\,\mathrm{MeV}$

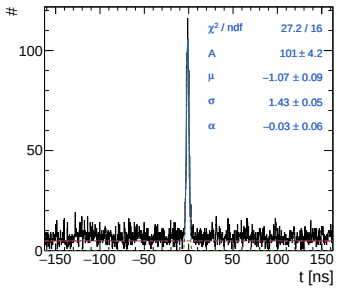

Θ_A, $1-60$, $268-284\,\mathrm{MeV}$

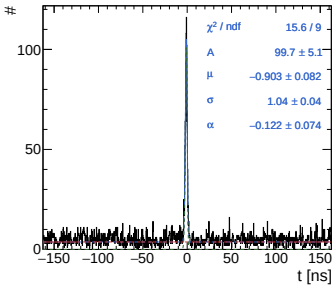

Θ_B, $1-60$, $444-467\,\mathrm{MeV}$

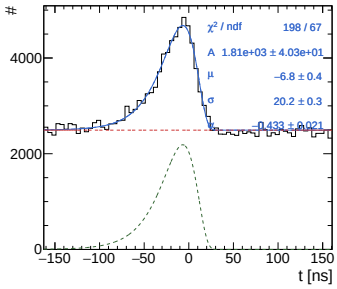

Θ_B, $121-180$, $16-18\,\mathrm{MeV}$

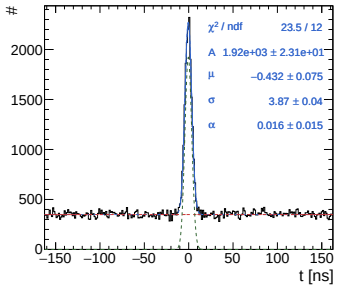

Θ_A, $121-180$, $42-47\,\mathrm{MeV}$

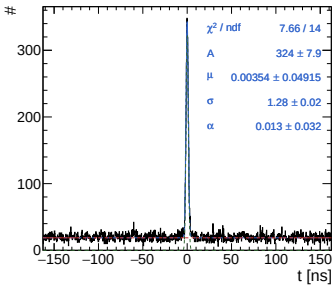

Θ_B, $121-180$, $358-378\,\mathrm{MeV}$

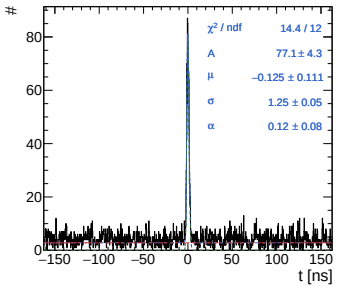

Θ_A, $121-180$, $885-922\,\mathrm{MeV}$

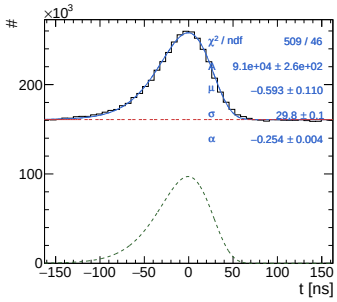

Θ_A, $301-1\,381$, $5-6\,\mathrm{MeV}$

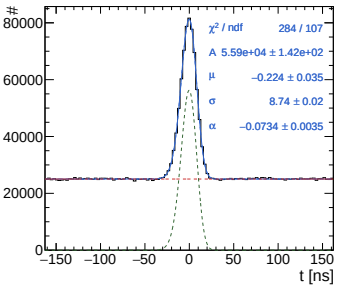

Θ_B, $301-1\,380$, $16-18\,\mathrm{MeV}$

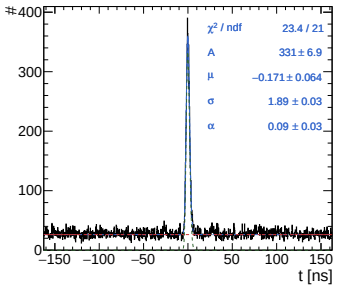

Θ_A, $301-1\,380$, $569-596\,\mathrm{MeV}$

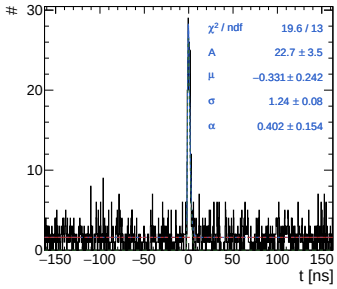

Θ_B, $301-1\,380$, $814-849\,\mathrm{MeV}$

Figure A.3: Fits of a Novosibirsk function (cf. Eqn. 5.2) to time distributions of the Crystal Barrel detector using Tagger bars as reference detector (TDC branch). Examples are shown for different thresholds Θ_A or Θ_B, different index regions with approximately constant threshold and different energies of the crystals. Only signals from photons originating from a π^0 decay during data taking in May 2018 are considered. The resulting time resolution is shown in Fig. 5.3.

A.3 Method for Selecting TDC Times

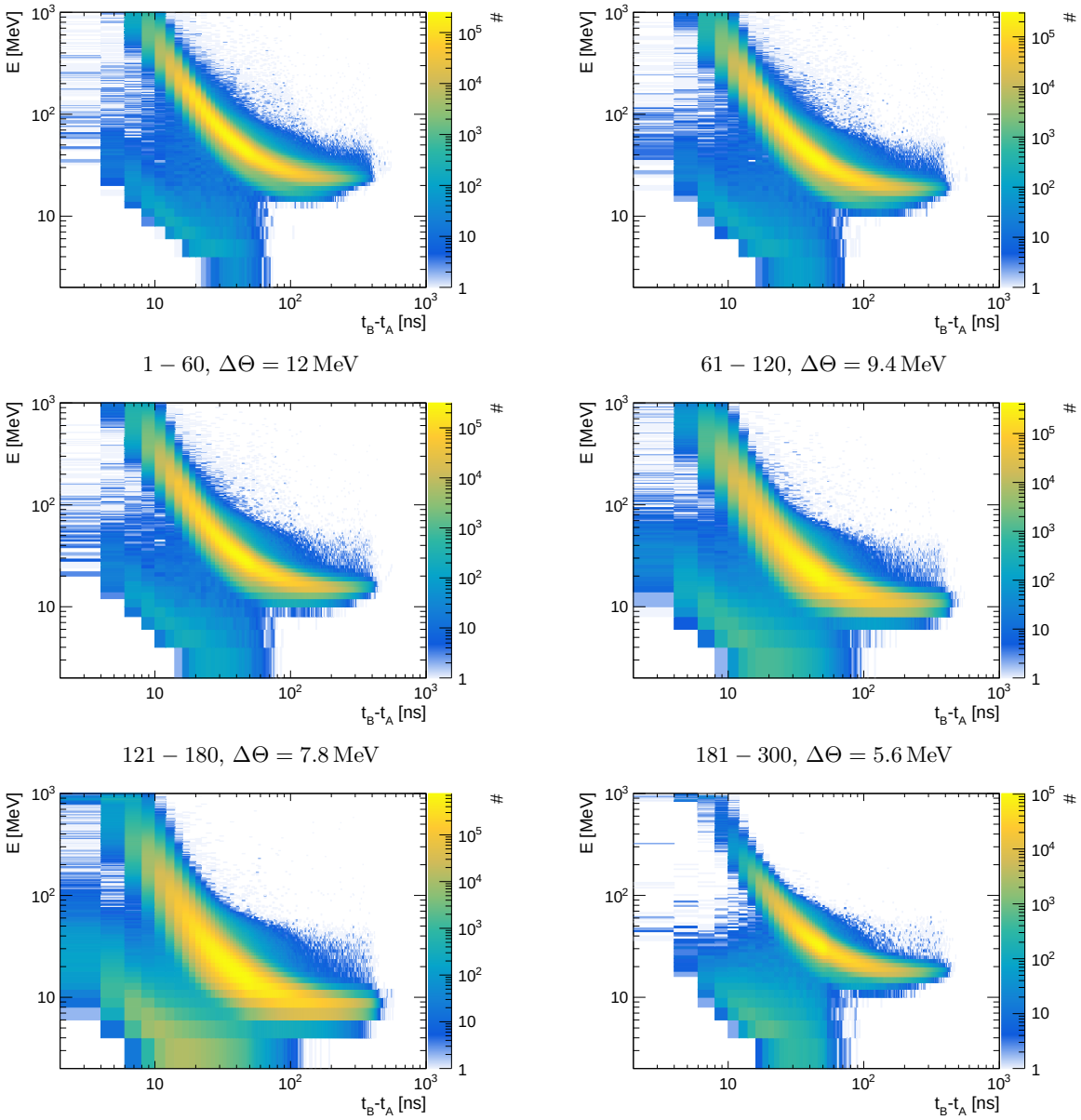

$1-60,\ \Delta\Theta = 12\,\text{MeV}$

$61-120,\ \Delta\Theta = 9.4\,\text{MeV}$

$121-180,\ \Delta\Theta = 7.8\,\text{MeV}$

$181-300,\ \Delta\Theta = 5.6\,\text{MeV}$

$301-1\,380,\ \Delta\Theta = 4.3\,\text{MeV}$

$1\,381-1\,440,\ \Delta\Theta = 9\,\text{MeV}$

Figure A.4: Relation between the time difference $\Delta t_{AB} = t_B - t_A$ and energy (QDC) for crystals exhibiting a pure AB pattern around trigger time ($-200-200\,\text{ns}$) during data taking in May 2018. Different crystal regions with different threshold configuration are shown. The deviating accumulations at small values correspond to events that only have a timestamp at threshold B due to the influence of noise. However, their actual energy is lower. As a result, the time difference Δt_{AB} is too small. The distribution using the normalized energy $\frac{E}{\Theta_B - \Theta_A}$ is shown in Fig. A.6 (top). Example fits to single normalized distributions are shown in Fig. A.7.

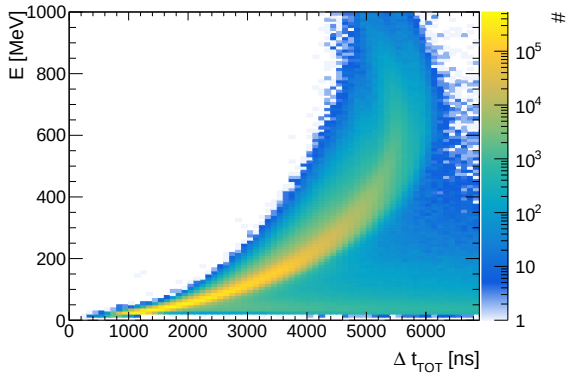

$1-60$, $\Theta_B = 23.3\,\mathrm{MeV}$

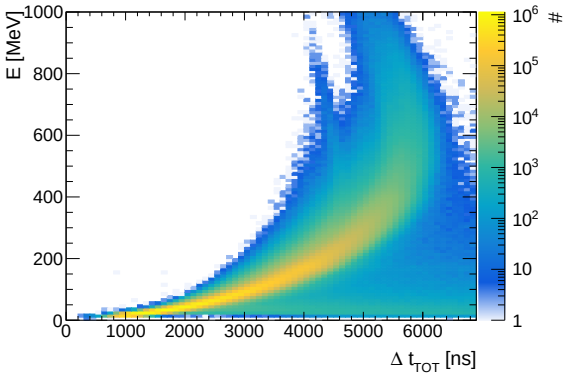

$61-120$, $\Theta_B = 18.2\,\mathrm{MeV}$

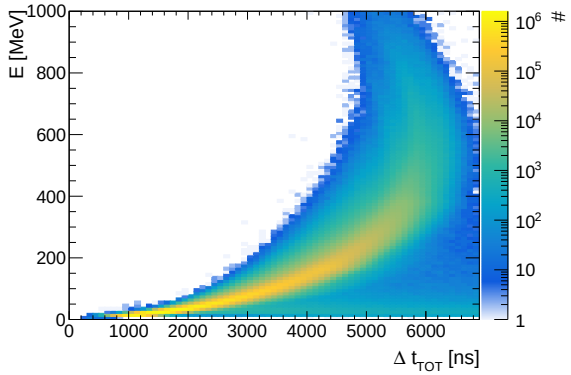

$121-180$, $\Theta_B = 14.9\,\mathrm{MeV}$

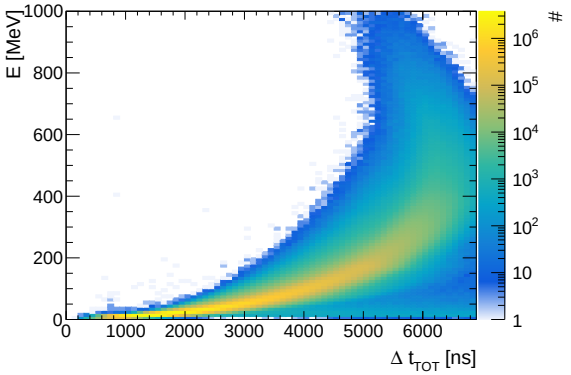

$181-300$, $\Theta_B = 10.6\,\mathrm{MeV}$

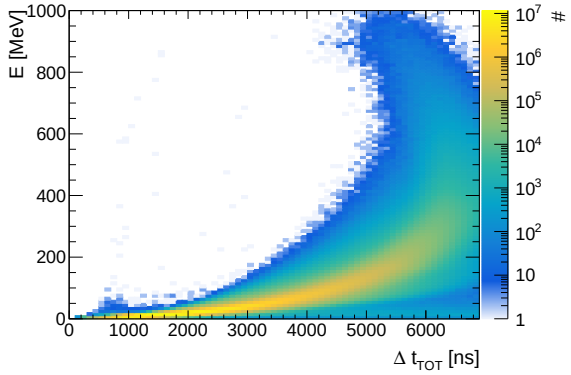

$301-1\,380$, $\Theta_B = 8.2\,\mathrm{MeV}$

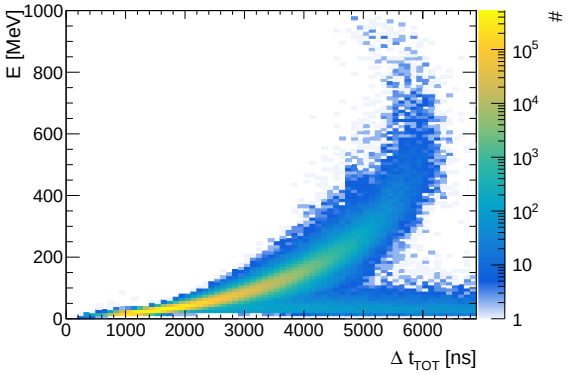

$1\,381-1\,440$, $\Theta_B = 17.5\,\mathrm{MeV}$

Figure A.5: Relation between time-over-threshold at threshold B $\Delta t_{\mathrm{TOT}} = t_{B_2} - t_{B_1}$ and energy for crystals exhibiting a pure ABB pattern around trigger time ($-200-200\,\mathrm{ns}$) during data taking in May 2018. Different crystal regions with different threshold configuration are shown. At low energies, pile-up events lead to a flat band that expands to high Δt_{TOT}. The second tail at high energies for index region $61-120$ arises from a crystal with deviating threshold setting. The distribution using the normalized energy $\frac{E}{\Theta}$ is shown in Fig. A.6 (bottom). Example fits to single normalized distributions are shown in Fig. A.8.

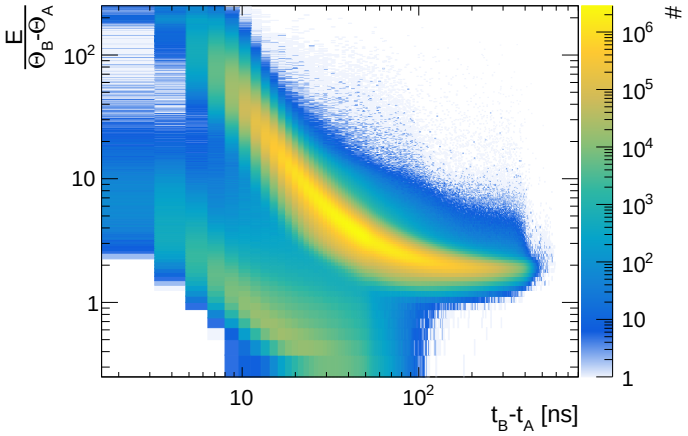

Δt_{AB}

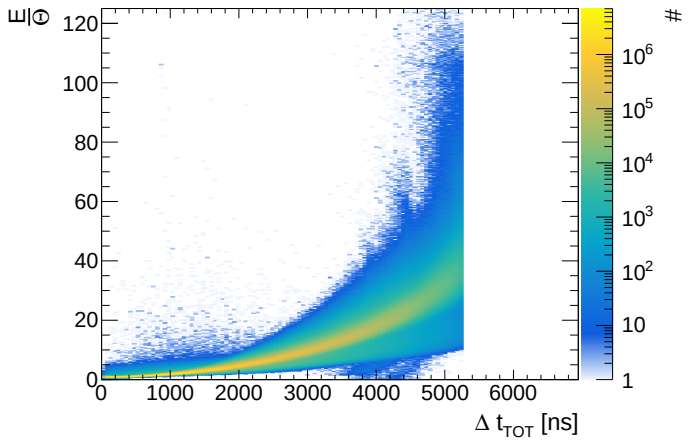

Δt_{TOT}

Figure A.6: Relation between the time difference $\Delta t_{AB} = t_B - t_A$ (top) and time-over-threshold at threshold B $\Delta t_{\mathrm{TOT}} = t_{B_2} - t_{B_1}$ (bottom) with normalized energy (QDC) $\frac{E}{\Theta_B - \Theta_A}$ and $\frac{E}{\Theta}$, respectively. Example fits to single distributions are shown in Fig. A.7 and Fig. A.8.

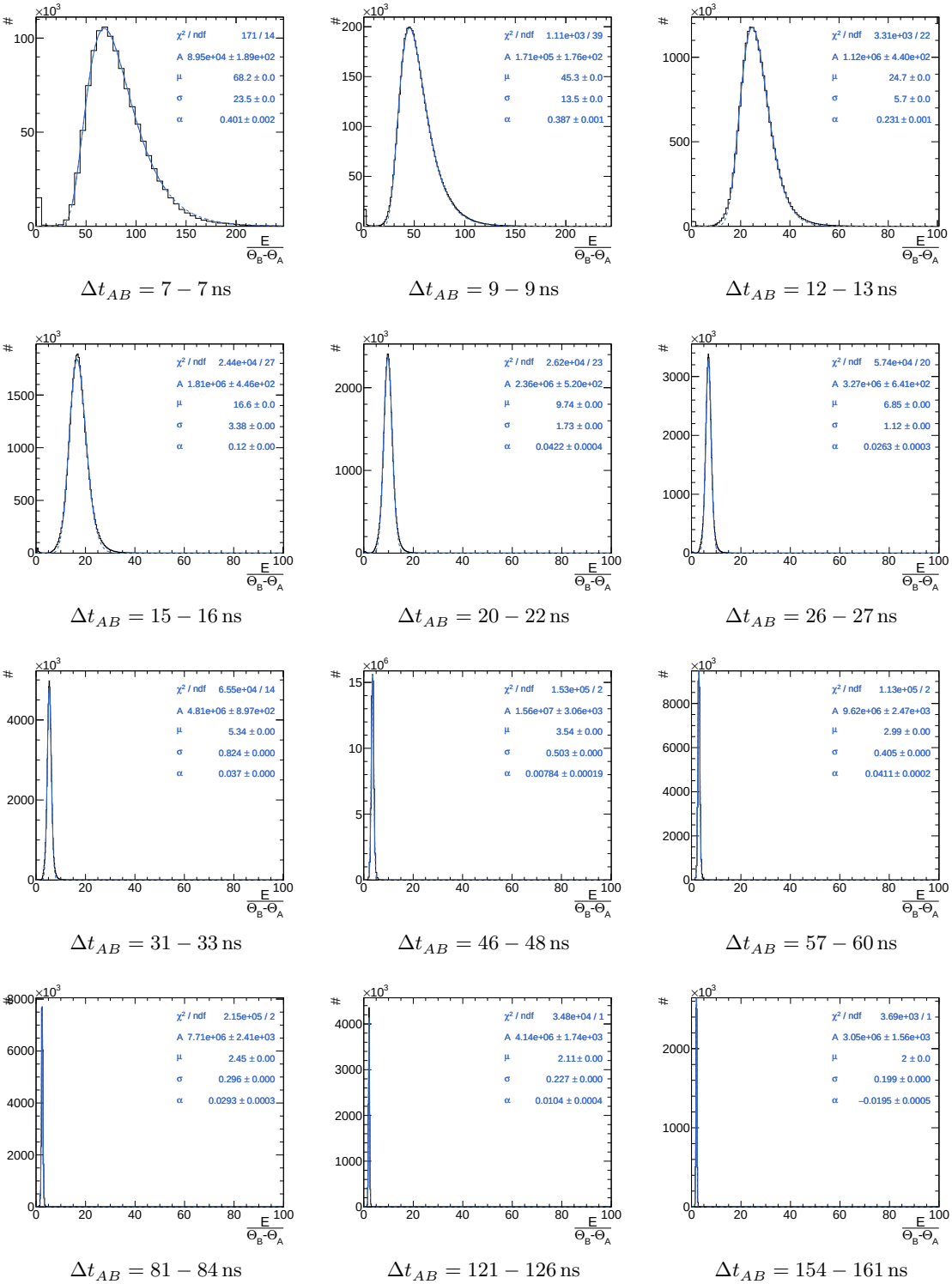

Figure A.7: Fits of a Novosibirsk function (cf. Eqn. 5.2) to distributions from Fig. A.6 (top) as function of $\Delta t_{AB} = t_B - t_A$. Examples are shown for different ranges of Δt_{AB}. Notice the different scale on the x-axis for the first two plots. The resulting dependency is shown in Fig. 5.7 (right).

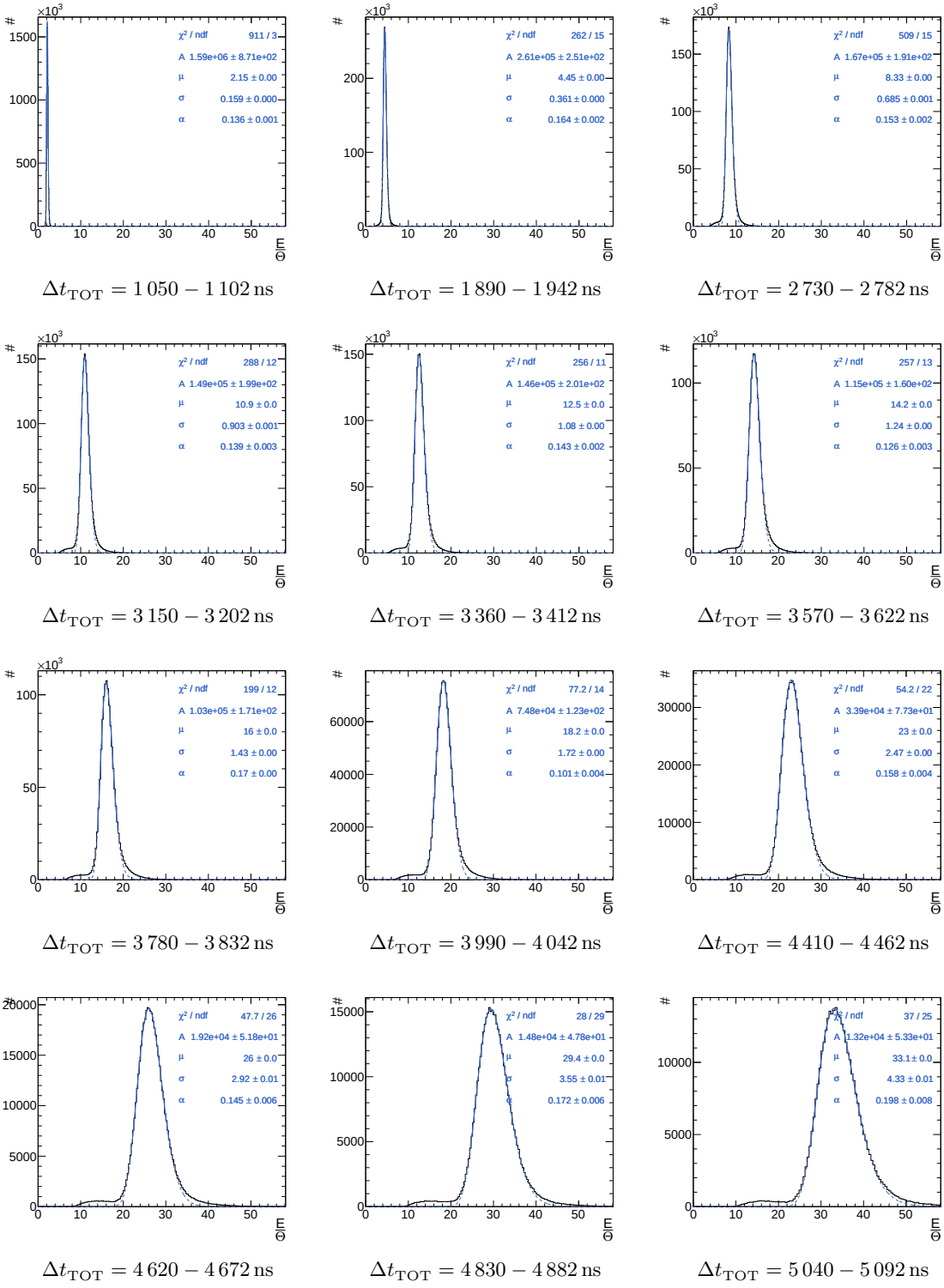

Figure A.8: Fits of a Novosibirsk function (cf. Eqn. 5.2) to distributions from Fig. A.6 (bottom) as function of $\Delta t_{\mathrm{TOT}} = t_{B_2} - t_{B_1}$. Examples are shown for different ranges of Δt_{TOT}. The resulting dependency is shown in Fig. 5.8 (right).

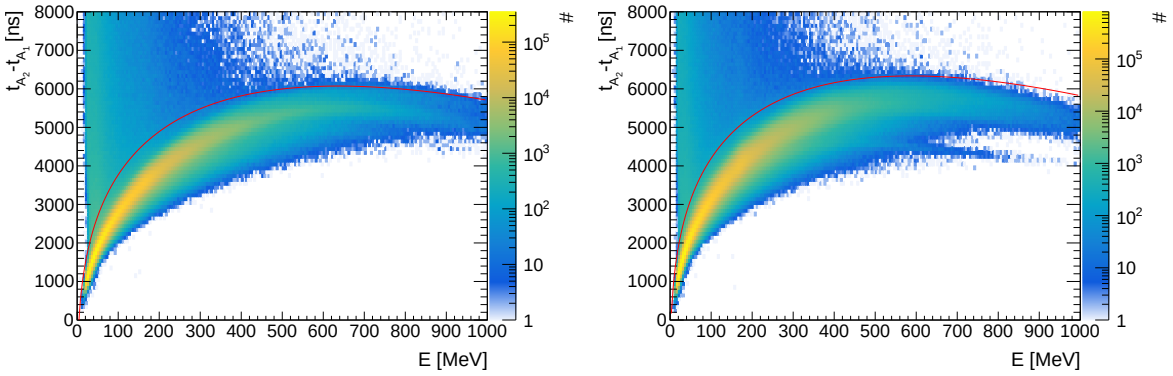

$1 - 60$, $\Theta_A = 11.3\,\mathrm{MeV}$

$61 - 120$, $\Theta_A = 8.8\,\mathrm{MeV}$

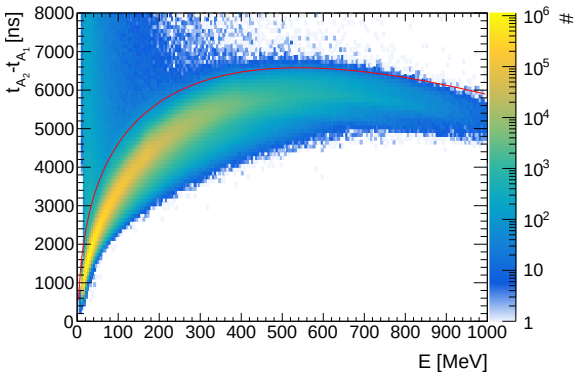

$121 - 180$, $\Theta_A = 7.1\,\mathrm{MeV}$

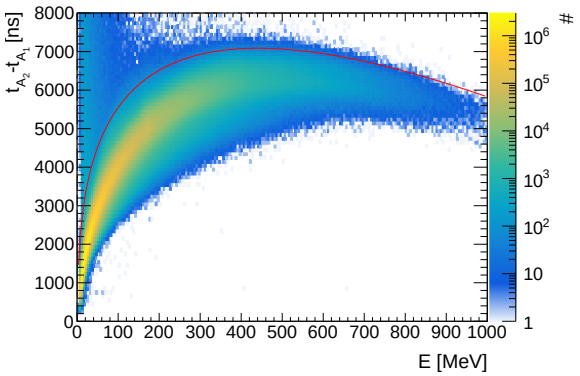

$181 - 300$, $\Theta_A = 5\,\mathrm{MeV}$

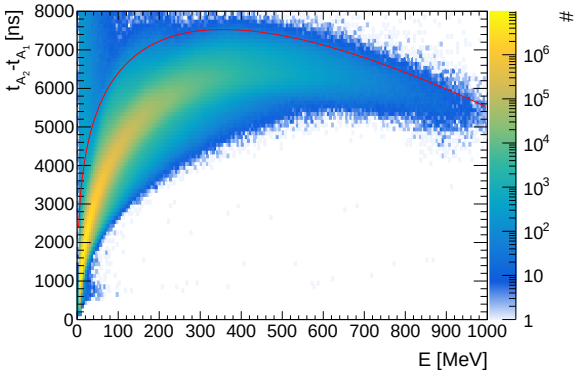

$301 - 1\,380$, $\Theta_A = 3.9\,\mathrm{MeV}$

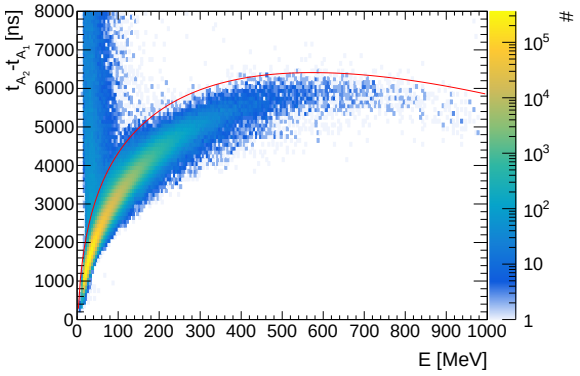

$1\,381 - 1\,440$, $\Theta_A = 8.5\,\mathrm{MeV}$

Figure A.9: Artificial dead time $\tau_{\mathrm{dead}} = t_{A_2} - t_{A_1}$ as function of energy (TDC) with pure ABA pattern around trigger time ($-200 - 200\,\mathrm{ns}$) during data taking in May 2018. Different crystal regions with different threshold configuration are shown. The fitted dependency of artificial dead time on energy and threshold (cf. Eqn. 5.14) is shown as red lines. The second tail at high energies for index region $61 - 120$ arises from a crystal with deviating threshold setting. Example distributions are shown in Fig. A.10.

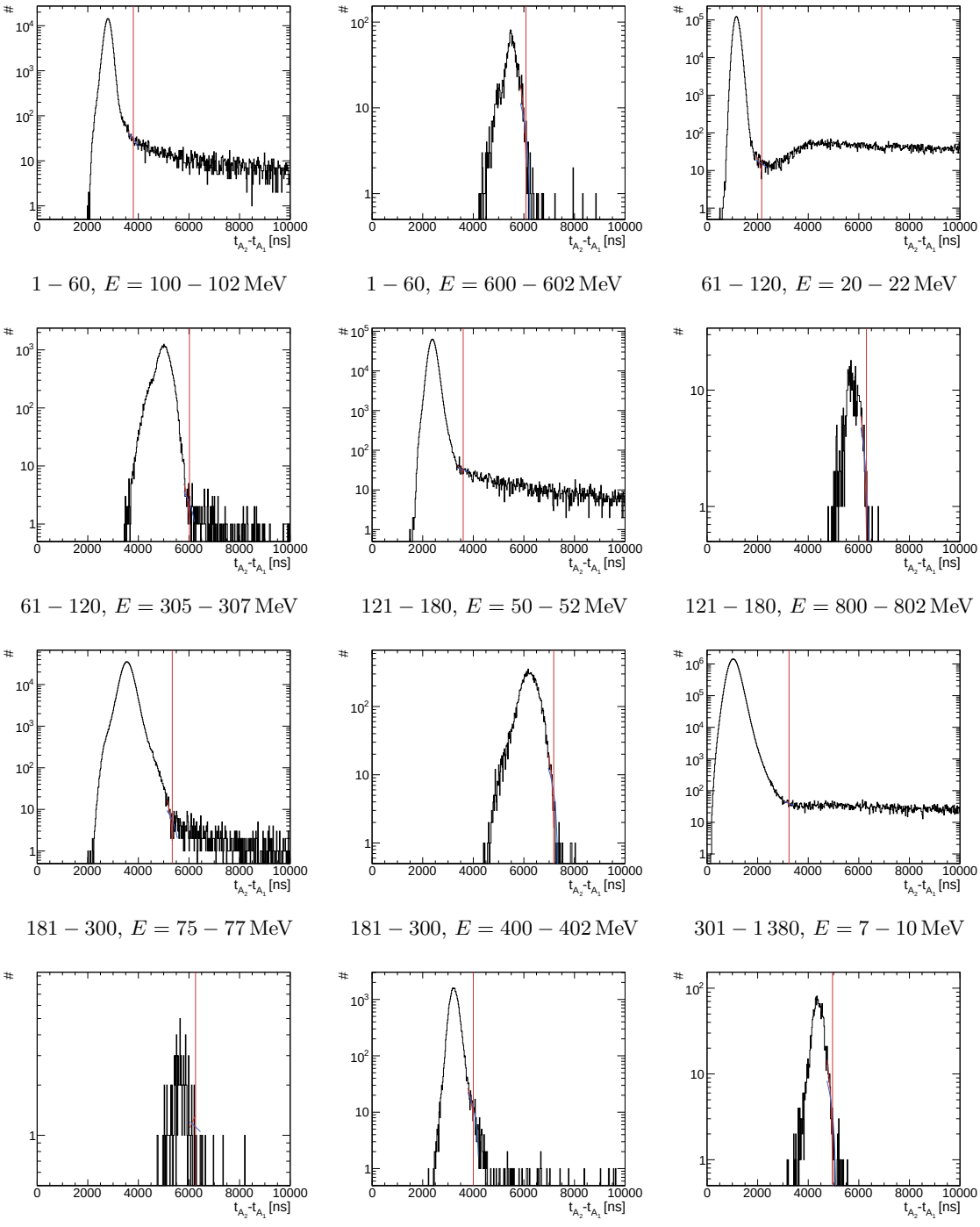

$1-60,\ E=100-102\,\mathrm{MeV}$ | $1-60,\ E=600-602\,\mathrm{MeV}$ | $61-120,\ E=20-22\,\mathrm{MeV}$

$61-120,\ E=305-307\,\mathrm{MeV}$ | $121-180,\ E=50-52\,\mathrm{MeV}$ | $121-180,\ E=800-802\,\mathrm{MeV}$

$181-300,\ E=75-77\,\mathrm{MeV}$ | $181-300,\ E=400-402\,\mathrm{MeV}$ | $301-1\,380,\ E=7-10\,\mathrm{MeV}$

$301-1\,380,\ E=900-902\,\mathrm{MeV}$ | $1\,381-1\,440,\ E=100-102\,\mathrm{MeV}$ | $1\,381-1\,440,\ E=200-202\,\mathrm{MeV}$

Figure A.10: Single distributions from Fig. A.9 as function of energy E (TDC). Examples are shown for different combinations of index regions with approximately constant threshold and the energy of the crystals. The transition between the distribution related to noise on the trailing edge and random coincidences is determined using linear functions. As soon as the slope of a linear function fitted to surrounding points shows a flat behavior the transition point is found (red line). The resulting dependency is shown in Fig. 5.10 (right).

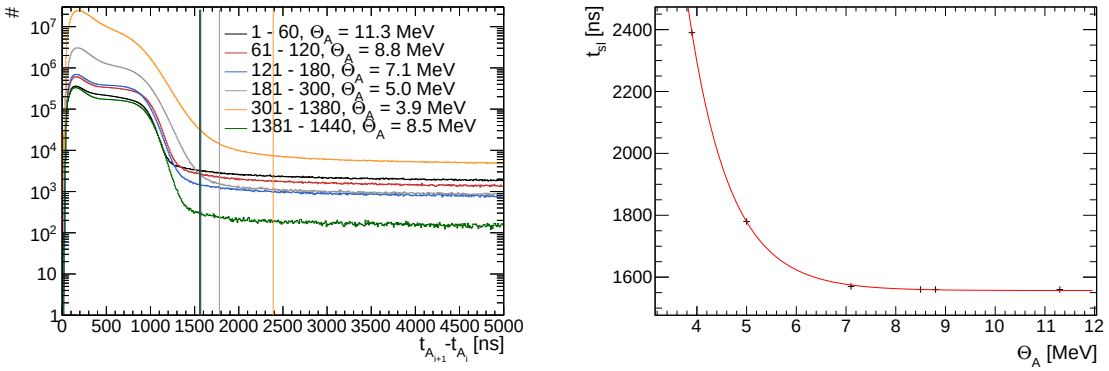

Subsequent time differences

Fit to transitions points

Figure A.11: Left: Subsequent time differences in crystals which only contain timestamps at threshold A during data taking in May 2018. The maximal time difference used for grouping timestamps via the single-linkage procedure is defined to be the transition point to a flat behavior created by random coincidences. Right: Fit of Eqn. A.1 to the threshold dependent transition points.

A.4 Clustering of A timestamps

In situations where only timestamps are available at threshold A, no artificial dead time can be applied. Instead, these timestamps are grouped into pulses according to the principle of single-linkage. The time difference for the single-linkage principle t_{sl} is determined by examination of subsequent time differences in crystals which only contain timestamps at threshold A (cf. Fig. A.11 (left)). At some time difference, a transition to random coincidences is visible. Preceding entries can be associated with the behavior of a group. The determination of the transition point is based on the same procedure as already used for the determination of the artificial dead time. The dependence on the threshold is then described by a simple fit (cf. Fig. A.11 (right))

$$t_{\mathrm{sl}}(\Theta_A) = [0] \cdot \exp\Big[[1] \cdot (\Theta_A - [2])\Big] + [3] \tag{A.1}$$

with parameters

$$\begin{aligned}
[0] &= (82.5 \pm 0.5) \times 10^4 \\
[1] &= (-1.20 \pm 0.02) \\
[2] &= (-1.84 \pm 0.04) \\
[3] &= (1.556 \pm 0.002) \times 10^3.
\end{aligned}$$

An exception applies to timestamps at threshold A which occur shortly before a AB pattern, i.e. the beginning of a new pulse. These timestamps are likely to correspond to noise at the leading edge. Thus, timestamps at threshold A which occur 300 ns before an AB pattern are discarded.

APPENDIX B

Event Selection

This appendix presents additional material to Chapter 7. Section B.1 presents the cut ranges for the coplanarity, missing mass, invariant mass, and polar angle difference. The color scale is chosen so that yellow areas correspond to regions where wide cuts are applied and blue areas correspond to regions where narrow cuts are applied. In addition, the application of these cuts is illustrated in a series of example distributions for 5-PED, 4.5-PED and 4-PED events (cf. Fig. B.3 to B.12). The distributions can be used to get a feel for the effect of the cut ranges. They also give transparent insight into the performance of the carbon scaling, which is explained in Chapter 8. The scale on the y-axis is kept constant to give a sense of the statistics in the different kinematic regions. Section B.2 and B.3 show the impact of cuts and the kinematic fit for 4.5-PED and 4-PED events. The distributions for 5-PED events are presented in the work. Section B.4 presents the event distributions after event selection for 5-PED, 4.5-PED and 4-PED events. Finally, in Section B.5 a collection of example fits determining the Q-factor are shown. They can be used to assess the quality of the fitting method. The background ξ for certain combinations of kinematic variables is also presented, as well as the size of hyperspheres.

B.1 Cut Ranges of Kinematic Cuts

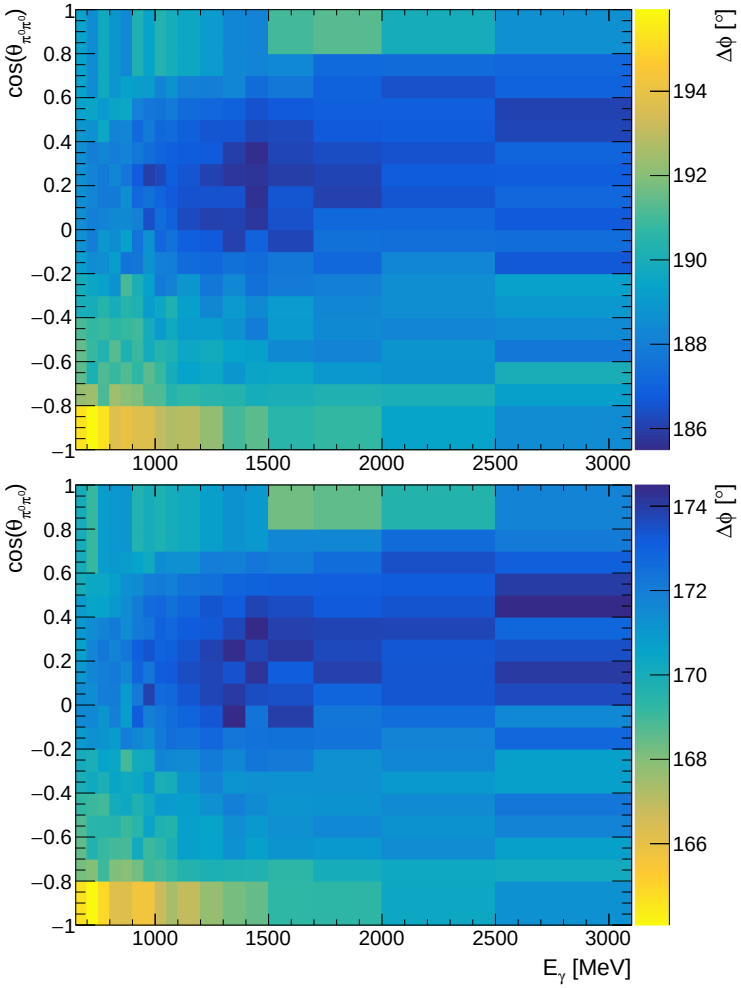

Coplanarity

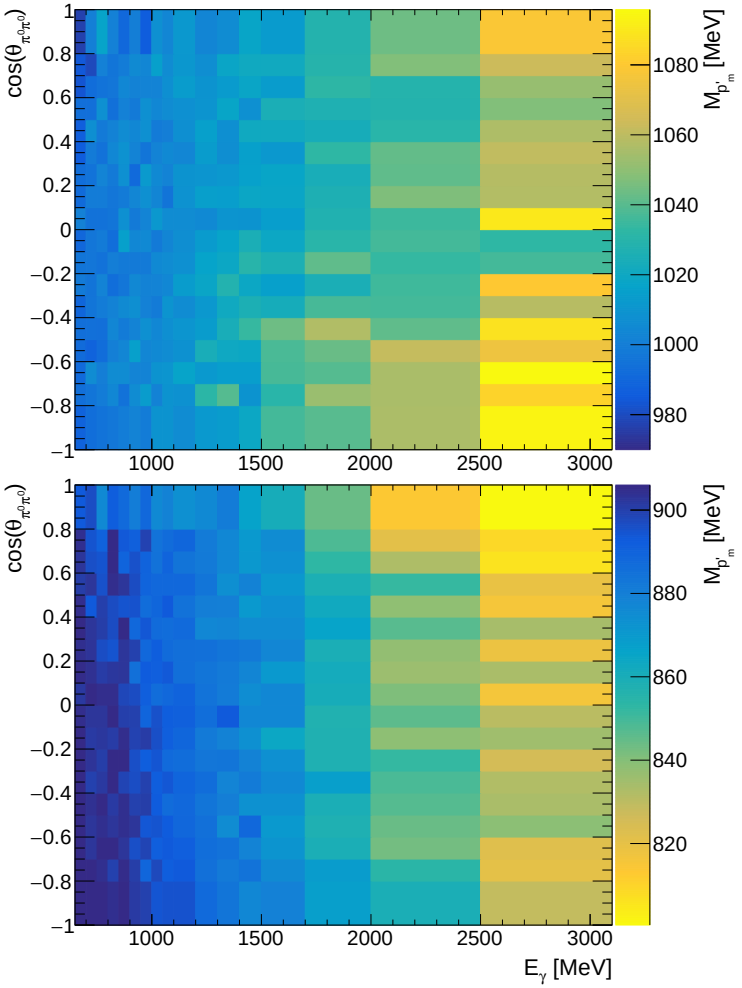

Missing mass

Figure B.1: Cut ranges for coplanarity and missing mass distributions as function of the beam energy E_γ and the cosine of the polar angle of the mesons in the CMS $\cos(\theta_{\pi^0\pi^0})$.

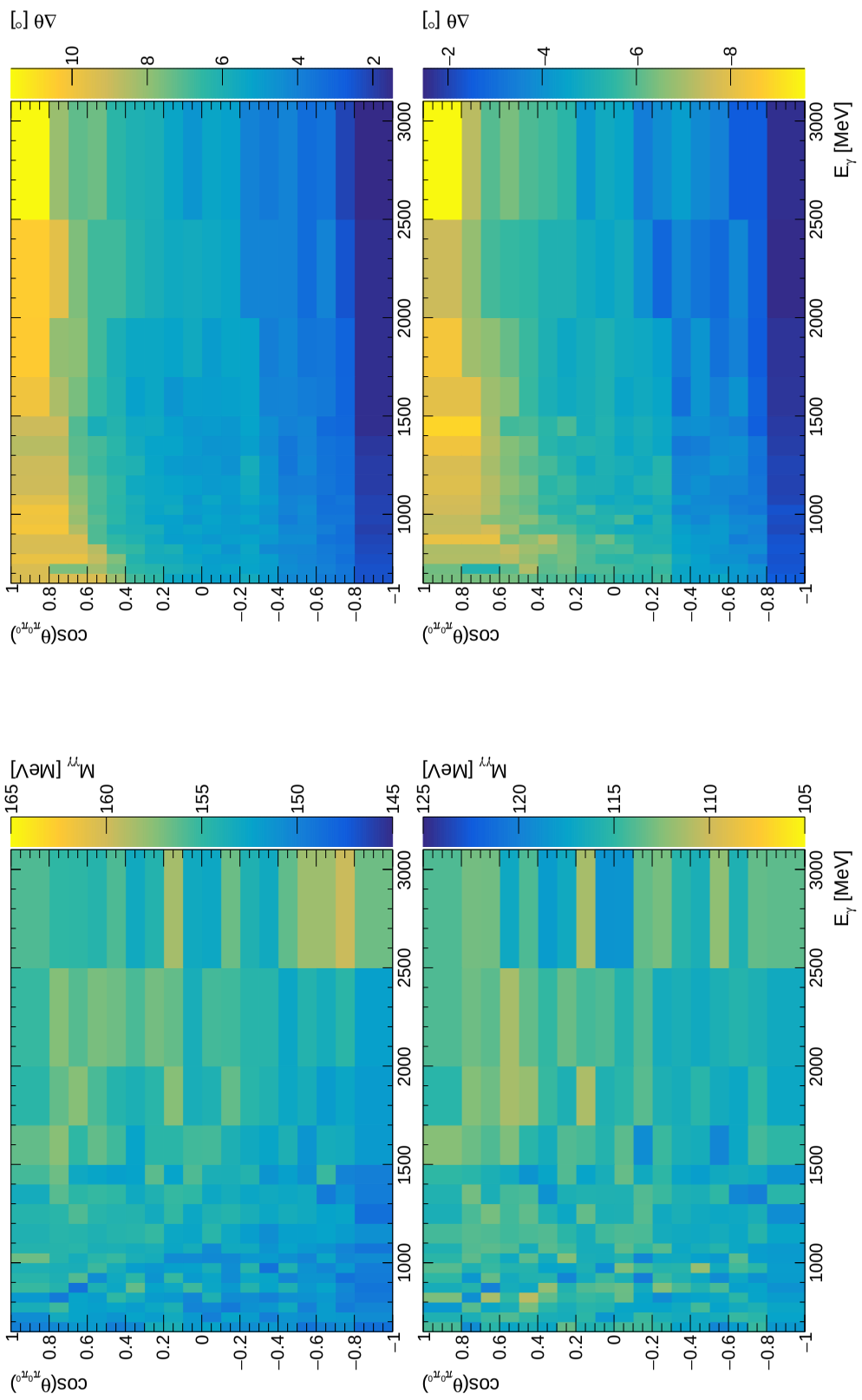

Polar angle difference

Invariant mass

Figure B.2: Cut ranges for invariant mass and polar angle distributions as function of the beam energy E_γ and the cosine of the polar angle of the mesons in the CMS $\cos(\theta_{\pi^0\pi^0})$.

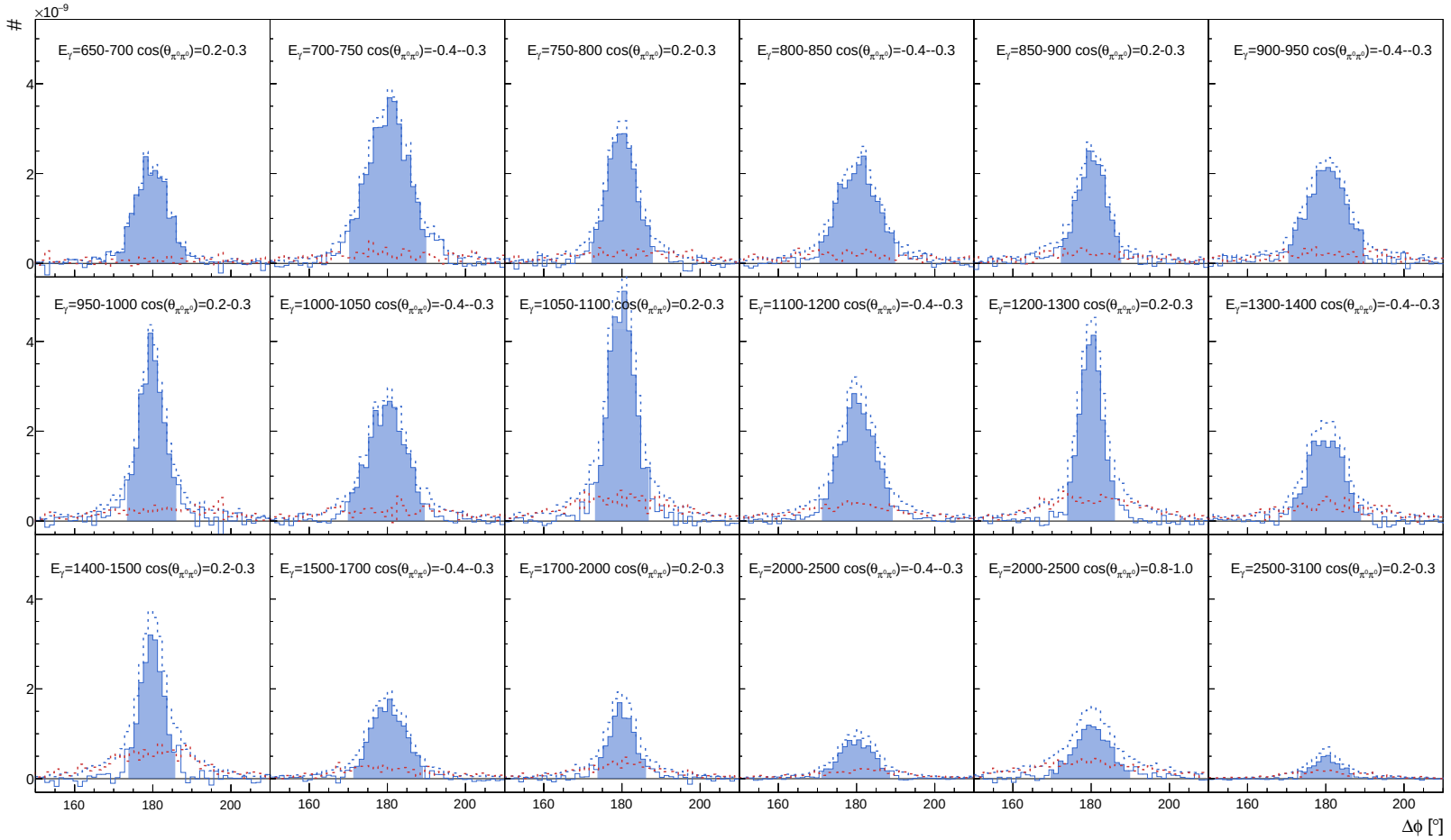

Figure B.3: Coplanarity distribution of 5-PED events for a collection of different E_γ and $\cos(\theta_{\pi^0\pi^0})$ bins for data taken in December 2017, May 2018, February 2019, and June 2021. The bins are randomly selected from areas where 5-PED events are expected. The butanol distribution before carbon subtraction and the scaled carbon distribution are shown as dashed lines. The butanol distribution with carbon subtraction is shown as solid line. The filled area corresponds to the cut range from Fig. B.1. In every case, all kinematic cuts are applied except of the one shown here.

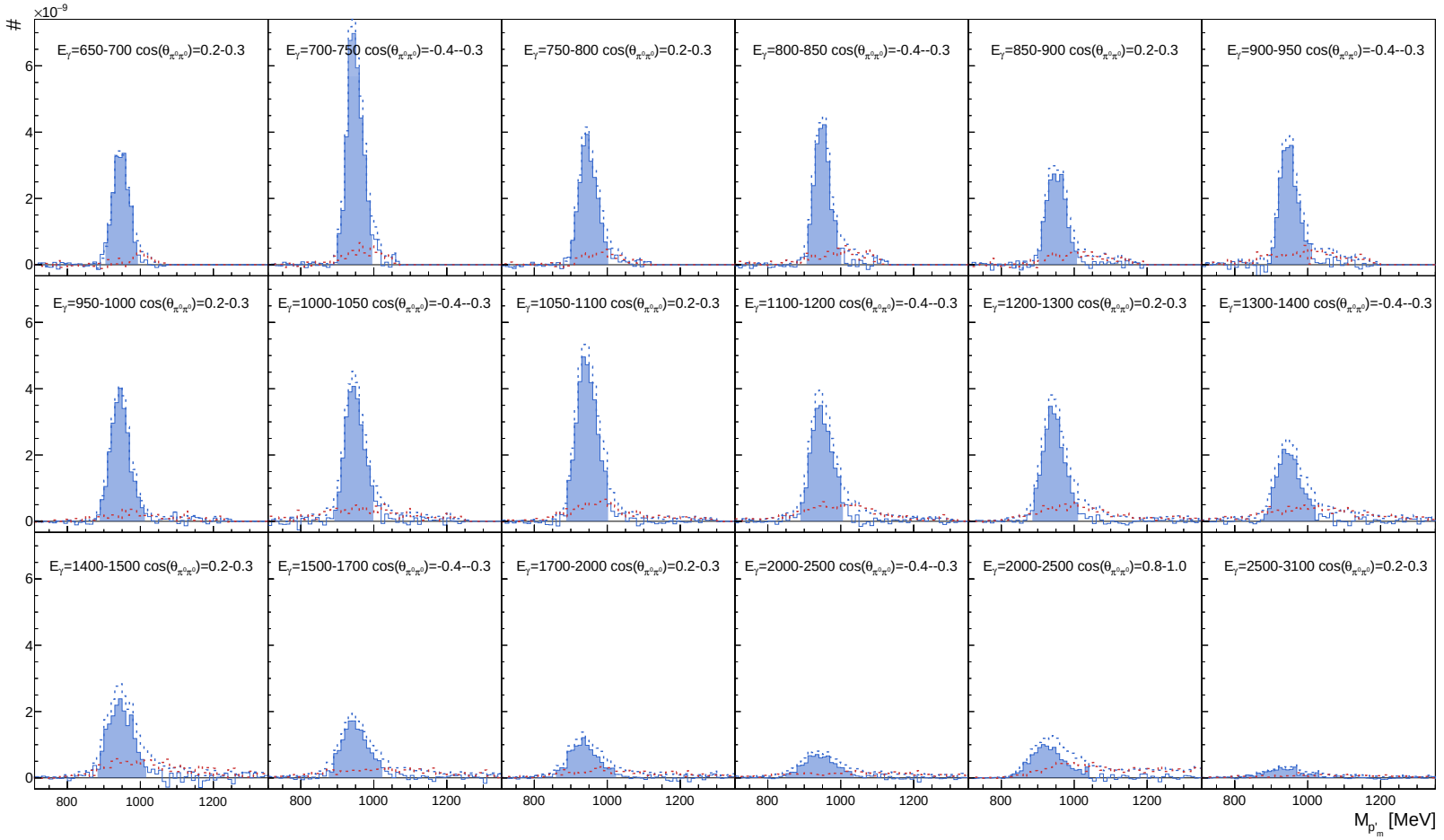

Figure B.4: Missing mass distribution of 5-PED events for a collection of different E_γ and $\cos(\theta_{\pi^0\pi^0})$ bins for data taken in December 2017, May 2018, February 2019, and June 2021. The bins are randomly selected from areas where 5-PED events are expected. The butanol distribution before carbon subtraction and the scaled carbon distribution are shown as dashed lines. The butanol distribution with carbon subtraction is shown as solid line. The filled area corresponds to the cut range from Fig. B.1. In every case, all kinematic cuts are applied except of the one shown here.

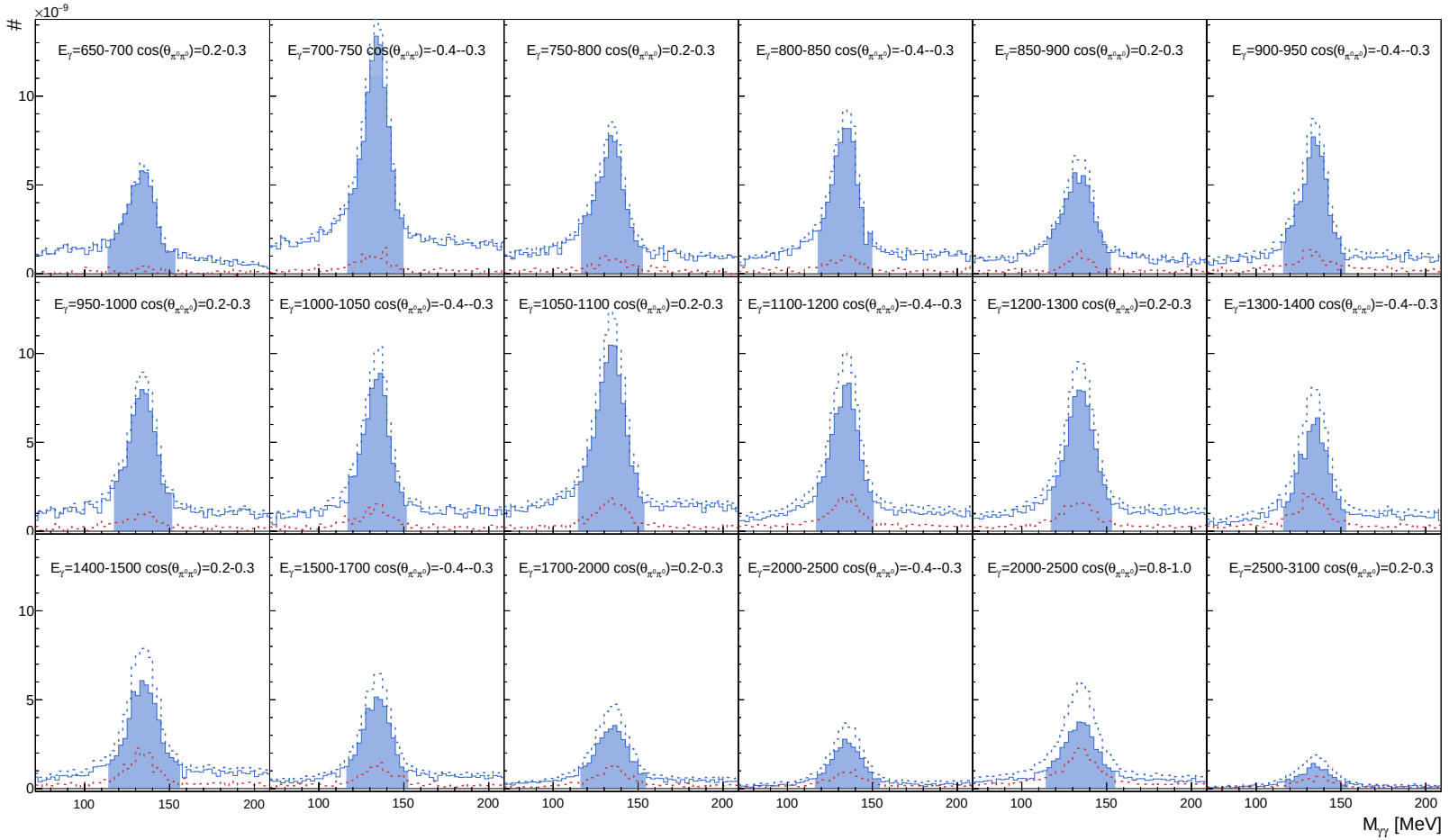

Figure B.5: Invariant mass distribution of 5-PED events for a collection of different E_γ and $\cos(\theta_{\pi^0\pi^0})$ bins for data taken in December 2017, May 2018, February 2019, and June 2021. The bins are randomly selected from areas where 5-PED events are expected. The butanol distribution before carbon subtraction and the scaled carbon distribution are shown as dashed lines. The butanol distribution with carbon subtraction is shown as solid line. The filled area corresponds to the cut range from Fig. B.2. In every case, all kinematic cuts are applied except of the one shown here.

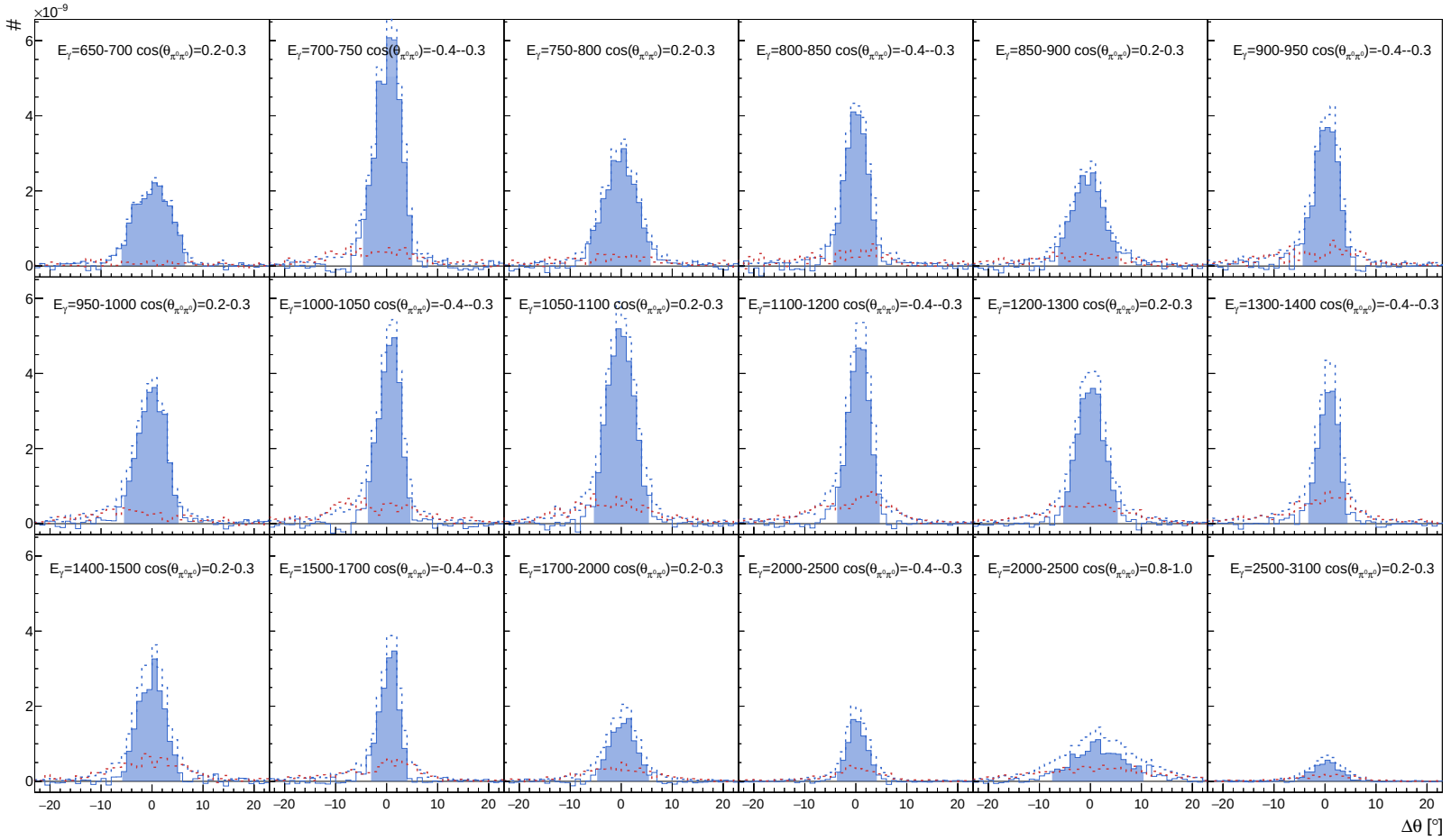

Figure B.6: Polar angle distribution of 5-PED events for a collection of different E_γ and $\cos(\theta_{\pi^0\pi^0})$ bins for data taken in December 2017, May 2018, February 2019, and June 2021. The bins are randomly selected from areas where 5-PED events are expected. The butanol distribution before carbon subtraction and the scaled carbon distribution are shown as dashed lines. The butanol distribution with carbon subtraction is shown as solid line. The filled area corresponds to the cut range from Fig. B.2. In every case, all kinematic cuts are applied except of the one shown here.

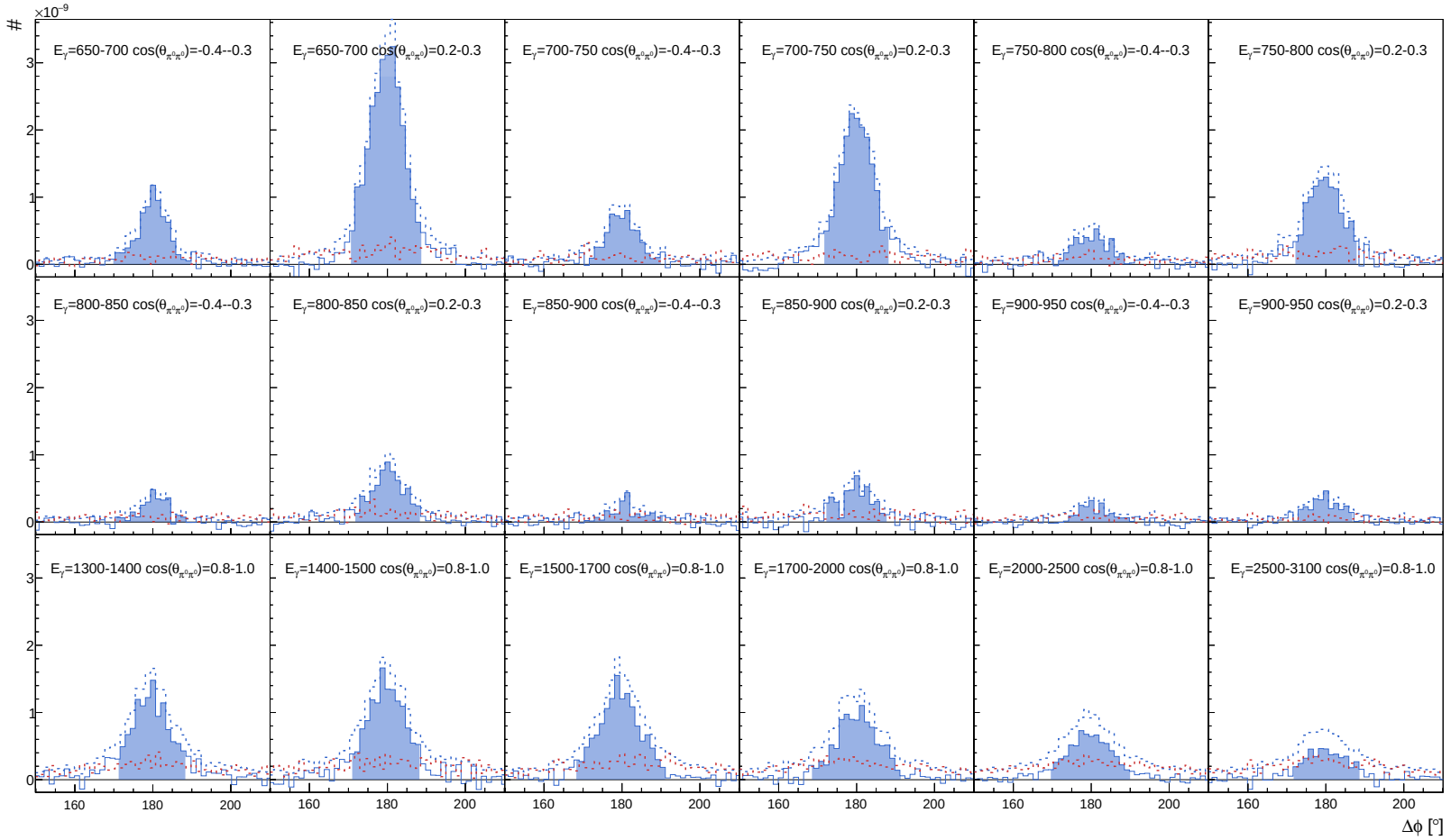

Figure B.7: Coplanarity distribution of 4.5-PED events for a collection of different E_γ and $\cos(\theta_{\pi^0\pi^0})$ bins for data taken in December 2017, May 2018, February 2019, and June 2021. The bins are randomly selected from areas where 4.5-PED events are expected. The butanol distribution before carbon subtraction and the scaled carbon distribution are shown as dashed lines. The butanol distribution with carbon subtraction is shown as solid line. The filled area corresponds to the cut range from Fig. B.1. In every case, all kinematic cuts are applied except of the one shown here.

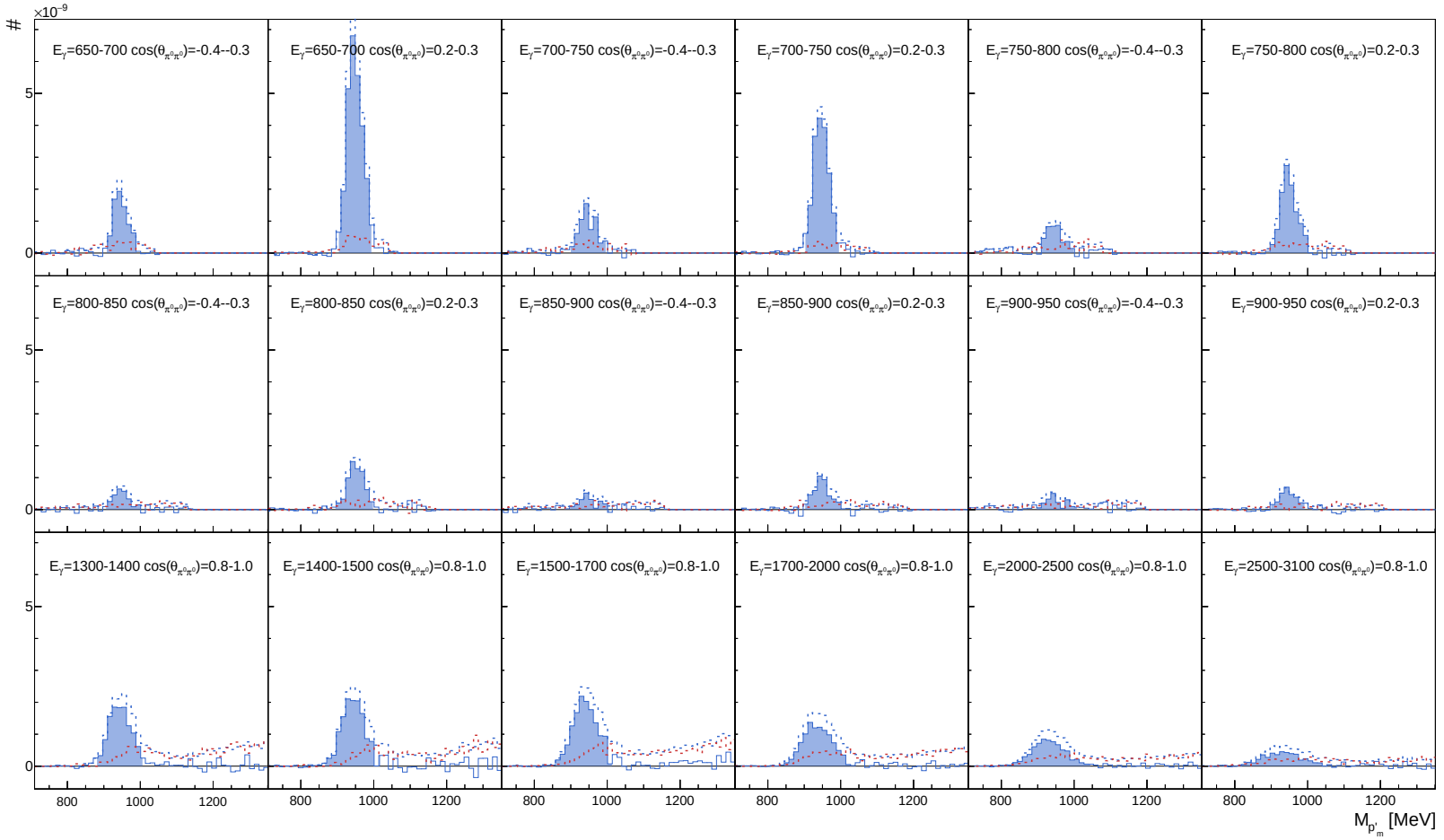

Figure B.8: Missing mass distribution of 4.5-PED events for a collection of different E_γ and $\cos(\theta_{\pi^0\pi^0})$ bins for data taken in December 2017, May 2018, February 2019, and June 2021. The bins are randomly selected from areas where 4.5-PED events are expected. The butanol distribution before carbon subtraction and the scaled carbon distribution are shown as dashed lines. The butanol distribution with carbon subtraction is shown as solid line. The filled area corresponds to the cut range from Fig. B.1. In every case, all kinematic cuts are applied except of the one shown here.

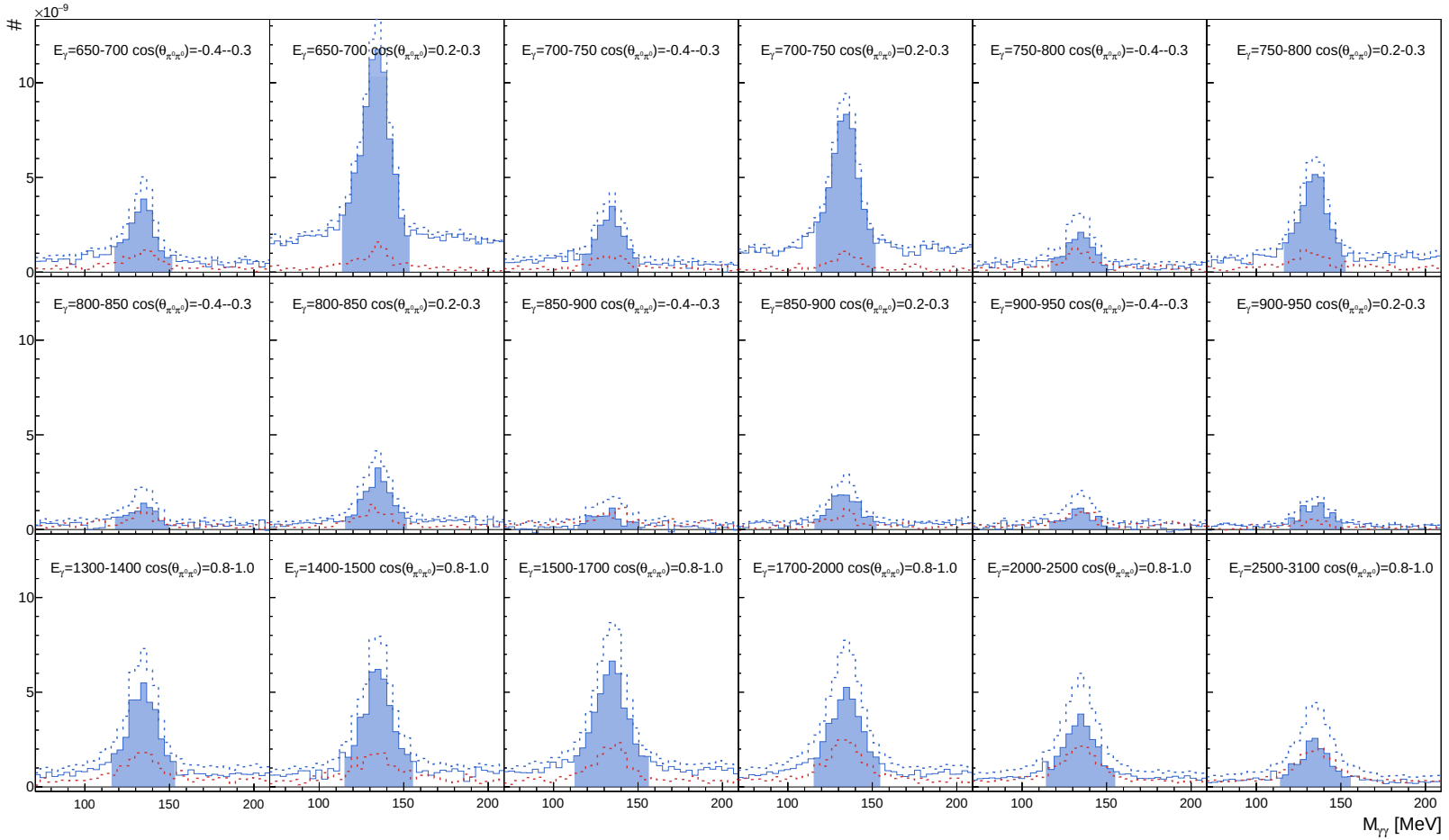

Figure B.9: Invariant mass distribution of 4.5-PED events for a collection of different E_γ and $\cos(\theta_{\pi^0\pi^0})$ bins for data taken in December 2017, May 2018, February 2019, and June 2021. The bins are randomly selected from areas where 4.5-PED events are expected. The butanol distribution before carbon subtraction and the scaled carbon distribution are shown as dashed lines. The butanol distribution with carbon subtraction is shown as solid line. The filled area corresponds to the cut range from Fig. B.2. In every case, all kinematic cuts are applied except of the one shown here.

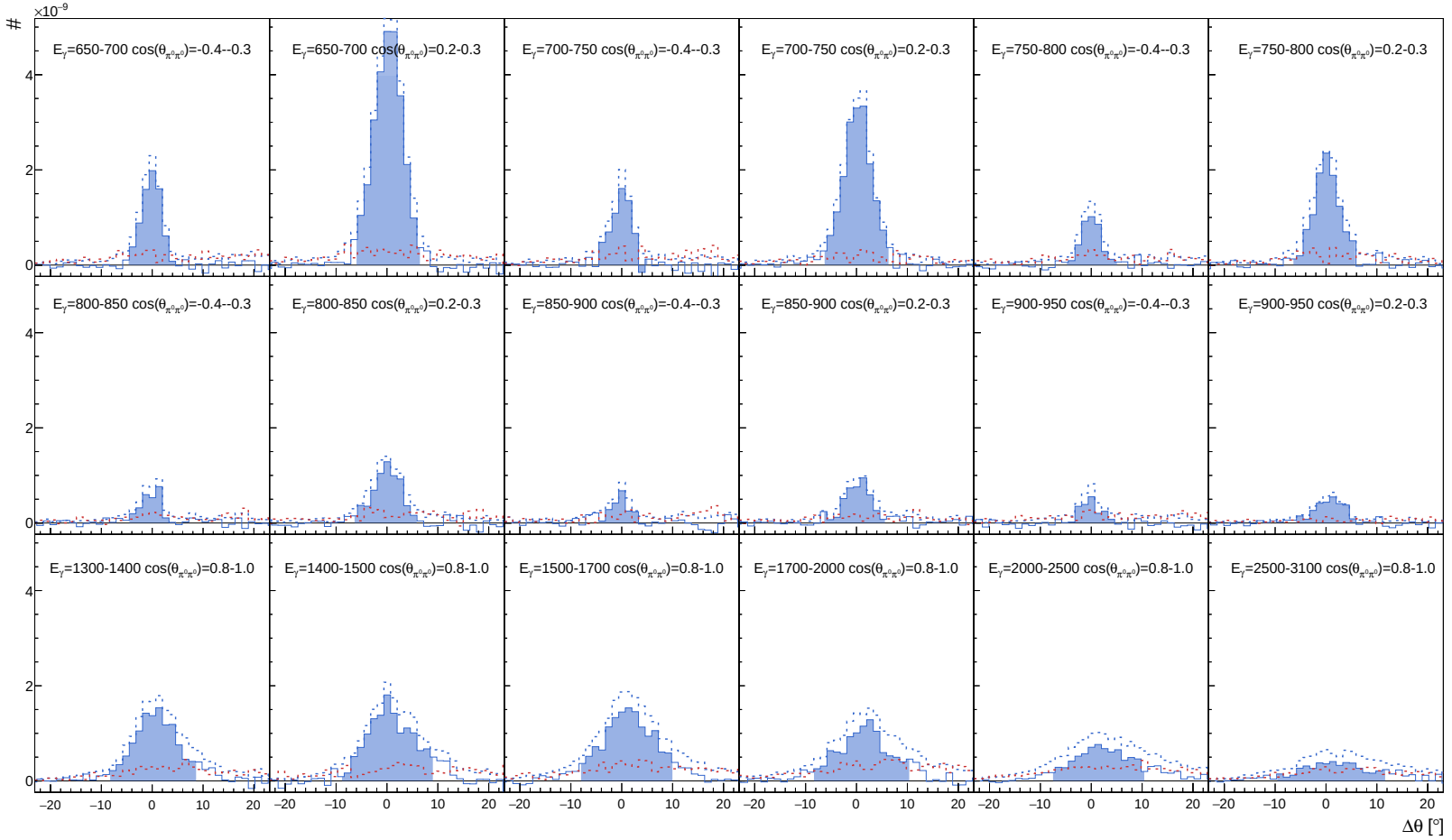

Figure B.10: Polar angle distribution of 4.5-PED events for a collection of different E_γ and $\cos(\theta_{\pi^0\pi^0})$ bins for data taken in December 2017, May 2018, February 2019, and June 2021. The bins are randomly selected from areas where 4.5-PED events are expected. The butanol distribution before carbon subtraction and the scaled carbon distribution are shown as dashed lines. The butanol distribution with carbon subtraction is shown as solid line. The filled area corresponds to the cut range from Fig. B.2. In every case, all kinematic cuts are applied except of the one shown here.

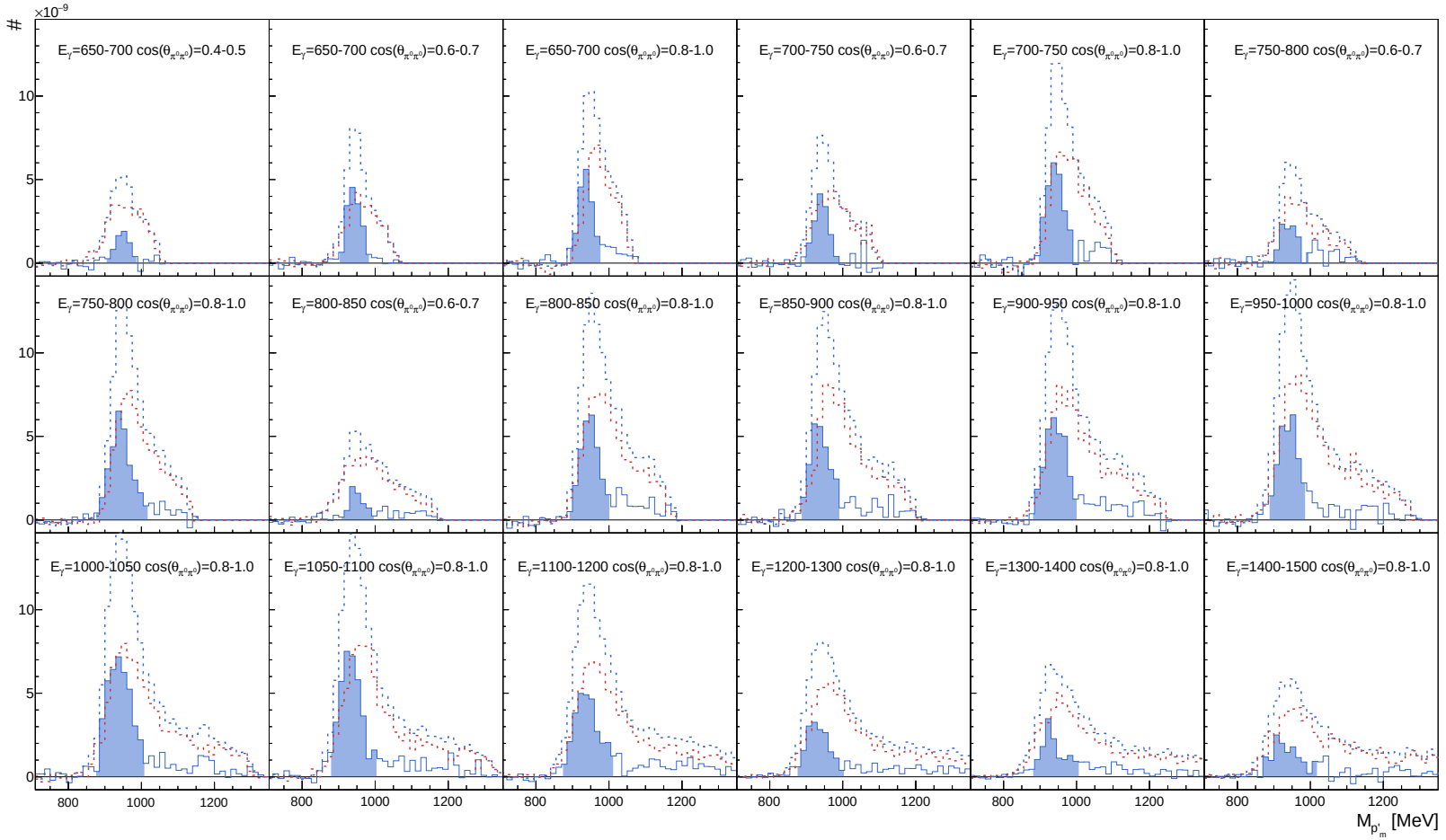

Figure B.11: Missing mass distribution of 4-PED events for a collection of different E_γ and $\cos(\theta_{\pi^0\pi^0})$ bins for data taken in December 2017, May 2018, February 2019, and June 2021. The bins are randomly selected from areas where 4-PED events are expected. The butanol distribution before carbon subtraction and the scaled carbon distribution are shown as dashed lines. The butanol distribution with carbon subtraction is shown as solid line. The filled area corresponds to the cut range from Fig. B.1. In every case, all kinematic cuts are applied except of the one shown here.

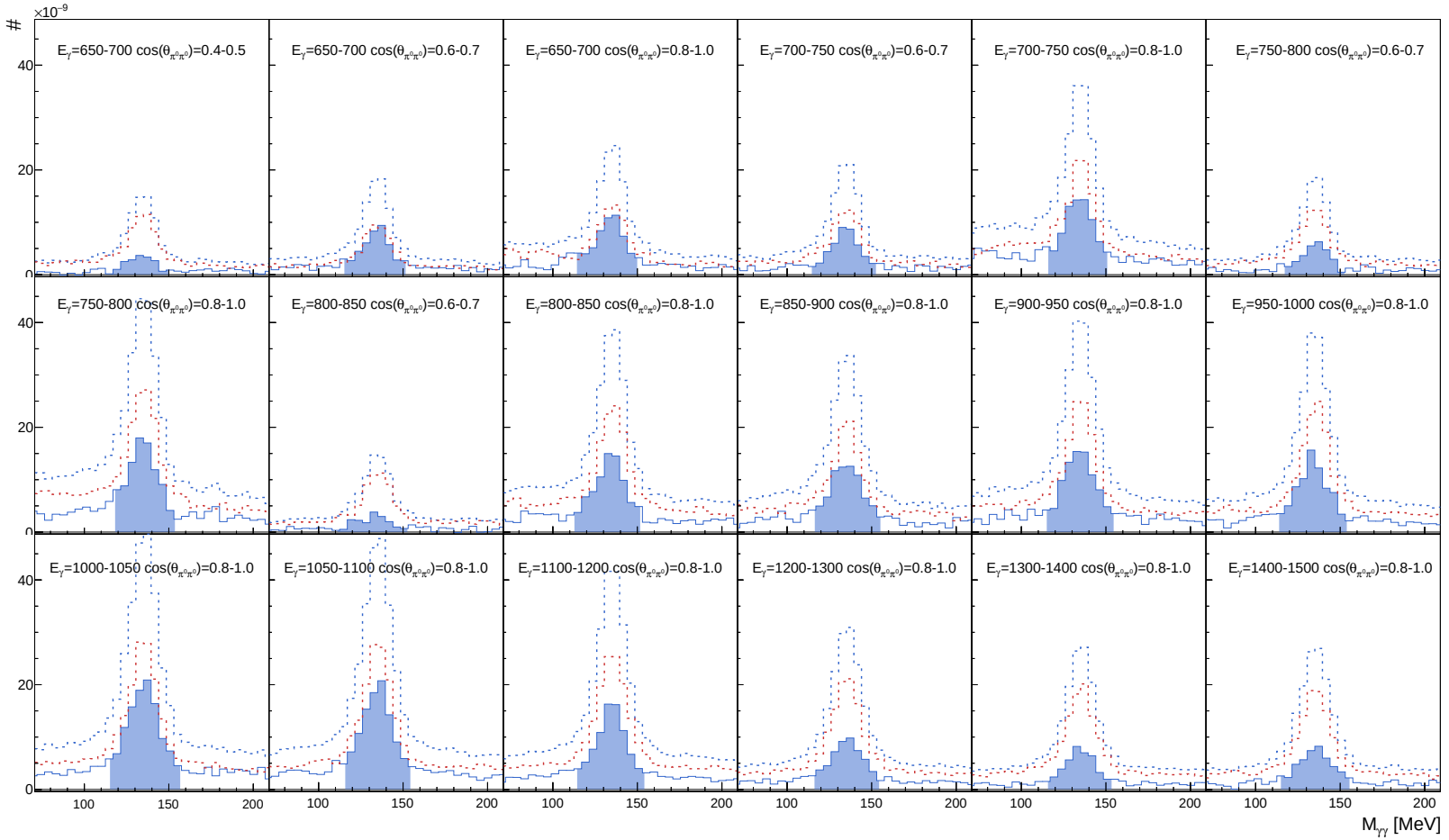

Figure B.12: Invariant mass distribution of 4-PED events for a collection of different E_γ and $\cos(\theta_{\pi^0\pi^0})$ bins for data taken in December 2017, May 2018, February 2019, and June 2021. The bins are randomly selected from areas where 4-PED events are expected. The butanol distribution before carbon subtraction and the scaled carbon distribution are shown as dashed lines. The butanol distribution with carbon subtraction is shown as solid line. The filled area corresponds to the cut range from Fig. B.2. In every case, all kinematic cuts are applied except of the one shown here.

B.2 Effect of Cuts on 4.5-PED and 4-PED Events

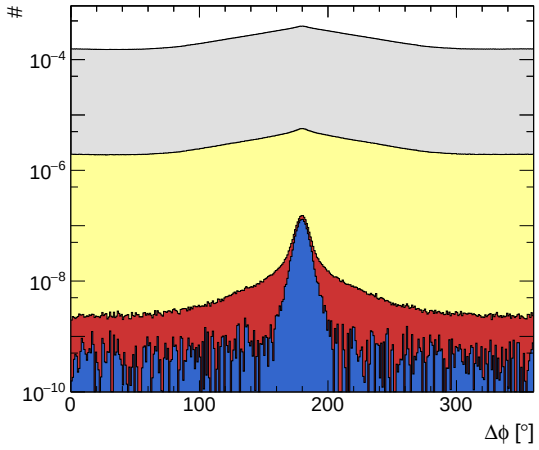

Coplanarity

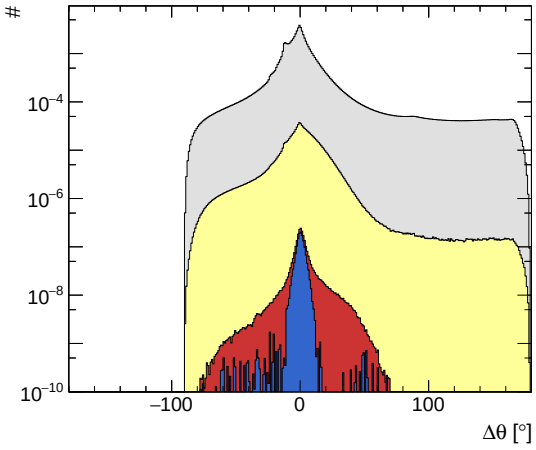

Polar angle difference

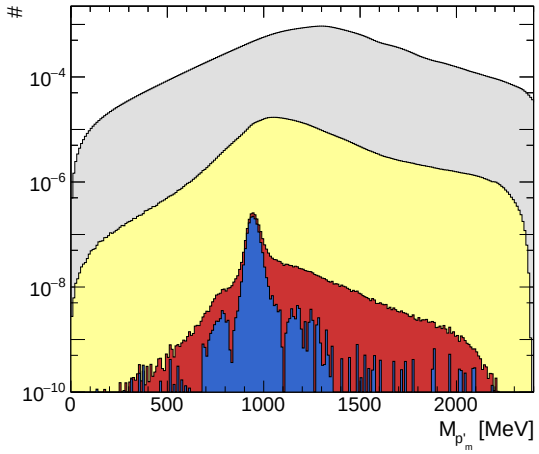

Missing mass

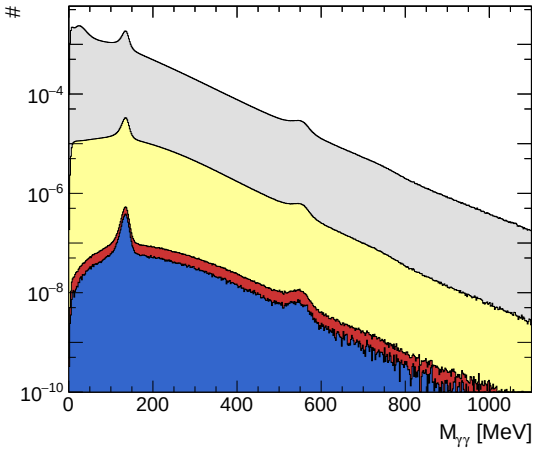

Invariant mass

Figure B.13: Effect of the cuts on the kinematic variables for 4.5-PED events. The distributions before any cuts, before kinematic cuts but with time cuts as well as the distributions after kinematic cuts are shown. In each case, all kinematic cuts are applied except the one shown in the picture. For completeness, the distribution after carbon subtraction is also shown. Flux normalization is applied. The combined data of December 2017, May 2018, February 2019, and June 2021 is used. Note that the y-axis is logarithmic.

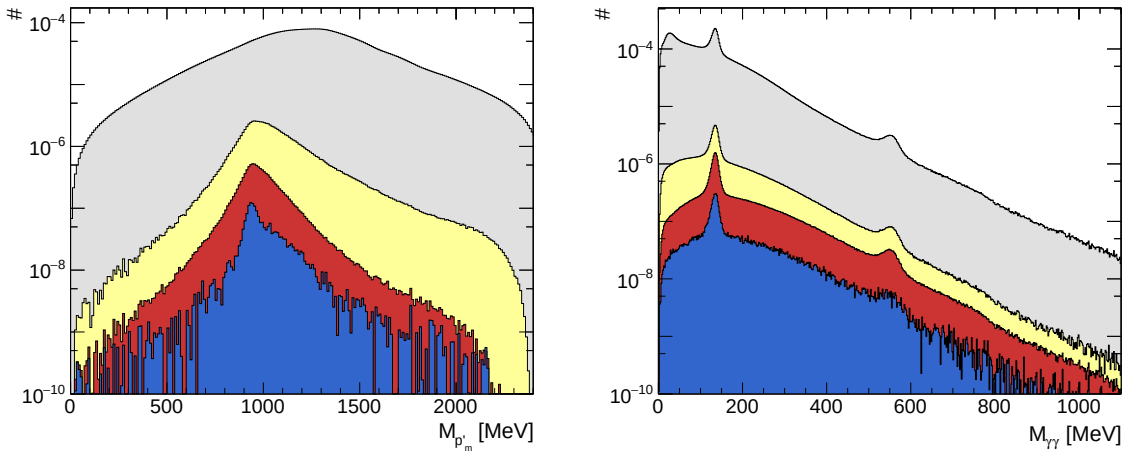

Missing mass Invariant mass

Figure B.14: Effect of the cuts on the kinematic variables for 4-PED events. For a description, cf. Fig. B.13

B.3 Effect of Kinematic Fit on 4.5-PED and 4-PED Events

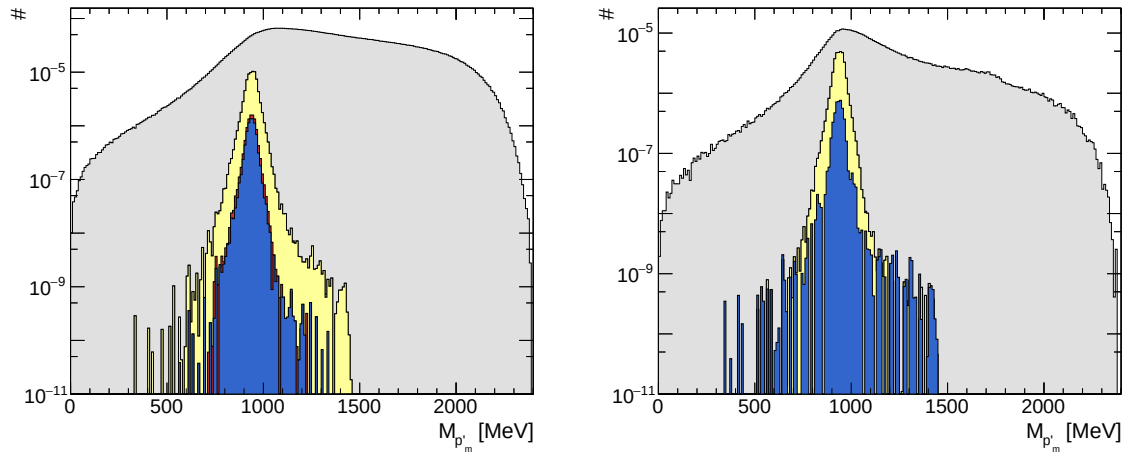

4.5-PED 4-PED

Figure B.15: Effect of the kinematic fit on the missing mass distribution for 4.5-PED and 4-PED events. Since the missing mass after the kinematic fit is limited to the literature value, the measured values are used. The distribution after time cuts but before cuts on the CL is shown as well as the distribution with cut on the hypothesis and additional cut on the anti-hypothesis. The anti-cut has only a small effect and is not visible (the yellow distribution is on top of the green distribution). The distribution after angle cuts is also shown, as is the final distribution after carbon subtraction. In each case, flux normalization is applied (cf. Section 8.3.1). Note that the y-axis is logarithmic.

B.4 Distribution of Events

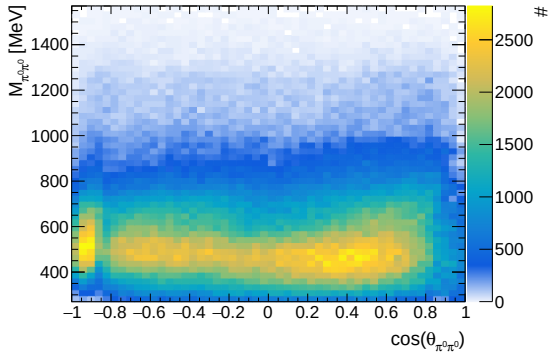

$\cos(\theta_{\pi^0\pi^0})$ vs. $M_{\pi^0\pi^0}$

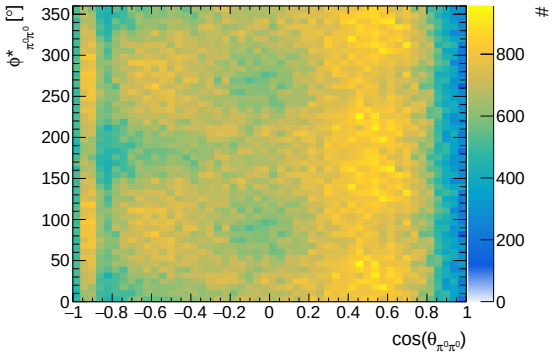

$\cos(\theta_{\pi^0\pi^0})$ vs. $\phi^*_{\pi^0\pi^0}$

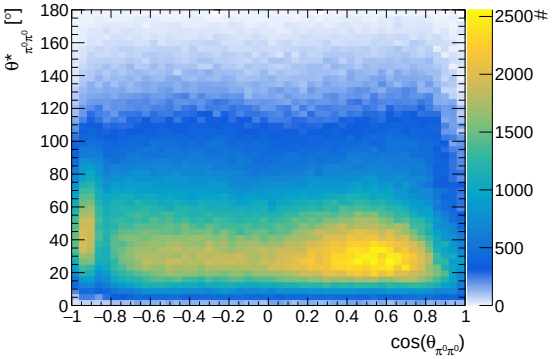

$\cos(\theta_{\pi^0\pi^0})$ vs. $\theta^*_{\pi^0\pi^0}$

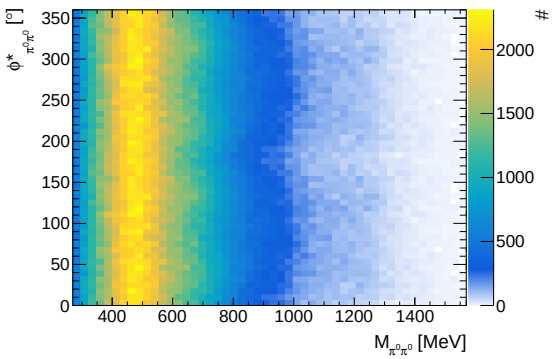

$M_{\pi^0\pi^0}$ vs. $\phi^*_{\pi^0\pi^0}$

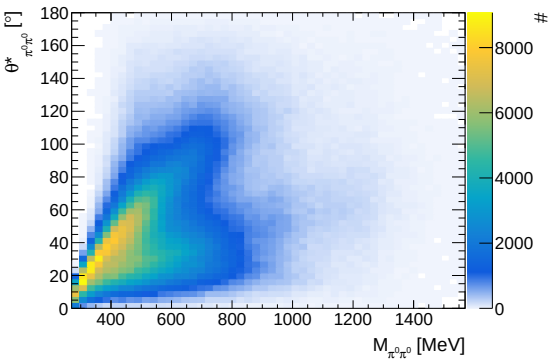

$M_{\pi^0\pi^0}$ vs. $\theta^*_{\pi^0\pi^0}$

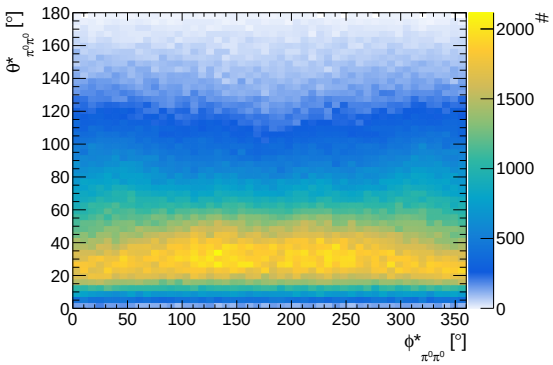

$\phi^*_{\pi^0\pi^0}$ vs. $\theta^*_{\pi^0\pi^0}$

Figure B.16: Distribution of $p\pi^0\pi^0$ events for different kinematic regions. Carbon subtraction (cf. Section 8.3) is performed. All PED classes from December 2017, May 2018, February 2019 and June 2021 are used. The distributions for kinematic variables as function of beam energy E_γ are shown in Fig. 7.10.

B.5 Event Based Q Factor Method

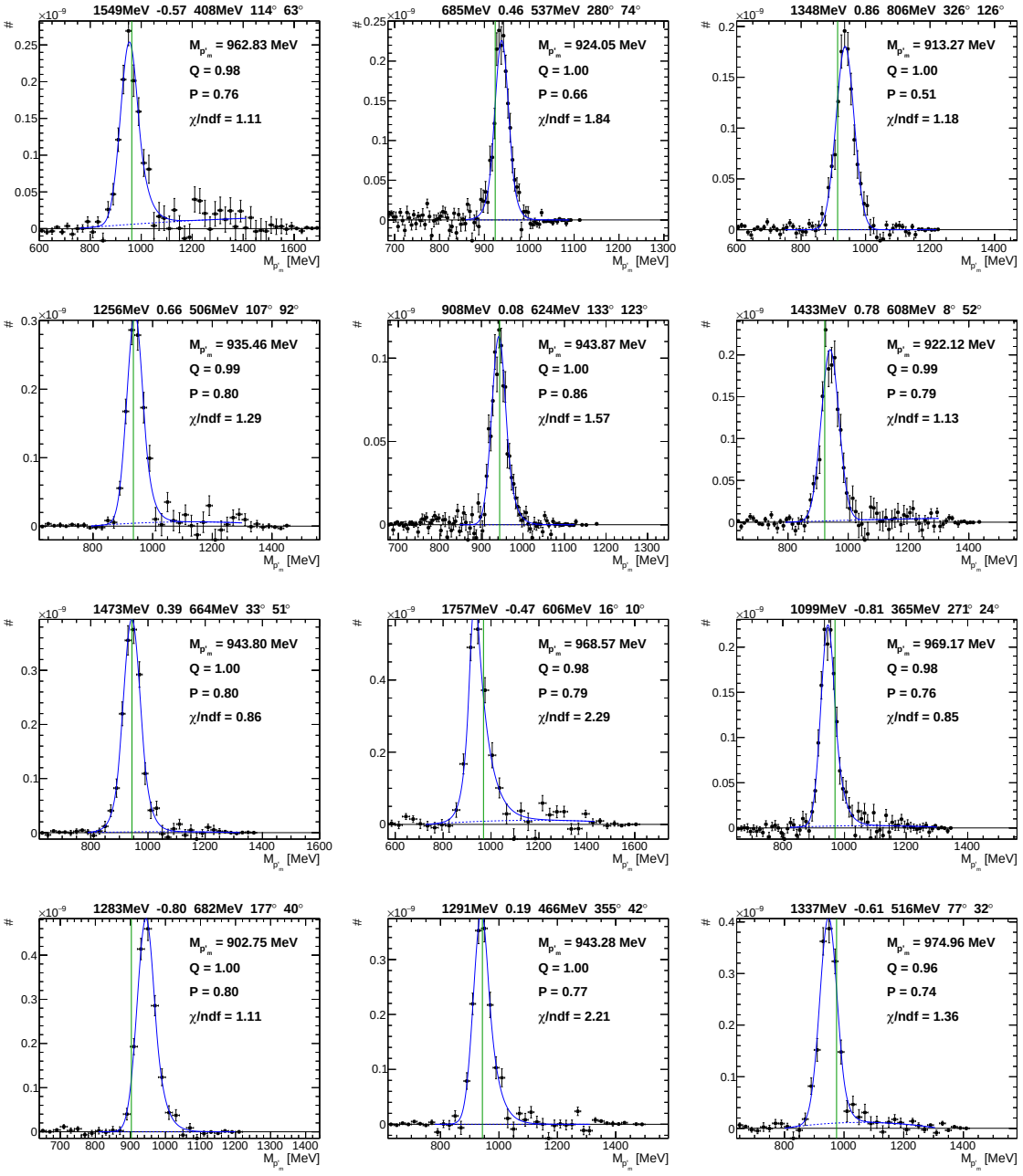

Figure B.17: Fits I of Eqn. 7.12 to the invariant mass distribution of the missing proton for a random collection of points with the kinematic variables $(E_\gamma, \cos(\theta_{\pi^0\pi^0}), M_{\pi^0\pi^0}, \phi^*_{\pi^0\pi^0}, \theta^*_{\pi^0\pi^0})$. The green line represents the missing mass $M_{p'_m}$ of the current point. At this position, the Q-factor is determined. Note that binning varies between the distributions.

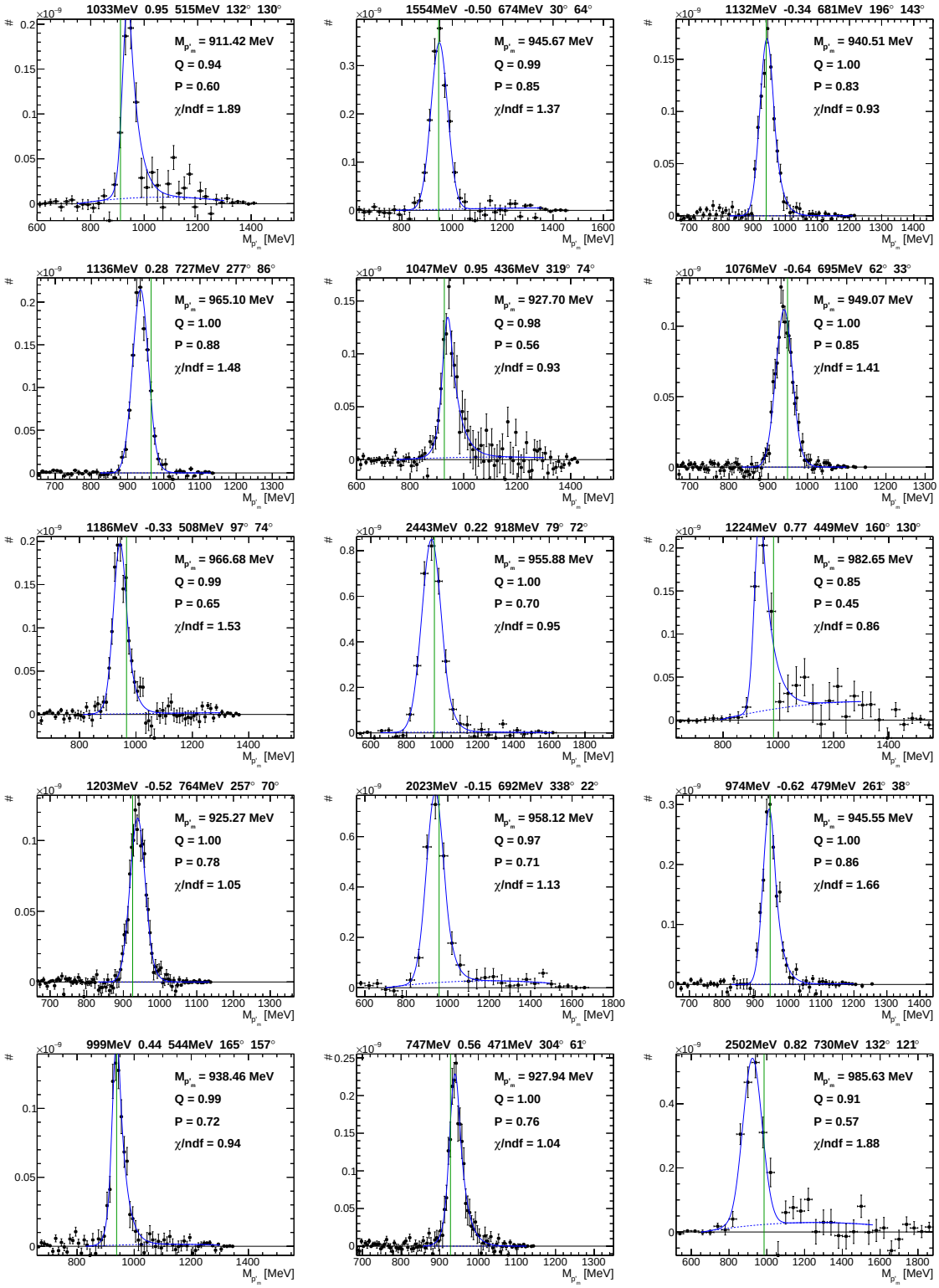

Figure B.18: Fits II of Eqn. 7.12 to the invariant mass distribution of the missing proton for a random collection of points with the kinematic variables $(E_\gamma, \cos(\theta_{\pi^0\pi^0}), M_{\pi^0\pi^0}, \phi^*_{\pi^0\pi^0}, \theta^*_{\pi^0\pi^0})$. For a description, cf. Fig. B.17.

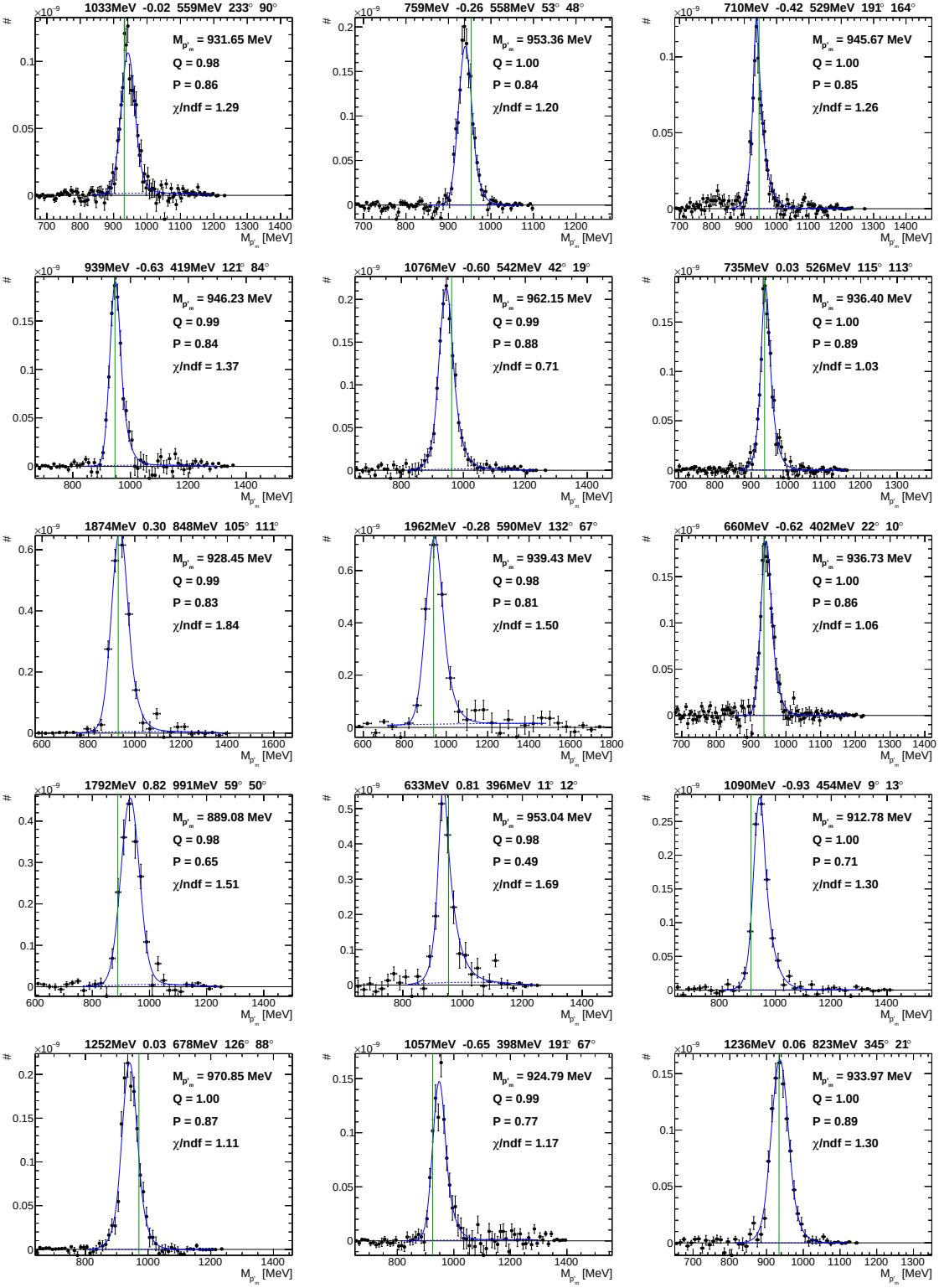

Figure B.19: Fits III of Eqn. 7.12 to the invariant mass distribution of the missing proton for a random collection of points with the kinematic variables $(E_\gamma, \cos(\theta_{\pi^0\pi^0}), M_{\pi^0\pi^0}, \phi^*_{\pi^0\pi^0}, \theta^*_{\pi^0\pi^0})$. For a description, cf. Fig. B.17.

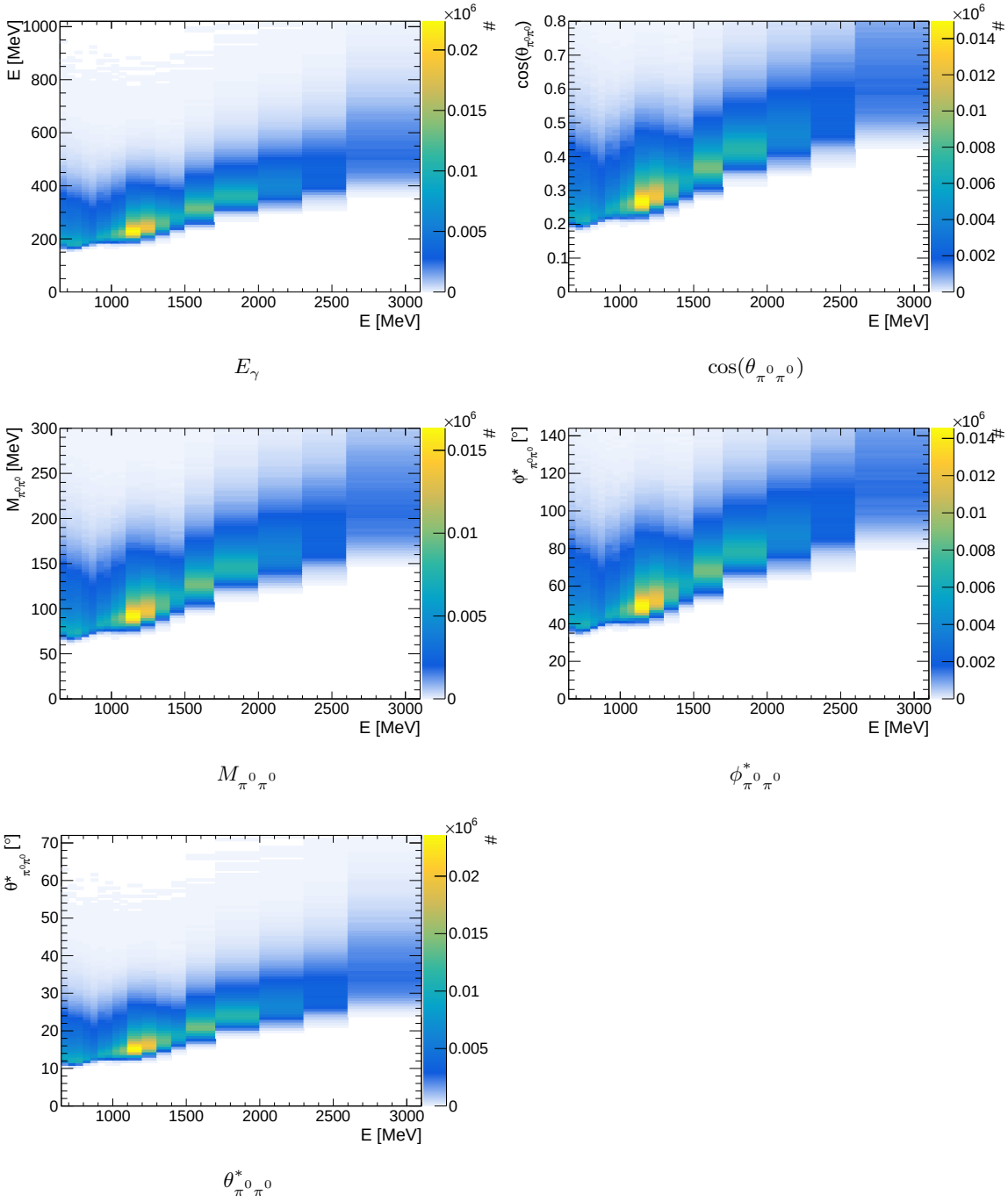

Figure B.20: The total radius of all hyperspheres along each semi-axis $(E_\gamma, \cos(\theta_{\pi^0\pi^0}), M_{\pi^0\pi^0}, \phi^*_{\pi^0\pi^0}, \theta^*_{\pi^0\pi^0})$ as a function of the beam energy E_γ.

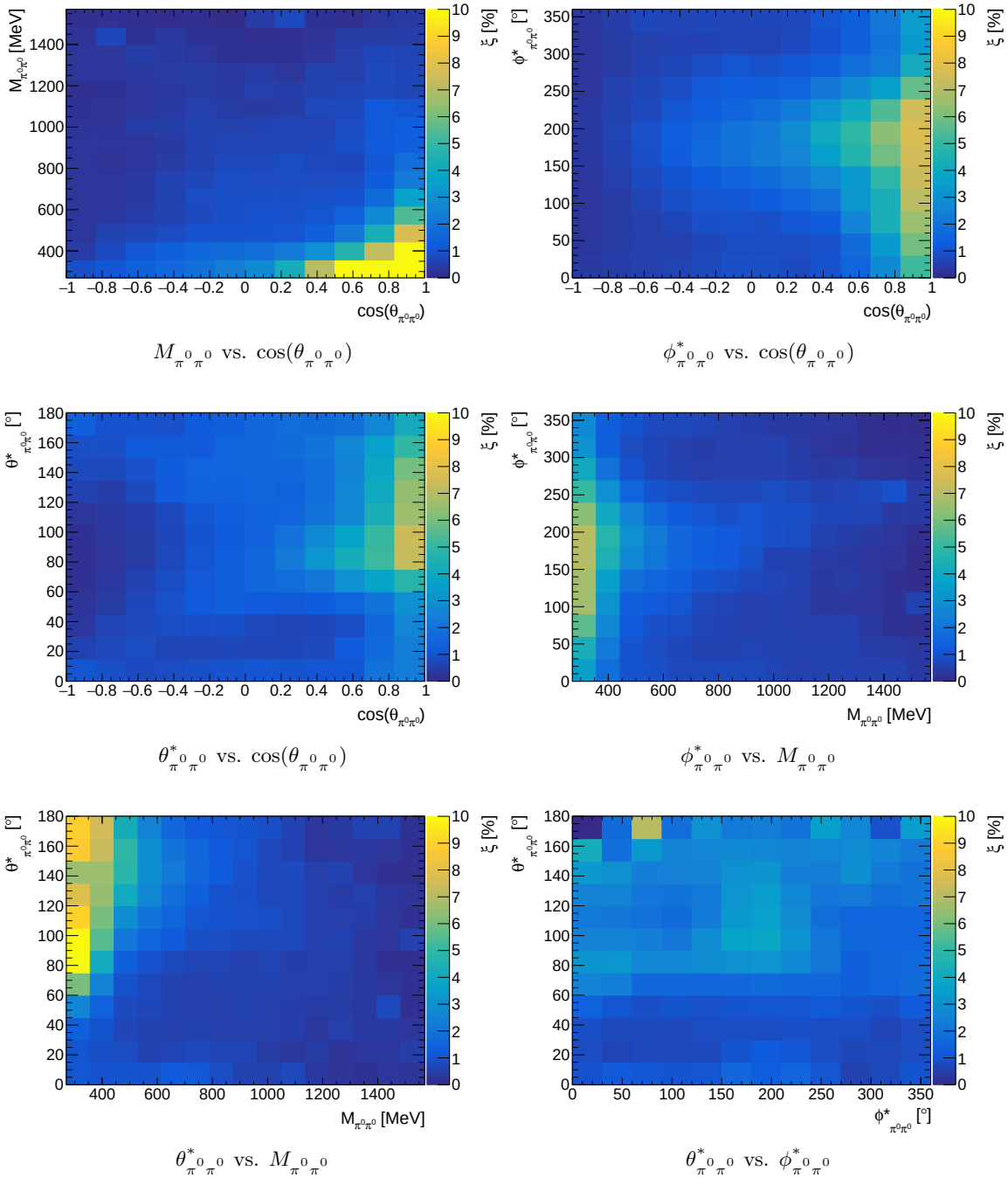

$M_{\pi^0\pi^0}$ vs. $\cos(\theta_{\pi^0\pi^0})$ | $\phi^*_{\pi^0\pi^0}$ vs. $\cos(\theta_{\pi^0\pi^0})$

$\theta^*_{\pi^0\pi^0}$ vs. $\cos(\theta_{\pi^0\pi^0})$ | $\phi^*_{\pi^0\pi^0}$ vs. $M_{\pi^0\pi^0}$

$\theta^*_{\pi^0\pi^0}$ vs. $M_{\pi^0\pi^0}$ | $\theta^*_{\pi^0\pi^0}$ vs. $\phi^*_{\pi^0\pi^0}$

Figure B.21: Background ξ for different kinematic regions. The background for kinematic variables as function of beam energy E_γ is shown in Fig. 7.14.

APPENDIX C

Determination of Polarization Observables

This appendix presents additional material to Chapter 8. In Section C.1, the dilution factor d is presented for various combinations of kinematic variables. In Section C.2, the distributions and normalized residuals of the background polarization observables within the Monto Carlo simulation are presented. The normalized residuals are calculated as the deviations of the extracted polarization observables from the corresponding input parameters normalized to the statistical error (cf. Eqn. 8.33). If the resulting distributions correspond to normal distributions with mean 0 and width 1, the values are in agreement. The distributions of the coefficients used to model the inefficiency in the simulation are shown in the end.

C.1 Dilution Factor d

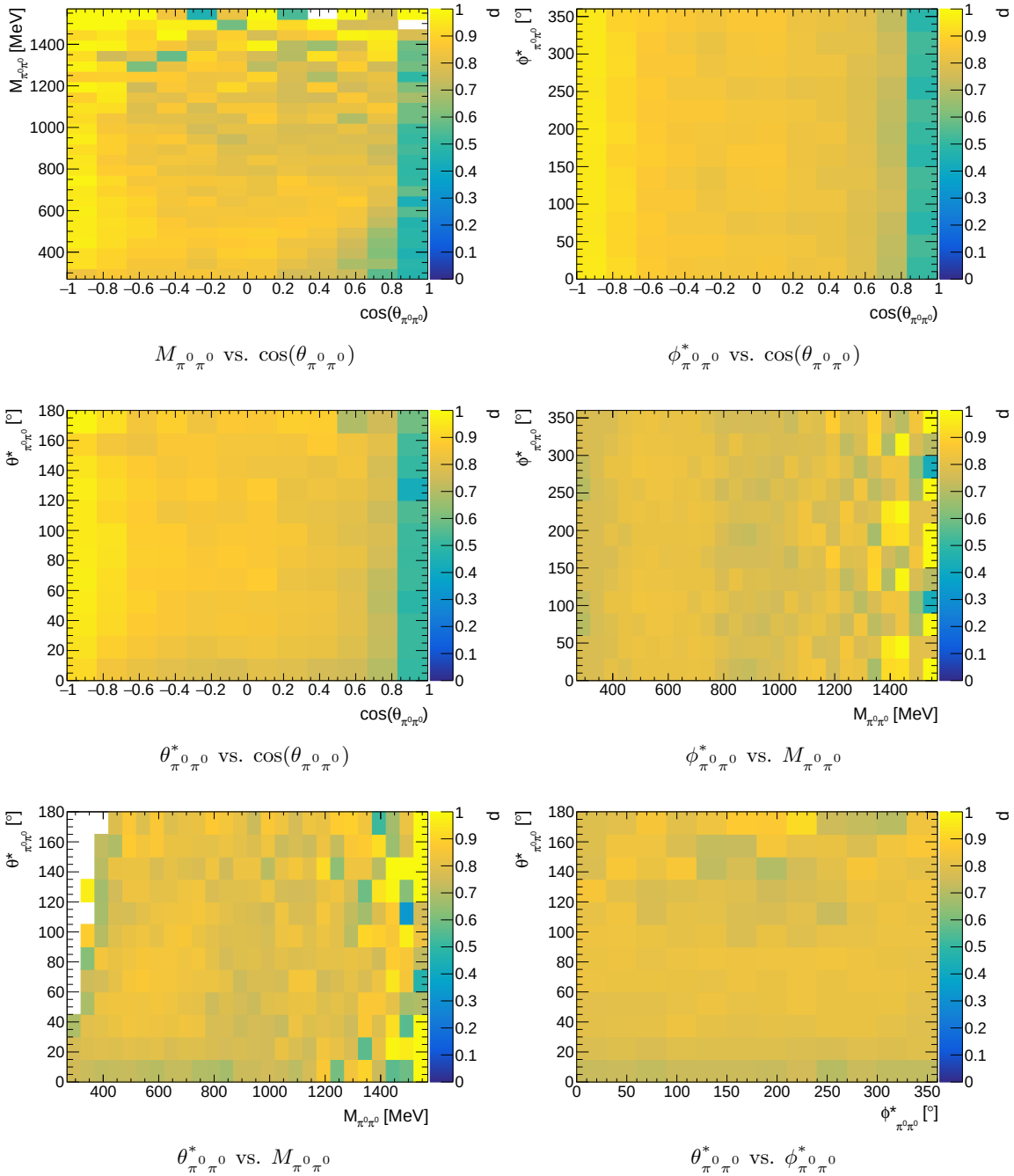

Figure C.1: Dilution factor d for different kinematic regions for the combined data from December 2017, May 2018, February 2019 and June 2021. The dilution factor for kinematic variables as function of beam energy E_γ is shown in Fig. 8.13.

C.2 Toy Monte Carlo Simulation

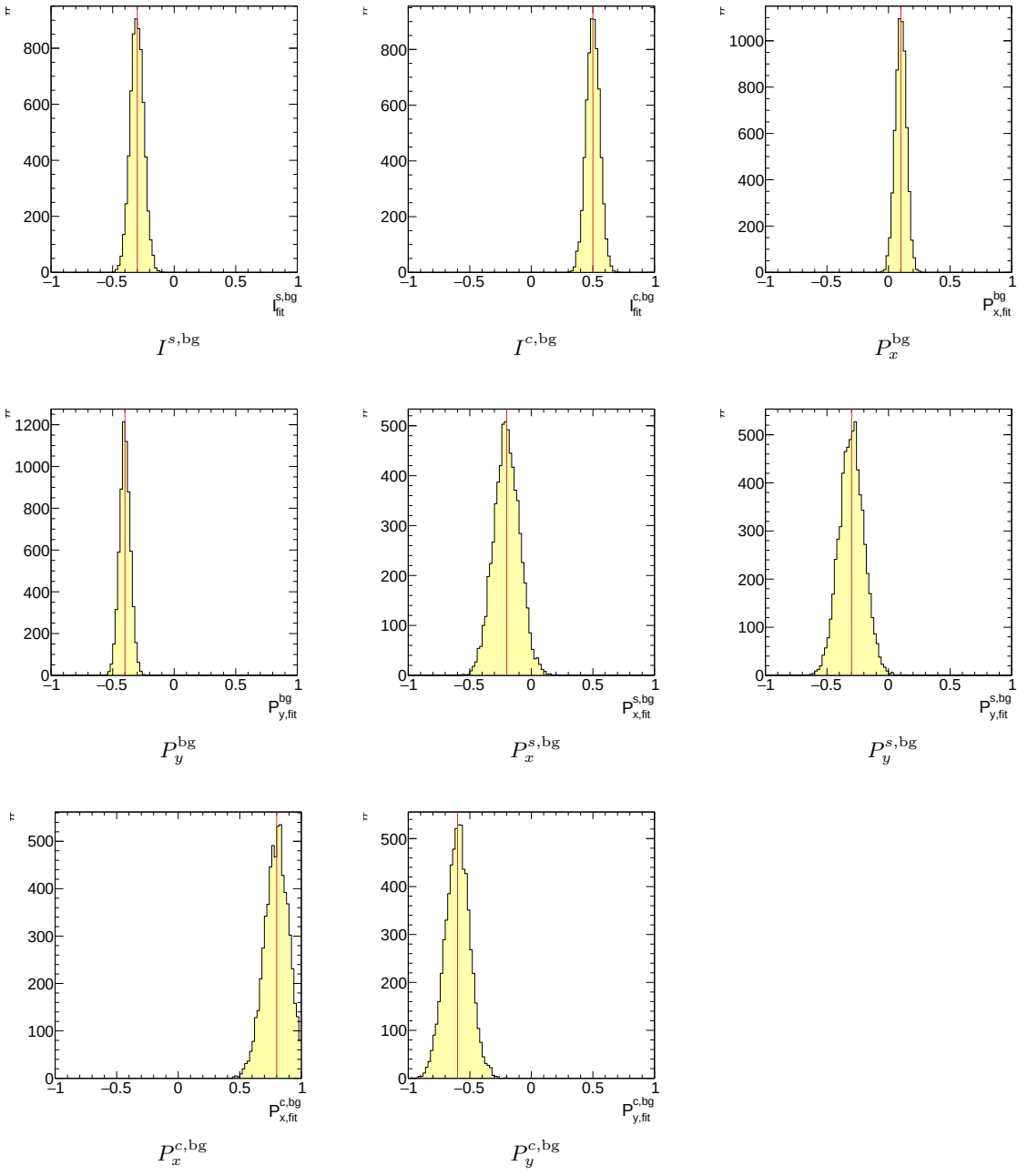

Figure C.2: Distributions of background polarization observables after 6400 Monte Carlo simulations. The input parameters are listed in Table 8.5 and marked as red lines. The corresponding distributions of the normalized residuals are shown in Fig. C.3.

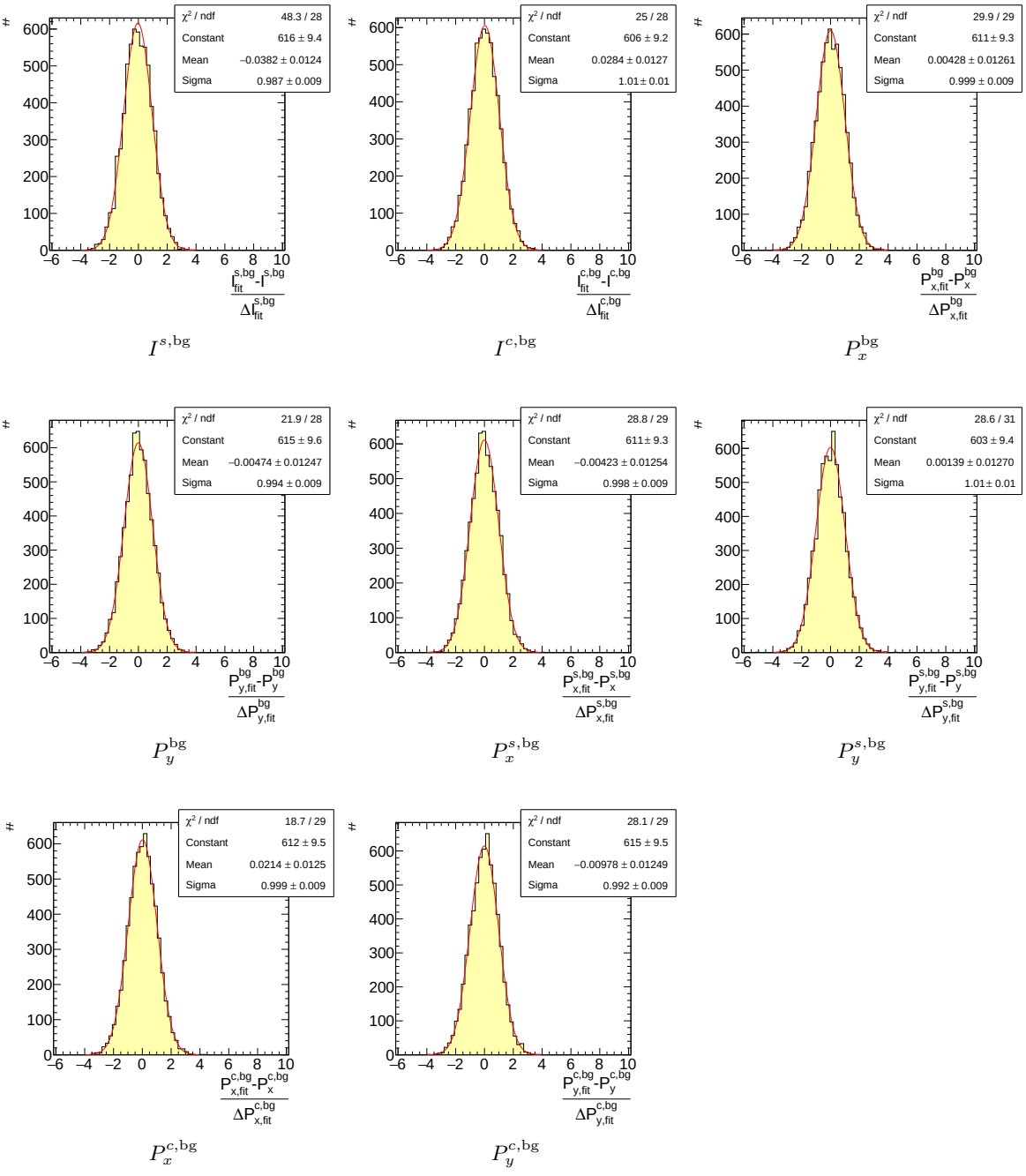

Figure C.3: Normalized residuals of extracted background polarization observables after 6400 Monte Carlo simulations (cf. Eqn. 8.33). If the resulting distributions correspond to a normal distributions with mean 0 and width 1, the extracted values are in agreement with the simulation.

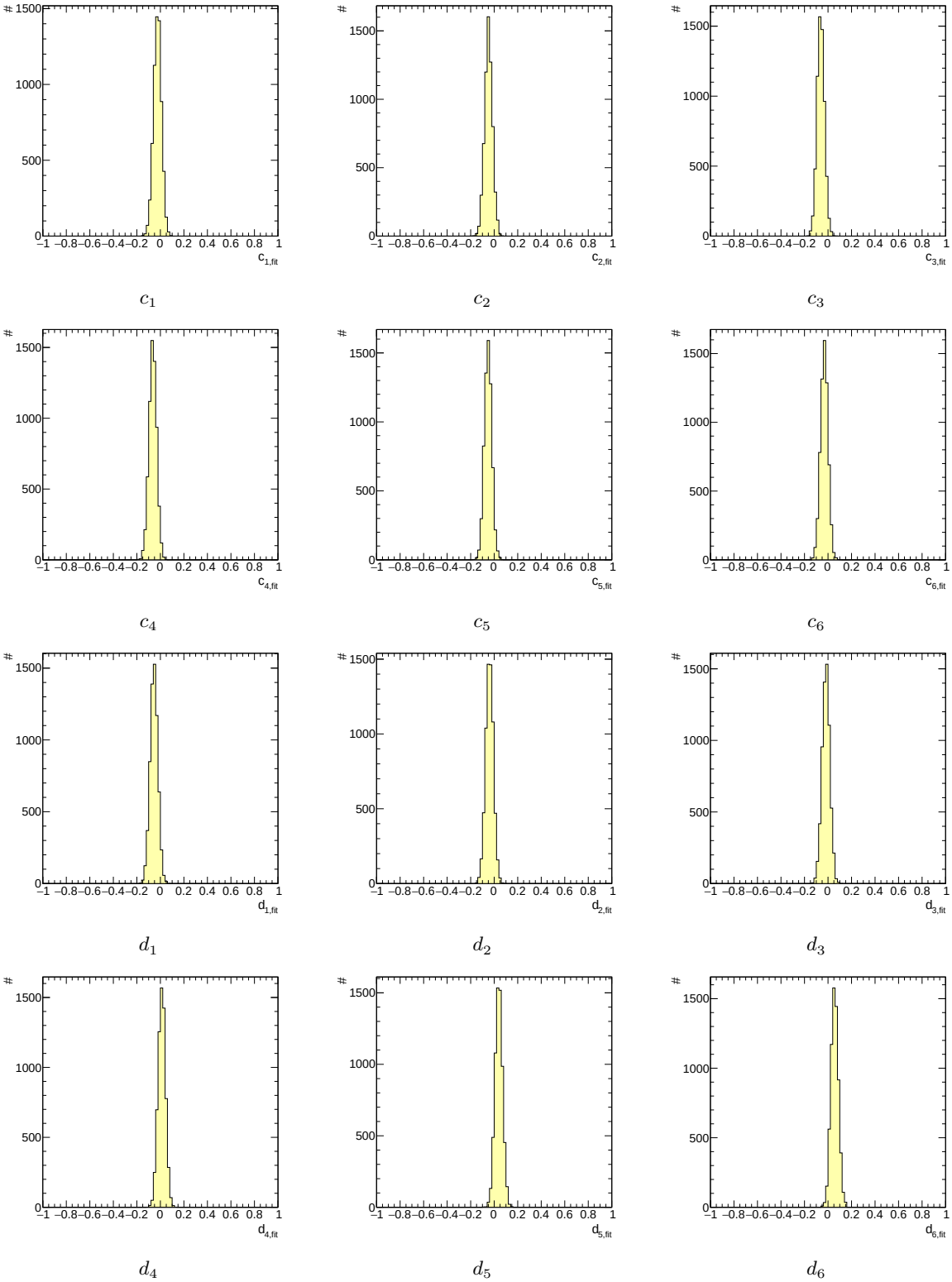

c_1 c_2 c_3

c_4 c_5 c_6

d_1 d_2 d_3

d_4 d_5 d_6

Figure C.4: Distributions of coefficients c_{1-6} and d_{1-6} for the detector efficiency after 6400 Monte Carlo simulations.

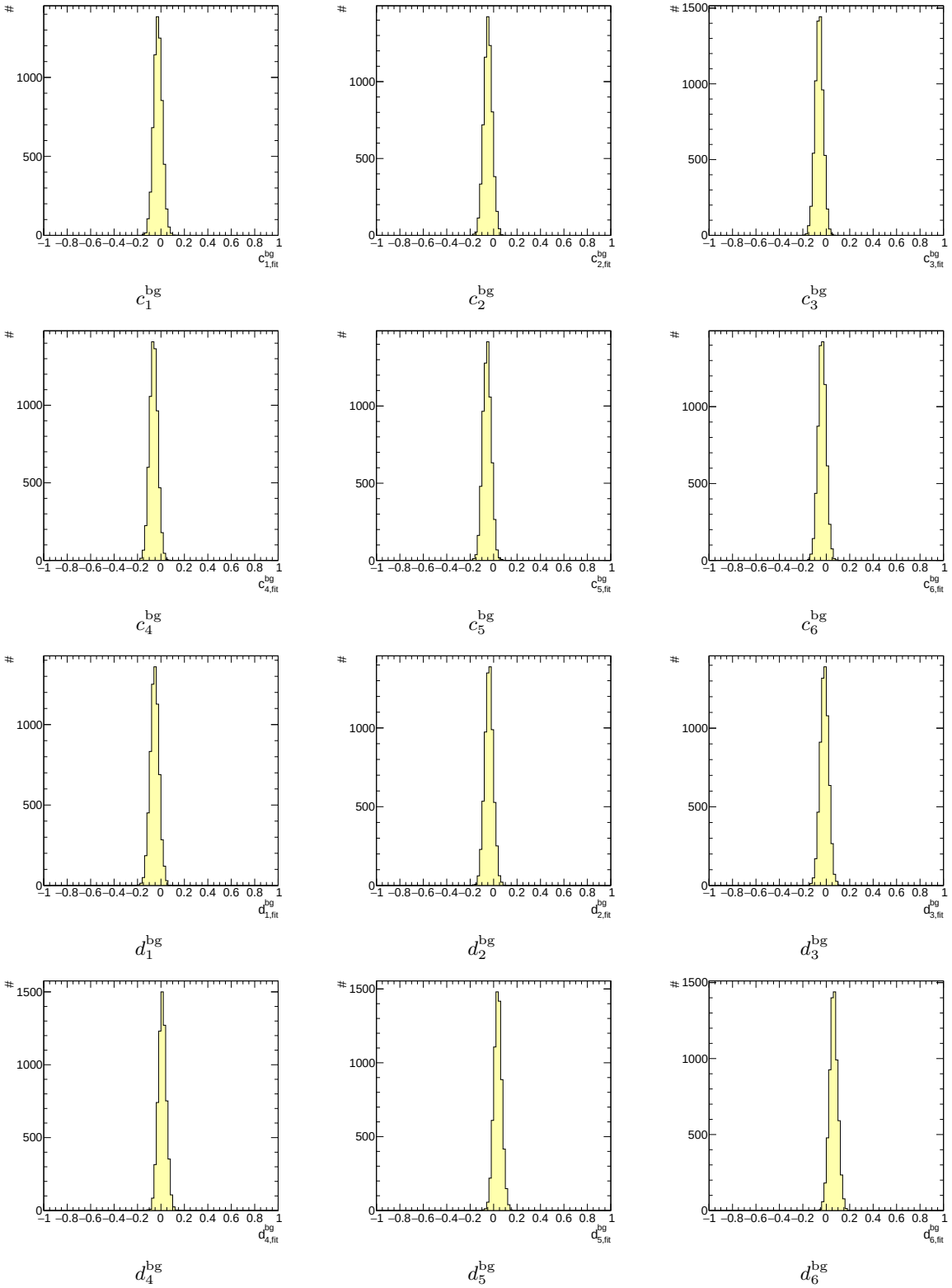

c_1^{bg} c_2^{bg} c_3^{bg}

c_4^{bg} c_5^{bg} c_6^{bg}

d_1^{bg} d_2^{bg} d_3^{bg}

d_4^{bg} d_5^{bg} d_6^{bg}

Figure C.5: Distributions of coefficients c_{1-6}^{bg} and d_{1-6}^{bg} for the detector efficiency after 6400 Monte Carlo simulations.

APPENDIX D

Discussion of the Results

This appendix presents additional material to Chapter 9. In Section D.1, additional views on the comparison of the different periods of data taking are presented, including 4-PED events. In Section D.2, additional views on the comparison of the polarization observables extracted in this work with Seifen et al. [20] are presented. Only 5-PED and 4.5-PED events are used for the comparison. Additional material on the final results of this work is included in the Section E to H.

D.1 Comparison of the Different Periods of Data Collection

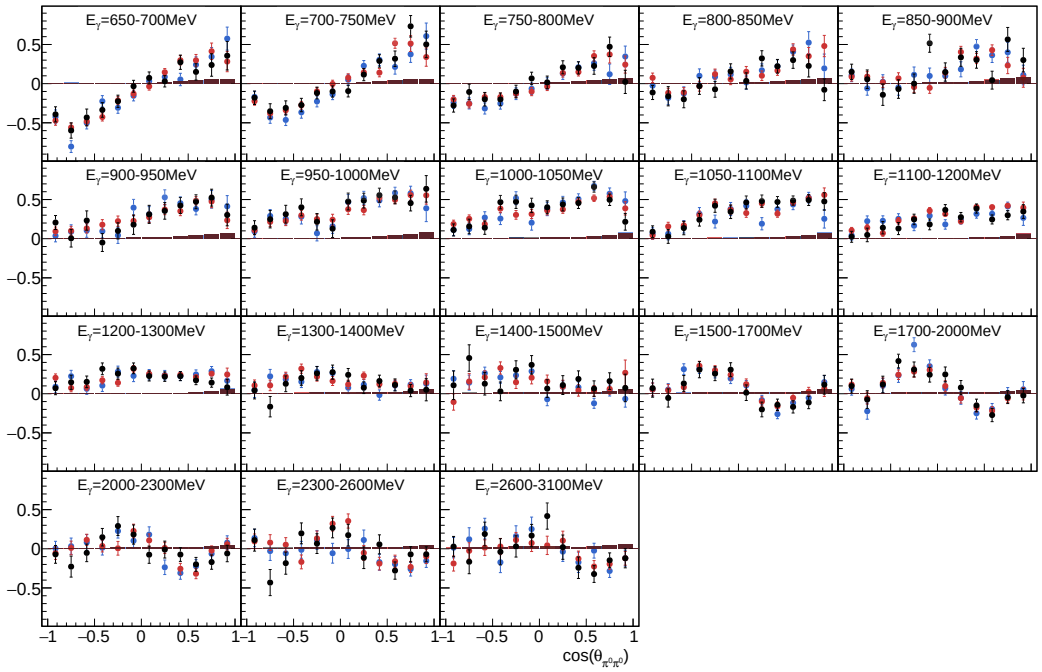

Figure D.1: Target asymmetry P_y as function of $\left(E_\gamma, \cos(\theta_{\pi^0\pi^0})\right)$ for 5-PED, 4.5-PED and 4-PED events. The different periods of data taking **December 2017**, May 2018 and February 2019 are compared. June 2021 is not used in the comparison because it excludes 4-PED. The systematic uncertainties are shown as bars on the x-axis.

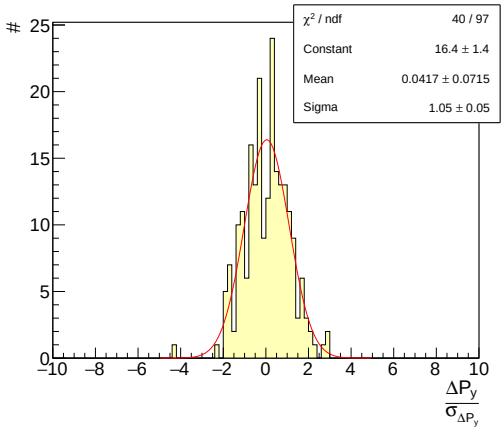

Dec 2017 & May 2018

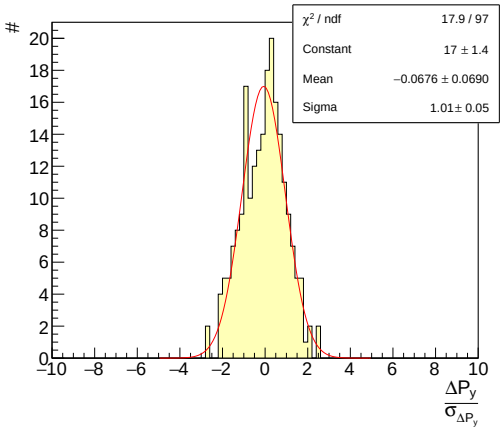

Dec 2017 & Feb 2019

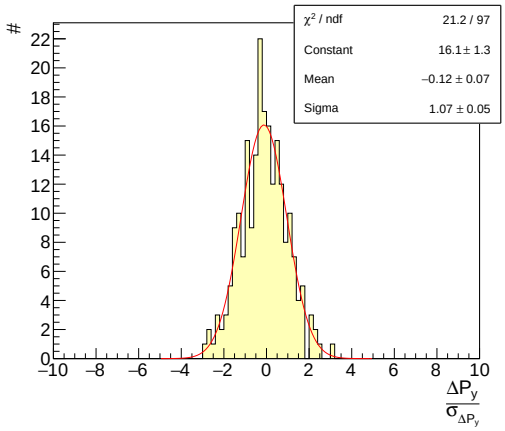

May 2018 & Feb 2019

Figure D.2: Residuals of the target asymmetry P_y for 5-PED, 4.5-PED and 4-PED events normalized to the statistical error for each combination of the three different periods of data taking December 2017, May 2018 and February 2019. June 2021 is not used in the comparison because it excludes 4-PED events.

D.2 Comparison to Existing Data

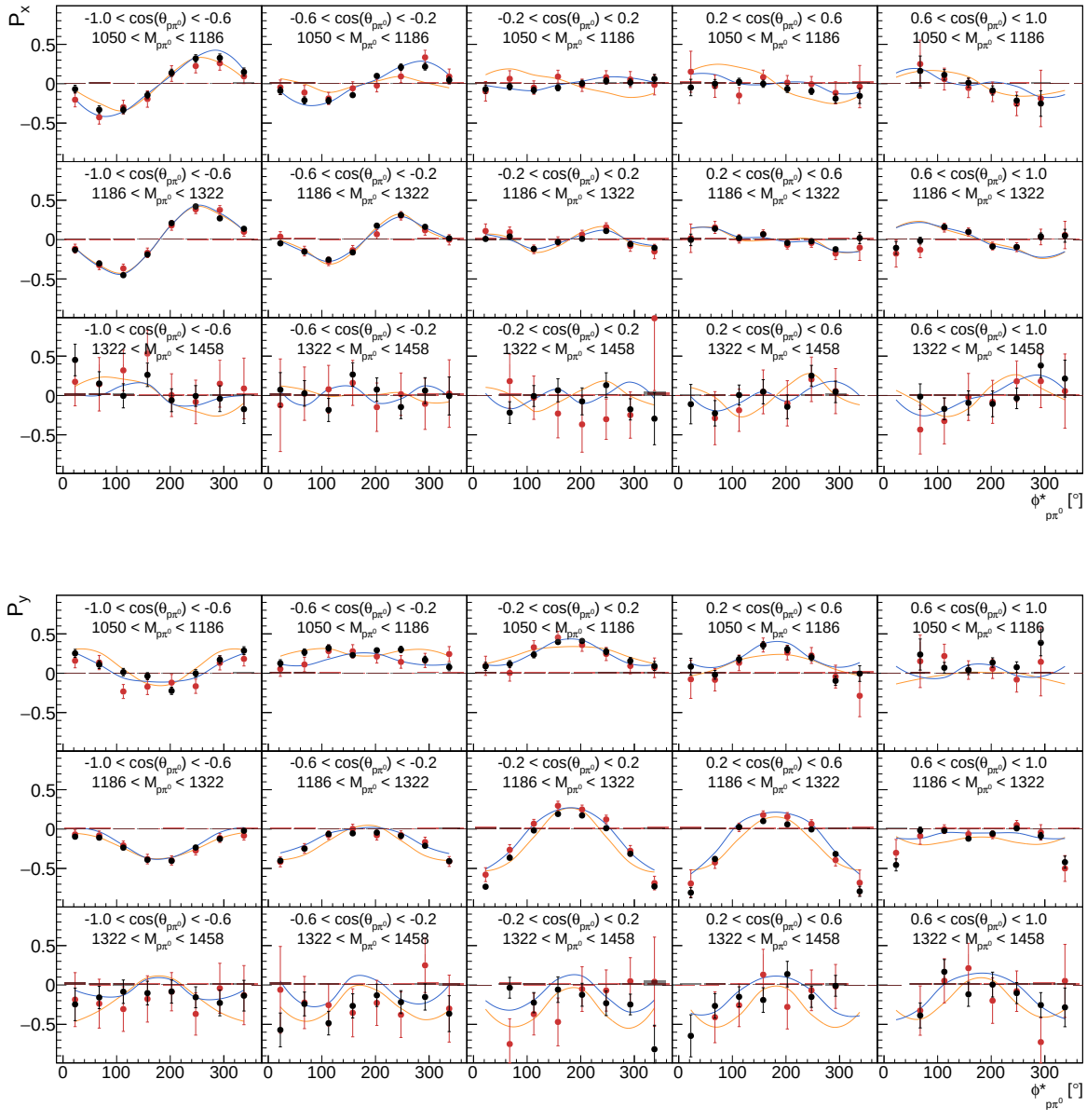

$E_\gamma = 650 - 800\,\mathrm{MeV}$

Figure D.3: Target asymmetries P_x, P_y for 5-PED and 4.5-PED events for a specific energy range $E_\gamma = 650 - 800\,\mathrm{MeV}$ as function of $(\cos(\theta_{p\pi^0}), M_{p\pi^0}, \phi^*_{p\pi^0})$. The **combined data of this work** is shown in comparison to Seifen et al. [20]. The systematic uncertainties are shown as bars on the x-axis. For completeness, model predictions of BnGa-2022 and BnGa-2014 are already presented.

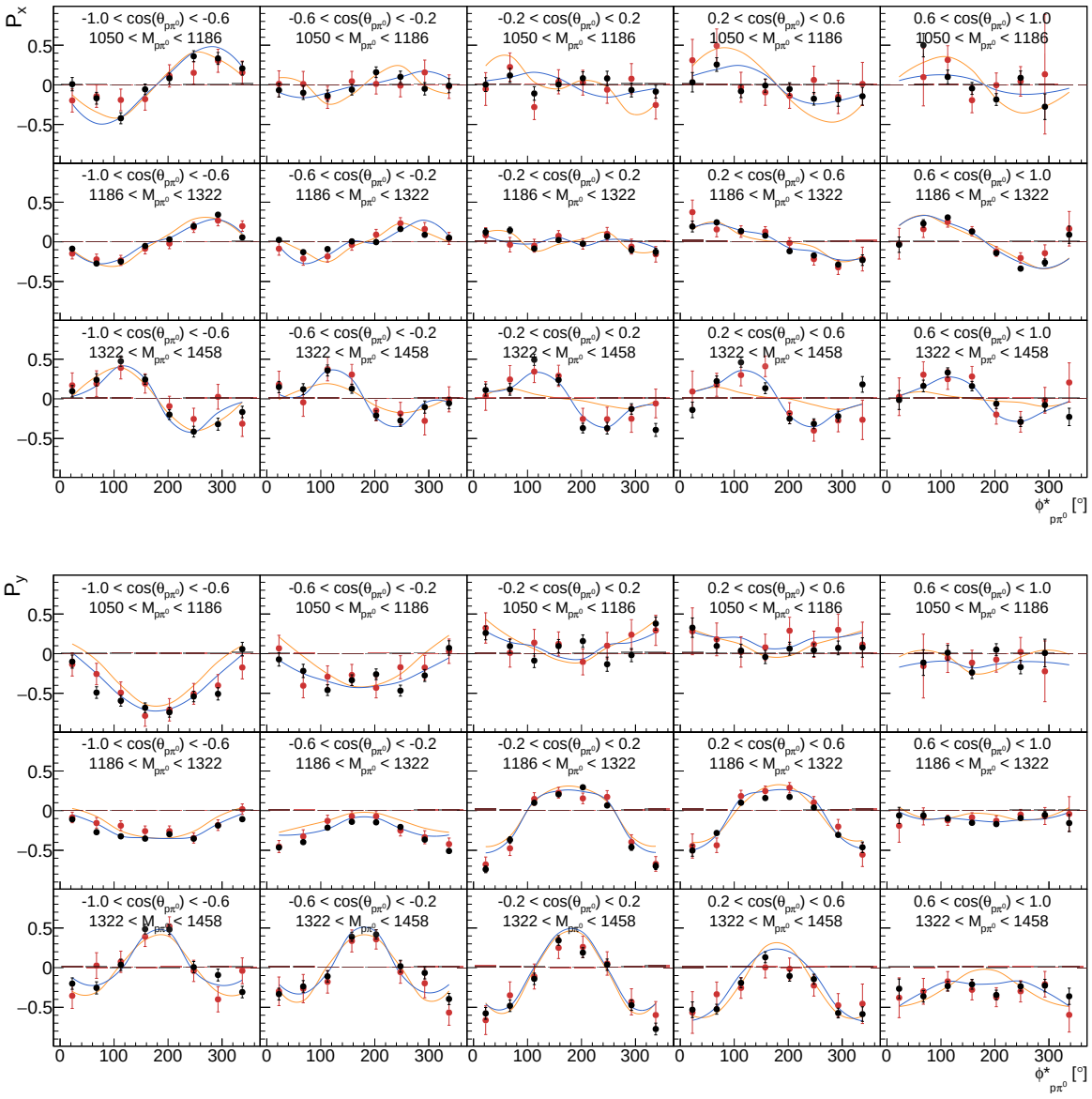

$E_\gamma = 800 - 950\,\mathrm{MeV}$

Figure D.4: Target asymmetries P_x, P_y for 5-PED and 4.5-PED events for a specific energy range $E_\gamma = 800 - 950\,\mathrm{MeV}$ as function of $(\cos(\theta_{p\pi^0}), M_{p\pi^0}, \phi^*_{p\pi^0})$. For a description, cf. Fig. D.3.

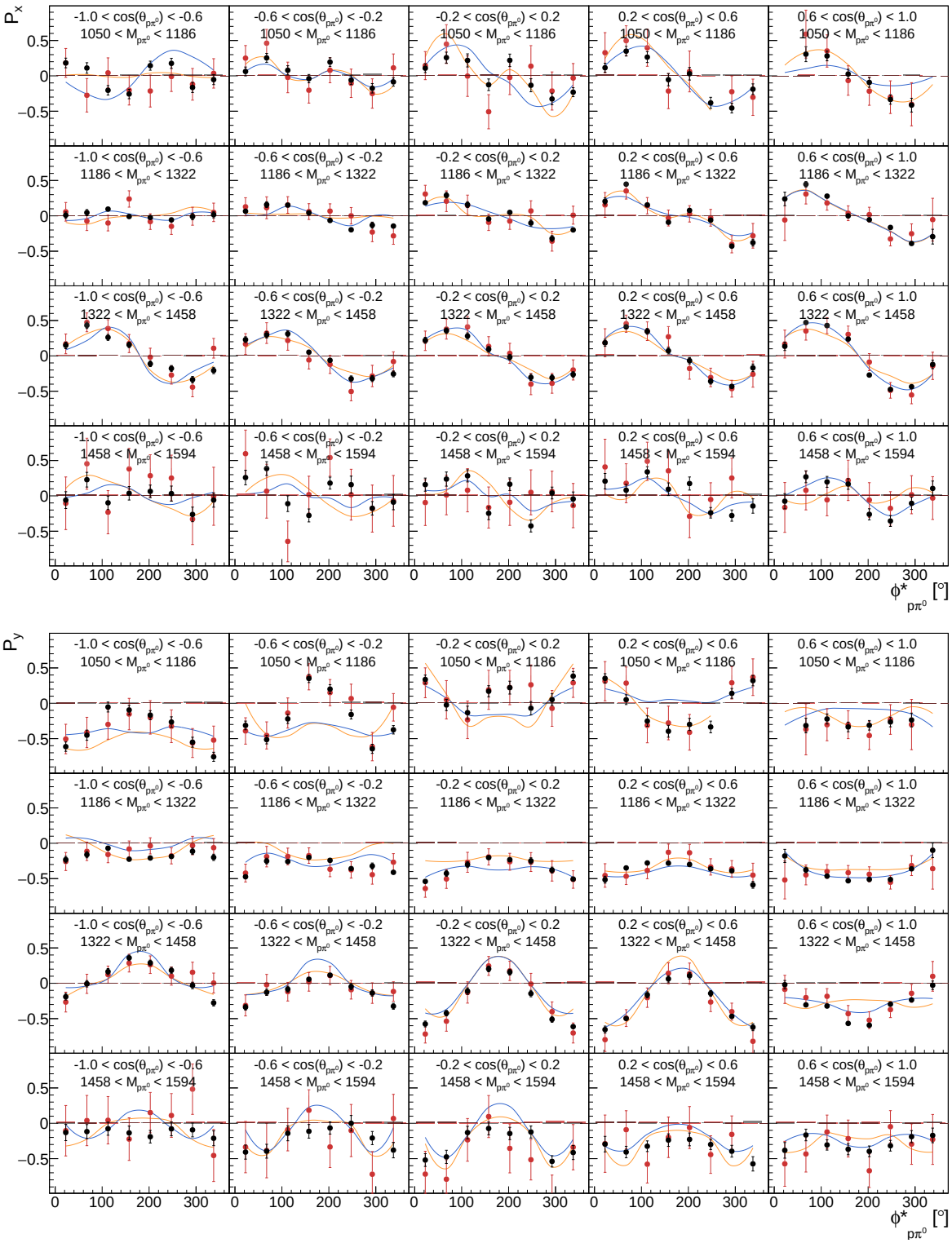

$E_\gamma = 950 - 1\,100\,\mathrm{MeV}$

Figure D.5: Target asymmetries P_x, P_y for 5-PED and 4.5-PED events for a specific energy range $E_\gamma = 950 - 1\,100\,\mathrm{MeV}$ as function of $(\cos(\theta_{p\pi^0}), M_{p\pi^0}, \phi^*_{p\pi^0})$. For a description, cf. Fig. D.3.

APPENDIX E

P_x, P_y in Two Dimensions

In this appendix, final results on single polarization observables P_x, P_y are presented in two dimensions. For the extraction of the results, the combined data of four periods of data taking are used: December 2017, May 2018, February 2019 and June 2021. In each case, 5-PED, 4.5-PED and 4-PED events are included for a complete coverage of the kinematic region. An exception is June 2021, for which 4-PED events are excluded (cf. Section 8.3.2.3). Combinations of kinematic variables for which the observables are expected to be zero when integrated over ϕ^* are excluded (see Section 8.2.1). The results are compared with the model predictions of BnGa-2022 and BnGa-2014. The systematic uncertainties of the results are shown as bars on the x-axis.

$\pi^0\pi^0$-System

The series of Fig. E.1 to E.14 deals with observables extracted in the $\pi^0\pi^0$-system.

- Fig. E.1 to E.5 shows the observables in bins of E_γ.
- Fig. E.6 to E.9 shows the observables in bins of $\cos(\theta_{\pi^0\pi^0})$.
- Fig. E.10 to E.12 shows the observables in bins of $M_{\pi^0\pi^0}$.
- Fig. E.13 to E.14 shows the observables in bins of $\phi^*_{\pi^0\pi^0}$.

$p\pi^0$-System

The series of Fig. E.15 to E.28 deals with observables extracted in the $p\pi^0$-system.

- Fig. E.15 to E.19 shows the observables in bins of E_γ.
- Fig. E.20 to E.23 shows the observables in bins of $\cos(\theta_{p\pi^0})$.
- Fig. E.24 to E.26 shows the observables in bins of $M_{p\pi^0}$.
- Fig. E.27 to E.28 shows the observables in bins of $\phi^*_{p\pi^0}$.

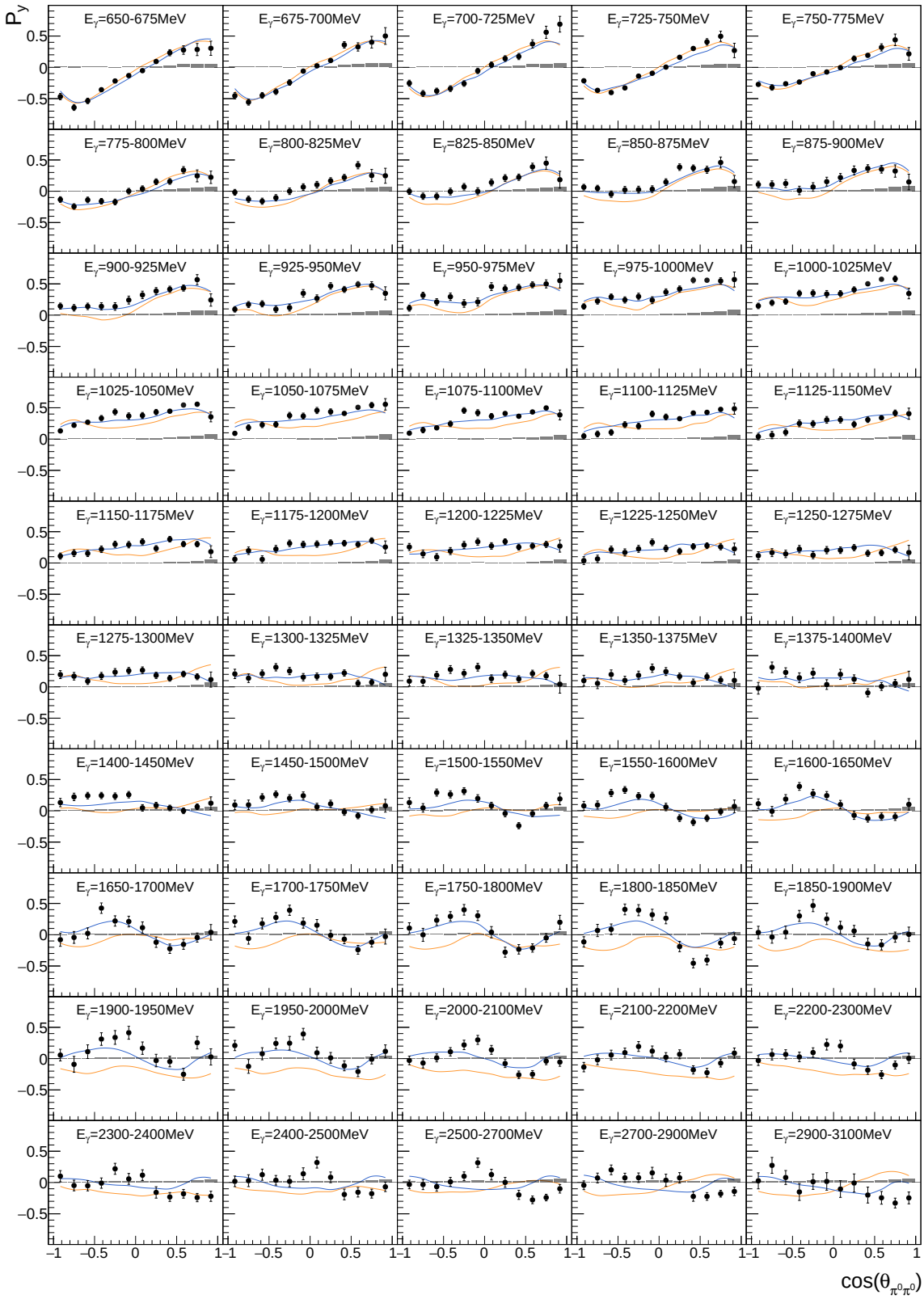

Figure E.1: Target asymmetry P_y as function of $\left(E_\gamma, \cos(\theta_{\pi^0\pi^0})\right)$. The **combined data of this work** is shown as well as the model predictions BnGa-2022 and BnGa-2014.

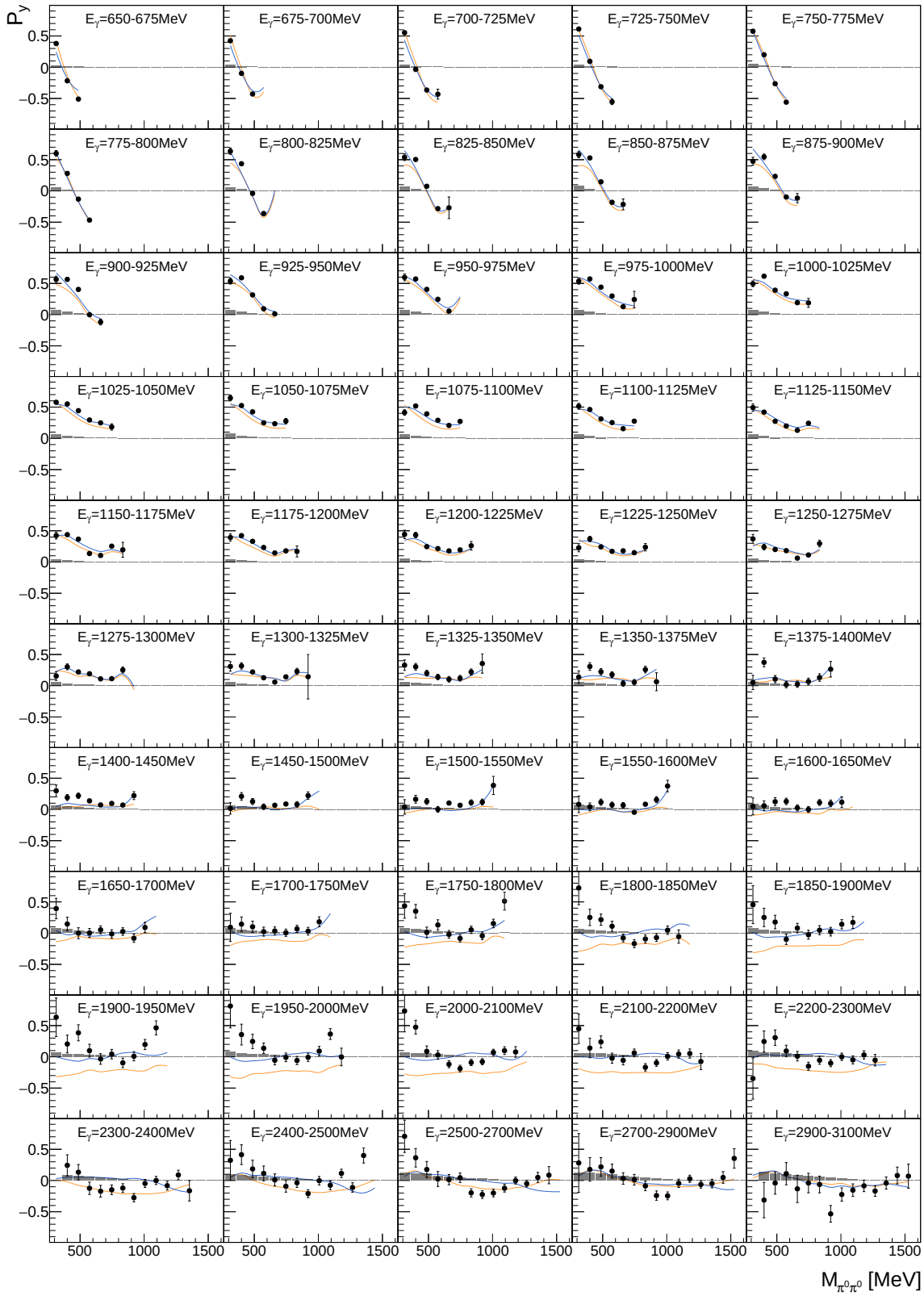

Figure E.2: Target asymmetry P_y as function of $\left(E_\gamma, M_{\pi^0\pi^0}\right)$. The **combined data of this work** is shown as well as the model predictions BnGa-2022 and BnGa-2014.

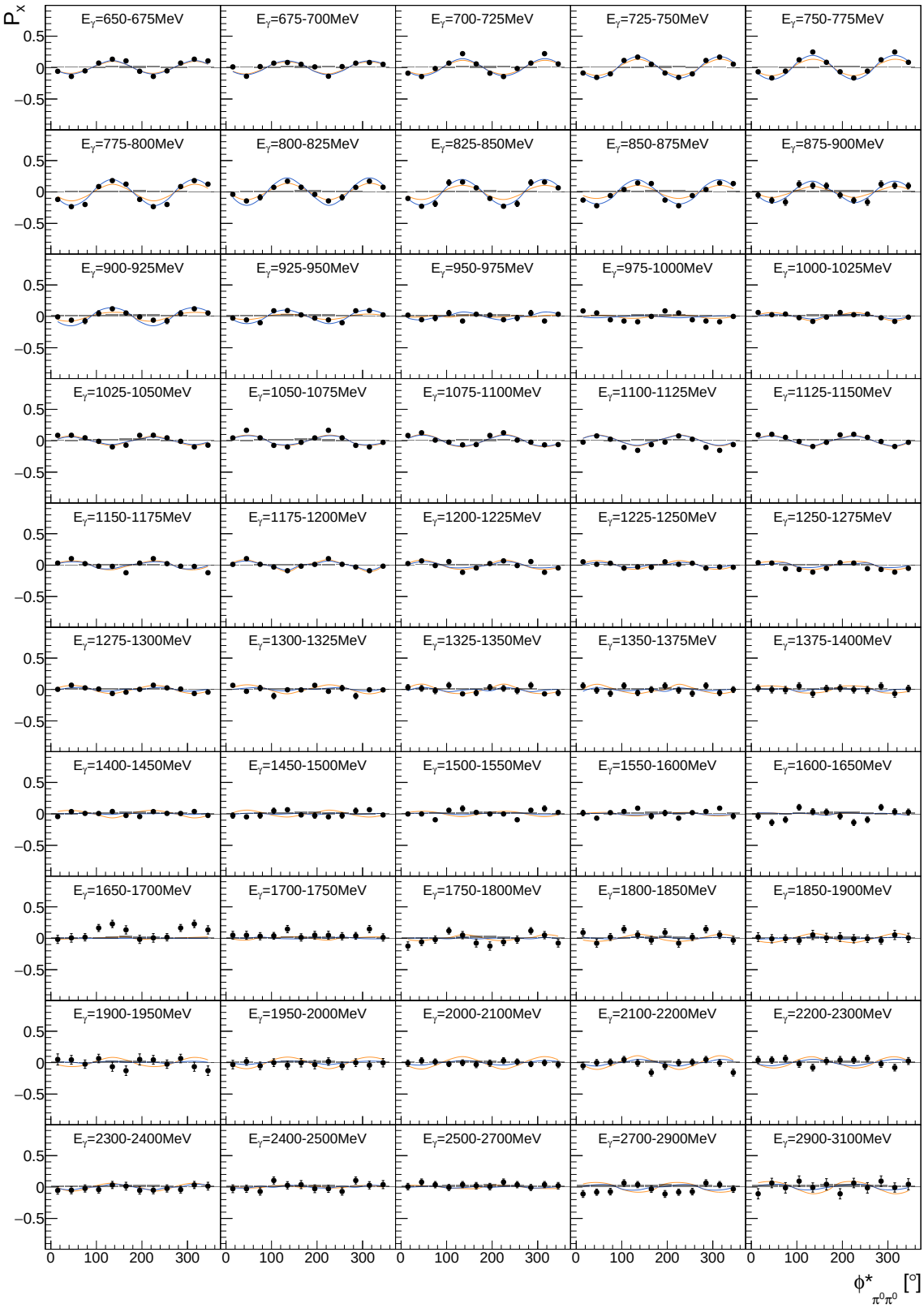

Figure E.3: Target asymmetry P_x as function of $\left(E_\gamma, \phi^*_{\pi^0\pi^0}\right)$. The **combined data of this work** is shown as well as the model predictions BnGa-2022 and BnGa-2014.

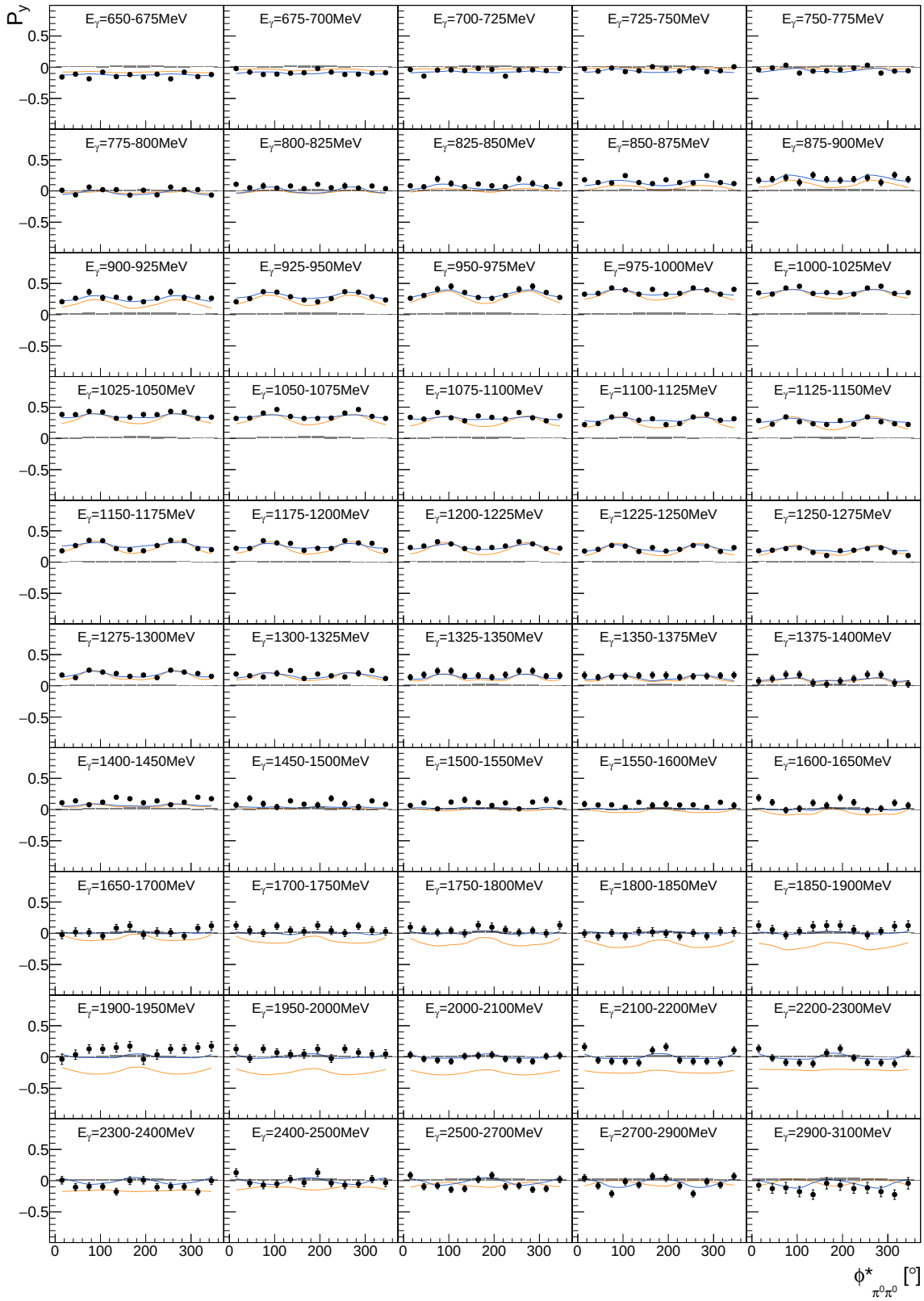

Figure E.4: Target asymmetry P_y as function of $\left(E_\gamma, \phi^*_{\pi^0\pi^0}\right)$. The **combined data of this work** is shown as well as the model predictions BnGa-2022 and BnGa-2014.

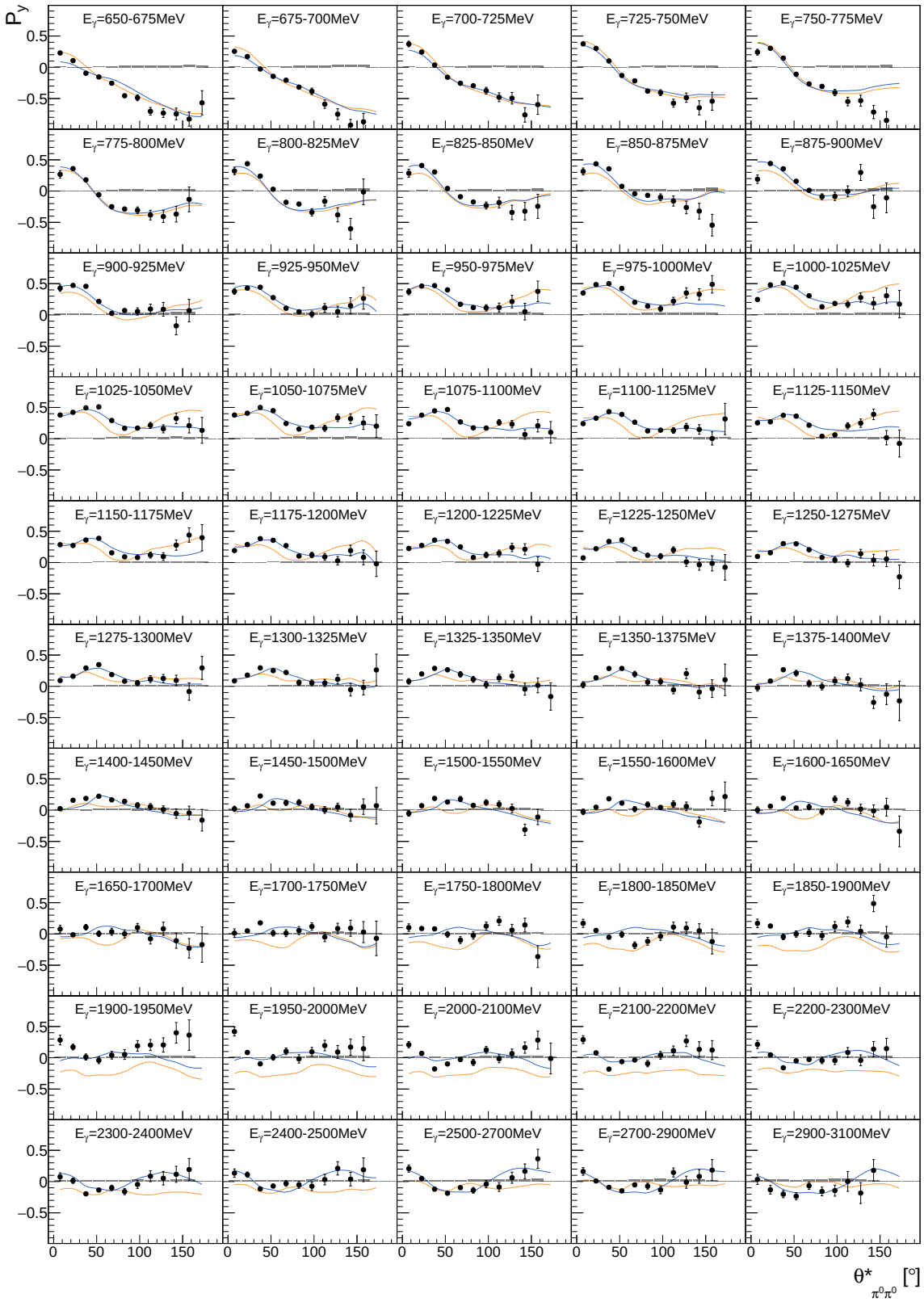

Figure E.5: Target asymmetry P_y as function of $\left(E_\gamma, \theta^*_{\pi^0\pi^0}\right)$. The **combined data of this work** is shown as well as the model predictions BnGa-2022 and BnGa-2014.

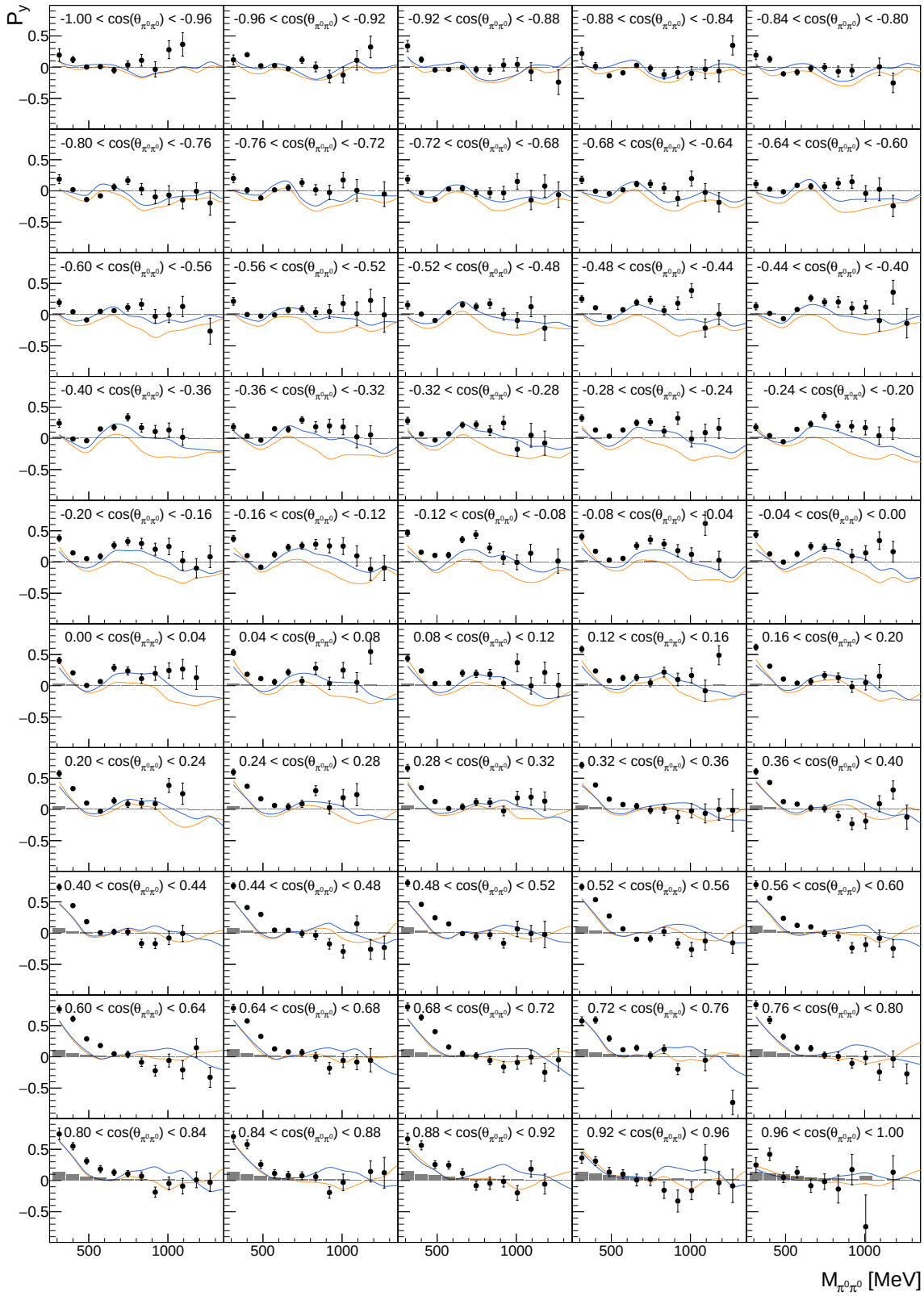

Figure E.6: Target asymmetry P_y as function of $\left(\cos(\theta_{\pi^0\pi^0}), M_{\pi^0\pi^0}\right)$. The **combined data of this work** is shown as well as the model predictions BnGa-2022 and BnGa-2014.

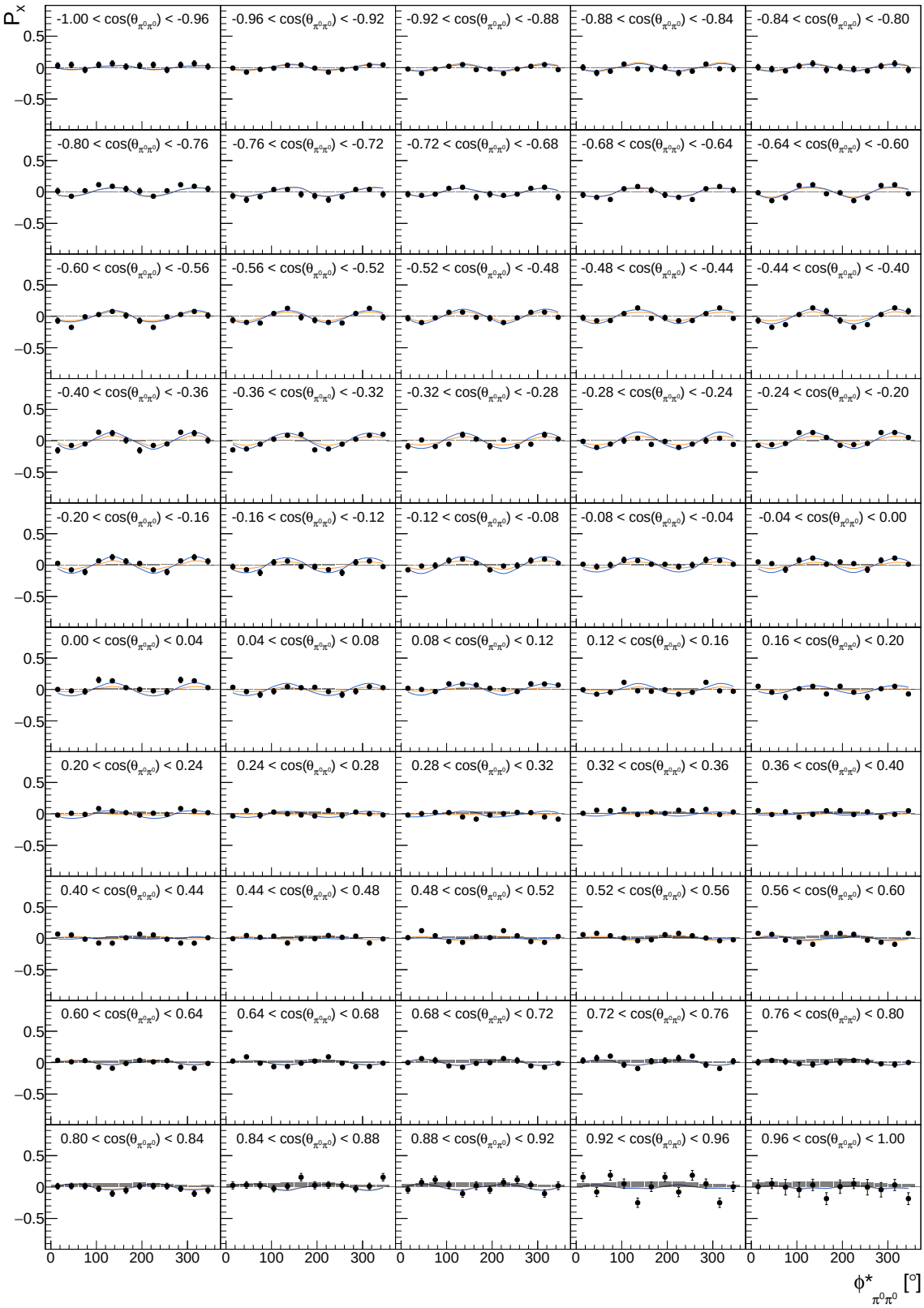

Figure E.7: Target asymmetry P_x as function of $\left(\cos(\theta_{\pi^0\pi^0}), \phi^*_{\pi^0\pi^0}\right)$. The **combined data of this work** is shown as well as the model predictions BnGa-2022 and BnGa-2014.

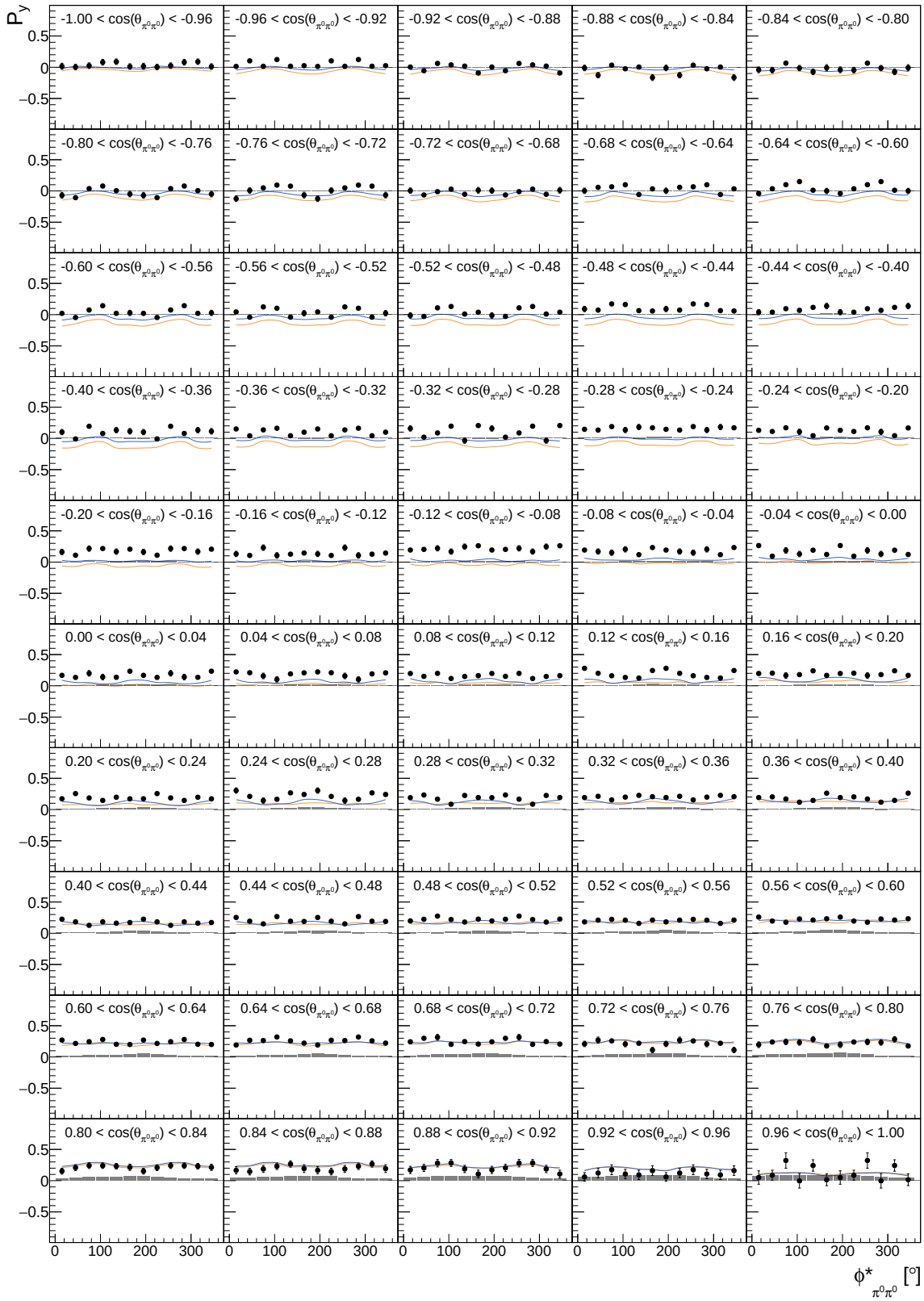

Figure E.8: Target asymmetry P_y as function of $\left(\cos(\theta_{\pi^0\pi^0}), \phi^*_{\pi^0\pi^0}\right)$. The **combined data of this work** is shown as well as the model predictions BnGa-2022 and BnGa-2014.

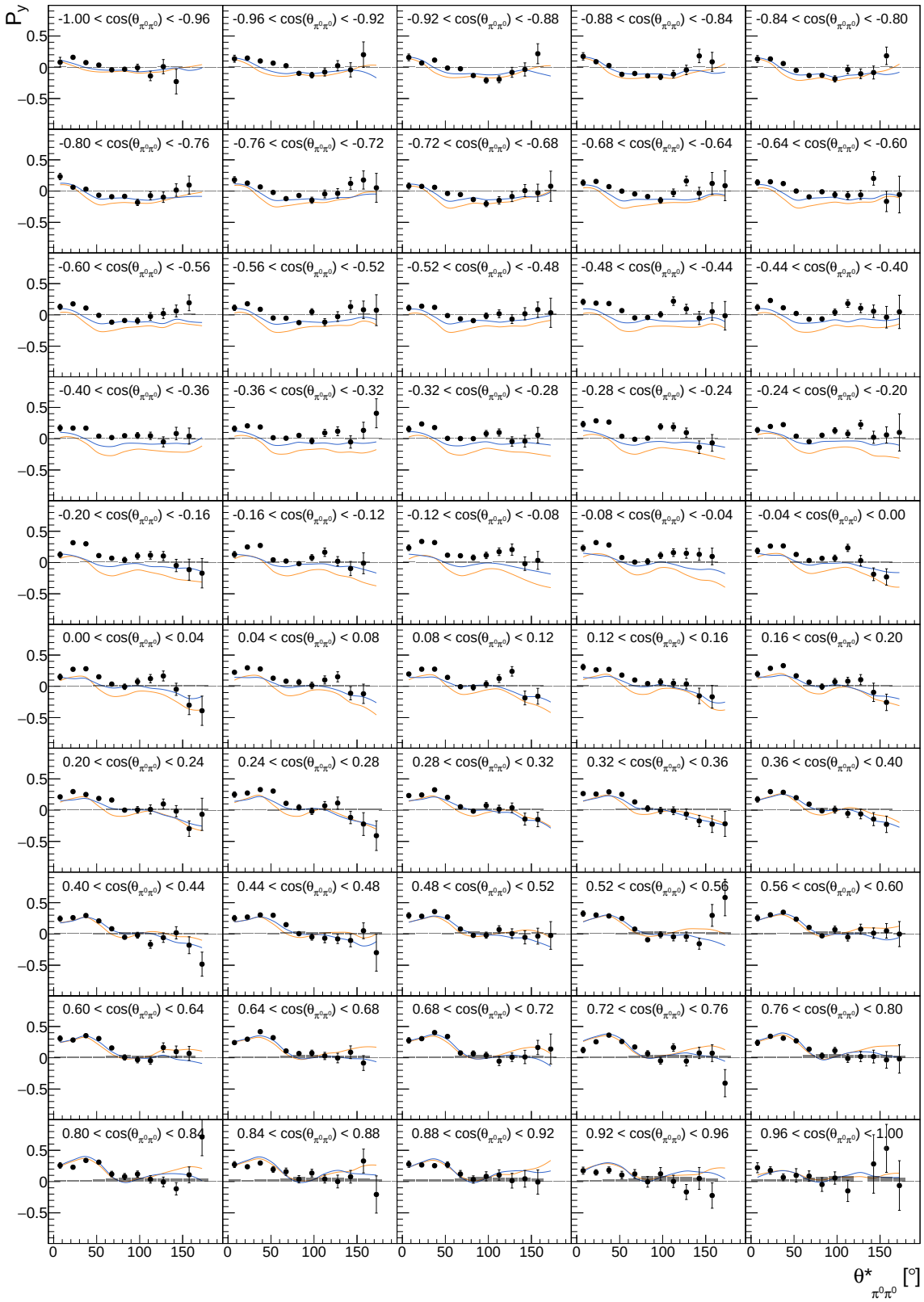

Figure E.9: Target asymmetry P_y as function of $\left(\cos(\theta_{\pi^0\pi^0}), \theta^*_{\pi^0\pi^0}\right)$. The **combined data of this work** is shown as well as the model predictions BnGa-2022 and BnGa-2014.

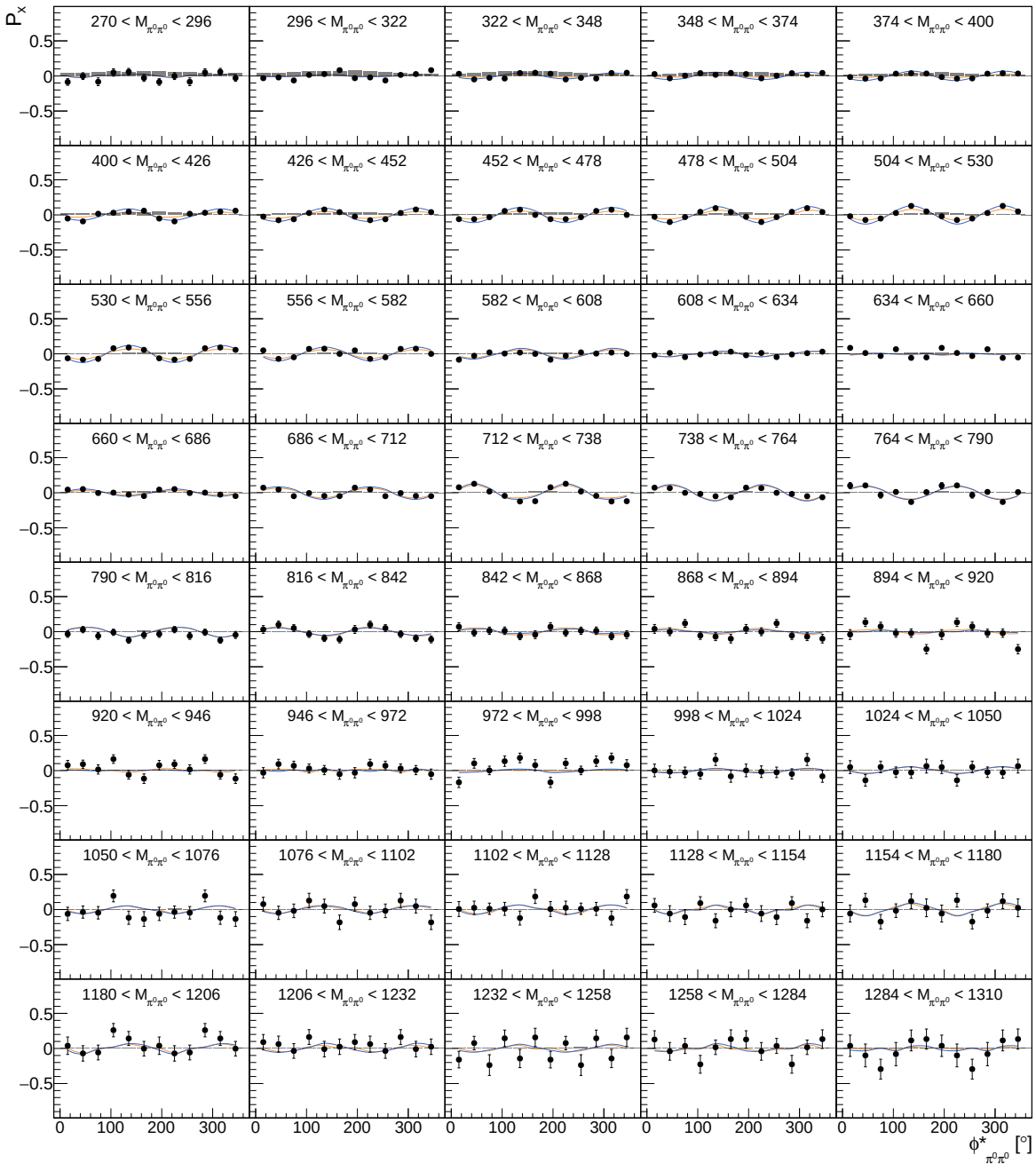

Figure E.10: Target asymmetry P_x as function of $\left(M_{\pi^0\pi^0}, \phi^*_{\pi^0\pi^0}\right)$. The **combined data of this work** is shown as well as the model predictions BnGa-2022 and BnGa-2014.

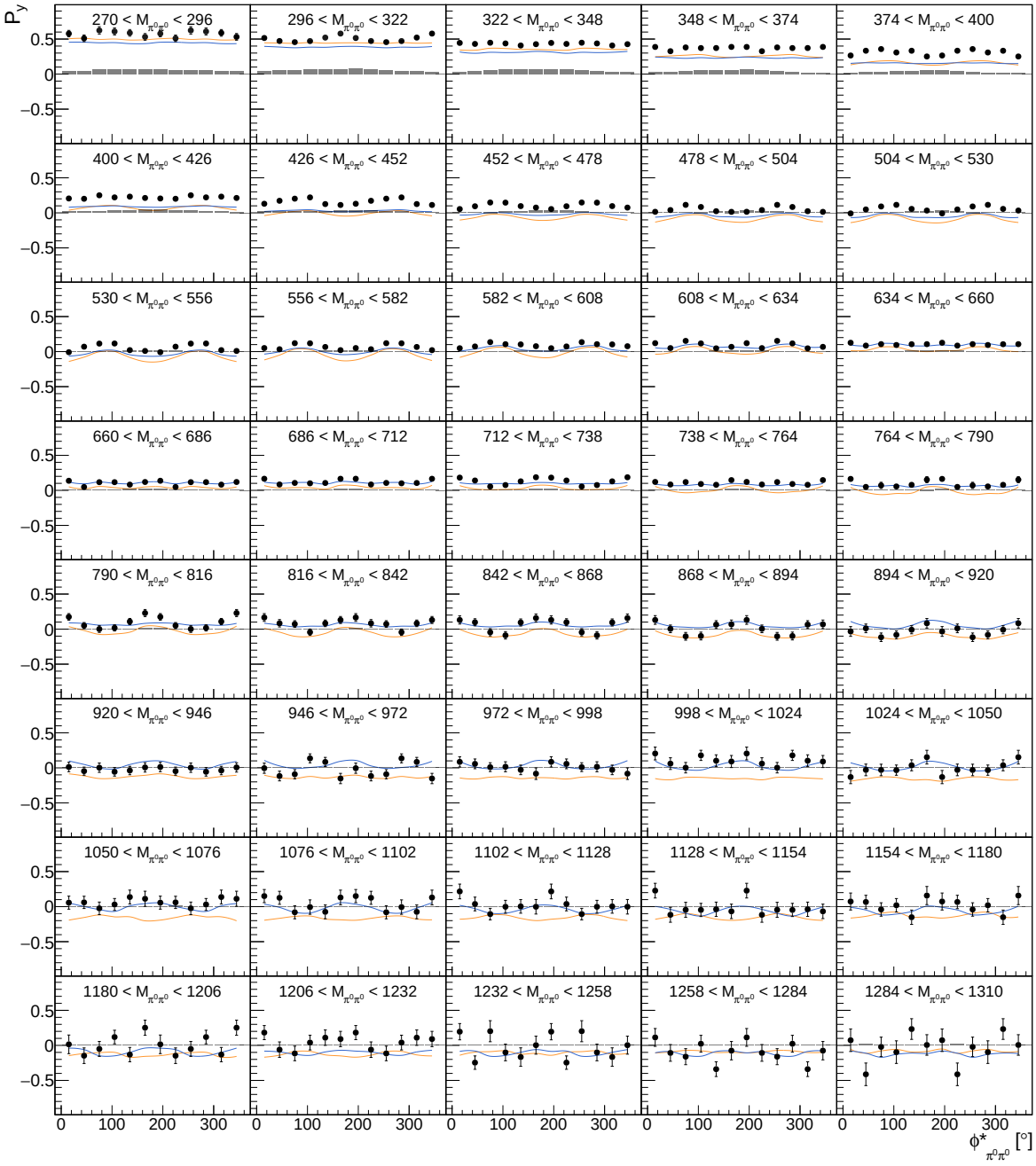

Figure E.11: Target asymmetry P_y as function of $\left(M_{\pi^0\pi^0}, \phi^*_{\pi^0\pi^0}\right)$. The **combined data of this work** is shown as well as the model predictions BnGa-2022 and BnGa-2014.

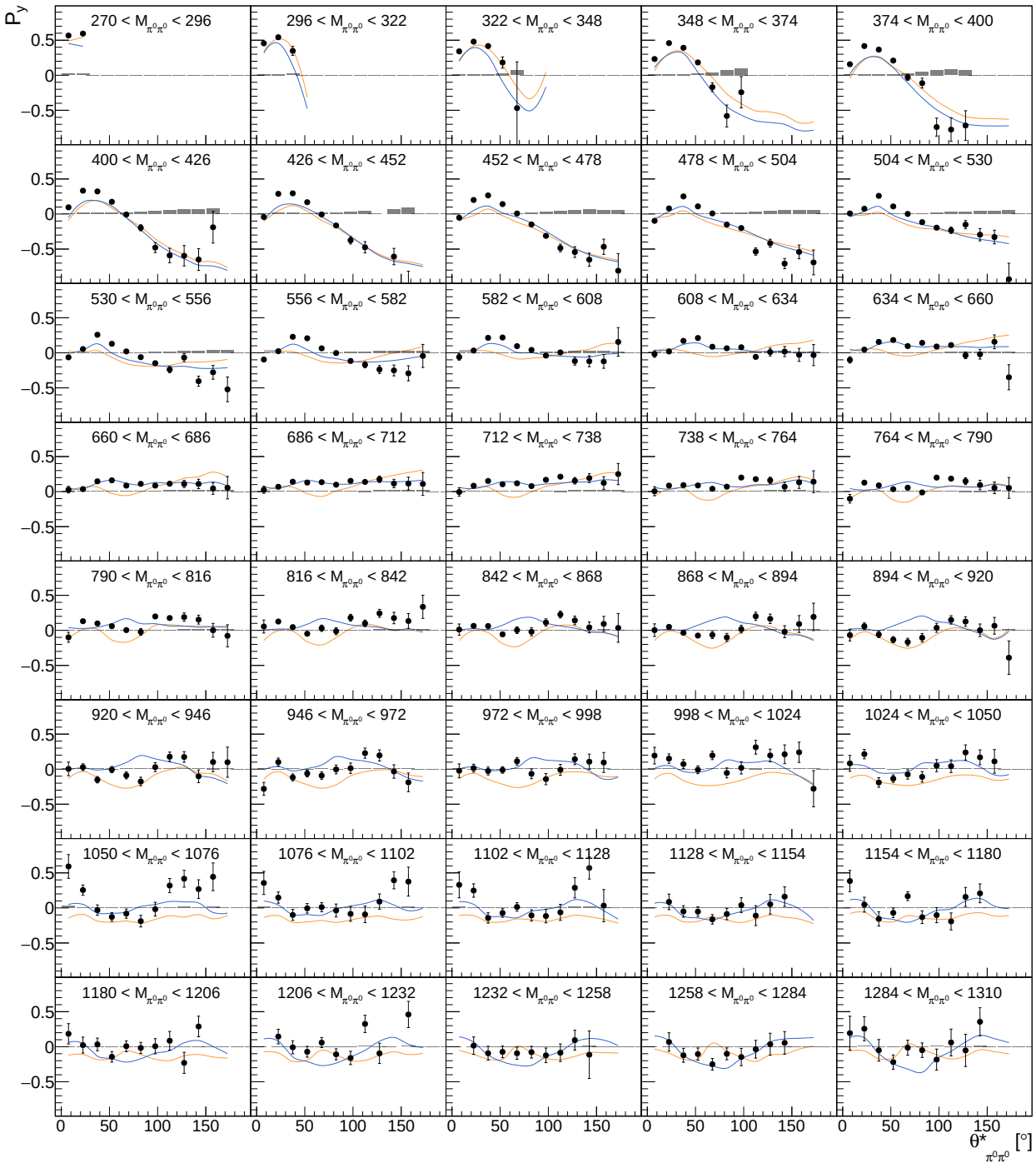

Figure E.12: Target asymmetry P_y as function of $\left(M_{\pi^0\pi^0}, \theta^*_{\pi^0\pi^0}\right)$. The **combined data of this work** is shown as well as the model predictions BnGa-2022 and BnGa-2014.

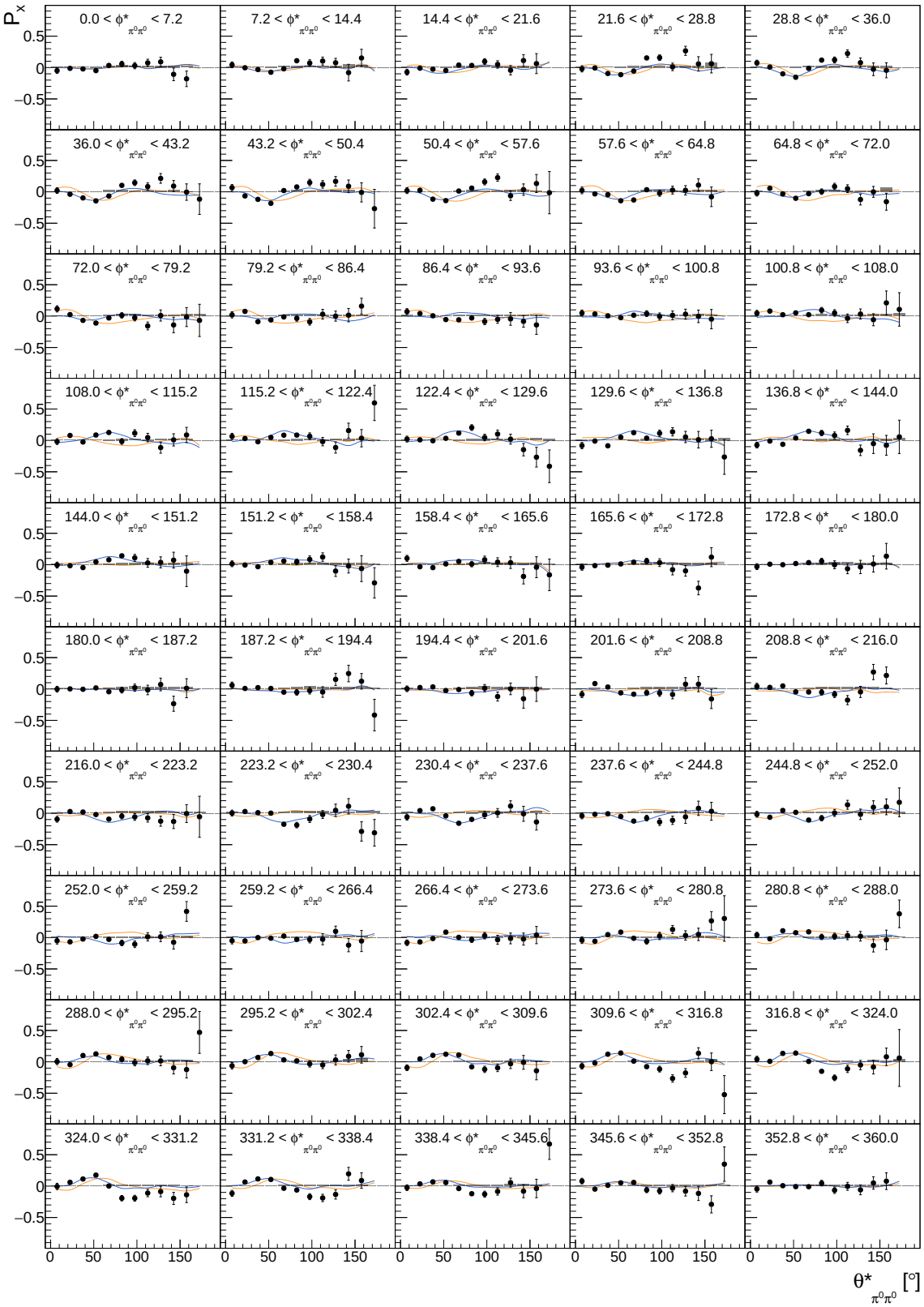

Figure E.13: Target asymmetry P_x as function of $\left(\phi^*_{\pi^0\pi^0}, \theta^*_{\pi^0\pi^0}\right)$. The **combined data of this work** is shown as well as the model predictions BnGa-2022 and BnGa-2014.

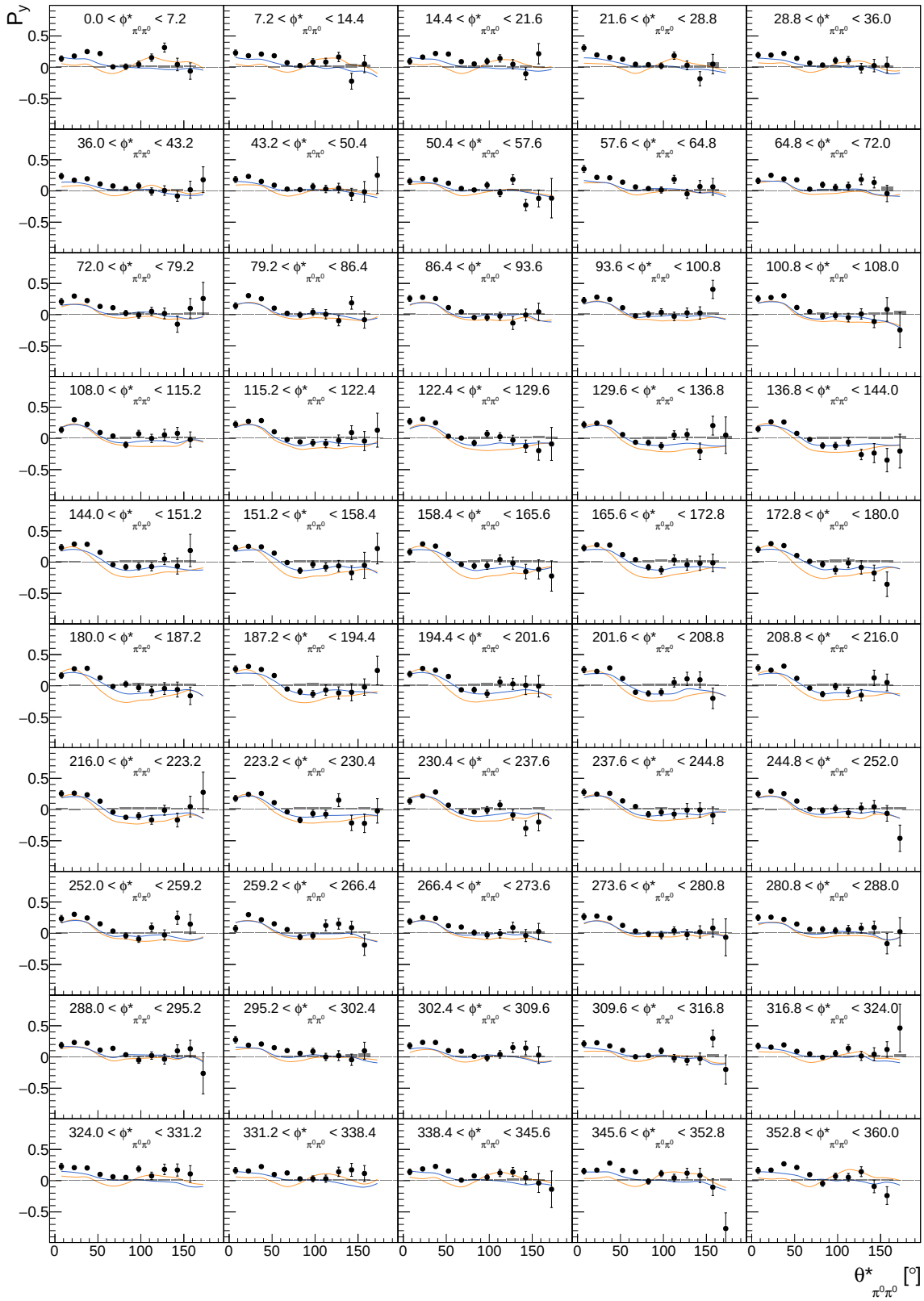

Figure E.14: Target asymmetry P_y as function of $\left(\phi^*_{\pi^0\pi^0}, \theta^*_{\pi^0\pi^0}\right)$. The **combined data of this work** is shown as well as the model predictions BnGa-2022 and BnGa-2014.

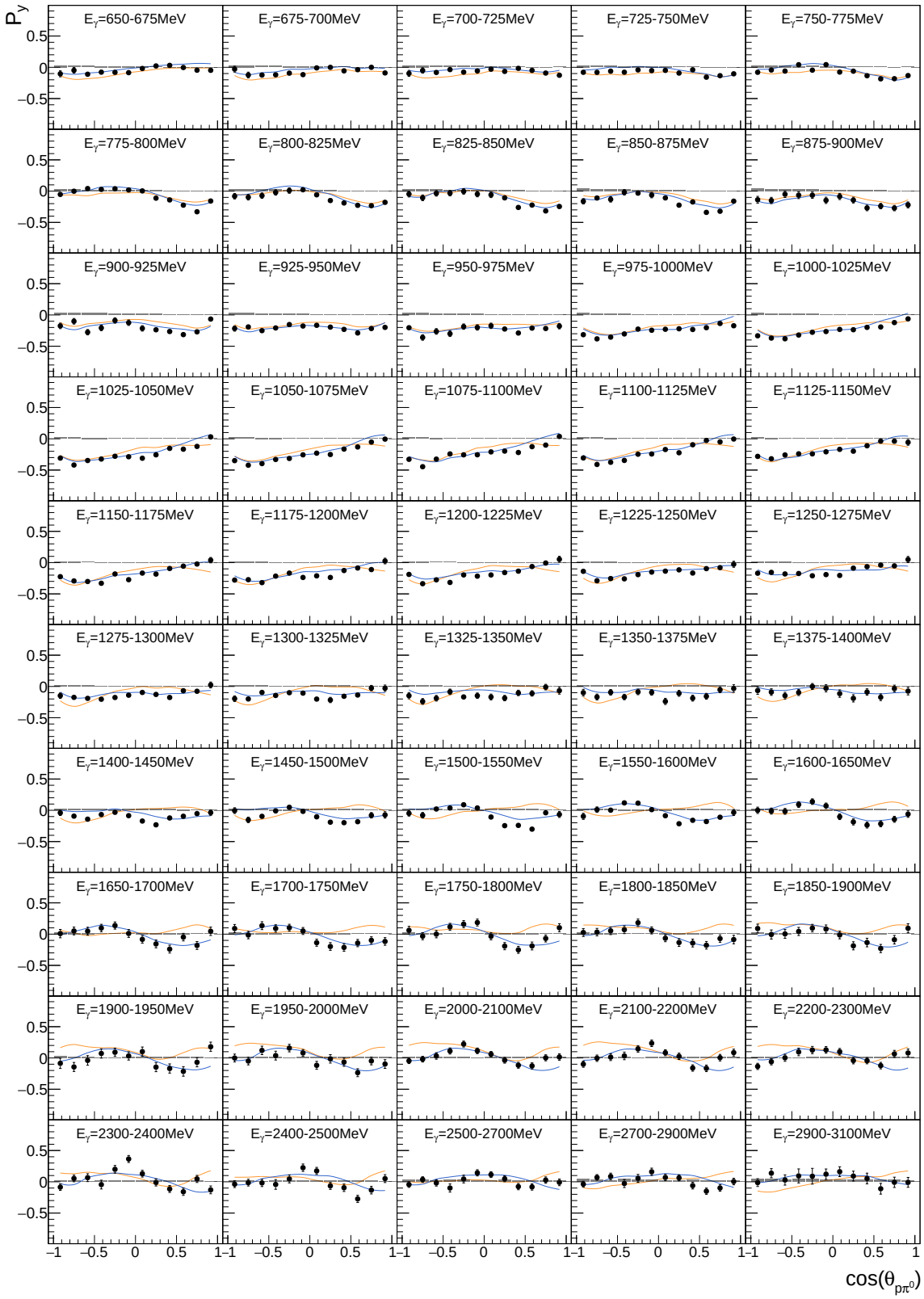

Figure E.15: Target asymmetry P_y as function of $\left(E_\gamma, \cos(\theta_{p\pi^0})\right)$. The **combined data of this work** is shown as well as the model predictions BnGa-2022 and BnGa-2014.

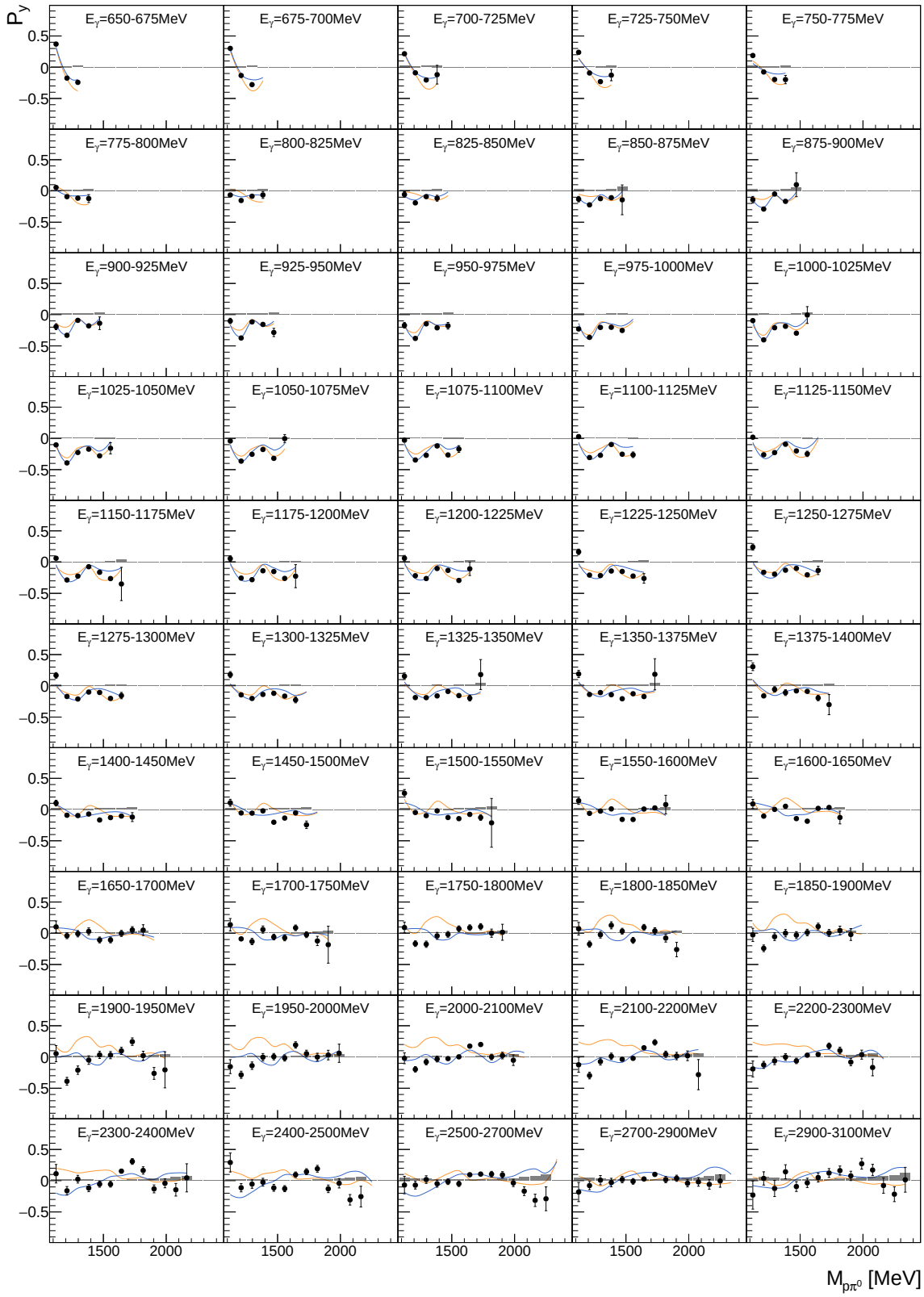

Figure E.16: Target asymmetry P_y as function of $\left(E_\gamma, M_{p\pi^0}\right)$. The **combined data of this work** is shown as well as the model predictions BnGa-2022 and BnGa-2014.

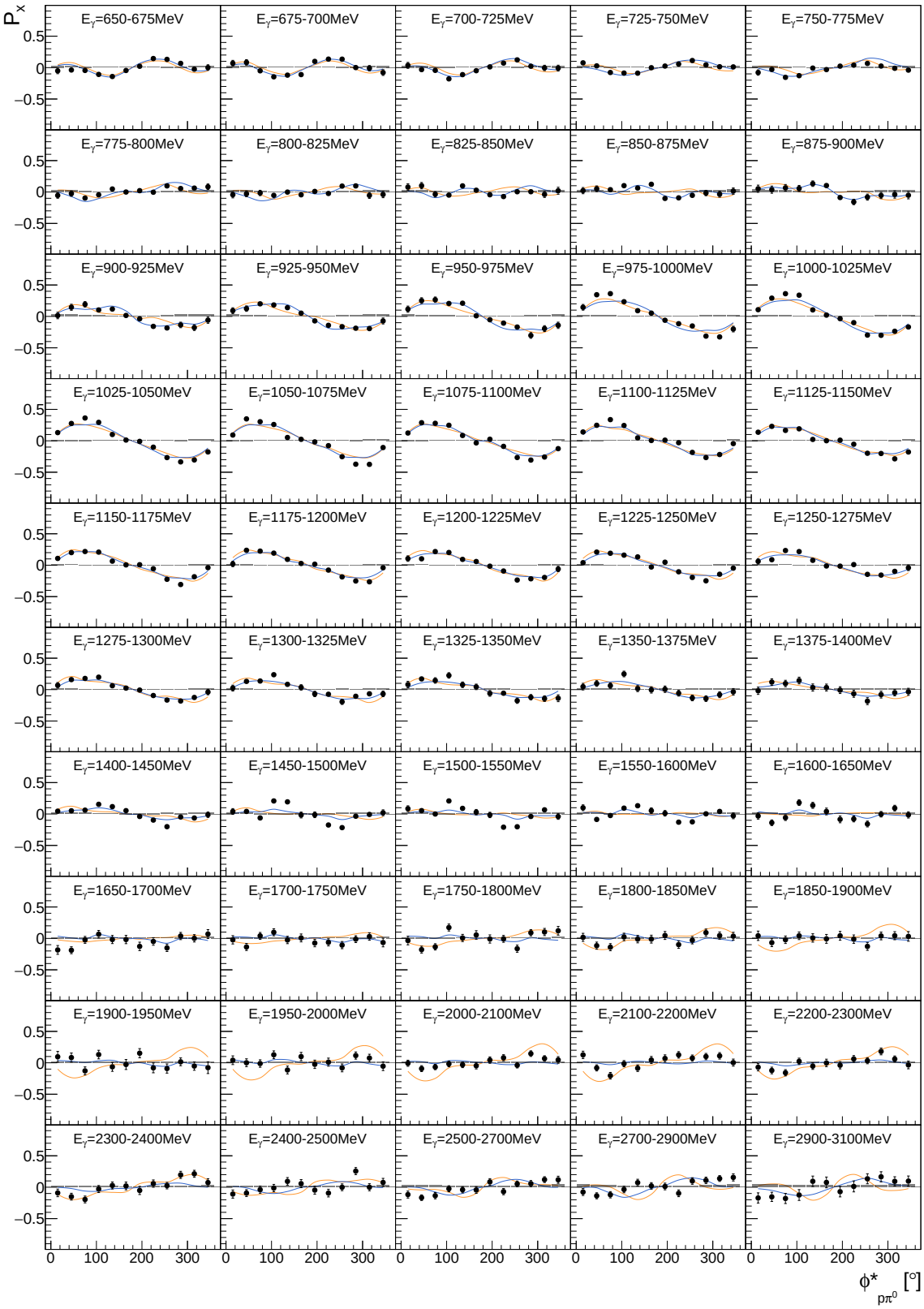

Figure E.17: Target asymmetry P_x as function of $\left(E_\gamma, \phi^*_{p\pi^0}\right)$. The **combined data of this work** is shown as well as the model predictions BnGa-2022 and BnGa-2014.

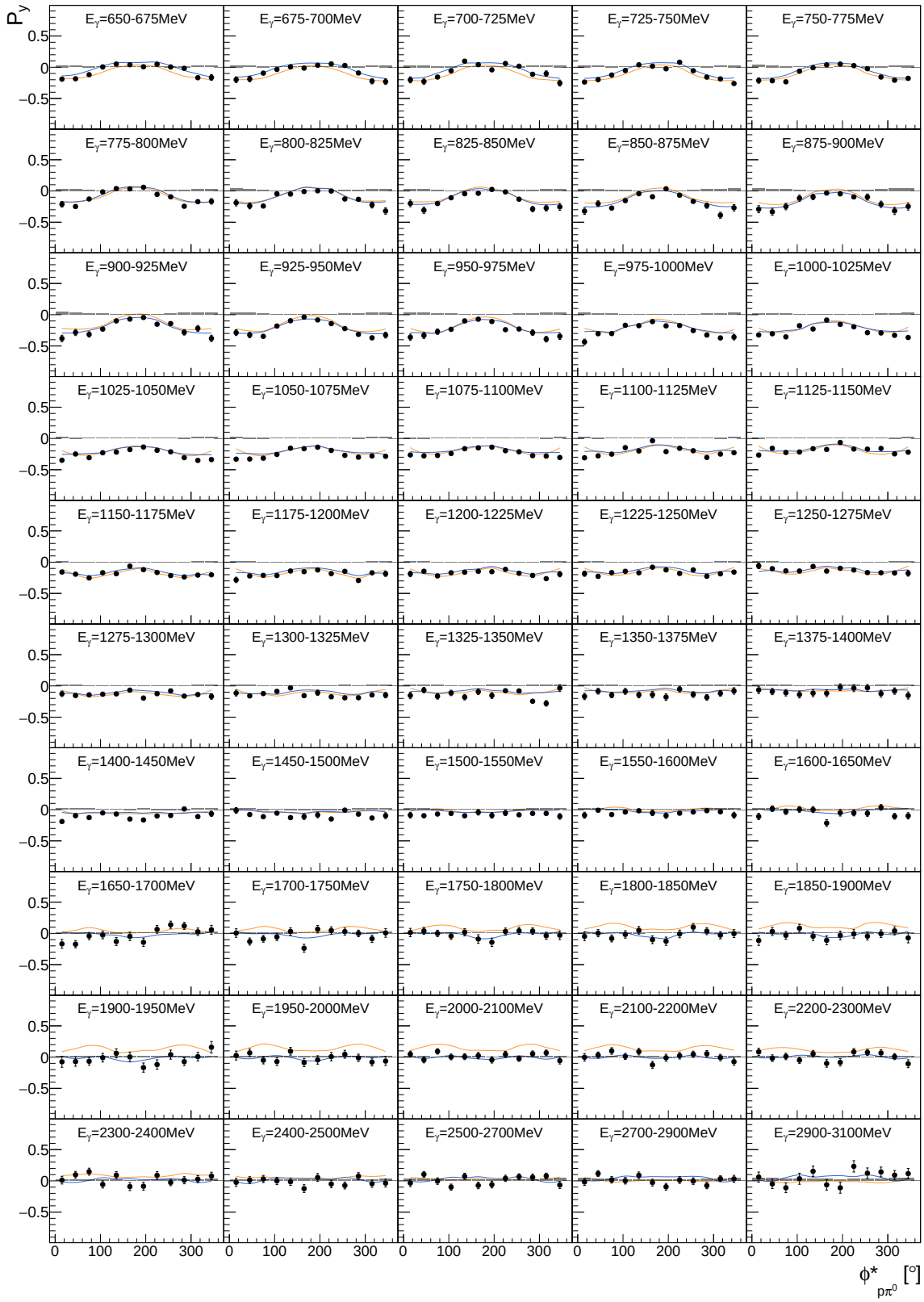

Figure E.18: Target asymmetry P_y as function of $\left(E_\gamma, \phi^*_{p\pi^0}\right)$. The **combined data of this work** is shown as well as the model predictions BnGa-2022 and BnGa-2014.

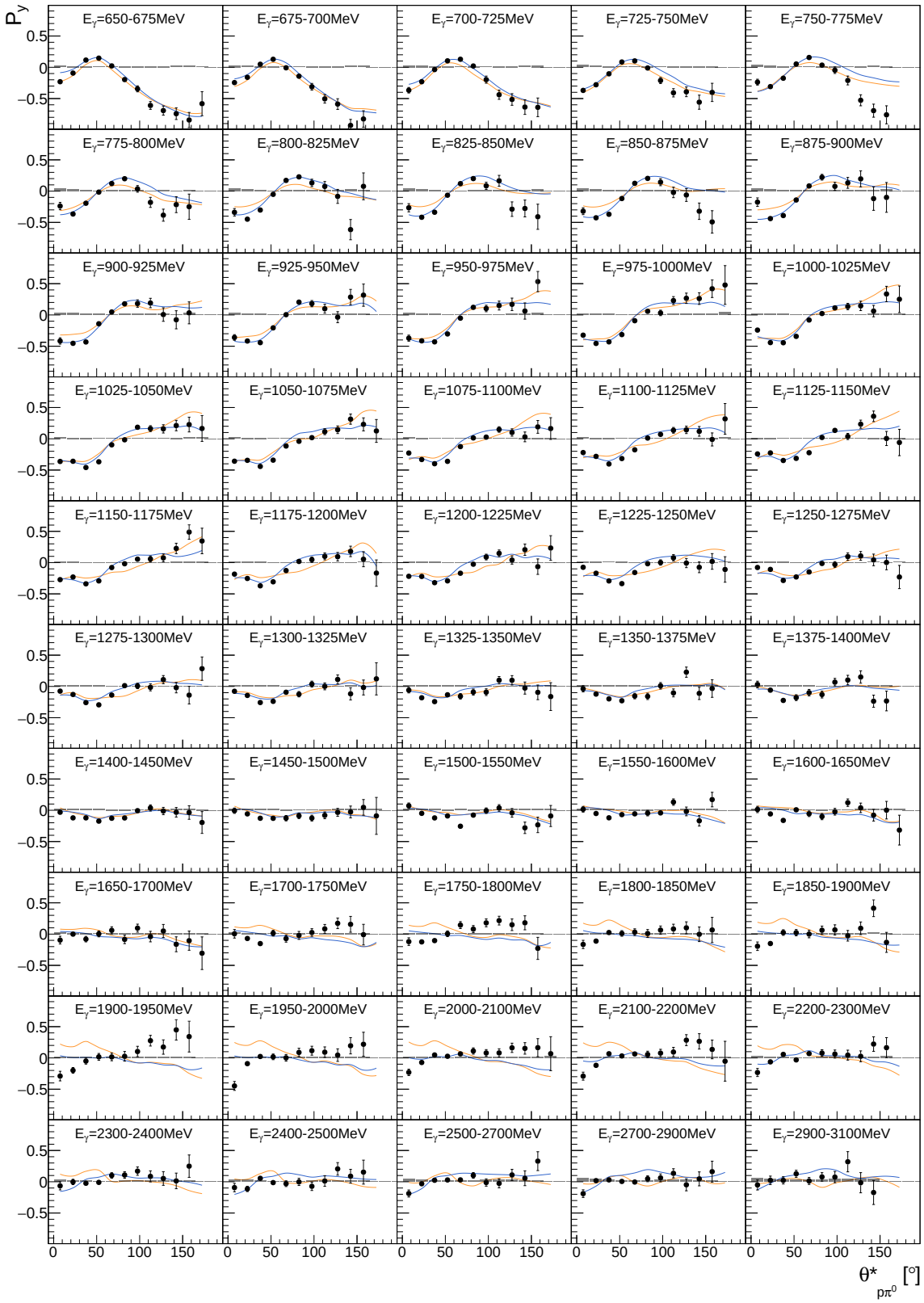

Figure E.19: Target asymmetry P_y as function of $\left(E_\gamma, \theta^*_{p\pi^0}\right)$. The **combined data of this work** is shown as well as the model predictions BnGa-2022 and BnGa-2014.

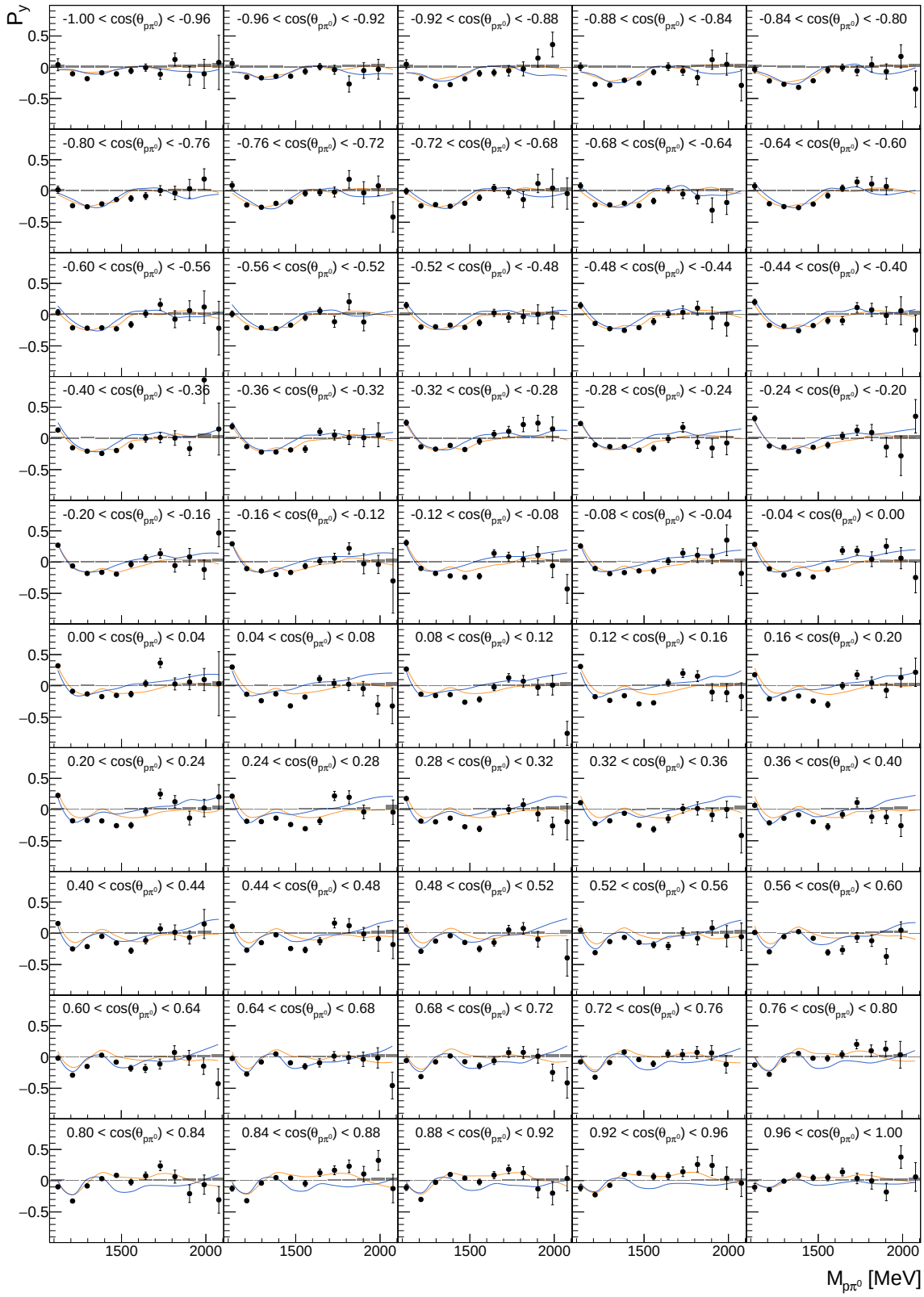

Figure E.20: Target asymmetry P_y as function of $\left(\cos(\theta_{p\pi^0}), M_{p\pi^0}\right)$. The **combined data of this work** is shown as well as the model predictions BnGa-2022 and BnGa-2014.

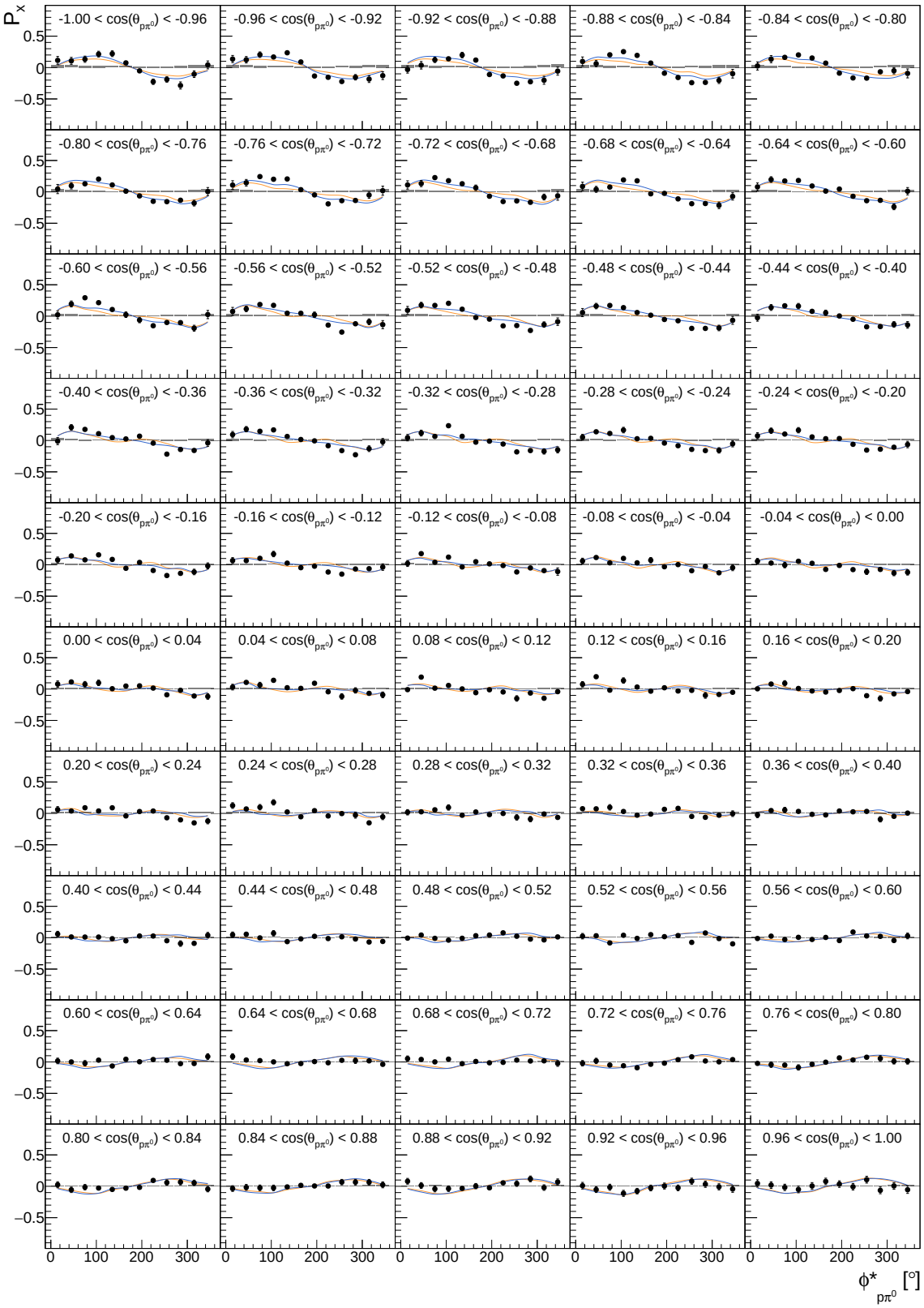

Figure E.21: Target asymmetry P_x as function of $\left(\cos(\theta_{p\pi^0}), \phi^*_{p\pi^0}\right)$. The **combined data of this work** is shown as well as the model predictions BnGa-2022 and BnGa-2014.

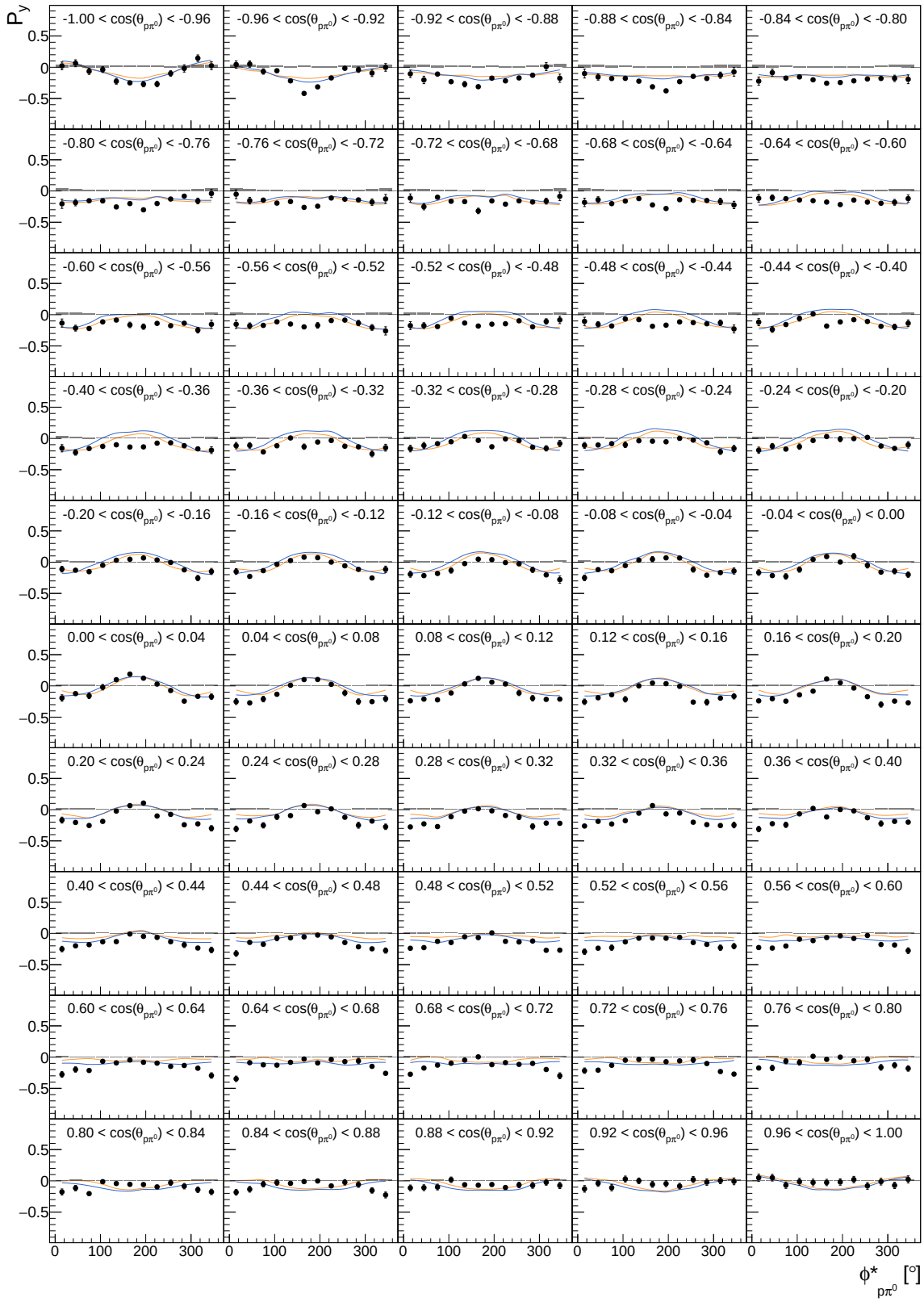

Figure E.22: Target asymmetry P_y as function of $\left(\cos(\theta_{p\pi^0}), \phi^*_{p\pi^0}\right)$. The **combined data of this work** is shown as well as the model predictions BnGa-2022 and BnGa-2014.

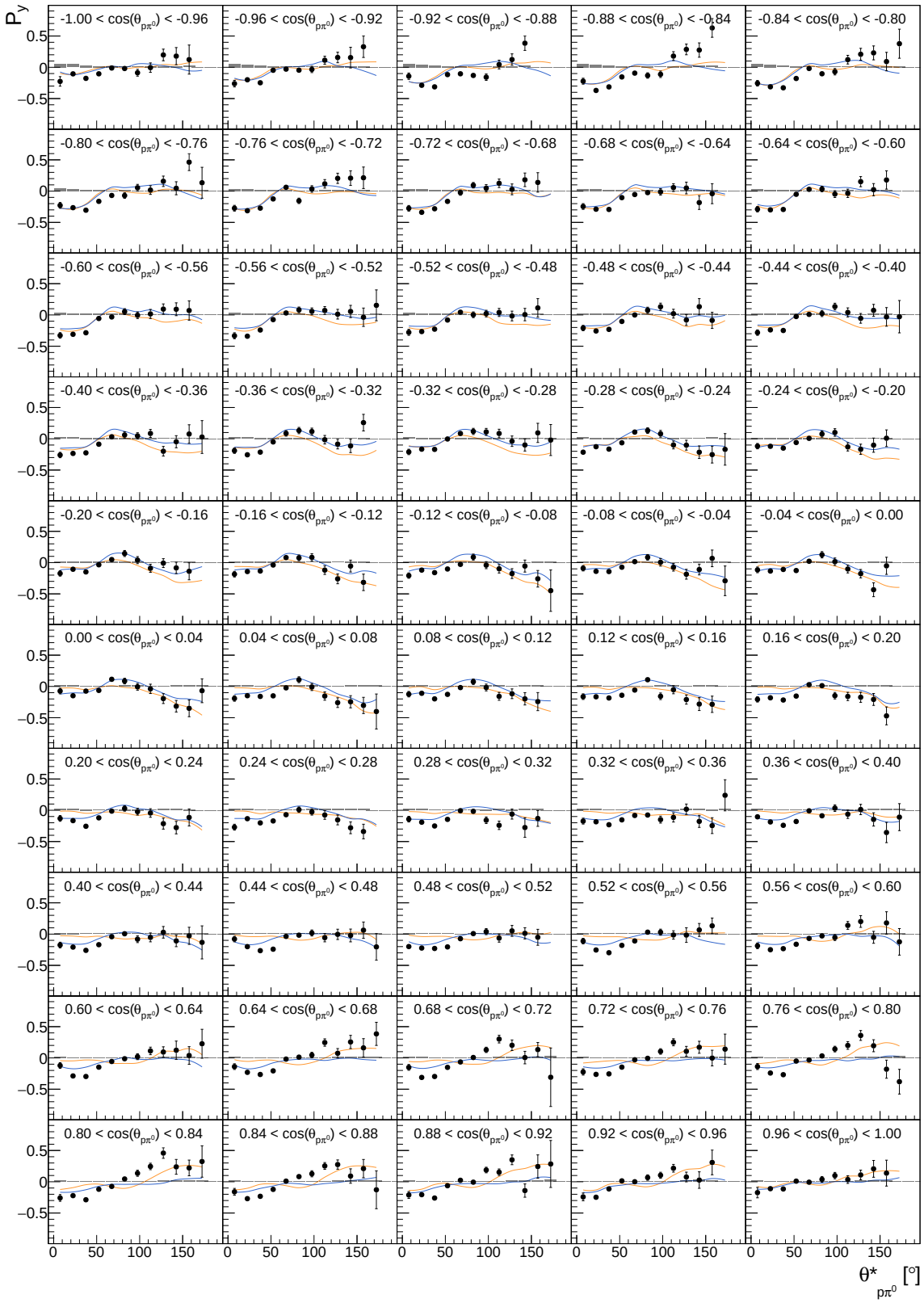

Figure E.23: Target asymmetry P_y as function of $\left(\cos(\theta_{p\pi^0}), \theta^*_{p\pi^0}\right)$. The **combined data of this work** is shown as well as the model predictions BnGa-2022 and BnGa-2014.

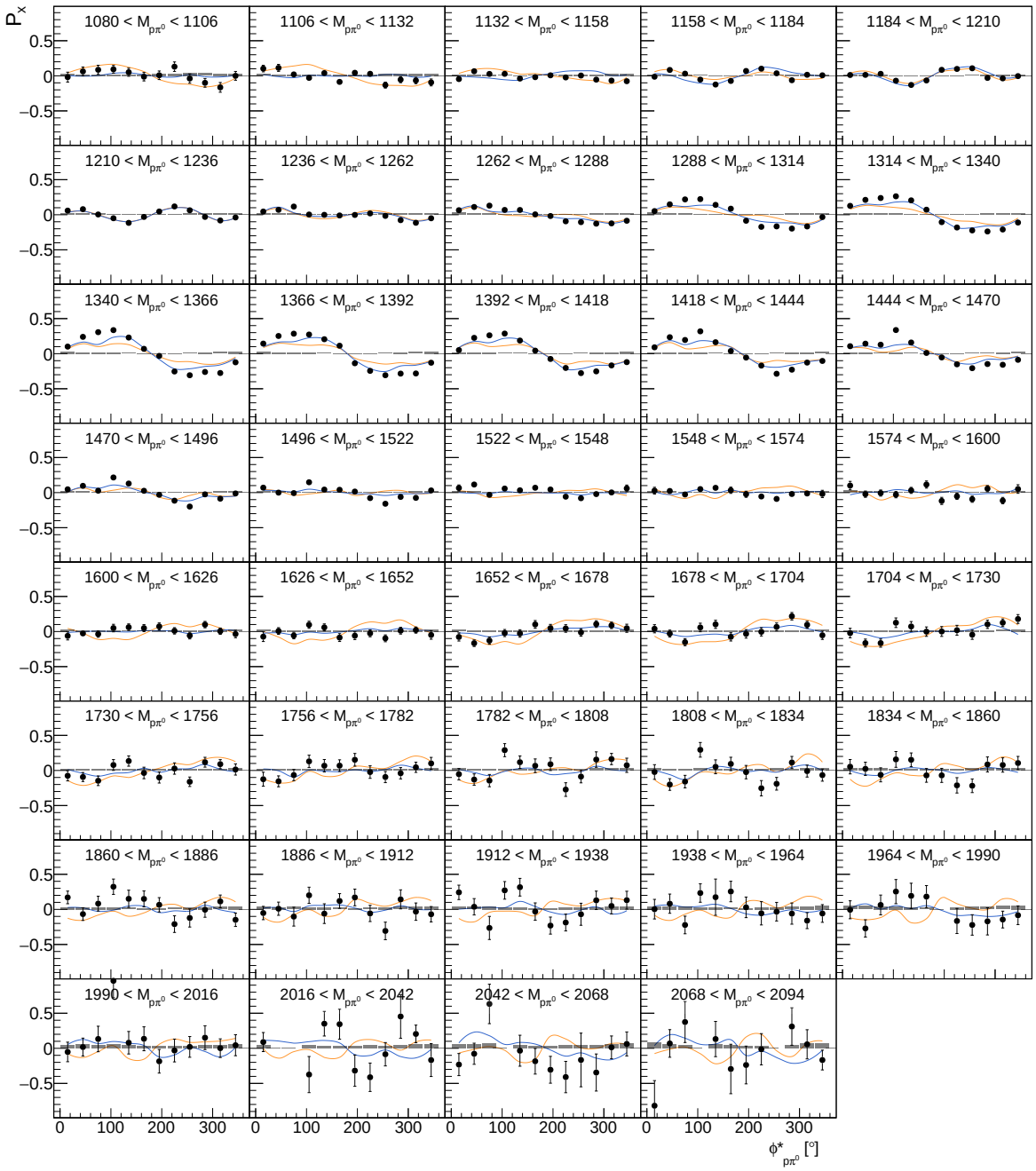

Figure E.24: Target asymmetry P_x as function of $\left(M_{p\pi^0}, \phi^*_{p\pi^0}\right)$. The **combined data of this work** is shown as well as the model predictions BnGa-2022 and BnGa-2014.

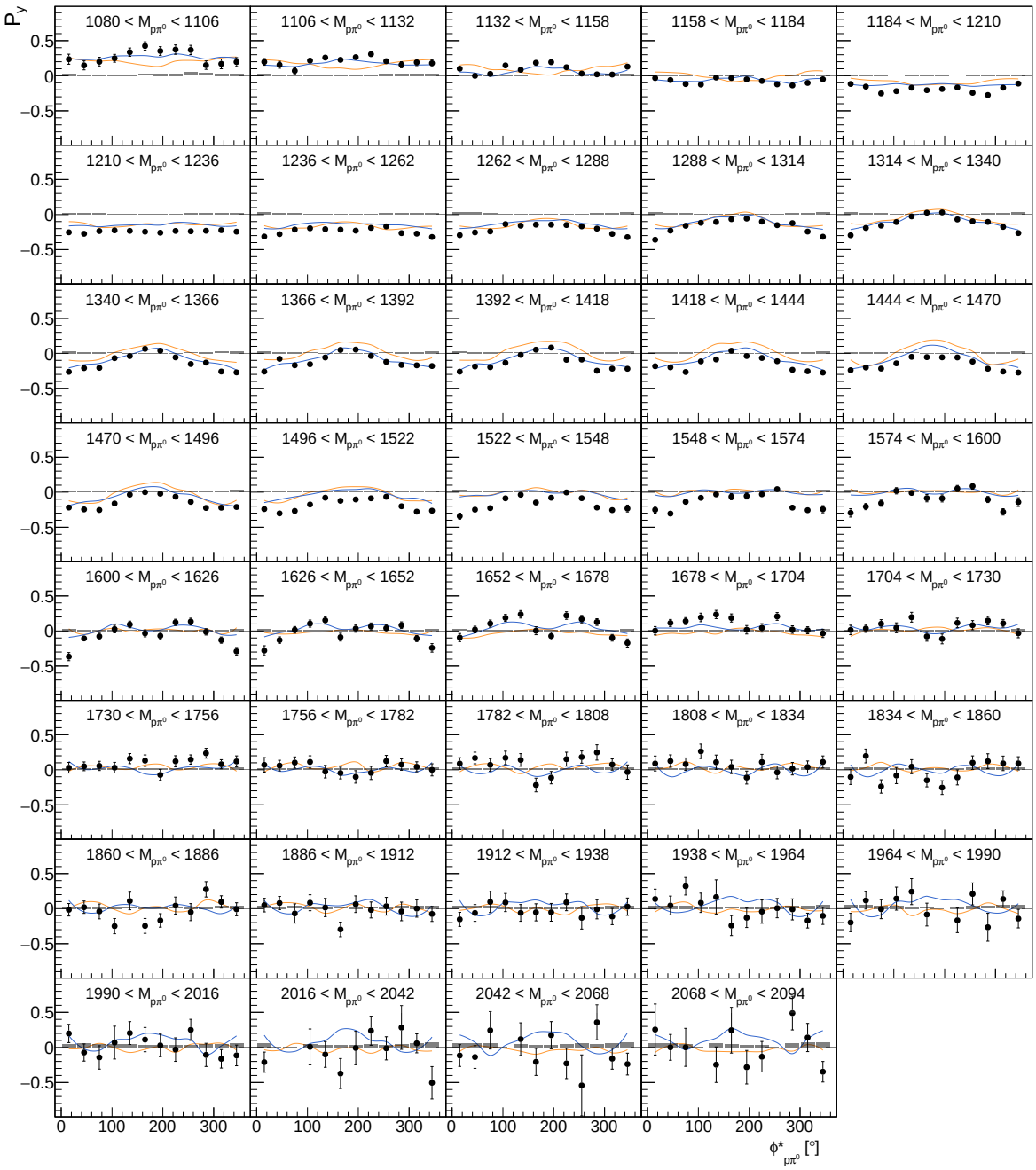

Figure E.25: Target asymmetry P_y as function of $\left(M_{p\pi^0}, \phi^*_{p\pi^0}\right)$. The **combined data of this work** is shown as well as the model predictions BnGa-2022 and BnGa-2014.

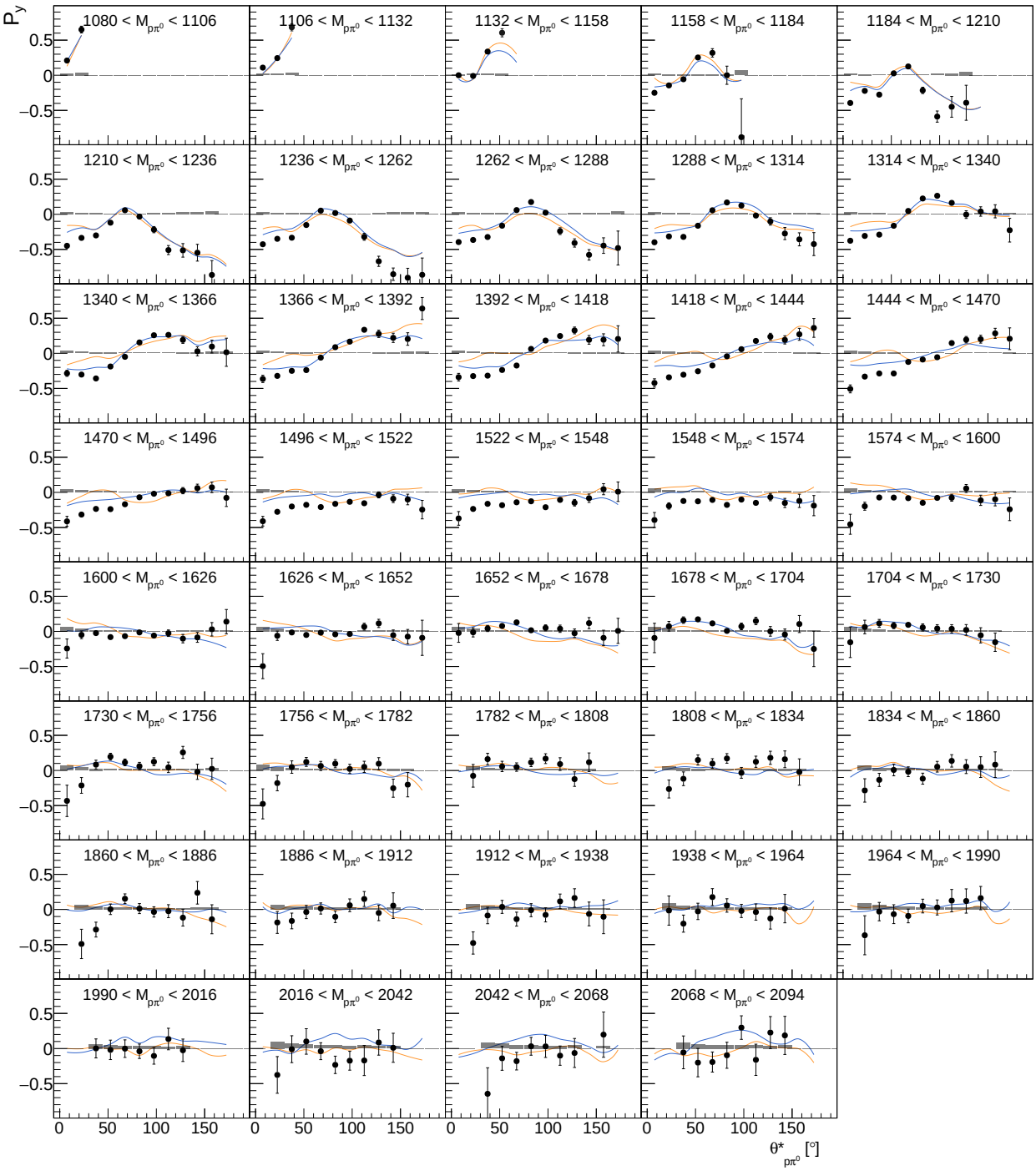

Figure E.26: Target asymmetry P_y as function of $\left(M_{p\pi^0}, \theta^*_{p\pi^0}\right)$. The **combined data of this work** is shown as well as the model predictions BnGa-2022 and BnGa-2014.

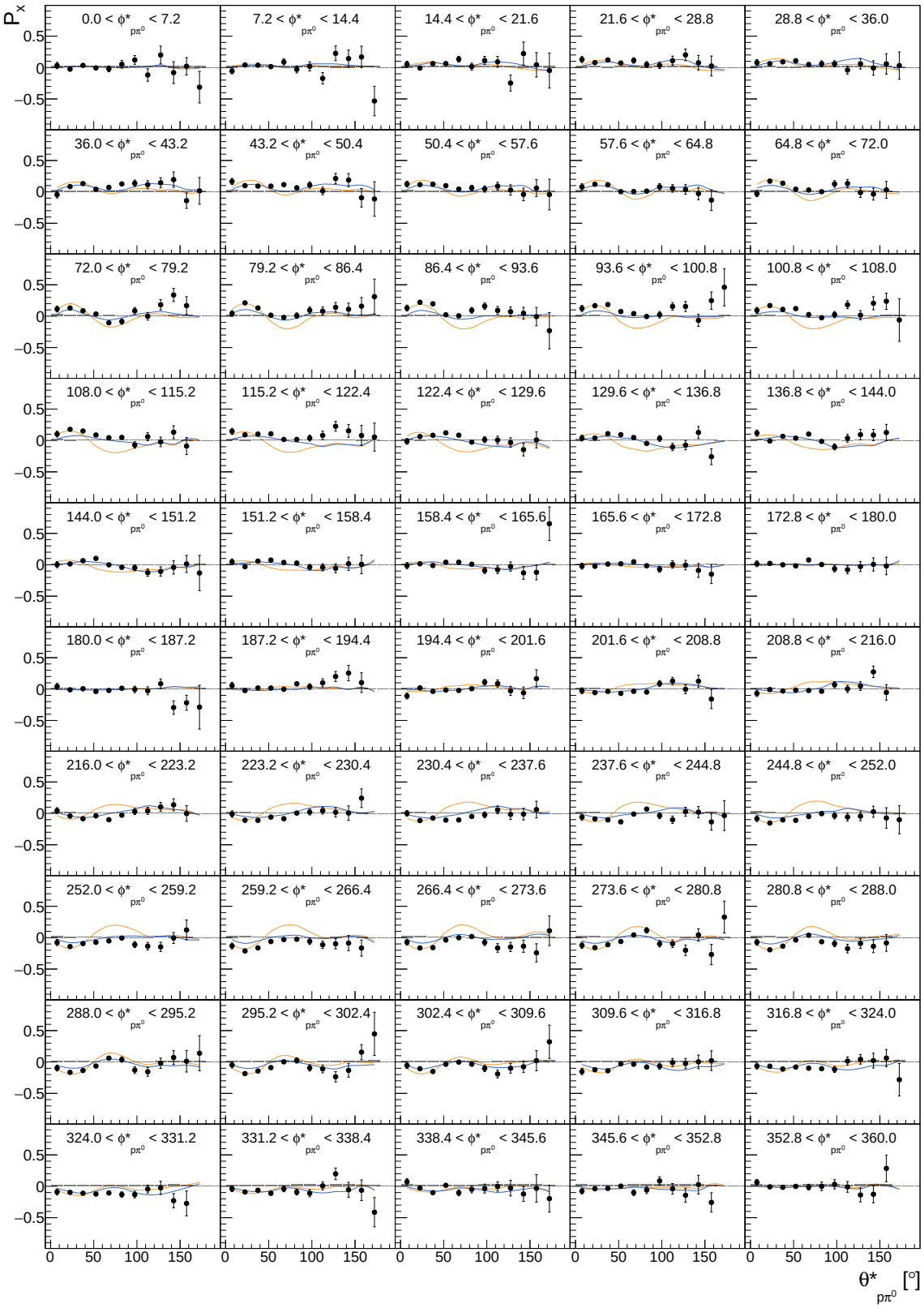

Figure E.27: Target asymmetry P_x as function of $\left(\phi^*_{p\pi^0}, \theta^*_{p\pi^0}\right)$. The **combined data of this work** is shown as well as the model predictions BnGa-2022 and BnGa-2014.

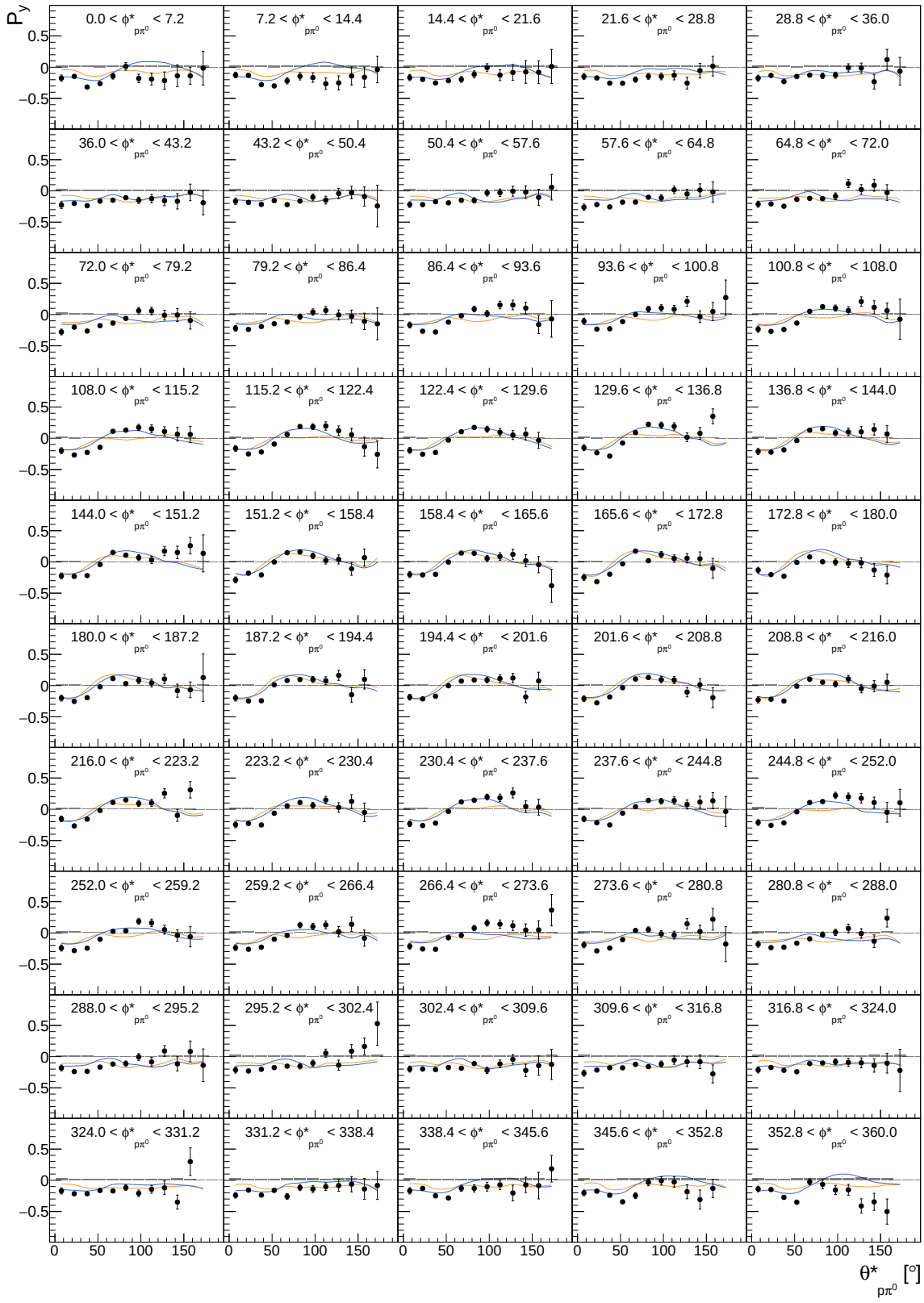

Figure E.28: Target asymmetry P_y as function of $\left(\phi^*_{p\pi^0}, \theta^*_{p\pi^0}\right)$. The **combined data of this work** is shown as well as the model predictions BnGa-2022 and BnGa-2014.

APPENDIX F

P_x^s, P_y^s, P_x^c, P_y^c in Two Dimensions

In this appendix, final results on double polarization observables P_x^s, P_y^s, P_x^c, P_y^c are presented in two dimensions. For the extraction of the results, the combined data of four periods of data taking are used: December 2017, May 2018, February 2019 and June 2021. In each case, 5-PED, 4.5-PED and 4-PED events are included for a complete coverage of the kinematic region. An exception is June 2021, for which 4-PED events are excluded (cf. Section 8.3.2.3). Combinations of kinematic variables for which the observables are expected to be zero when integrated over ϕ^* are excluded (see Section 8.2.1). The results are compared with the model predictions of BnGa-2022 and BnGa-2014. The systematic uncertainties of the results are shown as bars on the x-axis.

$\pi^0\pi^0$-System

The series of Fig. F.1 to F.8 deals with observables extracted in the $\pi^0\pi^0$-system.

- Fig. F.1 to F.3 shows the observables in bins of E_γ.
- Fig. F.4 to F.5 shows the observables in bins of $\cos(\theta_{\pi^0\pi^0})$.
- Fig. F.6 to F.7 shows the observables in bins of $M_{\pi^0\pi^0}$.
- Fig. F.8 shows the observables in bins of $\phi^*_{\pi^0\pi^0}$.

$p\pi^0$-System

The series of Fig. F.9 to F.16 deals with observables extracted in the $p\pi^0$-system.

- Fig. F.9 to F.11 shows the observables in bins of E_γ.
- Fig. F.12 to F.13 shows the observables in bins of $\cos(\theta_{p\pi^0})$.
- Fig. F.14 to F.15 shows the observables in bins of $M_{p\pi^0}$.
- Fig. F.16 shows the observables in bins of $\phi^*_{p\pi^0}$.

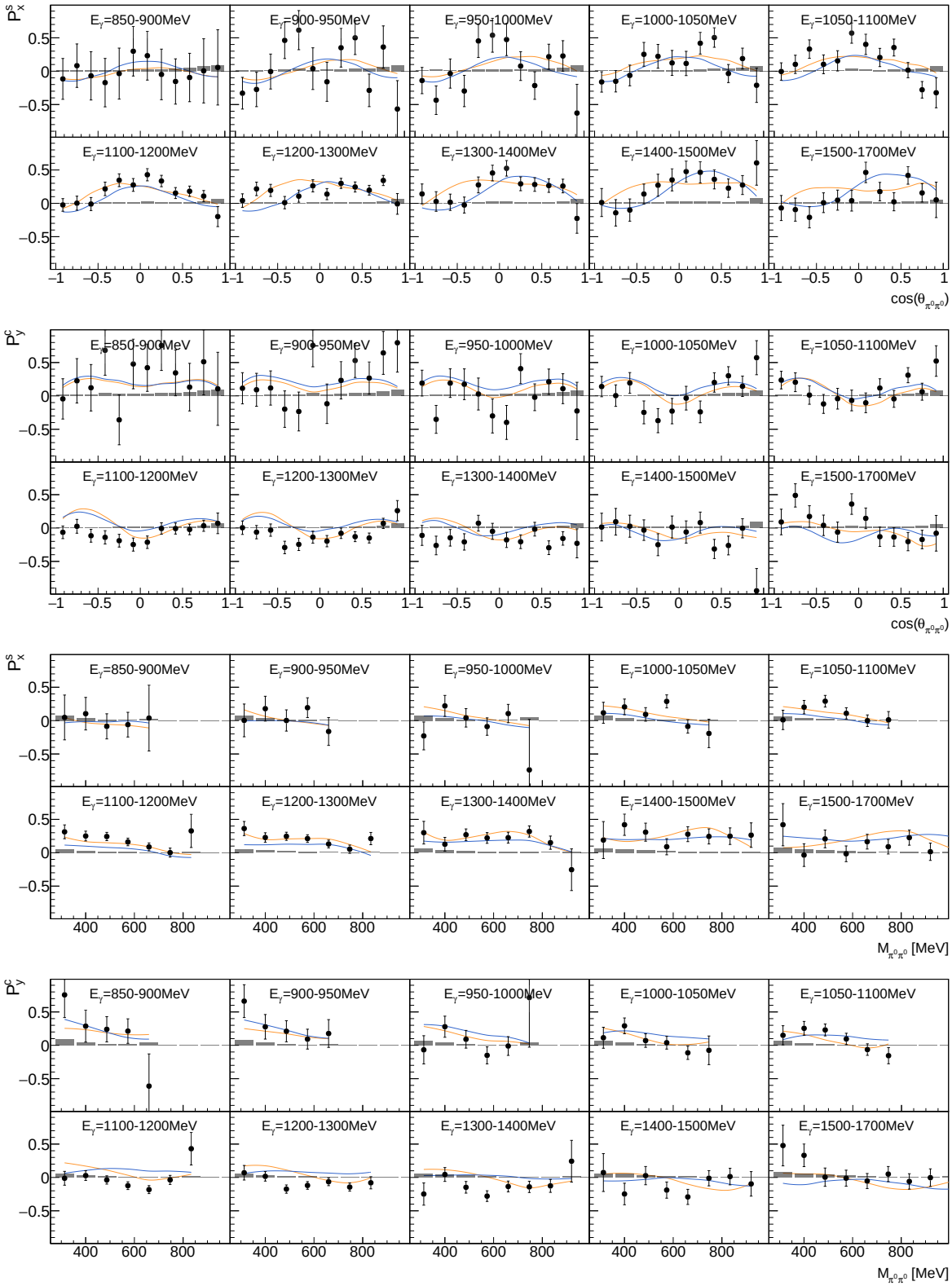

Figure F.1: Double polarization observable P_x^s, P_y^c as function of $(E_\gamma, \cos(\theta_{\pi^0\pi^0}))$ and $(E_\gamma, M_{\pi^0\pi^0})$. The **combined data of this work** is shown as well as the model predictions BnGa-2022 and BnGa-2014.

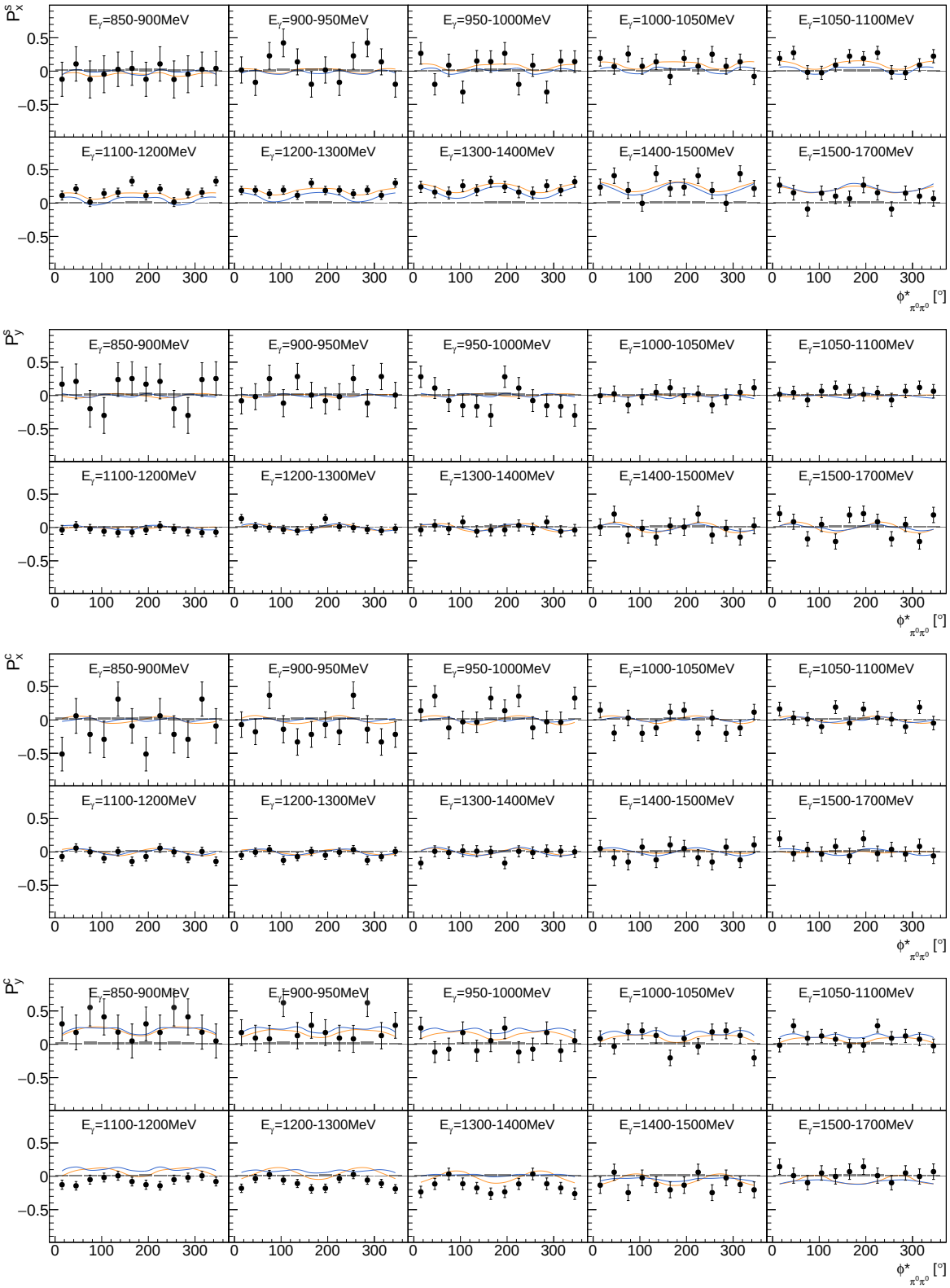

Figure F.2: Double polarization observable P^s_x, P^s_y, P^c_x, P^c_y as function of $(E_\gamma, \phi^*_{\pi^0\pi^0})$. The **combined data of this work** is shown as well as the model predictions BnGa-2022 and BnGa-2014.

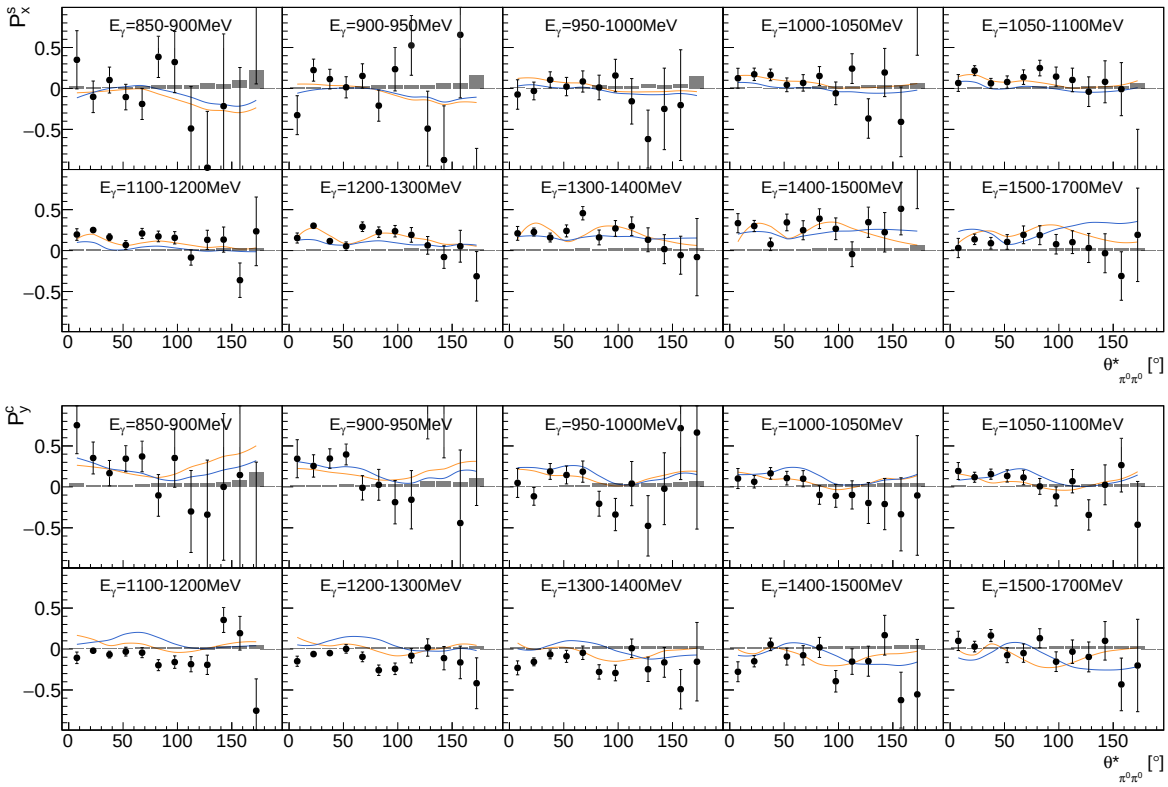

Figure F.3: Double polarization observable P_x^s, P_y^c as function of $(E_\gamma, \theta^*_{\pi^0\pi^0})$. The **combined data of this work** is shown as well as the model predictions BnGa-2022 and BnGa-2014.

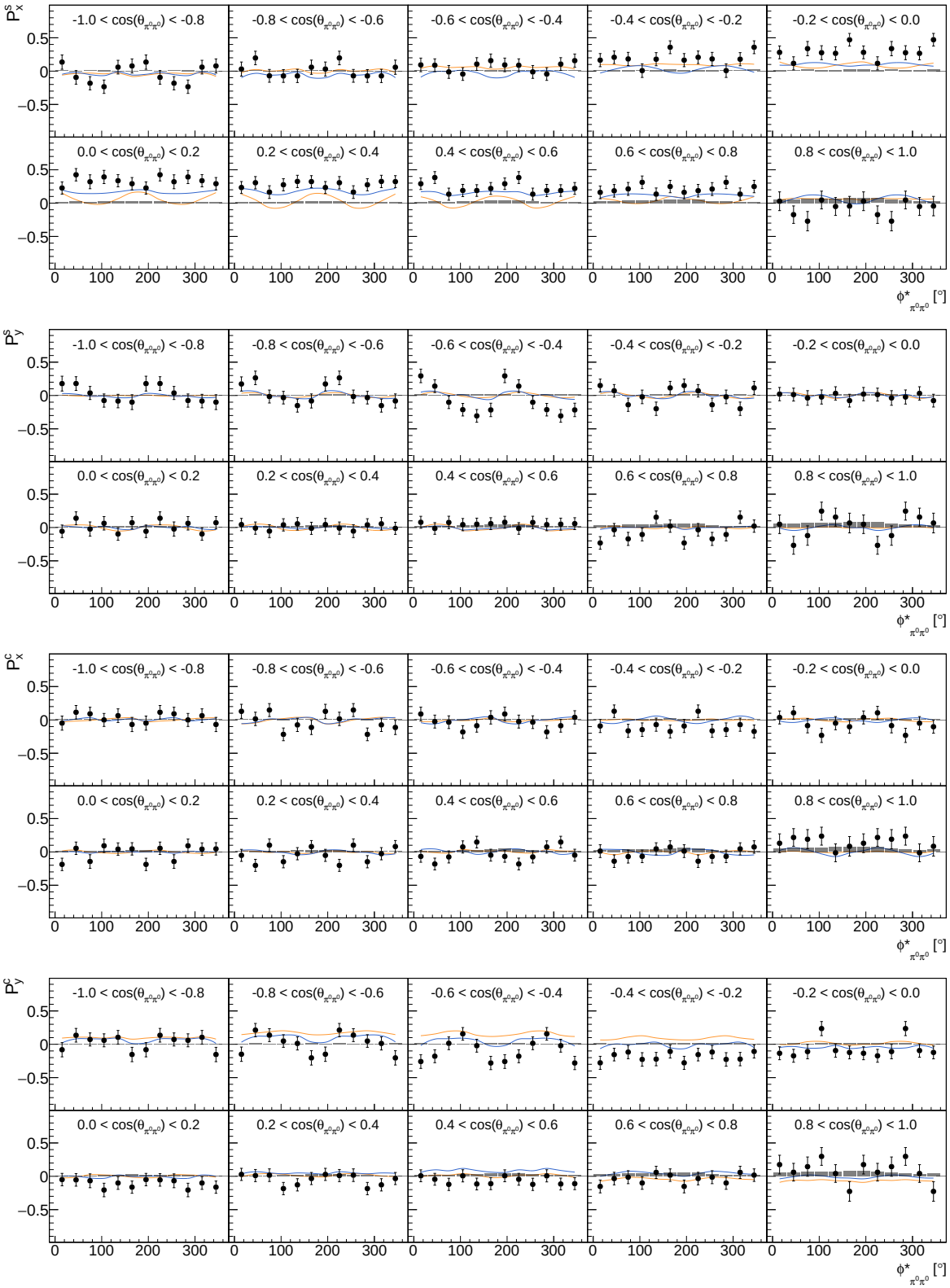

Figure F.4: Double polarization observable P_x^s, P_y^s, P_x^c, P_y^c as function of $(\cos(\theta_{\pi^0\pi^0}), \phi^*_{\pi^0\pi^0})$. The **combined data of this work** is shown as well as the model predictions BnGa-2022 and BnGa-2014.

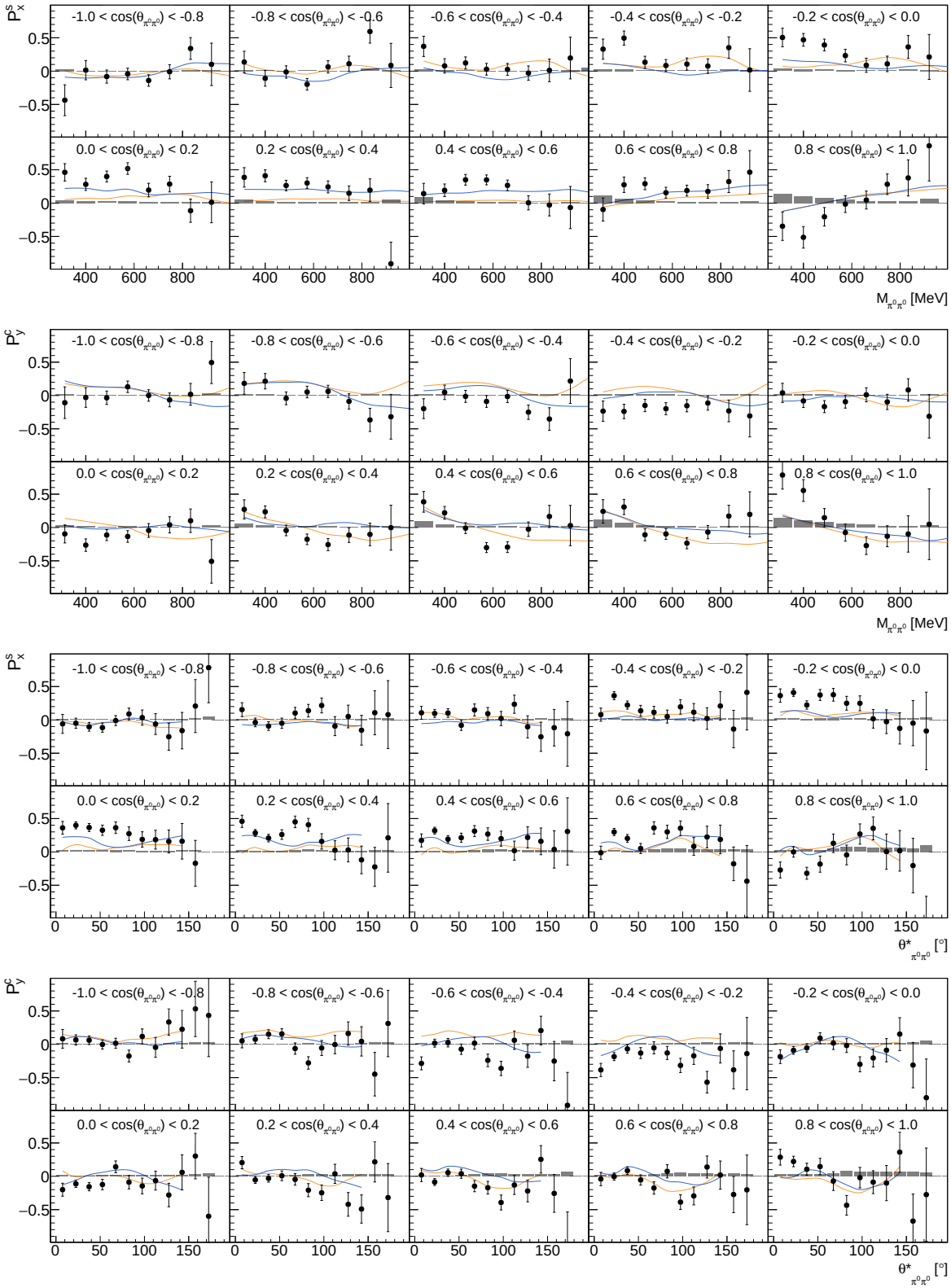

Figure F.5: Double polarization observable P_x^s, P_y^c as function of $(\cos(\theta_{\pi^0\pi^0}), M_{\pi^0\pi^0})$ and $(\cos(\theta_{\pi^0\pi^0}), \theta^*_{\pi^0\pi^0})$. The **combined data of this work** is shown as well as the model predictions BnGa-2022 and BnGa-2014.

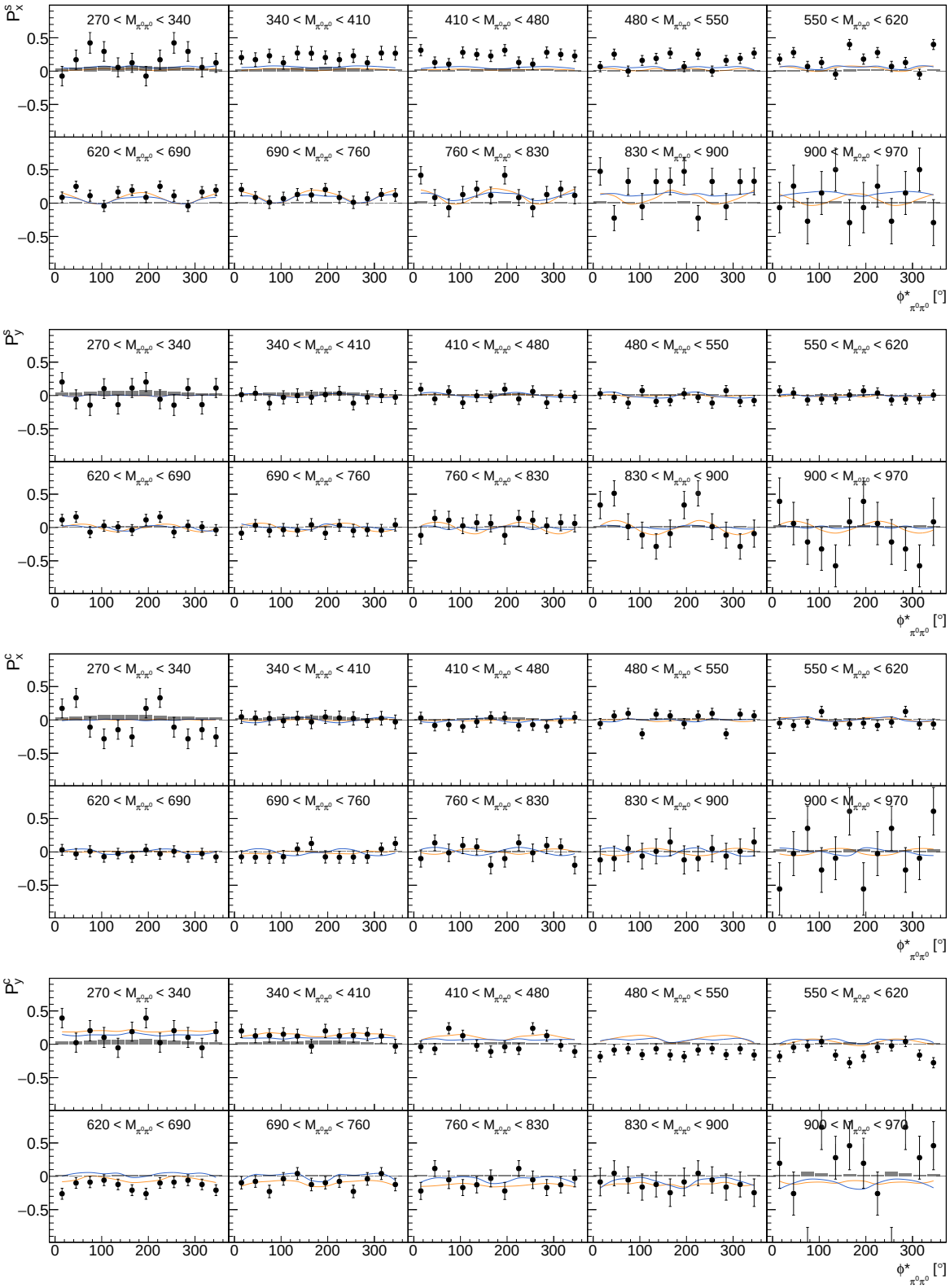

Figure F.6: Double polarization observable P^s_x, P^s_y, P^c_x, P^c_y as function of $(M_{\pi^0\pi^0}, \phi^*_{\pi^0\pi^0})$. The **combined data of this work** is shown as well as the model predictions BnGa-2022 and BnGa-2014.

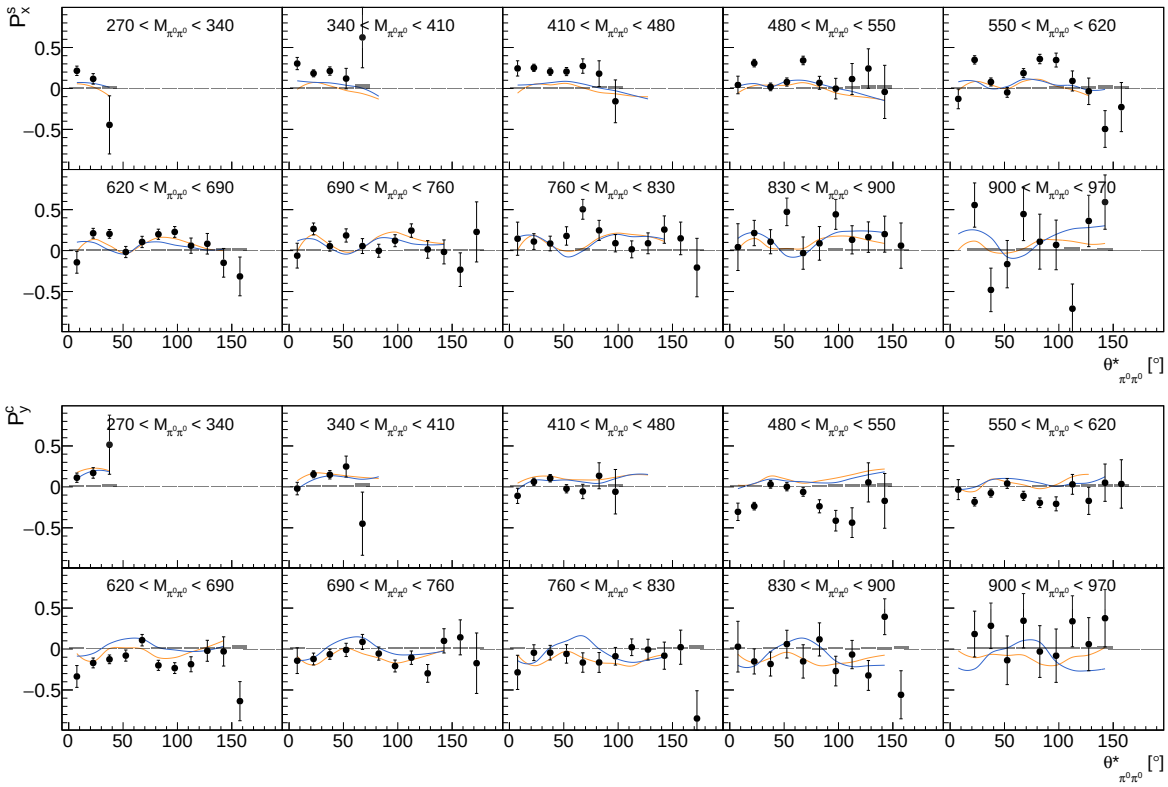

Figure F.7: Double polarization observable P_x^s, P_y^c as function of $(M_{\pi^0\pi^0}, \theta^*_{\pi^0\pi^0})$. The **combined data of this work** is shown as well as the model predictions BnGa-2022 and BnGa-2014.

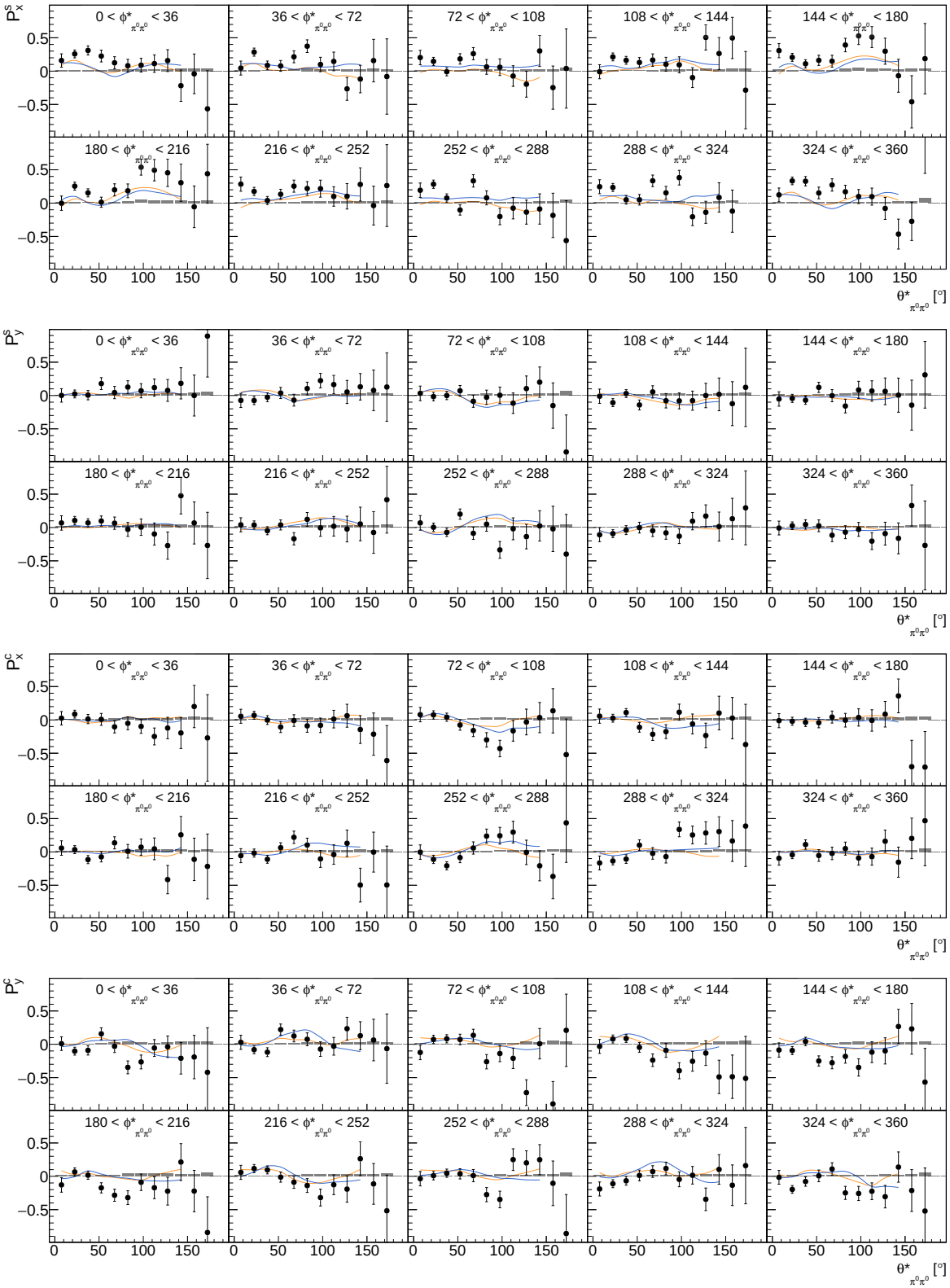

Figure F.8: Double polarization observable P_x^s, P_y^s, P_x^c, P_y^c as function of $(\phi^*_{\pi^0\pi^0}, \theta^*_{\pi^0\pi^0})$. The **combined data of this work** is shown as well as the model predictions BnGa-2022 and BnGa-2014.

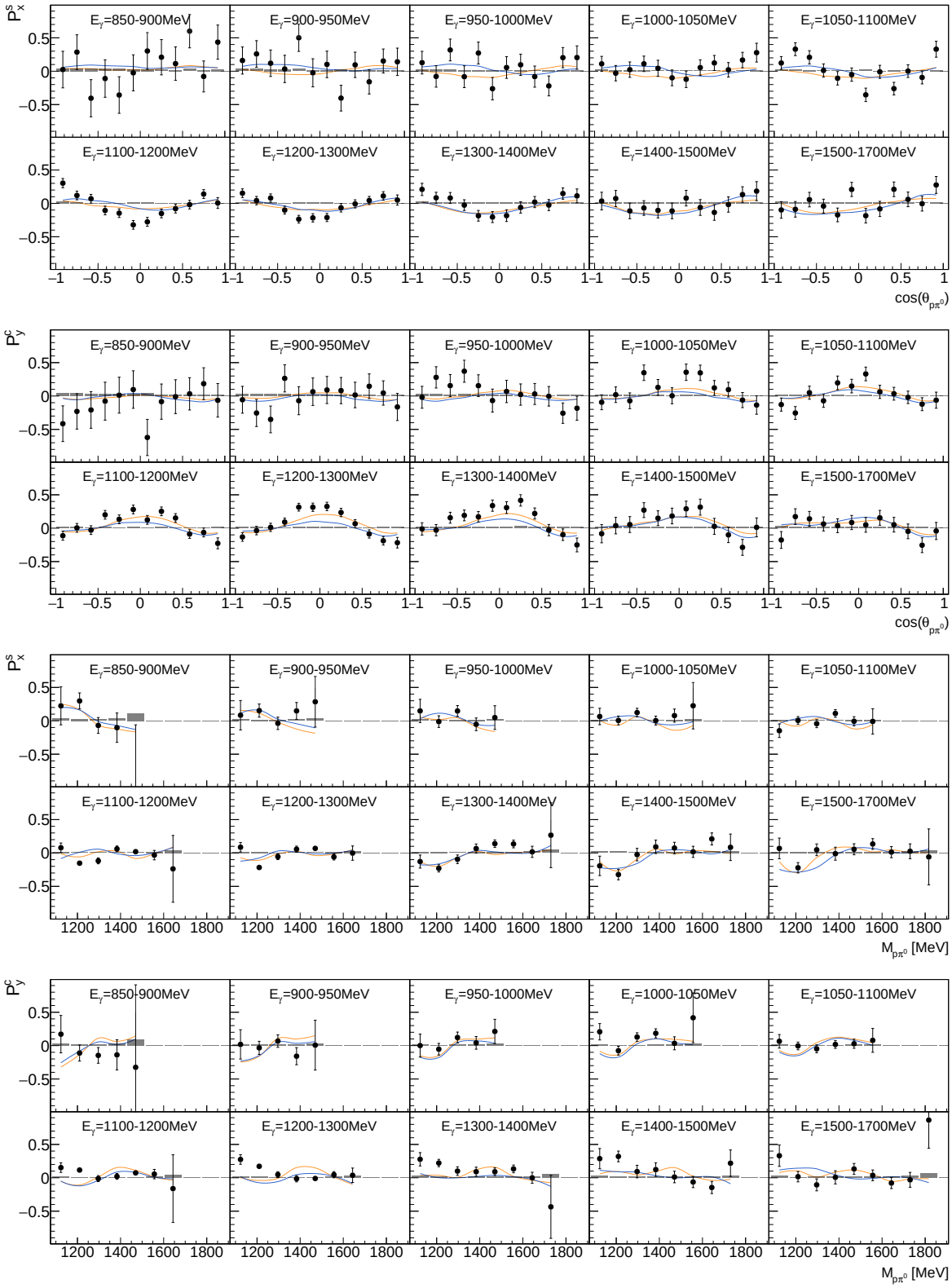

Figure F.9: Double polarization observable P_x^s, P_y^c as function of $(E_\gamma, \cos(\theta_{p\pi^0}))$ and $(E_\gamma, M_{p\pi^0})$. The **combined data of this work** is shown as well as the model predictions BnGa-2022 and BnGa-2014.

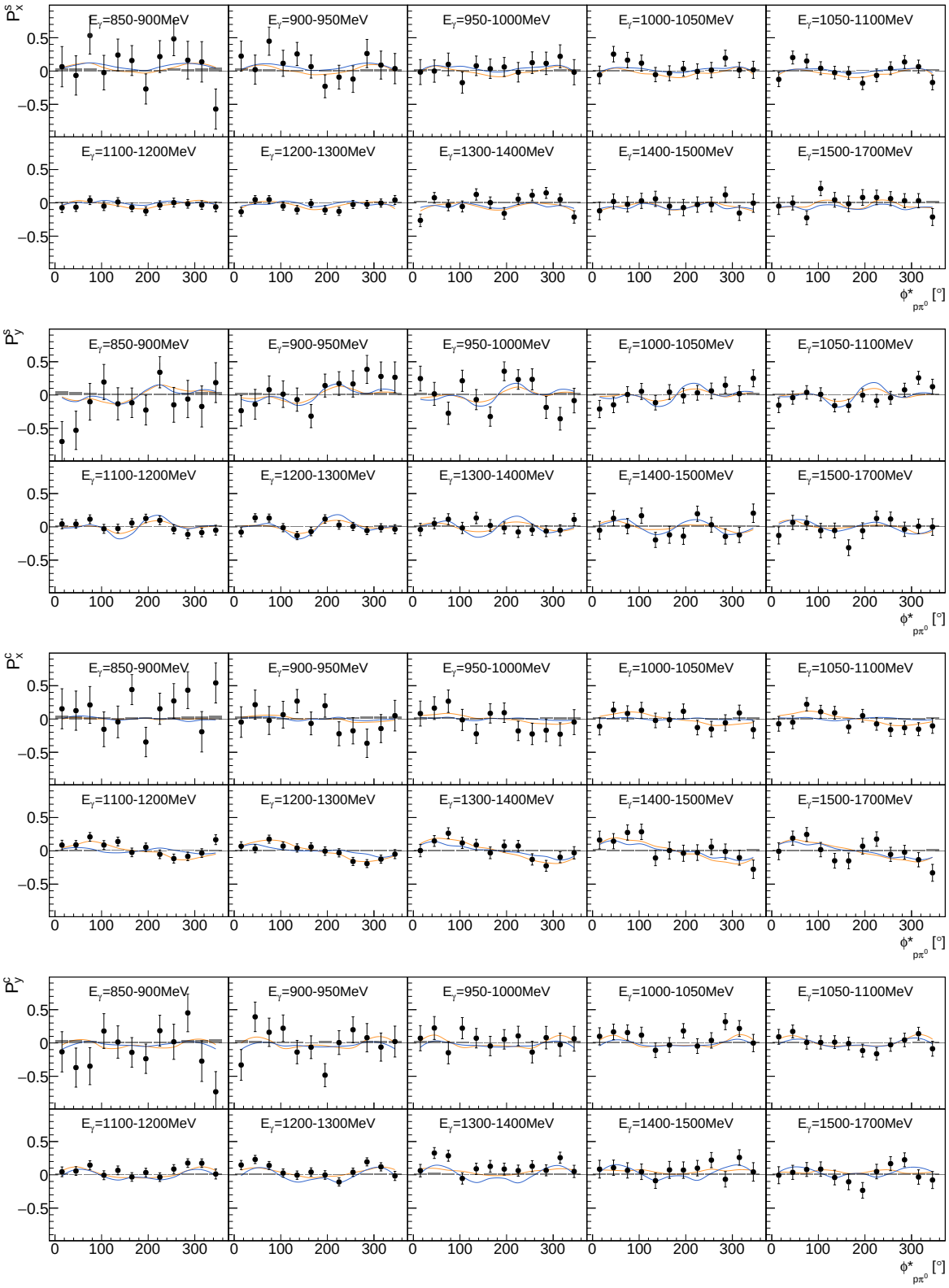

Figure F.10: Double polarization observable P^s_x, P^s_y, P^c_x, P^c_y as function of $(E_\gamma, \phi^*_{p\pi^0})$. The **combined data of this work** is shown as well as the model predictions BnGa-2022 and BnGa-2014.

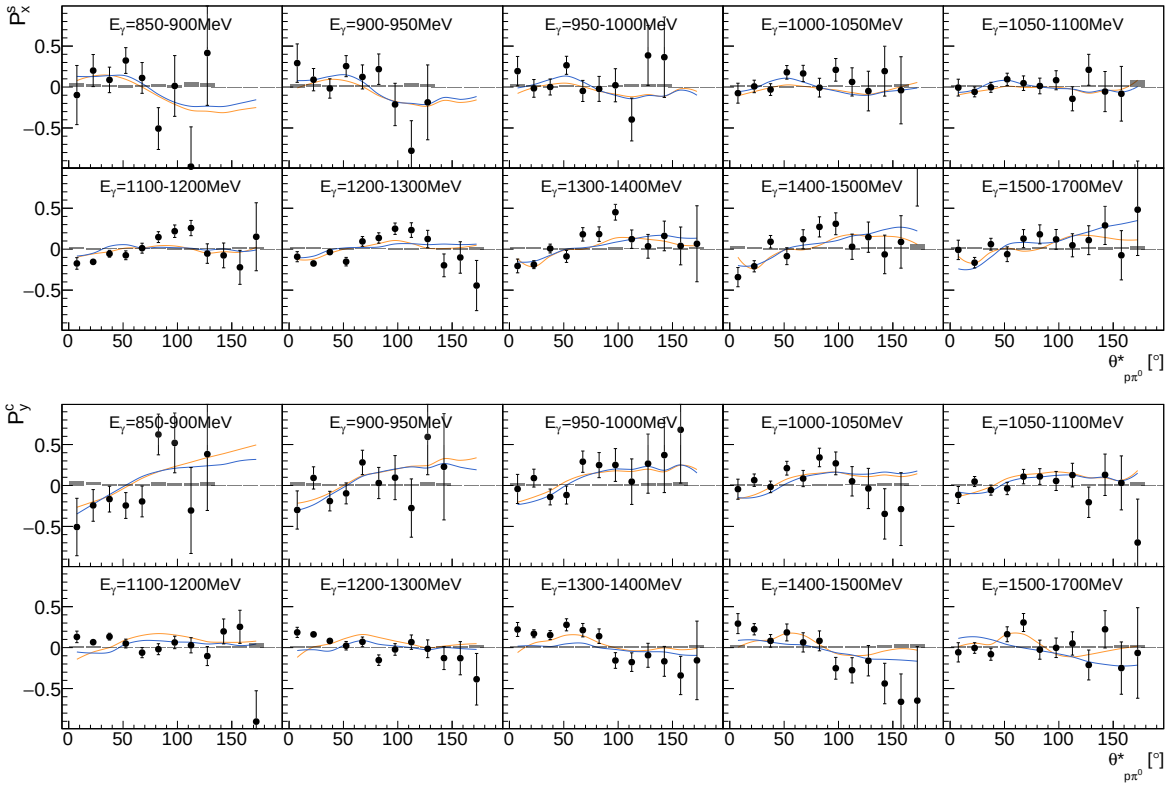

Figure F.11: Double polarization observable P_x^s, P_y^c as function of $(E_\gamma, \theta^*_{p\pi^0})$. The **combined data of this work** is shown as well as the model predictions BnGa-2022 and BnGa-2014.

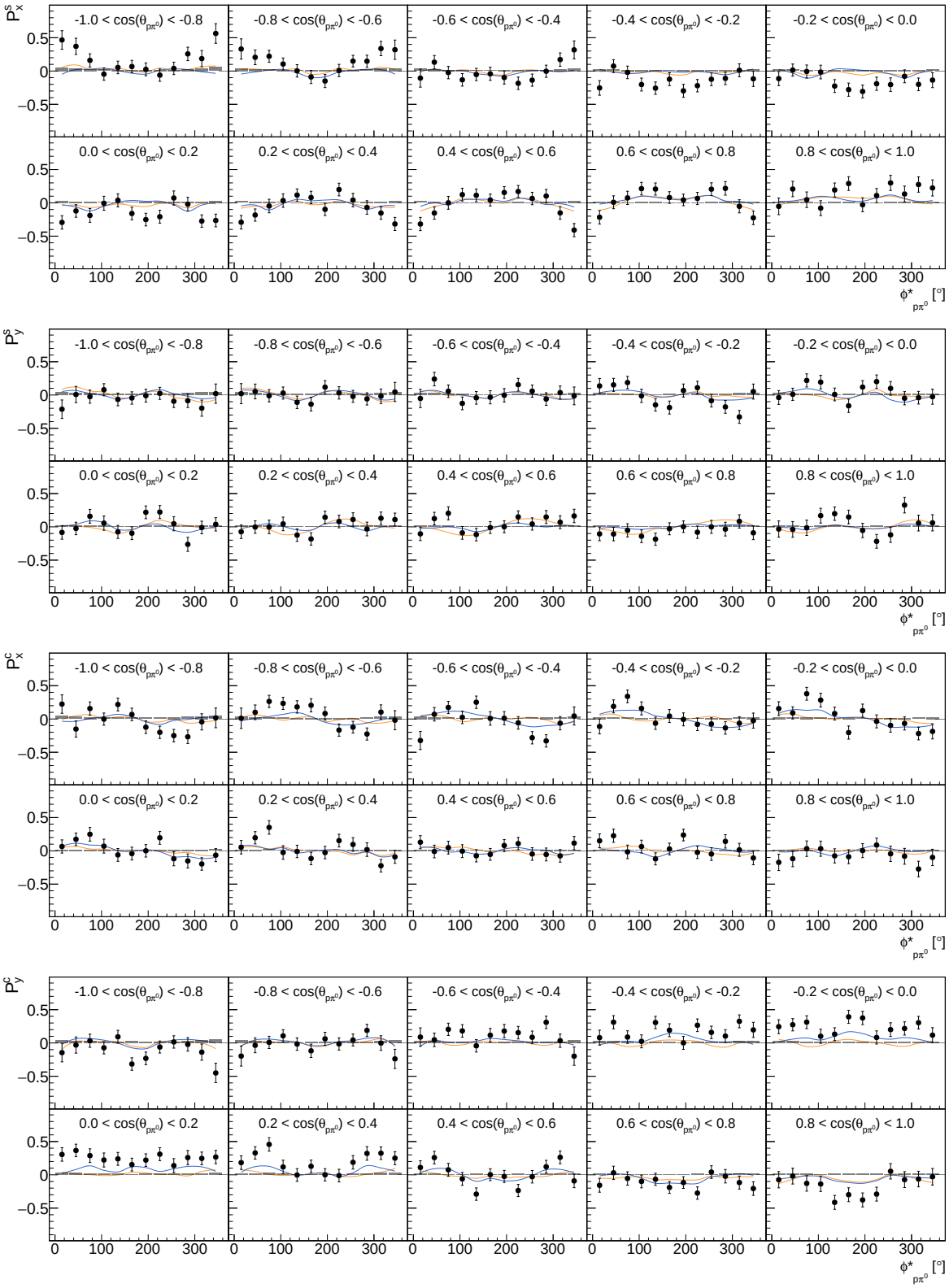

Figure F.12: Double polarization observable P_x^s, P_y^s, P_x^c, P_y^c as function of $(\cos(\theta_{p\pi^0}), \phi^*_{p\pi^0})$. The **combined data of this work** is shown as well as the model predictions BnGa-2022 and BnGa-2014.

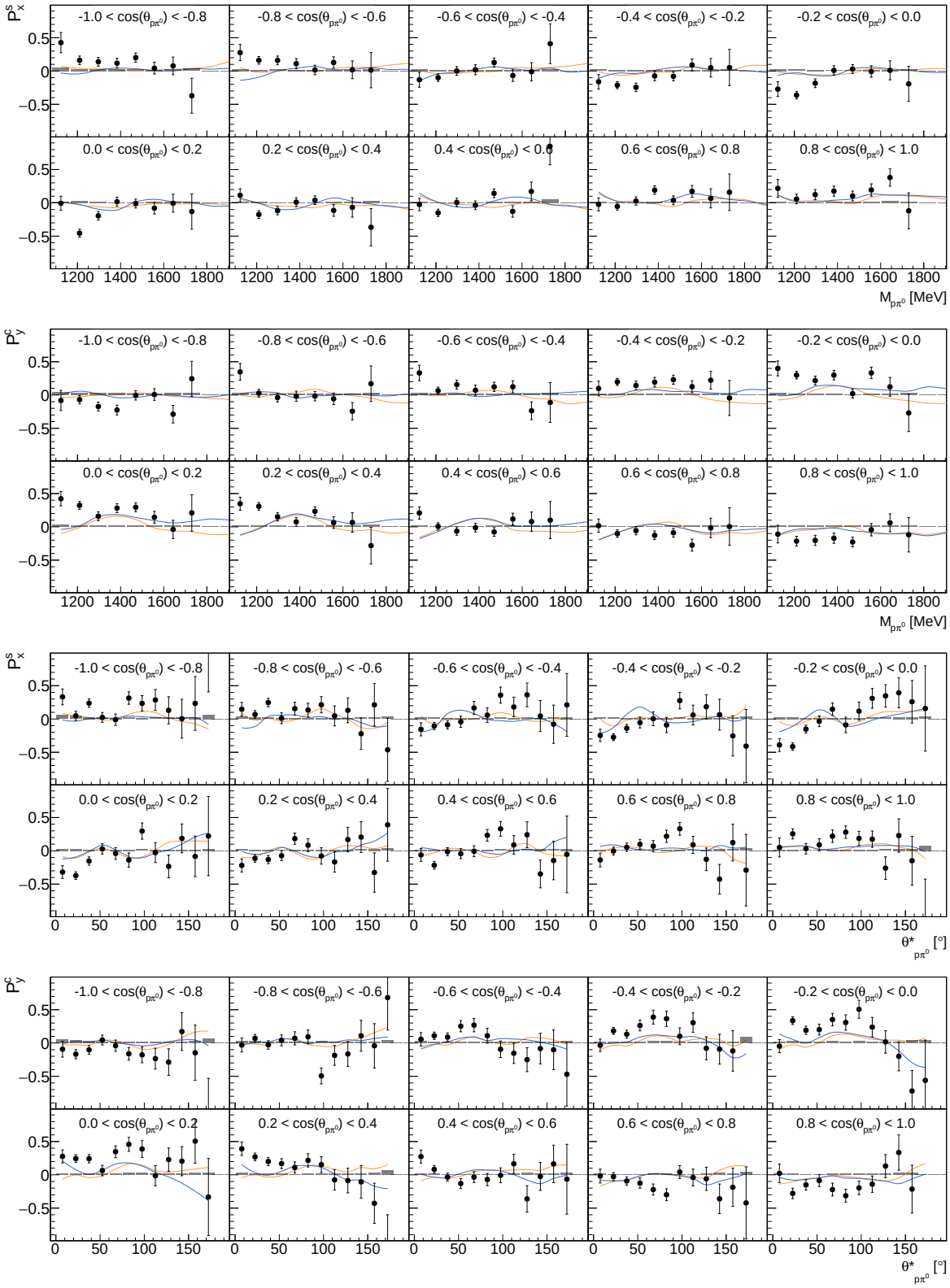

Figure F.13: Double polarization observable P_x^s, P_y^c as function of $(\cos(\theta_{p\pi^0}), M_{p\pi^0})$ and $(\cos(\theta_{p\pi^0}), \theta^*_{p\pi^0})$. The **combined data of this work** is shown as well as the model predictions BnGa-2022 and BnGa-2014.

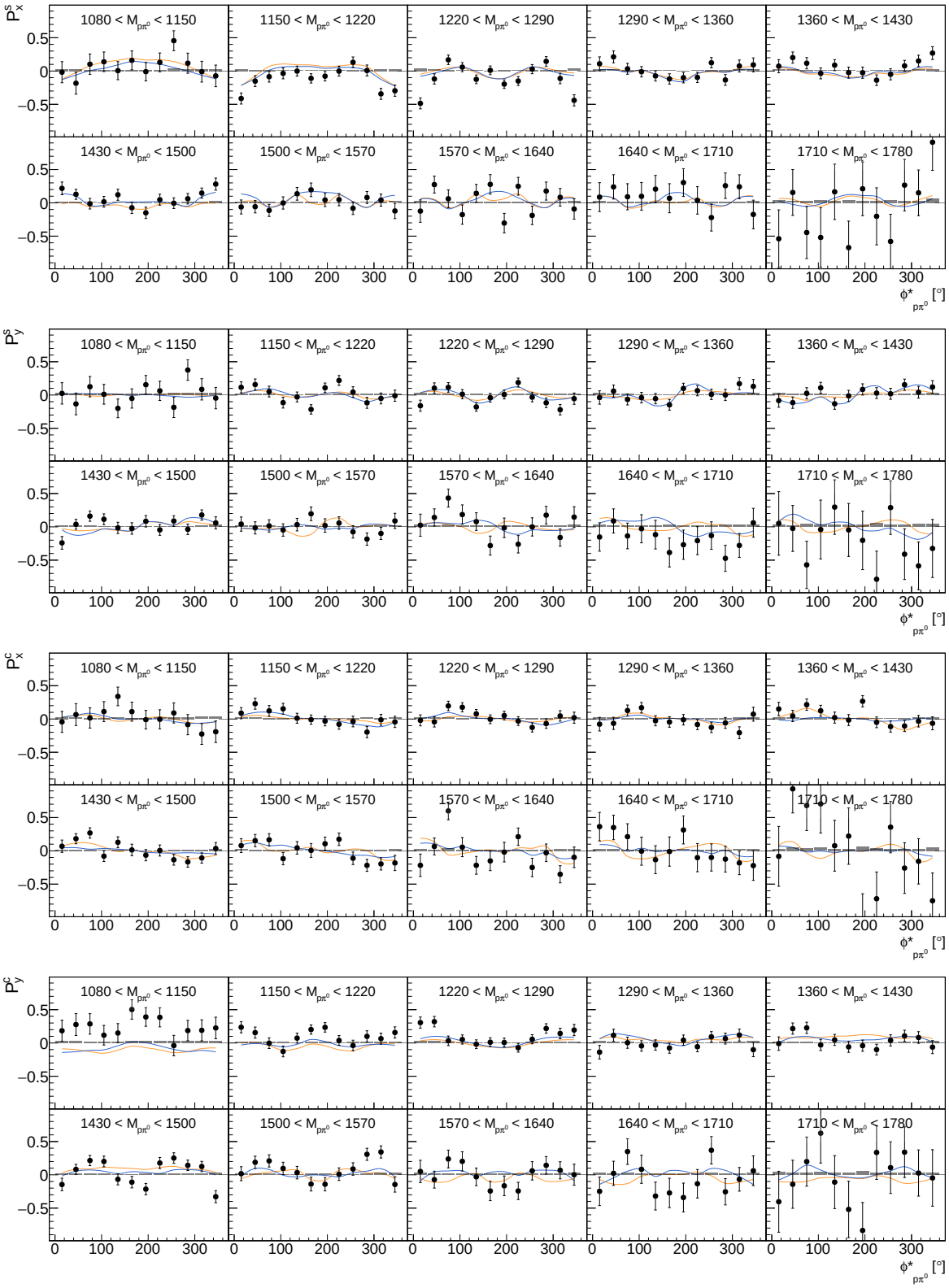

Figure F.14: Double polarization observable P_x^s, P_y^s, P_x^c, P_y^c as function of $(M_{p\pi^0}, \phi^*_{p\pi^0})$. The **combined data of this work** is shown as well as the model predictions BnGa-2022 and BnGa-2014.

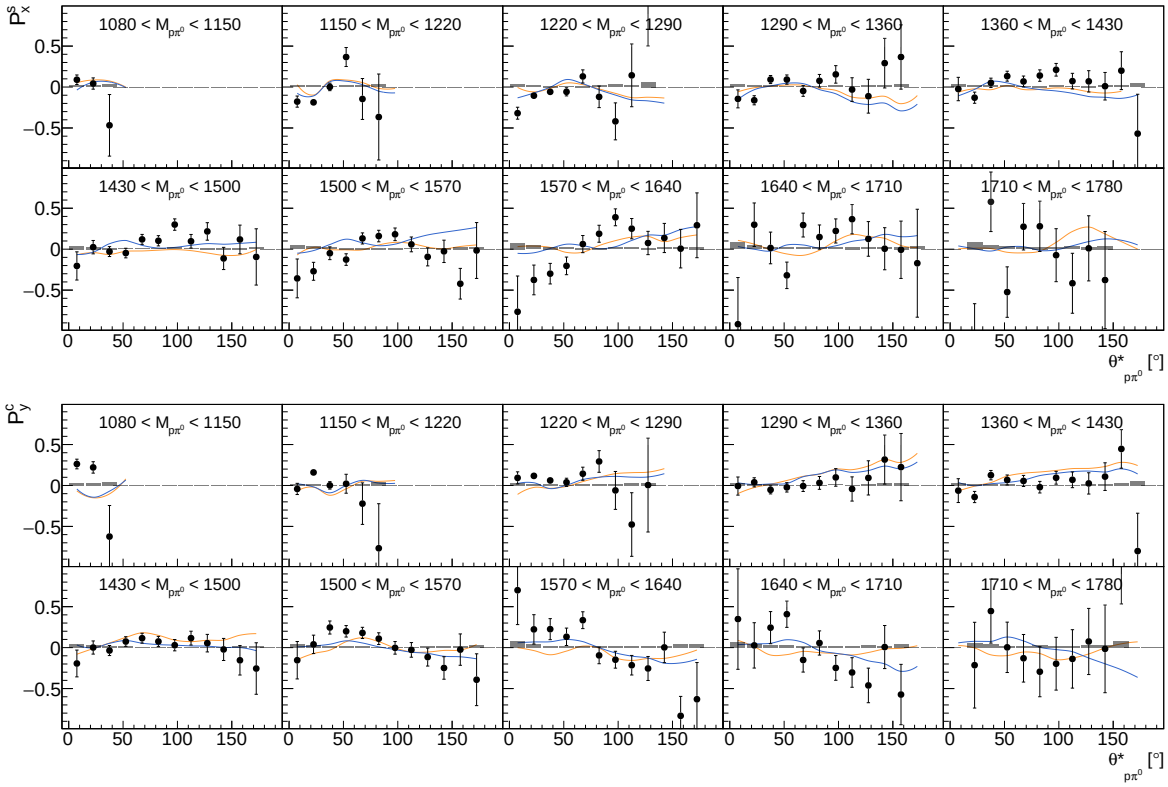

Figure F.15: Double polarization observable P_x^s, P_y^c as function of $(M_{p\pi^0}, \theta^*_{p\pi^0})$. The **combined data of this work** is shown as well as the model predictions BnGa-2022 and BnGa-2014.

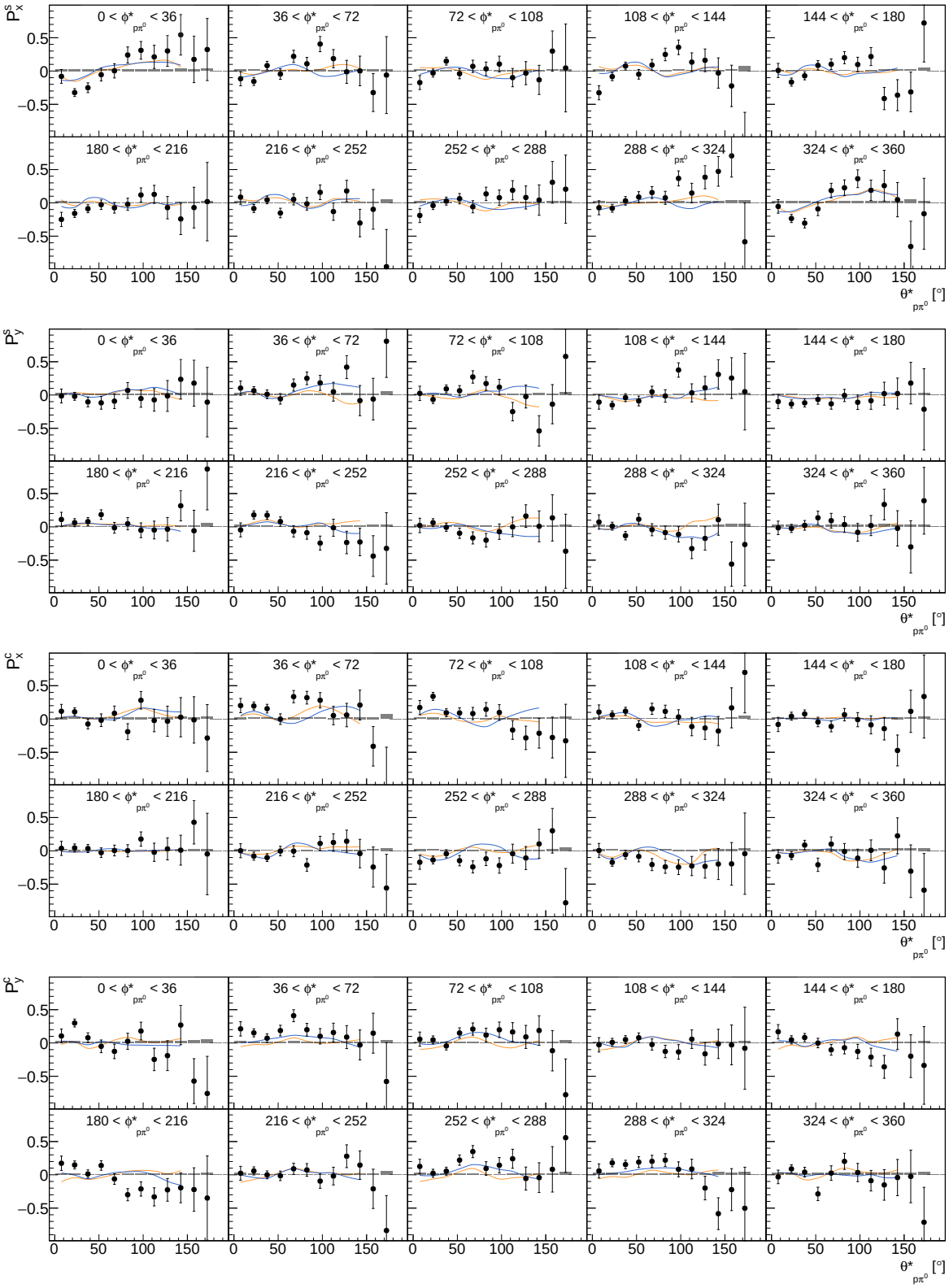

Figure F.16: Double polarization observable P^s_x, P^s_y, P^c_x, P^c_y as function of $(\phi^*_{p\pi^0}, \theta^*_{p\pi^0})$. The **combined data of this work** is shown as well as the model predictions BnGa-2022 and BnGa-2014.

APPENDIX G

P_x, P_y in Four Dimensions

In this appendix, final results of the single polarization observables P_x, P_y in four dimensions are presented. Each figure represents a selected energy range. In each figure (energy range), the extracted observables are presented as a function of $(\cos(\theta), M, \phi^*)$. For the extraction of the results, the combined data of four periods of data taking are used: December 2017, May 2018, February 2019 and June 2021. In each case, 5-PED, 4.5-PED and 4-PED events are included for a complete coverage of the kinematic region. An exception is June 2021, for which 4-PED events are excluded (cf. Section 8.3.2.3). The results are compared with the model predictions of BnGa-2022 and BnGa-2014. The systematic uncertainties of the results are shown as bars on the x-axis.

$\pi^0\pi^0$-System

The series of Fig. G.1 to G.10 deals with observables extracted in the $\pi^0\pi^0$-system.

$p\pi^0$-System

The series of Fig. G.11 to G.20 deals with observables extracted in the $p\pi^0$-system.

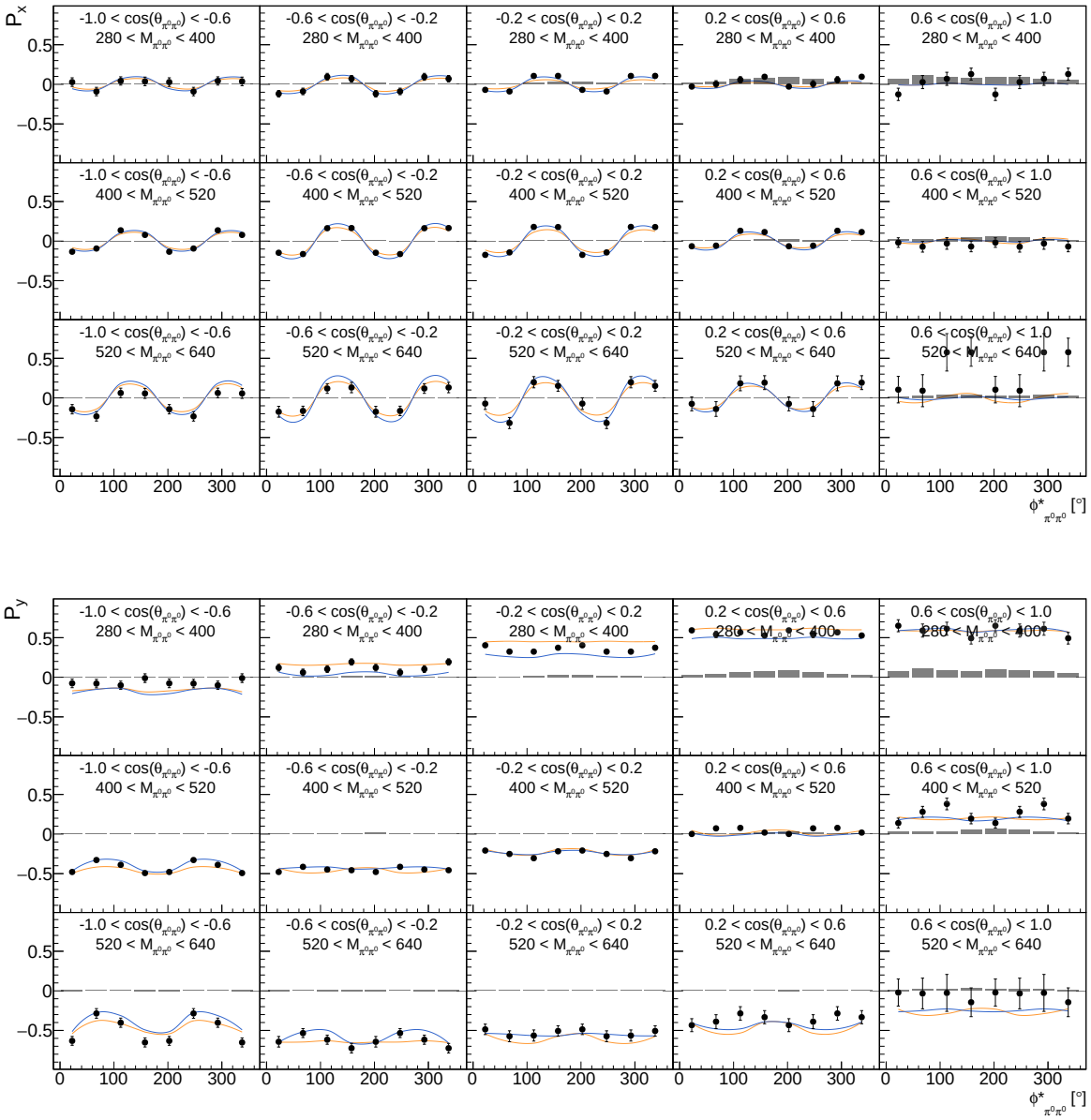

$E_\gamma = 650 - 800\,\mathrm{MeV}$

Figure G.1: Target asymmetries P_x, P_y for a specific energy range $E_\gamma = 650 - 800\,\mathrm{MeV}$ as function of $\left(\cos(\theta_{\pi^0\pi^0}), M_{\pi^0\pi^0}, \phi^*_{\pi^0\pi^0}\right)$. The **combined data of this work** is shown as well as the model predictions BnGa-2022 and BnGa-2014.

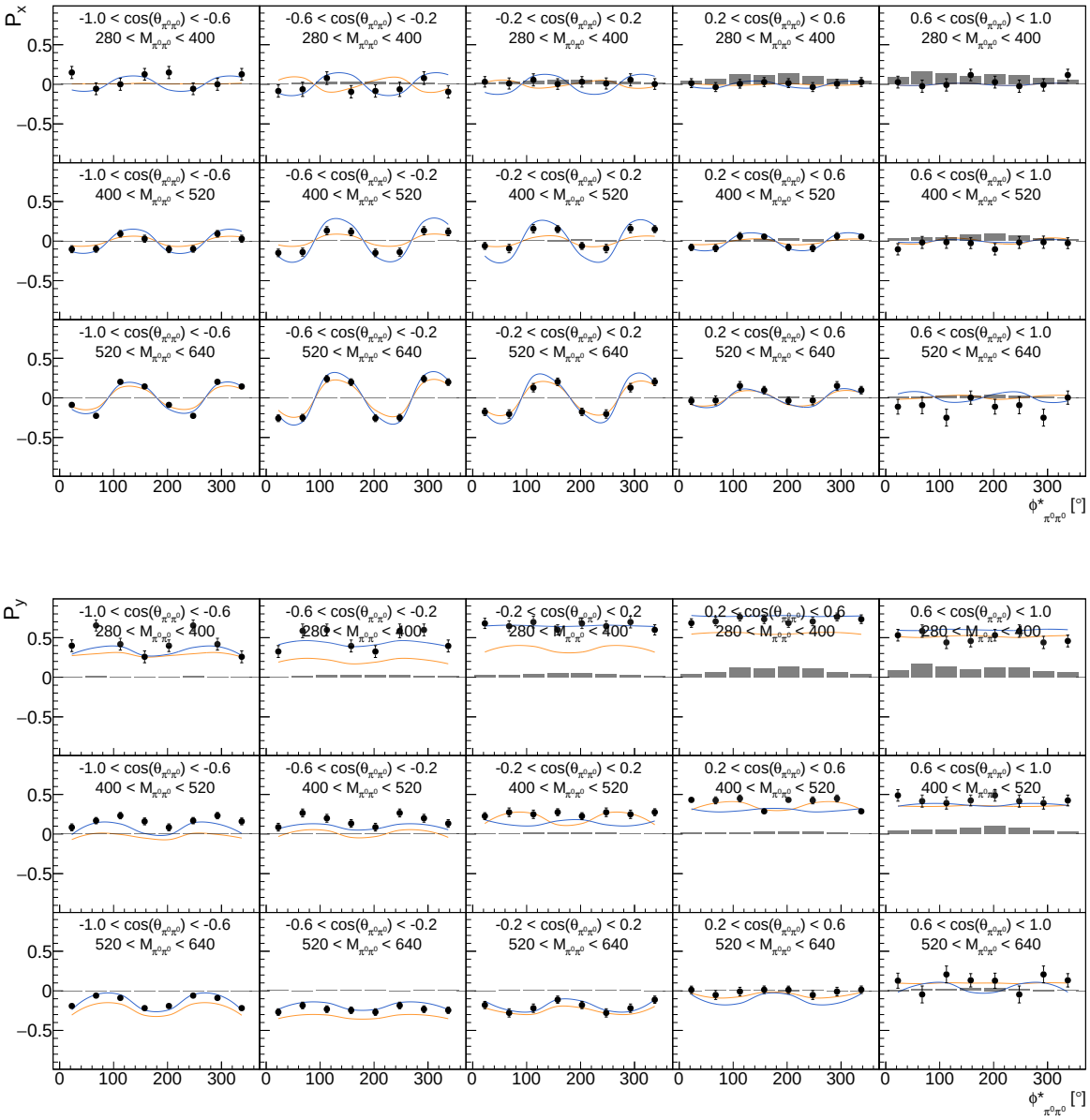

$E_\gamma = 800 - 950\,\mathrm{MeV}$

Figure G.2: Target asymmetries P_x, P_y for a specific energy range $E_\gamma = 800 - 950\,\mathrm{MeV}$ as function of $\left(\cos(\theta_{\pi^0\pi^0}), M_{\pi^0\pi^0}, \phi^*_{\pi^0\pi^0}\right)$. The **combined data of this work** is shown as well as the model predictions BnGa-2022 and BnGa-2014.

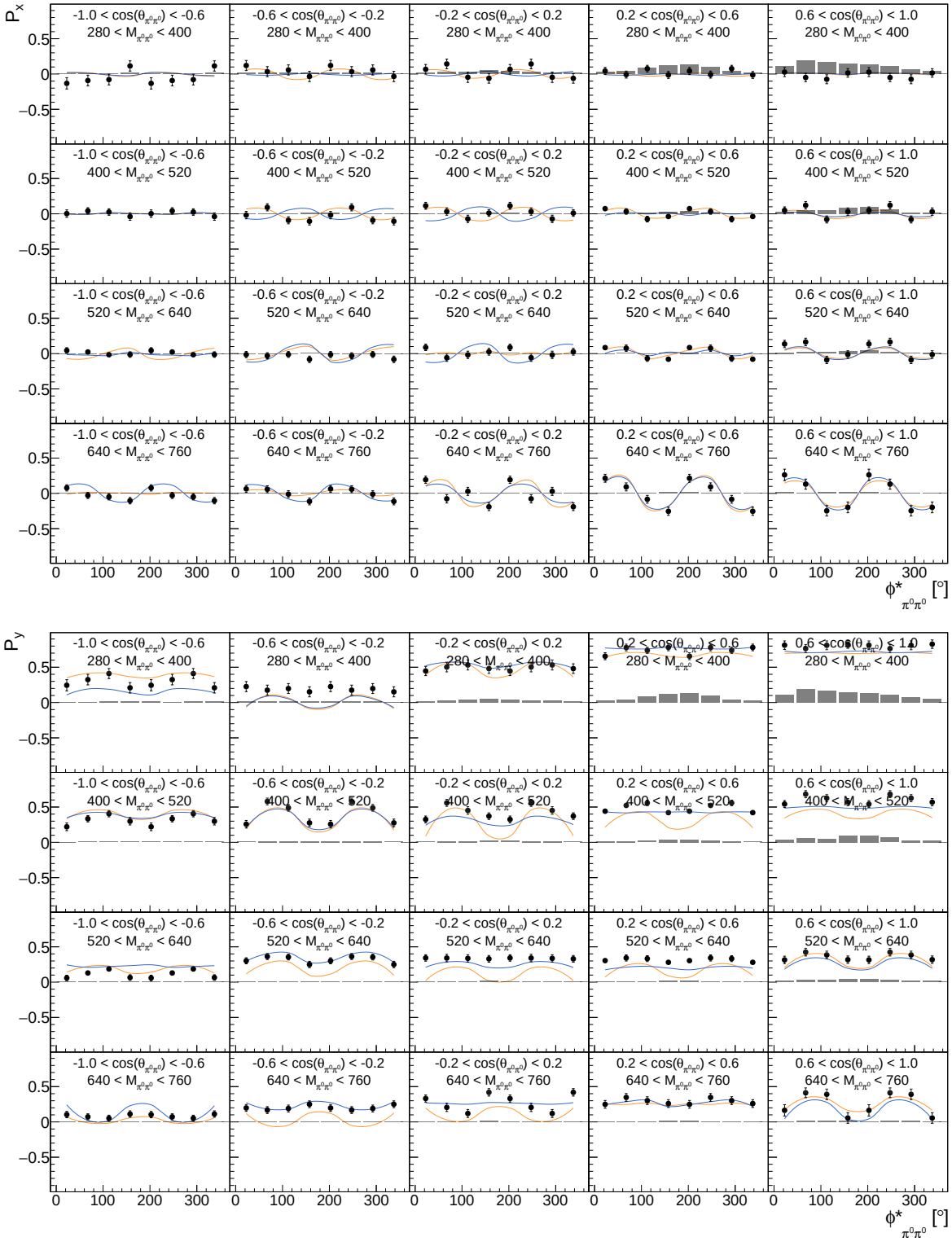

$E_\gamma = 950 - 1\,100\,\mathrm{MeV}$

Figure G.3: Target asymmetries P_x, P_y for a specific energy range $E_\gamma = 950 - 1\,100\,\mathrm{MeV}$ as function of $\left(\cos(\theta_{\pi^0\pi^0}), M_{\pi^0\pi^0}, \phi^*_{\pi^0\pi^0}\right)$. The **combined data of this work** is shown as well as the model predictions BnGa-2022 and BnGa-2014.

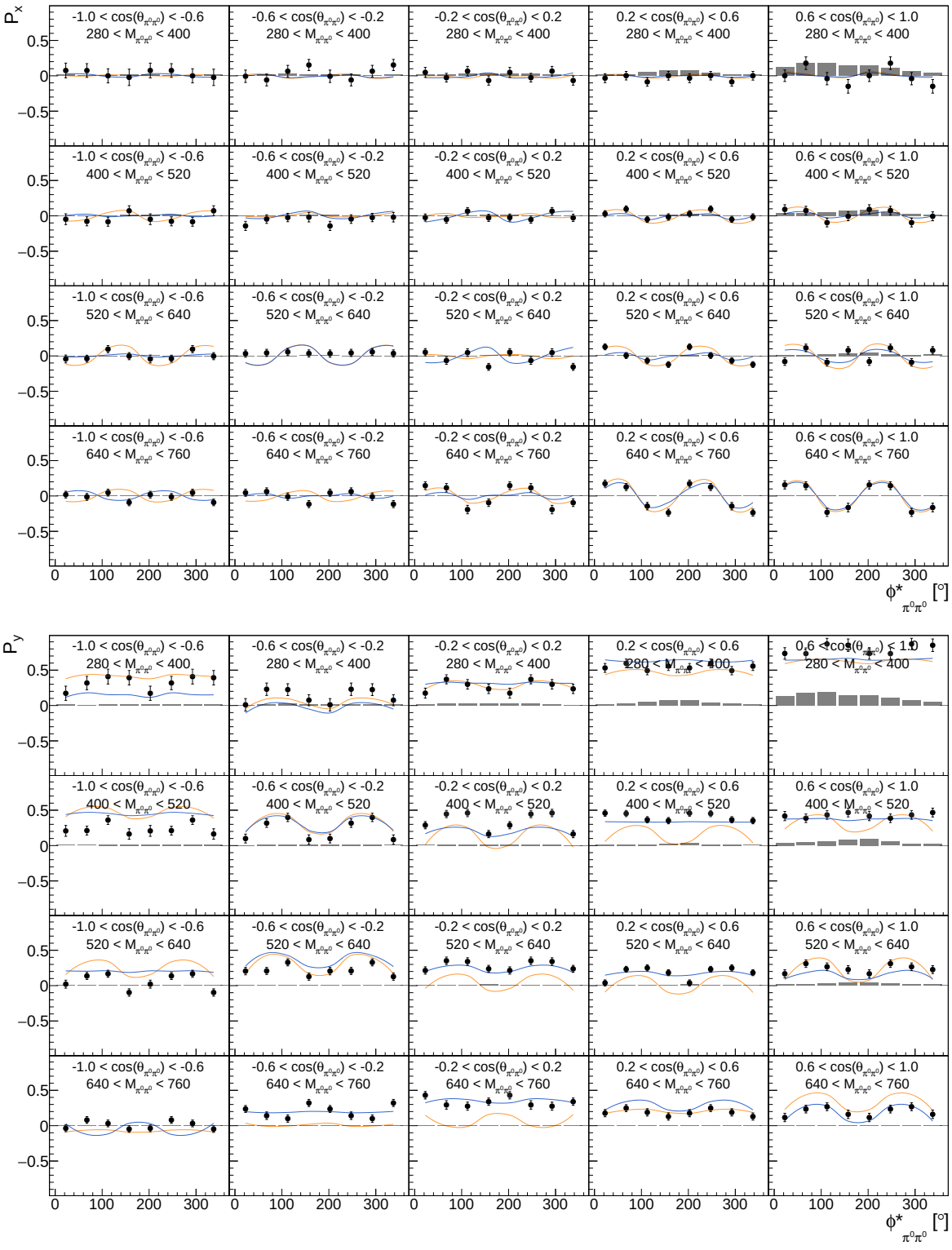

$E_\gamma = 1\,100 - 1\,250\,\mathrm{MeV}$

Figure G.4: Target asymmetries P_x, P_y for a specific energy range $E_\gamma = 1\,100 - 1\,250\,\mathrm{MeV}$ as function of $\left(\cos(\theta_{\pi^0\pi^0}), M_{\pi^0\pi^0}, \phi^*_{\pi^0\pi^0}\right)$. The **combined data of this work** is shown as well as the model predictions BnGa-2022 and BnGa-2014.

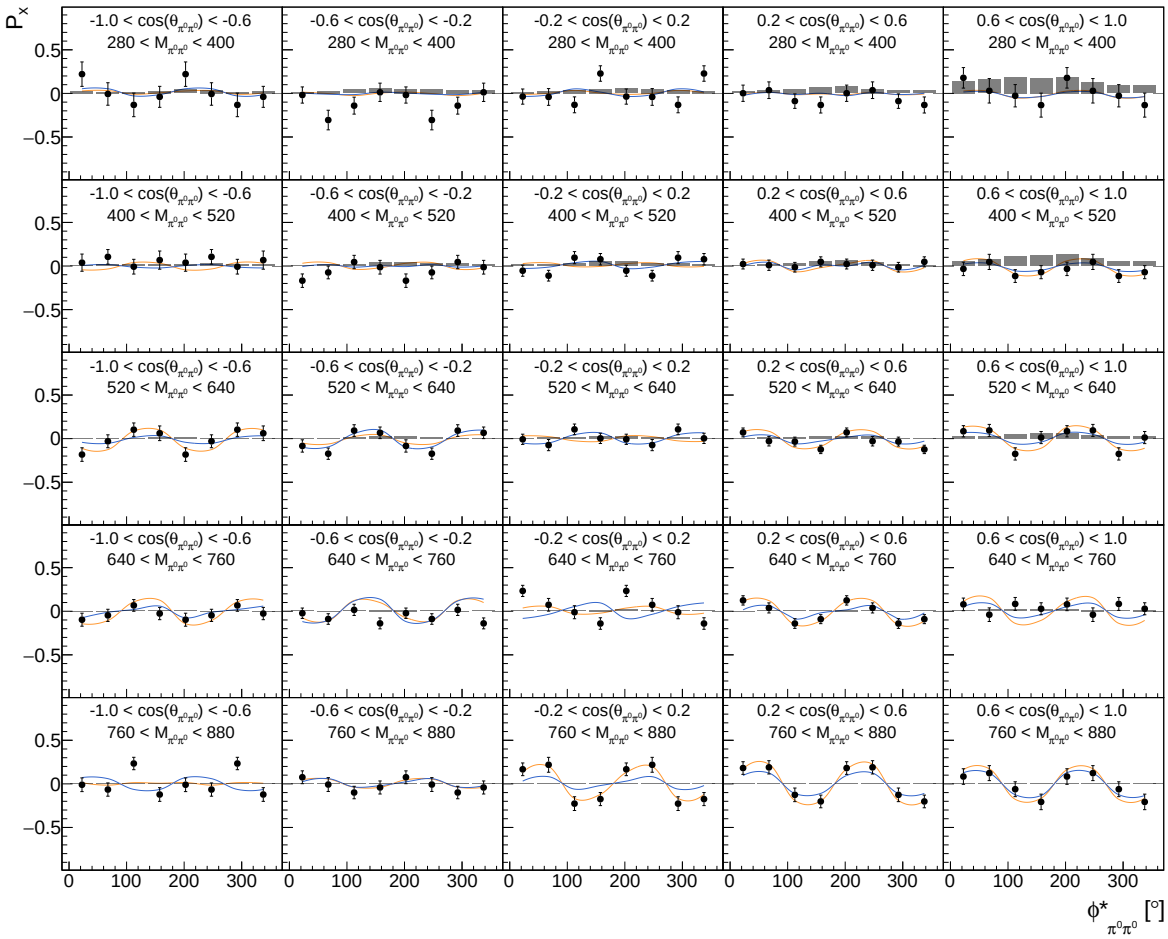

$E_\gamma = 1\,250 - 1\,400\,\text{MeV}$

Figure G.5: Target asymmetry P_x for a specific energy range $E_\gamma = 1\,250 - 1\,400\,\text{MeV}$ as function of $\left(\cos(\theta_{\pi^0\pi^0}), M_{\pi^0\pi^0}, \phi^*_{\pi^0\pi^0}\right)$. The **combined data of this work** is shown as well as the model predictions BnGa-2022 and BnGa-2014.

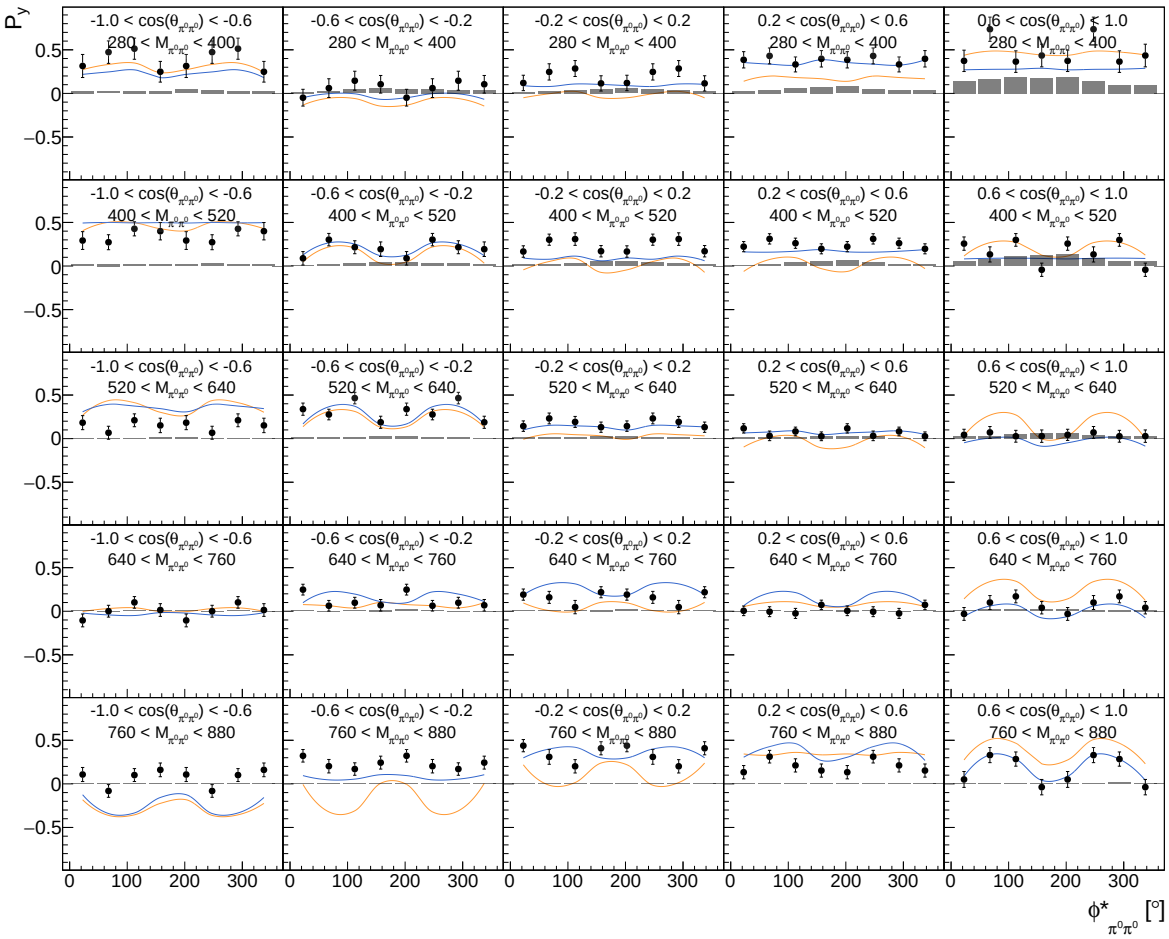

$E_\gamma = 1\,250 - 1\,400\,\text{MeV}$

Figure G.6: Target asymmetry P_y for a specific energy range $E_\gamma = 1\,250 - 1\,400\,\text{MeV}$ as function of $\left(\cos(\theta_{\pi^0\pi^0}), M_{\pi^0\pi^0}, \phi^*_{\pi^0\pi^0}\right)$. The **combined data of this work** is shown as well as the model predictions BnGa-2022 and BnGa-2014.

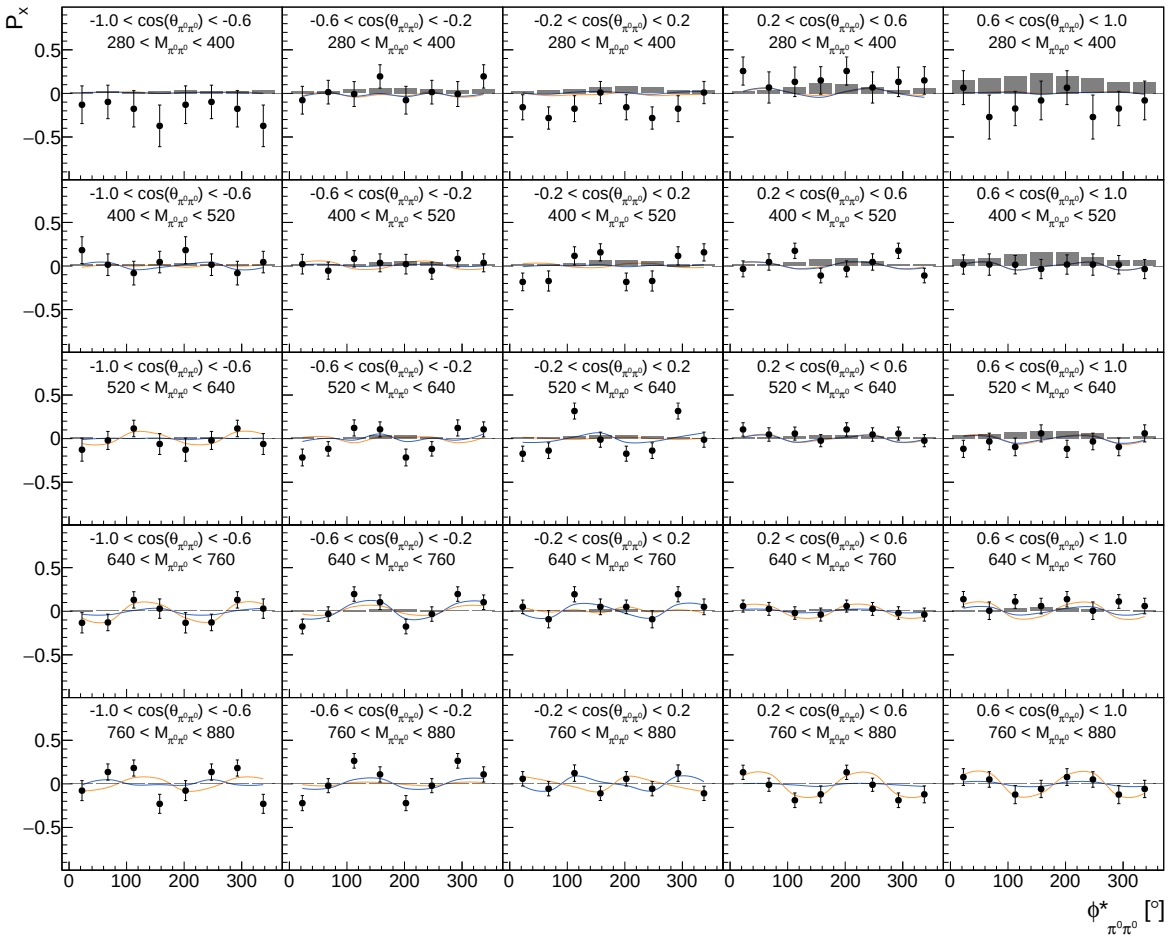

$E_\gamma = 1\,400 - 1\,550\,\text{MeV}$

Figure G.7: Target asymmetry P_x for a specific energy range $E_\gamma = 1\,400 - 1\,550\,\text{MeV}$ as function of $\left(\cos(\theta_{\pi^0\pi^0}), M_{\pi^0\pi^0}, \phi^*_{\pi^0\pi^0}\right)$. The **combined data of this work** is shown as well as the model predictions BnGa-2022 and BnGa-2014.

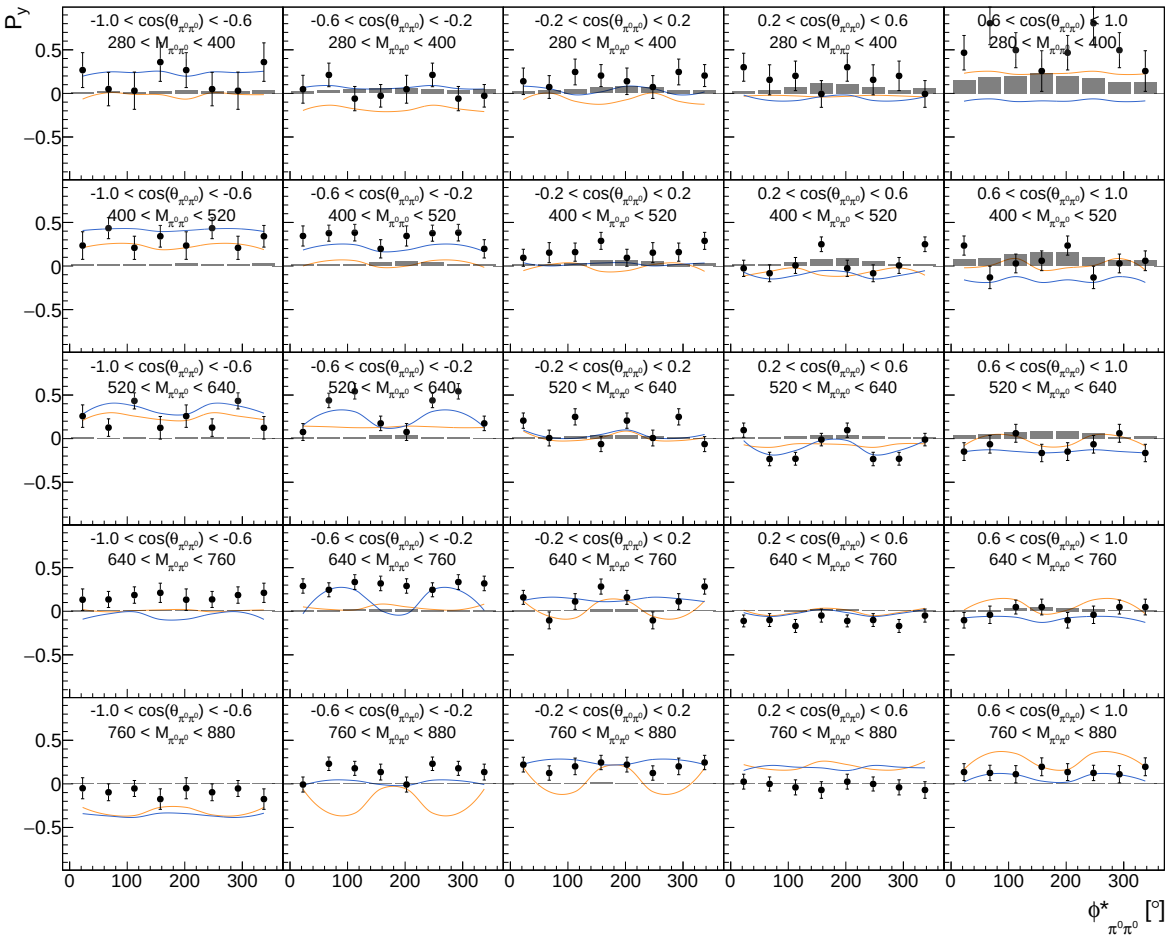

$E_\gamma = 1\,400 - 1\,550\,\mathrm{MeV}$

Figure G.8: Target asymmetry P_y for a specific energy range $E_\gamma = 1\,400 - 1\,550\,\mathrm{MeV}$ as function of $\left(\cos(\theta_{\pi^0\pi^0}), M_{\pi^0\pi^0}, \phi^*_{\pi^0\pi^0}\right)$. The **combined data of this work** is shown as well as the model predictions BnGa-2022 and BnGa-2014.

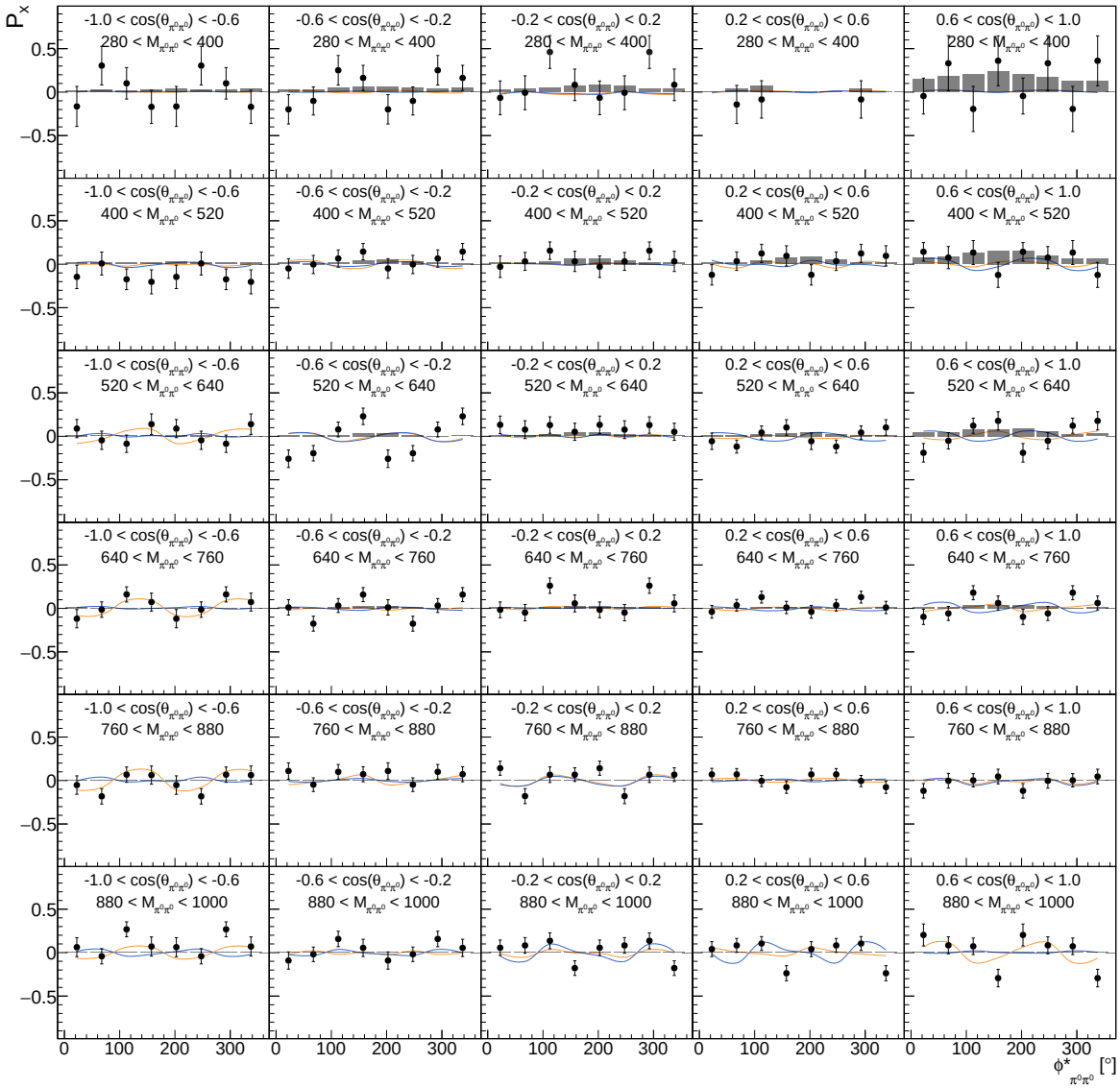

$E_\gamma = 1\,550 - 1\,850\,\text{MeV}$

Figure G.9: Target asymmetry P_x for a specific energy range $E_\gamma = 1\,550 - 1\,850\,\text{MeV}$ as function of $\left(\cos(\theta_{\pi^0\pi^0}), M_{\pi^0\pi^0}, \phi^*_{\pi^0\pi^0}\right)$. The **combined data of this work** is shown as well as the model predictions BnGa-2022 and BnGa-2014.

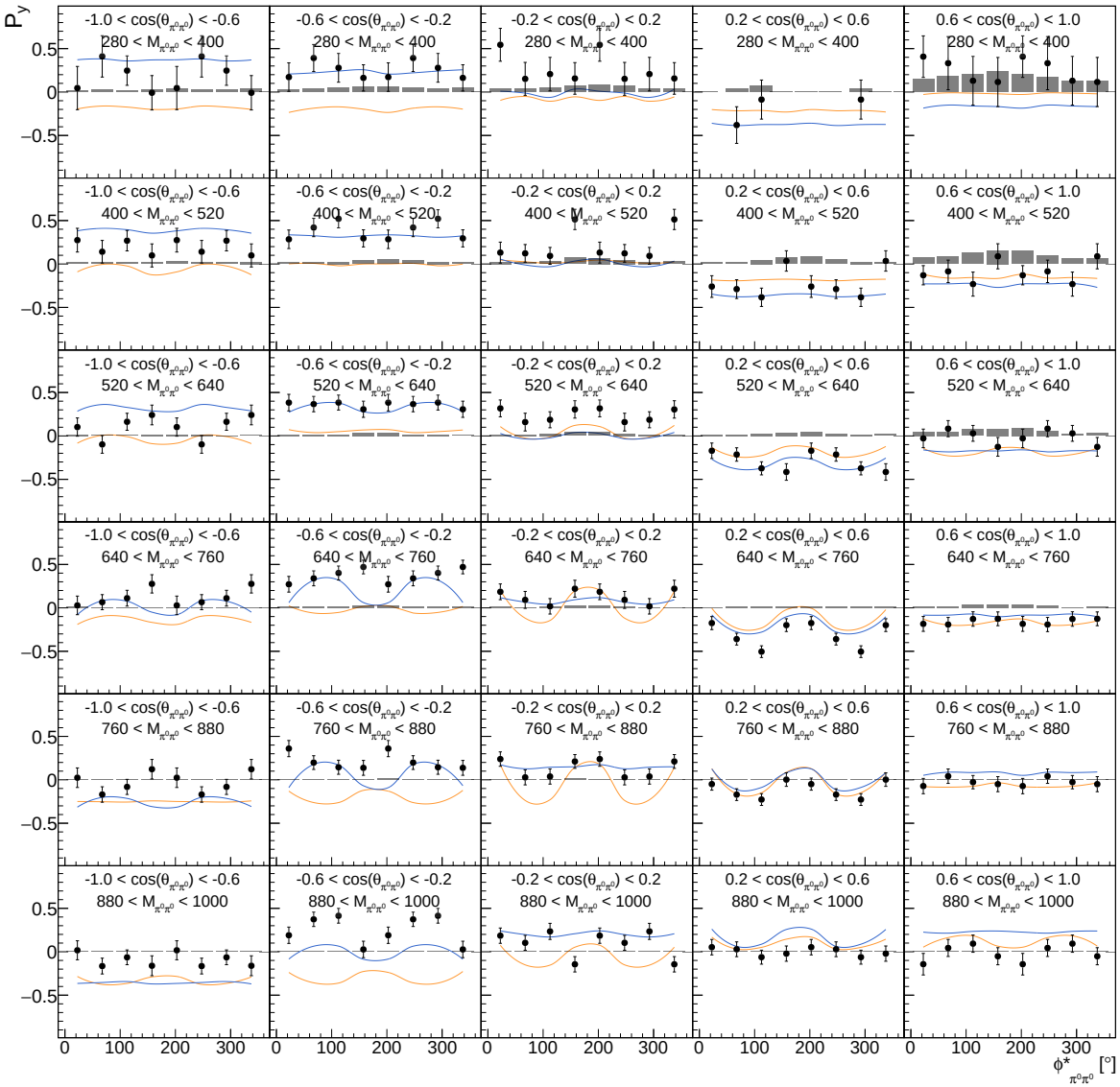

$E_\gamma = 1\,550 - 1\,850\,\mathrm{MeV}$

Figure G.10: Target asymmetry P_y for a specific energy range $E_\gamma = 1\,550 - 1\,850\,\mathrm{MeV}$ as function of $\left(\cos(\theta_{\pi^0\pi^0}), M_{\pi^0\pi^0}, \phi^*_{\pi^0\pi^0}\right)$. The **combined data of this work** is shown as well as the model predictions BnGa-2022 and BnGa-2014.

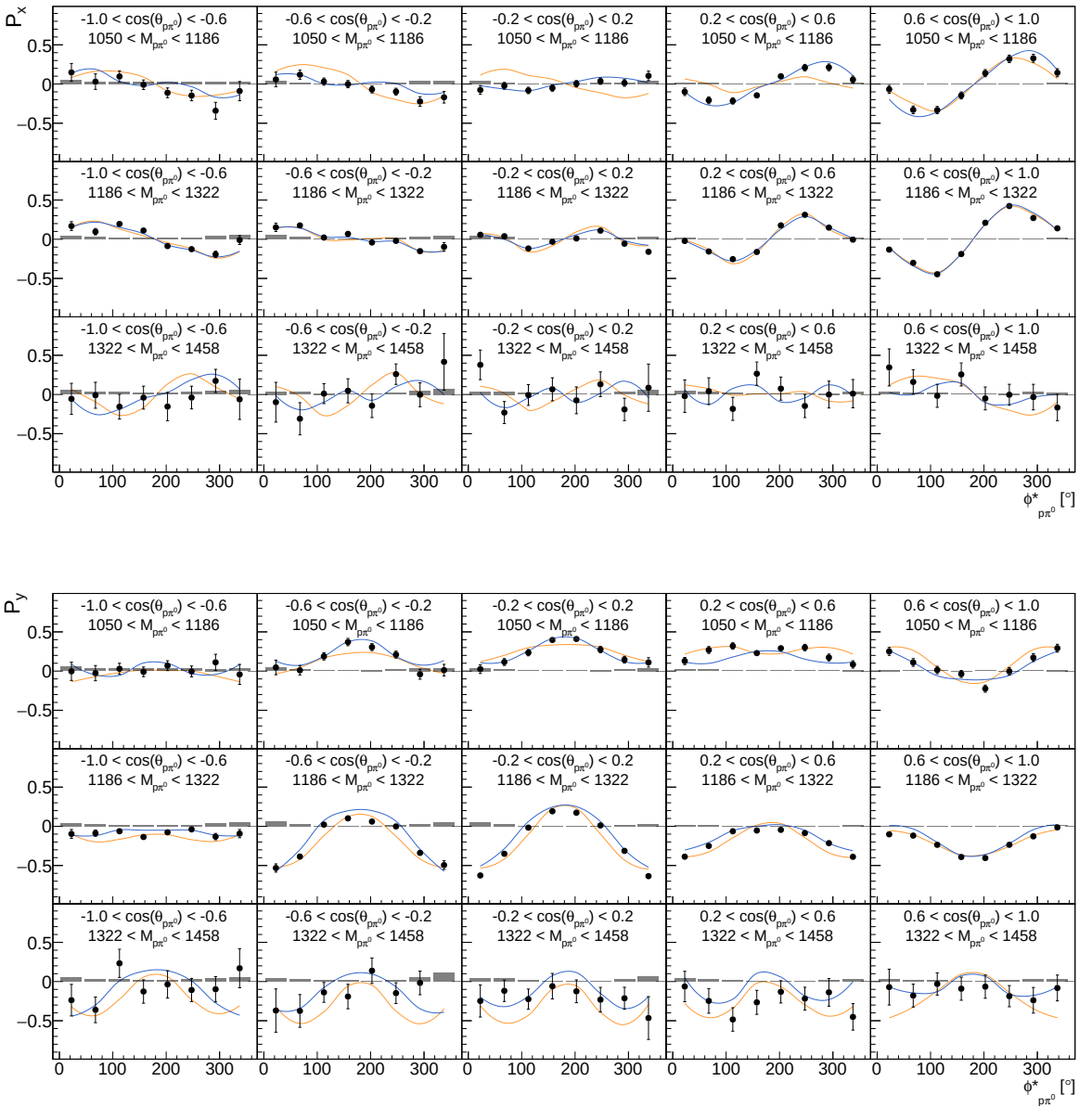

$E_\gamma = 650 - 800\,\mathrm{MeV}$

Figure G.11: Target asymmetries P_x, P_y for a specific energy range $E_\gamma = 650 - 800\,\mathrm{MeV}$ as function of $\left(\cos(\theta_{p\pi^0}), M_{p\pi^0}, \phi^*_{p\pi^0}\right)$. The **combined data of this work** is shown as well as the model predictions BnGa-2022 and BnGa-2014.

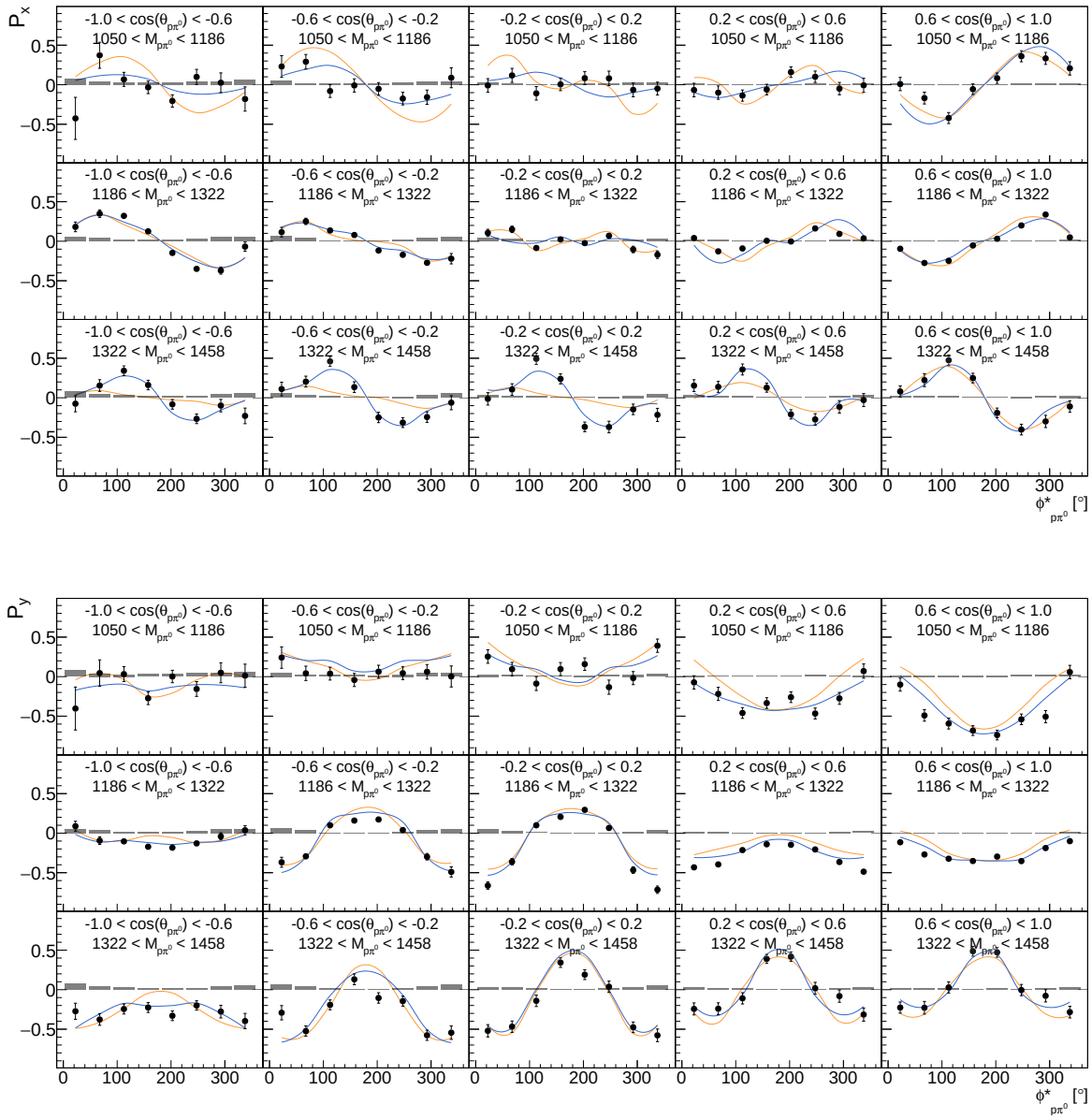

$E_\gamma = 800 - 950\,\mathrm{MeV}$

Figure G.12: Target asymmetries P_x, P_y for a specific energy range $E_\gamma = 800 - 950\,\mathrm{MeV}$ as function of $\left(\cos(\theta_{p\pi^0}), M_{p\pi^0}, \phi^*_{p\pi^0}\right)$. The **combined data of this work** is shown as well as the model predictions BnGa-2022 and BnGa-2014.

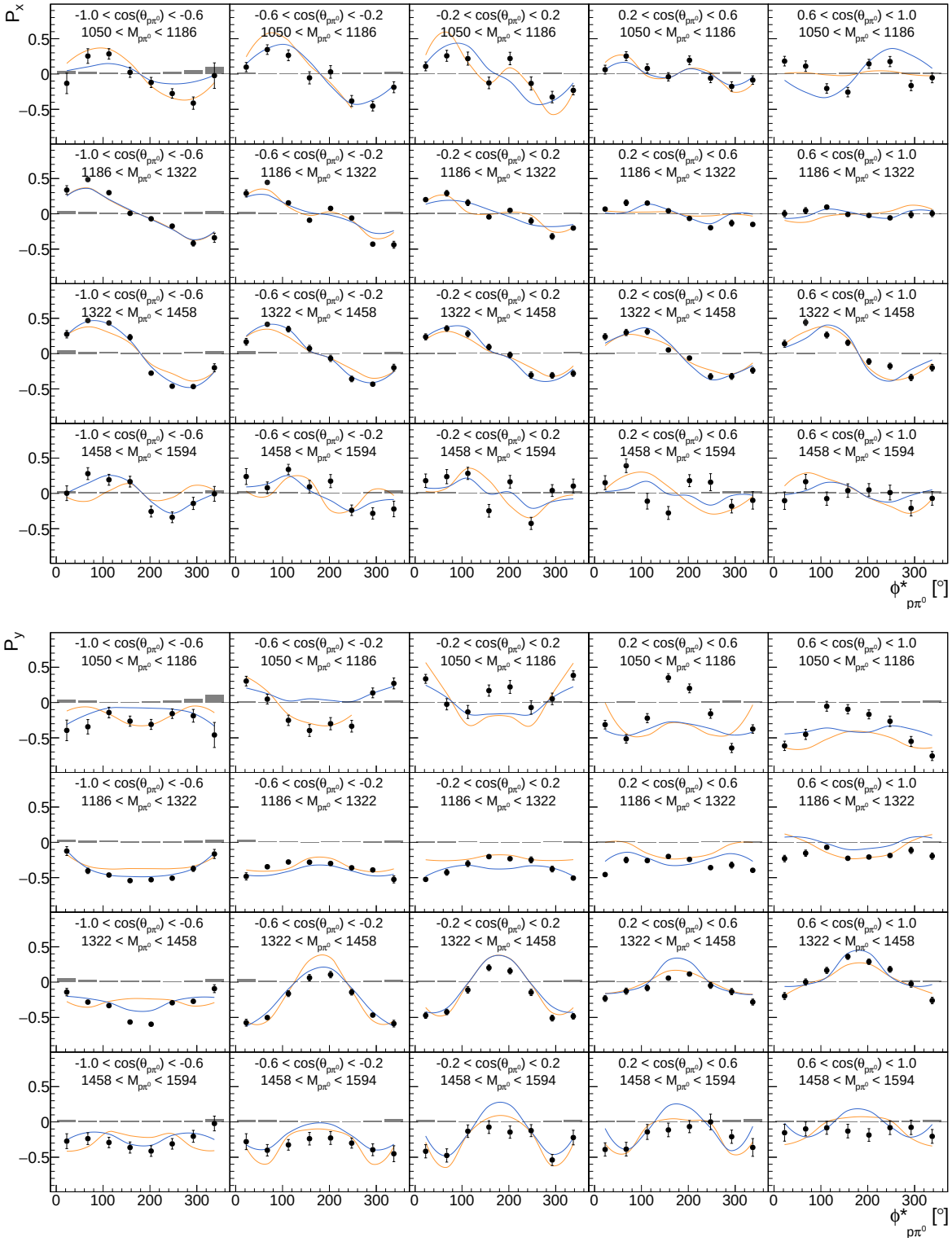

$E_\gamma = 950 - 1\,100\,\text{MeV}$

Figure G.13: Target asymmetries P_x, P_y for a specific energy range $E_\gamma = 950 - 1\,100\,\text{MeV}$ as function of $\left(\cos(\theta_{p\pi^0}), M_{p\pi^0}, \phi^*_{p\pi^0}\right)$. The **combined data of this work** is shown as well as the model predictions BnGa-2022 and BnGa-2014.

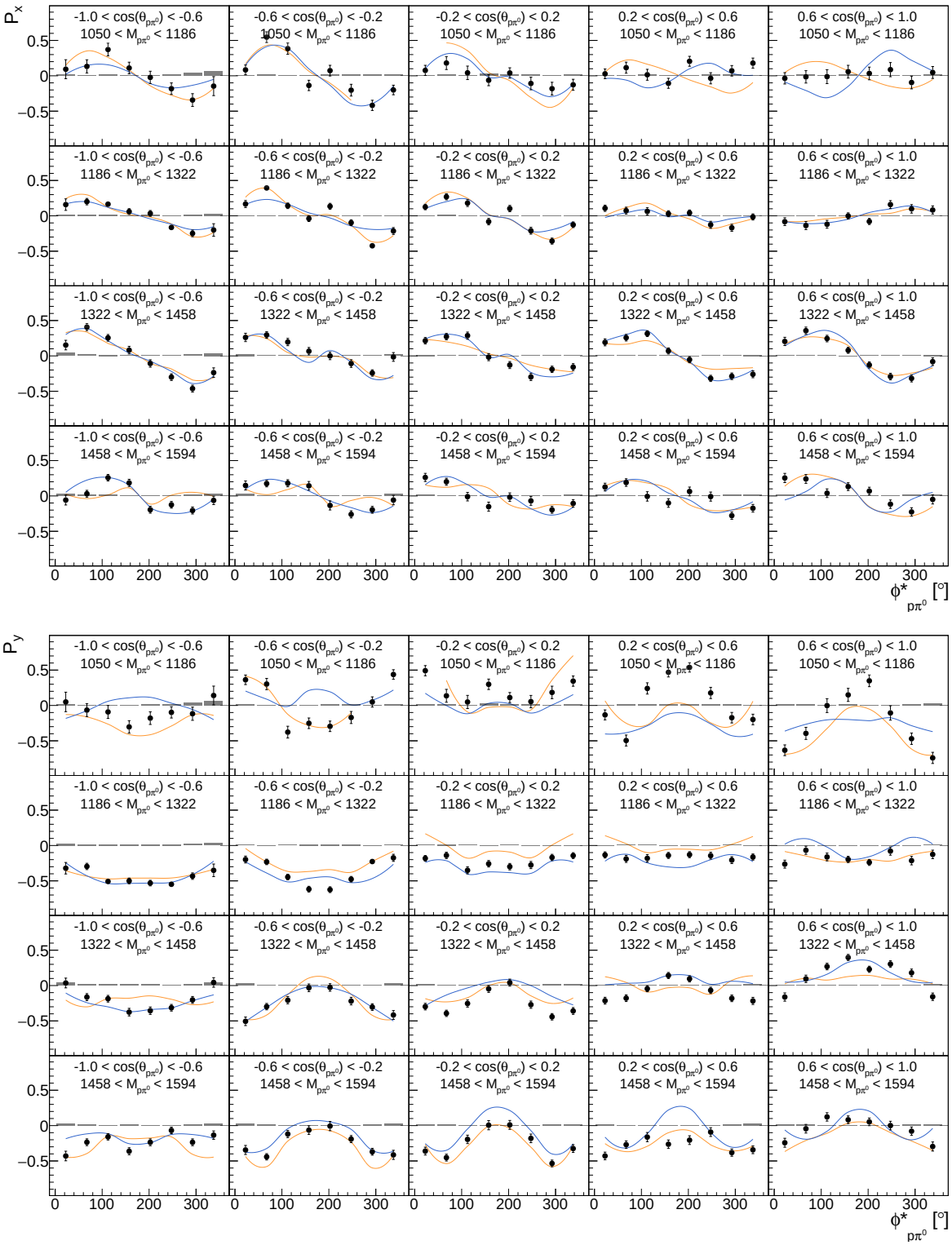

$E_\gamma = 1\,100 - 1\,250\,\mathrm{MeV}$

Figure G.14: Target asymmetries P_x, P_y for a specific energy range $E_\gamma = 1\,100 - 1\,250\,\mathrm{MeV}$ as function of $\left(\cos(\theta_{p\pi^0}), M_{p\pi^0}, \phi^*_{p\pi^0}\right)$. The **combined data of this work** is shown as well as the model predictions BnGa-2022 and BnGa-2014.

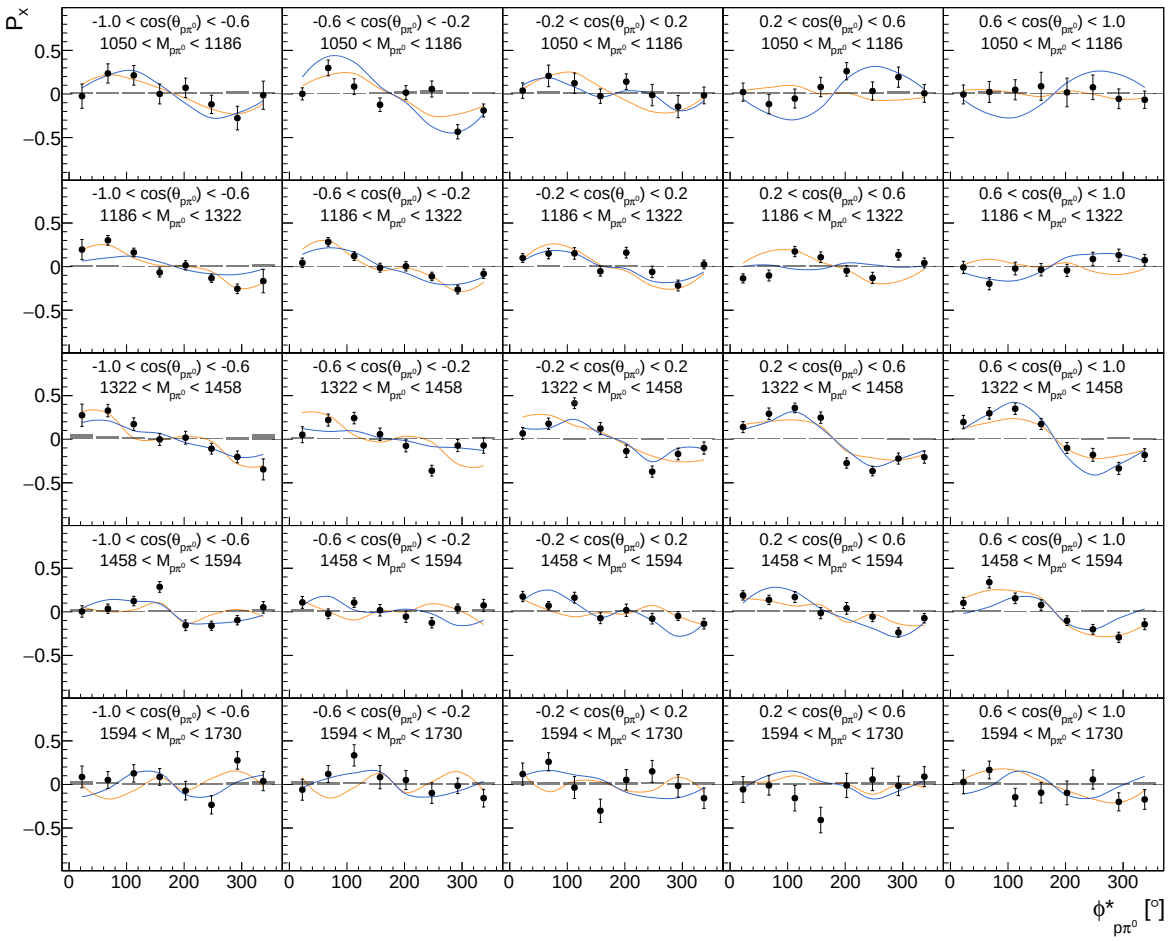

$E_\gamma = 1\,250 - 1\,400\,\text{MeV}$

Figure G.15: Target asymmetry P_x for a specific energy range $E_\gamma = 1\,250 - 1\,400\,\text{MeV}$ as function of $\left(\cos(\theta_{p\pi^0}), M_{p\pi^0}, \phi^*_{p\pi^0}\right)$. The **combined data of this work** is shown as well as the model predictions BnGa-2022 and BnGa-2014.

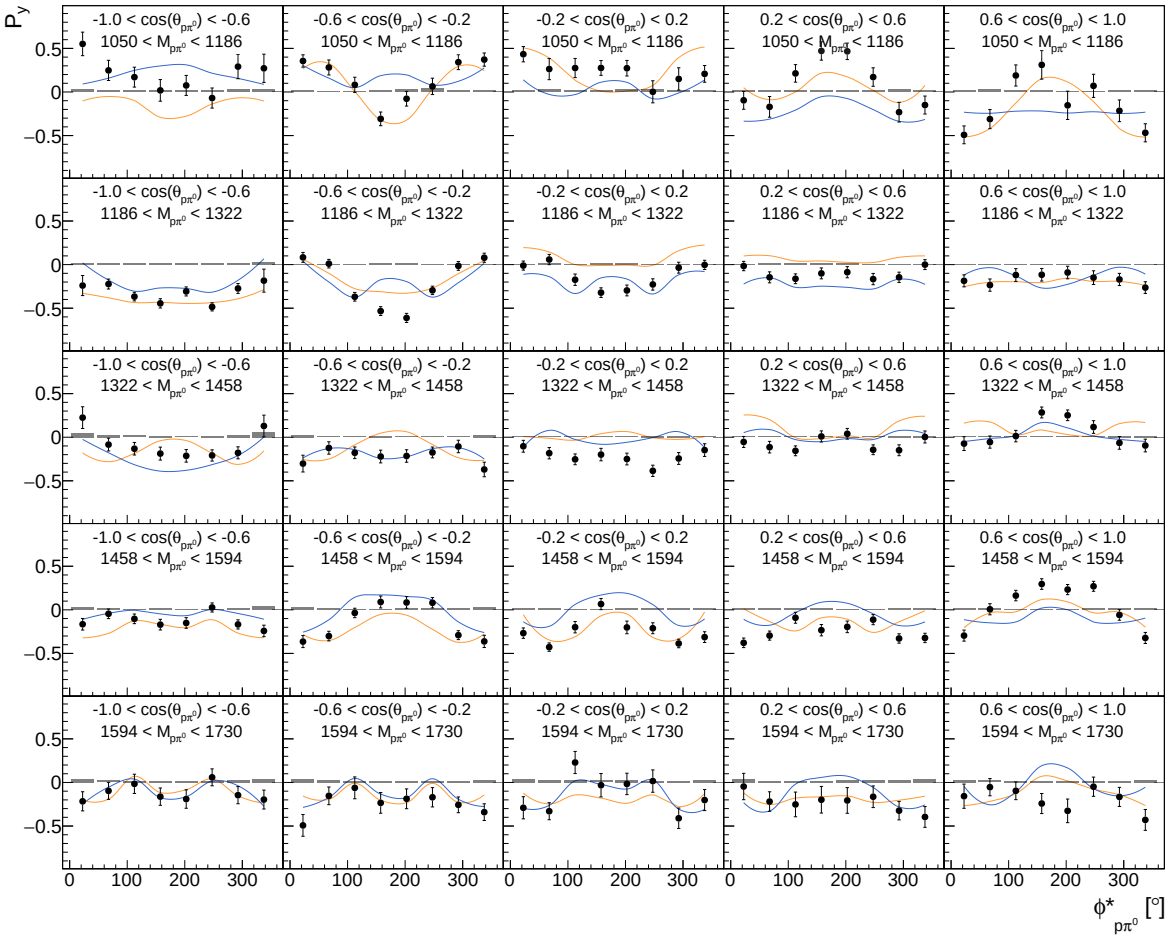

$E_\gamma = 1\,250 - 1\,400\,\text{MeV}$

Figure G.16: Target asymmetry P_y for a specific energy range $E_\gamma = 1\,250 - 1\,400\,\text{MeV}$ as function of $\left(\cos(\theta_{p\pi^0}), M_{p\pi^0}, \phi^*_{p\pi^0}\right)$. The **combined data of this work** is shown as well as the model predictions BnGa-2022 and BnGa-2014.

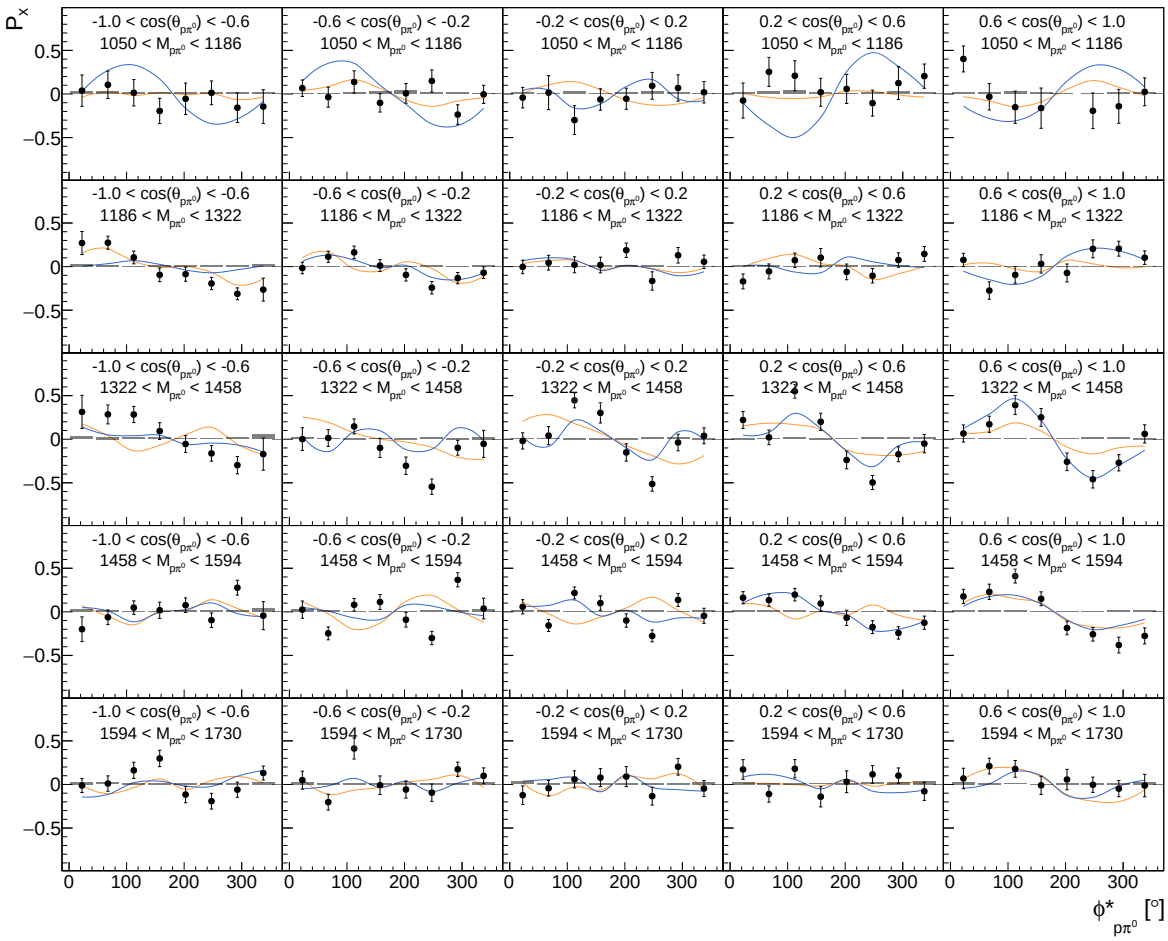

$E_\gamma = 1\,400 - 1\,550\,\text{MeV}$

Figure G.17: Target asymmetry P_x for a specific energy range $E_\gamma = 1\,400 - 1\,550\,\text{MeV}$ as function of $\left(\cos(\theta_{p\pi^0}), M_{p\pi^0}, \phi^*_{p\pi^0}\right)$. The **combined data of this work** is shown as well as the model predictions BnGa-2022 and BnGa-2014.

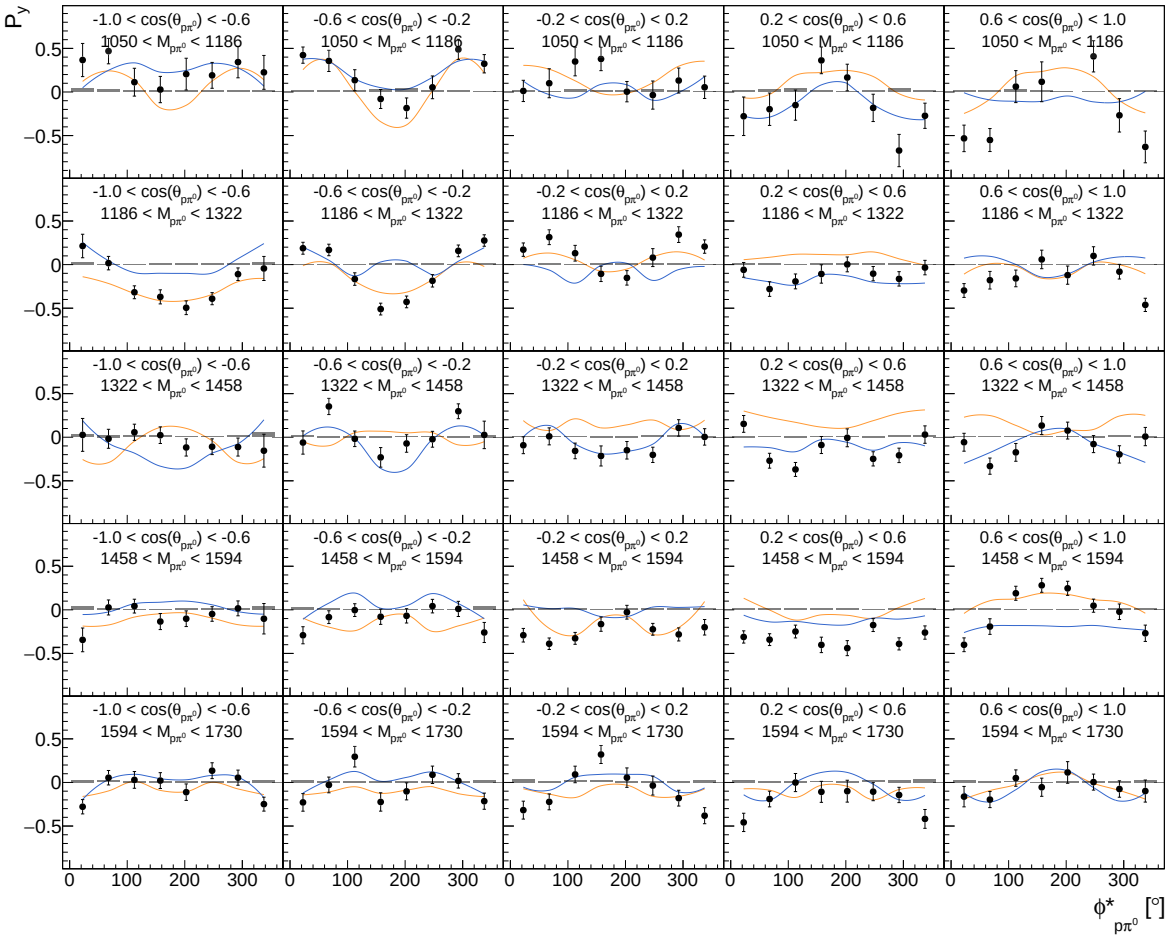

$E_\gamma = 1\,400 - 1\,550\,\mathrm{MeV}$

Figure G.18: Target asymmetry P_y for a specific energy range $E_\gamma = 1\,400 - 1\,550\,\mathrm{MeV}$ as function of $\left(\cos(\theta_{p\pi^0}), M_{p\pi^0}, \phi^*_{p\pi^0}\right)$. The **combined data of this work** is shown as well as the model predictions BnGa-2022 and BnGa-2014.

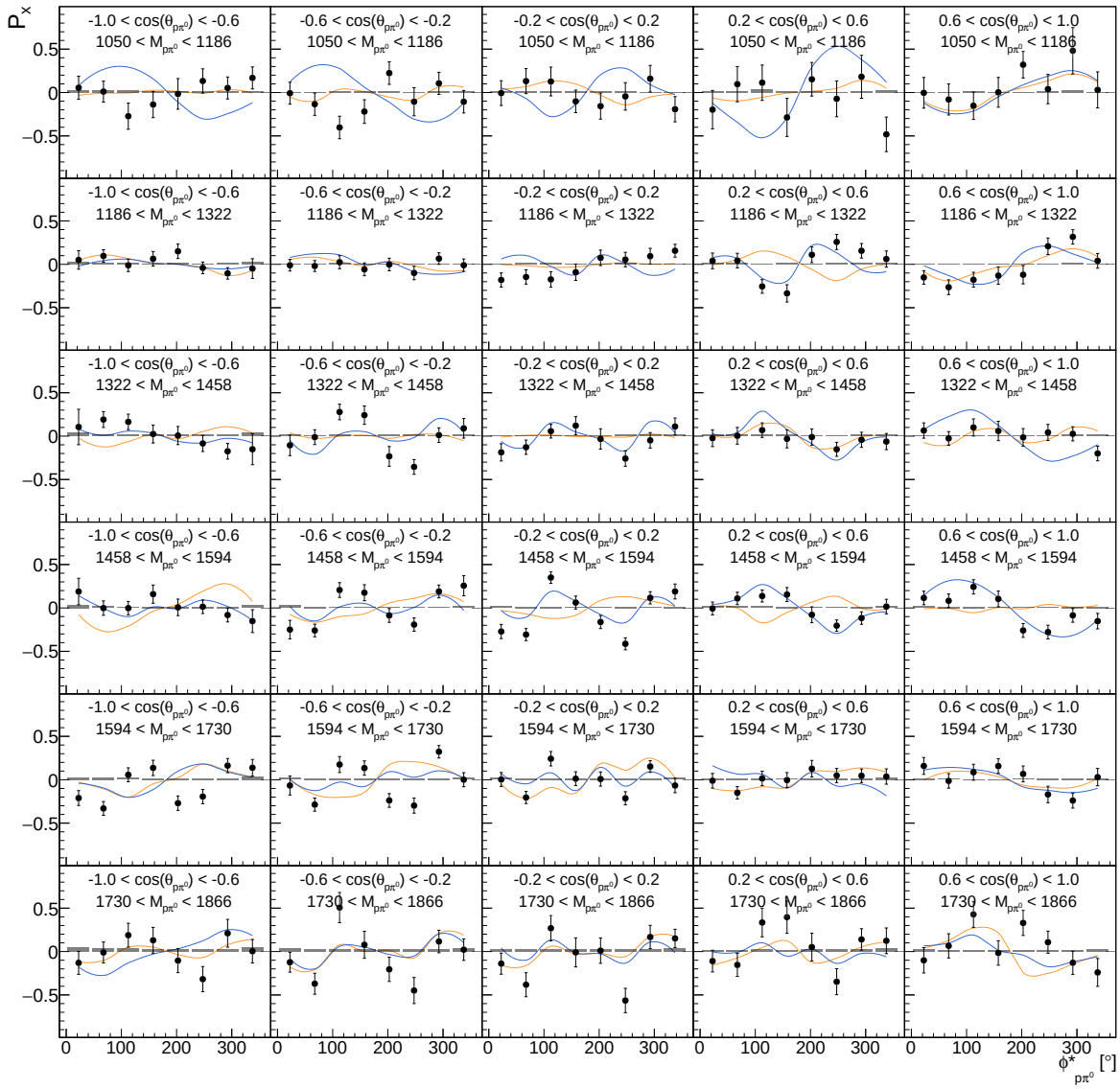

$E_\gamma = 1\,550 - 1\,850\,\text{MeV}$

Figure G.19: Target asymmetry P_x for a specific energy range $E_\gamma = 1\,550 - 1\,850\,\text{MeV}$ as function of $\left(\cos(\theta_{p\pi^0}), M_{p\pi^0}, \phi^*_{p\pi^0}\right)$. The **combined data of this work** is shown as well as the model predictions BnGa-2022 and BnGa-2014.

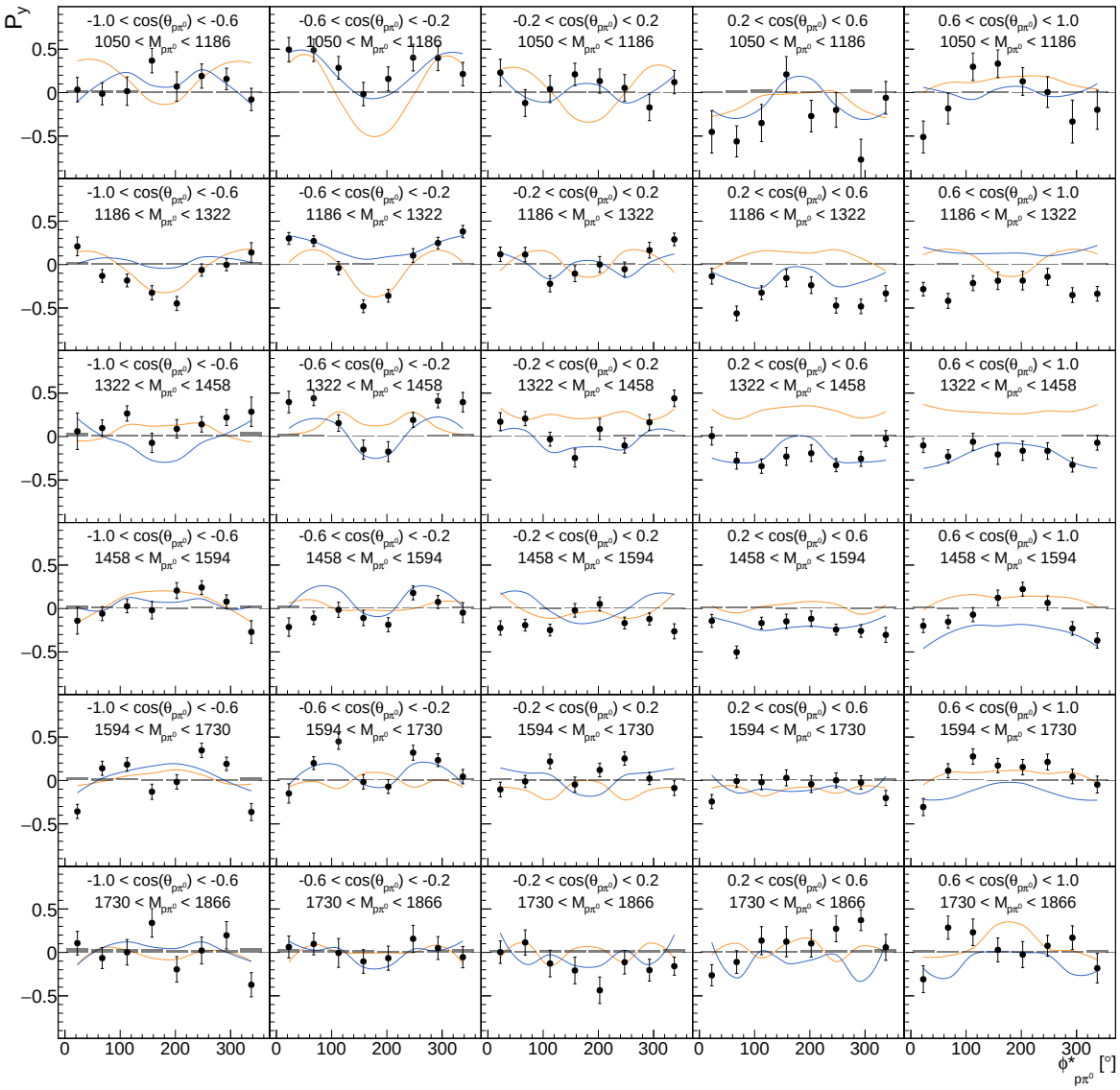

$E_\gamma = 1\,550 - 1\,850\,\mathrm{MeV}$

Figure G.20: Target asymmetry P_y for a specific energy range $E_\gamma = 1\,550 - 1\,850\,\mathrm{MeV}$ as function of $\left(\cos(\theta_{p\pi^0}), M_{p\pi^0}, \phi^*_{p\pi^0}\right)$. The **combined data of this work** is shown as well as the model predictions BnGa-2022 and BnGa-2014.

APPENDIX H

P_x^s, P_y^s, P_x^c, P_y^c in Four Dimensions

In this appendix, final results of the double polarization observables P_x^s, P_y^s, P_x^c, P_y^c in four dimensions are presented. Each figure represents a selected energy range. In each figure (energy range), the extracted observables are presented as a function of $(\cos(\theta), M, \phi^*)$. For the extraction of the results, the combined data of four periods of data taking are used: December 2017, May 2018, February 2019 and June 2021. In each case, 5-PED, 4.5-PED and 4-PED events are included for a complete coverage of the kinematic region. An exception is June 2021, for which 4-PED events are excluded (cf. Section 8.3.2.3). The results are compared with the model predictions of BnGa-2022 and BnGa-2014. The systematic uncertainties of the results are shown as bars on the x-axis.

$\pi^0\pi^0$-System

The series of Fig. H.1 to H.4 deals with observables extracted in the $\pi^0\pi^0$-system.

$p\pi^0$-System

The series of Fig. H.5 to H.8 deals with observables extracted in the $p\pi^0$-system.

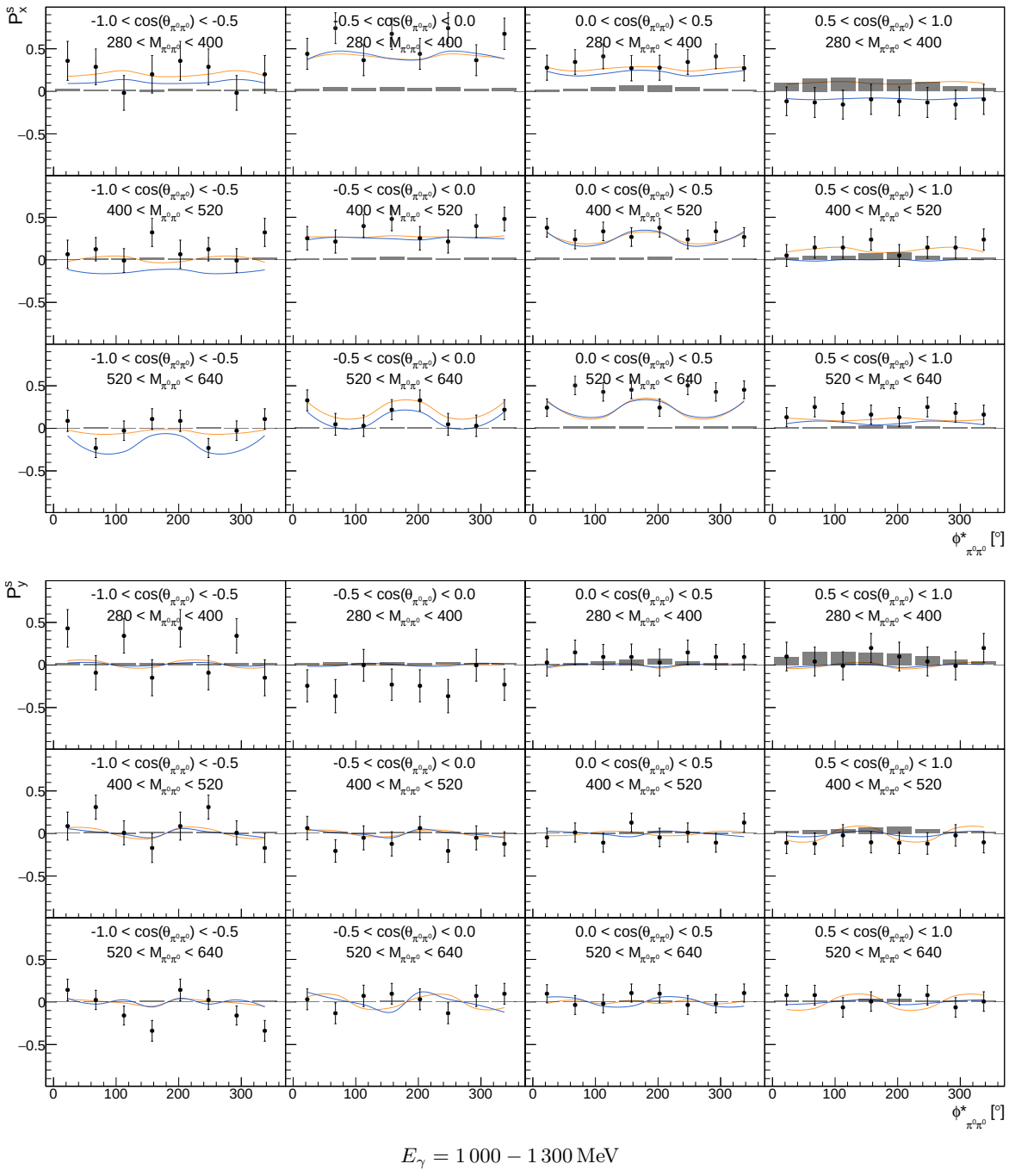

$E_\gamma = 1\,000 - 1\,300\,\mathrm{MeV}$

Figure H.1: Double polarization observables P_x^s, P_y^s for a specific energy range $E_\gamma = 1\,000 - 1\,300\,\mathrm{MeV}$ as function of $\left(\cos(\theta_{\pi^0\pi^0}), M_{\pi^0\pi^0}, \phi^*_{\pi^0\pi^0}\right)$. The **combined data of this work** is shown as well as the model predictions BnGa-2022 and BnGa-2014.

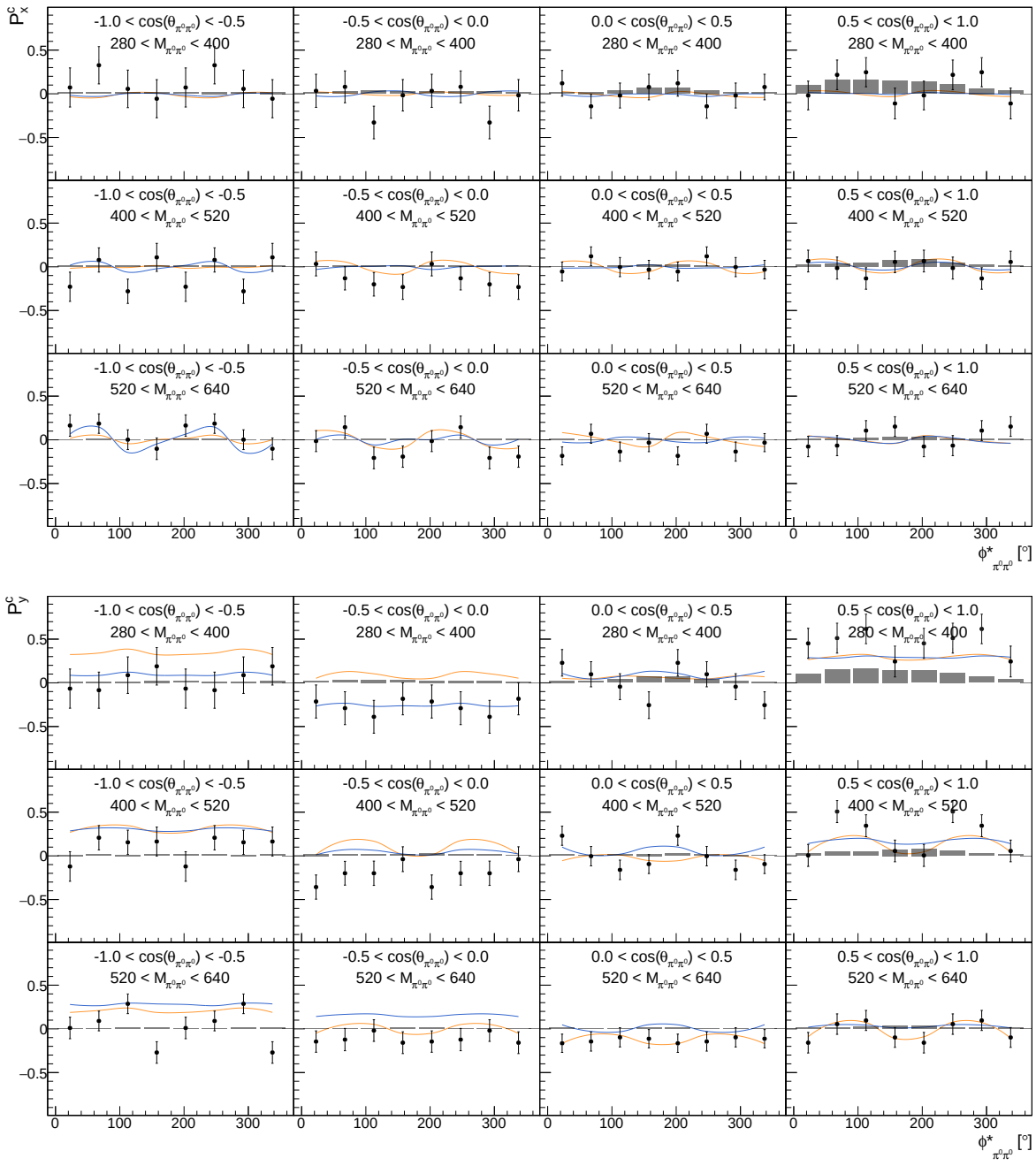

$E_\gamma = 1\,000 - 1\,300\,\text{MeV}$

Figure H.2: Double polarization observables P_x^c, P_y^c for a specific energy range $E_\gamma = 1\,000 - 1\,300\,\text{MeV}$ as function of $\left(\cos(\theta_{\pi^0\pi^0}), M_{\pi^0\pi^0}, \phi^*_{\pi^0\pi^0}\right)$. The **combined data of this work** is shown as well as the model predictions BnGa-2022 and BnGa-2014.

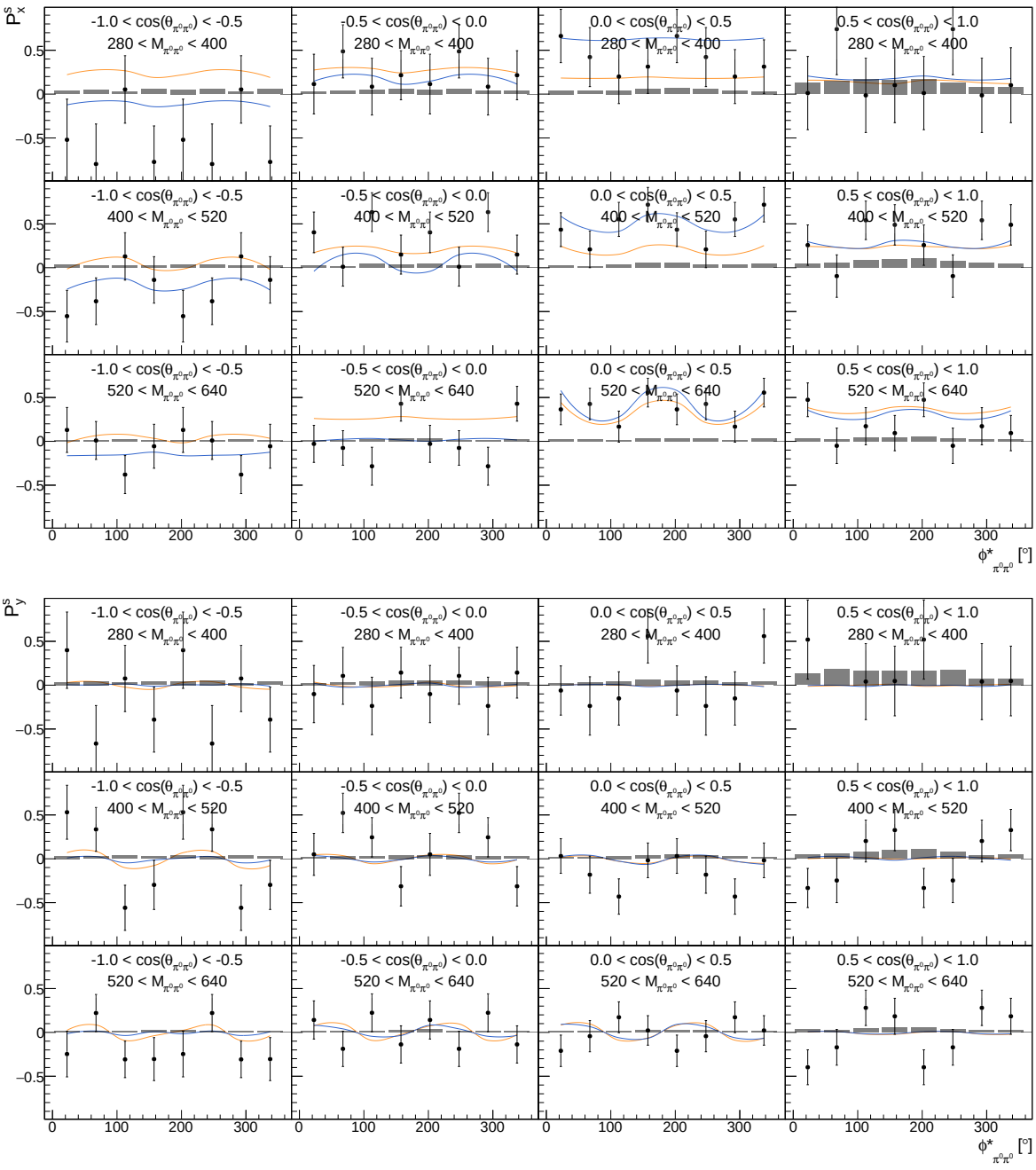

$E_\gamma = 1\,300 - 1\,600\,\mathrm{MeV}$

Figure H.3: Double polarization observables P_x^s, P_y^s for a specific energy range $E_\gamma = 1\,300 - 1\,600\,\mathrm{MeV}$ as function of $\left(\cos(\theta_{\pi^0\pi^0}), M_{\pi^0\pi^0}, \phi^*_{\pi^0\pi^0}\right)$. The **combined data of this work** is shown as well as the model predictions BnGa-2022 and BnGa-2014.

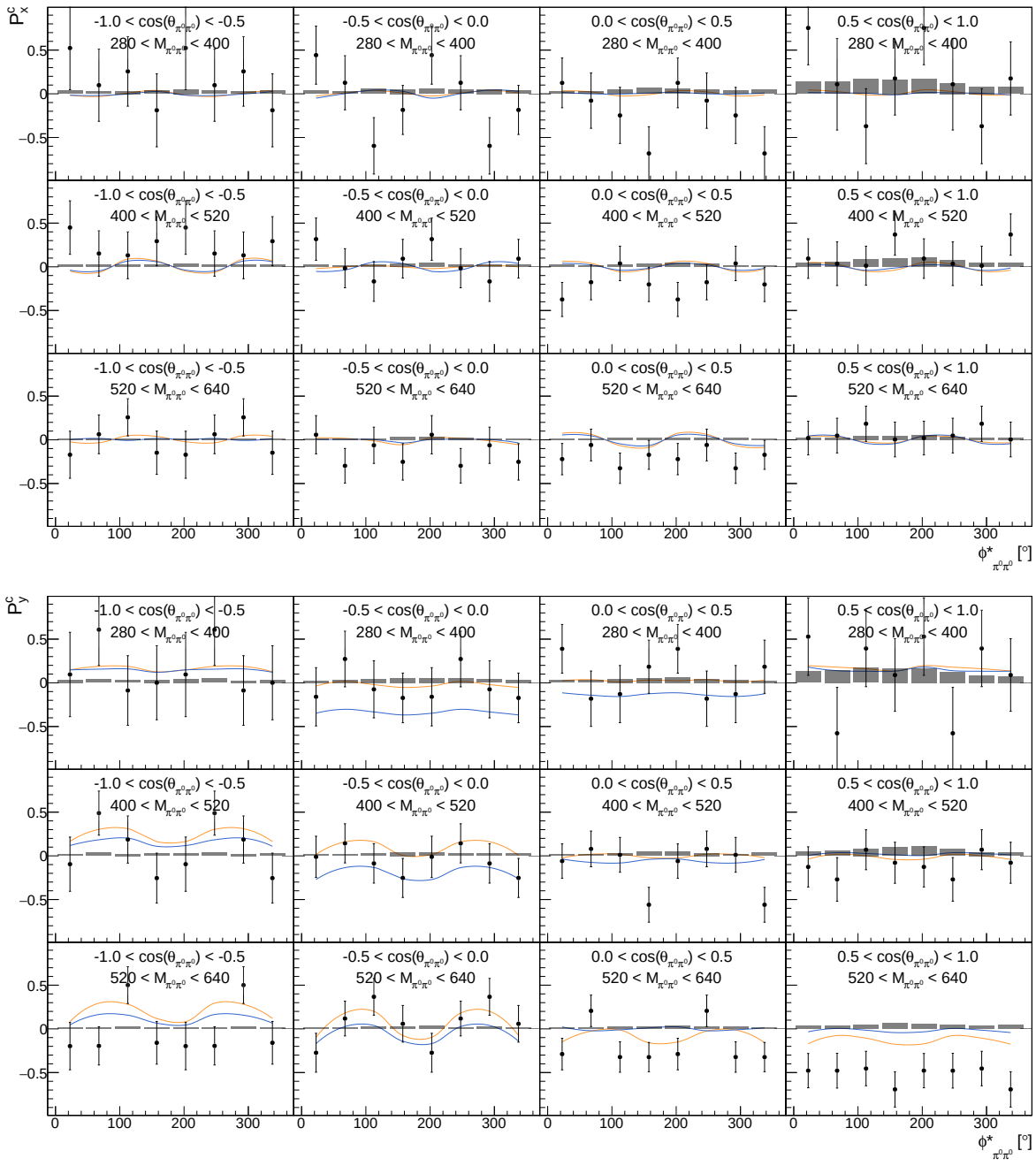

$E_\gamma = 1\,300 - 1\,600\,\text{MeV}$

Figure H.4: Double polarization observables P_x^c, P_y^c for a specific energy range $E_\gamma = 1\,300 - 1\,600\,\text{MeV}$ as function of $\left(\cos(\theta_{\pi^0\pi^0}), M_{\pi^0\pi^0}, \phi^*_{\pi^0\pi^0}\right)$. The **combined data of this work** is shown as well as the model predictions BnGa-2022 and BnGa-2014.

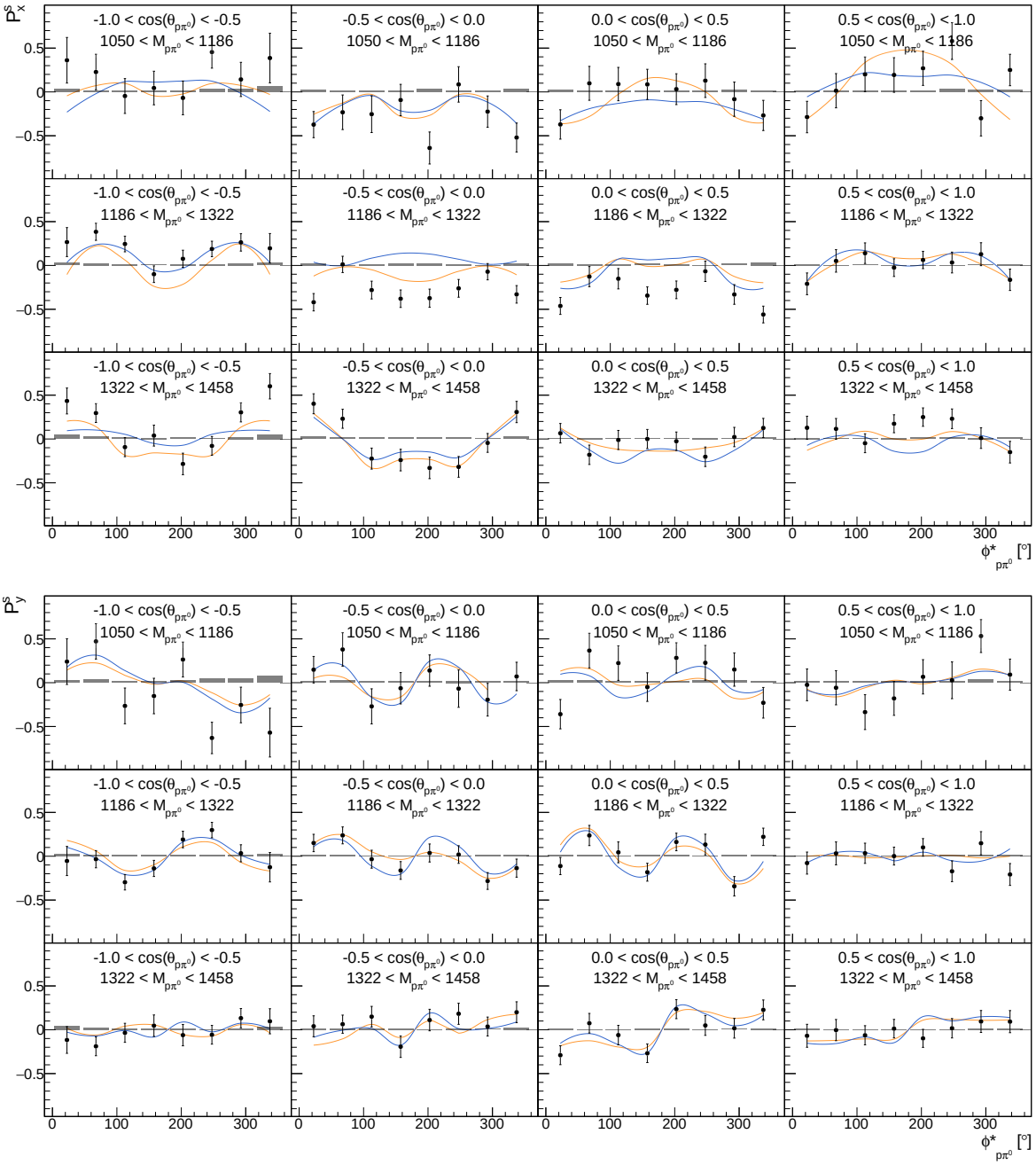

$E_\gamma = 1\,000 - 1\,300\,\text{MeV}$

Figure H.5: Double polarization observables P_x^s, P_y^s for a specific energy range $E_\gamma = 1\,000 - 1\,300\,\text{MeV}$ as function of $\left(\cos(\theta_{p\pi^0}), M_{p\pi^0}, \phi^*_{p\pi^0}\right)$. The **combined data of this work** is shown as well as the model predictions BnGa-2022 and BnGa-2014.

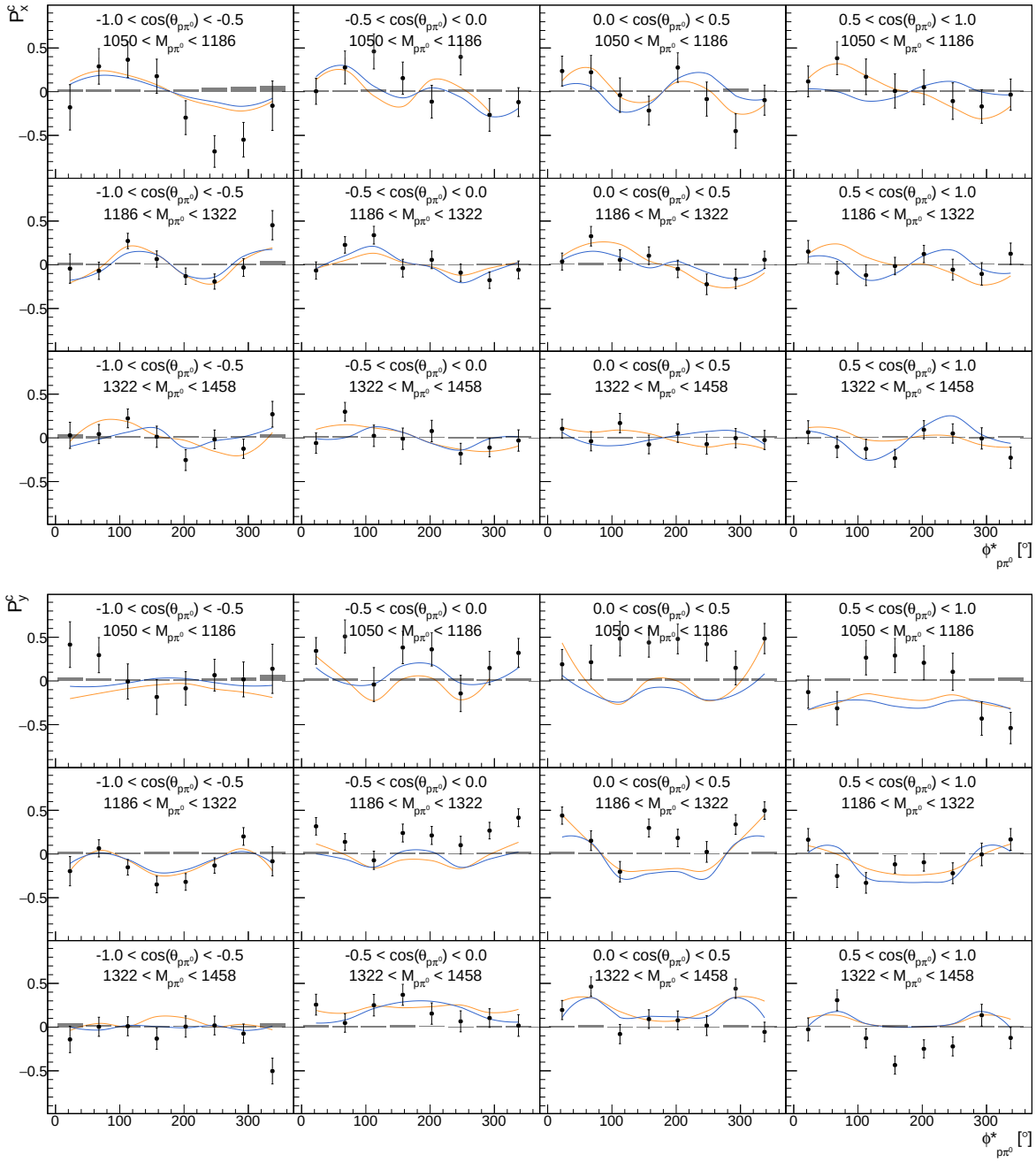

$E_\gamma = 1\,000 - 1\,300\,\mathrm{MeV}$

Figure H.6: Double polarization observables P_x^c, P_y^c for a specific energy range $E_\gamma = 1\,000 - 1\,300\,\mathrm{MeV}$ as function of $\left(\cos(\theta_{p\pi^0}), M_{p\pi^0}, \phi^*_{p\pi^0}\right)$. The **combined data of this work** is shown as well as the model predictions BnGa-2022 and BnGa-2014.

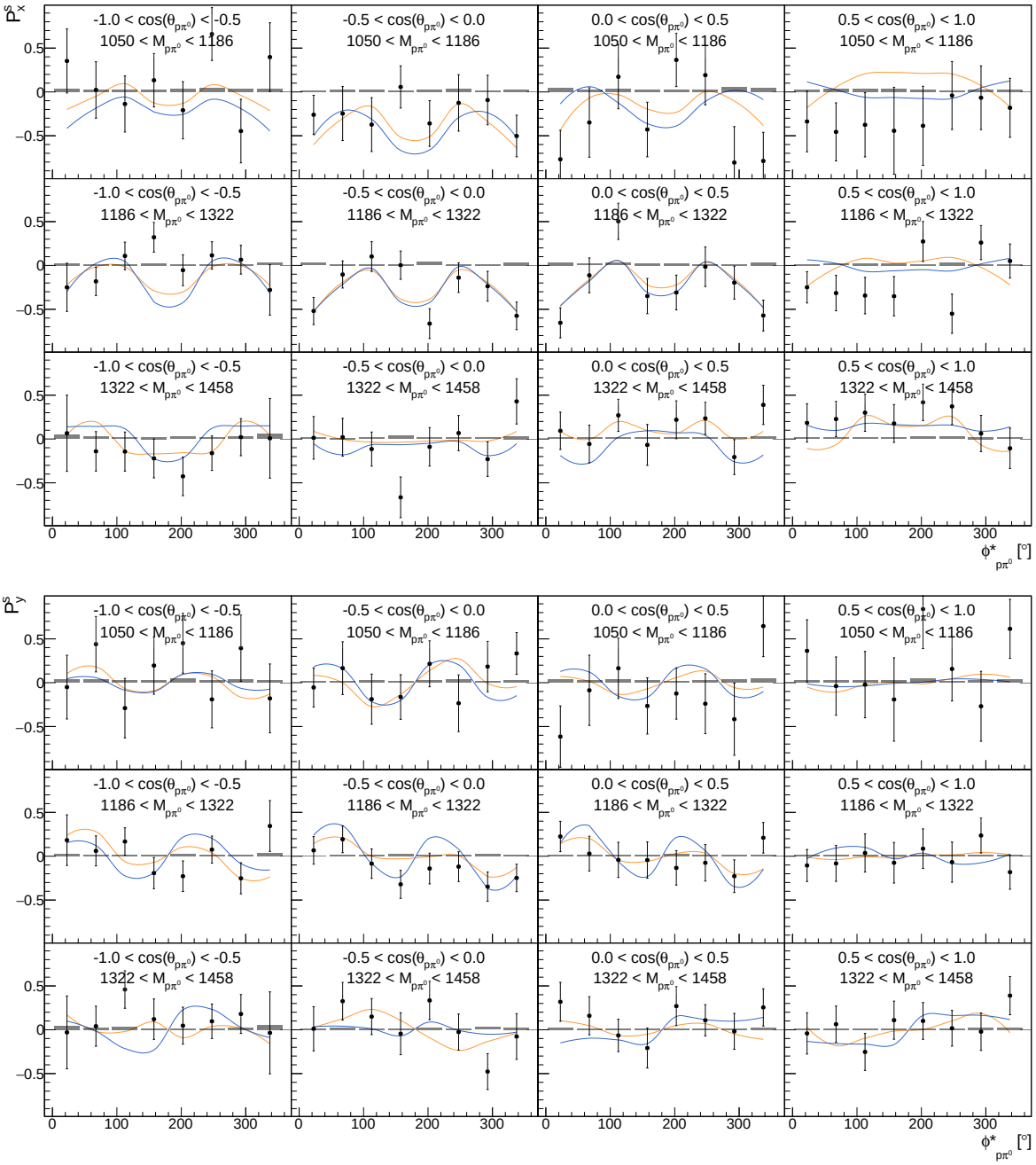

$E_\gamma = 1\,300 - 1\,600\,\text{MeV}$

Figure H.7: Double polarization observables P_x^s, P_y^s for a specific energy range $E_\gamma = 1\,300 - 1\,600\,\text{MeV}$ as function of $\left(\cos(\theta_{p\pi^0}), M_{p\pi^0}, \phi^*_{p\pi^0}\right)$. The **combined data of this work** is shown as well as the model predictions BnGa-2022 and BnGa-2014.

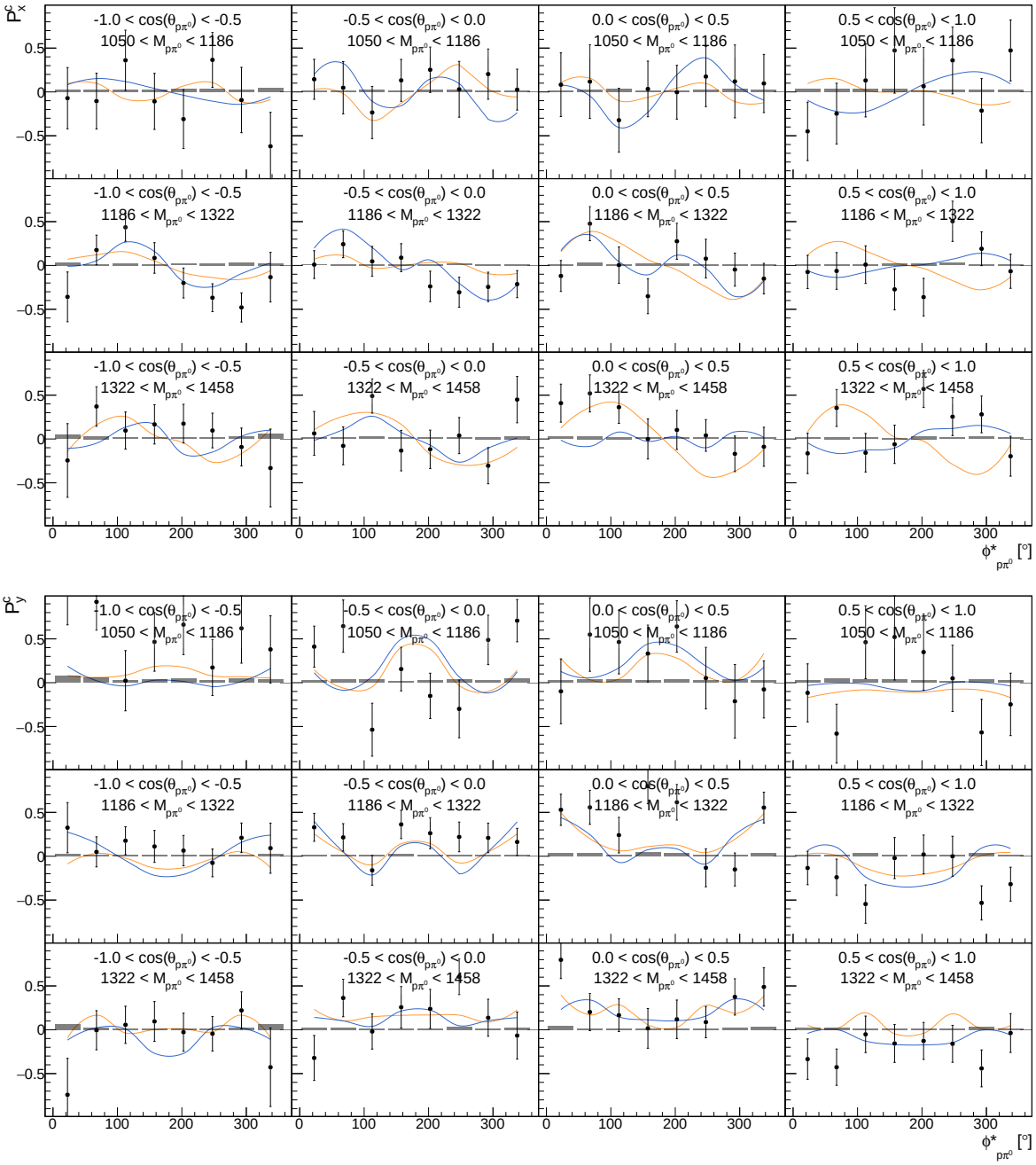

$E_\gamma = 1\,300 - 1\,600\,\mathrm{MeV}$

Figure H.8: Double polarization observables P_x^c, P_y^c for a specific energy range $E_\gamma = 1\,300 - 1\,600\,\mathrm{MeV}$ as function of $\left(\cos(\theta_{p\pi^0}), M_{p\pi^0}, \phi^*_{p\pi^0}\right)$. The **combined data of this work** is shown as well as the model predictions BnGa-2022 and BnGa-2014.

Bibliography

[1] S. L. Glashow, *Partial Symmetries of Weak Interactions*, Nucl. Phys. **22** (1961) 579.

[2] A. Salam, *Weak and Electromagnetic Interactions*, Conf. Proc. **C680519** (1968) 367.

[3] S. Weinberg, *A Model of Leptons*, Phys. Rev. Lett. **19** (1967) 1264.

[4] D. Griffiths, *Introduction to Elementary Particles*, 2nd Edition, Wiley-VCH, 2008.

[5] M. Gell-Mann, *The Eightfold Way: A Theory of strong interaction symmetry*, (1961).

[6] M. Gell-Mann, *Symmetries of Baryons and Mesons*, Phys. Rev. **125** (3 1962) 1067.

[7] S. Navas et al., *Review of particle physics*, Phys. Rev. D **110** (2024) 030001.

[8] G. Aad et al., *Observation of a new particle in the search for the Standard Model Higgs boson with the ATLAS detector at the LHC*, Physics Letters B **716** (2012) 1, ISSN: 0370-2693.

[9] B. Povh et al., *Teilchen und Kerne: Eine Einführung in die physikalischen Konzepte*, 8. Auflage, Springer-Verlag, 2009.

[10] R. Feynman, *Quantum Electrodynamics: A Lecture Note and Reprint Volume*, Frontiers in Physics : A Lecture Note and Reprint Series, W.A. Benjamin, 1962.

[11] D. J. Gross and F. Wilczek, *Ultraviolet Behavior of Non-Abelian Gauge Theories*, Phys. Rev. Lett. **30** (26 1973) 1343.

[12] H. D. Politzer, *Reliable Perturbative Results for Strong Interactions?* Phys. Rev. Lett. **30** (26 1973) 1346.

[13] K. G. Wilson, *Confinement of quarks*, Phys. Rev. D **10** (8 1974) 2445.

[14] P. Achard et al., *Measurement of the running of the electromagnetic coupling at large momentum-transfer at LEP*, Physics Letters B **623** (2005) 26, ISSN: 0370-2693.

[15] N. Isgur and G. Karl, *Hyperfine interactions in negative parity baryons*, Physics Letters B **72** (1977) 109, ISSN: 0370-2693.

[16] U. Löring, K. Kretzschmar, B. Metsch, and H. R. Petry, *Relativistic quark models of baryons with instantaneous forces*, The European Physical Journal A - Hadrons and Nuclei **10** (2001) 309, ISSN: 1434-601X.

[17] U. Löring, B. Metsch, and H. R. Petry, *The light-baryon spectrum in a relativistic quark model with instanton-induced quark forces*, The European Physical Journal A - Hadrons and Nuclei **10** (2001) 395, ISSN: 1434-601X.

[18] M. Ronniger and B. C. Metsch, *Effects of a spin-flavour-dependent interaction on the baryon mass spectrum*, The European Physical Journal A **47** (2011) 162, ISSN: 1434-601X.

[19] A. Thiel et al.,
Three-Body Nature of N^* and Δ^* Resonances from Sequential Decay Chains,
Phys. Rev. Lett. **114** (9 2015) 091803.

[20] T. Seifen et al., *Polarization observables in double neutral pion photoproduction*, (2022), arXiv: 2207.01981 [nucl-ex].

[21] V. Sokhoyan et al., *High-statistics study of the reaction $\gamma p \to p2\pi^0$*,
The European Physical Journal A **51** (2015) 95, ISSN: 1434-601X.

[22] R. P. Feynman, *Space-Time Approach to Non-Relativistic Quantum Mechanics*,
Rev. Mod. Phys. **20** (2 1948) 367.

[23] R. Sommer, *Scale setting in lattice QCD*, 2014, arXiv: 1401.3270 [hep-lat].

[24] R. G. Edwards, J. J. Dudek, D. G. Richards, and S. J. Wallace,
Excited state baryon spectroscopy from lattice QCD, Phys. Rev. D **84** (7 2011) 074508.

[25] S. Weinberg, *Phenomenological Lagrangians*,
Physica A: Statistical Mechanics and its Applications **96** (1979) 327, ISSN: 0378-4371.

[26] J. Gasser and H. Leutwyler, *Chiral perturbation theory to one loop*,
Annals of Physics **158** (1984) 142, ISSN: 0003-4916.

[27] C. D. Roberts and A. G. Williams,
Dyson-Schwinger equations and their application to hadronic physics,
Progress in Particle and Nuclear Physics **33** (1994) 477, ISSN: 0146-6410.

[28] G. Eichmann and C. S. Fischer,
Baryon Structure and Reactions from Dyson–Schwinger Equations,
Few-Body Systems **60** (2018) 2, ISSN: 1432-5411.

[29] H. Sanchis-Alepuz and R. Williams, *Recent developments in bound-state calculations using the Dyson –Schwinger and Bethe–Salpeter equations*,
Computer Physics Communications **232** (2018) 1.

[30] J. Maldacena, *The Large-N Limit of Superconformal Field Theories and Supergravity*,
International Journal of Theoretical Physics **38** (1999) 1113, ISSN: 1572-9575.

[31] O. Aharony, S. S. Gubser, J. Maldacena, H. Ooguri, and Y. Oz,
Large N field theories, string theory and gravity, Physics Reports **323** (2000) 183,
ISSN: 0370-1573.

[32] G. Höhler, *Pion Nucleon Scattering. Part 1 & 2*, ed. by H. Schopper,
accessed 2023-07-16.

[33] R. A. Arndt, W. J. Briscoe, I. I. Strakovsky, and R. L. Workman,
Extended partial-wave analysis of πN scattering data, Phys. Rev. C **74** (2006) 045205,
arXiv: nucl-th/0605082.

[34] A. Thiel et al.,
Well-established nucleon resonances revisited by double-polarization measurements,
Phys. Rev. Lett. **109** (2012) 102001, arXiv: 1207.2686 [nucl-ex].

[35] A. V. Anisovich et al.,
Properties of baryon resonances from a multichannel partial wave analysis,
Eur. Phys. J. A **48** (2012) 15, arXiv: 1112.4937 [hep-ph].

[36] A. Thiel et al.,
Double-polarization observable G in neutral-pion photoproduction off the proton,
The European Physical Journal A **53** (2017) 8.

[37] F. Afzal et al.,
Observation of the pη' Cusp in the New Precise Beam Asymmetry Σ Data for $\gamma p \to p\eta$,
Phys. Rev. Lett. **125** (2020) 152002, arXiv: 2009.06248 [nucl-ex].

[38] J. Müller et al., *New data on $\gamma p \to \eta p$ with polarized photons and protons and their implications for $N^* \to N\eta$ decays*, Physics Letters B **803** (2020) 135323,
ISSN: 0370-2693.

[39] J. Hartmann, *Double polarisation experiments in meson photoproduction*, EPJ Web Conf. **130** (2016) 01011, ed. by A. Wrońska, A. Magiera, C. Guaraldo, and H. Ströher, arXiv: 1609.06946 [nucl-ex].

[40] S. Garni et al., *Target and beam-target asymmetries for the $\gamma p \to \pi^0\pi^0 p$ reaction*, (2022), arXiv: 2207.14079 [hep-ex].

[41] F. Cividini et al., *Measurement of the helicity dependence for single π^0 photoproduction from the deuteron*, Eur. Phys. J. A **58** (2022) 113,
arXiv: 2203.00535 [nucl-ex].

[42] C. Mullen et al.,
Single π^0 production off neutrons bound in deuteron with linearly polarized photons,
Eur. Phys. J. A **57** (2021) 205, arXiv: 2103.08400 [nucl-ex].

[43] W. J. Briscoe et al., *Cross section for $\gamma n \to \pi^0 n$ at the Mainz A2 experiment*,
Phys. Rev. C **100** (2019) 065205, arXiv: 1908.02730 [nucl-ex].

[44] K. Chan et al., *Measurement of the helicity asymmetry $\mathbb{E}$ for the $\vec{\gamma}\vec{p} \to p\pi^0$ reaction in the resonance region*, 2023, arXiv: 2305.08616 [nucl-ex].

[45] N. Zachariou et al.,
Beam-spin asymmetry Σ for Σ^- hyperon photoproduction off the neutron,
Physics Letters B **827** (2022) 136985, ISSN: 0370-2693.

[46] A. Celentano et al.,
First measurement of direct photoproduction of the $a_2(1320)^0$ meson on the proton,
Phys. Rev. C **102** (3 2020) 032201.

[47] N. Zachariou et al.,
Beam–target helicity asymmetry E in $K^+\Sigma^-$ photoproduction on the neutron,
Physics Letters B **808** (2020) 135662, ISSN: 0370-2693.

[48] A. Thiel, F. Afzal, and Y. Wunderlich, *Light Baryon Spectroscopy*,
Progress in Particle and Nuclear Physics **125** (2022) 103949, ISSN: 0146-6410.

[49] W. Roberts and T. Oed,
Polarization observables for two-pion production off the nucleon,
Phys. Rev. C **71** (5 2005) 055201.

[50] P. Kroenert, Y. Wunderlich, F. Afzal, and A. Thiel,
Minimal complete sets for two pseudoscalar meson photoproduction,
Phys. Rev. C **103** (2021) 014607, arXiv: 2009.04356 [nucl-th].

[51] I. Aitchison, *The K-matrix formalism for overlapping resonances*,
Nuclear Physics A **189** (1972) 417, ISSN: 0375-9474.

[52] S. U. Chung et al., *Partial wave analysis in K matrix formalism*,
Annalen Phys. **4** (1995) 404.

[53] A. V. Anisovich et al.,
Properties of baryon resonances from a multichannel partial wave analysis,
The European Physical Journal A **48** (2012) 15, ISSN: 1434-601X.

[54] A. V. Anisovich, V. A. Nikonov, and A. V. Sarantsev,
Bonn-Gatchina Partial-Wave Analysis (BnGa), https://pwa.hiskp.uni-bonn.de.

[55] A. Sarantsev, "Properties of Baryons from Bonn-Gatchina Partial Wave Analysis,"
Proceedings of the 10th International Workshop on the Physics of Excited Nucleons (NSTAR2015),
eprint: https://journals.jps.jp/doi/pdf/10.7566/JPSCP.10.010005.

[56] L. Tiator, D. Drechsel, and S. Kamalov, *MAID Partial-Wave Analysis*,
https://maid.kph.uni-mainz.de.

[57] D. Drechsel, O. Hanstein, S. Kamalov, and L. Tiator, *A unitary isobar model for pion photo- and electroproduction on the proton up to 1 GeV*,
Nuclear Physics A **645** (1999) 145.

[58] D. Drechsel, S. S. Kamalov, and L. Tiator, *Unitary isobar model –MAID2007*,
The European Physical Journal A **34** (2007) 69, ISSN: 1434-601X.

[59] W. Briscoe, M. Doering, H. Haberzettl, I. Strakovsky, and R. Workman,
SAID Partial-Wave Analysis, https://gwdac.phys.gwu.edu.

[60] R. A. Arndt, I. I. Strakovsky, R. L. Workman, and M. M. Pavan,
Updated analysis of πN elastic scattering data to 2.1 GeV: The baryon spectrum,
Phys. Rev. C **52** (4 1995) 2120.

[61] R. A. Arndt, W. J. Briscoe, I. I. Strakovsky, and R. L. Workman,
Extended partial-wave analysis of πN scattering data,
Phys. Rev. C **74** (4 2006) 045205.

[62] M. Döring, J. Haidenbauer, and D. Rönchen,
Jülich-Bonn-Washington Partial-Wave Analysis,
https://collaborations.fz-juelich.de/ikp/meson-baryon/main.

[63] M. Döring, C. Hanhart, F. Huang, S. Krewald, and U.-G. Mei ßner,
Analytic properties of the scattering amplitude and resonances parameters in a meson exchange model, Nuclear Physics A **829** (2009) 170.

[64] M. Döring, C. Hanhart, F. Huang, S. Krewald, and U.-G. Mei ßner, *The role of the background in the extraction of resonance contributions from meson–baryon scattering*,
Physics Letters B **681** (2009) 26.

[65] A. V. Anisovich et al., *The impact of new polarization data from Bonn, Mainz and Jefferson Laboratory on $\gamma p \to \pi N$ multipoles*,
The European Physical Journal A **52** (2016) 284, ISSN: 1434-601X.

[66] J. Ahrens et al., *Intermediate resonance excitation in the $\gamma p \to p\pi_0\pi_0$ reaction*,
Physics Letters B **624** (2005) 173, ISSN: 0370-2693.

[67] M. Dieterle et al.,
Helicity-Dependent Cross Sections for the Photoproduction of π^0 Pairs from Nucleons,
Phys. Rev. Lett. **125** (6 2020) 062001.

[68] M. Dieterle et al., *Photoproduction of π^0-pairs off protons and off neutrons*,
The European Physical Journal A **51** (2015) 142, ISSN: 1434-601X.

[69] M. Oberle et al., *Measurement of the beam-helicity asymmetry $I^{\odot}$ in the photoproduction of π^0-pairs off the proton and off the neutron*,
Physics Letters B **721** (2013) 237.

[70] V. L. Kashevarov et al., *Experimental study of the $\gamma p \to \pi^0\pi^0 p$ reaction with the Crystal Ball/TAPS detector system at the Mainz Microtron*,
Physical Review C **85** (2012).

[71] F. Zehr et al., *Photoproduction of $\pi^0\pi^0$ - and $\pi^0\pi+$ -pairs off the proton from threshold to the second resonance region*,
The European Physical Journal A **48** (2012) 98, ISSN: 1434-601X.

[72] D. Krambrich et al.,
Beam-Helicity Asymmetries in Double-Pion Photoproduction off the Proton,
Physical Review Letters **103** (2009).

[73] U. Thoma et al., *N^* and Δ^* decays into $N\pi^0\pi^0$*, Physics Letters B **659** (2008) 87.

[74] M. Kotulla et al., *Double π^0 photoproduction off the proton at threshold*,
Physics Letters B **578** (2004) 63, ISSN: 0370-2693.

[75] Y. Assafiri et al., *Double π^0 Photoproduction on the Proton at GRAAL*,
Phys. Rev. Lett. **90** (22 2003) 222001.

[76] M. Wolf et al., *Photoproduction of neutral pion pairs from the proton*,
The European Physical Journal A - Hadrons and Nuclei **9** (2000) 5, ISSN: 1434-601X.

[77] F. Härter et al.,
Two neutral pion photoproduction off the proton between threshold and 800 MeV,
Physics Letters B **401** (1997) 229, ISSN: 0370-2693.

[78] A. Braghieri et al., *Total cross section measurement for the three double pion photoproduction channels on the proton*, Physics Letters B **363** (1995) 46,
ISSN: 0370-2693.

[79] M. Urban, *Design eines neuen Lichtpulsersystems sowie Aufbau und Inbetriebnahme der neuen APD Auslese für das Crystal-Barrel-Kalorimeter*,
PhD thesis: Rheinische Friedrich-Wilhelms-Universität Bonn, 2018.

[80] C. Honisch, *Design, Aufbau und Test einer neuen Ausleseelektronik für das Crystal-Barrel-Kalorimeter*,
PhD thesis: Rheinische Friedrich-Wilhelms-Universität Bonn, 2015.

[81] P. Klassen,
Entwicklung eines neuen Cluster-Finders für das Crystal-Barrel-Kalorimeter,
PhD thesis: Rheinische Friedrich-Wilhelms-Universität Bonn, 2025.

[82] J. Müllers, *An FPGA-based Sampling ADC for the Crystal Barrel Calorimeter*,
PhD thesis: Rheinische Friedrich-Wilhelms-Universität Bonn, 2019.

[83] *CBELSA/TAPS Experiment*, https://www1.cb.uni-bonn.de.

[84] W. Hillert, "The Bonn Electron Stretcher Accelerator ELSA: Past and future,"
vol. 28, 2006 139, ISBN: 978-3-540-36753-6.

[85] F. Frommberger, *Private communication*, 2024.

[86] D. Proft, *Optimierung des Beschleunigerbetriebs für Experimente zur Hadronen- und Detektorphysik an der Elektronen-Stretcher-Anlage ELSA*,
PhD thesis: Rheinische Friedrich-Wilhelms-Universität Bonn, 2019.

[87] W. Leo,
Techniques for Nuclear and Particle Physics Experiments: A How-to Approach.
Second Revised Edition, Springer-Verlag, 1904.

[88] H. Bethe and W. Heitler,
On the stopping of fast particles and on the creation of positive electrons,
Proc. R. Soc. Lond. A **146** (1934) 83.

[89] U. Timm, *Coherent Bremsstrahlung of Electrons in Crystals*,
Fortschritte der Physik **17** (1969) 765, eprint:
`https://onlinelibrary.wiley.com/doi/pdf/10.1002/prop.19690171202`.

[90] S. Kammer, *Strahlpolarimetrie am CBELSA/TAPS Experiment*,
PhD thesis: Rheinische Friedrich-Wilhelms-Universität Bonn, 2010.

[91] H. Eberhardt, *Bestimmung von Polarisationsobservablen in der π^0 und ω Photoproduktion am Proton mit dem CBELSA/TAPS-Experiment*,
PhD thesis: Rheinische Friedrich-Wilhelms-Universität Bonn, 2012.

[92] K. Livingston,
The Stonehenge technique. A method for aligning coherent bremsstrahlung radiators,
Nuclear Instruments and Methods in Physics Research Section A: Accelerators, Spectrometers, Detectors and Associated Equipment **603** (2009) 205.

[93] F. Natter, P. Grabmayr, T. Hehl, R. Owens, and S. Wunderlich, *Monte Carlo simulation and analytical calculation of coherent bremsstrahlung and its polarisation*,
Nuclear Instruments and Methods in Physics Research Section B: Beam Interactions with Materials and Atoms **211** (2003) 465, ISSN: 0168-583X.

[94] H. Olsen and L. C. Maximon, *Photon and Electron Polarization in High-Energy Bremsstrahlung and Pair Production with Screening*, Phys. Rev. **114** (3 1959) 887.

[95] H. Eberhardt, *Messung der Targetpolarisation und Detektorstudie für das Møllerpolarimeter des Crystal-Barrel-Aufbaus an ELSA.*,
Diploma thesis: Rheinische Friedrich-Wilhelms-Universität Bonn, 2006.

[96] M. Gottschall et al.,
Measurement of the helicity asymmetry E for the reaction $\gamma p \to \pi^0 p$,
The European Physical Journal A **57** (2021) 40, ISSN: 1434-601X.

[97] M. Grüner, *Private communication*, 2024.

[98] E. Aker et al., *The Crystal Barrel spectrometer at LEAR*,
Nucl. Instrum. Meth. **A321** (1992) 69.

[99] C. Wendel, *Design und Aufbau eines Szintillationsdetektors zur Identifizierung geladener Teilchen im Crystal-Barrel-Vorwärtsdetektor*,
PhD thesis: Rheinische Friedrich-Wilhelms-Universität Bonn, 2008.

[100] R. Novotny, *The BaF2 Photon Spectrometer TAPS*,
Nuclear Science, IEEE Transactions on **38** (1991).

[101] D. Kaiser,
Aufbau und Test des Gas-Cerenkov-Detektors für den Crystal-Barrel-Aufbau an ELSA,
Diploma thesis: Rheinische Friedrich-Wilhelms-Universität Bonn, 2007.

[102] J. Dielmann, *Entwicklung, Aufbau und Test eines Detektors zur Bestimmung des Photonenflusses an der Bonner Photonenmarkierungsanlage*,
Diploma thesis: Rheinische Friedrich-Wilhelms-Universität Bonn, 2008.

[103] J. Hartmann, *Zeitkalibrierung und Photonenflussbestimmung für das Crystal-Barrel-Experiment an ELSA*,
Diploma thesis: Rheinische Friedrich-Wilhelms-Universität Bonn, 2008.

[104] G. Suft et al.,
A scintillating fibre detector for the Crystal Barrel experiment at ELSA,
Nuclear Instruments and Methods in Physics Research Section A: Accelerators, Spectrometers, Detectors and Associated Equipment **538** (2005) 416, ISSN: 0168-9002.

[105] A. Fösel, *Entwicklung und Bau des Innendetektors für das Crystal Barrel Experiment an ELSA/Bonn*, PhD thesis: Friedrich-Alexander-Universität Erlangen, 2001.

[106] M. Grüner,
Modifikation und Test des Innendetektors für das Crystal Barrel Experiment.,
Diploma thesis: Rheinische Friedrich-Wilhelms-Universität Bonn, 2006.

[107] C. Hammann, *Aufbau eines Flüssigwasserstofftargets zur Durchführung von Kalibrationsmessungen am Crystal-Barrel Experiment an ELSA*,
Diploma thesis: Rheinische Friedrich-Wilhelms-Universität Bonn, 2009.

[108] C. Bradtke et al., *A new frozen-spin target for 4π particle detection*,
Nucl. Instrum. Meth. **A436** (1999) 430.

[109] H. Dutz, *Private communication*, 2024.

[110] G. Reicherz et al., *The Bonn polarized target NMR-system*,
Nuclear Instruments and Methods in Physics Research Section A: Accelerators, Spectrometers, Detectors and Associated Equipment **356** (1995) 74, Proceedings of the Seventh International Workshop on Polarized Target Materials and Techniques, ISSN: 0168-9002.

[111] J. Hoff., *Development of a MiniTAPS Trigger Board for the Crystal Barrel/TAPS Experiment at ELSA*,
Master's thesis: Rheinische Friedrich-Wilhelms-Universität Bonn, 2019.

[112] C. Schmidt et al., *ExPlORA*, `https://explora.cb.uni-bonn.de`.

[113] R. Brun and F. Rademakers, *ROOT - An Object Oriented Data Analysis Framework*, vol. A389, `http://root.cern.ch/`, 1997.

[114] F. Kalischewski, *Development of a new simulation for the CBELSA/TAPS experiment using Virtual Monte Carlo*,
Diploma thesis: Rheinische Friedrich-Wilhelms-Universität Bonn, 2011.

[115] R. Brun, F. Bruyant, M. Maire, A. C. McPherson, and P. Zanarini, *GEANT3*, (1987).

[116] S. Agostinelli et al., *Geant4—a simulation toolkit*,
Nuclear Instruments and Methods in Physics Research Section A: Accelerators, Spectrometers, Detectors and Associated Equipment **506** (2003) 250, ISSN: 0168-9002.

[117] P. Hoffmeister,
Das Datenerfassungssystem für das Crystal-Barrel/TAPS-Experiment an ELSA,
PhD thesis: Rheinische Friedrich-Wilhelms-Universität Bonn, 2019.

[118] D. Piontek,
Entwicklung eines Online-Monitors für das Crystal-Barrel-Experiment an ELSA,
Diploma thesis: Rheinische Friedrich-Wilhelms-Universität Bonn, 2007.

[119] *CBELSA/TAPS Rundatabase*, `https://rundatabase.cb.uni-bonn.de`.

[120] A. Thiel, *Aufbau einer computergesteuerten Experimentüberwachung für den Crystal-Barrel-Aufbau an ELSA.*,
Diploma thesis: Rheinische Friedrich-Wilhelms-Universität Bonn, 2006.

[121] J. Müllers, *Design and Test of a Slowcontrol for the APD Upgrade of the Crystal Barrel Calorimeter*,
Master's thesis: Rheinische Friedrich-Wilhelms-Universität Bonn, 2013.

[122] *CBELSA/TAPS Slowcontrol Webpage*, `https://slowcontrol.cb.uni-bonn.de`.

[123] *CBELSA/TAPS Analyse Database*,
`https://www.cb.uni-bonn.de/AnalyseDB-1.20`.

[124] *CBELSA/TAPS Calibration Website*, `https://www.cb.uni-bonn.de/calibration`.

[125] C. Honisch et al.,
The new APD-Based Readout of the Crystal Barrel Calorimeter – An Overview, 2023, arXiv: `2212.12364 [physics.ins-det]`.

[126] H. Van Pee, *Private communication*, 2024.

[127] M. Grodzicka et al.,
Characterization of CsI:Tl at a wide temperature range (-40 °C to +22 °C),
Nuclear Instruments and Methods in Physics Research A **707** (2013) 73.

[128] H. Kolanoski and N. Wermes, *Teilchendetektoren: Grundlagen und Anwendungen.*

[129] S.-G. Crystals, *Cesium Iodide Scintillation Material*, https://www.luxiumsolutions.com/files/886/download, 2020.

[130] J. Kataoka et al., *Recent progress of avalanche photodiodes in high-resolution X-rays and γ-rays detection*, Nuclear Instruments and Methods in Physics Research Section A: Accelerators, Spectrometers, Detectors and Associated Equipment **541** (2005) 398, Development and Application of Semiconductor Tracking Detectors, ISSN: 0168-9002.

[131] M. Groß, *Überwachung des APD-Verstärkungsfaktors der CsI(Tl)-Kristalle des Crystal Barrel Kalorimeters mittels Lichtpulsermessungen*, Bachelor's thesis: Rheinische Friedrich-Wilhelms-Universität Bonn, 2022.

[132] I. Keshelashvili, W. Erni, F. Müller, M. Steinacher, and B. Krusche, *Development of Low-Noise / Low-Power Preamplifier for the Readout of Inorganic Scintillators and their Mass Production Test System*, Journal of Physics: Conference Series **587** (2015) 012024.

[133] J. Bloemer, *Verbesserung der Online-Zeitauflösung für die neue APD-Auslese*, Bachelor's thesis: Rheinische Friedrich-Wilhelms-Universität Bonn, 2012.

[134] L. T. Corporation, *LT1715 - 4ns, 150MHz Dual Comparator with Independent Input/Output Supplies*, https://www.analog.com/media/en/technical-documentation/data-sheets/1715fa.pdf, 2020.

[135] Wikipedia contributors, *Constant fraction discriminator*, [Online; accessed 15-March-2025], 2025.

[136] H. Fischer et al., *Implementation of the dead time free F1 TDC in the COMPASS detector readout*, Nucl. Instrum. Meth. A **461** (2001) 507, ed. by G. Batignani, F. Cervelli, G. Chiarelli, and A. Scribano, arXiv: hep-ex/0010065.

[137] O. Freyermuth, *Studies of ω Photoproduction off Proton at the BGO-OD Experiment*, PhD thesis: PhD thesis: Rheinische Friedrich-Wilhelms-Universität Bonn, 2017.

[138] J. Bieling, *jTDC*, https://github.com/jobisoft/jTDC, 2015-2016.

[139] K. Esslinger, *CB CsI-Shaper*, Physik-Institut der Universität Zürich, 1989.

[140] LeCroy, *Datasheet 1885F ADC*, https://teledynelecroy.com/lrs/dsheets/1885f.htm.

[141] J. Macht, *Sampling-ADC based Pile-Up Recovery and Digital Signal Processing in the CBELSA/TAPS-Experiment*, PhD thesis in preparation: Rheinische Friedrich-Wilhelms-Universität Bonn, 2025.

[142] B. Otto, *Optimisation of the Sampling-ADC Readout of the Crystal Barrel Calorimeter*, Master's thesis: Rheinische Friedrich-Wilhelms-Universität Bonn, 2022.

[143] S. Ciupka, *Test and calibration of a module for the new Energy-sum trigger for the Crystal Barrel Calorimeter at ELSA*, Master's thesis: Rheinische Friedrich-Wilhelms-Universität Bonn, 2018.

[144] S. Ciupka,
Determination of the Polarisation Observables T,P and H in the reaction $\gamma p \to p\pi^0$,
PhD thesis in preparation: Rheinische Friedrich-Wilhelms-Universität Bonn, 2025.

[145] N. Stausberg, *Time Calibration and Target Asymmetry Determination for Single Meson-Photoproduction at the CBELSA/TAPS Experiment*,
Master's thesis: Rheinische Friedrich-Wilhelms-Universität Bonn, 2019.

[146] J. H. Müller, *Bestimmung der Doppelpolarisationsobservablen E in der Reaktion $\gamma p \to p\eta$ am CBELSA/TAPS-Experiment in Bonn*, PhD thesis, 2019.

[147] J. Junkersfeld,
Kalibration des Crystal-Barrel-ELSA Detektors mit Hilfe der Reaktion $\gamma p \to p\pi^0$,
Diploma thesis: Rheinische Friedrich-Wilhelms-Universität Bonn, 2000.

[148] N. Davis,
Das neue Crystal Barrel Lichtpulser-System: Untersuchung und Optimierung verschiedener Methoden zur Kalibration des High-Range-Bereiches der ADCs,
Bachelor's thesis: Rheinische Friedrich-Wilhelms-Universität Bonn, 2019.

[149] H. Ikeda et al., *A detailed test of the CsI(Tl) calorimeter for BELLE with photon beams of energy between 20 MeV and 5.4 GeV*,
Nuclear Instruments and Methods in Physics Research Section A: Accelerators, Spectrometers, Detectors and Associated Equipment **441** (2000) 401, ISSN: 0168-9002.

[150] B. Aubert et al.,
Measurement of branching fractions and CP and isospin asymmetries for $B \to K^*\gamma$,
Phys. Rev. D **70** (11 2004) 112006.

[151] J. Drinhaus, *Aufbau und Test einer 3x3-CsI(Tl)-Kristallmatrix am getaggten Photonenstrahl an ELSA*,
Diploma thesis: Rheinische Friedrich-Wilhelms-Universität Bonn, 2012.

[152] B. B. Rossi, *High-energy particles*, Prentice-Hall physics series,
New York, NY: Prentice-Hall, 1952.

[153] T. Seifen, *Verbesserung der Rekonstruktion und Entwicklung eines First-Level-Triggerschemas für das Crystal-Barrel-Kalorimeter*,
Diploma thesis: Rheinische Friedrich-Wilhelms-Universität Bonn, 2009.

[154] N. Stausberg, *Entwicklung einer Mesonenmassenkorrekturfunction für das Crystal-Barrel-Kalorimeter*,
Bachelor's thesis: Rheinische Friedrich-Wilhelms-Universität Bonn, 2016.

[155] T. Dahlke, *Bestimmung einer winkelabhängigen Energiekorrekturfunktion für das TAPS-Kalorimeter des Crystal-Barrel/TAPS-Experimentes an ELSA*,
Diploma thesis: Rheinische Friedrich-Wilhelms-Universität Bonn, 2008.

[156] R. Novotny, *Performance of the BaF2-calorimeter TAPS*,
Nuclear Physics B - Proceedings Supplements **61** (1998) 137, Proceedings of the Fifth International Conference on Advanced Technology and Particle Physics,
ISSN: 0920-5632.

[157] D.-M. Piontek and M. Grüner, *Hit-Reconstruction in ChaPI*, CB-TR16-Note (2008).

[158] J. Hartmann, *Measurement of Double Polarization Observables in the Reactions $\gamma p \to p\pi^0$ and $\gamma p \to p\eta$ with the Crystal Barrel/TAPS Experiment at ELSA*, PhD thesis: Rheinische Friedrich-Wilhelms-Universität Bonn, 2017.

[159] T. Seifen, *Messung von Polarisationsobservablen in der $2\pi^0$-Photoproduktion mit dem Crystal-Barrel/TAPS-Experiment*, PhD thesis: Rheinische Friedrich-Wilhelms-Universität Bonn, 2020.

[160] K. Fornet-Ponse, *Die Photonenmarkierungsanlage für das Crystal-Barrel/TAPS-Experiment an ELSA*, PhD thesis: Rheinische Friedrich-Wilhelms-Universität Bonn, 2009.

[161] M. Grüner, *Private communication*, 2023.

[162] R. Barlow, *Statistics: A Guide to the Use of Statistical Methods in the Physical Science*, John Wiley & Sons Ltd., 1993.

[163] S. Brandt, *Statistical and computational methods in data analysis.*

[164] P. Mahlberg, *Bestimmung der Strahlasymmetrien I_c und I_s für die Reaktion $\gamma p \to p\pi^0\pi^0$ mit dem CBELSA/TAPS-Experiment an ELSA*, PhD thesis in preparation: Rheinische Friedrich-Wilhelms-Universität Bonn, 2025.

[165] S. Das, *A simple alternative to the Crystal Ball function*, (2016), arXiv: `1603.08591 [hep-ex]`.

[166] M. Williams, M. Bellis, and C. A. Meyer, *Multivariate side-band subtraction using probabilistic event weights*, Journal of Instrumentation **4** (2009) P10003.

[167] I. Barker, A. Donnachie, and J. Storrow, *Complete experiments in pseudoscalar photoproduction*, Nuclear Physics B **95** (1975) 347, ISSN: 0550-3213.

[168] C. Rohlof and H. Dutz, *Effective densities and polarizations of the targets for the GDH-experiments at MAMI and ELSA*, Nuclear Instruments and Methods in Physics Research Section A: Accelerators, Spectrometers, Detectors and Associated Equipment **526** (2004) 126, Proceedings of the ninth International Workshop on Polarized Solid Targets and Techniques, ISSN: 0168-9002.

[169] N. I. of Standards and Technology, `https://www.nist.gov`.

[170] S. Ciupka, *Private communication*, 2024.

[171] M. Gottschall, *Bestimmung der Doppelpolarisationsobservablen E fuer die Reaktion $\gamma p \to p\pi^0$ am CBELSA/TAPS-Experiment*, PhD thesis: Rheinische Friedrich-Wilhelms-Universität Bonn, 2013.

[172] F. James, *Statistical Methods in Experimental Physics*, 2nd Edition, World Scientific Publishing, 2006.

[173] F. N. Afzal, *Measurement of the beam and helicity asymmetries in the reaction $\gamma p \to p\pi^0$ and $\gamma p \to p\eta$*, PhD thesis: Rheinische Friedrich-Wilhelms-Universität Bonn, 2019.

[174] J. Kreit, *Linear Polarisation per Spill*,
AG Thiel at University of Bonn (2023), In preparation.

List of Figures

List of Tables

Acknowledgements

This thesis would not have been possible without the support and contributions of many people, some of whom I would like to thank here.

I would like to thank Prof. Dr. Ulrike Thoma for giving me the opportunity to be part of her research group. I am grateful that I had the chance to write not only my bachelor's and master's theses in her group, but now also my dissertation.

I would also like to thank Prof. Dr. Reinhard Beck, PD Dr. Bastian Kubis, and Prof. Dr. Reinhard Klein for agreeing to be part of my thesis committee.

Furthermore, I would like to thank all members of the CBELSA/TAPS collaboration and the other research groups at the HISKP in Bonn. Special thanks go to Philipp Mahlberg and Tobias Seifen for their support and many discussions. I am also grateful to Jan Hartmann for his huge and continuous efforts to improve both the data acquisition and the data analysis. I would also like to thank Dr. Harald Van Pee and Ben Salisbury for their patience with my demanding use of the cluster.

Thank you very much to everyone who made my time at the University of Bonn an unforgettable experience.

Finally, I would like to thank my family and my wife Lina, who supported me throughout the entire journey.